FAA-RD-79-21

Project Report
ATC-88
Volume I

MLS Multipath Studies, Phase 3 Volume I: Overview and Propagation Model Validation/Refinement Studies

J. E. Evans
S. J. Dolinar
D. F. Sun
D. A. Shnidman

25 April 1979

Lincoln Laboratory
MASSACHUSETTS INSTITUTE OF TECHNOLOGY
LEXINGTON, MASSACHUSETTS

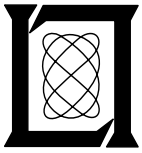

Prepared for the Federal Aviation Administration,
Washington, D.C. 20591

This document is available to the public through
the National Technical Information Service,
Springfield, VA 22161

1. Report No.	2. Government Accession No.	3. Recipient's Catalog No.
FAA-RD-79-21		

4. Title and Subtitle	5. Report Date
MLS Multipath Studies, Phase 3. Final Report, Volume I: Overview and Propagation Model Validation/Refinement Studies	25 April 1979
	6. Performing Organization Code

7. Author(s)	8. Performing Organization Report No.
J.E. Evans S.J. Dolinar D.F. Sun D.A. Shnidman	ATC-88, Volume I

9. Performing Organization Name and Address	10. Work Unit No. (TRAIS)
Massachusetts Institute of Technology Lincoln Laboratory P.O. Box 73 Lexington, MA 02173	11. Contract or Grant No. DOT-FA74-WAI-461
	13. Type of Report and Period Covered
12. Sponsoring Agency Name and Address Department of Transportation Federal Aviation Administration Systems Research and Development Service Washington, DC 20591	Project Report
	14. Sponsoring Agency Code

15. Supplementary Notes

The work reported in this document was performed at Lincoln Laboratory, a center for research operated by Massachusetts Institute of Technology under Air Force Contract F19628-78-C-0002.

16. Abstract

This report presents work done during phase 3 of the US national Microwave Landing System (MLS) program toward developing a computer simulation model of MLS multipath effects, the experimental validation of the model, and the application of the model to investigate multipath performance of ICAO proposals for the new approach and landing guidance system.

This first volume of the report presents an overview of the overall simulation results as well as a description of the refined mathematical models and validation of the propagation portion of the simulation. Specific propagation topics include:

1) preliminary results for validation of models for reflections from rough and/or rising terrain based on L-band field data.
2) validation of the models for building reflections based on field measurements at a number of operational airports.
3) validation and refinement of the models for angle guidance system shadowing by obstacles such as buildings and other objects.

17. Key Words	18. Distribution Statement
Microwave Landing System (MLS) Multipath Diffraction Shadowing Time Reference Scanning Beam (TRSB)	Document is available to the public through the National Technical Information Service, Springfield, Virginia 22151.

19. Security Classif. (of this report)	20. Security Classif. (of this page)	21. No. of Pages	
Unclassified	Unclassified	388	

ABSTRACT

This report presents work done during phase 3 of the US national Microwave Landing System (MLS) program toward developing a computer simulation model of MLS multipath effects, the experimental validation of the model, and the application of the model to investigate multipath performance of ICAO proposals for the new approach and landing guidance system. The model was developed by separately considering the characteristics of the four basic elements affecting system operation in a multipath environment, i.e., airport, flight profile, propagation and system elements. This modeling approach permits the examination of the effect on system performance of individual multipath performance factors such as: (a) reflections from terrain, aircraft, buildings with differing orientations, (b) shadowing by aircraft, buildings and convex runways (c) aircraft flight profiles and approach speeds, and (d) system design features to combat multipath.

This first volume of the report presents an overview of the overall simulation as well as a description of the refined mathematical models and validation of the propagation portion of the simulation. The overview discusses the background and motivation for this multiyear study and outlines the topics presented in the remainder of the report. Also contained in the overview is a cross reference between various MLS multipath performance topics and the Lincoln Laboratory project reports issued to date.

The remainder of this volume is concerned with validation and refinement of the propagation and flight profile models described in earlier Lincoln

reports. Specific topics include:

(1) preliminary results for validation of models for reflections from rough and/or rising terrain based on L band field data obtained at L.G. Hanscom Airport (Bedford, MA) and Ft. Devens, MA.

(2) validation of the models for building reflections based on elevation field measurements at JFK airport and azimuth field measurements at Miami International (Florida), Lambert International (St. Louis), Tulsa International (Oklahoma), Wright Patterson AFB (Ohio), and Sydney International (Australia). The azimuth field data analysis focused in particular on assessing the extent to which the reflected signals were spatially phase coherent as assumed in the propagation model.

(3) validation and refinement of the models for angle guidance system shadowing by obstacles such as buildings and other objects. The ray theory representation used previously has now been extended to handle a wider range of shadowing geometries (including the case of obstacles in the ground antenna near field).

(4) refinement of the flight profile model to fit a smooth curved path between pairs of non-connected linear segments.

The remaining volumes in this report will discuss other salient features of the Lincoln phase 3 studies:

volume 2 - presents the development and validation data for the models of the three MLS techniques (DLS, DMLS, and TRSB) assessed by ICAO.

volume 3 - results of comparative system studies including various scenarios and studies of specific issues which arose out of the scenarios.

volume 4 - users manual for the propagation and TRSB model computer programs.

ACKNOWLEDGMENTS

Many people from Lincoln Laboratory have contributed significantly to the results described in this volume. R. Sandholm of Lincoln developed much of the instrumentation used in the azimuth and the ground reflection multipath measurements.

P. Lanzilotti, J. Reid, A. Gregory, and J. Kalil assisted in the ground reflection measurement equipment development and maintenance, experiment execution, and data processing. P. Drouilhet provided substantial encouragement for the azimuth multipath measurements as well as acting as chief pilot. R. Moffatt assisted in the data analysis of the azimuth multipath experiments as well as developing much of the software for the refined shadowing models.

D. Vickers of the Federal Aviation Administration assisted in obtaining and analyzing much of the TRSB field data used in our studies. R. Cleary of the National Avionic Facility Experimental Center provided much of the equipment used in the azimuth multipath measurement program as well as the measurement vans and support personnel for the elevation multipath measurements.

Several Australian organizations made significant contributions to our work. G. Boyd and J. Brand of the Australian Department of Transport provided airport maps and field data for Sydney International Airport. Dr. G. Lucas and B. Oreb of the University of Sydney graciously shared much of their scale model range data (published and unpublished) on reflection and shadowing phenomena.

Finally, special mention must be made of the group 44 secretaries - Karen Roberts, Nancy Blue, Ida Johnston, and Diane Young - for their work on this report and the many earlier versions which were a part of US data submitted to ICAO.

TABLE OF CONTENTS

LIST OF TABLES

LIST OF ILLUSTRATIONS

List of Illustrations (Cont'd)

List of Illustrations (Cont'd)

List of Illustrations (Cont'd)

List of Illustrations (Cont'd)

List of Illustrations (Cont'd)

List of Illustrations (Cont'd)

List of Illustrations (Cont'd)

List of Illustrations (Cont'd)

List of Illustrations (Cont'd)

LIST OF ILLUSTRATIONS (Cont'd)

LIST OF ILLUSTRATIONS (Cont'd)

List of Illustrations (Cont'd)

I. INTRODUCTION AND OVERVIEW

This report represents the final report on a several year effort to develop and validate a comprehensive simulation of multipath effects due to shadowing and/or reflections on the microwave landing system (MLS). Our objective in this section is to describe the background and motivation for this effort as well as outlining the other sections of the report.

A. Background

The U.S. national MLS program had as its goal the development of a common civil/military system suitable for adoption as an international standard. The extensive considerations by the RTCA SC-117 [1] led to the selection of two air-derived concepts (scanning beam and doppler scan) which were actively developed in a joint DOT/DOD/NASA program culminating in the choice of the time reference scanning beam (TRSB) concept in 1974 [2, 8]. In addition, several alternative systems (both air-derived and ground-derived) were developed in other countries for consideration under International Civil Aviation Organization (ICAO) [4] and/or North Atlantic Treaty Organization (NATO) [5] programs.

The use of radio beams to provide information for instrument landings is subject to errors generated by reflection and/or shadowing of the radio signals by terrain, buildings and large nearby aircraft. Fig. 1-1 illustrates the phenomena of concern. The term "multipath" is used to describe the reflection/shadowing phenomena because several possible paths exist for signals to travel between the transmitter and receiver, as opposed to the single (direct) path assumed in initial system design.

Resistance to coherent interference (i.e., multipath) is a key technical issue in assessing both the relative and absolute capabilities of the various systems. Results of analyses in the national MLS program [11 - 13] as well as the results of a comprehensive study conducted for the NATO Industrial Advisory Group (NIAG) [75] suggested that large aircraft and/or vertical structures near the approach zone would be the major sources of error. The

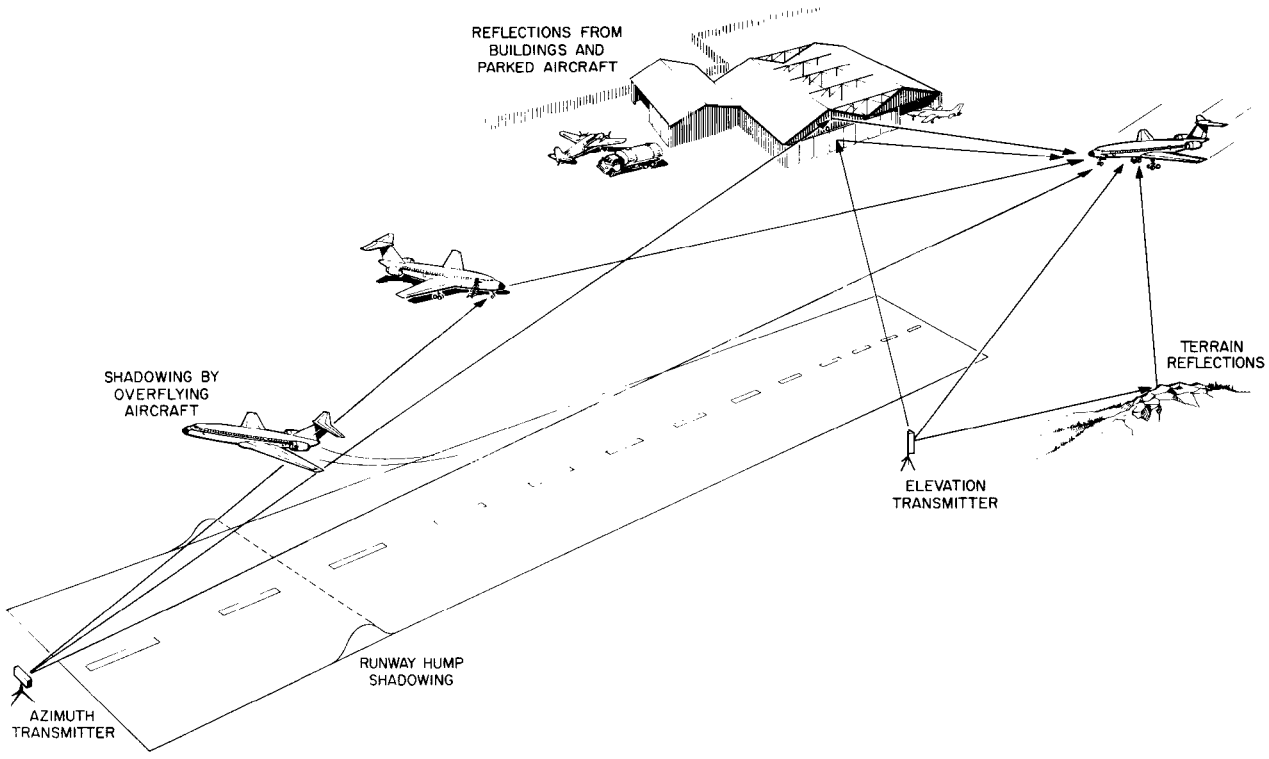

Fig.1-1. MLS multipath phenomena.

continuing construction of buildings in the vicinity of the approach and landing zone and the increasing use of wide body aircraft (both potentially significant multipath sources) emphasize the importance of multipath effects to the design and selection of any future landing guidance system.

Thus, to aid in the system selection, optimization, and standardization process, there was need for realistic multipath models of representative real-world airport environments. These multipath models could then be used in simulations, which include the landing system characteristics, to assess the potential strengths and weaknesses of each system when subjected to various levels of multipath interference.

1. Why Computer Simulation?

It is generally agreed that comparative multipath performance data can be obtained only by subjecting candidate systems to identical conditions. Obtaining such data through field tests is difficult when one considers the practical problems of providing instrumentation on the ground and in the aircraft sufficiently accurate to delineate system performance differences throughout a variety of flight profiles and airport environments.

For example, in both the U.S. [8] and the ICAO All Weather Operations Panel (AWOP) assessments [9] multipath test data was not useful for quantitative comparative purposes. Airport geometries differed, instrumentation was deficient, and the system hardware tested was not in all cases identical with that proposed.

There are several factors which make computer simulation a desirable way to compare system multipath performance:

(a) The techniques can be conveniently compared under a variety of identical airport and flight path conditions.

(b) It reduces the substantial expense and precision instrumentation associated with quantitatively meaningful field tests.

(c) It permits the investigation of the system sensitivity to multipath parameters.

(d) It enables one to compare performance for anticipated airport environments (e.g., with more and/or larger buildings than now exist).

In addition, it is even difficult to compare directly the results of field tests made at a given airport runway if important aspects of the multipath environment (e.g., terrain conditions, hangar door configurations, etc.) have changed during the time elapsed between the tests of the various systems.

Most importantly, MLS will be operational well into the 21st century; therefore, one must look into both present and anticipated airport situations. Because of the rapid construction in the vicinity of many of our airports, flight tests today will not accurately depict performance for the environment twenty years hence.

Computer simulation is the most practical technique available to perform the performance comparison. Models can be used to examine the sensitivity of the system to important airport features which may not yet be present at today's airports and field test sites. This in turn leads to a much better understanding of the strengths and deficiencies of the various systems when applied to the more complicated airport environment which could exist during the lifetime of MLS.

2. Requirements for the Study

The ultimate goal of this effort was to assess the effects of representative multipath environments on the performance of various candidate MLS. To accomplish this goal, it was necessary* to accomplish the following:

a. Scattering Multipath Models. Develop scattering multipath models intended for quantitative assessment of specific MLS systems and techniques. These models would be applicable to representative airports and should include only those objects/structures/terrain features which cause significant effects on the performance of a MLS equipped aircraft executing typical approach and landing profiles. The development of these models was to be primarily an analytical effort, although selected field measurements as a part of the MLS test program might be required for validation.

*The following paragraphs are drawn from the initial statement of work for the MLS studies program

The development of these models was accomplished in an iterative fashion, with the initial first order model being refined through selected detailed analytical studies and available experimental data from the MLS and other test programs. Two phases were identified:

1. The development of the first order models was based on the existing models derived from the MLS contractors, the NIAG study and earlier USAF studies. These models permitted an early preliminary assessment of multipath sensitivity for certain of the MLS candidates and served as the basis for more accurate (second order) simulation models.

2. Second order scattering models were to be developed which make better use of the MLS experimental data and incorporate a detailed representation of significant environmental features (i.e.,those features for which the landing systems were found to be particularly sensitive).

   Continuing refinement was to be made in the scattering models as the experimental data from other countries and from the MLS prototype development phase became available. These results were to provide validated models for implementation issues such as assessing the MLS "critical" and "sensitive" areas at specific airports.

b. MLS Multipath Performance Simulations. Investigate the multipath sensitivity of the MLS candidates by computer simulation. These simulations used the scattering models together with mathematical models of the various landing systems to dynamically simulate guidance performance. The system elements (signal formats, ground and airborne antenna locations and characteristics, and receiver signal processing routines) important for studies of multipath error effect were included in these simulations. These simulations were developed in an iterative fashion as follows:

1. An initial assessment was accomplished early in the program to serve as background material for suggesting critical experimental multipath tests for the various MLS systems and to identify key areas where additional systems description is required. To support this assessment, first order simulations for each MLS submitted as a candidate system to the ICAO were developed based on currently available information.

2. Second order simulations of those systems specified by the FAA were developed. Refinement of candidate system descriptions was accomplished as more information (including experimental data) became available. A more detailed assessment of the MLS systems designated by the FAA was conducted using the refined simulations. These provided an aid for assessing experimental system test results as well as suggesting additional tests for the various systems.

c. Users Manual.

So that the information gained from these multipath studies could be conveniently utilized by the FAA in MLS site and equipment selection, the computer programs developed were to be in a common scientific computer language and a users manual provided.

d. Indepth Studies of Important Issues.

The airport models utilized in the simulation studies necessarily were limited to a number of representative environments. To permit a deeper understanding of some of the multipath performance factors and differences which emerged during the course of the simulations, a number of analytical studies were carried out to better delineate the possible performance over the full range of expected MLS environments. These studies included the following issues:

1. Motion averaging as a means of reducing inbeam errors.

2. Static and dynamic multipath effects on the Doppler reference antenna.

3. Polarization.

4. Sensitive/critical areas studies.

5. Shadowing.

6. Receiver acquisition/validation algorithms.

B. OVERVIEW OF REPORT

In this section, we wish to briefly summarize the work accomplished over the past few years and to indicate the various Lincoln Laboratory ATC project reports in which the various issues have been reported. The preceding section described the major requirements of the study. Table 1-1 shows where each of these items has been reported. Since much of the work prior to spring 1976 was presented in a series of generally available reports, in this report we have attempted to:

(1) describe the previously reported work in fairly general terms

and (2) present the new results (many of which appeared in not generally available working papers) in much greater detail.

Thus, the remainder of this section will be an overview of the MLS multipath study which indicates where more detailed descriptions are available.

1. Computer Modeling of MLS Multipath Performance

The purpose of this section is to describe the procedure used to develop and validate the computer models. The general procedure used to estimate system performance with computer simulation is to separate the model into its basic elements and then to validate the model based on laboratory and field test results. This approach can be developed with various degrees of sophistication depending on the intended use of the model. For the purposes of a

TABLE 1-1

LINCOLN LABORATORY REPORTS ON PRINCIPAL TOPICS FOR MLS MULTIPATH STUDIES

	First Order Model and its Validation	Refined Model and its Validation
Scattering Model	ATC-55, ATC-63, ATC-68	ATC-68, volumes I and II of this report
Systems Models		
TRSB	ATC-63	Volume II of this report
DMLS	ATC-63	Volume II of this report
DLS	Reported in informal working papers	Volume II of this report
Multipath Performance Simulations		
AWOP "Standard" Scenarios	Informal working papers	Volume III of this report
Other AWOP Scenarios	Informal working papers	Volume III of this report
Validation Scenarios	Informal working papers	Volume III of this report
Other Scenarios	ATC-63	Volume III of this report
Users Manual	Reported in informal working papers	Volume IV of this report

Multipath Issues	Where Reported
Motion averaging	ATC-63
Polarization	ATC-58, ATC-63
TRSB sensitive/critical areas	ATC-63
Shadowing	Volumes I and III of this report
Effects unique to Doppler reference antenna signal	ATC-63, Volume III of this report
Receiver acquisition/validation algorithms	Volume III of this report

comparative assessment, several simplifications can be employed in the computation of the reflected signal components and the airport model. However, if one desired to predict performance on a specific flight at a specific airport, more detail must be included in the model concerning the installation coordinates, the aircraft profile, the significant features and precise locations of all reflecting or shadowing surfaces at an airport, etc.

In this section the elements of an MLS comparative simulation are defined followed by a discussion of the propagation and system models and their respective validation.

a. The Elements of an MLS Comparative Multipath Simulation

An MLS multipath simulation predicts the multipath error for an MLS technique on a given approach path to a specified airport environment. Four different elements are involved in the simulation process.

1. An airport model - the locations and composition of reflecting and shadowing obstacles, terrain features, and MLS antenna locations.
2. A flight profile model - the path flown by an aircraft.
3. A propagation model - this determines the radio signals at the receiver for each point along the flight path, taking into account the various multipath reflections.
4. A system model - this computes the receiver error caused by multipath for the specified equipment antenna patterns, scan format, and receiver processing algorithm.

Fig. 1-2 shows the relationship of these various elements to the outputs from the simulation. The airport and flight profile models consist of data specified by the user for any particular situation being investigated. The degree of approximation to an actual airport environment depends very heavily on the objectives of the particular simulation.

For example, in a comparative analysis, reflecting surfaces of a hangar might be represented by the simulation by a single flat plate. However, if it were necessary to predict system performance at an actual airport many plates (e.g. 40) of different shapes and sizes might be necessary to simulate the dominant reflecting surfaces.

The modeling process was relatively straightforward and has utilized a substantial data base which includes a significant amount of operational airport data. Much of the validation has been accomplished by separately validating the individual parts of the overall simulation rather than attempting to validate simultaneously all the various models by comparison of computer results with flight tests at an operational airport.

This segregation of individual components was deemed necessary for several reasons:

1. TRSB multipath errors in today's airports will be small, masked by the instrumentation accuracy, and hard to isolate into individual components.
2. Very precise tracking facilities are required for quantitative validation of the model with flight test data - these are often not available at operational airports.
3. Individual components of the total multipath error phenomena must be fully understood in order to predict future performance.

and

4. Very powerful tools such as specialized multipath measurement equipment and receiver bench simulators have been developed for experimental validation of the individual components.

However, in some cases, end-to-end validation by comparison with flight tests has been accomplished and several examples will be described in volume II.

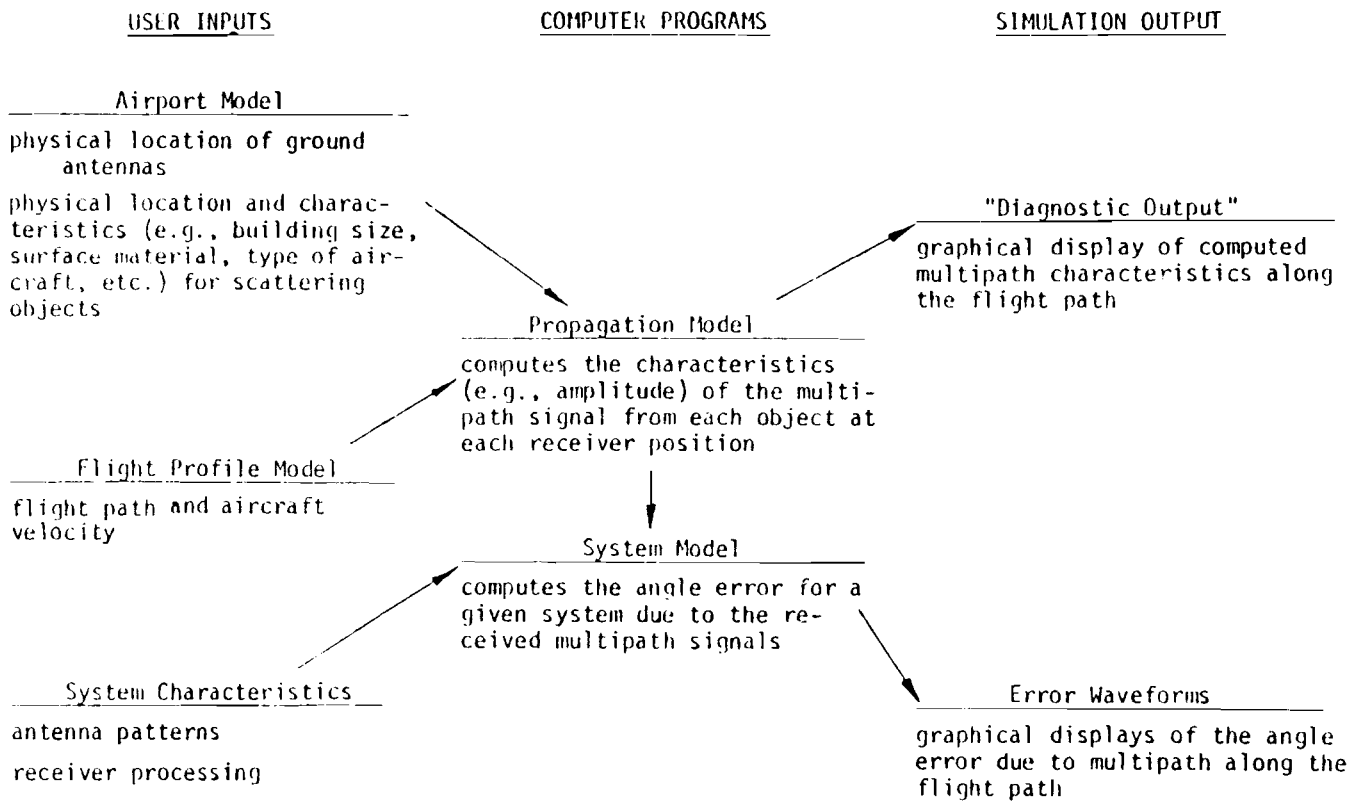

Fig.1-2. Relationship of the various elements in Lincoln Laboratory MLS multipath simulation.

b. Propagation Modeling

The purpose of this section is to present a brief discussion of the approach used in developing and validating the computer propagation model, i.e., the model which determines the multipath characteristics of obstacles found in airport environments. These models define:

1. The signals reflected from terrain, buildings, and aircraft

and 2. the changes in the direct signal characteristics due to shadowing by runway humps, buildings, and taxiing aircraft.

The task of modeling the reflection and shadowing phenomena at microwave frequencies is simplified by the optical-like properties of microwaves and the applicable experience from tracking radar operation at microwave frequencies. Additionally, there has been much work done in the MLS multipath area as summarized in Table 1-2. The wavelengths for MLS are considerably smaller than the obstacles;* thus, the scattering phenomena is very similar to that which occurs with optical systems and the regions of significant multipath can be determined by ray tracing such as illustrated in Fig. 1-3.

The modeling involves two distinct steps:

1. The very complicated real world objects are represented by certain simpler shapes which more readily lend themselves to practical computational procedures. As an example, aircraft fuselages are represented by metallic cylinders.

2. A computational algorithm of reasonable complexity for a modern computer is used to give a quantitative expression for the scattered signal parameters.

---

*by contrast, the ILS localizer wavelength is comparable to obstacle sizes (e.g., aircraft fuselage diameters), which leads to a quite difficult field theory problem.

TABLE 1-2

MAJOR SOURCES OF MLS MUTLIPATH ENVIRONMENT DATA FOR PROPAGATION MODEL DEVELOPMENT

	Reflections from:			Shadowing by:		
	Buildings	Aircraft	Other Sources	Aircraft	Runway Humps	Buildings
Qualitative Characteristics	1-3, 5-9 A 2 4 6 7 10 E	6 7 A 2-7, 9 E	6 A 4 7 E	1 2 5-7 A 2-6 E	1 2 5-7 A	2 3 6 7 A 3 7 E
Quantitative Characteristics						
Reflection coefficient	1 2 5-9 A 2 6-10 E	7 8 10 A 6 7 E	---	---	---	---
Spatial extent	1-3, 5-9 A 4 7-10 E	1-3, 5-9 A 4-9 E	4 7 E	1 2 6 7 A 2-7 E	2 5 7 A 5 7	2 3 7 A E
Size, distance factors	7 10 E	6 7 E	---	1 2 7 A 2-7 E	2 5 7 A 2 5 E	2 3 7 E
Secondary paths	7 A 5 7 9 E	7 A E	---	2 7 A 2-7 E	2 7 A	3 7 A 1 3 E
Spatial coherence	1-3, 5-9 A 2-7 9 E	1-3, 5-9 A 7 E	---	1 2 7 A 2 3 5 E	2 7 A 2 5 E	2 3 7 A 3 7 E

1. Univ. of Trondheim Electronics Research Laboratory (Norway) [10, 75]
2. Royal Aircraft Establishment (UK) [15]
3. Australian Dept. of Tansport/Univ. of Sydney (Australia) [16,18, 37, 38, 80]
4. Tests of scanning beam systems prior to MLS program [19-21]
5. FAA scanning beam MLS contractor studies and tests [12, 22, 23]
6. FAA doppler scan MLS contractor studies and tests [11, 13, 24, 25]
7. M.I.T. Lincoln Laboratory [26-30]
8. US Army [31, 32]
9. US Airforce/IITRI [33-35]
10. Space Research Center/ Post Office (UK) [36]

A = analytical or theoretical study

E = experimental study

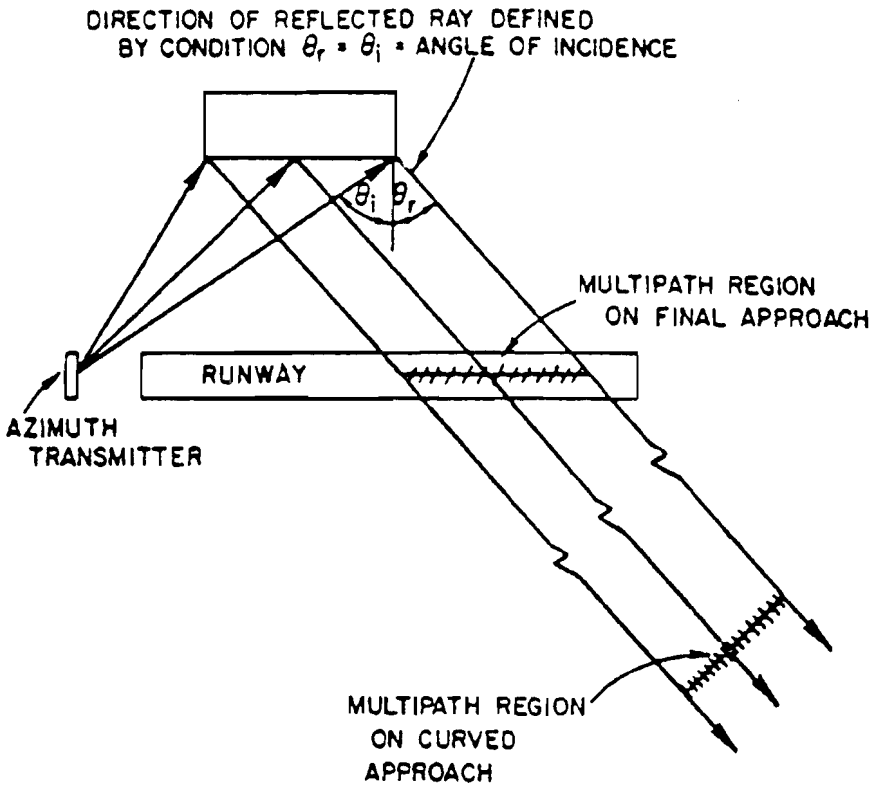

Fig.1-3. Determination of MLS multipath regions by ray tracing.

Terrain Reflection Modeling

The terrain is typically represented by a collection of rectangular and triangular plates, each with prescribed orientation, roughness, and dielectric constant. By varying these parameters, one can assess the sensitivity of performance to terrain type (e.g., dry ground vs. snow). The multipath levels are computed by a numerical Kirchoff-Fresnel integral (or, a simplified approximation).

Building Reflection Modeling

Buildings are represented by one or more rectangular plates of prescribed orientation and surface material. The various plates represent salient features of a building such as the doors of a hangar. By allowing each plate to have a different surface material characterization, inhomogeneous surfaces (e.g., concrete walls with metal doors) can be modeled. Consideration is also made for secondary ground reflection paths. The levels are computed assuming Fresnel diffraction is applicable and then using closed form Fresnel integral expressions.

Aircraft Reflection Modeling

For aircraft, it is essential to consider the curvature of the surfaces as this tends to spread the reflections over a much greater region than would be the case with flat plates. The fuselages and tail fins are both modeled as cylinders or a section thereof. The resulting multipath levels are computed by a combination of Fresnel diffraction (integrals) and geometric optics. The shadowing of the azimuth (localizer) signal by runway humps also requires explicit consideration of the surface curvature, and is computed by similar mathematical algorithms.

Shadowing

Shadowing by buildings or aircraft causes both an attenuation and distortion of the transmitted wavefront. Both of these factors are considered in the models for shadowing. The shadowing obstacles are represented by one or more rectangular plates which approximate the object silhouette. Similar techniques have been successfully used in studying the effects of widebody aircraft on the ILS [3].

The details of the first and second order models have been described in earlier Lincoln Laboratory reports [28, 29]. In chapter IV of this report, we describe several refinements to the shadowing model in the areas of secondary paths involving ground reflections and shadowing by obstacles in the near field of the ground antenna.

c. Propagation Validation

An essential feature of the MLS multipath model development was validation of the model by comparison with appropriate field data. The principal focus has been on data at a carrier frequency of 5.1 GHz (C band), although some comparisons have been made at 15 GHz (Ku band) and 1090 MHz (L band). The key points addressed in the validation were:

1. Does the physical model assumed for the scatterers at the airport make sense: For example, do buildings scatter much like a flat plate coplanar with the vertical walls? Do aircraft tail fins yield reflections over a range of angles corresponding to a section of a cylinder? How many scatterers need to be modeled in a given environment?

2. With appropriate specification of parameters such as dielectric constant and surface roughness, do the quantitative predictions of the model agree well with the field data?

To address these issues, an initial set of MLS multipath measurement programs were conducted at operational airports [e.g., Logan International, Boston, MA (BOS), Wright-Patterson Air Force Base, Dayton, Ohio, and Long Beach, California] as well as at airports primarily devoted to test activity (e.g., Wallops Island, VA., and RAE Bedford, UK). The results of those initial measurements and model validation tests have been reported in several earlier Lincoln Laboratory reports [26-30]. It was concluded from these various measurement programs that:

1. Significant specular multipath levels were associated with the specular reflections from building walls or aircraft. The buildings could generally be classified in one of two categories:
   a. Those with complex surfaces (broken columns, jet ways, etc.) and low reflection levels

   and

   b. Those with simple (e.g., homogeneous flat plate) surfaces which yielded higher levels. In particular, many of the complicated features (delivery trucks, luggage carts, etc.) in a terminal area may be ignored as far as modeling significant multipath is concerned.

2. The predictions of the model for simple surfaces (e.g., flat building walls and aircraft) were quantatatively in good agreement with the field measurement results.

More recently, additional model validation tests have been carried out to address several issues of particular concern:

1. The nature of ground reflected signals from rough and/or rising terrain. This study, which included L band field measurements at L.G. Hanscom airport, Bedford, MA and Ft. Devens, MA, is reported in Chapter II of this volume.

2. The existence of high level azimuth building reflection multipath which is phase coherent over MLS measurement periods (e.g., 200 ms). This study, which included measurements at Miami International, St. Louis (STL), Tulsa International, Oklahoma (TUL) and WPAFB, is reported in chapter III of this volume.

3. The levels and spatial character of elevation building reflections. This study, which was done in connection with the TRSB field trials at J.F. Kennedy International, New York (JFK), is reported in chapter III of this volume.

4. Errors due to azimuth and elevation shadowing by plates, buildings, and aircraft. Scale model measurements made by the Air Navigation Group at the Univ. of Sydney [37-38, 80] and the results of TRSB and DMLS field tests at Aeroparque, Buenos Aires, Argentina; Brussels International, Belgium; NAFEC, New Jersey; and JFK; New York have been utilized to refine and validate the shadowing models. The scale model and NAFEC results are presented in Chapter IV of this volume while the Aeroparque, Brussels, and JFK data is discussed in volume II of this report.

d. System Modeling

The development and validation of the final system models for the MLS techniques proposed to ICAO was based on the states' proposals to ICAO [6, 7, 16, 65]. It was agreed that each proposing state should furnish sufficient data to enable any interested party* to simulate that system. A multipath subgroup was established by working group A (WG-A) of the ICAO AWOP to facilitate the exchange of this detailed technical data. This included antenna patterns, scanning mechanizations, and receiver processing algorithms [65].

In all cases, the received signal is modeled as a superposition of the received direct path signal and a number of replicas of it, each having its own amplitude, delay, code angle and Doppler shift. The system model then determines the error by taking into account the nature of the transmitted signals and the proposed signal processing.

The model construction was facilitated by two factors. First, the signal transmission and signal processing used for the MLS techniques is similar in many respects to radar and radio astronomy systems (e.g., interferometry, "monopulse", and "sliding window" trackers). Thus, there is an extensive data base of literature and practical experience from which to draw. Sec-

*For example, the United Kingdon AWOP panel member presented scanning beam simulations based on US data while the US AWOP member presented simulations of Doppler scan and DLS techniques based on the UK and FRG proposals.

ondly, it was decided to focus on predicting errors due to multipath alone since 1) including other error sources (e.g., quantization effects) would greatly complicate the results without yielding data that was not already available from the test site field test data and 2) the principal objective of the simulations was to identify the multipath sensitivities of the various systems.

1. TRSB Model

For the time reference scanning beam system (TRSB), the waveform at a given code angle is generated by the passage of the scanned beam as shown in Fig. 1-4. The functional form of the beam waveform is determined from measured or theoretical patterns as illustrated in Fig. 1-5.* By superimposing the beam patterns corresponding to the various signal paths, the net received envelope is determined. The remainder of the model parallels the microprocessor based receiver processing [69]. A tracking gate is centered on the largest consistent envelope peak, and the beam arrival angle is calculated by finding the times at which the leading and trailing edges of the received envelope cross a threshold. Various checks and tracking algorithms are applied to each measurement before it is presented as angle data. The TRSB model is presented in depth in chapter I of Volume II.

2. DMLS Model

For the Doppler scan system (DMLS), the waveform at a given code angle is a time gated sinusoid whose angle code frequency is generated by commutation of excitation along a line array as shown in Fig. 1-6. By superposing the sinusoids corresponding to the various signal paths, the net received waveform is determined. The UK Doppler digital correlation receiver [7, 67, 68] has been modeled. The processor determines the signal frequency, by

---

*The pattern for an azimuth thinned phased array proposed for relatively benign sites is illustrated. Other patterns modeled and validated include the fully filled phased array for Azimuth and the COMPACT phase array implementation for elevation, both of which have low sidelobes.

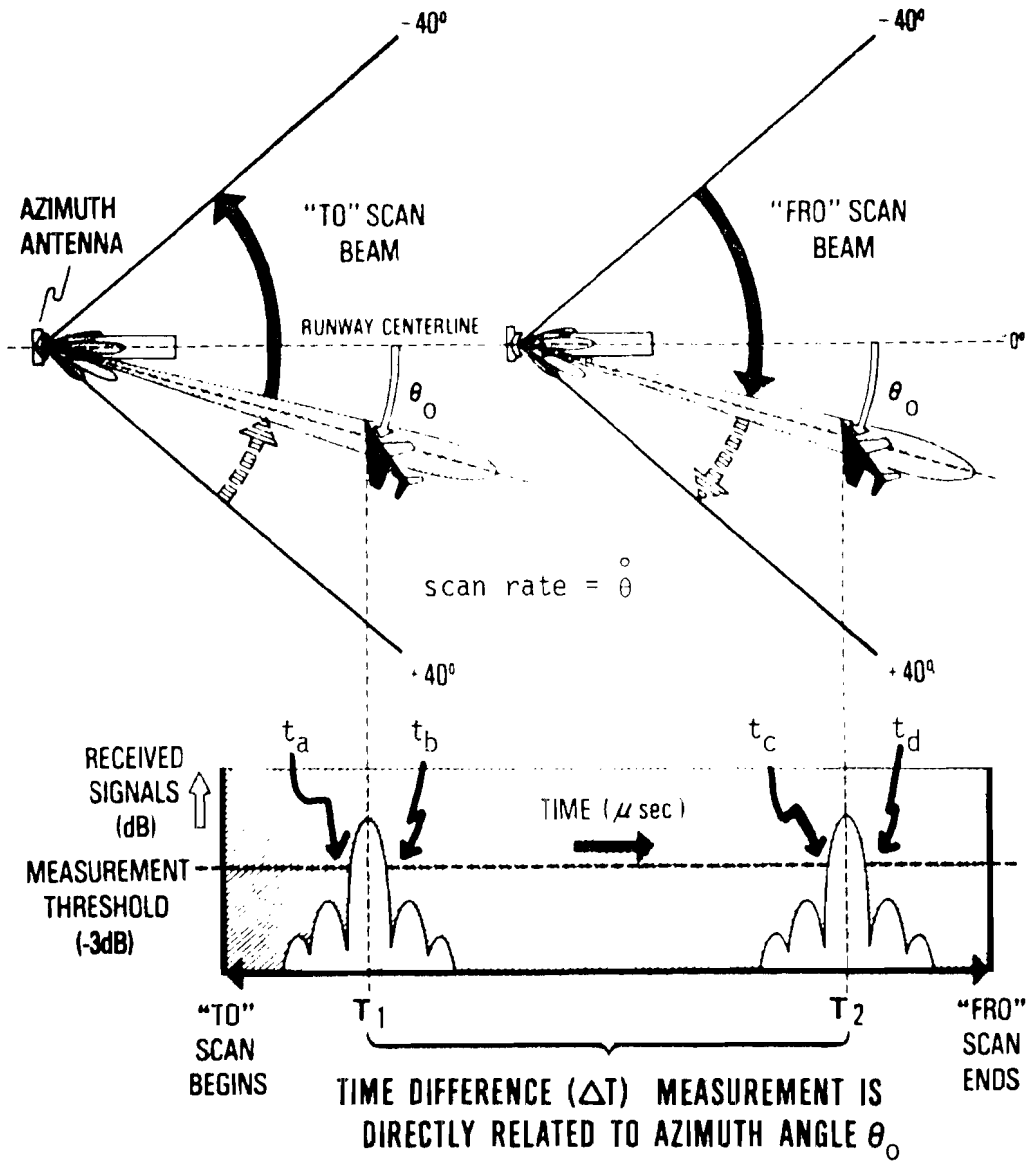

Fig.1-4. TRSB bi-direction scan format.

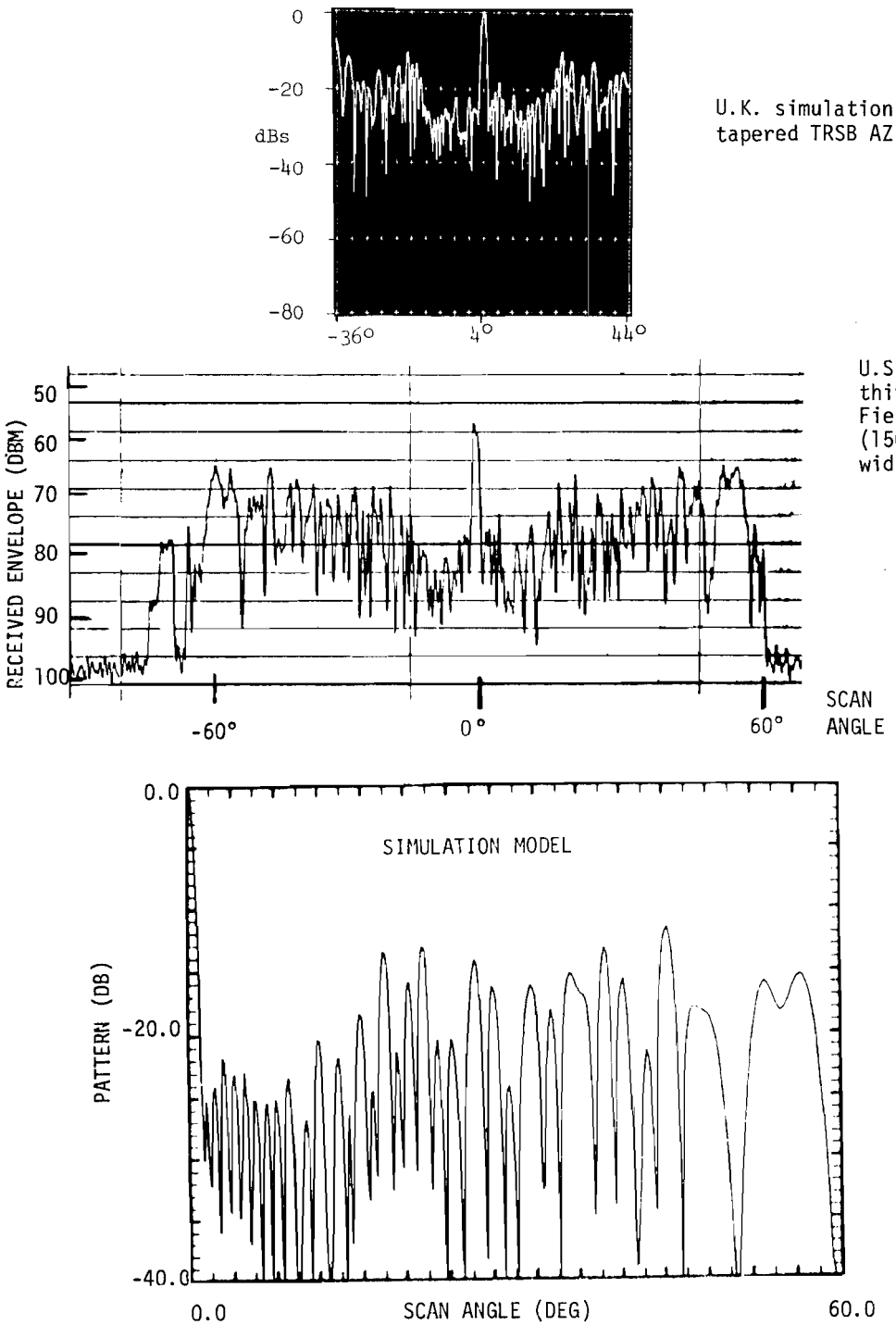

Fig.1-5. Measured and theoretical beam patterns for density tapered TRSB azimuth array.

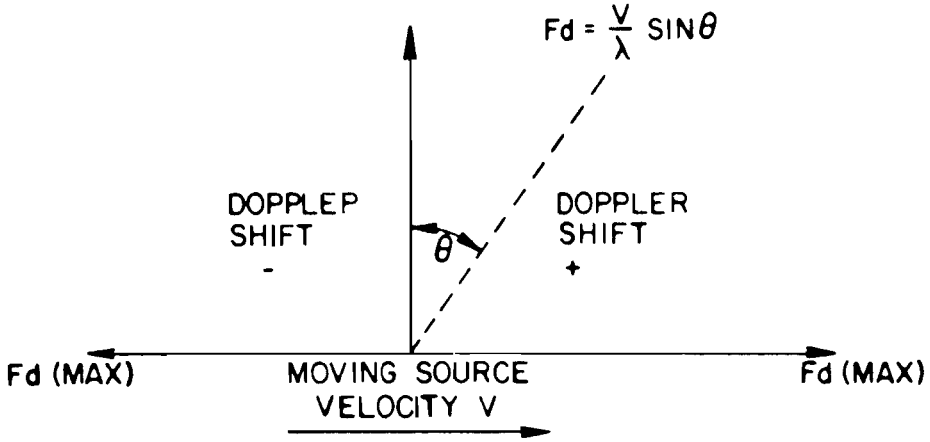

(a) THE DOPPLER PRINCIPLE

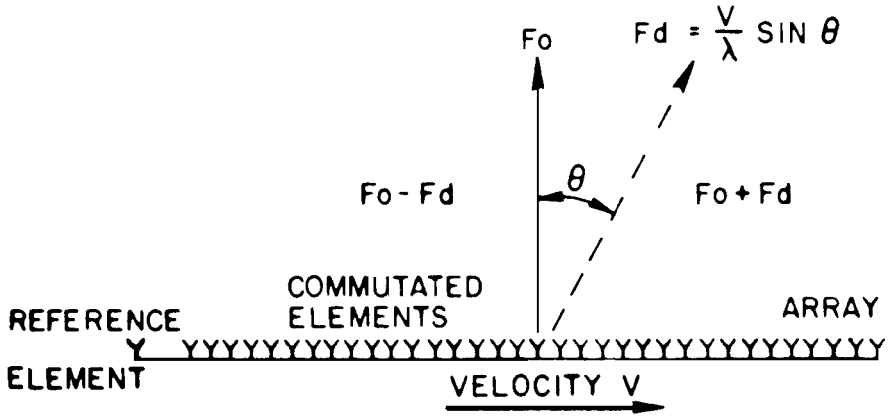

(b) DOPPLER APPLIED TO MLS

Fig.1-6. Generation of Doppler signal in space.

performing spectral analysis of the dtected signal (see Fig. 1-7) over a coarse/fine frequency grid in the equivalent coverage volume. The spectral analysis is performed by correlating the incoming waveforms with quadrature components of the tracked frequency so as to produce sum (Σ) and difference (Δ) filter outputs for each scan. The ratio (Δ/Σ) is used as an error signal to drive the correlator frequency to the frequency of the incoming signal. Multipath components serve to change the Σ and Δ values such that the tracker frequency is not equal to the direct signal frequency. The computer model, which is presented in detail in section III of Volume II, determines the resultant values of Σ and Δ for each scan by closed form analytical expressions with the digital tracking loop dynamics being emulated as in the actual receiver. Various checks are applied to each measurement before it is presented as angle data.

3. DLS Model

The DLS received signal at a given antenna is a superposition of ICAO L band DME pulses corresponding the the various transmitter to receiver paths. The DLS ground system makes measurements of the amplitude and phase of the received signal at a number of ground antennas, with the angle code information being contained in the phase difference between the direct signal received at the various antennas as shown in figure 1-8. These measurements are first combined to yield "virtual antenna" outputs with interferometric processing being used to determine the angle bearing of the aircraft [6, 66, 70]. The angle data is then transmitted to the aircraft by time position coded pulses following the normal DME reply as shown in figure 1-9. The computer model, which is presented in Chapter V of Volume II, determines the net received signal at each antenna using measured and theoretical patterns, and then performs the same processing that is used in the DLS ground system. Validity tests and filtering algorithms are applied to the received angle data before it is presented.

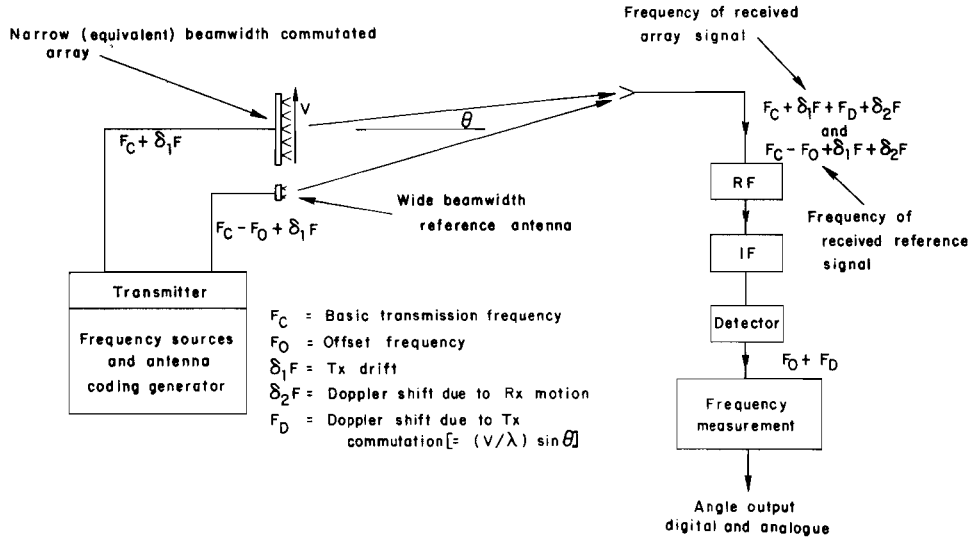

DMLS receiver seeks to determine F_D to within several Hz
However, $\delta_1 F$ and $\delta_2 F$ are unknown quantities whose magnitudes are 1-10 kHz

∴ DMLS array signal frequency is measured relative to reference signal frequency

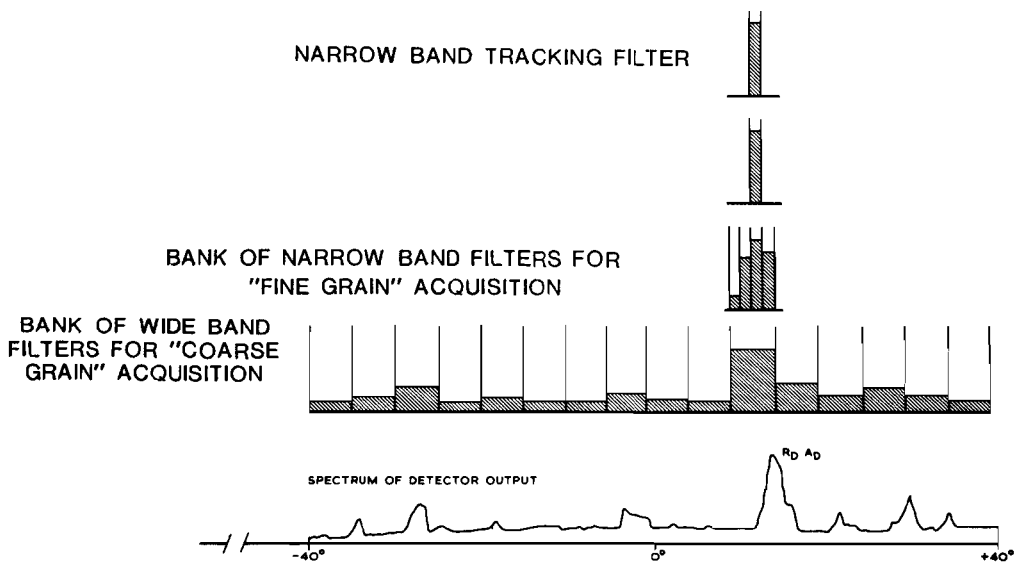

OPERATION OF DMLS CORRELATION PROCESSOR

Fig.1-7. Angle estimation by DMLS receiver.

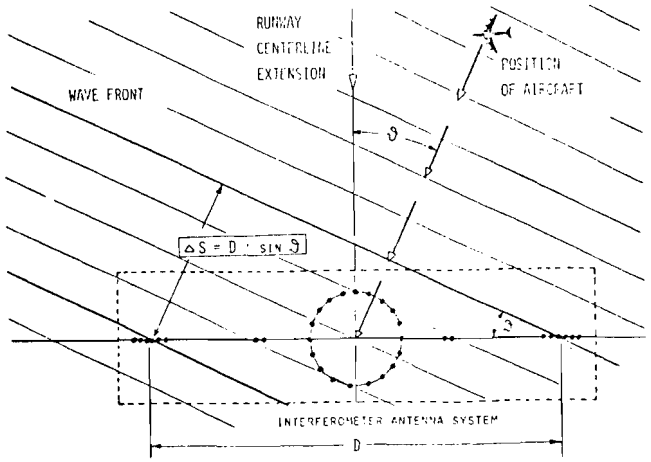

(a)

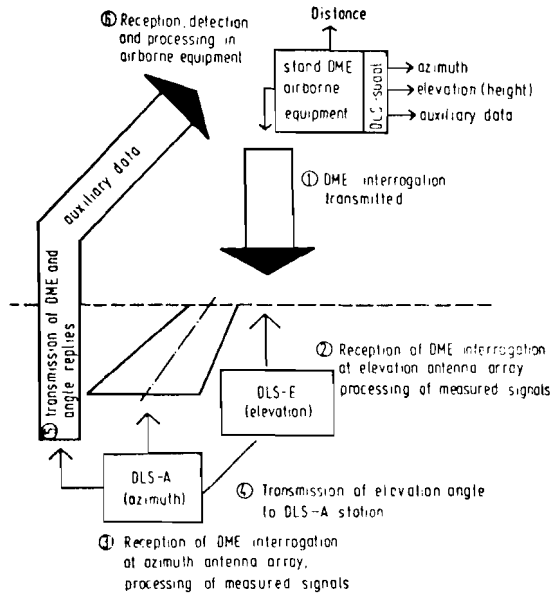

(b)

Fig.1-8(a-b). (a) Principle of the DME-based landing system DLS. (b) DLS signal flow.

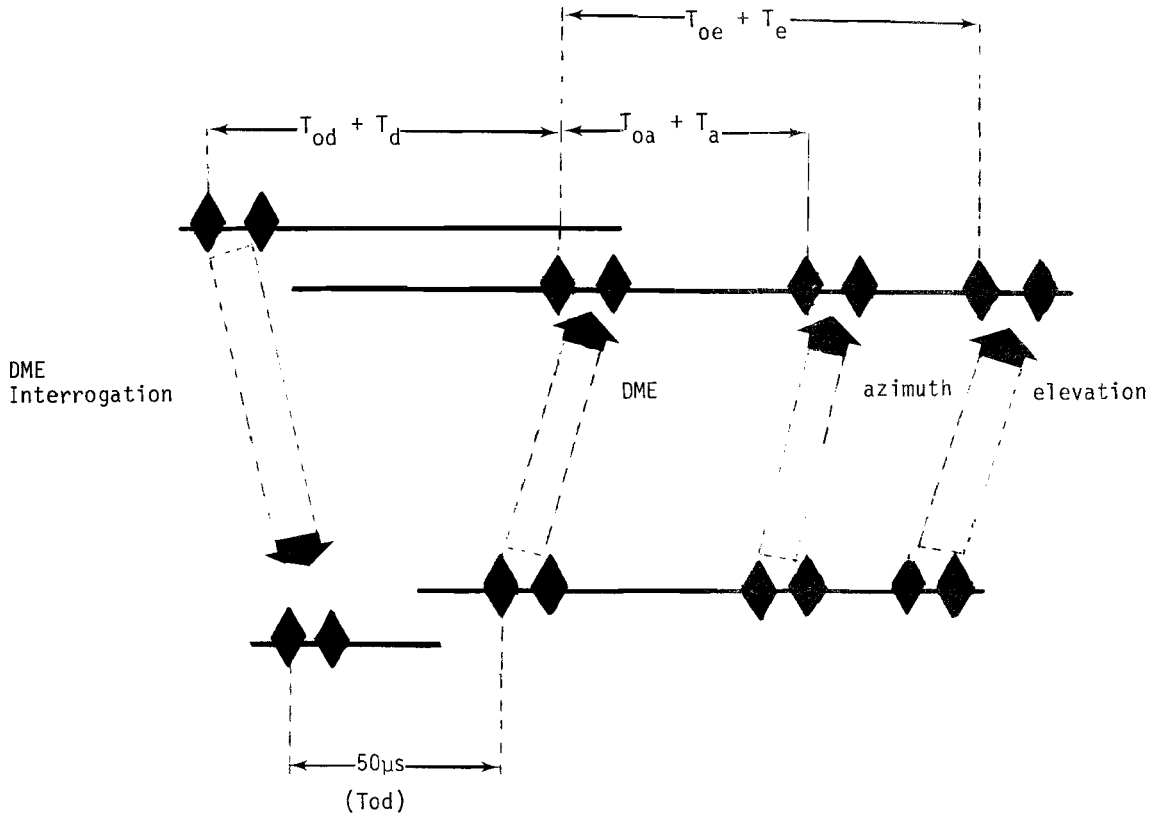

Ta - time equivalent to azimuth
Td - time equivalent to distance
Te - time equivalent to elevation
Toa, Tod, Toe - bias time intervals

Fig.1-9. DLS signal format.

e. System Model Validation

Model validation is a process by which one gains sufficient confidence in the operation of the simulation model to rely upon its predictions for previously untested situations. The primary validation tool is the comparison of model outputs to other data calculated for or experimentally measured in corresponding situations and to explain both the similarities and discrepancies which are evident. For each of the MLS system models, and for the TRSB model in particular, theoretical calculations, bench test experiments, and field tests have all been used as data inputs to the validation process illustrated in Fig. 1-10. This section traces the path by which the conclusions of the individual tests have culminated in validation of the simulation for the purpose of the comparative simulations.

The validation process is most usefully viewed within the context of its primary modeling objectives, which are:

(i) Representative received signal-in-space model in the presence of multipath sources,

(ii) Receiver modeling at the functional signal processing level,

(iii) Emphasis upon multipath-induced effects, and not elements of clean accuracy such as front end noise, beam stepping quantization, receiver time and amplitude quantization, etc.

The use of field data and theoretical (analytical studies as a validation input is familiar to most readers; however, the hybrid bench simulators merit some discussion. As an aid to system performance analysis and optimization, the UK and US constructed laboratory test sets which can inject into an actual MLS receiver the waveform corresponding to reception of a direct signal and a single multipath signal [7, 71]. Since the characteristics of the direct and multipath signals (e.g., amplitude, rf phase and angle code) are fairly tightly controlled, such bench data is quite useful for system model validation.

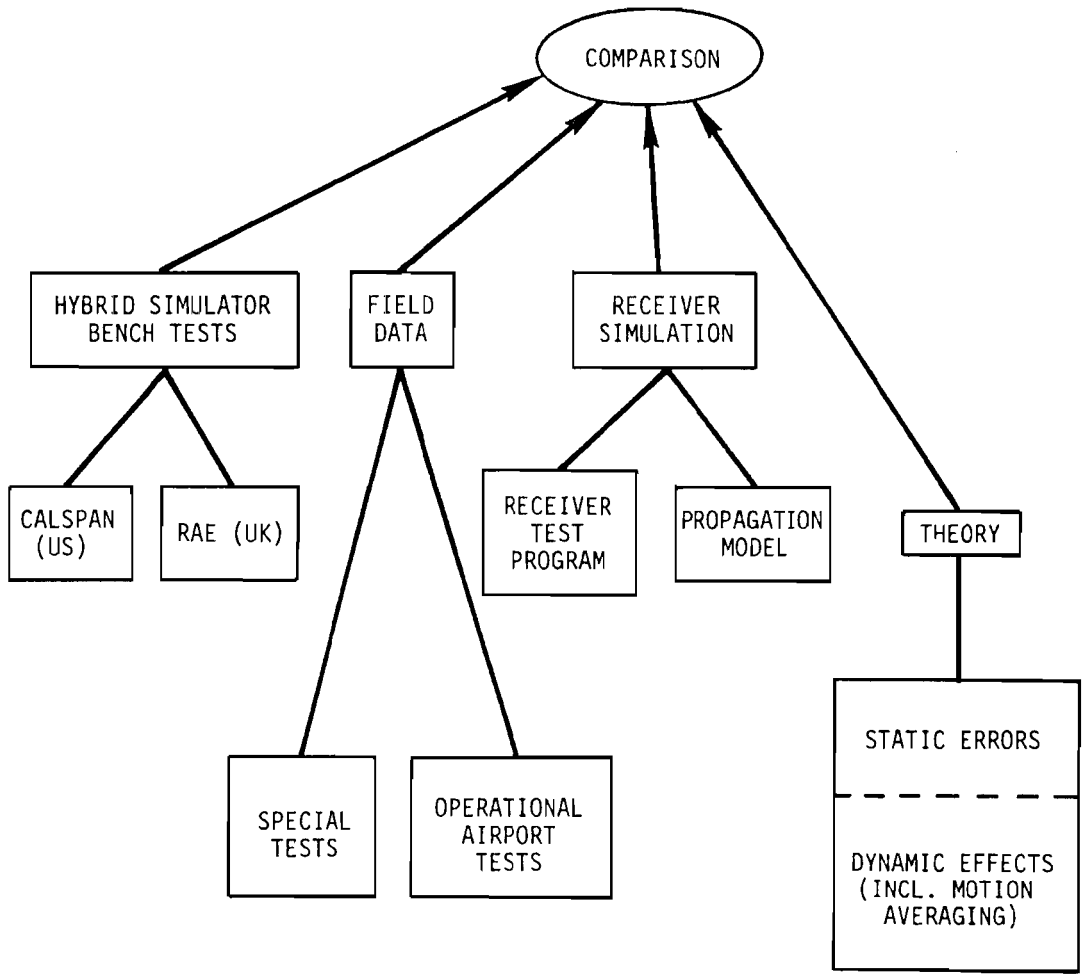

Fig.1-10. Elements of system model validation process.

(1) TRSB Model Validation

The TRSB model validation, which is described in detail in section II of volume II, was accomplished by a several step procedure. First, the model for the receiver envelope processor was validated by comparison with the results of hybrid simulator tests at CALSPAN Corporation [71] and with analytical (theoretical) results [28]. Then, the received signal and antenna models were validated by comparison with field tests.* For example, the sidelobe model for the azimuth array was validated by results from the ICAO AWOP "standard" screen multipath tests [72], while the mainlobe model was validated by screen and operational airport building reflection tests [28, 73, 7, 4] as well as shadowing tests [31, 73].

(2) DMLS Model Validation

The DMLS model validation, which is described in detail in section IV of volume II, was principally accomplished by comparison with the RAE hybrid bench simulator data. This simulator emulates the DMLS dynamic antenna scanning mechanisms in the course of generating the simulated received signal which is input to the DMLS receiver under test. Thus, there was a lesser need to rely on field tests for received signal model validation. This lesser need for DMLS field data was fortuitous because the bulk of the DMLS controlled multipath field tests were carried out with signal formats and receiver processing which were quite different from that proposed and modeled. However, a limited amount of DMLS field data involving building reflections and shadowing for the proposed system were obtained in early 1978 and are compared with the simulation results in chapter IV of volume II.

---

*The CALSPAN simulator makes assumptions regarding the received antenna patterns which are similar to those utilized in the Lincoln computer model; thus, the hybrid simulator data cannot by itself validate the received signal model.

(3) DLS Model Validation

The proposed DLS signal processing is to be accomplished digitally on a digital computer. Thus, DLS computer model justification/validation was less of a problem for the other two techniques. The validity of the processor computer code was established by developing the model in cooperation with the FRG technical experts who had coded the DLS testbed computer and, by comparing the program results with known analytical results for the processors used. In addition, the received signal model was validated by comparison with very limited FRG field measurements using a repeater to generate synthetic mutlipath signals. Both types of validation results are reported in chapter VI of volume II of this report.

2. Application of Computer Modeling to MLS Comparative Assessment

In this section, the application of computer modeling is discussed with emphasis on defining system sensitivities to multipath effects. As mentioned earlier, this consisted of simulations of the various systems in representative airport environments and indepth analysis of various issues which arose out of the modeling/simulation studies. Since the driving factor for much of the analysis was the scenario simulations, it is necessary to provide some perspective on the overall MLS multipath threat and the differences between the comparative scenarios and actual airports.

An important part of the Lincoln MLS multipath studies was a survey of a number of major airports to identify and characterize existing multipath sources (e.g., building locations, sizes and surface composition) [27]. These airport survey results are useful in providing perspective on the current likelihood of encountering significant MLS multipath. A study of airport maps for eleven major U.S. and foreigh airports [Chicago (O'Hare), London (Heathrow), Los Angeles, Melbourne, Miami, Minneapolis/St. Paul, New York City (Kennedy), Paris (Orly), Philadelphia, San Francisco, Tulsa] together with on-site inspection of the U.S. airports, showed that over 50% of the run-

way ends were free of buildings which could produce significant azimuth multipath when on final approach. Some 88% of the runway ends were free of buildings which could produce significant elevation multipath.

These statistics suggest that in many cases susceptibility to building multipath may not be a factor in the MLS installation, thus permitting the use of lower cost/capability versions of the MLS. Moreover, these statistics suggest that tests at an "average" current airport are unlikely to encounter "stressful" multipath conditions. On the other hand, there are some runways where significant multipath levels could be encountered with the existing buildings, and we can anticipate that the number of airport buildings will increase in the future. One must focus attention on these stressful situations in comparing the candidate systems.

Most of the controversy that has arisen with respect to the comparative simulations vis-a-vis actual airports and/or field tests have been concerned with the airport models, not with the propagation or system models. Much of the difficulty has arisen from misunderstanding as to the objectives of the various simulations and poor choice of words in describing the models.

Two general classes of simulation have been conducted for the various interested parties: sensitivity simulations and airport specific simulations. Sensitivity simulations are primarily concerned with identifying system sensitivities to general airport features (e.g., building and aircraft locations).

The airport models for the AWOP scenarios* presented in volume III related to sensitivity simulations and were developed for the most part by placing simulated buildings at the locations of actual buildings at actual airports. It was agreed that the buildings assumed in some simulation runs were to be higher and/or more reflective than the actual buildings so as to compare all

---

*e.g., the "standard" scenarios agreed on by AWOP [66, 72] and/or the additional scenarios generated by the FRG, Netherlands, U.K., and U.S.

the systems in the more challenging environment that could exist when MLS is implemented [72]. Also, it was agreed to simplify the airport features by representing the buildings by uniform flat plates, terrain as a horizontal flat sheet, etc., [66]. This was done because inclusion of fine detail (for example, the precise locations and shapes of windows in airport buildings) would so complicate the resulting simulation that one might never achieve the desired understanding of system behavior. Thus, although those scenarios were derived from actual airports, the simulation results could not be directly related to MLS performance at the airport from which the scenario was derived. Although this point was well understood within AWOP [66], confusion was created outside AWOP by the (unfortunate) use of actual airport names to designate the AWOP scenarios derived from those airports.

Airport specific simulations, intended to predict MLS performance at a given airport on a particular flight path, require utilization of very detailed airport data in generating the airport model. As discussed in volume II of this report, airport specific simulations were utilized to validate the multipath simulations. Careful site surveys were made to determine precise transmitter and scattering object locations, terrain features (e.g., grass height and ground contours), building surface composition, taxiing and parked aircraft locations, etc. Additionally, precise aircraft flight profile data was necessary in many cases to give a close replication of resultant error waveform.

In both cases, the simulation outputs (recall Fig. 1-2) have been designed so as to yield a better understanding of <u>why</u> the systems errors occured in a given region. This is accomplished by graphical displays of key multipath parameters (e.g., amplitude, angle with respect to the direct signal) along the flight path as well as the "raw" receiver errors before data validity checks and multiple measurement averaging take place.

In discussing the simulation results, it is convenient to discuss separately the cases of azimuth and elevation angle performance, since the nature of the multipath threat is somewhat different for these. Also, in our discussion it will be useful to divide the multipath into two categories:

"in-beam" = multipath which has an angle code close (e.g., within two ground antenna beamwidths) to that of the direct signal

and

"out-of-beam" = multipath with an angle code well removed from that for the direct signal (e.g., an angle code separation of more than two beamwidths)

The above terminology is drawn from radar applications where "in-beam" denotes a situation in which two targets are difficult to resolve.

The scenarios simulated considered both in-beam and out-of-beam multipath as indicated in Table 1-3. We see that a wide variety of multipath threats were considered in both airport specific and comparative scenarios. An airport specific scenario based on the field test for a given system, is reported in the volume II chapter discussing validation for that system model. The results for a comparative scenario (using either an airport specific or a comparative airport model) are reported in volume

The conclusions reached by AWOP from these various simulations and other relevant data (e.g., field test results, theoretical analyses and simulations presented by others) was that [9]:

(1) All systems will be affected by azimuth or elevation diffraction phenomena when the line of sight is partially or totally blocked. Avoidance of such situations will need to be considered in MLS siting; however, there is not a significant difference between the systems with respect to shadowing performance.

(2) TRSB is highly resistant to high level out-of-beam azimuth multipath due to the low antenna sidelobes and tracking logic. With DMLS, there is an increased possibility of degraded performance due to reference signal multipath effects. The assessed DLS configuration had poor out-of-beam azimuth performance due to high antenna sidelobes and difficulties in maintaining track during periods of high multipath levels.

TABLE 1-3

MLS MULTIPATH SCENARIOS PRESENTED IN THIS REPORT

Scenario	Type of Scenario*	Volume where Reported	TYPE OF MULTIPATH ENCOUNTERED+ Azimuth in beam	Azimuth out of beam	Elevation in beam	Elevation out of beam
AWOP #1,4,6,7,8 (JFK)	C	III	5	1	1 2	5
AWOP #2 (LAX)	C	III	5	1 2	1	5
AWOP #3 (Crissey)	C	III	5	2	2	5
AWOP #5 (JFK)	C	III	4 5	2	-	-
Hagenberg "TRSB Stressful" #1	C	III	-	-	2	5
Hagenberg "TRSB Stressful" #2	C	III	5	2	-	-
Salzburg (FRG)	C	III	5	5	-	5
Shadowing B707 (UK)	C	III	3 5	-	-	-
TRSB CV880 overflight	AS/C	II, III	3 5	-	-	-
ILS Monitor Shadowing (Buenos Aires)	AS/C	II, III	-	-	3	5
Hercules Shadowing (Brussels)	AS	II	-	-	3	5
Building reflections (Brussels)	AS/C	III	5	2	-	-
Building reflections (Sydney)	C	III	5	2	-	-
JFK Flight Tests	AS	II	-	-	2 4	5
	C	III	5	2	-	-

* C = Comparative
AS = Airport Specific

\+ Airport Multipath types:
1 aircraft specular reflections
2 building specular reflections
3 shadowing by aircraft
4 shadowing by buildings
5 ground specular reflections

(3) DMLS and TRSB elevation multipath performance against in-beam elevation reflections were comparable and within the AWOP accuracy limits even for difficult scenarios. The DLS errors for the assessed implementation were generally larger than those of the other two systems due to the wider beamwidth of the DLS elevation arrays.

(4) All three systems gave satisfactory performance against out-of-beam elevation multipath (principally ground specular reflections) in the scenarios assessed.

During the course of the simulation studies, a number of multipath performance factors proved significant enough to warrant separate indepth studies. The studies which are reported in volume III include:

1. Shadowing phenomena (Chapter II) - here the focus was on comparative system response to several simultaneous in-beam multipath signals since shadowing can typically be represented as several in-beam multipath components (see Chapter IV of the present volume).

2. DMLS dynamic reference effects (chapter III) - the use of two radiated signals which are multiplicatively combined in the DMLS receiver gives rise to several multipath performance issues not found in the other systems. These phenomena include:

   (a) "reference scalloping" - frequency modulation of the reference by out-of-beam multipath yields in-beam interference signals at the output of the DMLS detector.

   (b) AGC effects - dynamic variation in the DMLS AGC during a scan produces changes on the effective beam patterns.

   (c) "array scalloping" - receiver motion induced Doppler shifts on the commutated DMLS signal cause multipath from a scatterer which is physically "out-of-beam" to have an in-beam frequency code.

(d) "lateral diversity" - simultaneous lateral shifts of the DMLS elevation sideband and carrier radiating elements are utilized to spread the received bandwidth or to induce changes in the relative phase of certain error causing detector output terms. This permits a reduction of certain types of in-beam elevation errors by a method other than motion averaging. The focus of our work has been on quantifying the benefits from lateral diversity and identifying possible problems which would need to be addressed in any follow-on studies

3. Acquisition/validation (Chapter IV) - it is essential that a MLS technique avoid displaying highly erroneous angle data. High level out-of-beam azimuth multipath is of particular concern since a poorly designed system might commence a track on such multipath which would be difficult to distinguish from a valid track. Thus, an important issue is the ability of the various systems to distinguish between valid and invalid tracks on the basis of single and multiple measurements.

4. TRSB slew limiter studies (Chapter II) - the TRSB receiver performs data validity checks (slew limiting) and filtering (averaging) on the raw angle data before outputting it. Certain of these data validity checks can significantly effect the multipath performance.

C. MLS SIMULATION COMPUTER PROGRAMS

This section provides a brief summary of version 2.0 of the MLS simulation computer program. A more complete description of the programs is contained in the user's manual, which is volume IV in this report. The MLS simulation programs are written in the FORTRAN IV computer language and has been successfully utilized on computers in the United Kingdom and Federal Republic of Germany. It has three major parts; multipath parameter computations and graphical output, system error computations, and error manipulation and plotting. The relationship of these various parts is shown in figure 1-2.

The propagation model takes an airport environment* specified by the user (in a block data subroutine) and computes the multipath characteristics (level, separation angle, etc.). Flight paths between up to 35 segments are computed from waypoints supplied in a block data subroutine , with the corresponding perturbation smoothing points. A special version of the flight path generating routine is also provided which fits a smooth curved path between pairs of non-connected linear segments (see chapter V of this volume).

For a given flight path, a loop over all the evaluation points is established to calculate the receiver coordinates as illustrated in figure 1-11. At each evaluation point, the program loops through all transmitter locations, e.g., all angle functions such as azimuth, elevation, and DME. For a fixed transmitter-receiver geometry, a second loop is established to calculate the multipath parameters for each scattering object in the airport model. Multipath amplitude levels are determined as though the transmitter antenna pattern were omnidirectional. The multipath information to be passed to the receiver subroutines consists of the relative multipath amplitude, phase, time delay, azimuth and elevation planar angles specifying the direction of propagation of the direct wave and fractional Doppler shift.

Editing follows, so as to remove minor components. These multipath characteristics are then written to a user specified data set (usually a digital tape). Multipath diagnostics are plotted along with an airport map showing the placement of obstacles. The multipath programs require approximately 325K bytes of storage on the Lincoln IBM 370/168 computer.** The amount of computer time used depends on the number of obstacles and data points used; for a 'typical' 200 point run with 10 scatterers and no perturbation smoothing, 2 minutes of cpu (computer) time is required on the Lincoln IBM 370/168 computer.

---

* e.g., transmitter, building and aircraft locations, building sizes, terrain electrical properties, etc.

** In addition, the Laboratory IBM/370 system typically requires 120K - 200K bytes of additional memory for the operating system.

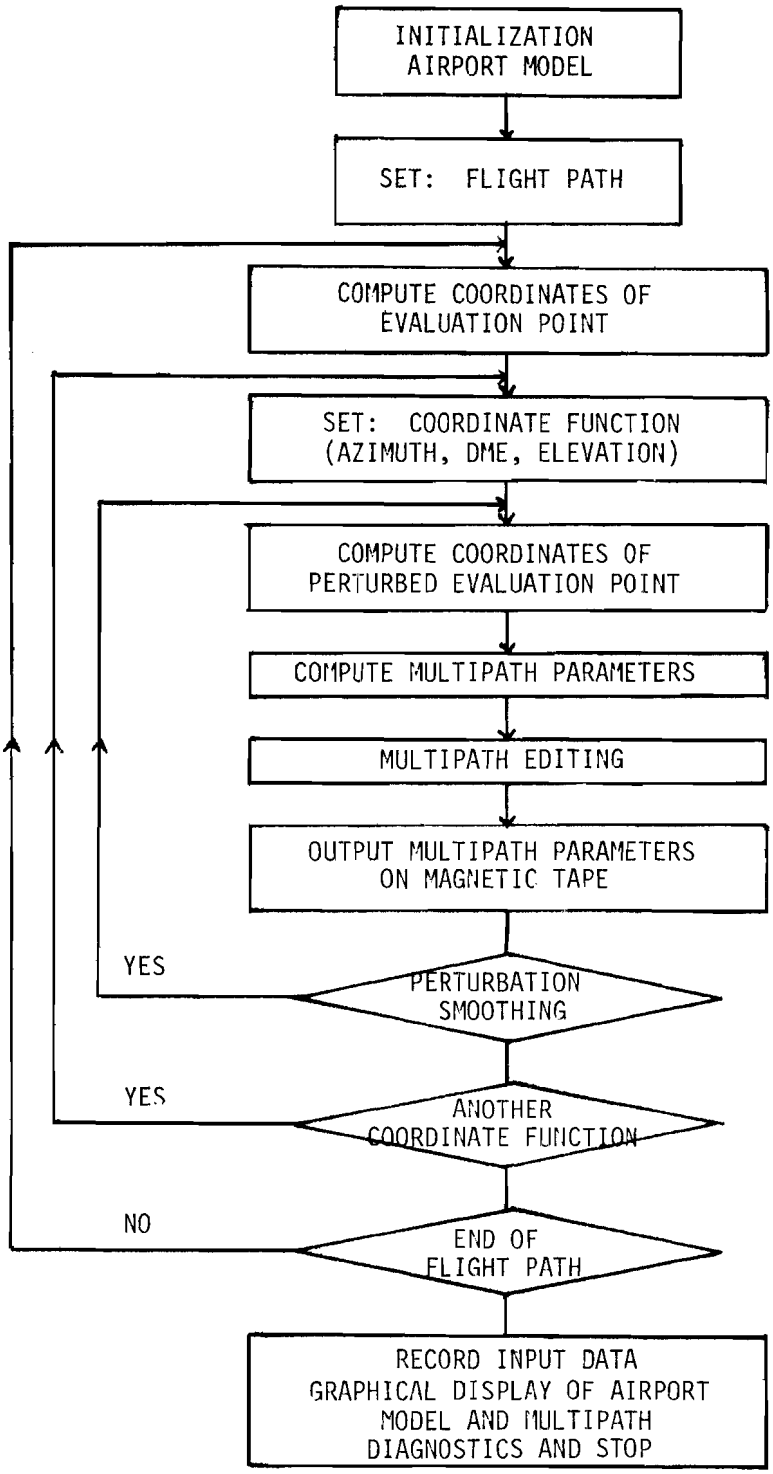

Fig.1-11. Flow chart for multipath section of computer program.

The system model part of the simulation takes TRSB system parameters (initialized in the block data subroutine and/or provided in special subroutines), reads the multipath data generated by the propagation model, and computes the resulting errors, as illustrated in Fig. 1-12. The program takes these errors and writes them out on a data set (typically a digital tape) to be used by the third part of the simulation. For a 'typical' run with 200 points, no perturbation smoothing or static errors, and 10 scatterers, it takes about three to ten minutes of cpu time for the TRSB elevation system to be processed. This time is highly dependent on the number of multipath components and beam patterns utilized. The TRSB azimuth system typically runs 2-3 times faster than the elevation system. The system model programs require about 200K bytes of storage on the Lincoln 370 computer. A plotting program takes the error generated by the receiver routines, asks which specific plots are disired, and plots them.

The graphical routines used the the simulation are from the Integrated Graphics System of the Datagraphix Company with some modification by the Lincoln Laboratory support staff. The simulation program generates these graphical outputs on a Tektronix storage scope. The multipath part of the simulation produces a printout of the parameters used in the simulation run, an airport map locating the obstacles and transmitters, and multipath diagnostics. These diagnostics contain information about the multipath amplitude and separation angles along the flight path, indicating the obstacles which generate significant multipath components.

The system model part of the simulation itself generates no plots. The receiver error plotting program writes out a title page identifying the run, and then plots for a specific system the azimuth, DME, and elevation errors along the flight path. If desired, x, y, z positional errors from the corresponding system can be plotted. Plots of the means, standard deviations, and peak errors can be obtained if perturbation smoothing was used. The single measurement errors are plotted over the dynamic errors with a different symbol. Also, if desired, the error histories may be passed through digital filters to give the "path following", "control motion", and "rate" error characteristics.

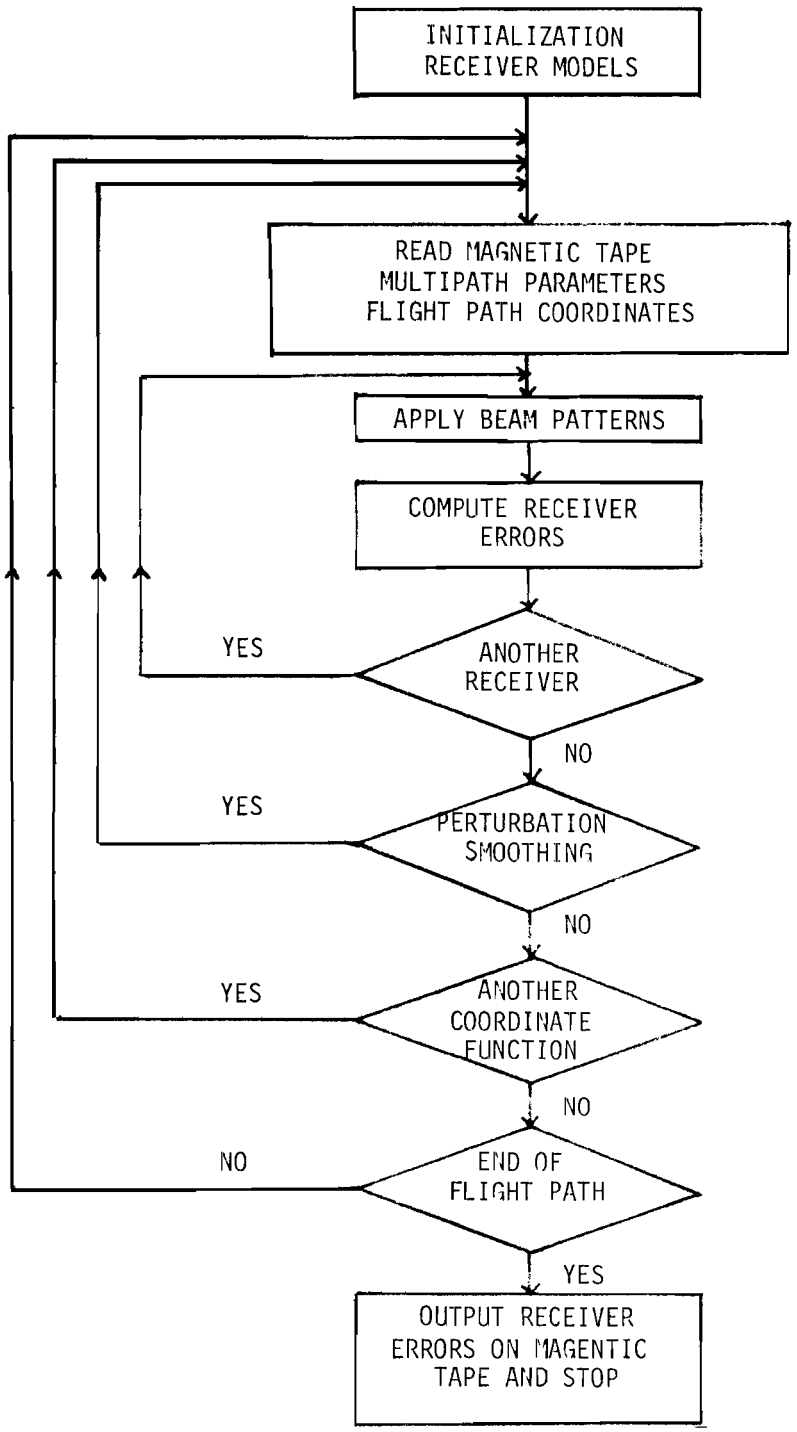

Fig.1-12. Flow chart for receiver section of computer program.

These plotting routines exist in separate subroutines in all except a few cases. No propagation or system model routine directly calls any plotting routine. Thus, the program may be adapted to other installations not having the Lincoln graphical routines.

The simulation routines involved with the computation of multipath receiver errors were written to be as independent as possible. That is, they essentially do not depend on the calling routine. In order for routines to work faster and more efficiently, especially when doing perturbation smoothing, some routines do have knowledge of the structure of the calling routine. However, the complexity this introduces is fairly small and, as a result, these routines can be used independently for a variety of other studies. For instance, the routines were used with very few changes for the critical areas studies [28].

Similarly, several test programs have been written which can check out the various multipath and receiver routines and/or be used as a tool in multipath measurement test design, system optimization, etc. Specific test programs include multipath from a single multipath obstacle (TESTMLT) and performance of a specific receiver when one or more multipath components are present (RCVTST). These Fortran routines are highly interactive and generate graphical ouput, so specific cases can be examined easily and in great detail.

II. GROUND REFLECTION MODEL VALIDATION STUDIES

A. Introduction

The validation of the MLS multipath propagation model by comparison with appropriate field measured data has been an important feature in the process of the model refinement. In the case of specular reflections from the ground, virtually no quantitative MLS field data was available which could be compared in detail with the propagation model. This was a quite undesirable situation since the nature of the ground reflection environment is an important factor in MLS antenna optimization and sitting. Some limited L-band experimental data of the type required became available as a consequence of a Department of Defense program at Lincoln Laboratory and was analyzed in the course of the phase III studies. Field measurement results for the ground reflections in various terrain conditions and their comparisons with the MLS computer simulation results are the subjects to be discussed in this section.

Field measurements were made in the fall of 1977 and the spring of 1978 at Hanscom Air Force Base (AFB) and Fort Devens, using an existing measurement facility [39] with some modifications. These sites offered an opportunity to compare ground reflection multipath at:

1. a flat site which provides good ILS guidance (Hanscom).
2. a site with both upsloping and downsloping local slopes within a roughly level horizon (Ft. Devens golf course).

Also, there were considerable differences in vegetation height between the various locations with the golf course providing the lowest vegetation heights.

The choice of using much of the equipment used in a previous FAA program was simple, since that equipment needed only to be fitted with a new receiving antenna array and antenna/channel multiplexing scheme. The new receiving antenna array consisted of eleven L-band dipoles with the aperture of 26λ. The measurements were made at 1090 MHz with the signal transmitted from a standard ATC transponder on board an aircraft. The field data were taken in terms of the RF phase and amplitude received at each of the eleven dipoles for the aperture sampling processing [40].

Conventionally, the comparison between the field measured data and the corresponding computer simulation results are made on the basis of multipath levels (i.e., M/D ratios) and/or angle errors (azimuthal or elevation angle) along the flight or measurement paths. Here, however, a different approach was taken to make these comparisons. For each transmitter position along the flight path, the received signals at the ground antenna array were processed to estimate the angular power spectrum, i.e., the distribution of the received signal power as a function of the elevation angle. This angular power spectrum was then compared with that predicted by the MLS computer simulation. With this approach, in addition to the M/D ratios, several other features in the received signal can be used for comparison, such as the number and the arrival angles of the multipath components.

In addition to the field measurements to collect ground reflection data, a terrain survey was made for several measurement sites at Hanscom Air Force Base and Fort Devens. These terrain survey data were used to construct the physical model of the ground around each measurement site for the computer simulation run.

The remainder of this section will proceed as follows. The subsection B will discuss the method used for the propagation model validation. The experimental hardware involved in the field measurments will be described in the subsection C. The data analysis results from the field measurements and the MLS computer simulation runs will be presented in the subsection D, together with a brief description of the field measurements conducted and data reduction procedure. The last subsection will summarize the results.

B. Method Used for Propagation Model Validation

As mentioned earlier, the MLS computer simulation propagation model was validated by the field measured and simulated angular power spectra. For our ground reflection measurements, the angular power spectrum is the distribution of the received signal power as a function of the elevation angle. For the field measurements, this approach involves the estimation of the angular power spectrum from the measured complex signal (i.e., the RF phase and the

amplitude) at each dipole of the receiving antenna array. For the MLS simulation results, before the angular power spectrum can be estimated, the complex signal at each dipole of the receiving antenna has to be generated first from the output of the MLS multipath simulation run [28, 29]. And the MLS multipath simulation run needs as its input some appropriate ground model for the terrain involved in the field measurement.

In the results presented in the following subsection D, three kinds of angular power spectra were calculated from both the field measured data and the correspond MLS multipath simulation runs. They are (1) the conventional beamforming (or beamsum, BS) spectrum, which is analogous to a received TRSB envelope, (2) the maximum likelihood (ML) spectrum, and (3) the maximum entropy (ME) spectrum. There has been much discussion of the latter two spectral estimation techniques in the geophysics array processing and time series analysis literature [42-49] because they appear to offer a better capability for resolving signal components which are too close together in elevation angle to be resolved by technique (1). Thus, in this subsection we will only briefly describe these spectral estimation methods. Also, here we will discuss the approach which we took to construct the ground model used in the MLS multipath simulation.

1. Spectral estimation

To facilitate the description of various spectral estimates, the vector notation will be used. The column vectors and matrices are presented by the underlined lower-case letters. The asterisk (*) denotes conjugate transposition. Underlined upper-case letters represent Hermitian matrices. In the following, we will define some vectors and matrices which will be used in the description of various spectral estimates.

The column vector $\underline{s}$ represents the complex sensor outputs from the receiving antenna array, i.e., s_i is the complex signal received at i-th dipole. The (i,j)-th element of the cross-spectral (or covariance) matrix, $\underline{R}$, was estimated by that of the sample covariance matrix $\hat{\underline{R}}$, i.e.,

$$R_{ij} \approx \hat{R}_{ij} = s_i^* s_j + 0.001\, \varepsilon_o^2\, \delta_{ij} \qquad (1)$$

where ε_o^2 is the minimum of $|s_i|^2$, i = 1, N (N is the total number of dipoles in the receiving antenna array). The second term in (1) is added so that $\hat{\underline{R}}$ will not be singular. The column vector $\underline{v}$ represents the steering (or probing) vector whose i-th element is given by

$$v_i = \exp[j\, kz_i \sin\theta] \tag{2}$$

where $j = \sqrt{-1}$

k = wave number = $2\pi/\lambda$

z_i = distance of i-th dipole from the array origin

θ = elevation angle

The steering vector $\underline{v}$ physically represents the received signal vector corresponding to a unit plane wave arriving from elevation angle θ.

The ML spectral estimation had its genesis in the seismic array beamforming under conditions of directional interference [43]. The ML method passes undistortedly a plane wave coming from direction θ while suppressing in an optimum least-squares sense those plane waves from directions other than θ. The angular power spectrum estimated from the ML method, $P_{ML}(\theta)$, is given by

$$P_{ML}(\theta) = (\underline{v}^* \hat{\underline{R}}^{-1} \underline{v})^{-1} \tag{3}$$

The estimate (3) may be contrasted to the standard beam sum angular power estimate, $P_{BS}(\theta)$, of

$$P_{BS}(\theta) = \underline{v}^* \hat{\underline{R}}\, \underline{v} = |\underline{v}^*\, \underline{s}|^2 = |\Sigma\, s_i\, e^{-jkz_i \sin\theta}\,^2| \tag{4}$$

The conventional beamforming method, which yields the estimate (4), simply time-aligns the arrivals of wavefronts coming from the direction θ It is essentially equal to the received TRSB envelope on a TO-scan of the elevation (or flare) antenna for a uniformly weighted aperture distribution.

The use of the maximum entropy method (MEM) for high resolution spectral estimation has been justified by a variety of arguments [44, 45, 46, 47, 48, 49, 50]. For the application to our ground reflection data, the physically most meaningful argument is that the received angular power spectrum can be fitted with a finite number of poles which correspond to the multipath components arriving at the receiving antenna array.

This definition is equivalent to assuming that the signal at the n-th antenna can be represented as a linear combination of the samples on the antennas immediately above or below the given antenna. If $\underline{a}$ denotes the corresponding linear predictor coefficients which are determined from the data, the MEM angular power spectrum estimate, $P_{MEM}(\theta)$, is given by

$$P_{MEM}(\theta) = P_N \, \Delta / |V^* \, \underline{\Gamma}|^2 \qquad (5)$$

where $\underline{\Gamma} = [1, -\underline{a}]$ is the vector corresponding to the residual error in the parameter estimation procedure, P_N is estimated rms residual error and Δ is the spacing between the antennas. For the results presented here, the P_N and $\underline{a}$ were determined directly from the measured (complex) antenna outputs using the so-called Burg technique [49].

2. Ground Model

Figure 2-1 shows a terrain height profile for the ground in front of our receiving antenna array at one of the measurement sites. For the MLS multipath simulation run, the ground was physically modeled as a series of rectangular plates with their slopes coincident with the terrain height profile. As shown in Fig. 2-1, for this particular ground, the terrain profile was fitted with eight straight line segments with various slopes. These straight line segments represent the end view of the rectangular plates in the ground model. The top view of this particular ground model is also shown in Fig. 2-1.

Those ground plates which were closer to the receiving antenna array were further divided into several smaller rectangular plates in order to make the variation among the distances from the receiving antenna to various

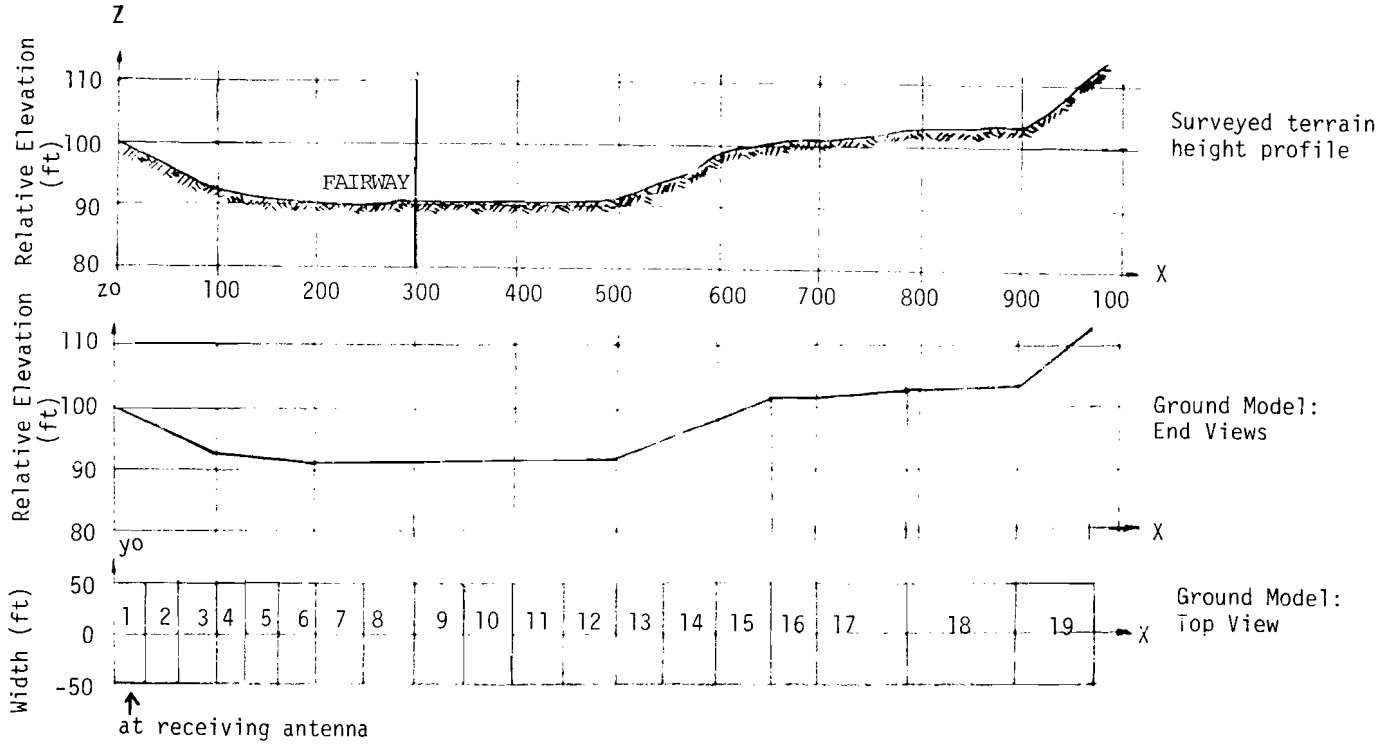

Fig.2-1. Construction of ground model from terrain survey.

points on any given rectangular plate as small as practical. This is to comply as closely as is practical with one of the assumptions made in the propagation model, that the distances from the receiver (or the transmitter) to various points on the same reflection plate are constant [29]. Thus, for a given terrain profile, the final ground model to be input to the MLS multipath simulation run usually consisted of a fairly large number of rectangular plates. For example, the final ground model for the terrain shown in Fig. 2-1 was formed by nineteen rectangular plates.

In order to accommodate these many ground plates in the MLS multipath simulation run, these ground plates were treated as tilted buidling plates because in the computer simulation program the maximum number of the reflection plates which can be handled as ground reflection is ten while the maximum number of the reflection plates which can be handled as building reflection is fifty. In practice, treating the ground plates as tilted building plates in the computer simulation should be all right, provided that:

1. we only consider the reflection ray X-O-R [29] in the building reflection calculation,

2. we only consider the specular ground reflection,

3. we use an appropriate complex dielectric constant corresponding to the type of ground involved in the field measurement. (For our measurement sites, the ground was covered with grass), and

4. the cross-tilt of the ground can be ignored, i.e., the slope of any ground plate in the direction perpendicular to the X-axis as shown in Fig. 2-1 is zero.

C. Experimental Hardware

The experimental system used in the field measurement is described in this subsection. As mentioned earlier, the existing facility from the previous PALM program [39]formed the mainbody of the current experimental system. Some modifications were made in the recording procedure of the incoming signal and several pieces of new hardware (a receiving antenna array and an Eclipse computer) were

installed. Hence, the discussion of the experimental hardware will emphasize these modifications to the existing equipment.

The equipment (Figs. 2-2 and 2-3) consists of a receiving antenna array (consisting of eleven L-band dipoles), a theodolite (to measure the true aircraft elevation angle), an electronics van, a standard ATC transponder (used as a transmitter) on board the aircraft, and a motor generator for the power supply in the field. The van contains an ATCRBS interrogator with a roof mounted broad beam horn antenna, a standard ATC transponder for equipment calibration purpose, an operator's console to monitor the measurement, a five-channel RF receiver, timing and control circuitry, equipment to digitize data and to store it on the magnetic tape for off-line processing on a general purpose computer, and an Eclipse computer with a display terminal, a copier and a tape drive for the on-site processing.

The measured data are recorded digitally on both magnetic tape and disk. The data stored includes amplitude for each of the eleven dipoles, the differential phase (in-phase and quadrature component) for ten antennas referenced to the first, theodolite bearing, range to the aircraft, meteorological data, date and time of day.

In the following, we will only describe the equipment set-up which differs from the previous FAA measurement program. For the descriptions of the original equipment, such as the RF receiver subsystem and the data processing subsystem (i.e., timing and control circuitry, equipment to digitize and to record data), please refer to the technical note published for that program [39]. Also, we will discuss procedures involved in a typical measurement mission and equipment calibration.

1. Equipment Set-Up

The experimental configuration for the measurement missions is shown in Fig. 2-3. The standard ATC transponder on board the aircraft is a Narco vacuum tube beacon transponder which has been wired to reply to B-mode interrogations at 1090 MHz. This permits us to avoid synchronous garble and to have improved

Fig.2-2. Experimental system for ground reflection data collection.

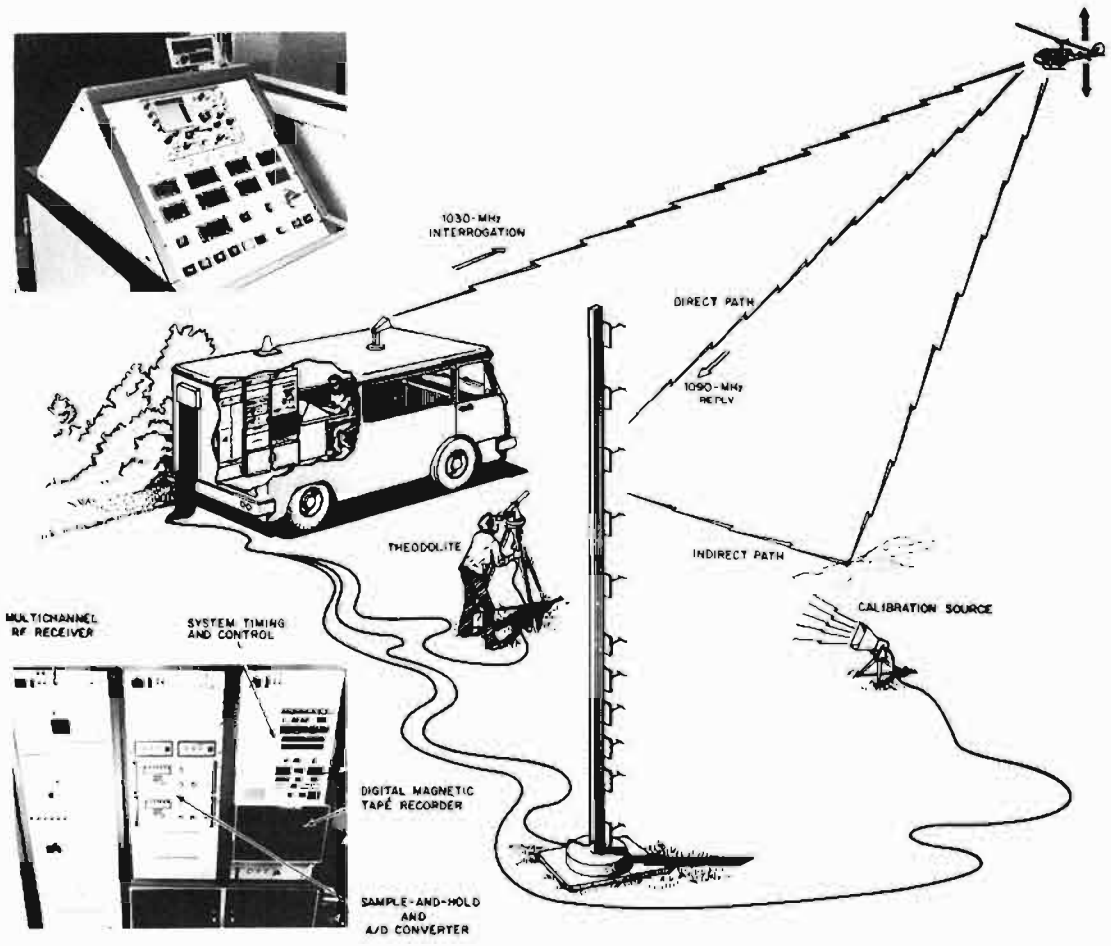

Fig.2-3. Terrain multipath experimental configuration.

transmitter frequency stability.* The receiving antenna array consists of eleven L-band vertical dipole antennas with reflectors mounted on a 30-foot vertical mast. The arrangement of the dipoles in the array is shown in Fig. 2-4. Antennas #1, #2, #3, #4, #5, #6, #7, #8, and #9 are equally spaced with 3.24λ separation between the neighboring antennas. This results in a linear array of 26λ height. Antennas #2, #2.5, #3, #3.5, and #4 are also equally spaced; however, the spacing between two neighboring antennas is only 1.62λ which yields total array height of 6.5λ. For the results presented in the following subsection D , the measured data were obtained from nine equally-spaced dipoles of the large array with aperture of 26λ. This large array gave much better resolution for the angular power spectrum. The small array of 6.5λ aperture was for other data collection purposes. Typical E-plane and H-plane radiation patterns measured at 1090 MHz for the dipole antenna used in the receiving antenna array are shown in Figs. 2-5 and 2-6, respectively. These eleven dipoles antennas are fairly identical, in terms of the voltage standing wave ratio (VSWR), the 3 dB beamwidth in the E-plane and H-plane pattern (at 1090 MHz) and the antenna gain. Table 2-1 presents the measured values of the VSWR, 3 dB beamwidth and the gain for these eleven dipole antennas.

Since the RF receiver only has five channels, the recordings of the incoming replies at the eleven antennas are grouped into three modes, A, B, and C. As shown in Fig. 2-4, Mode A records the output of antennas #9, #7, #5, #3 and #1 through channels #1, #2, #3, #4, and #5, respectively; Mode B records the output of antennas #8, #6, #4, #2, and #1 through channels #1, #2, #3, #4 and #5, respectively; and Mode C records the output of antennas #3.5, #2.5, #4, #2, and #3 through channels #1, #2, #3, #4, and #5, respectively. In the normal measurement mode, measurements are made on successive replies in the order ABC ABC ABC A. Since the replies are normally 0.1 seconds apart (10 Hz interrogation rate), the aircraft position and multipath change are negligible during the time required to measure on all three modes.

---

*By virtue of the quartz crystal frequency reference in the NARCO transponder.

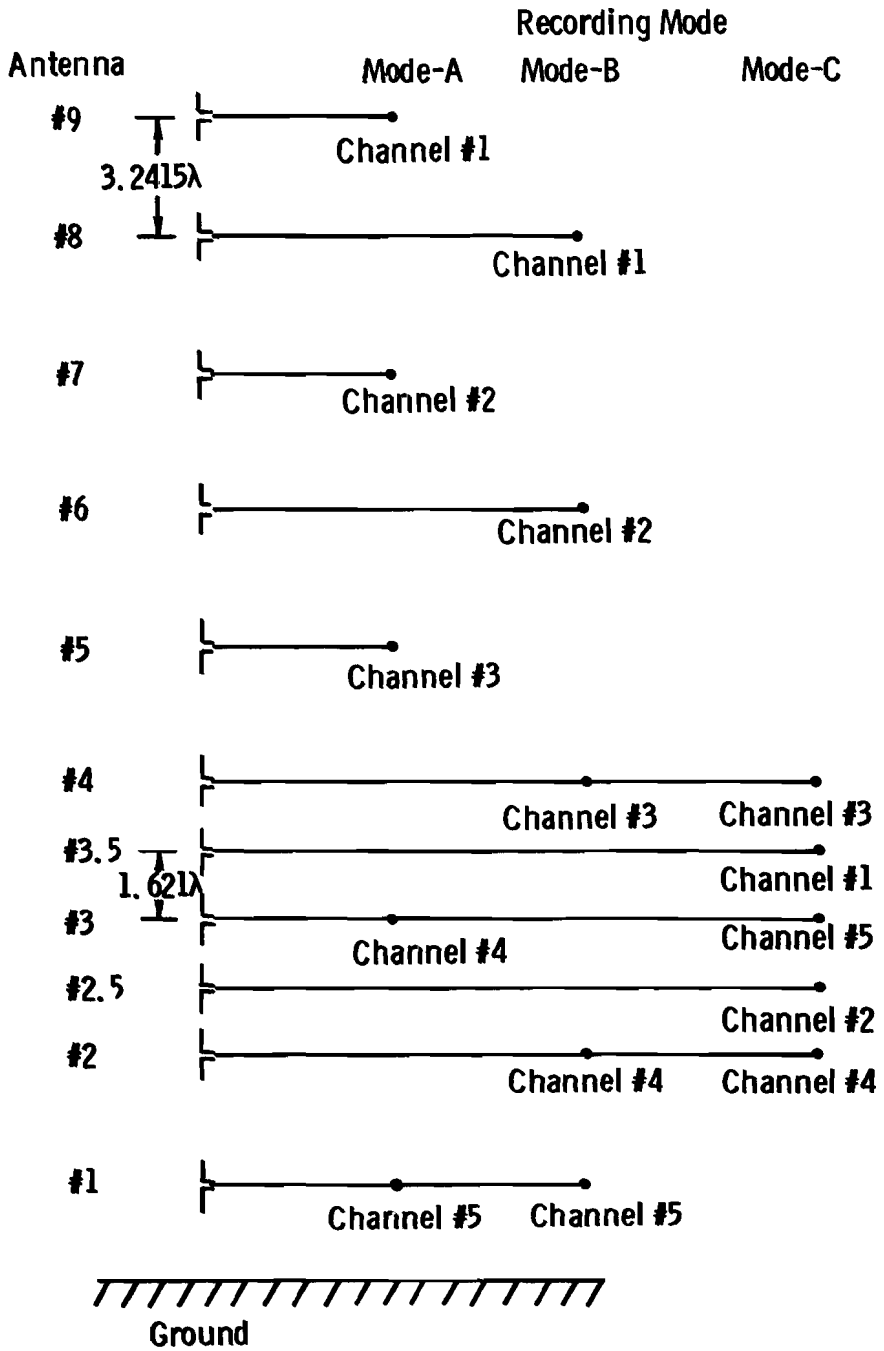

Fig.2-4. Relation of dipole antennas in the array to recording channels.

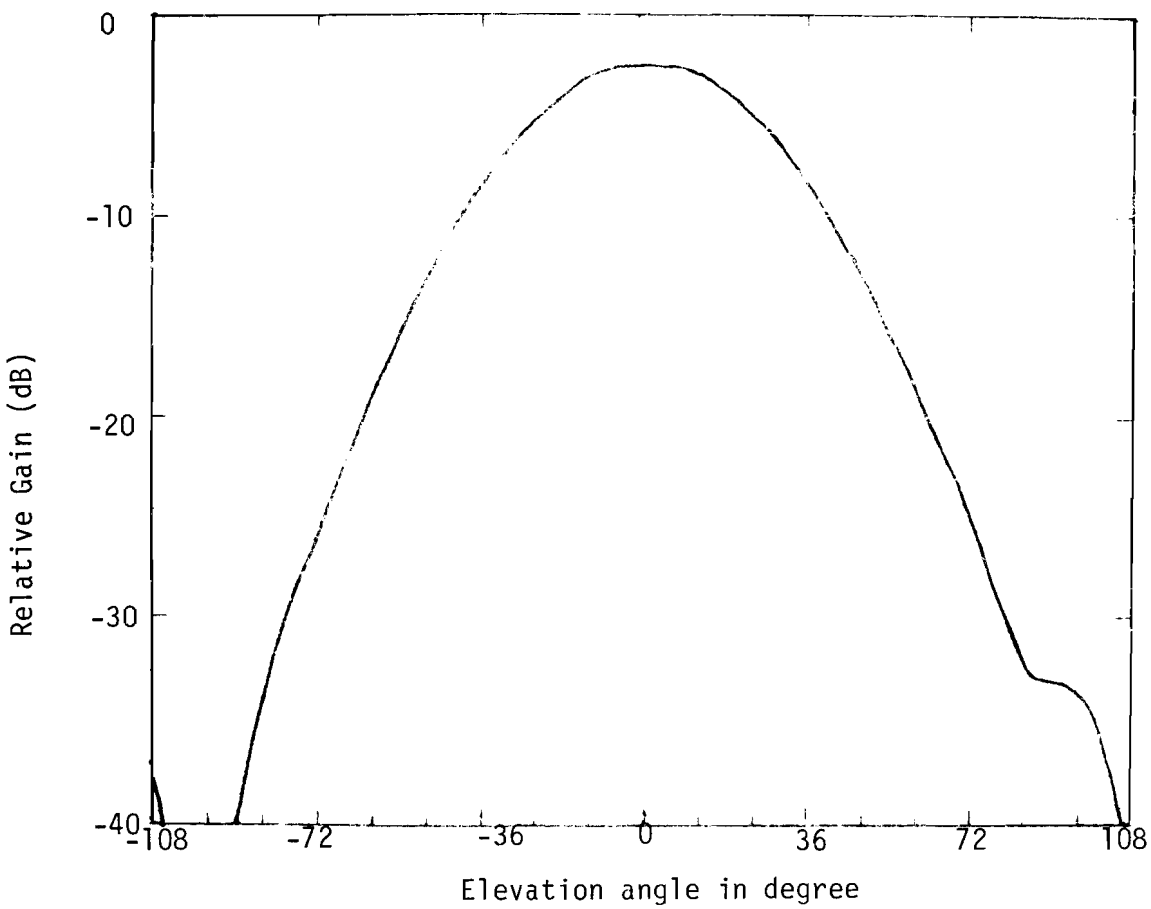

Fig.2-5. E-plane radiation pattern.

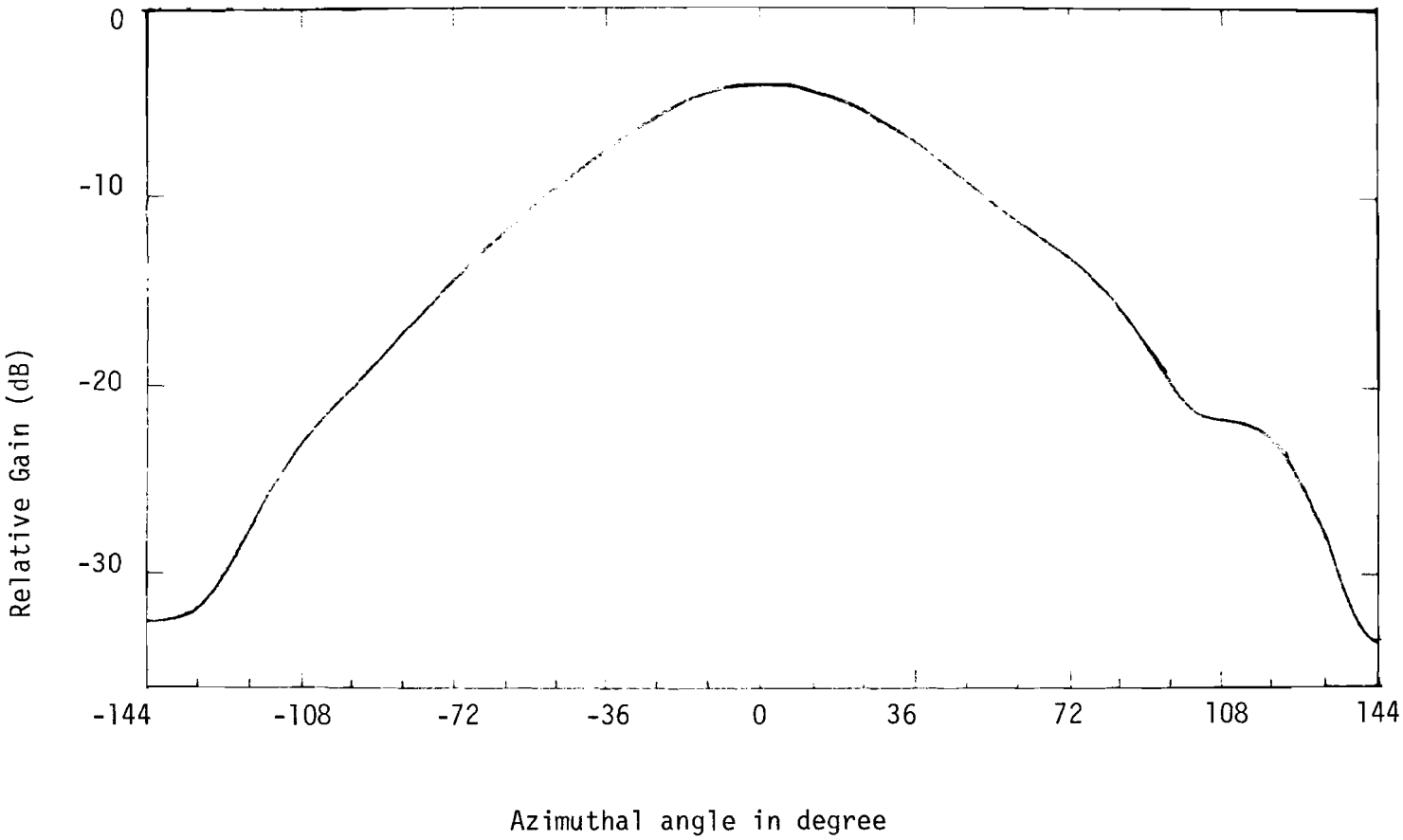

Fig. 2-6. H-plane radiation pattern.

TABLE 2-1

CHARACTERISTICS OF THE DIPOLE ANTENNAS IN THE RECEIVING ANTENNA ARRAY

Antenna	VSWR @ 1.090 MHz	3dB BEAMWIDTH H-plane	3dB BEAMWIDTH E-plane	Gain H-plane	Gain E-plane
9	1.55:1	70°	51°	0*dB	0*dB
8	1.58	68	51	0	-.2
7	1.53	70	51	-.1	-1.5
6	1.53	71	52	0	-.3
5	1.41	69	53	+.1	-.7
4	1.52	71	51	-.1	-.5
3.5	1.59	69	51	0	-.6
3	1.45	70	52	-.1	-1.2
2.5	1.57	69	51	-.1	-1.4
2	1.59	68	52	0	-1.3
1	1.51	70	51	0	0

*used as reference

By the "two identical antenna" method of measuring gain, the absolute gain of antenna 8 or 6 is 8.8 dB

The calibration radiator is for the purpose of external calibration of each dipole antenna together with its connecting cable. At the present time, we use two thin-wire dipoles as calibration radiators. One thin-wire dipole is closely coupled to the reference antenna (antenna #1 for Mode A and Mode B, and antenna #3 for Mode C) and the other is closely coupled to the antenna which is to be calibrated as shown in Fig. 2-7.

The Eclipse computer, together with a display terminal and a tape drive, serves the following purposes in a measurement mission: (1) monitoring the equipment calibration to see if all five RF channels are functioning normally, (2) recording the measured data on its magnetic disk and (3) performing the on-site processing of the measured data right after each measurement to see if the measurement was properly made.

2. Measurement Procedure

For a typical field measurement mission, the mission procedure consists of the following steps:

a. Equipment set-up, checking and calibration before the aircraft flight:

This includes the internal amplitude and phase calibration for the five-channel RF receiver, the external amplitude and phase calibration for each individual dipole antenna together with its connecting cable, and the theodolite calibration. The calibration data are recorded in calibration files on both disk and magnetic tapes in addition to the displays on the CRT screen.

b. The aircraft flights:

For each aircraft flight, the aircraft transponder replies received at each dipole antenna and the theodolite tracking are digitally recorded in data files on both disk and magnetic tape. The theodolite electric readout is checked before and after each flight to insure that the theodolite had not been disturbed during the flight. The Eclipse computer

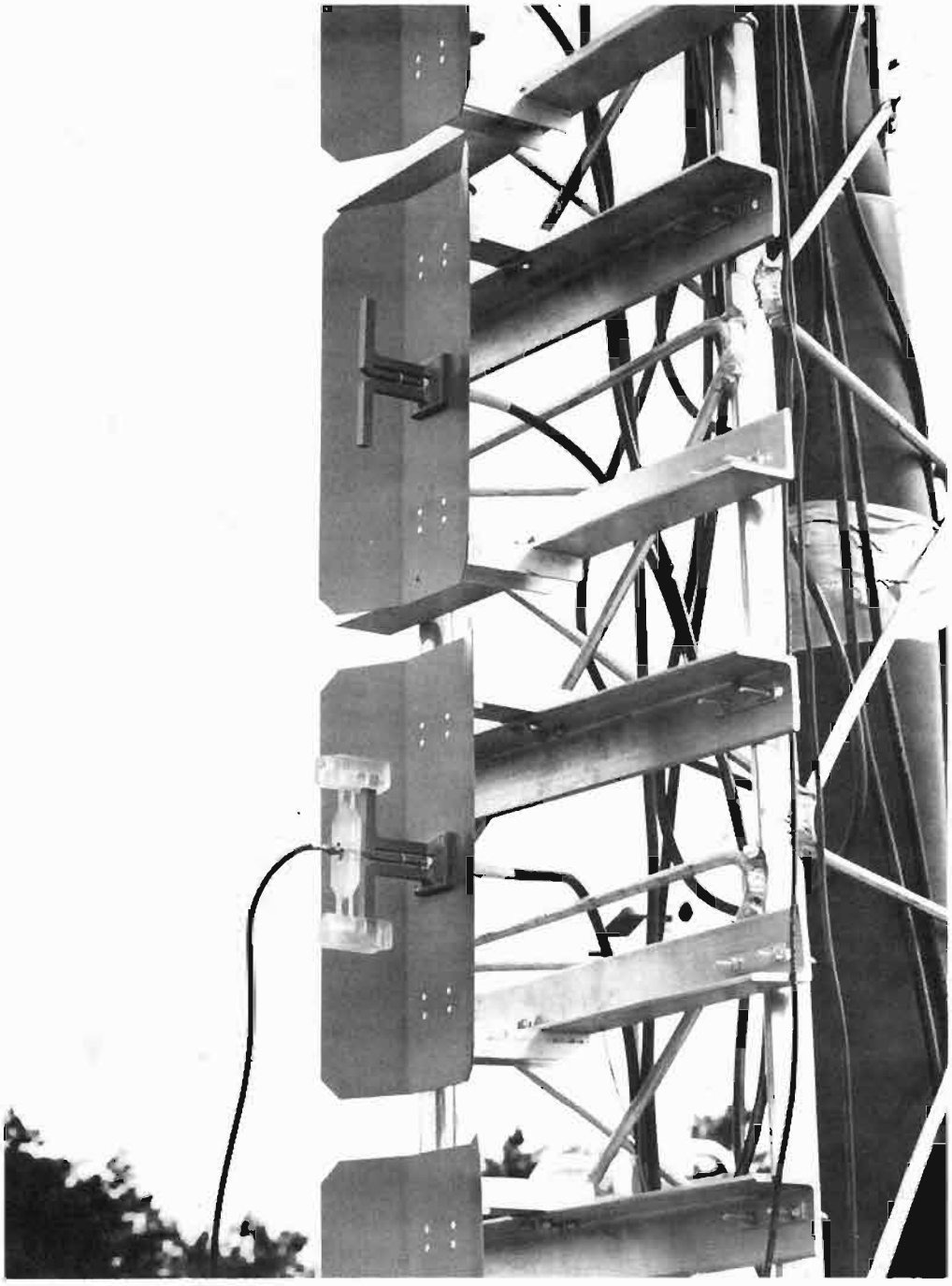

Fig.2-7. Coupling mechanism for external calibration.

will do the on-site processing of the measured flight data right after each flight, if necessary.

c. Equipment calibration after the aircraft flight:

This includes the internal amplitude and phase calibration for the five-channel RF receiver. This post-mission calibration is to check if there is any drift in the characteristics of the RF channels during the mission.

The activities during the mission are recorded on audio tape for the reconstruction of the mission log later on. After the mission, the calibration and flight data recorded on the magnetic tape are processed on the Lincoln IBM 370 computer.

3. Equipment Calibration

As described in subsection C-2, the internal calibration was made before and after each measurement mission. Also, the external calibration was made for each mission. These equipment calibration data were to be used in the construction of the look-up tables for the processing of the measured flight data.

a. Internal calibration

The internal calibration is to calibrate the five RF receiver channels. This includes amplitude and phase calibration.

The internal amplitude calibration is accomplished by internally feeding the output of the transponder inside the van to the receiver IF and recording the output of A/D converter in digital counts for transponder attenuations from 0 to -80 dB. A typical set of internal amplitude look-up curves, made from the internal amplitude calibration, is shown in Fig. 2-8. The amplitude characteristic is seen to be logarithmic over a dynamic rage of approximately 60 dB with a slope of $\approx$ 0.7 dB/digital count (this yield a 0.35 dB peak quantization error and a 0.2 dB rms quantization error). Each point

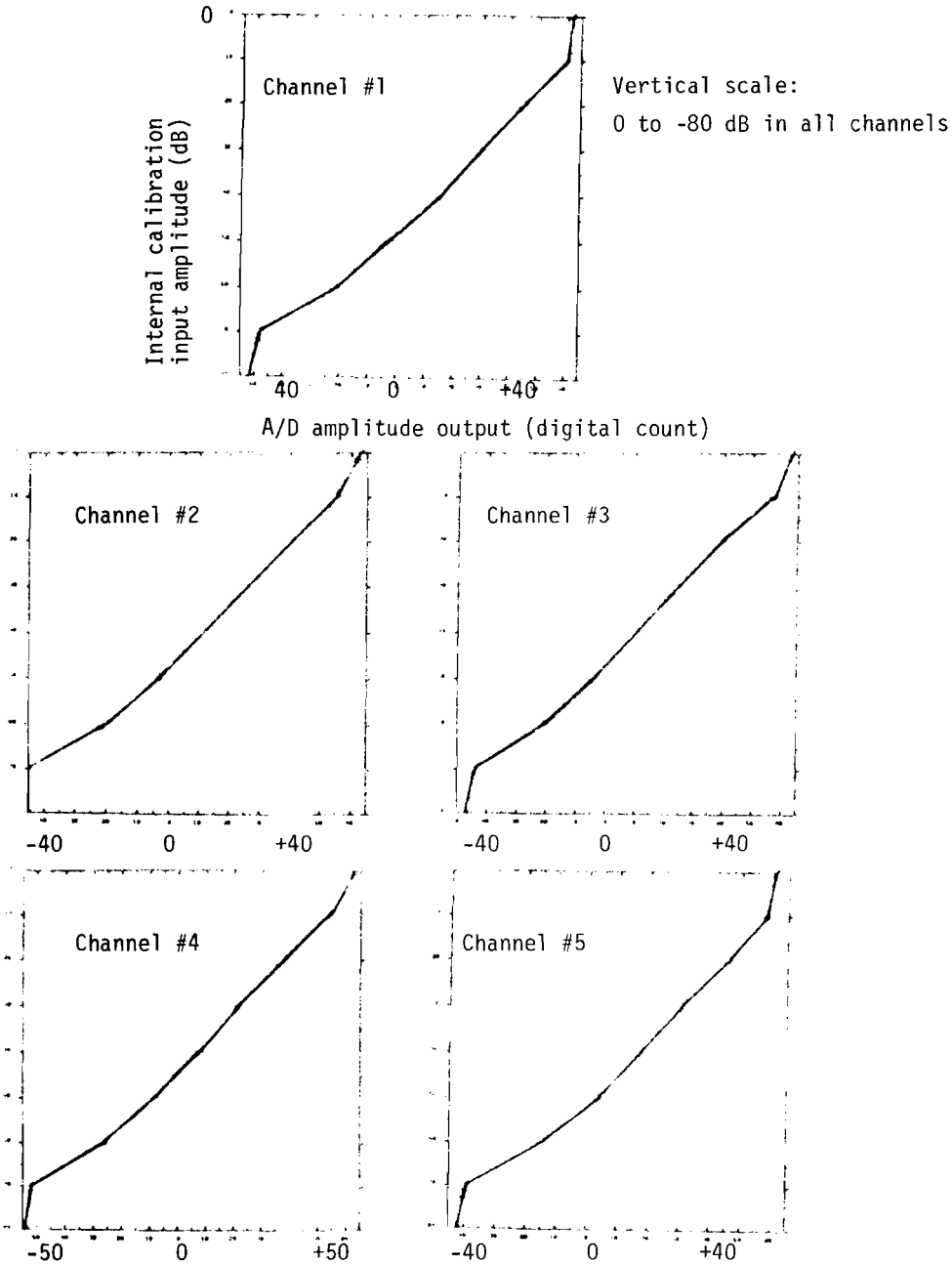

Fig.2-8. RF receiver channel amplitude output characteristics.

The internal phase calibration is accomplished by internally feeding the output of the transponder inside the van to the IF receiver and recording the phase detector output data in A/D counts in terms of the in-phase (I) and quadrature (Q) components. The input to the IF receiver is varied from 0° to 360° in 32 steps, by means of a digital phase shifter. In the internal phase calibration, channel #5 was used as a reference channel. The digital phase shifter was calibrated on a network analyzer. Precise phase values (to 0.05°) for each digital setting were stored in a look-up table. A typical set of internal phase look-up curves, made from the measured I and Q, is shown in Fig. 2-9. The quantization errors for the phase measurement are 0.5° (peak error) and 0.3° (rms). Each point in Fig. 2-9 represents the average of measurements on 50 pulses. The standard deviation of these measurements is approximately 0.4 digital counts.

From examining these calibration data, we found that the RF receiver was quite stable during any given measurement mission. The amplitude look-up curves for five channels were all very linear from -60 dB to -10 dB and the phase look-up curves for all four channels were fairly linear between 0° and 360°.

b. External calibration

As described in subsection C-1, two identical thin-wire dipoles are used as the external calibration radiators. The output from the transponder inside the van is equally split to feed two calibration thin-wire dipoles. The calibration is carried out in two runs: (1) calibration for each antenna in Mode A and Mode B with one calibration thin-wire dipole coupled to reference antenna #1, and (2) calibration for each antenna in Mode C with one calibration thin-wire dipole coupled to reference antenna #3. The external phase calibration is obtained for each antenna together with its connecting cable in terms of I and Q component from the phase detector output. The "antenna lag" of each antenna* relative to the reference antenna is then calculated from these I and Q values. The external amplitude calibration is also obtained by recording A/D converter amplitude output for the antenna under calibration and for the reference antenna.

---

*i.e., the phase difference due to cable length difference and/or front end amplifier phase shift.

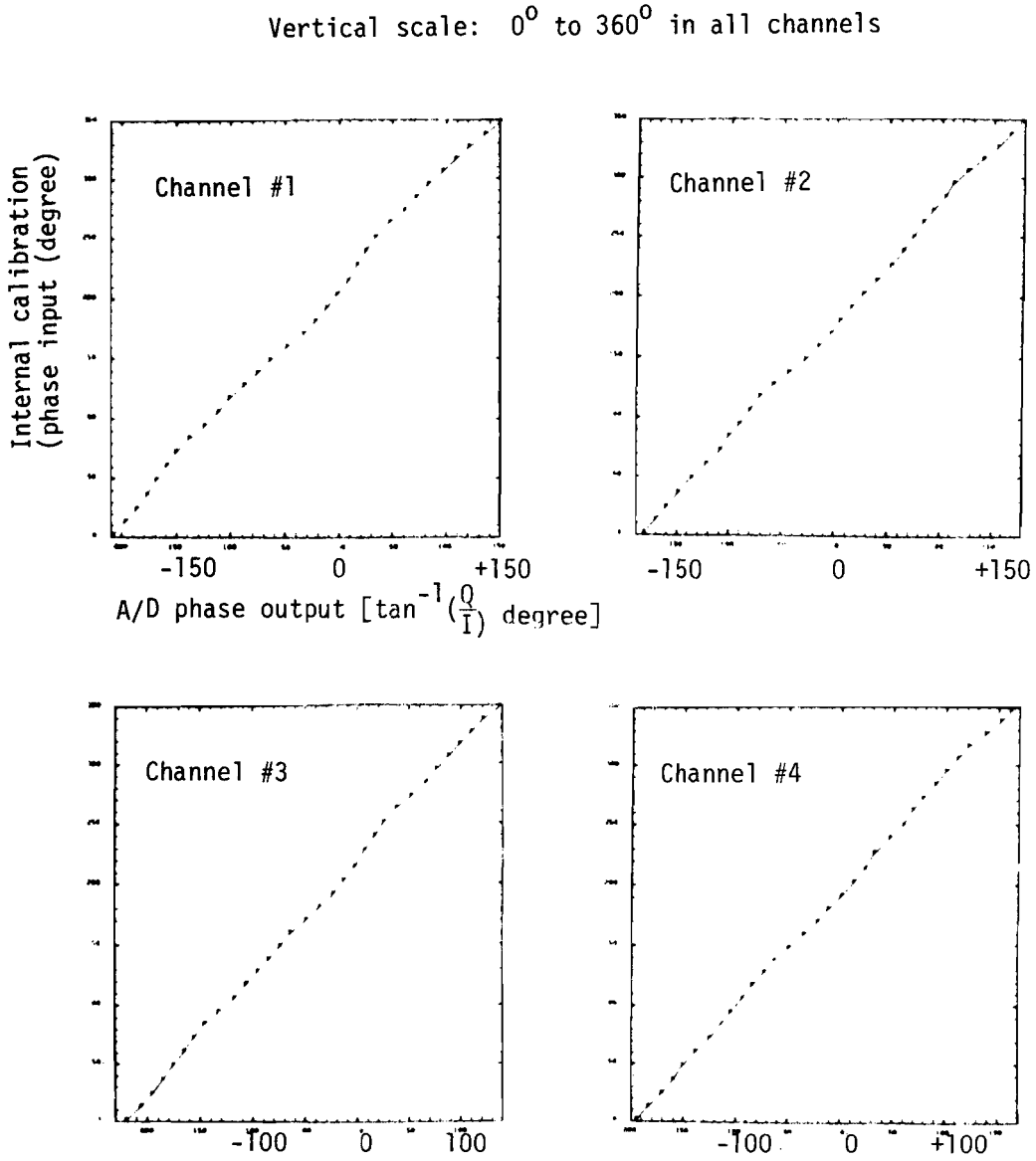

Fig.2-9. RF receiver channel phase output characteristics: channel #5 as reference.

In addition to the external calibration taken at each measurement mission using the above mentioned method, a special measurement mission was conducted at the Antenna Test Range of Lincoln Laboratory to obtain external calibration data using a known source in the far field to illuminate all eleven dipole antennas at the same time. At the Antenna Test Range, the receiving antenna array was laid sideways on the ground. The eleven dipole antennas became a horizontal array and were simultaneously illuminated by the radiation from an L-band dish at 2000 feet away. This arrangement of the antenna array ensured that the external calibration of each dipole antenna was made under the identical environment. The external calibration made at the Antenna Test Range indicated that there was almost no amplitude variation amoung the 11 dipoles. Also, the calculated antenna lag of each dipole together with its connecting cable from this external calibration was compared and validated with that taken at several measurement missions in the field.

D. Experiment Results

In this subsection, we will first briefly describe the field measurements conducted for gathering the ground reflection data and the terrain conditions around various measurement sites at Hanscom AFB and Fort Devens. The data reduction procedure involved in processing the filed measured data and in obtainning the MLS multipath simulation results will also be described. The data analysis results will then be presented and the comparison between the field measurement results and the MLS computer simulation predicted results will be made in terms of the angular power spectrum.

1. Measurements at Hanscom AFB and Fort Devens

a. Hanscom AFB

Figure 2-10 shows a simple map of the measurement site at Hanscom AFB. Also shown in this map is the terrain height profile along one of the radial lines from the receiving antenna array. The ground from the receiving antenna down to the overrun area is fairly flat, with a slight downward slope of 1.5° in front of the receiving antenna. Figure 2-11 shows a photograph taken at the receiving antenna toward the overrun area. The ground mostly was covered with grass of varying heights. Terrain profile survey was made along those radial lines, as shown in Fig. 2-10.

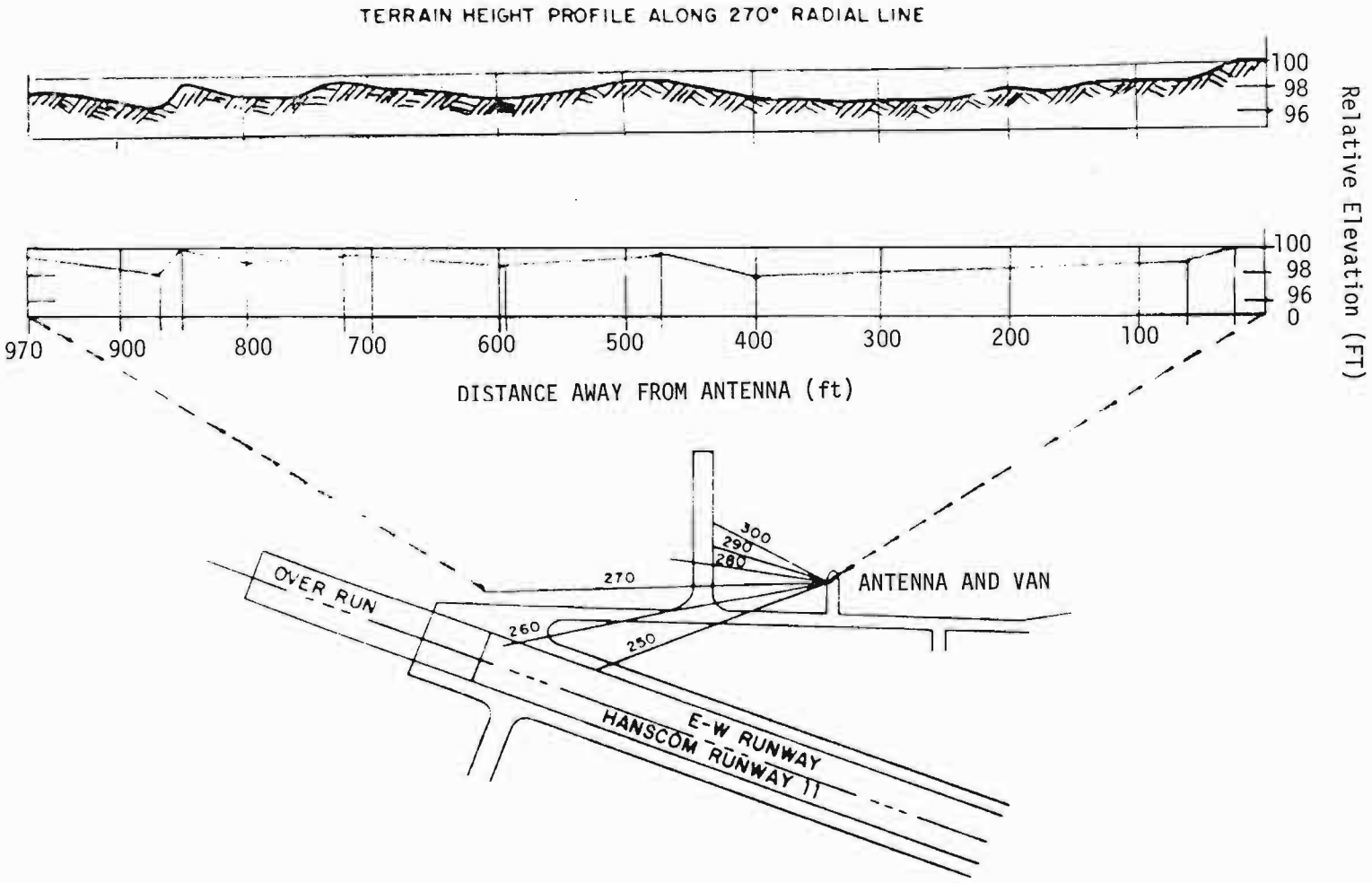

Fig.2-10. Measurement site at Hanscom Air Force Base.

Fig.2-11. Hanscom Air Force Base: ground in front of the receiving antenna towards overrun area.

Measurements were made with a single engine aircraft and a helicopter. For the single engine aircraft, measurements were taken from two basic flight profiles: (1) over-head flight along extended runway centerline (Hanscom runway 11 along 290°) with a change in heading to 277° at the middle marker at various constant altitudes and (2) flight along a constant circular arc (radius ≈ 4 nmi) at a constant elevation angle ($\theta \approx 4°$). The elevation angles of the aircraft for these flights ranged from 1° to 9°. For the helicopter, the flight patterns were straight up and down at the overrun area (range ≈ 0.5 nmi) and at a distance of about 3 nmi. The elevation angles range from 0° to 23°.

The earlier measurements at Hanscom AFB with the single engine aircraft were mostly for the purpose of checking out the equipment and computer programs. The measured data used for the analysis were mostly from the helicopter flights at the overrun area along the 270° radial line. Consequently, the ground model for the MLS multipath simulation runs was made from the terrain profile along the 270° radial line as shown in Fig. 2-10.

b. Fort Devens

Measurements were made at two areas in Fort Devens, namely the golf course and the drop zone. Fig. 2-12 shows a map of the measurement site at the golf course, six measurement points along three radial lines from the receving antenna array were chosen, covering a 35° sector. The terrain height profile survey was made along these three radial lines. Figs. 2-13 through 2-15 present the terrain height profiles along these three radial lines, together with the corresponding ground models used in the MLS multipath simulation runs. In general, the ground in front of the receiving antenna array has a noticeable downward sloping, followed by an upward sloping. The ground was uniformly covered by short grass, as shown in Fig. 2-16 which is a photograph taken at the receving antenna along the radial line O-B. Measurements at the golf course were made at two ragnes: the measurement points A, B, and C at 0.6 nmi and the measurement points D, E, and F at 1.5 nmi.

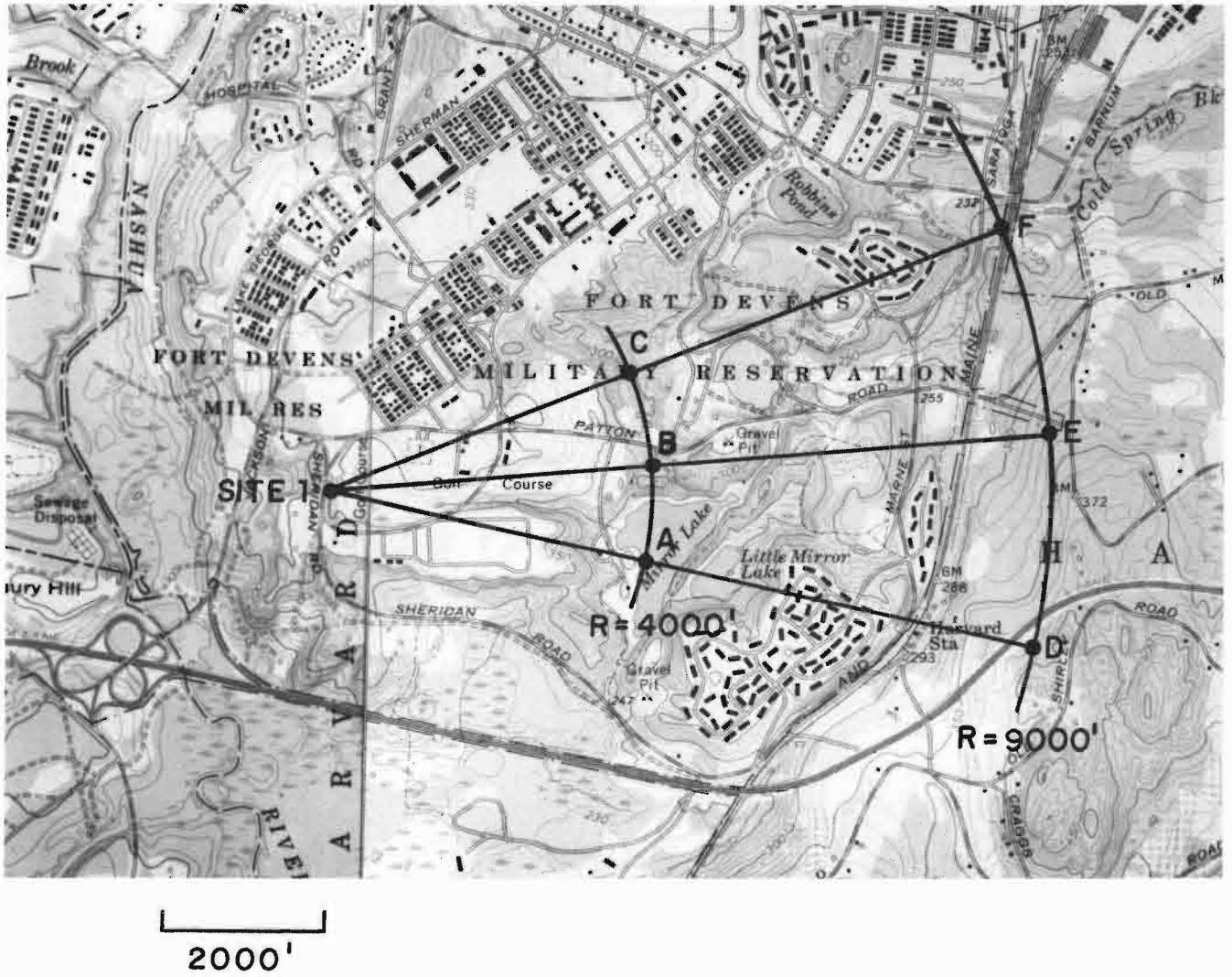

Fig. 2-12. Measurement site at golf course at Fort Devens.

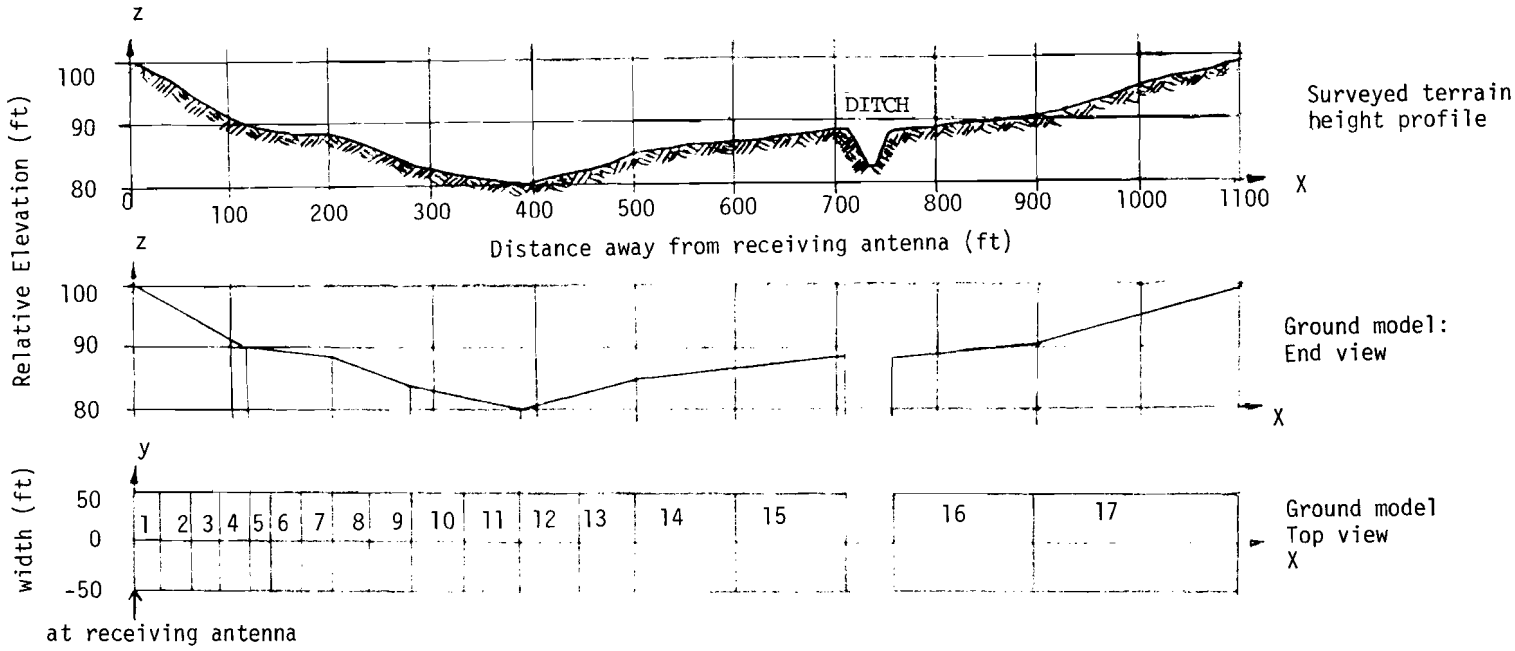

Fig.2-13. Terrain height profile at golf course of Fort Devens: along radial line O-A.

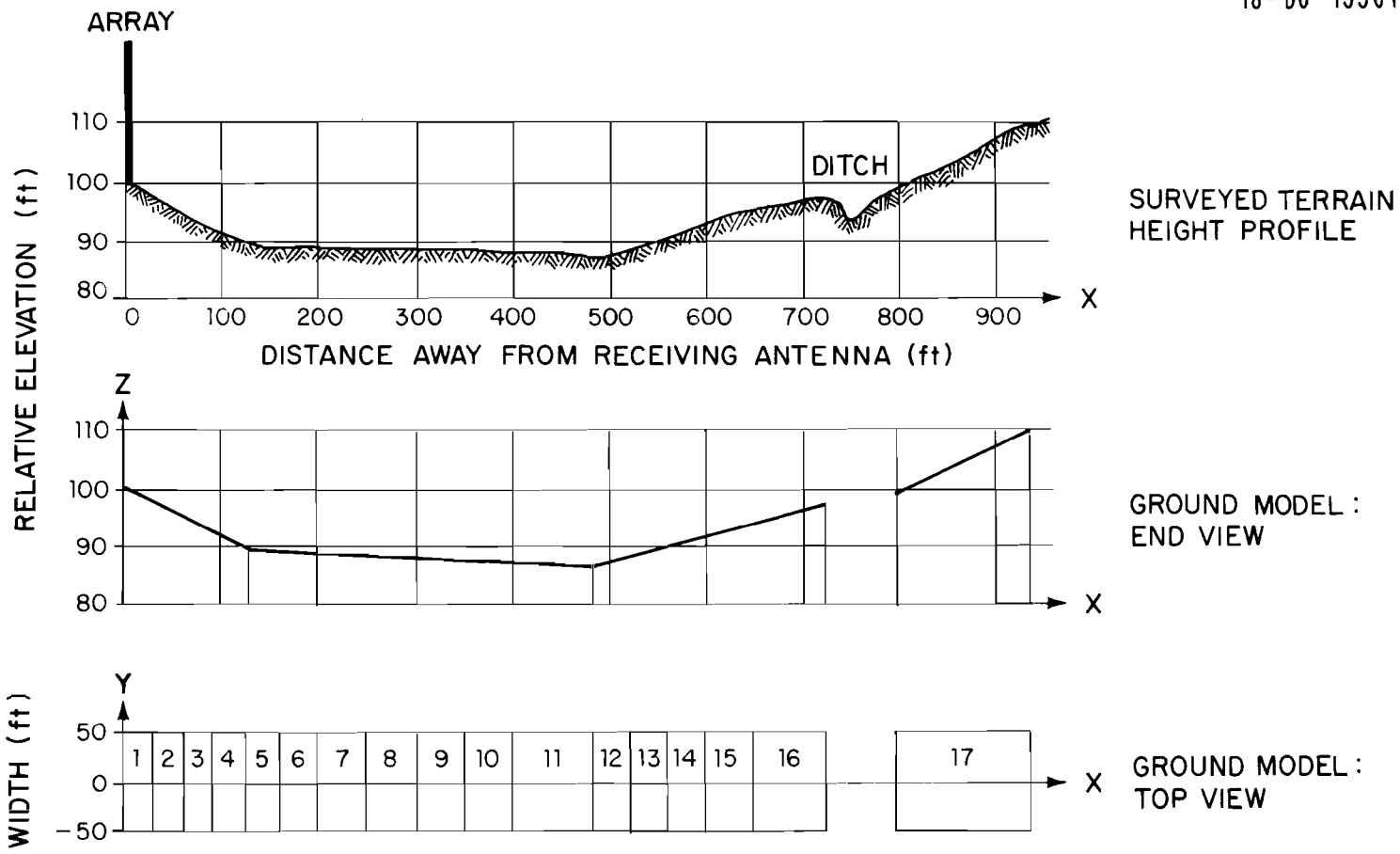

Fig.2-14. Terrain height profile at golf course of Fort Devens: along radial line O-B.

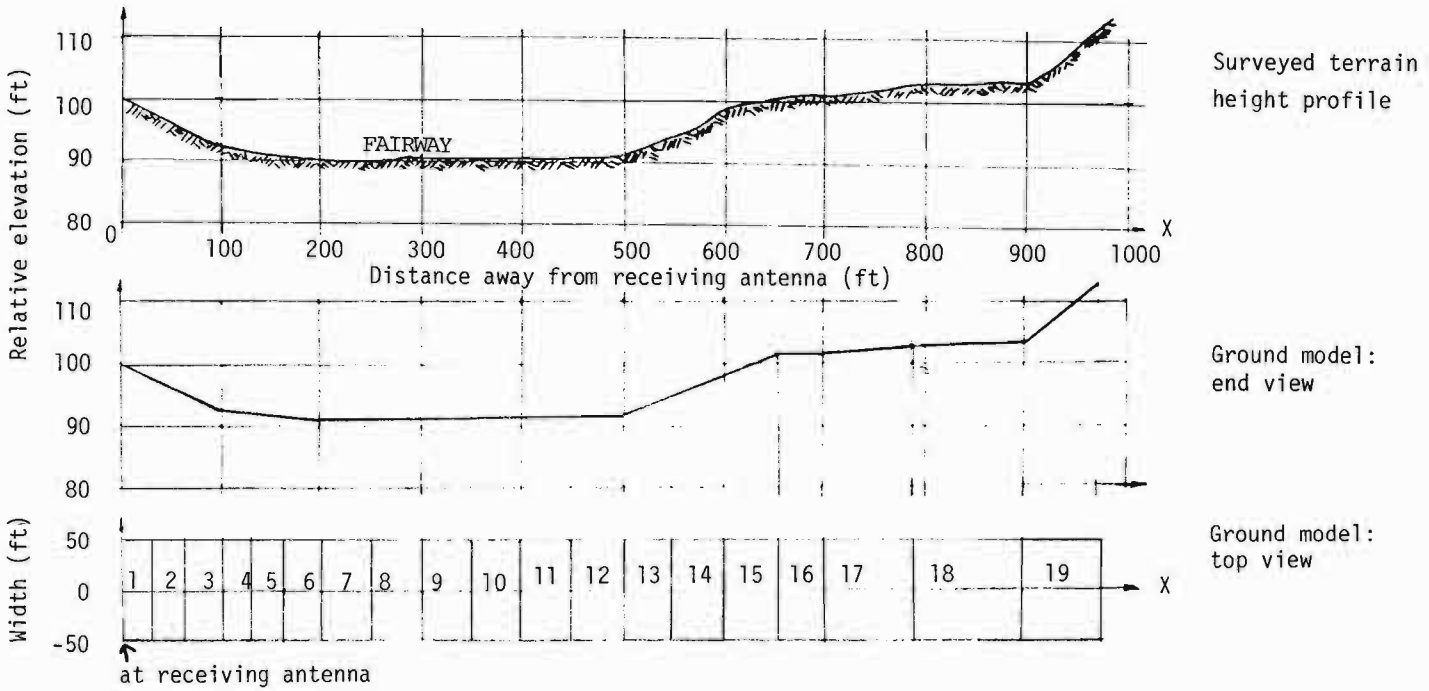

Fig.2-15. Terrain height profile at golf course of Fort Devens: along radial line O-C.

Fig. 2-16. Golf course at Fort Devans: ground in front of the receiving antenna along radial line O-B.

Figure 2-17 shows a similar map of the measurement site at the drop zone. Seven measurement points were chosen along four radial lines from the receiving antenna, covering a 180° sector. To date, measurements were made for two ranges (0.5 nmi and 1.6 nmi) at points A, B, C, and D in the northeastern sector. A terrain height profile survey has not yet been done for the drop zone. To illustrate the terrain condition around this measurement site, Fig. 2-18 shows a photograph taken at the receiving antenna along the radial line O-A. It can be seen that the ground in front of the receiving antenna slopes downward slightly to the foot of a small hill whose summit is about 0.4 nmi from the receiving antenna with an elevation of 135 feet relative to the ground at the receiving antenna. The ground was covered by grass and a number of small shrubs.

All measurements at Fort Devens were taken with the helicopter. The flight paths were all straight up and down, covering the elevation from the line of sight to about 8°.

2. Data Reduction Procedure

The procedure involved in processing the field measured data is shown as a block diagram in Fig. 2-19. Also shown in this figure is the corresponding procedure in obtaining the MLS computer simulation results to be compared with the field measurement results.

The measured I and Q values recorded on magnetic tape or disk for each dipole antenna are subjected to phase detector and antenna lag correction using the appropriate phase look-up tables obtained from equipment phase calibration as described in subsection C. This yields the phases of the incoming signal at the locations of nine equally-spaced dipole antennas in the receiving antenna array. The measured amplitude for each antenna is also corrected using the appropriate amplitude look-up tables obtained from equipment amplitude calibration to yield the corresponding amplitude of the incoming signal at that antenna. These corrected phases and amplitudes, representing the incoming signal waveform sampled by the receiving antenna array, are used to obtain angular power spectral estimates of the incoming signal from various spectral estimation methods described in subsection B, namely, conventional beamforming, the maximum likelihood estimate, and the maximum entropy estimate.

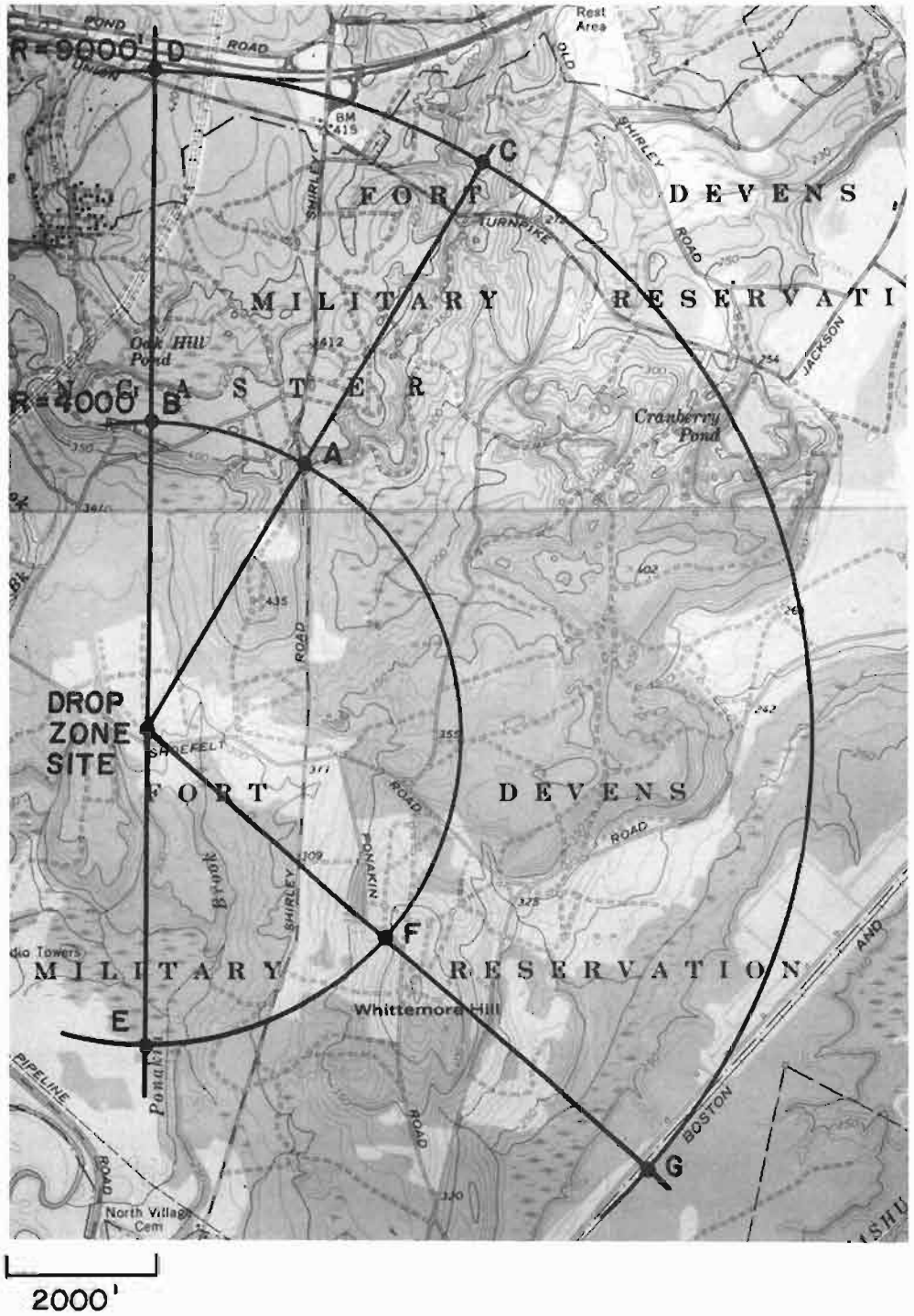

Fig. 2-17. Measurement site at drop zone of Fort Devens.

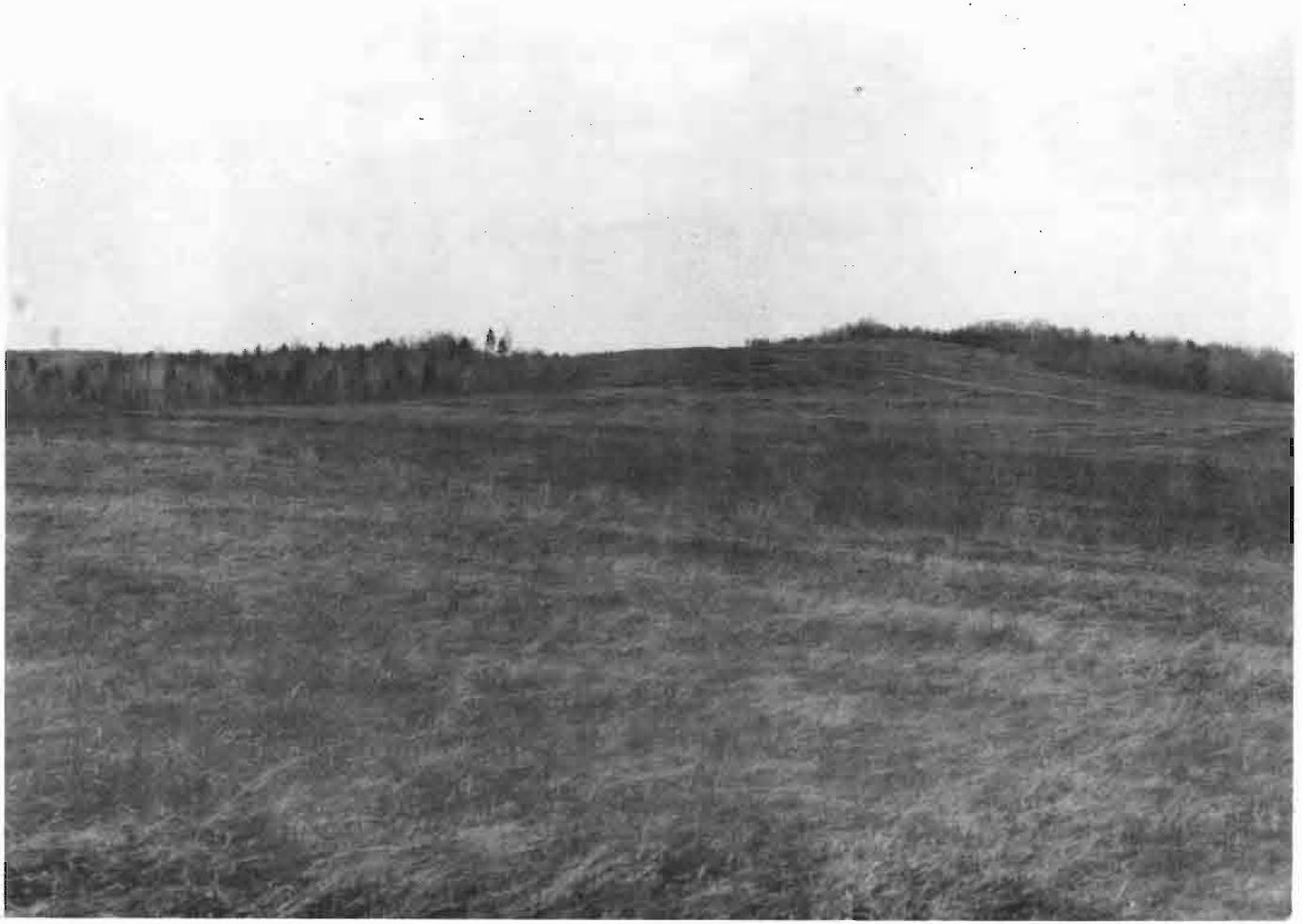

Fig.2-18. Drop zone at Fort Devens: ground in front of the receiving antenna along radial line O-A.

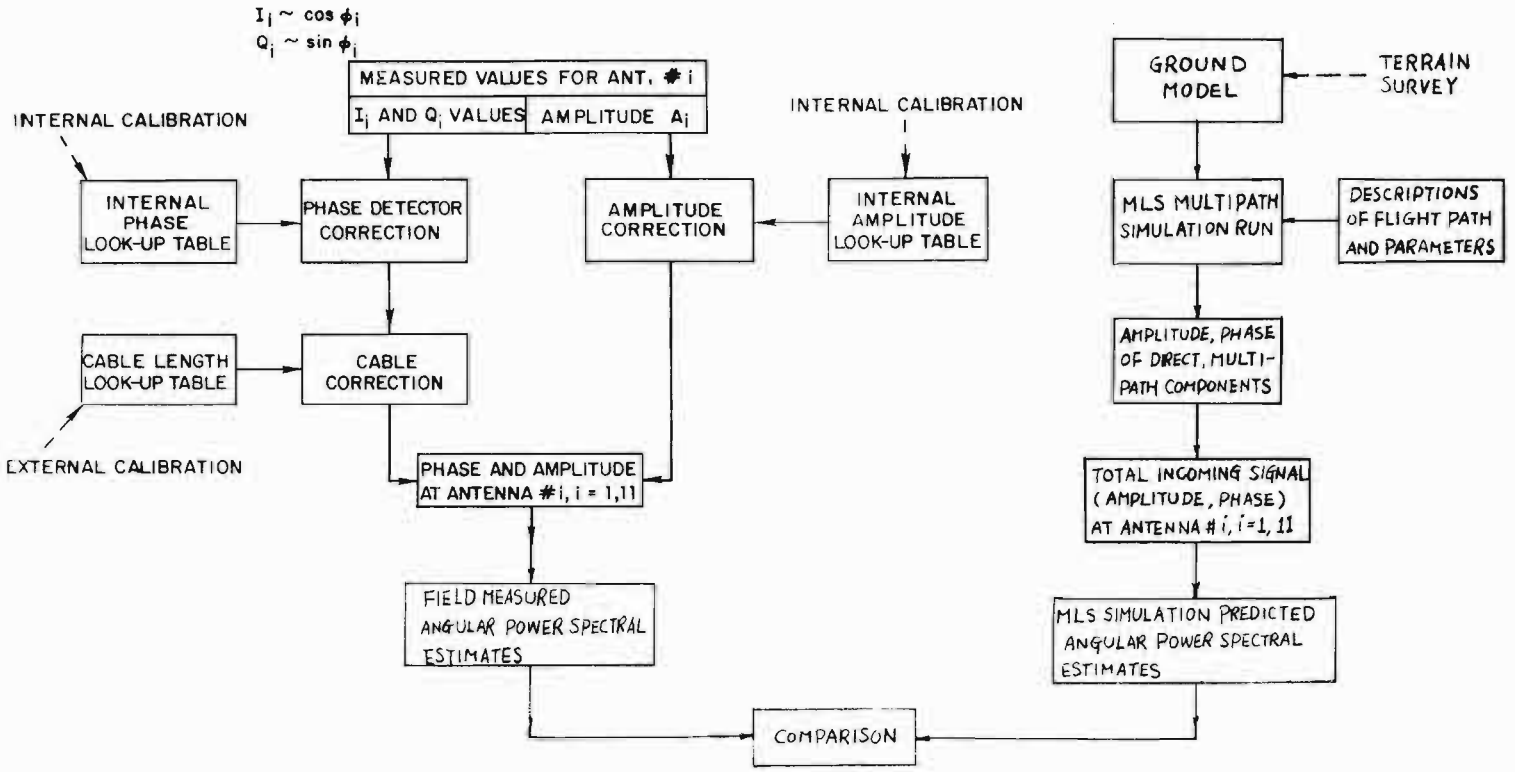

Fig. 2-19. Data reduction procedure.

The process of obtaining the corresponding angular power spectral estimates from the MLS computer simulation is depicted in Fig. 2-19. Appropriate ground model (obtained from the terrain height profile survey as described in subsection B) and flight path descriptions are supplied to the MLS multipath simulation run. The output of the MLS multipath simulation run yields the predicted amplitudes and phases of various multipath components relative to the direct signal and their corresponding arrival angles at the phase center of the receiving antenna array. The total incoming signal at each dipole antenna in the receiving antenna array is constructed from these predicted multipath components, in addition to the direct signal, based on the assumption of multiple plane wave arrivals. The predicted amplitudes and phases of the total incoming signal for the nine equally-spaced dipole antennas are then used to obtain the angular power spectra.

3. Data Analysis Results

Data analysis results presented in this subsection were obtained from the field measured data and the corresponding MLS multipath simulation runs for the measurements taken at Hanscom AFB runway 11 overrun area and at the golf course of Fort Devens. The results for the measurements at the drop zone of Fort Devens were not given here, because the terrain height profile survey for the drop zone has not yet been used to generate the MLS computer simulation results for comparison.

Comparison between the field measurement results and the corresponding MLS computer simulation predicted results was made on the following features: (1) the general appearances of all three kinds of angular power spectra (i.e., beamsum (BS), maximum likelihood (ML) and maximum entropy (ME) spectra) and (2) the number, the arrival elevation angles, and the multipath levels (i.e., M/D ratios) of the multipath arrivals indicated in the angular power spectra. The second feature was estimated from the ME angular power spectrum, since it offered higher resolution. The M/D ratios of the multipath signals to the direct signal were estimated from the spectral peaks and the widths of those spectral peaks which corresponded to the multipath and the direct signals, since it was shown that the area under a ME spectral peak provided a good estimate of the power in the corresponding component [46].

In making the comparison, one cannot expect the detailed spectral shape (e.g., sidelobe structure, background spectrum level) to be identical since several field measurement factors have been ignored. These factors include:

(1) instrumental errors such as quantization errors and front end noise
(2) diffuse scattering from hills at off-azimuth angles
(3) deviations of the actual flight paths from the assumed path*
(4) not considering tilts of the ground plates in the cross range direction
(5) ignoring near field effects in computing the individual antenna outputs

Keeping these factors in mind, in general, the MLS computer simulation results could explain quite well the features observed in the field measurement results, such as the number of the ground reflection components, their arrival angles and M/D ratios.

In the following, the results from the comparison between the field measurement results and the corresponding MLS computer simulation predicted results will be discussed and some representative angular power spectral esimates will be given. To facilitate the comparison, in each figure shown below, the angular power spectral estimates from the field measured data are shown at the top and those predicted by the MLS computer simulation are given at the bottom. The BS, ML, and ME spectrum are plotted with the symbols 'B', 'O', and 'X', respectively. The true elevation angle of the direct signal (for the field measurement results, this is the theodolite tracking angle) is indicated by a vertical line with the symbol 'C'.

Certain aspects of the measured multipath environment are of interest above and beyond the agreement with the current propagation model. One of the important issues is whether the reflections are specular in nature as opposed to being diffuse. Specular reflections act as image sources of energy emanating from the specular reflection point, which in turn gives rise to an impulse-like peak in the received angular power spectrum. When the reflecting surface is electrically rough, an extended area may have small facets which individually yield very low specular reflections.

*Only the aircraft elevation and range are obtained in the measurement recording.

superposition of the many small reflections acts as an extended source of radiation with an amplitude best characterized as a sample function from a random process. The corresponding angular power spectrum is expected to have one or more wide peaks corresponding to the extended source angles.

One of the important issues under study in the field measurement program is the relative levels of the diffuse and specular reflections and, in particular, the diffuse reflection levels near the radio horizon. Theoretical studies [51] have suggested that there is a "bright" diffuse reflection spot near the radio horizon which could be an important limiting factor in system performance since the corresponding separation angle between direct and reflected signals is approximately 1/2 that of the nominal specular reflection over flat terrain.

Another factor which can yield reduced separation angles is upsloping terrain. It can be shown that the separation angle over terrain which is upsloping at an angle α is

$$\theta'_{sep} \approx \theta_{sep} - 2\alpha \qquad (6)$$

where θ_{sep} = separation angle between the direct and specular reflection had the terrain been flat

α = terrain upward tilt along the line of sight path from ground antenna to aircraft

Conventionally, MLS elevation antenna design and siting has been based on (6) with $\alpha = 0$. Consequently, when $\alpha > 0$, the design margin may be significantly reduced if the reflection levels for rising terrain are similar to those for flat terrain.

Terrain which is both upsloping and downsloping may be "focusing" in the sense that more than one specular reflection is present at a given time. The "focusing ground" case is of interest in that the net multipath level could possibly exceed unity whereas systems designers typically consider a maximum M/D level of unity.

Several factors which tend to reduce the multipath reflection threat are also of interest:

(1) absorption by vegetation

(2) reduction of the specular levels by roughness effects [52, 53]

(3) shielding of the reflecting region by objects (e.g., trees) or terrain [52].

The roughness reduction is viewed as potentially quite important since theory and limited experiments (primarily over sea [53] suggest that there is an exponential-quadratic dependence on irregularity height and grazing angle of the form:

$$\rho_{roughness} = \exp[-2\ (2\pi\ \delta h \sin \theta_g/\lambda)\ ] \qquad (7)$$

where $\delta h/\lambda$ rms height variation in wavelengths and θ_g is the grazing angle [53]. These various factors typically would cause the multipath levels to be reduced with possibly a broadening of the specular peaks.

a. Hanscom AFB

Figures 2-20 through 2-25 show the representative angular power spectral estimates for the measurements taken at Hanscom AFB. These spectra were for the helicopter over the Hanscom runway 11 overrun area (see Fig. 2-10) at various elevation angles. As described in subsection D-1-a, the terrain consists of a fairly flat grass field in front of the receiving antenna array at this measurement site. Hence, it is expected that the ground reflected signal would be primarily a specular reflection from the ground which had been attenuated by the grass cover.

For the helicopter at elevation angle $\theta = 8.6°$ (Fig. 2-20), no obvious multipath components are observed in both the field measurement and the MLS computer simulation, although the background spectral level is higher in the field measurement results. This was expected because the reflection coefficient of typical ground at L-band is quite low in this (Brewster angle) region. At $\theta = 5.2°$ (Fig. 2-21), both field measurement results and the

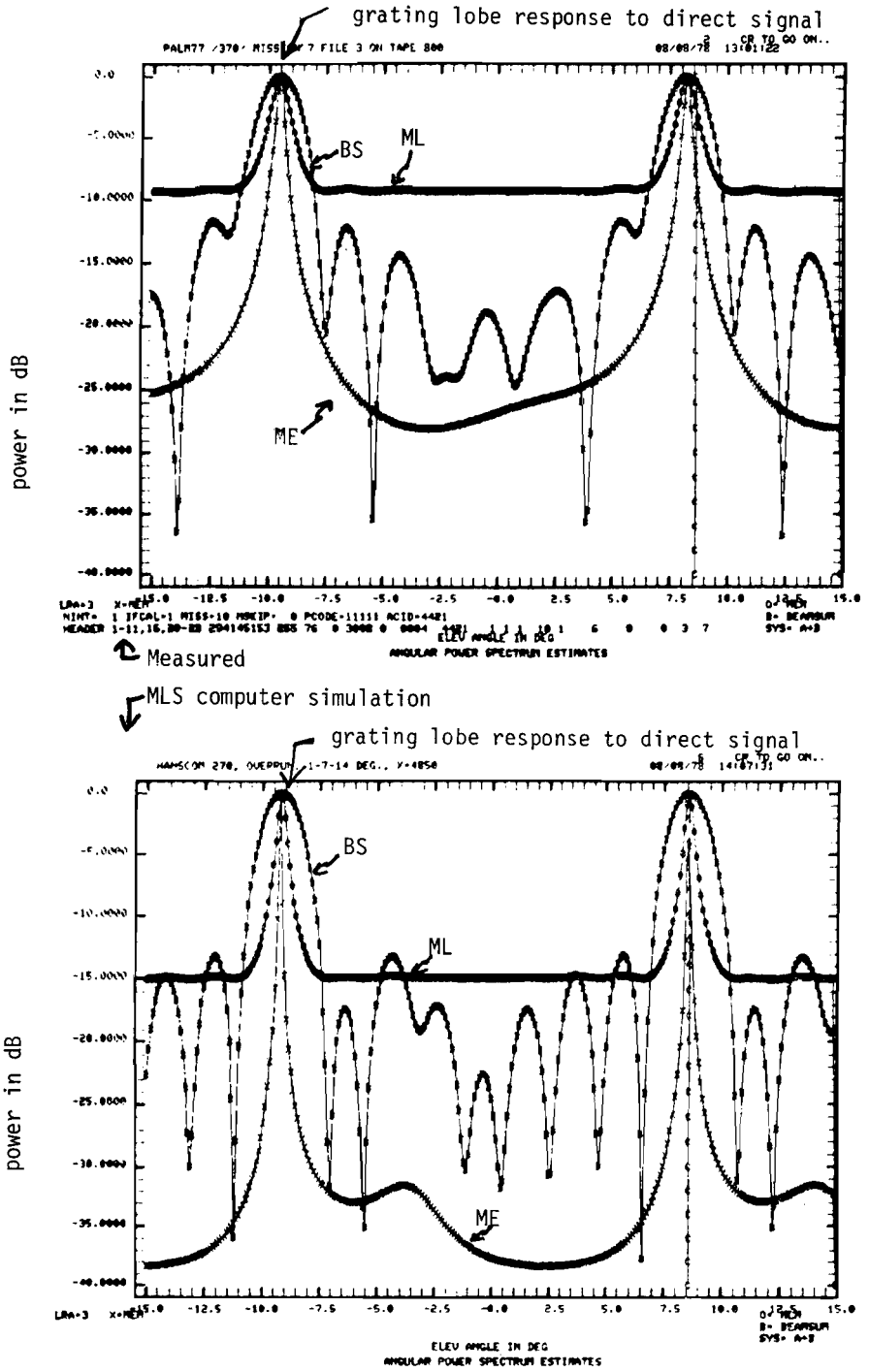

Fig. 2-20. Hanscom AFB measurements: $\theta = 8.6^{o}$.

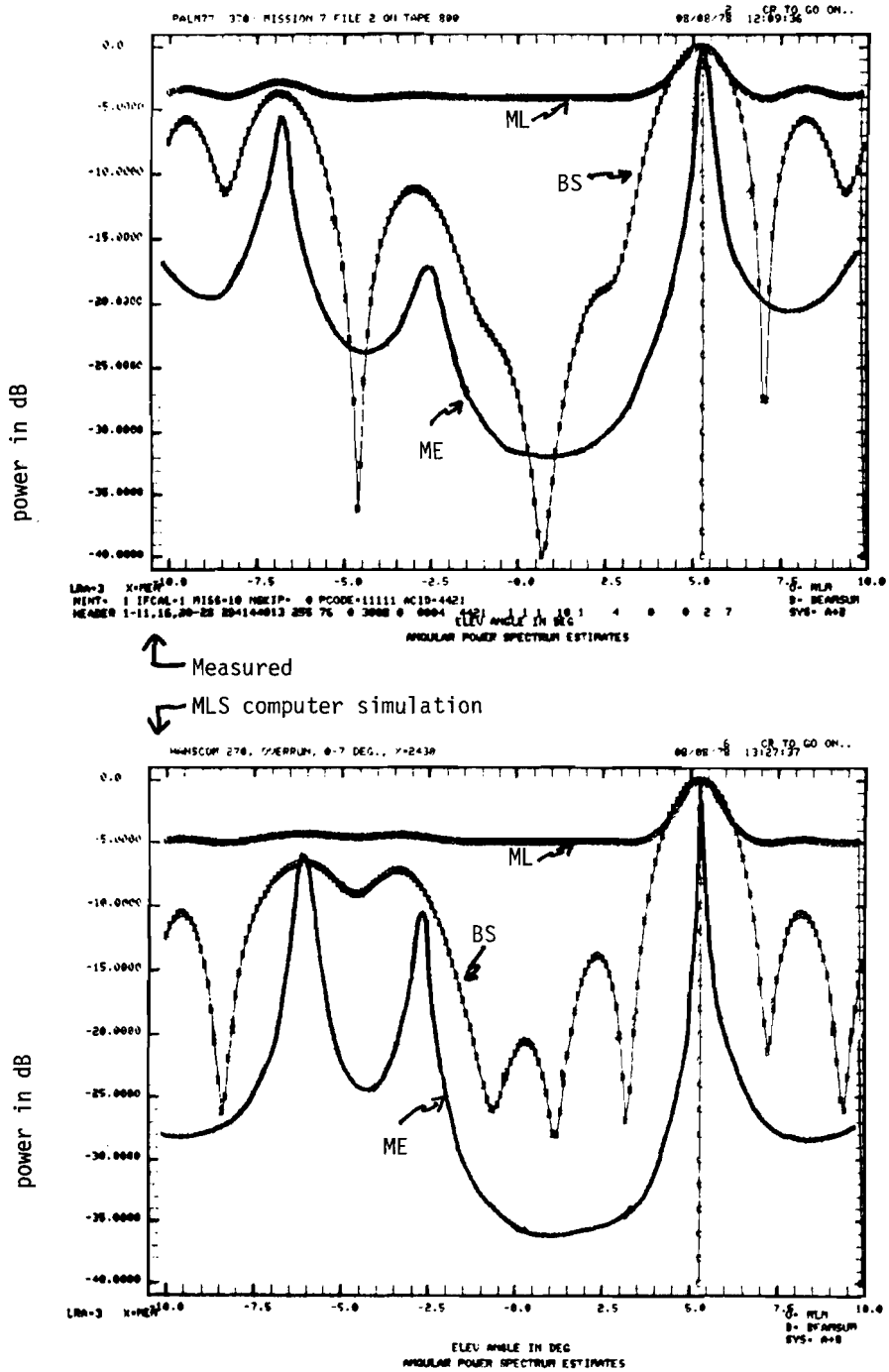

Fig. 2-21. Hanscom AFB measurements: $\theta = 5.2^{o}$.

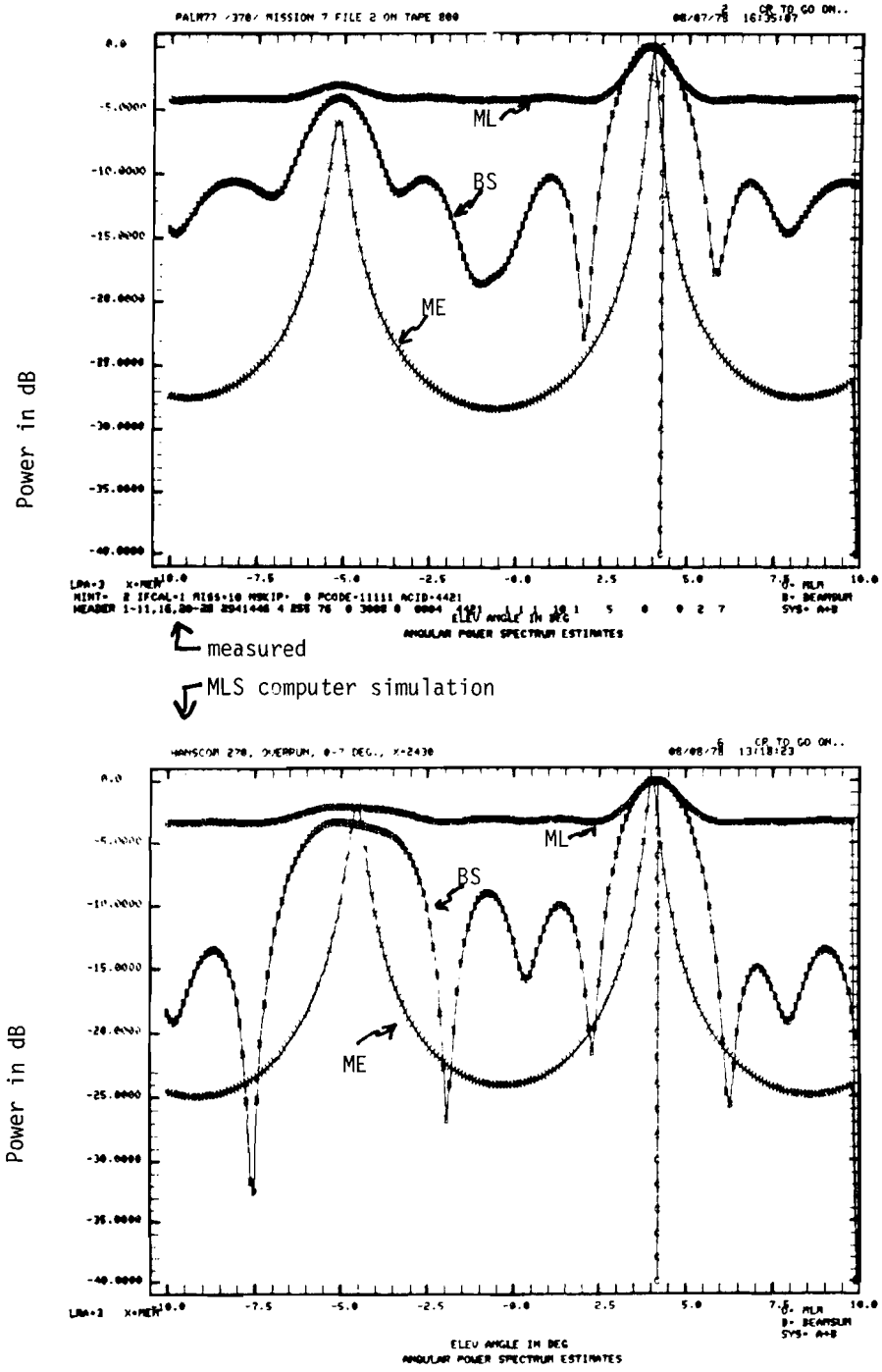

Fig. 2-22. Hanscom AFB measurements: $\theta = 4.2^{o}$.

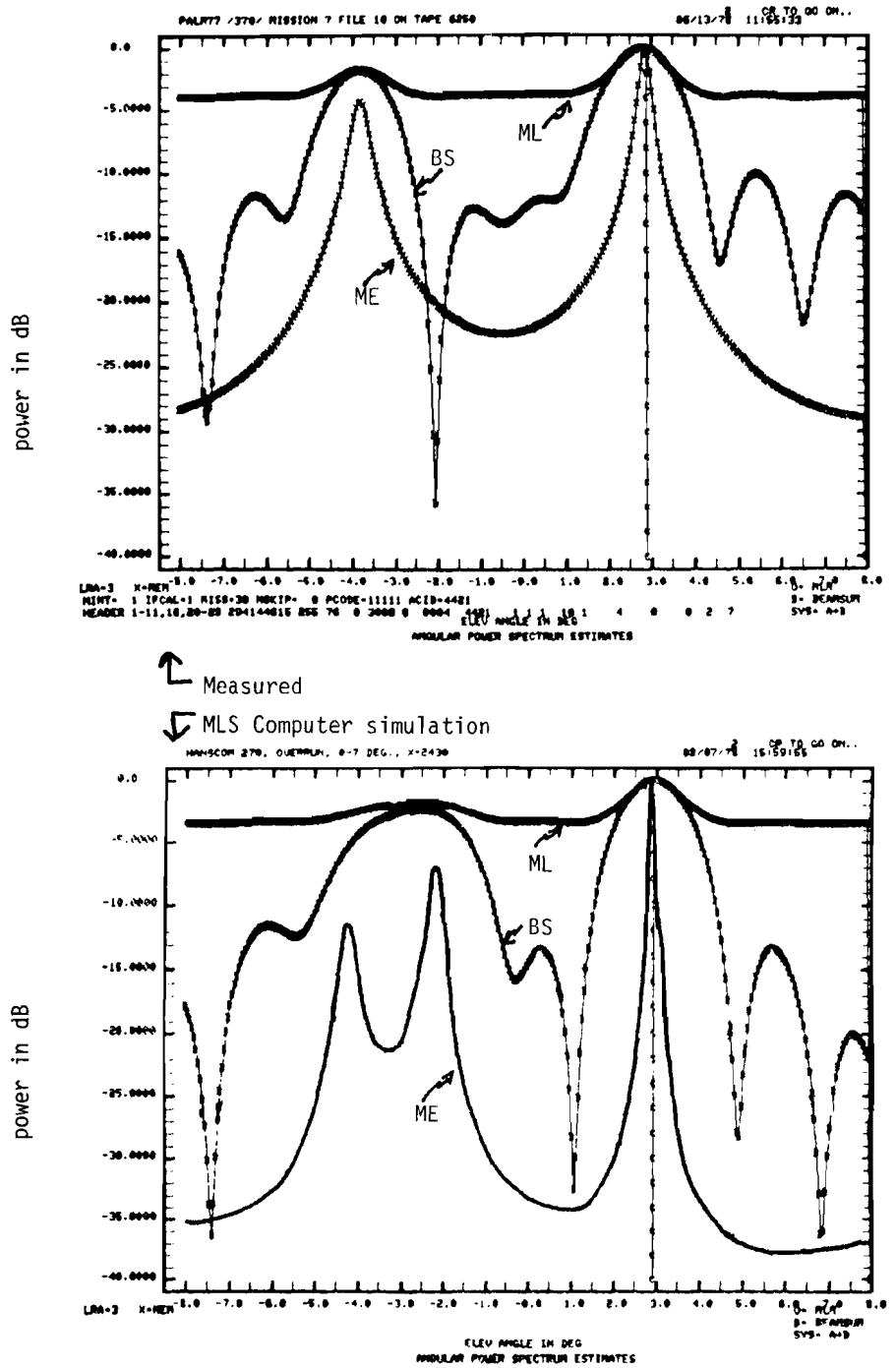

Fig. 2-23. Hanscom AFB measurements: $\theta = 2.9^{o}$.

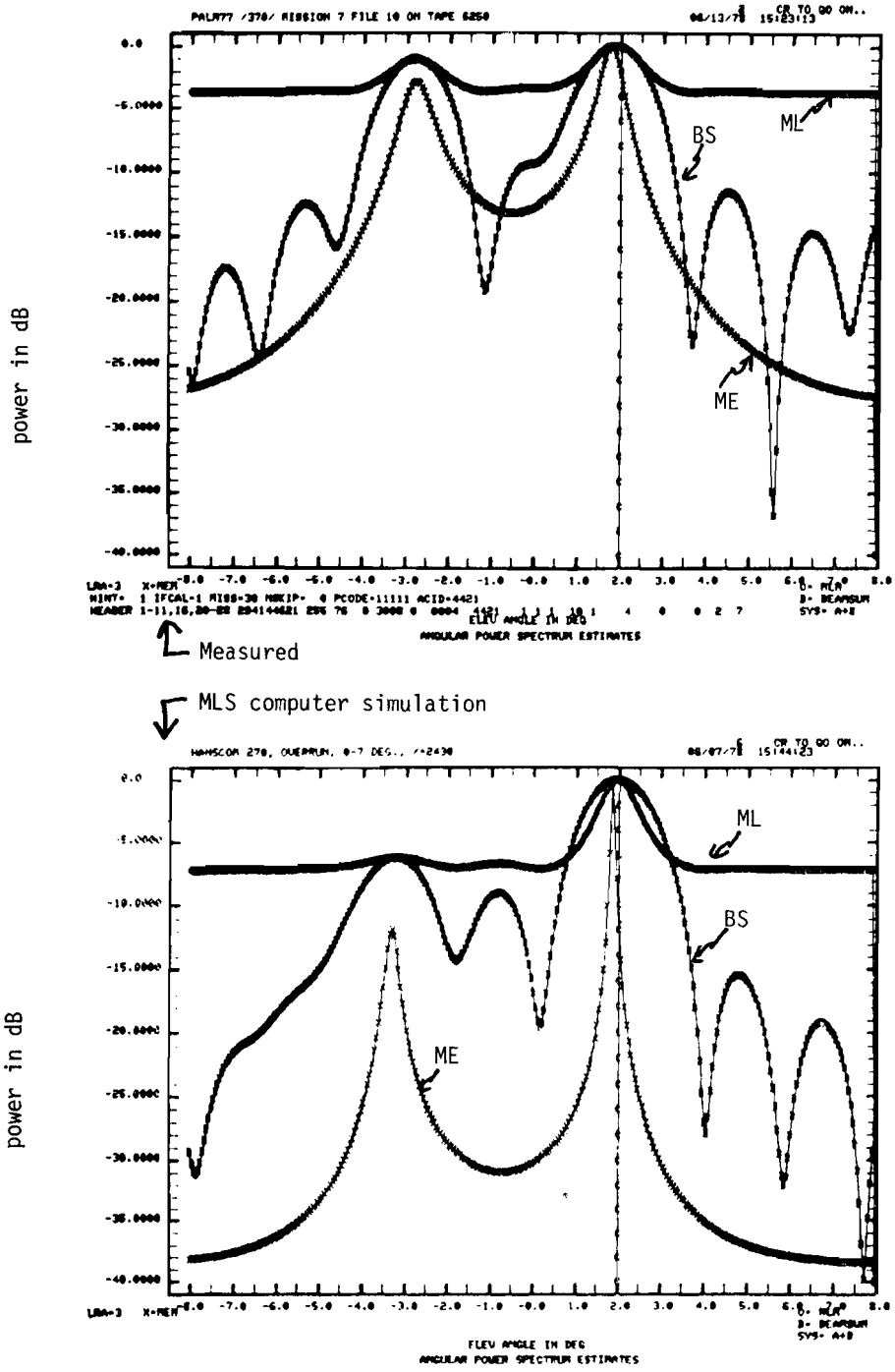

Fig. 2-24. Hanscom AFB measurements: $\theta = 2.0^{o}$.

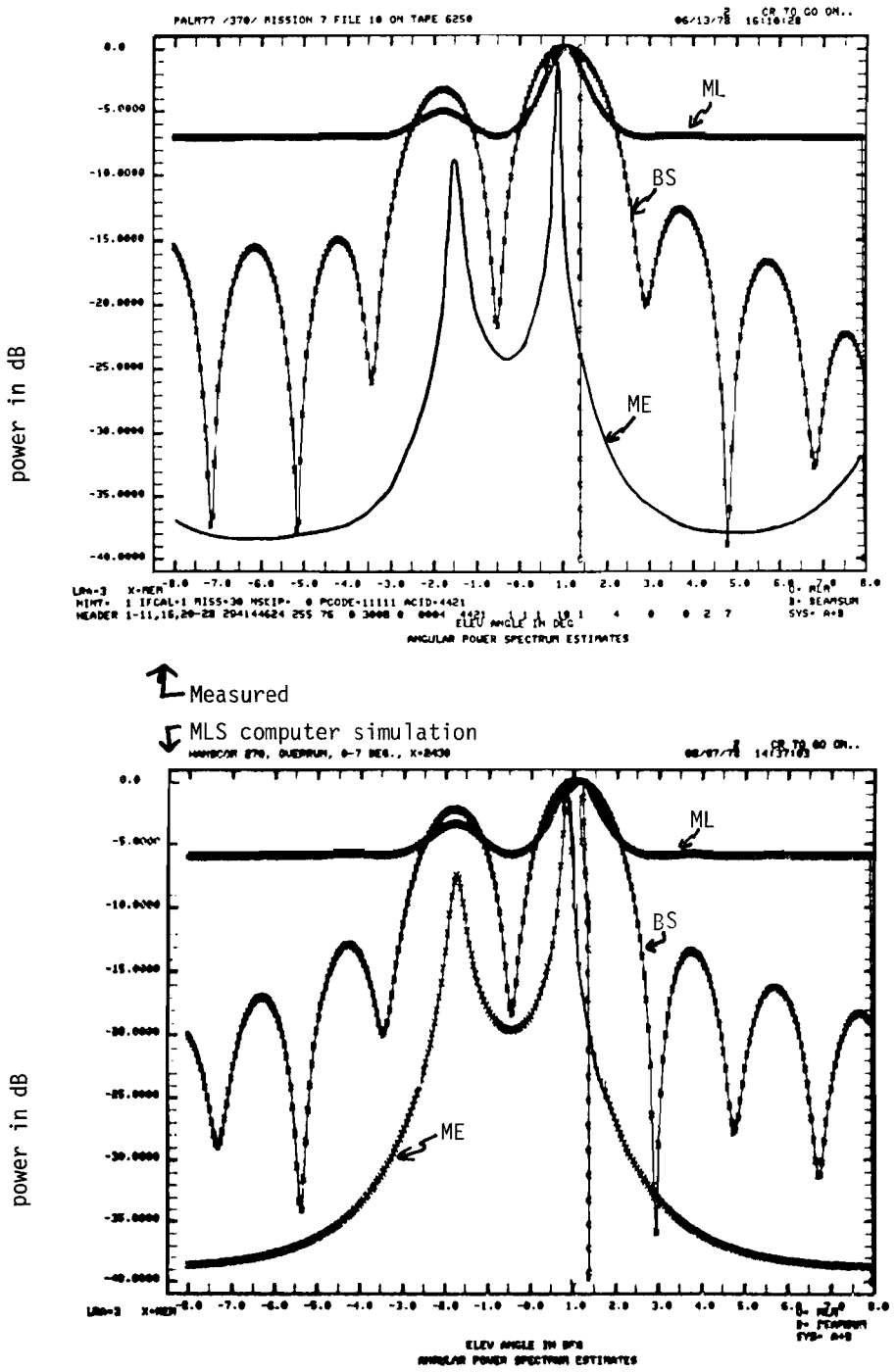

Fig. 2-25. Hanscom AFB measurements: $\theta = 1.4^{o}$.

MLS computer simulation preidcted results indicate that there are two ground reflected signals, one near $\theta = -2.5°$ and the other around $\theta = -6.5°$; although noticeable difference in the sidelobe structure is observed in the BS spectra. At $\theta = 4.2°$ (Fig. 2-22), one ground reflection around $\theta = -5.0°$ is clearly shown by both the field measurement and the MLS computer simulation, with both indicating similar multipath level of this ground reflected signal (M/D $\approx$ -3 dB). At $\theta = 2.9°$ (Fig. 2-23), the BS and the ML spectrum of the MLS computer simulation results are very similar to those of the field measurement results. However, the ME spectrum of the MLS computer simulation results has two spectral peaks at the negative elevation angle while the field measurement results indicate one only. At $\theta = 2.0°$ and 1.4°, both field measurement and the MLS computer simulation give quite similar spectra, with the MLS computer simulation results yielding somewhat lower multipath level for $\theta = 2.0°$.

For the measurements taken at Hanscom AFB, the results from the comparison can be summarized as follows:

(1) the background spectral level of the ML or the ME spectrum for the field measurement results usually is higher than that for the MLS computer simulation predicted results, especially at higher elevation angle. This could arise either from complexities in the reflection environment not simulated (e.g., diffuse reflections) or from instrumental errors (e.g., A/D quantization noise, residual calibration error).

(2) the sidelobe structure in the BS spectrum is somewhat different between the field measurement results and the MLS computer simulation results. This might be due to the fact that the noise interference in the field measurement has not been accounted for in the MLS multipath simulation or due to residual antenna calibration errors.

(3) Both field measurement results and the corresponding MLS computer simulation results yield fairly accurate elevation angle estimates of the direct signal.

(4) In most cases, the number of the ground reflected signals indicated by the field measurement results is the same as that predicted by the MLS computer simulation results. On a couple of occasions (e.g., the one shown in Fig. 2-23), the MLS computer simulation results (the ME spectrum only) yield one more ground reflection than the field measurement results has called for. This probably is due to the improper division of the ground plates in modeling the terrain

(5) The estimated arrival angles of the ground reflections from the MLS computer simulation results agree quite well with those observed in the field measurement results, although they are not exactly identical. This slight difference in the estimated arrival angles of the ground reflections probably is attributed partially to the assumption of the plane wave arrivals for the multipath components made in the MLS multipath simulation run and partially to the fact that the detailed flight path is not known exactly.

(6) The estimated M/D ratios are fairly similar between the field measurement results and the MLS computer simulation results, with the latter showing slightly lower multipath level.

To illustrate the sort of numbers which were extracted from the angular power spectra and were used in the comparison, Table 2-2 gives the estimated elevation angles of the direct and the ground reflected signals and their M/D ratios for some of the field measurement results and the corresponding MLS computer simulation results.

b. Fort Devens

As described in the subsection D-1-b, field measurements at the golf course of Fort Devens were made in three radial directions, i.e., the radial lines O-A, O-B, and O-C (see Fig. 2-12). Terrain at the golf course has more features (i.e., ground drops and rises more often and more steeply) than that at the Hanscom AFB (Figs. 2-13 to 2-15). Consequently, we can expect to see effects on both the field measurement results and the MLS computer simulation results.

TABLE 2-2

HANSCOM AIR FORCE BASE MEASUREMENTS

Measurement Point	Elevation Angle of Helicopter	Estimated Angle of Direct Signal (Helicopter)		Estimated Angle (θ_r) and M/D ratio of Ground Reflected Signal				
		measured	MLS simulation	#	measured		MLS simulation	
					θ_r	M/D(db)	θ_r	M/D (db)
Runway 11 overrun area	8.6°	8.3°	8.6°	–	–	–	–	–
	5.2°	5.2°	5.2°	1	-2.5°	-9.2	-2.6°	-7.2
				2	-6.8°	-3.2	-6.4°	-3.0
	4.2°	4.0°	4.0°	1	-5.0°	-3.0	-4.6°	-2.0
	2.9°	2.9°	2.9°	1	-3.8°	-2.2	-4.2°	-3.0
				2	–	–	-2.1°	-1.0
	2.0°	1.7°	1.8°	1	-2.9°	-1.6	-3.3°	-2.5
	1.4°	0.9°	0.9°	1	-1.5°	-3.0	-1.7°	-3.5

In fact, we found that the agreement between the MLS computer simulation predicted results and the field measurement results was poor in most cases for the measurements taken in the radial directions O-A and O-C. However, we found fairly good agreement between two sets of results for the measurements at the radial direction O-B. This probably can be explained by the following facts:

(1) Terrain along the radial line O-B varies much more slowly than that along the radial line O-A, or O-C, as can be seen in the terrain height profiles shown in Figs. 2-13 to 2-15. Thus, the ground model (consisting of several simple rectangular plates) used in the MLS multipath simulation run for the measurements taken in the radial direction O-B probably is a much better approximation of the true terrain than those for the measurements made the radial directions O-A and O-C.

(2) The cross-tilt of the ground, which was not taken into account in the MLS multipath simulation, probably can not be ignored for the terrain along the radial lines O-A and O-C.

(3) The location of the measurement point B on the radial line O-B can be more accurately determined than that of the measurement point A or C, because the radial line O-B passes through an obvious landmark (a small white house at the end of the golf course) at the golf course. This should make the flight path used in the MLS multipath simulation run closer to that in the field measurement.

Figures 2-26 and 2-27 show two examples of the angular power spectral estimates for the measurements at point A (Fig. 2-12) on the radial line O-A. For the helicopter at the elevation angle $\theta = 13°$ (Fig. 2-26), both field measurement results and the MLS computer simulation results give very accurate estimates of the direct signal arrival angle at $\theta = 1.3°$ and the background spectral levels are quite similar. Also, the two sets of results both suggest one ground reflection. However, the estimated arrival angle of this ground reflected signal from the MLS computer simulation results differs a lot from that of the field measurement results, $\theta \approx -6.5°$ vs. $\theta \approx -9.0°$. For $\theta = 2.6°$ (Fig. 2-27), it can be seen that the MLS computer simulation results differ noticeably from the field measurement results.

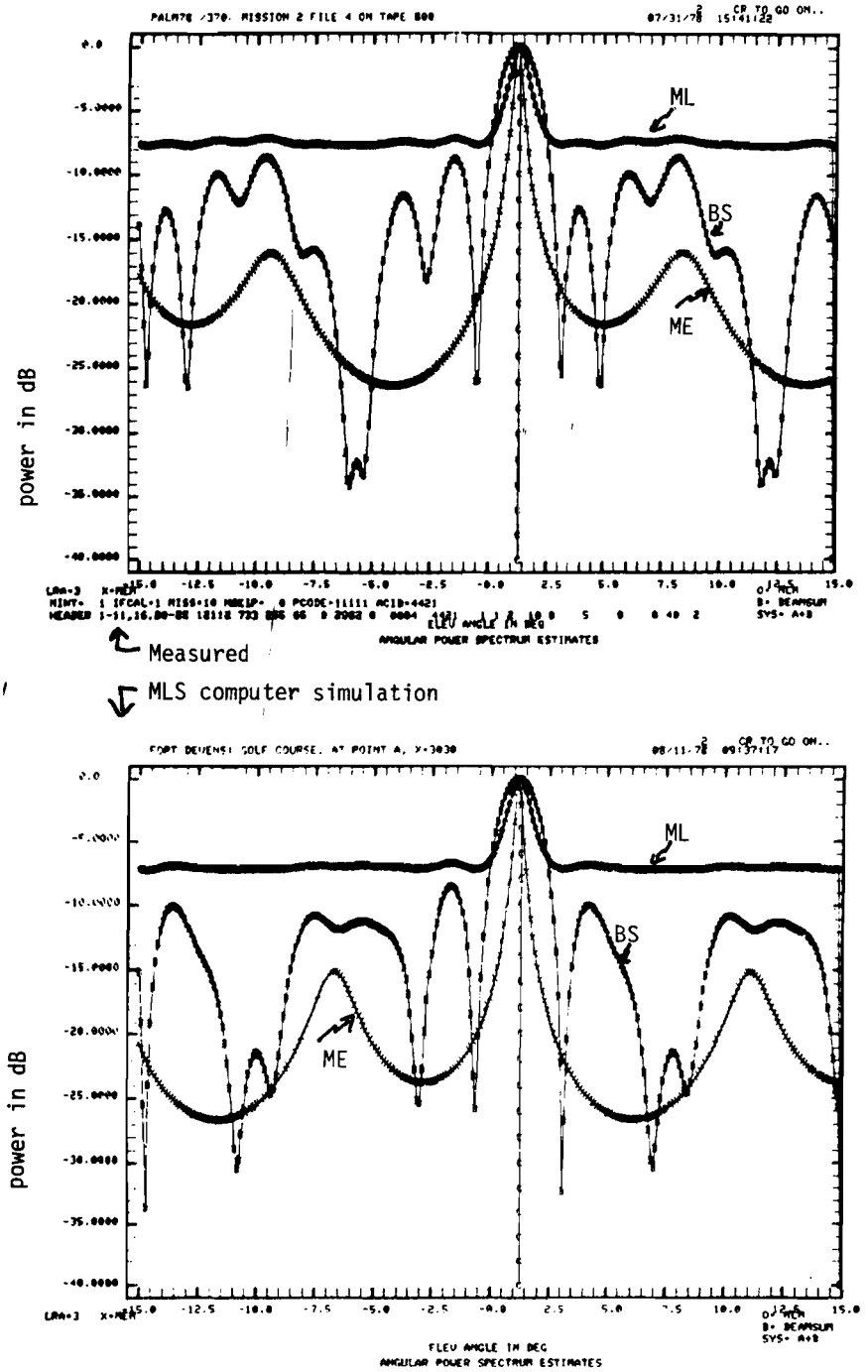

Fig. 2-26. Fort Devens measurement (golf course): $\theta = 1.3^{o}$.

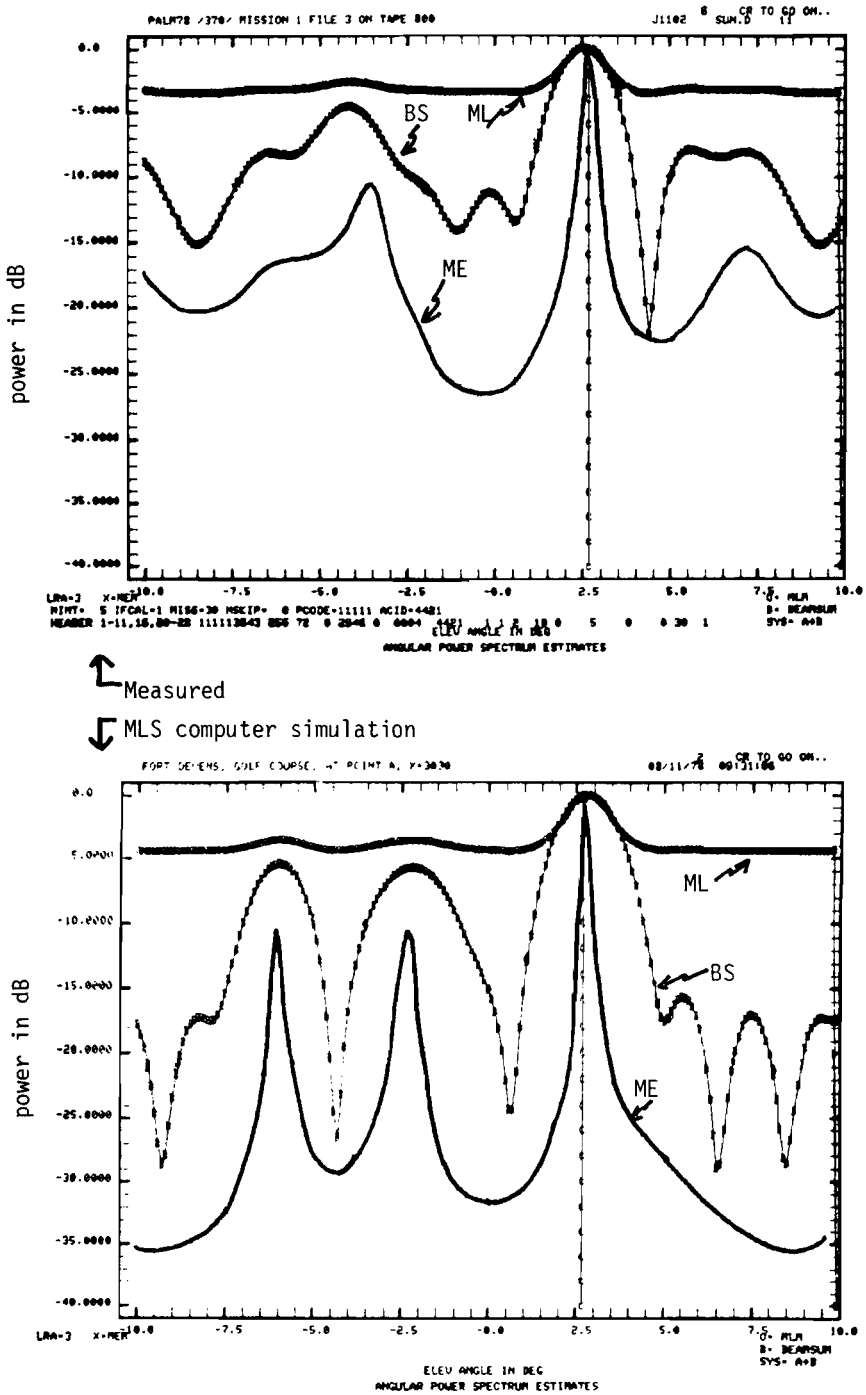

Fig. 2-27. Fort Devens measurement (golf course): $\theta = 2.6^{o}$.

Figures 2-28 and 2-29 show similar examples for measurements taken at point C (Fig. 2-12) on the radial line O-C. For the helicopter at the elevation angle $\theta = 3.2°$ (Fig. 2-28), the agreement in terms of the estimated elevation angles of the direct and the ground reflected signals and the M/D ratio seems fair between the MLS computer simulation results and the field measurement results. For $\theta = 4.9°$ (Fig. 2-29), the agreement between the two sets of results is poor.

Figures 2-30 through 2-33 show similar examples for the filed measurements made at point B (Fig. 2-12) on the radial line O-B. As mentioned earlier, the agreement between the MLS computer simulation results and the field measurement results is quite good, as can be seen in these figures. For the helicopter at the elevation angle $\theta = 3.2°$ (Fig. 2-30), the two sets of results both yield fairly good angle estimates of the direct signal, both suggest a ground reflected signal arriving at -5.0°, and both give similar multipath levels for this ground reflected signal. For $\theta = 4.2°$ (Fig. 2-31), the MLS computer simulation results and the field measurement results both yield very good angle estimates of the direct signal and both indicate the existence of two ground reflected signals, one at -6.0° and the other at -1.7°, with the latter having a lower multipath level. For $\theta = 5.2°$ (Fig. 2-33), the two sets of results both indicate the arrival of two ground reflected signals, one at -7.5° and the other at -2.5°, with the former having a higher M/D ratio. In all these examples, the differences between the MLS computer simulation results and the field measurement results in background spectral level and the sidelobe structure are similar to those observed in the Hanscom AFB measurements.

In summary, the overall agreement (and, sources of differences) between the computer simulation results and field measurements at the Fort Devens golf course are similar to those encountered with the Hanscom data except for the cross filtered terrain effects which are visible in the field measurements in the radial direction O-A and O-C. Table 2-3 tabulates the esimated elevation arrival angles of the direct and ground reflected signals and their M/D ratios for some of the field measurement results and corresponding MLS computer simulation results.

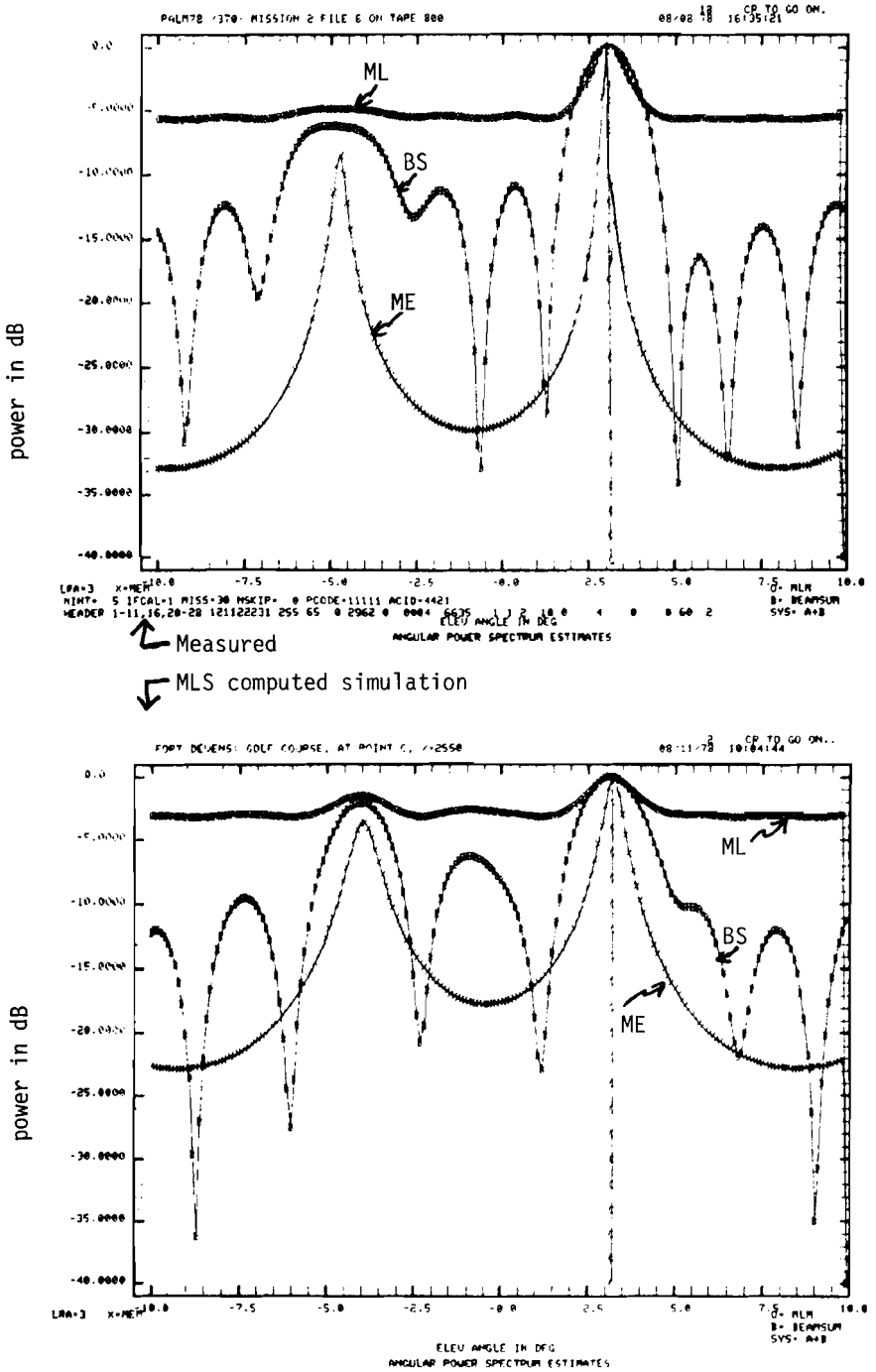

Fig. 2-28. Fort Devens measurement (golf course): $\theta = 3.2^{o}$.

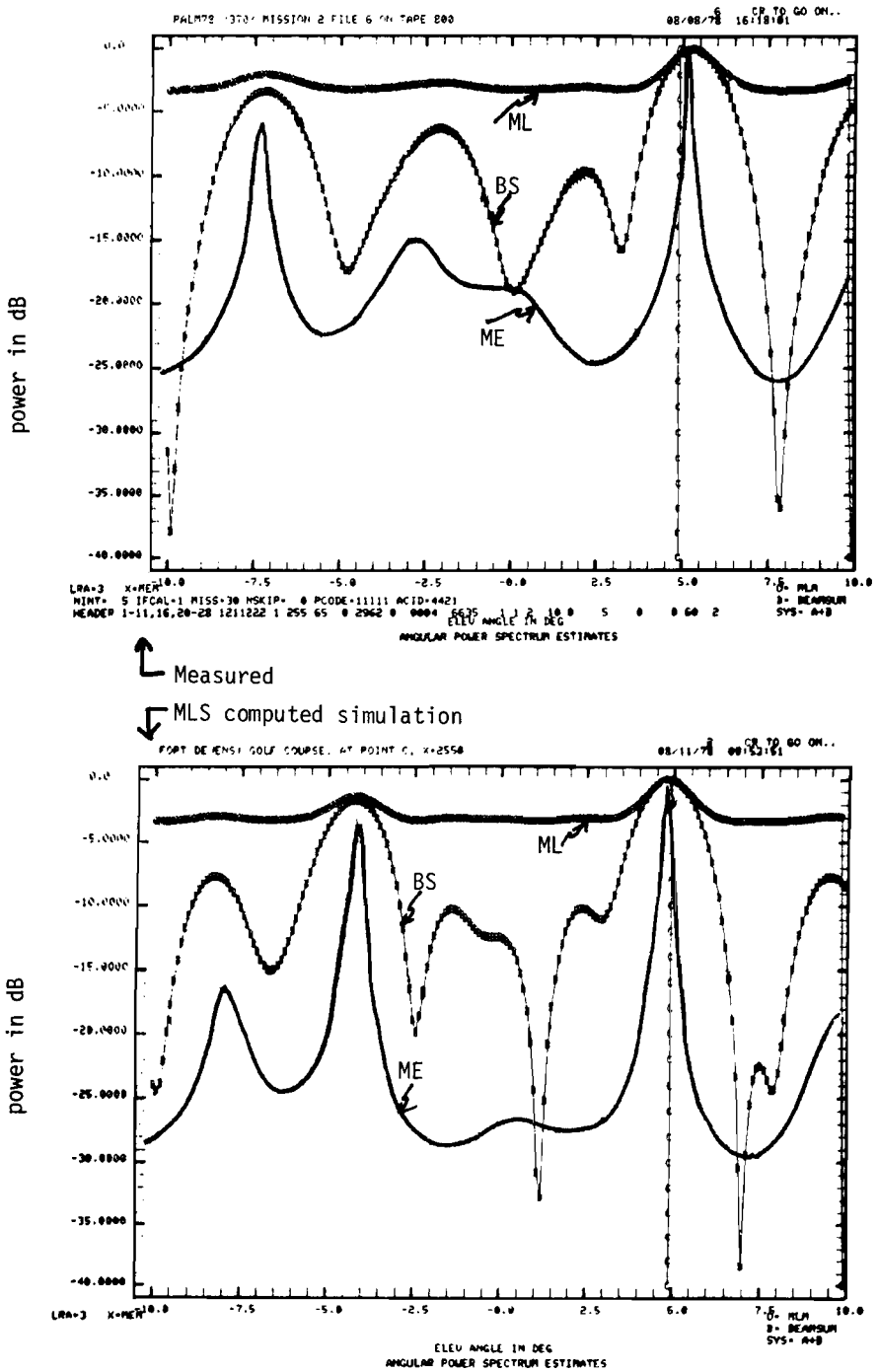

Fig. 2-29. Fort Devens measurement (golf course): $\theta = 4.9^{o}$.

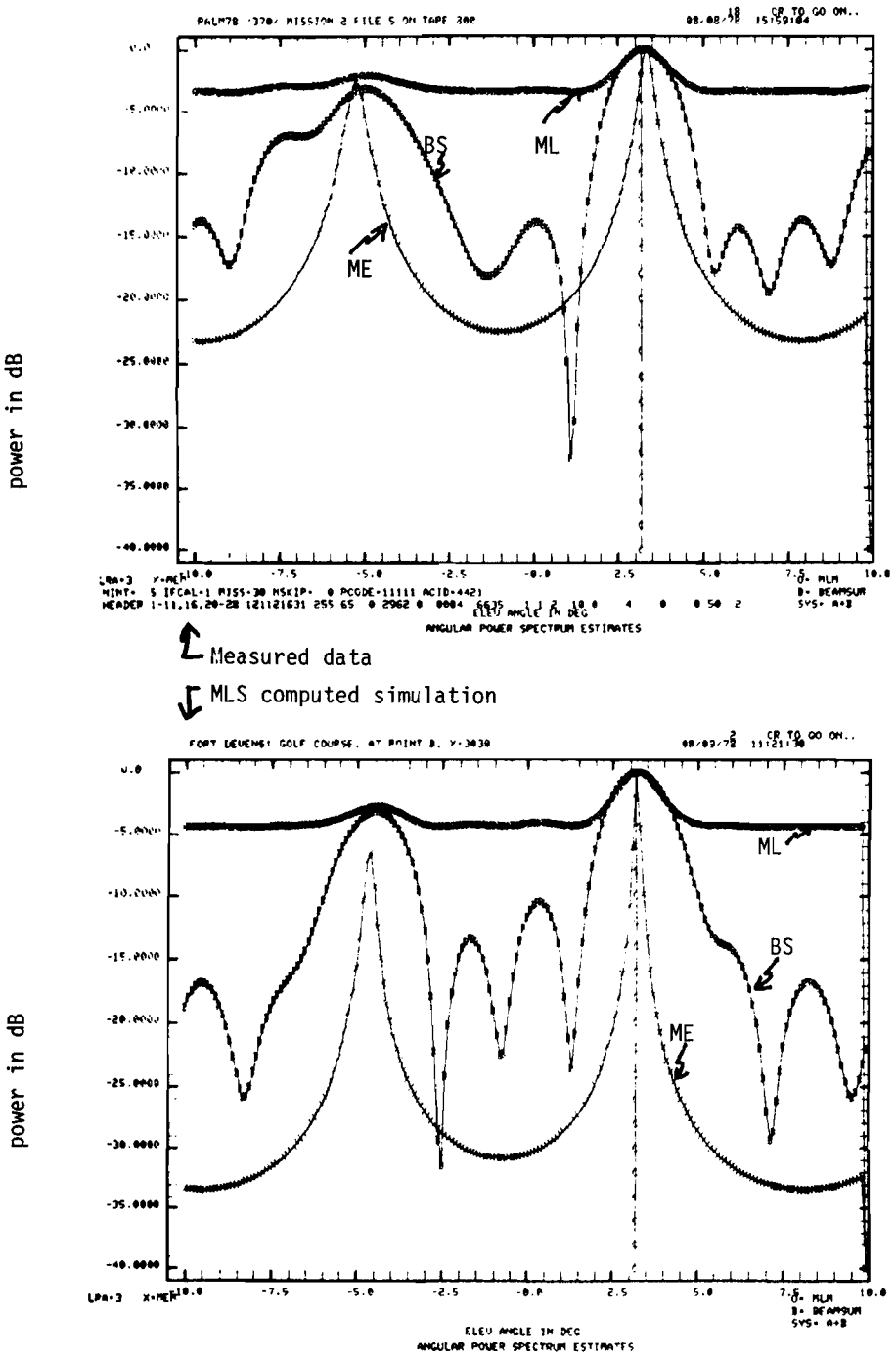

Fig. 2-30. Fort Devens measurement (golf course): $\theta = 3.2^{o}$.

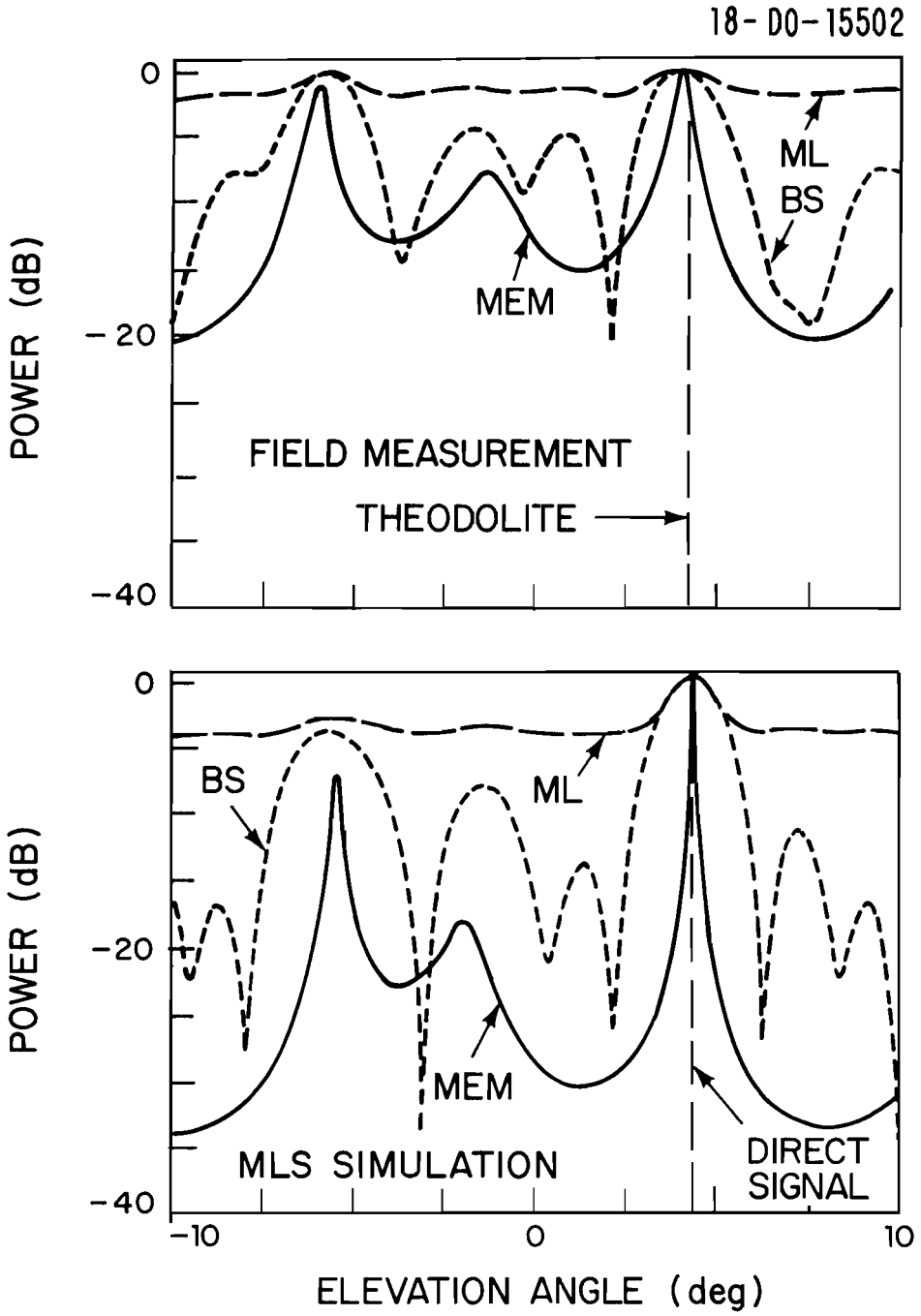

Fig. 2-31. Fort Devens measurement (golf course): $\theta = 4.2^{o}$.

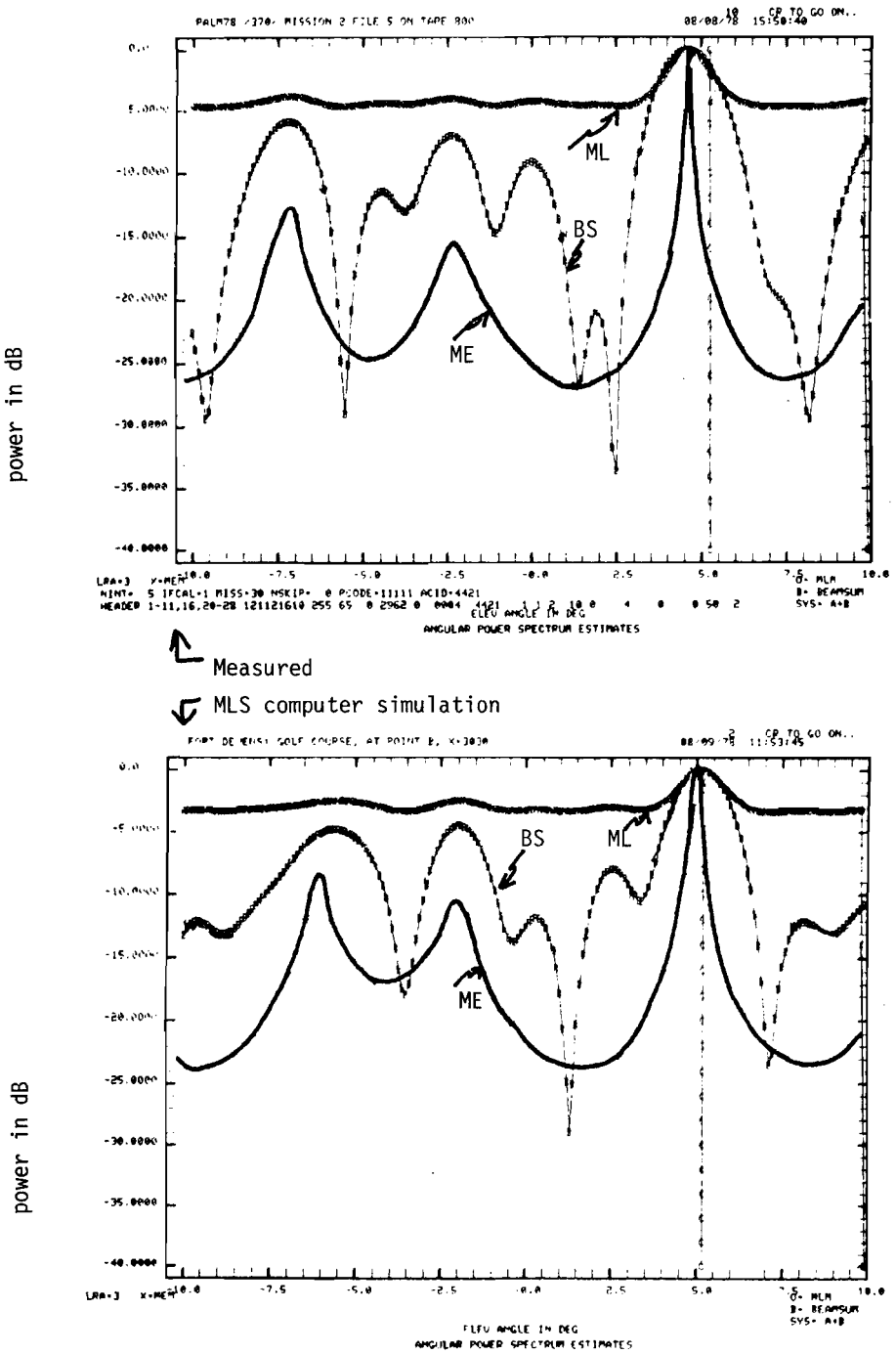

Fig. 2-32. Fort Devens measurement (golf course): $\theta = 5.2^{o}$.

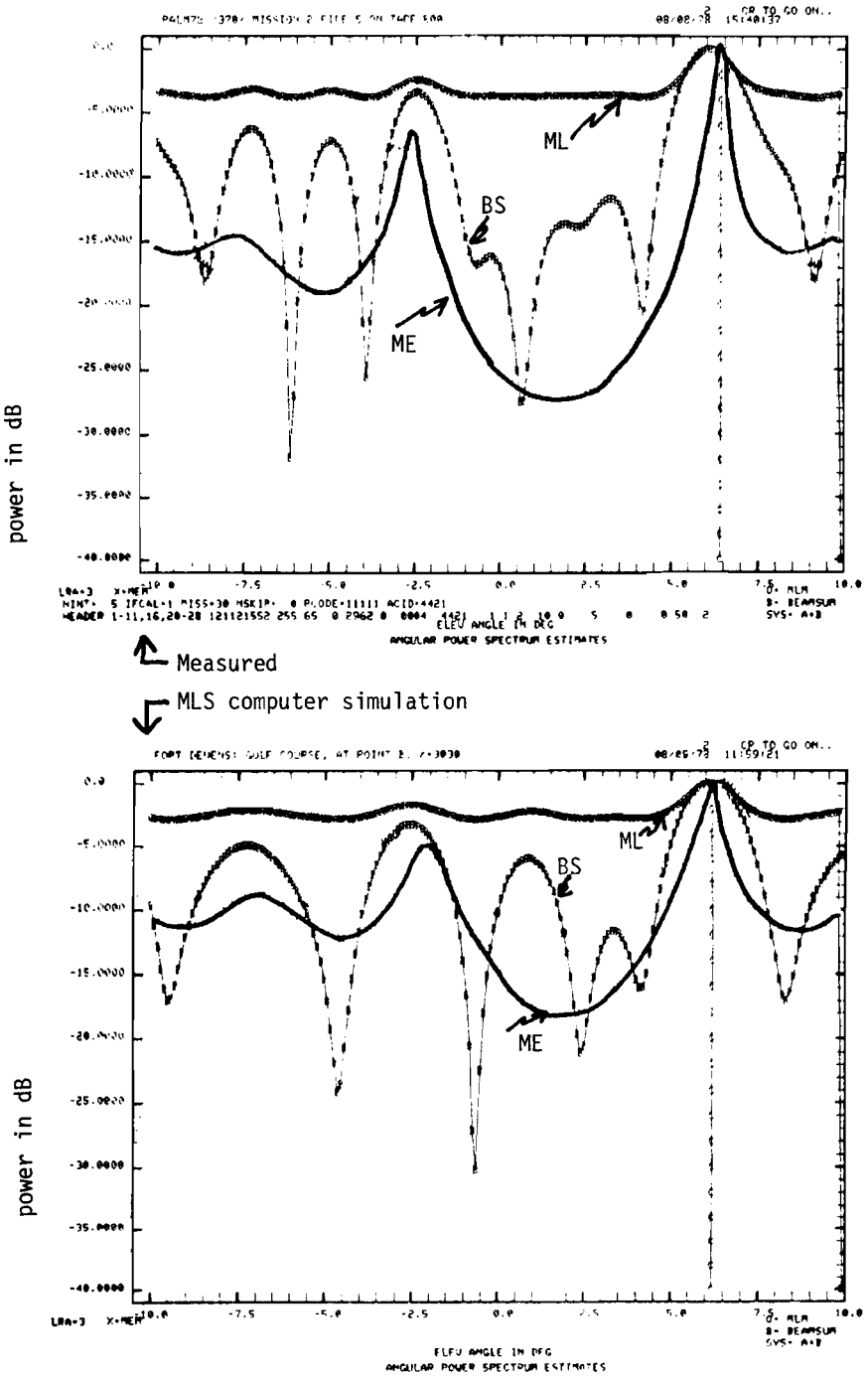

Fig. 2-33. Fort Devans measurement (golf course): θ=6.2° at measurement point B.

E. Summary

Field measuremtns for collection the ground reflection data have been taken at several sites at Hanscom Air Force Base and Fort Devens. The field measurement results and the corresponding MLS computer simulation results have been compared in terns of their angular power spectra for a variety of measurements made at these sites. In most cases, especially when the terrain variation was simple and could be quite accurately modeled as a series of simple rectrangular ground plates (such as for those measurements at Hanscom AFB and in the radial direction O-B at the Fort Devens golf course), fairly good agreement between the MLS computer simulation results and the field measurements was obtained in terms of the estimated elevation angles of the direct signal and the ground reflected signals, the number of the ground reflected signals and their multipath levels. However, when the assumptions which were made in the MLS computer simulation run were not reasonably satisfied in the field measurement environment, especially when the terrain variation was more complex and could not be easily and accurately represented by several simple rectangular plates, then one could not expect them to make meaningful comparison between the MLS computer simulation results and the field measurement results. Recognizing this limitation, the agreement between the MLS computer cimulation results and the field measurement results for the ground reflection measurements at the Hanscom AFB and Fort Devens is reasonably good. In the next phase of the MLS studies, more accurate terrain surveys will be made at these sites and the ground reflection model will be refined to overcome the shortcomings identified above.

Too little data has been obtained to date to warrant any firm conclusions regarding the various multipath environment issues discussed in Secion C.3. However, several preliminary judgements seem warranted:

(1) the bulk of the reflections appear to be specular in nature and to be explained by the flat plate models utilized in the MLS propagation model.

TABLE 2-3

FORT DEVENS MEASUREMENTS: GOLF COURSE

Measurement Point	Elevation Angle of Helicopter	Estimated Angle of Direct Signal (Helicopter)		Estimated Angle (θ_r) and M/D ratio of Ground Reflected Signal				
		measured	MLS simulation	#	measured		MLS simulation	
					θ_r	M/D(db)	θ_r	M/D (db)
A	1.3°	1.2°	1.2°	1	-9.2°	-7.7	-6.5°	-6.5
	2.6°	2.6°	2.6°	1	-3.6°	-3.5	-2.4°	-5.0
				2	—	—	—	—
B	3.2°	3.2°	3.2°	1	-5.2°	-2.5	-4.7°	-3.8
	4.2°	3.9°	4.2°	1	-1.5°	-2.4	-2.0°	-7.0
				2	-6.1°	1.0	-6.1°	-1.0
	5.2°	4.6°	4.9°	1	-1.7°	-7.2	-2.0°	-4.6
				2	-7.1°	-6.0	-6.2°	-3.3
	6.2°	6.2°	6.2°	1	-2.5°	-3.6	-1.9°	-2.0
				2	-7.5°	-5.5	-7.0°	-2.0
C	3.2°	3.0°	3.2°	1	-4.7°	-5.0	-4.0°	-1.8
	4.9°	5.2°	4.9°	1	-2.7°	-7.2	-4.0°	-1.2
				2	-7.5	-6.0	-7.7°	-6.0

(2) high L-band reflection levels (e.g., $\geq$ 3 dB) can be encountered at low elevation angles with a fairly high (e.g., > 1 wavelength) grass cover).

(3) no evidence of a "bright" diffuse reflection spot at the horizon is evident in the data to date

(4) upsloping terrain can yield fairly high level reflections with the predicted decrease in separation angle

(5) "focusing" terrain reflections can arise when the requisite terrain contours occur.

It should be emphasized that the above statements are based only on L-band data and may not apply at C-band due to the 5:1 change in wavelength. In some areas, such as the effect of vegetation height, it is clear that more measurements will have to be made at the same sites with a variety of terrain conditions (e.g., vegetation height) if one is to achieve a careful quantitative characterization of multipath. Improved data processing algorithms would be of aid in better resolving and quantifying the various data features at very low elevation angles.

III. BUILDING REFLECTIONS

A. Van Measurements at John F. Kennedy (JFK) International Airport, New York

Figure 3-1 shows a map of JFK airport with the antenna locations used for TRSB tests on runway 13L. This particular runway offers a generally benign azimuth multipath environment, but the elevation multipath environment can be quite demanding due to the presence of large hangars abreast of the runway threshold.

In the field trials, relatively few azimuth multipath effects were noted save for some shadowing at very wide angles due to polse, etc., near the azimuth site. However, in some cases, discernible and fairly sizable elevation multipath effects were observed due to shadowing and/or reflections. Thus, the validation studies focused on the elevation phenomena.

In addition to the flight tests, a series of static and moving van measurements were made of the multipath levels and TRSB errors in the near threshold region. These are particularly useful in providing data free of tracker contamination effects. The results reported in this section were obtained from the static and moving van measurements in December 1977 and March 1978.

In the following, the December 1977 and the March 1978 JFK measurements with the MLS van will be discussed separately, each together with the MLS computer simulation results. We must emphasize here that the measurement path would have to be known to a fraction of a wavelength (e.g., 0.6 cm) to give exact equivalence of the simulated and the field measured error waveforms. Since this levels of detail was not available, one could only expect large scale features (e.g., error magnitude and region) to be equivalent.

1. 13-14 DECEMBER 1977 MEASUREMENTS

a. Measurement Environment

Figure 3-2 gives a sketch which shows the location of the MLS (TRSB) EL1 antenna and the hangars (HGRs) of interest near the landing threshold of JFK runway 13L. The EL1 was sited at 250 feet north of runway 13L centerline (CL) and 769 feet after the landing threshold. Elevation multipath effects

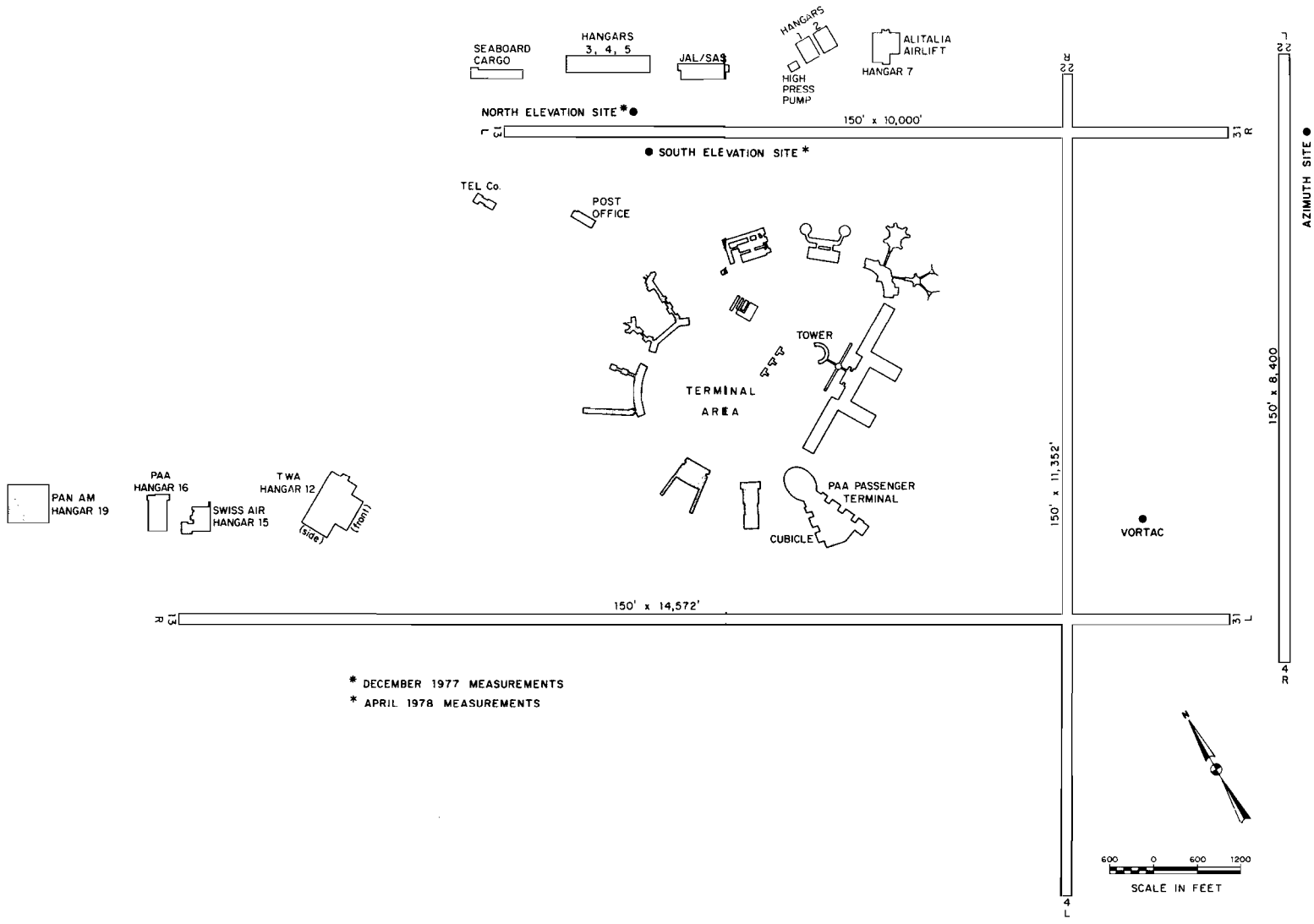

Fig. 3-1. John F. Kennedy International Airport (JFK).

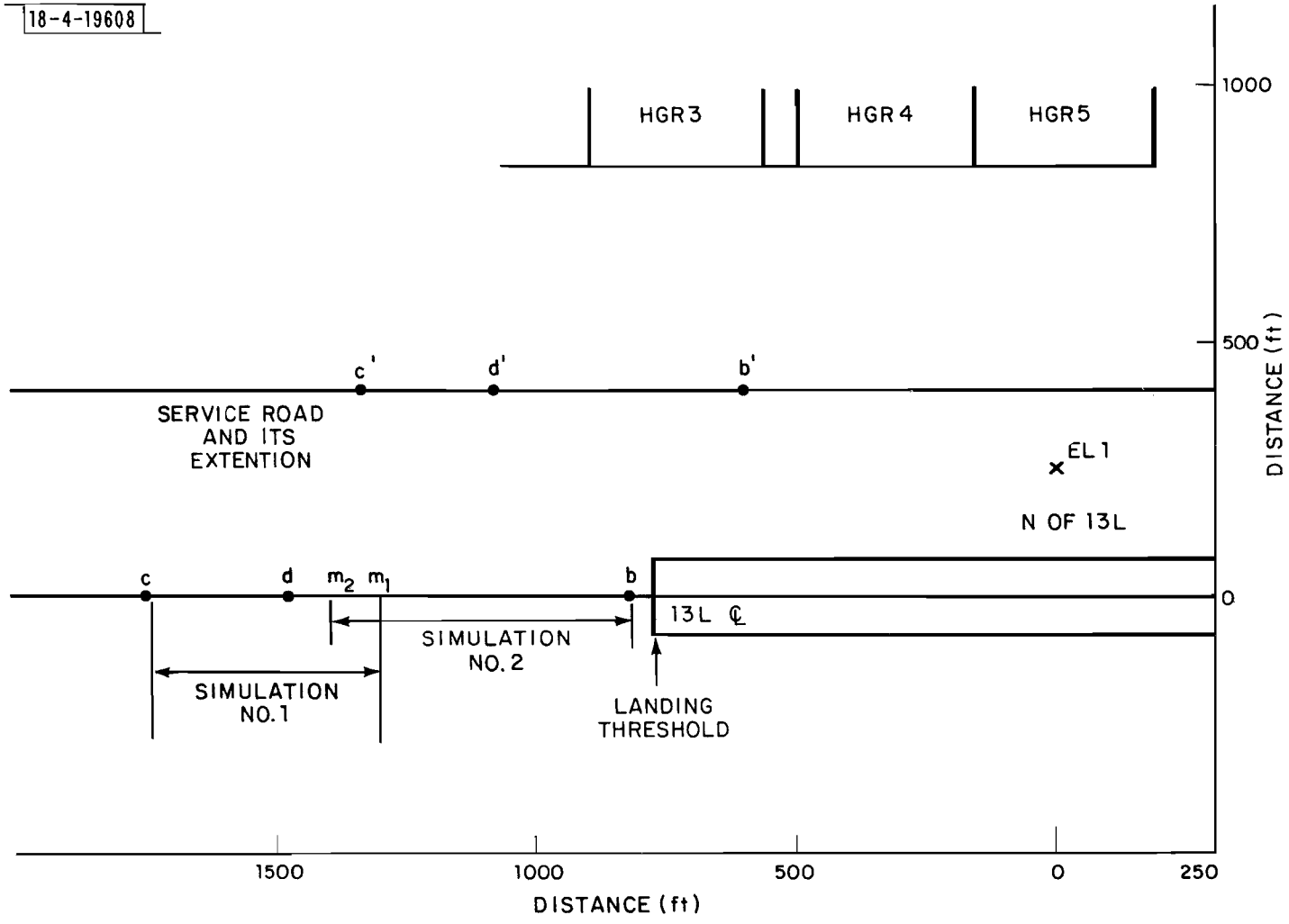

Fig. 3-2. Location of MLS van measurements at JFK runway 13L, December 1977.

were expected from HGRs 3 and 4 for our measurements. The hangar fronts are parallel to runway 13L CL and are 838.5 feet north of runway 13L CL with the end corner of HGR3 at 131 feet before the landing threshold. Fig. 3-3 shows the detailed engineering drawing of HGR3. HGRs 3 and 4 are identical, with a low brick building between them. Figs. 3-4 and 3-5 show photographs of the hangar front surface.

Measurements were made with a Bendix "small community" TRSB receiver on the MLS van. The EL1 antenna was a Bendix "basic narrow" antenna with a 1.5° beamwidth.

b. Measurements Made

Horizontal cuts were made on runway 13L CL with the MLS van moving from points b to c (Fig. 3-2) at 10 mph and with the receiving antenna mast at 25' and 44' height. First, a directional receiving antenna (20° beamwidth horn) was aimed at EL1. This should yield the signal level and elevation angle of the direct signal. Second, the directional horn was aimed at hangars to obtain the characteristics of the multipath signals from the hangars. Third, an omni antenna (180° beamwidth horn) was pointed along the runway 13L CL to simulate the elevation signal received by a landing aircraft on 13L. Similar horizontal cuts were also made along the service road from b' to c', as shown in Fig. 3-2. Also, several vertical cuts were made at points b', c' and d' on the service road.

c. Measurement Results

Since there was an active (unmonitorable) AGC in the receiver used in the measurements,* the measured log-video amplitudes of the multipath and the direct signals could not be used to obtain the meaningful amplitude ratios of the multipath and the direct signals, i.e., M/D ratios. Also, the reflection coefficients for various parts of the hangars could not be estimated from the measurements of the vertical cuts on the service road. However, the errors in the elevation angle estimated due to the multipath from the hangars can be computed from the elevation angle read out obtained in the measurements. Table 3-1 lists the

---

*The Bendix AGC is a long time constant AGC which responds to the net received azimuth and elevation signals including the DPSK omni radiated data.

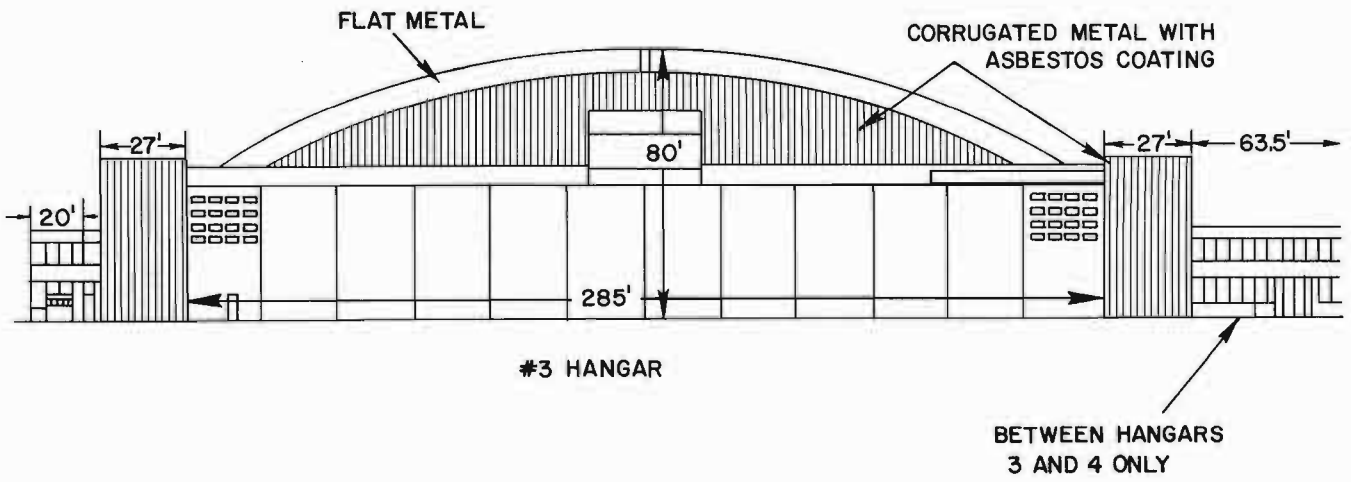

Fig. 3-3. Runway facing profile of hangar 3 at JFK.

Fig.3-4. Hangar 3 near JFK runway 13L - 31R.

Fig.3-5. Hangar 3 near JFK runway 13L - 31R.

TABLE 3-1

ELEVATION ANGLE ERRORS FOR JFK DECEMBER 1977
HORIZONTAL CUT ALONG RUNWAY 13L CENTERLINE,
RECEIVER HEIGHT = 44 FEET.

ε_θ = Elevation angle error = $\theta_{omni} - \theta_{D\,H}$

where θ_{omni} = measured elevation angle with omni horn pointing along 13L CL

θ_{DH} = measured elevation angle with directional horn pointing along EL1

X_c = distance in feet after point c

X_c	ε_θ	X_c	ε_θ	X_c	ε_θ	X_c	ε_θ
(at c) 0	0.055	101.64	-0.01	203.21	-0.015	315.22	-0.012
4.62	0.015	106.26	-0.01	207.90	-0.025	321.59	0.008
9.24	0.02	110.88	-0.03	212.52	-0.045	327.96	0.012
13.86	-0.015	115.50	-0.012	217.14	-0.035	334.33	-0.005
18.48	0.0	120.12	-0.015	221.76	-0.035	340.70	-0.01
23.10	0.0	124.74	-0.01	226.38	-0.009	(at m_2) 347.07	-0.02
27.72	-0.01	129.36	0.003	231.00	-0.01	353.44	0.03
32.34	-0.01	133.98	-0.017	235.62	-0.005	359.81	0.045
36.96	0.0	138.60	-0.011	240.24	-0.035	366.18	0.02
41.58	-0.015	143.22	-0.02	244.86	-0.015	372.55	-0.02
46.20	-0.025	147.84	-0.015	249.48	-0.033	378.92	-0.01
50.82	-0.033	152.46	-0.03	254.10	-0.042	385.29	-0.01
55.44	0.007	157.08	-0.01	258.72	-0.027	391.66	0.018
60.06	0.008	161.70	-0.015	263.34	-0.003	398.03	-0.029
64.68	0.002	166.32	-0.015	267.96	-0.02	404.40	-0.008
69.30	0.002	170.94	-0.038	272.58	0.025	410.77	-0.011
73.92	-0.015	175.56	-0.032	(at d) 277.20	0.040	417.14	0.0
78.54	-0.005	180.18	-0.040	283.37	0.0	423.51	-0.005
83.16	0.0	184.80	-0.02	289.74	-0.015	429.88	-0.015
87.78	-0.03	189.42	0.024	296.11	-0.005	436.25	0.002
92.40	-0.005	194.04	-0.012	302.48	-0.025	442.62	0.01
97.02	0.01	198.66	-0.02	308.85	-0.009	(at m_1) 448.99	0.01

TABLE 3-1 (contd.)

X_c	ε_θ	X_c	ε_θ	X_c	ε_θ	X_c	ε_θ
455.36	-0.015	576.39	-0.016	697.42	-0.002	818.45	0.027
461.73	0.0	582.76	0.0	703.79	-0.025	824.82	0.038
468.1	-0.02	589.13	-0.015	710.16	-0.065	831.19	-0.015
474.47	-0.02	595.50	-0.026	716.53	-0.008	837.56	0.04
480.84	-0.008	601.87	-0.003	722.90	0.02	843.93	0.04
487.21	0.02	608.24	-0.009	729.27	-0.05	850.30	0.035
493.58	0.017	614.61	0.015	735.64	-0.055	856.67	0.005
499.95	-0.03	620.98	-0.038	742.01	-0.005	863.04	-0.018
506.32	0.01	627.35	-0.01	748.38	-0.035	869.41	0.063
512.69	-0.019	633.72	-0.003	754.75	-0.015	875.78	0.047
519.06	-0.023	640.09	0.018	761.12	-0.02	882.15	0.033
525.43	-0.02	646.46	-0.015	767.49	-0.035	888.52	0.014
531.00	-0.017	652.83	-0.025	773.86	-0.011	894.89	-0.087
538.17	-0.01	659.20	0.0	780.23	0.0	901.26	-0.074
544.54	-0.02	665.57	-0.013	786.60	-0.1	907.63	-0.033
550.91	-0.02	671.94	0.03	792.97	0.018	914.00	-0.032
557.28	-0.035	678.31	-0.067	799.34	0.034	920.37	-0.055
563.65	-0.01	684.68	0.004	805.71	0.03	(at b) 926.74	-0.01
570.02	-0.019	691.05	-0.06	812.08	-0.015		

difference between the elevation angle readout for the omni horn pointing along runway 13L CL and that for the directional horn pointing at EL 1. These differences will yield the elevation angle errors at various points along the measurement path on runway 13L CL. In general, the errors were smaller than 0.05 degrees. These errors will be compared with the predicted error trace from the corresponding MLS simulation run.

d. MLS Simulation Runs

MLS simulations were made for the horizontal cut along the runway 13L CL. The measurement path from point c to the landing threshold was simulated in two runs, as indicated in Fig. 3-2. The first run covered the path from point c to point m_1 which was 530 feet before the landing threshold. For this run, the multipath was expected from HGR3, the center building (CNT) and part of HGR4. We used a 40-plate model for HGR3 and a 5-plate model for the center building, as shown in Fig. 3-6. The part of HGR4 which was involved in this run was modeled with 5 plates, B8 to B12 shown in Fig. 3-6. The second run covered the path from point m_2, which was 100 feet before the point m_1, to the landing threshold. For this run, the multipaths were expected from part of HGR3, CNT, and HGR4. Hangars were modeled similarly to the first run.

The M/D ratios for the first and the second runs are shown in Figs. 3-7 and 3-8, respectively. The multipath levels from the measurements are also shown in these figures. The measured and computer simulation predicted multipath levels both include the azimuth pattern of the elevation antenna. Although these measured multipath levels cannot be meaningfully compared with the simulation results, because of the AGC in the receiver during the measurement, the average fluctuation in the measured multipath levels can still be visualized in these figures. It can be seen that the M/D ratios fluctuate a lot along the path; however, the multipath levels are not high. The fluctuation of M/D ratios probably is due to the crossing of the Fresnel zone over the junction of two doors and the edges of pillars. Figs. 3-9 and 3-10 compare the measured and computer simulation predicted elevation angle errors. The measured errors were hand-reduced from receiver output records on a spatial grid which was coarser than

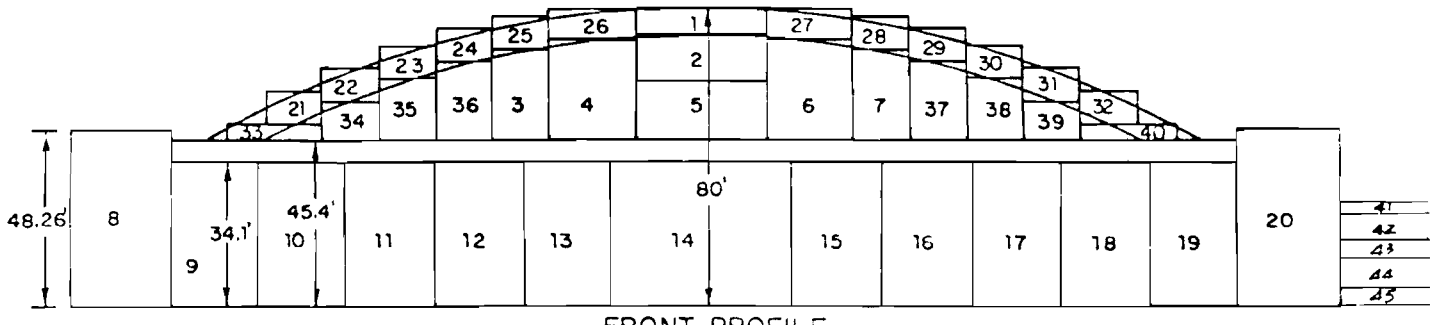

FRONT PROFILE

NOTE: Plates 41 to 45 were used to model the center building between HGRs 3 and 4.

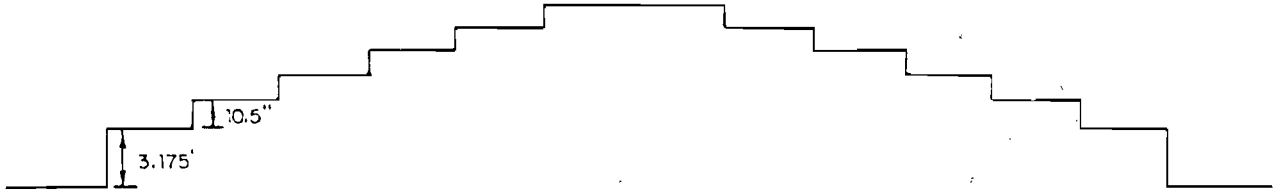

DETAILS OF DOOR STAGGERING

Fig. 3-6. Model for hangars 3 and 4 used in the simulation for December 1977 horizontal cut along JFK runway 13L centerline.

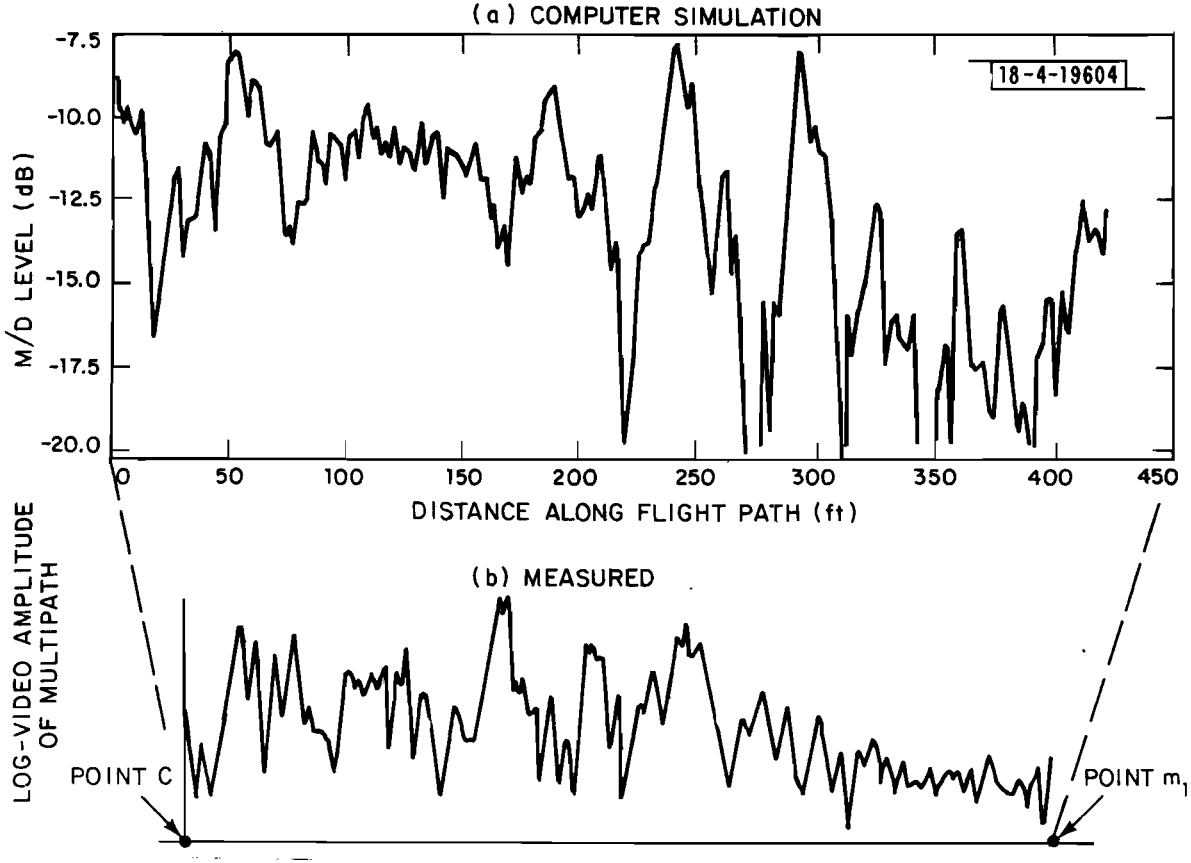

Fig. 3-7. Multipath levels of computer simulation and measured (with AGC) results for December 1977 horizontal cut along JFK runway 13L centerline: Receiver height = 44', run #1.

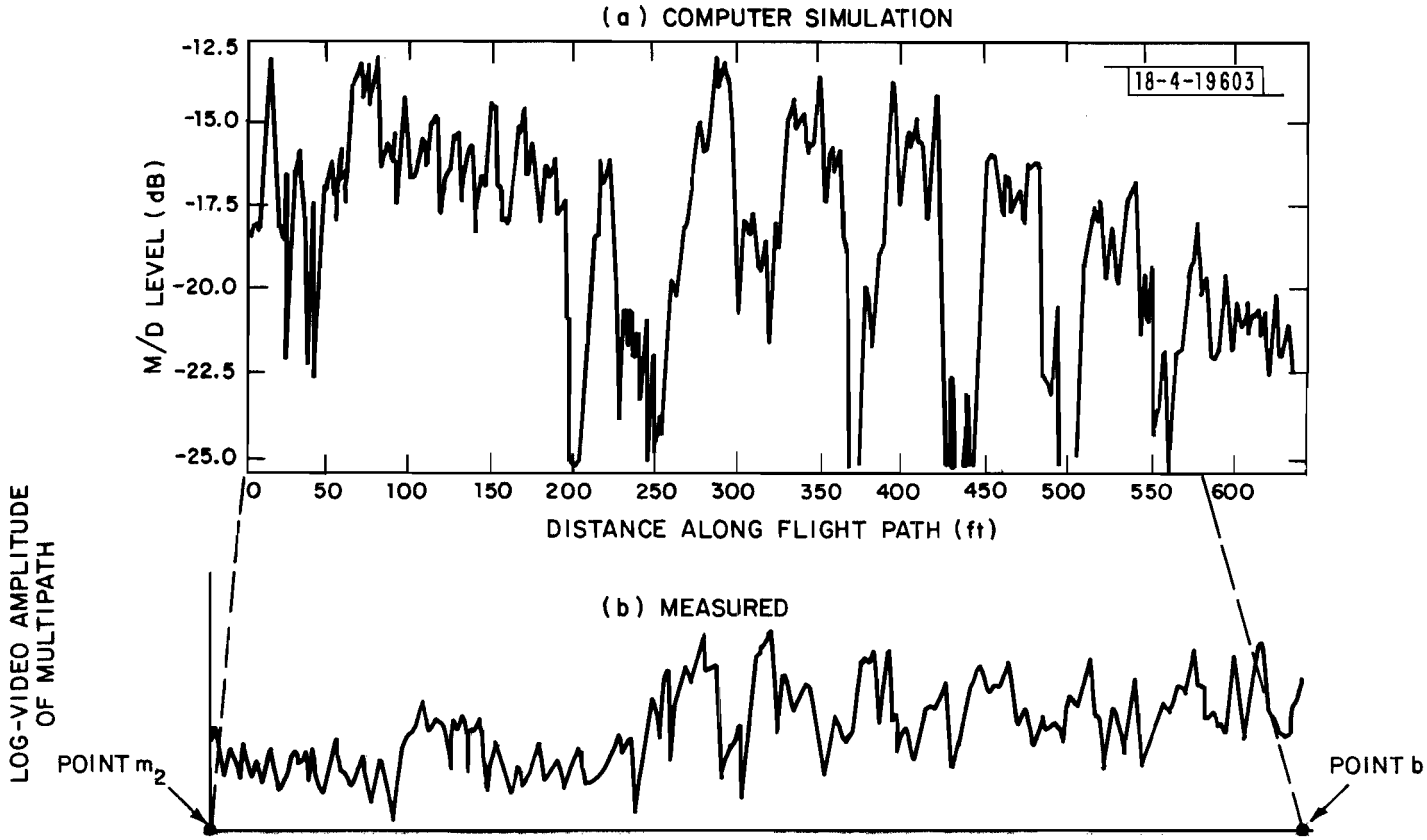

Fig. 3-8. Multipath levels of computer simulation and measured (with AGC) results for December 1977 horizontal cut along JFK runway 13L centerline: receiver height = 44', run #2.

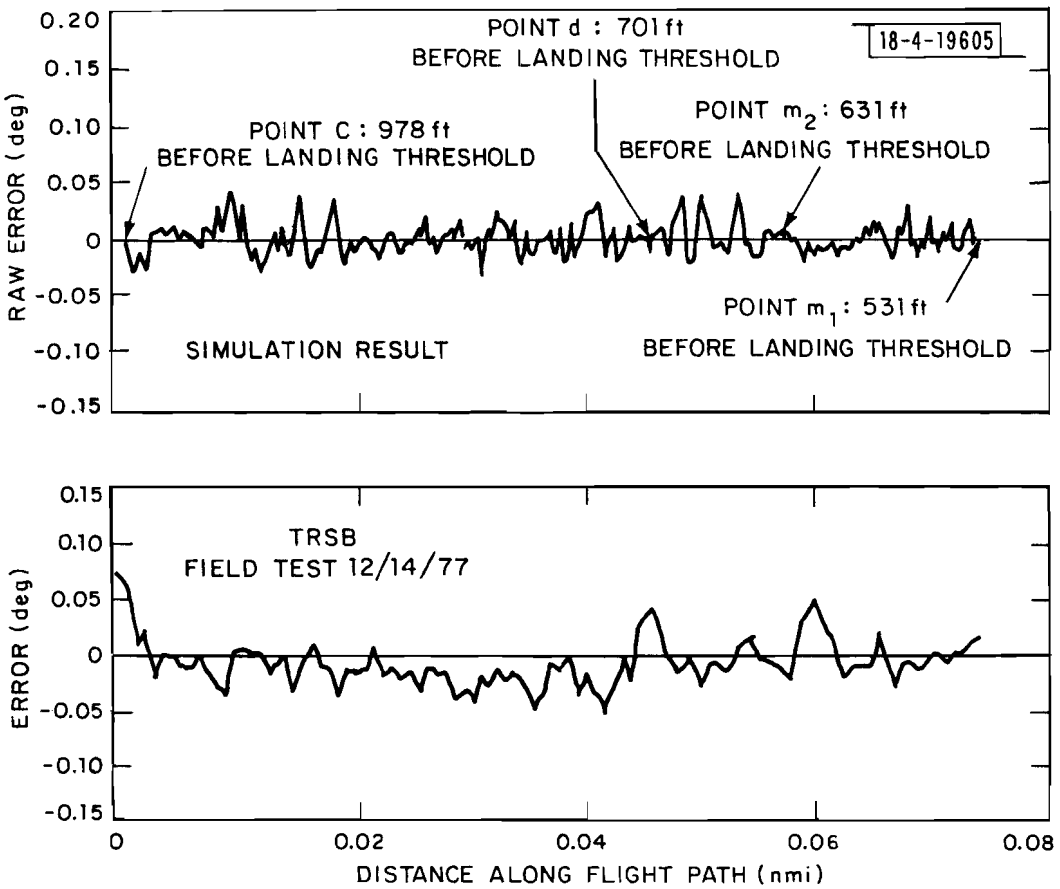

Fig. 3-9. Comparison of simulation with TRSB field data from moving van test on JFK runway 13L centerline.

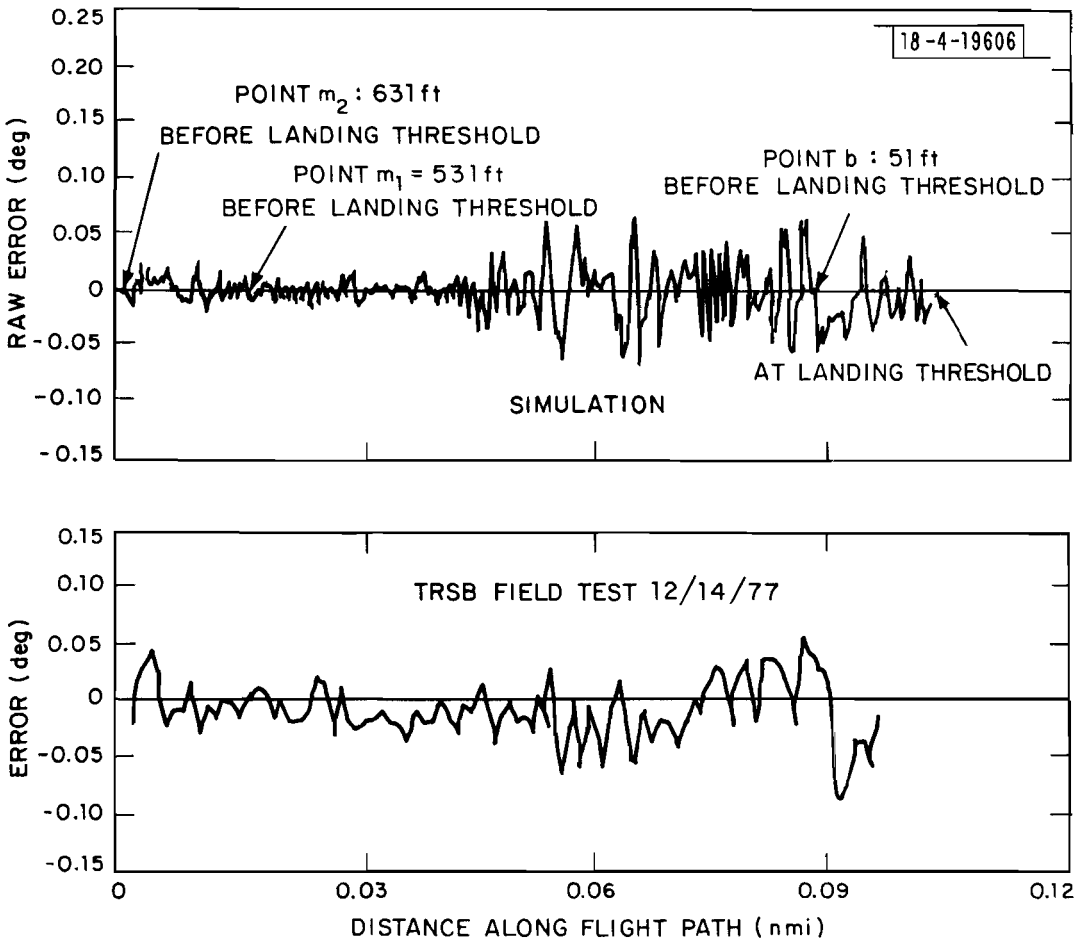

Fig. 3-10. Comparison of simulation with TRSB field data from moving van test on JFK runway 13L centerline.

that of the simulation. This results in an apparent difference in frequency content which probably does not reflect the actual situation. However, as shown in Figs. 3-9 and 3-10, we see that the magnitude of the angle error from the computer simulation agreed well with the field measurements. No significant angle errors (i.e., errors > 0.10°) were observed in the measurements or the simulation runs.

2. 2-3 MARCH 1978 MEASUREMENTS

a. Measurement Environment

Fig. 3-11 gives a sketch which shows the locations of the EL1 antenna and the hangars of interest near the landing threshold of JFK runway 13L. For this measurement, the EL1 antenna was sited at 250 feet south of runway 13L CL and 1019 feet after the landing threshold. The hangars involved in this measurement were the same as those involved in the December 1977 measurement. Measurements were made with a TRSB basic narrow receiver on the MLS van, with the AGC disabled. The EL1 antenna was a basic narrow antenna.

b. Measurements Made

Three vertical cuts were made at points A, B* and C*, as indicated in Fig. 3-11. The receiving antenna mast was moved from 30 foot height to a 70 foot height and measurements were made at every 2 foot interval. The same 20° directional horn and 180° omni horn were used in these measurements as those used in the December 1977 measurement, for the same purposes as described in subsection III-A-1-b. Also, six vertical cuts were made at points a, b, c, d, e, and f, 80 feet in front of HGR3 as shown in Fig. 3-11. These close-in measurements were for the purpose of estimating the reflection coefficients on various parts of HGR3.

---

*From the reflection geometry shown in Fig. 3-11, points B and C appear to be not the optimum locations for making the measurements. The cause of this apparent misplacement is that the locations of points B and C were determined from an FAA map which had an inaccurate location of the hangars relative to the runway 13L CL.

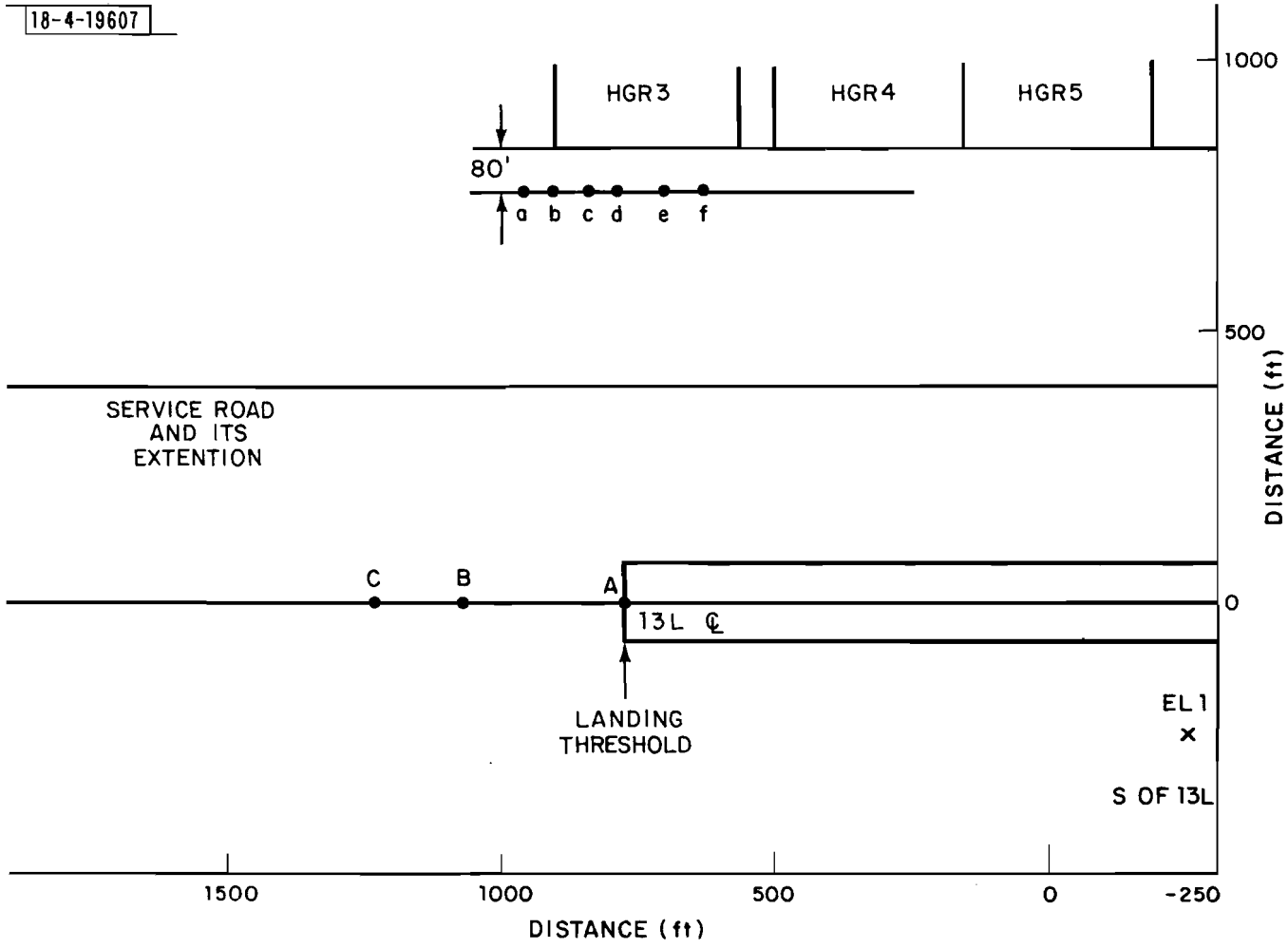

Fig. 3-11. Location of MLS van measurements at JFK runway 13L, March 1978.

c. Measurement Results

The received log-video amplitudes and the elevation angles were obtained for every 2 foot interval along the vertical cuts at points A, B, C, a, b, c, d, e, and f (Fig. 3-11). Since the receiver used in these measurements has no AGC, the measured log-video amplitudes can be used directly to obtain the M/D ratios to be compared with the computer simulation results. The measured results from the vertical cuts at point A, B, and C along the runway 13L CL will be compared with the computer simulation results. The measurements from the vertical cuts in front of HGR3 (points a, b, c, d, e, and f, in Fig. 3-11) yielded material reflection coefficients of 0.4 for the side pillars, 0.83 to 1.0 for the doors, and 0.71 for the arc above the door. The peak multipath levels observed for the vertical cuts on the runway 13L CL are -16 dB, -20 dB, and -12 dB at points A, B, and C, respectively. In general, the angle errors were less than 0.05 degrees.

d. Simulation Runs

The MLS simulation runs were made for the vertical cuts on the runway 13L CL. At point A, multipath was expected from HGR4. Therefore, HGR4 was modeled with a 50-plate model shown in Fig. 3-12. Each hangar door was modeled with 2 plates, an upper plate for the glass window/metal part of the door and a lower plate for the flat metal part of the door. At points B and C, the building model consisted of the right half of the HGR3 model, the center building (CNT) described earlier and the left half of the HGR4 model.

The M/D ratios from the simulation runs for the vertical cuts at point A, B, and C are shown in Fig. 3-13 through 3-15, respectively. Superimposed on these figures are the measured M/D ratios. The measured and the computer simulation predicted multipath levels both include the azimuth pattern of the EL1 antenna. The peak M/D ratios from the simulation runs are -18 dB, -22 dB, and -13 dB at points A, B, and C, respectively. These values agree well with the measurements. However, it should be noticed that the measured multipath level probably is sensitive to the detailed location of the measurement point on the runway 13L CL, judging from the fluctuation in the M/D ratios observed in the simulation runs for the December 1977 horizontal cut along the runway 13L CL, as shown in Figs. 3-7 and 3-8.

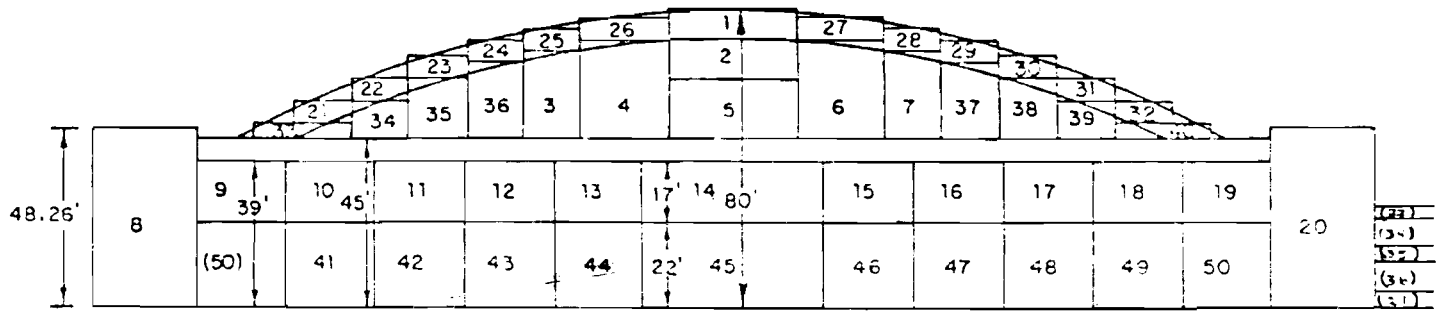

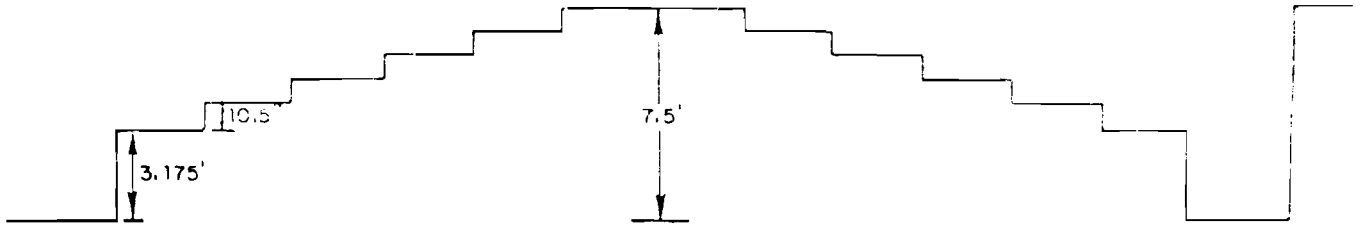

Fig. 3-12. Model for hangars 3 and 4 used in the simulation for March 1978 MLS static van measurements at JFK runway 13L.

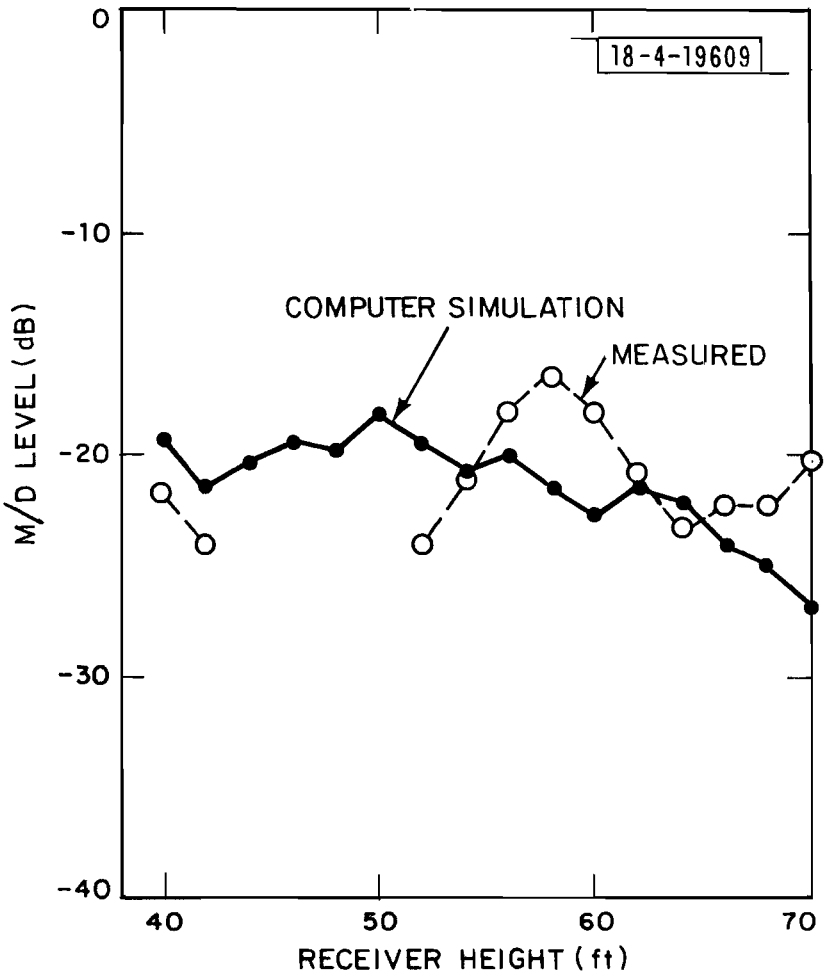

Fig.3-13. Comparison of measured and computed simulation predicted M/D levels for vertical cut at point A on JFK runway 13L centerline.

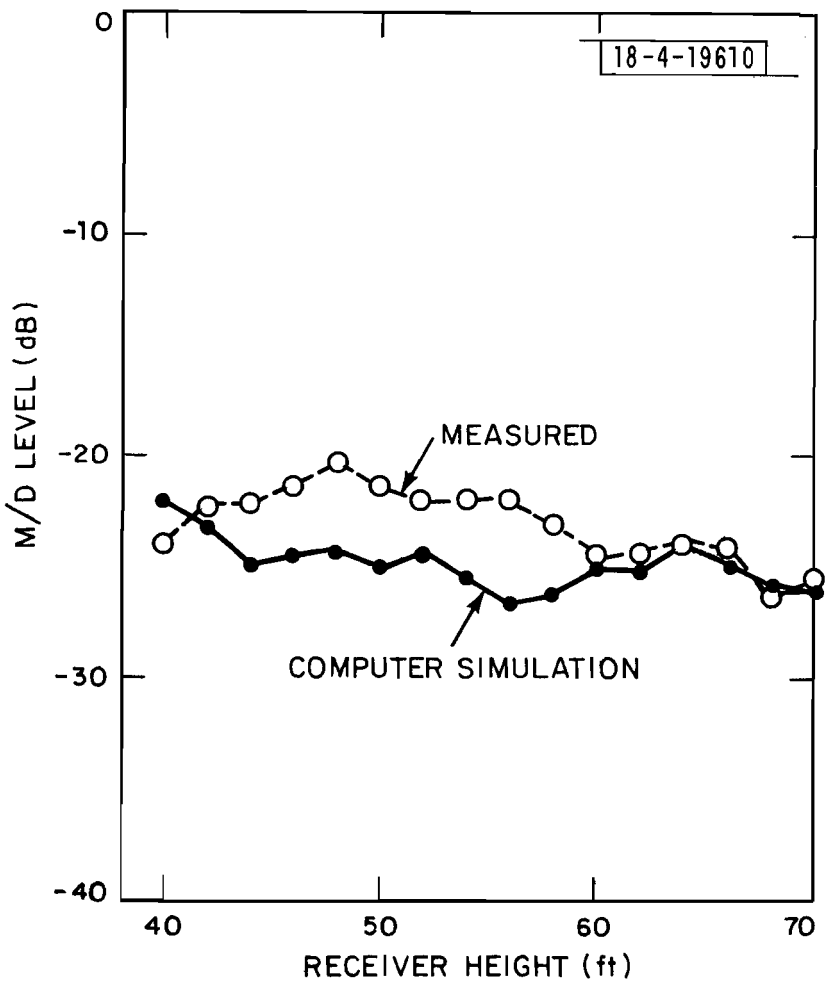

Fig.3-14. Comparison of measured and computed simulation predicted M/D levels for vertical cut at point B on JFK runway 13L centerline.

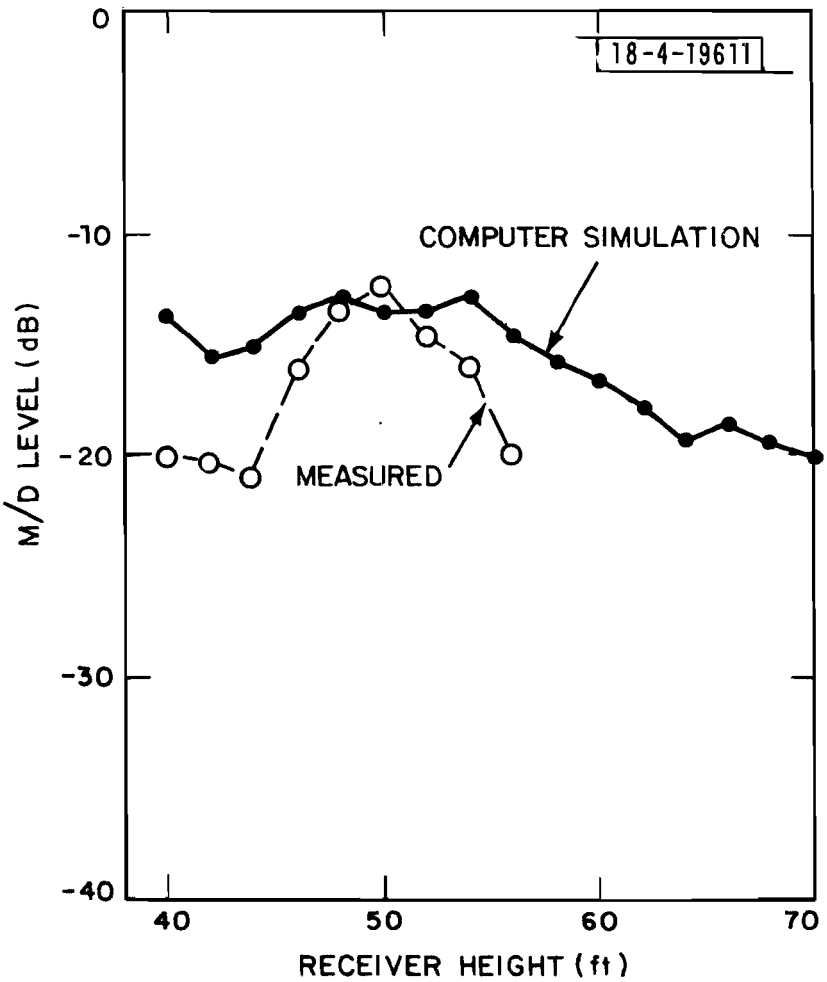

Fig.3-15. Comparison of measured and computed simulation predicted M/D levels for vertical cut at point C on JFK runway 13L centerline.

The errors in the elevation angles from the simulation runs are shown in Figs. 3-16 through 3-18. Also shown in these figures are the elevation angle errors from the measurements. The agreement between the simulation results and the measurement results is good for the magnitude of the angle error, although the sign of the angle error from the simulation does not quite follow the measurement. In considering these results, it should be noted that the intent had been to make the van vertical cuts at the locations in which the results should not be highly sensitive to the receiver position. Unfortunately, the survey data used to determine those points was subsequently found to be in error, with the end result being that the results at location C are particularly sensitive to the receiver location. In all cases, the sign of the angle error is very sensitive to the van lateral position.

3. Summary

The computer simulation results and the MLS field measurement data at JFK have been compared over a variety of static and moving van pole cuts. In all cases, insufficient accuracy in the airport geometry and the measurement paths of the pole cuts meant that only the gross error features (e.g., error magnitude, peak and region) could be meaningfully compared. Keeping these factors in mind, the overall agreement between computer simulation results and the JFK field measurement results is regarded as quite good.

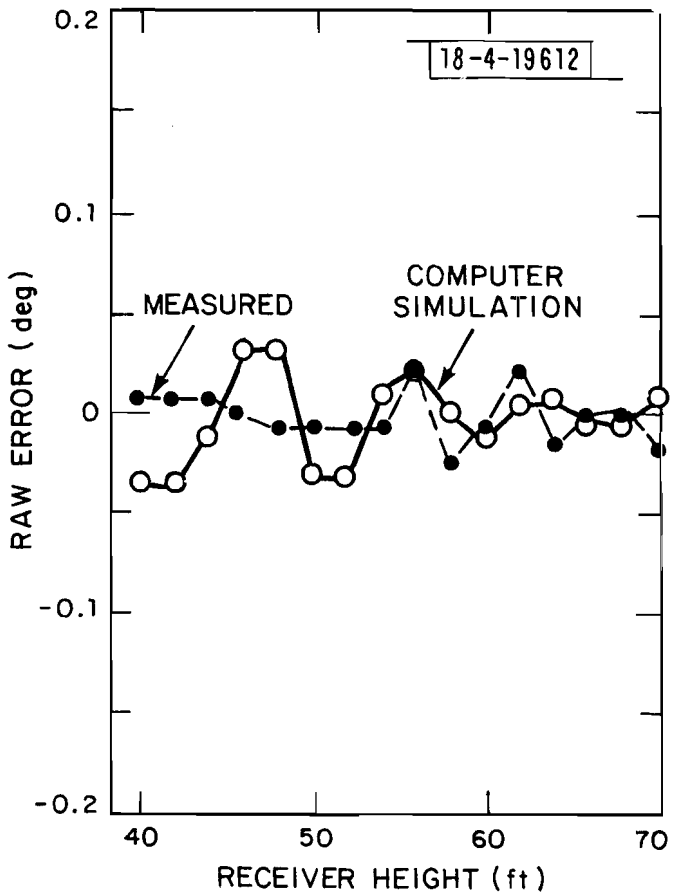

Fig.3-16. Comparison of measured and computed simulation predicted angle errors for vertical cut at point A on JFK runway 13L centerline.

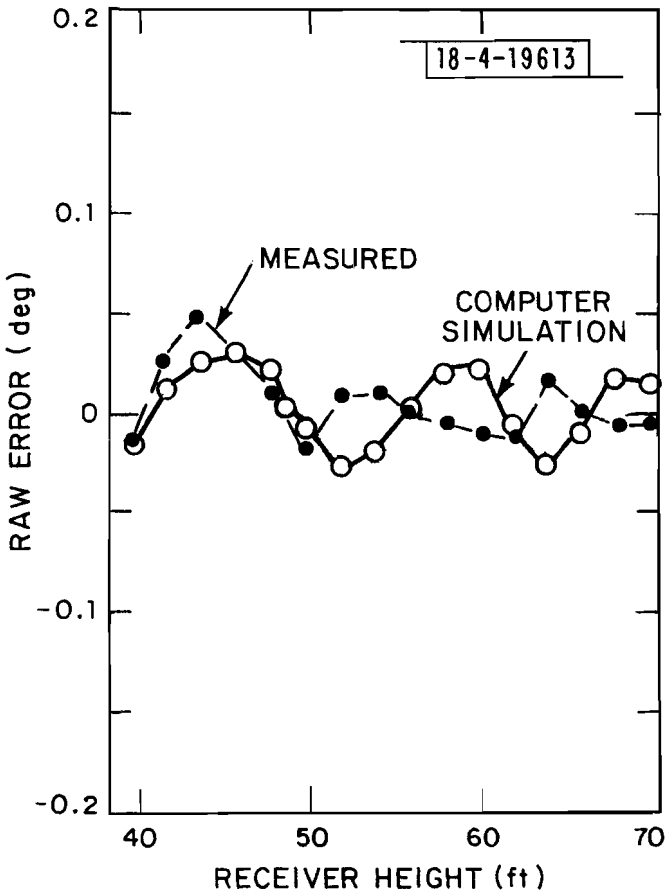

Fig.3-17. Comparison of measured and computed simulation predicted angle errors for vertical cut at point B on JFK runway 13L centerline.

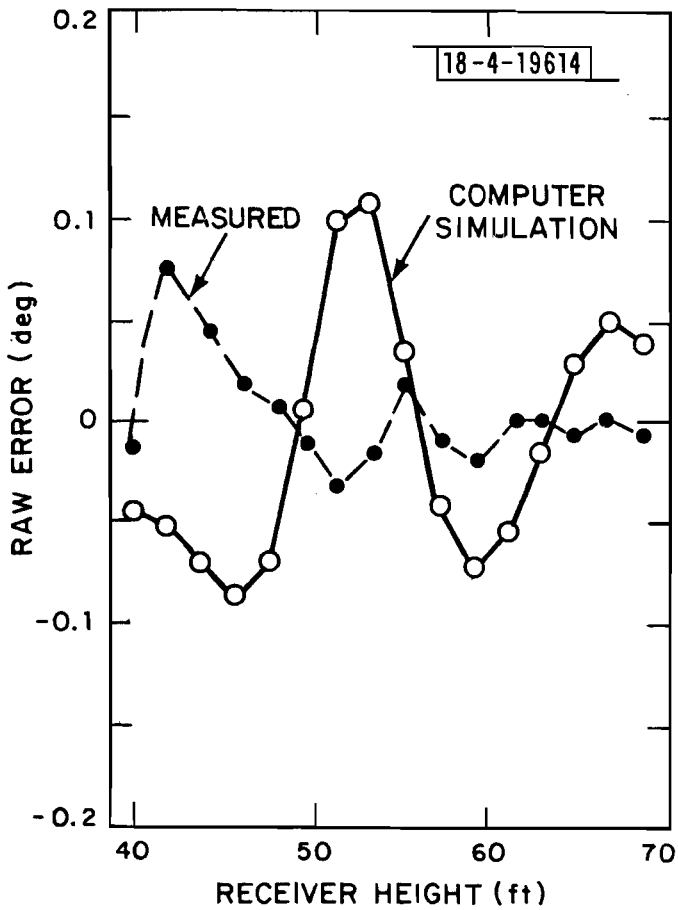

Fig.3-18. Comparison of measured and computed simulation predicted angle errors for vertical cut at point C of JFK runway 13L centerline.

B. Results of MLS Azimuth Multipath Measurements at Four Operational Airports

1. Introduction

The characteristics of MLS azimuth multipath at operational airports received considerable attention recently due to the differences in system azimuth multipath performance which emerged in the Lincoln computer simulations. Much of the initial MLS field testing was done at airports which were fairly benign from the viewpoint of natural azimuth multipath [9]. Similarly, most of the trials and/or demonstrations in connection with the ICAO AWOD meeting [58 - 63] were not conducted at sites which yielded high level azimuth multipath. Conducting full MLS field trials at an operational airport is a costly and logistically difficult task, thus a simple multipath measurement program was undertaken to characterize the multipath at several U.S. airports (St. Louis, Miami, Tulsa and Wright Patterson Air Force Base) whose geometry suggested the possibility of substantial multipath.

The specific objectives of the measurement program were to:

(1) confirm that azimuth multipath at operational airports can have the high levels, scalloping frequencies, and phase coherence* assumed in the computer simulations and analytic studies to date [10-15, 28, 29, 64].

(2) determine which, if any, of the airports would offer challenging multipath environments

(3) provide additional detailed data for validation of the Lincoln MLS propagation model.

All of these objectives were achieved in the measurement program. This section is primarily concerned with reporting the results which bear on objectives (1) and (2). A quantitative comparison of some of the field data with the propagation model is reported in Section C of this chapter.

*Phase coherence here refers to the stability of the scalloping frequency over an MLS measurement period of 30 msec (for DMLS) to 200 msec (for TRSB or DLS). This phase coherence is an important factor in motion averaging and DMLS reference scalloping effects.

The multipath measurement equipment is described in Section 2. A highly mobile equipment was desired which could measure the multipath parameters of greatest interest. This was accomplished by radiating a CW signal through a wide coverage antenna so that the direct signal and reflected signals were simultaneously received aboard an aircraft. The frequencies of the various received signals differ by the various Doppler shifts due to receiver motion (i.e., scalloping frequency)*, thus the multipath signal characteristics (e.g., level, scalloping frequency, scalloping frequency stability, and scatterer bearing from the aircraft) can be determined by spectrum analysis of the received signal as illustrated in Fig. 3-19. The received signals were coherently demodulated and recorded on analog tape. The analog tapes were then digitized and Fourier analyzed to determine the multipath environment at various points along the flight path. Figure 3-20 shows a typical spectrum plot from the data measured in the flare region at Wright Patterson.

Section 3 describes the multipath data reduction method. Fast Fourier transforms (FFT) were made of short segments of the data with time windows utilized to minimize sidelobe effects. This technique was applied to both the coherently demodulated signal and to the log video signal. Also reported in Section 3 are the results of bench tests, aircraft runup tests and flight tests to quantitatively characterize the received spectrum modifications due to the instrumentation and aircraft environment (e.g., vibration, propeller modulation).

Sections 4-7 describe the measurement results at St. Louis, Tulsa, Wright Patterson AFB and Miami, respectively. Each section starts with a description of the airport geometry map, the major multipath threats, and expected multipath regions. Next, the results of the spectrum analysis at various points along the flight path are shown. Finally, the field data is compared with the anticipated multipath regions.

Section 8 summarizes the results of the measurement program.

*This is precisely the physical phenomena which leads to the "reference scalloping" error mechanism in the Doppler scan technique which is discussed in Volume III of this report.

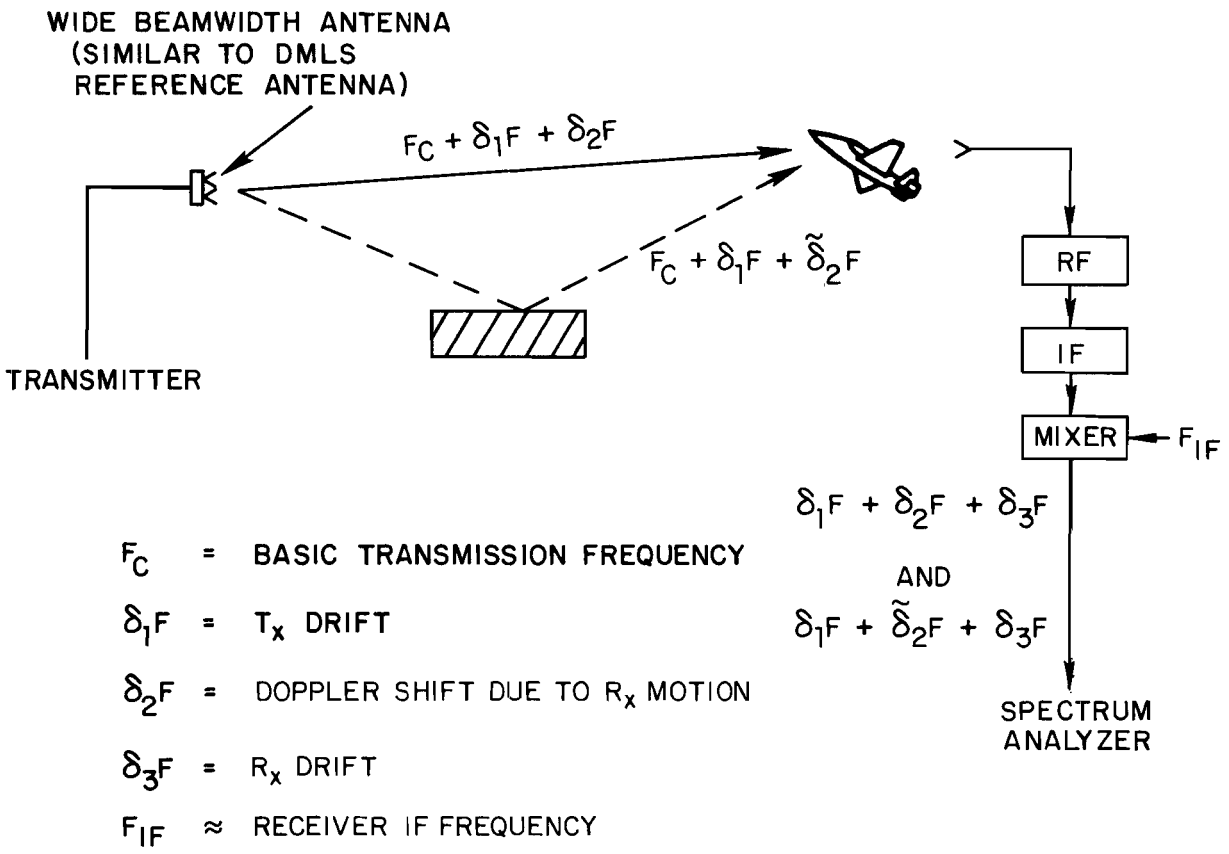

Fig. 3-19. Determination of multipath characteristics from spectrum analysis of received signal.

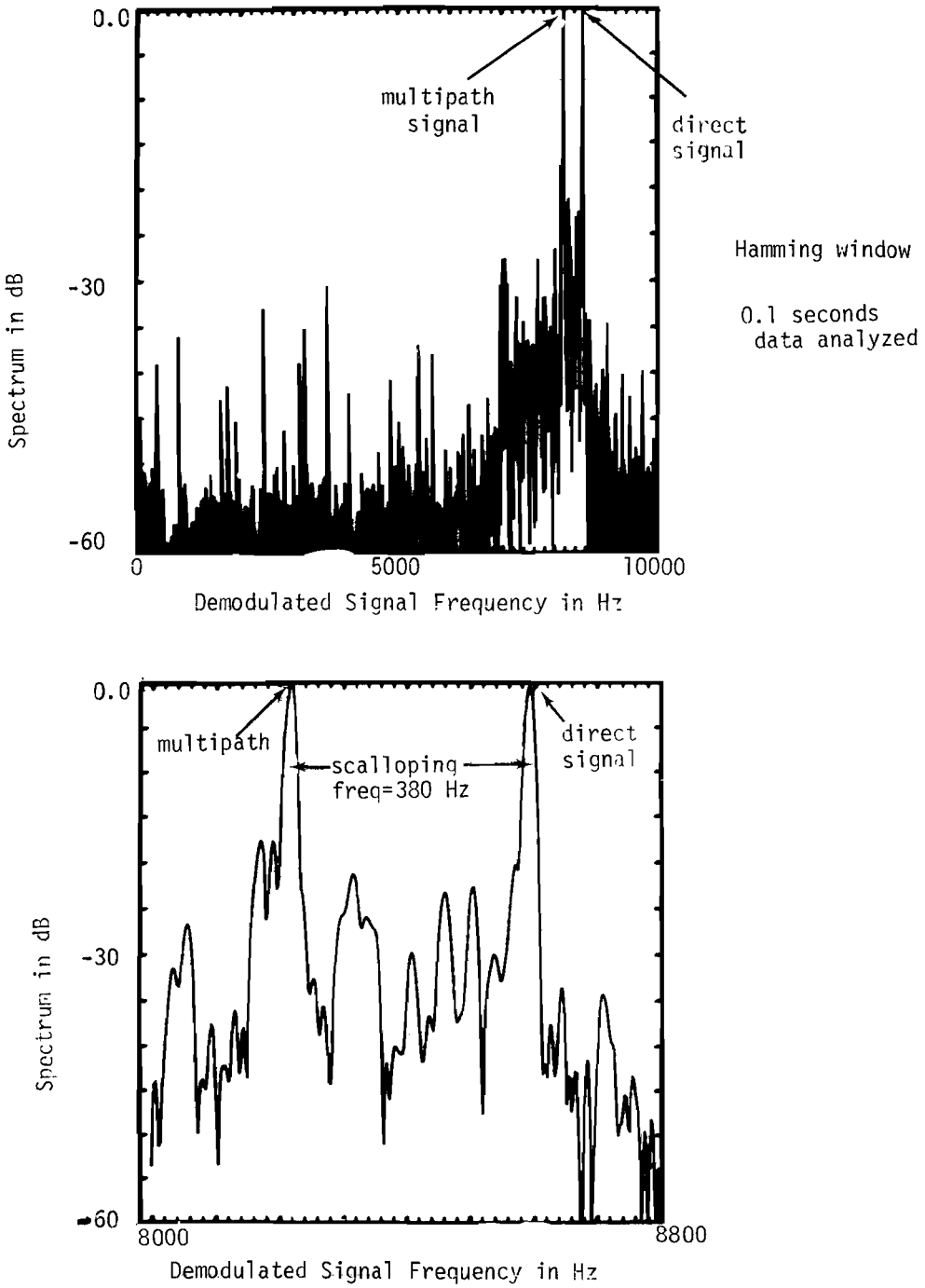

Fig.3-20. Spectrum of received signal at Wright Patterson AFB.

2. Equipment Configuration

The urgency of the MLS multipath field measurement program made it imperative that the technique chosen be relatively straightforward and that the required hardware components be readily available or easily and quickly fabricated. The method that was finally adopted is illustrated in the block diagrams of Figs. 3-21 and 3-22. Many of the components were borrowed from the FAA's inventory of MLS equipment spares. A few of the components as well as all mechanical mounting hardware associated with the aircraft and ground installations were fabricated at Lincoln Laboratory.

Basically the measurements involve use of a ground-based C-band transmitter and MLS wide beamwidth antenna to radiate a C W signal over a wide region of azimuth angles. The composite C W signal of interest consisting of the direct and reflected components is received, demodulated and recorded via an airborne TRSB phase II receiver and analog FM recorder. The recorded signals are later processed in the laboratory to extract information pertinent to characterization of the prominent reflecting surfaces.

a. Ground Equipment

Fig. 3-21 is a simplified block diagram of the ground-based transmitting equipment employed for the multipath measurements. A stable crystal-controlled exciter operating at a frequency of 5189.4 MHz is used to drive a TWT amplifier. The exciter output of +21 dBm is attenuated by 9 dB in order to match the signal level to the input range of the TWT amplifier. The amplifier has a gain of 30 dB and provides a maximum output of 15 watts CW.

The ground based antenna is an TRSB Forward Ident. column radiator manufactured by Bendix Corp. The azimuth and elevation patterns of the antenna are illustrated in Fig. 3-23 and 3-24. The peak gain of the antenna at an elevation angle of 2 degrees is approximately 14 dB.

Fig. 3-25 is a photograph of the ground-based antenna and transmitting equipment. The antenna mounting stand was designed with adjustable base pads in each of its three legs to allow for exact vertical alignment prior to each data recording mission.

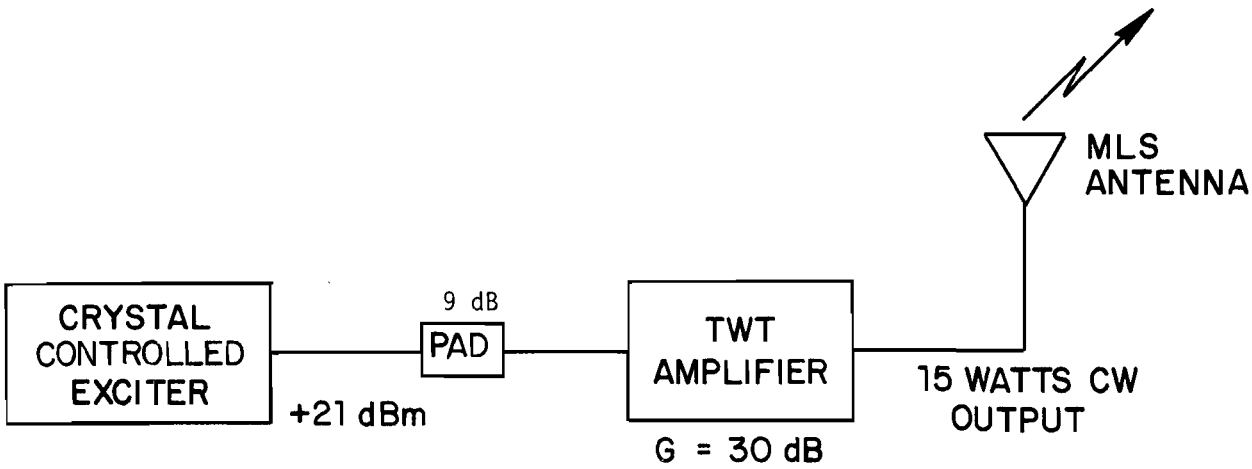

Fig. 3-21. Ground based transmitter configuration for MLS multipath measurements.

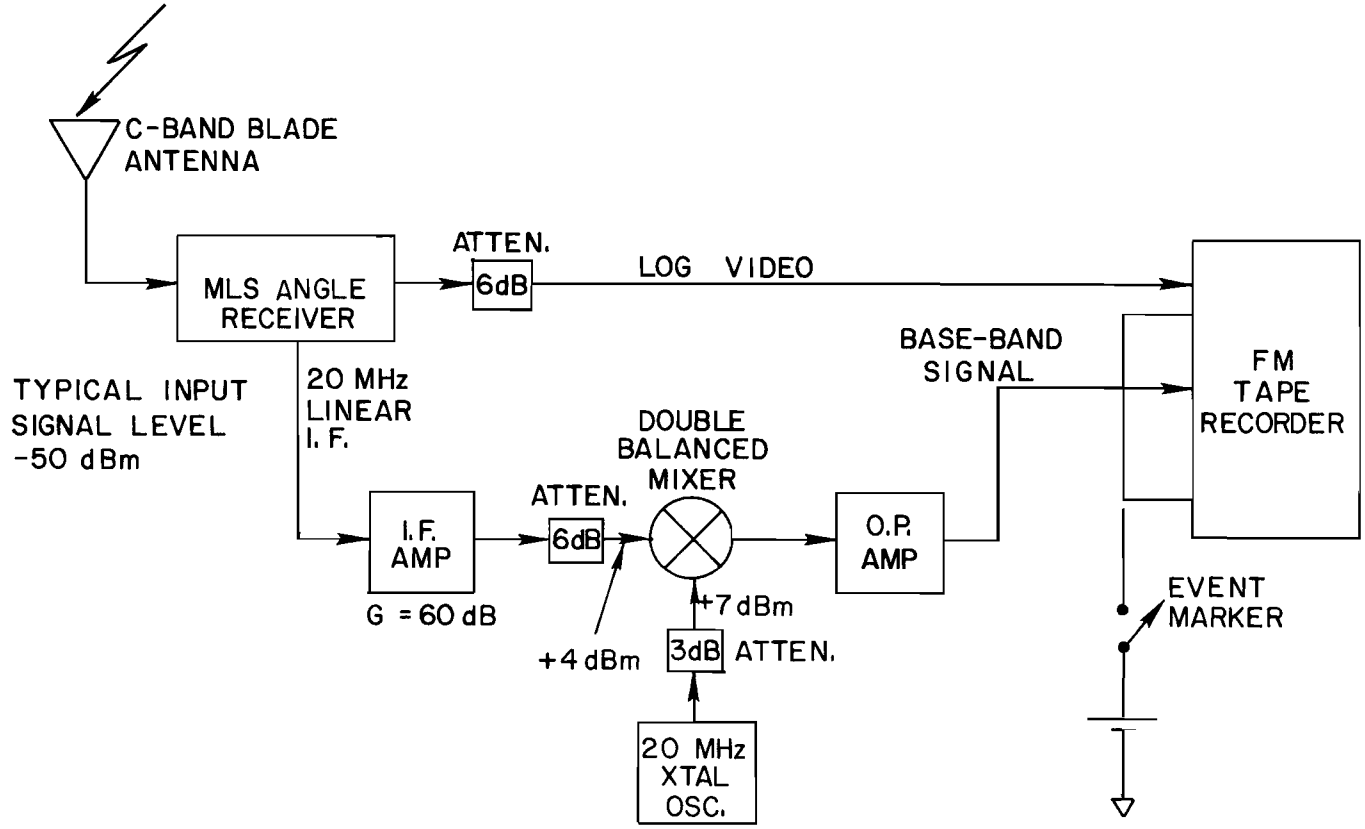

Fig. 3-22. A/C receiver/recording configuration for MLS multipath measurements.

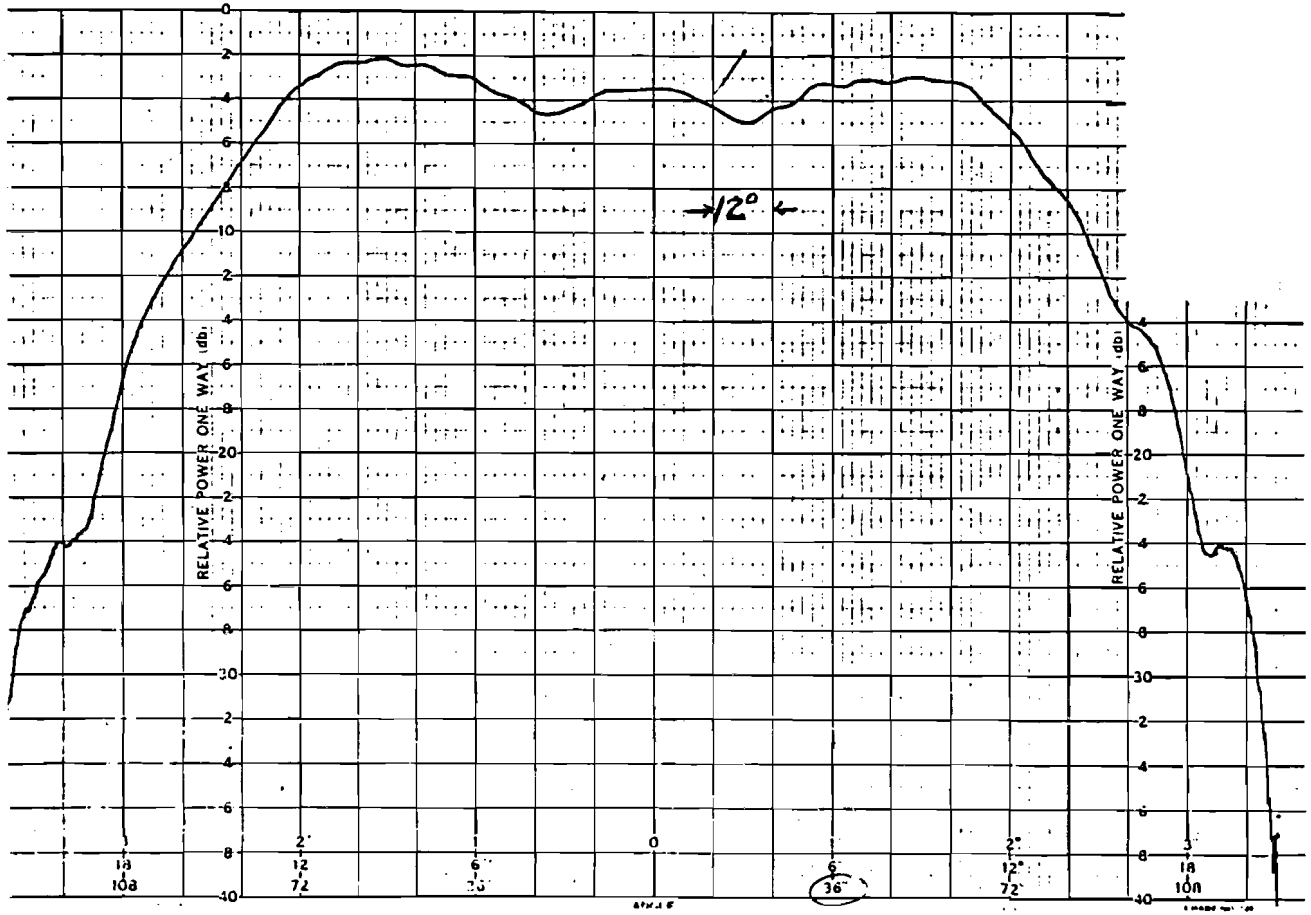

Vertical scale 2 dB/div
Horizontal scale 12 deg/div.

Fig. 3-23. Azimuth pattern-forward ident. antenna.

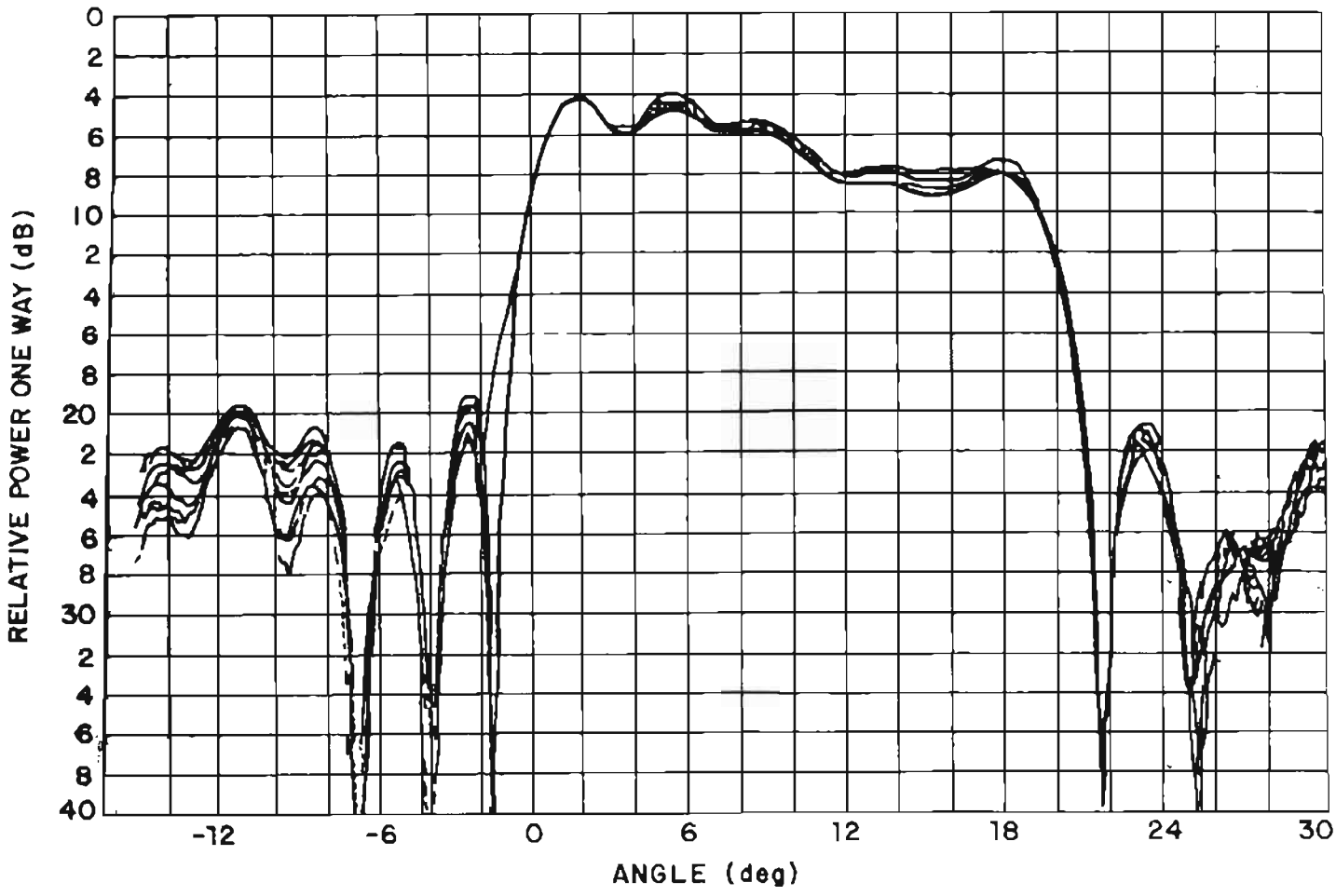

Fig. 3-24. Elevation patterns of MLS forward ident. antenna.

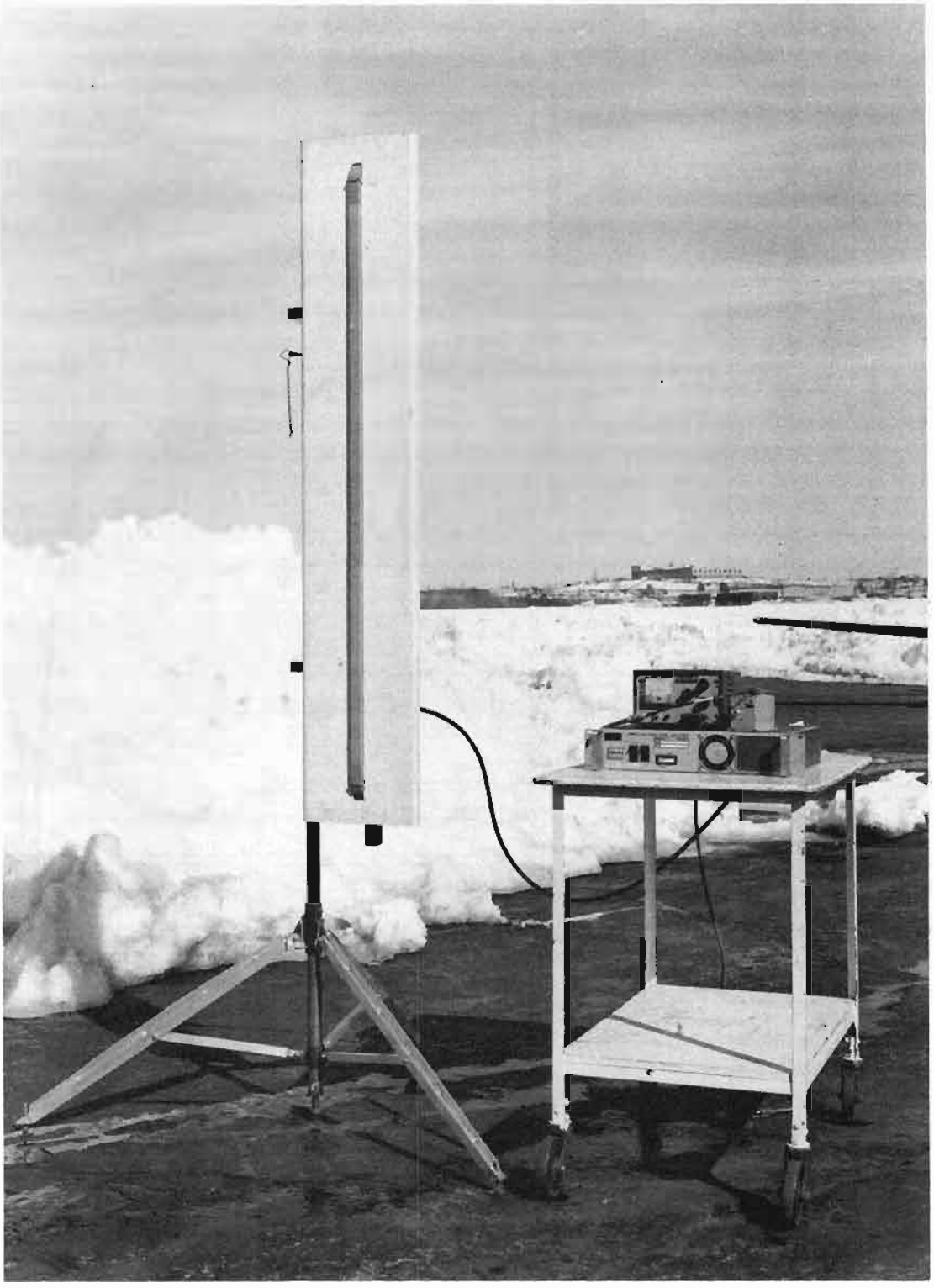

Fig. 3-25. MLS multipath measurement ground equipment.

b. Aircraft Equipment

Fig. 3-22 is a simplified block diagram of the receiving equipment used for the tests. The equipment was installed on board a Piper Navajo aircraft leased for the purpose. The photographs in Figs. 3-26 through 3-28 illustrate the aircraft and the mounting and location of the receiving equipment.

Reception of the composite signal is accomplished by use of a C-Band blade antenna mounted near the nose of the aircraft (see Fig. 3-29). The signal is then routed via 15 feet of RG-214 coaxial cable to a Bendix Phase II MLS angle receiver located in the cabin directly behind the pilot's seat. The RF, IF, and log detector portions of the Bendix receiver are used to generate the necessary signals for analog recording. A log detected video output is already available from the Bendix receiver. A minor modification was required in order to provide a linear 20 MHz IF signal output for spectral analysis. The IF output signal is then amplified and demodulated to a base-band signal (zero IF) by mixing with a stable-crystal controlled 20 MHz oscillator.

The overall RF and IF gain of the receiver path was chosen to provide the best match between expected RF input levels and receiver dynamic range. Typically the maximum RF signal input levels encountered for most of the data recording flights was on the order of -50 dBm. An overall gain of 54 dB results in an optimal IF signal level at the mixer of +4 dBm. The expected maximum signal levels of both the log detector and demodulator outputs are further adjusted to match the 1 volt RMS input requirement of the FM tape recorder for a nominal -50 dBm input.

The recorder is a 7-track Honeywell 5600 FM tape recorder with 4 channels for FM recording and 3 channels for direct recording. The log video and base-band signals as well as an event mark are recorded on the FM channels. An internally generated reference tone is recorded on a direct channel for later playback servo control.

Fig. 3-26. Test aircraft Piper Navajo.

Fig. 3-27. MLS multipath measurement airborne equipment.

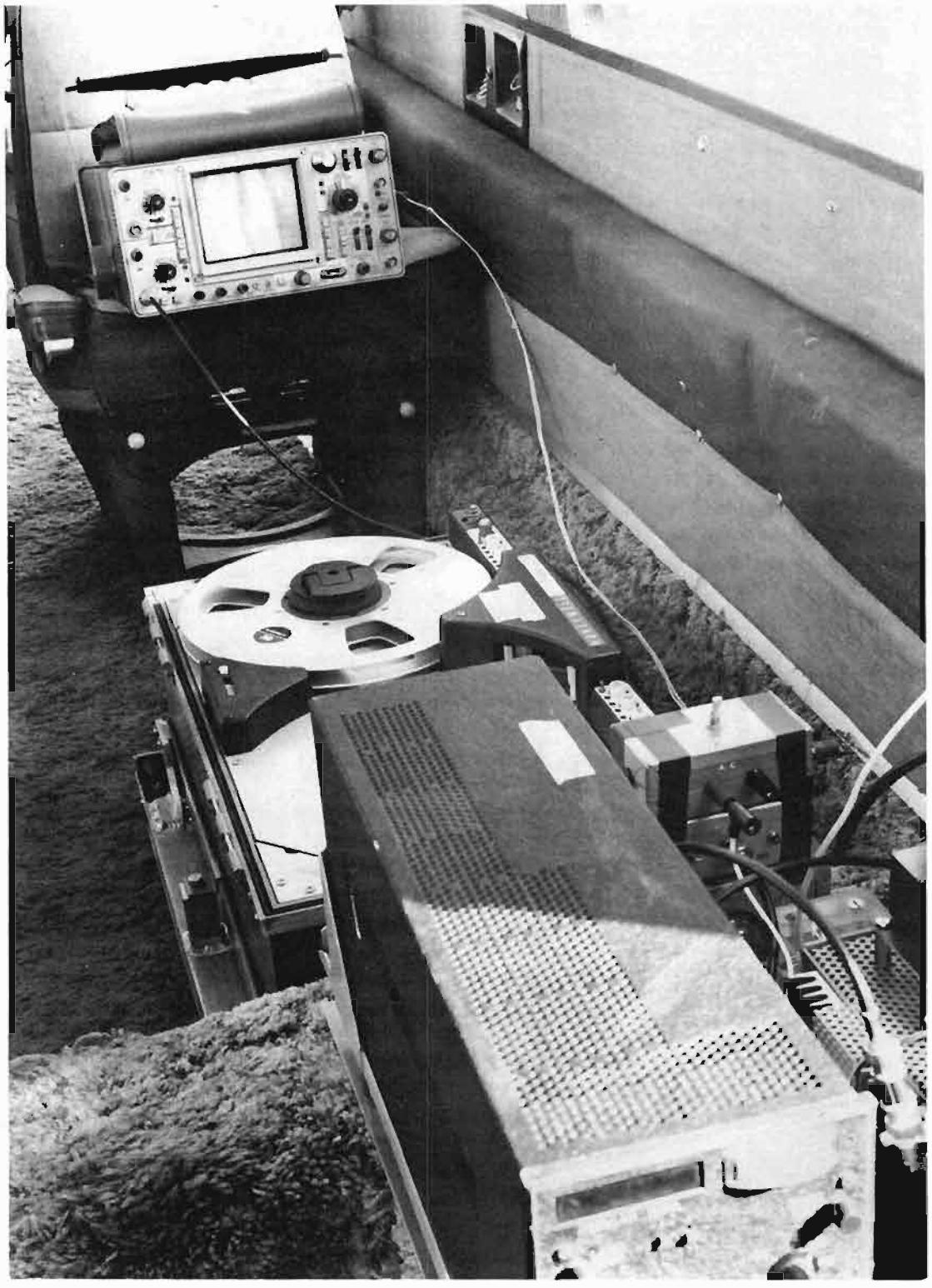

Fig. 3-28. MLS multipath measurement airborne equipment.

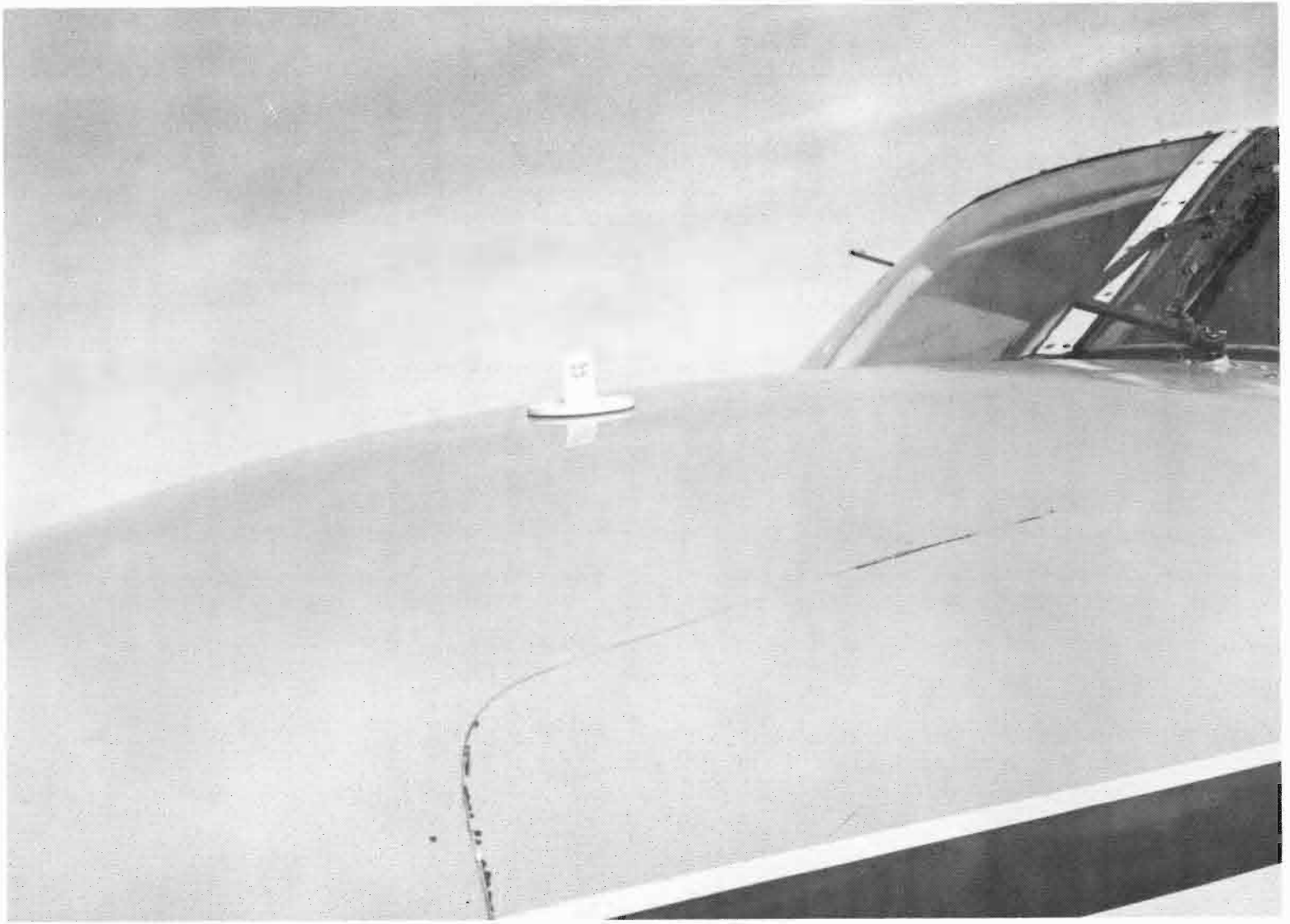

Fig. 3-29. Mounting location of A/C C-band blade antenna.

All of the data recording was made at a tape speed of 60 ips which results in an overall signal bandwidth of 40 KHz. Prior to a data recording run the local oscillator in the Phase II receiver was adjusted such that the demodulated center frequency was not zero but offset by approximately 5 KHz. The purpose was to insure that the slow thermal drifts of the various oscillators in the system would not cause the doppler frequency components of interest to fold over or become ambiguous during a data recording interval.

c. Timing and Digitization

To furnish a position reference for data analysis, a dc signal was switched onto one of the FM channels as the aircraft flew over a prominent landmark*, but before it entered the expected multipath region. By combining this known point with knowledge of the aircraft speed, we could make a fairly reasonable estimate (e.g., to within 100-200 feet) of aircraft position.

Before digitization, a standard IRIG time code was put on the analog tape and all recorded data then plotted out on an ultraviolet oscillograph. The scalloping on the log video (see figure 3-30) could then be used to define regions of substantial multipath which would then be analyzed in detail by the digital processing scheme of the next section. The data was digitized to 8 bits and recorded on an IBM compatible digital tape. The subsequent processing was then done on the laboratory IBM 370 timeshare system.

*e.g., a road or the end of the runway.

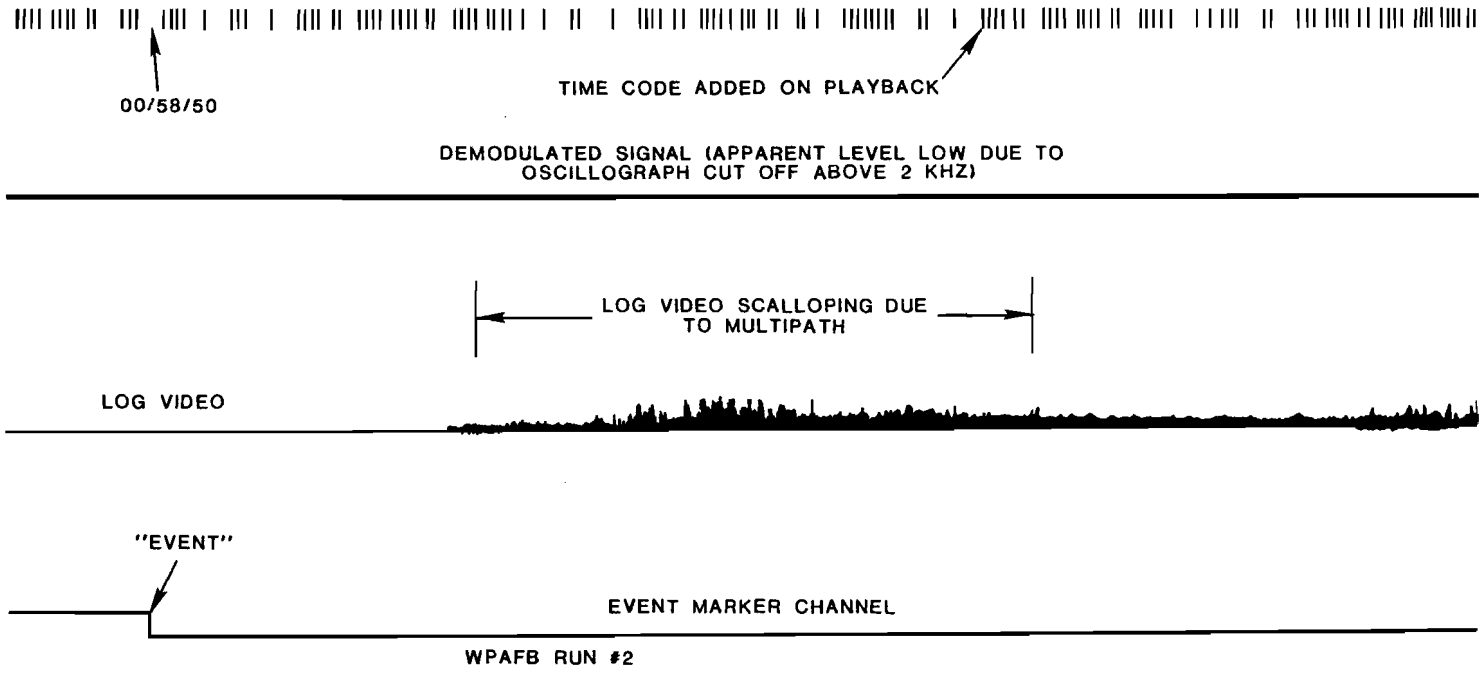

Fig. 3-30. Example of oscillograph recording.

3. Analysis Methods

In this section we discuss how the measured signals were processed to yield estimates of the multipath levels, scalloping frequencies, and scatterer location. First, we briefly review the theoretical background for our approach and then turn to some of the practical details including the expected spectrum effects due to local oscillator frequency drifts, aircraft vibration and propeller modulation.

a. Determination of Multipath Characteristics from Received CW Signal

The objective of this section is to briefly outline how one might analyze the received signal to determine multipath characteristics. We assume that the complex received signal as a function of time can be written as:

$$r(t) = \rho_d(t)\, e^{j(\omega_o+\omega_d)t} + \underbrace{\Sigma\, \rho_i(t)\, e^{j[\omega_o+\omega_i(t)]t + \phi_i}}_{\text{multipath signals}} \qquad (3\text{-}1)$$

direct signal

where

$\rho_d(t)$ = direct signal amplitude - expected to be slowly varying with time

ω_d = direct signal Doppler due to receiver motion
= $2\pi\ (\frac{v}{\lambda})\ \cos\beta_d$

β_d = angle of transmitter with respect to receiver velocity vector

$\rho_i(t)$ = multipath amplitude from ith scatterer (e.g., a door on a hangar)

$\omega_i(t)$ = multipath Doppler due to receiver motion = $2\pi\ \frac{v}{\lambda}\cos\ \beta_i$

β_i = angle of scatterer with respect to the receiver velocity vector

$\omega_{si}(t) = \omega_i(t) - \omega_d$ = scalloping frequency for ith scatterer

ϕ_i = rf phases for multipath signal with respect to the direct signal

ω_o = carrier frequency

Since cosβ is an even function of β, we see from (3-1) that there is a potential ambiguity as to which side of the receiver-transmitter axis corresponds to a given scalloping frequency. This was not a problem at the bulk of the test sites, since the buildings tended to be on one side of the runway.

The received envelope is simply $|r(t)|$. When a single multipath scatterer is present

$$|r(t)| = \rho_d(t) \left|1 + \frac{\rho_1(t)}{\rho_d(t)} e^{j[\omega_i(t)-\omega_d]t + \phi_1}\right| \qquad (3\text{-}2)$$

$$\triangleq \rho_d(t) \left|1 + \rho(t)\, e^{j\,\omega_s(t)t + \phi_1}\right|$$

where $\rho(t) \triangleq$ M/D ratio

$\omega_s(t) \triangleq \omega_{s1}(t)$

If $\rho(t)$, $\rho_d(t)$ and $\omega_s(t)$ are slowly varying with respect to the "average" values of $\omega_s(t)$, then $|r(t)|$ has the sinusoidal nature depicted in figure 3-31 where:

the distance between successive peaks = $1/\omega_s(t)$ (3-3)

the dB range between peaks and nulls = $20 \log_{10}\left(\frac{1+\rho}{1-\rho}\right)$ (3-4)

In the above case envelopes or a memoryless transformation thereof (e.g., log envelope) can be used to infer multipath amplitudes, coherence and angular location.* A serious problem in M/D ratio determination is that the case $\rho > 1$ cannot be distinguished from the case of $\rho < 1$ from the peak to null ratio (i.e., $\rho = x$ and $\rho = 1/x$ are indistinguishable).

If there are several signals present all with roughly the same value of $\omega_{si}(t)$, then one would get much the same behavior for r(t) as that shown above, except that now:

$$\rho(t)e^{j\phi_i} \sim \rho_i(t) + \sum_{k\neq i} \rho_i(t)e^{j[\omega_{sk}(t) - \omega_{si}(t)]t + \phi_k - \phi_i} \qquad (3\text{-}5)$$

The differing scalloping frequencies would cause the apparent reflection coefficient to vary faster than did the $\rho_i(t)$.

*angle location of the scatterer is determined from the equation $\beta_m = \cos^{-1}[\frac{\lambda}{2\pi v}\omega_s + \cos\beta_d]$ and knowledge of the aircraft velocity vector.

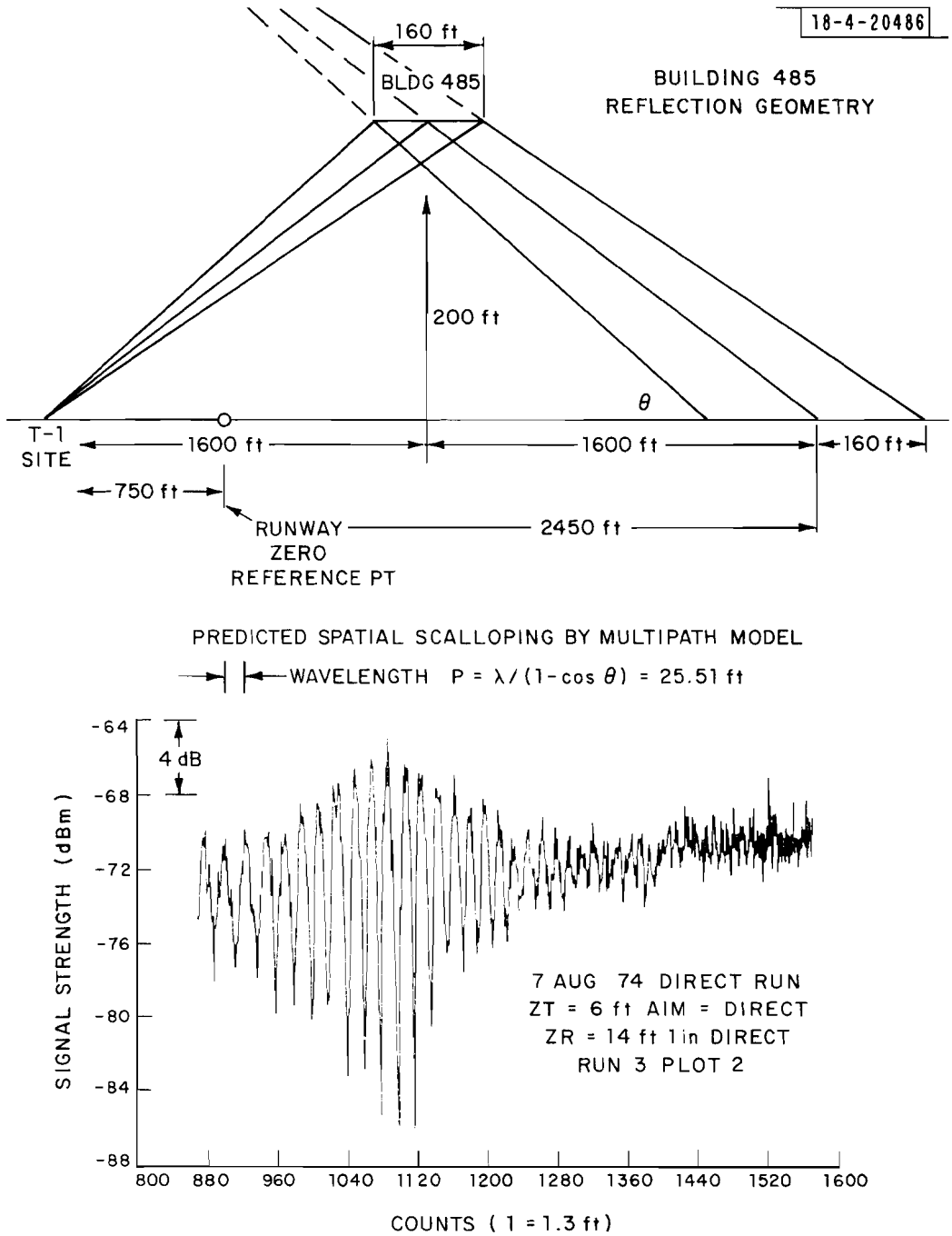

Fig. 3-31. Scalloping in net received signal amplitude for WPAFB building 485 measurements.

To give some perspective on the likely changes in the $\rho_i(t)$, let us consider a hangar at 10° azimuth with 25 foot wide staggered doors which is oriented to yield a scalloping frequency of 400 Hz for an aircraft at 110 knots approach velocity. The specular point would lie on a given door for approximately 0.13 seconds, which is approximately the 6 dB down width of $\rho(t)$ when the Fresnel zone radius is $\leq$ 25 feet.

If the scalloping frequencies are quite different, then the effective $\rho(t)$ varies so rapidly that one cannot determine $\rho(t)$ or ω_s (t) from equations (3-2) and (3-3).

The alternative is to perform a spectrum analysis on short (e.g., 0.1 second to 1.0 second) segments of r(t) as is discussed in the next section.

b. Fourier Analysis Approach

Since the various multipath signals have different frequencies, spectrum analysis is a natural approach to measuring the multipath parameters. This analysis was accomplished digitally by use of fast Fourier discrete transform techniques [54, 55] so as to achieve:

(1) simultaneous estimation over the whole frequency band of interest

(2) low spectral sidelobes

(3) repeatable and easily varied analysis intervals

The simultaneous estimation was viewed as important due to the drifts in ω_o due to changes in the transmitter and receiver local oscillator frequencies. Spectral sidelobes will be discussed below, while the utility of reprocessing digital data is well known.

The classical Fourier transform for continuous time functions is defined as:

$$F(\omega) = \int_{\infty}^{\infty} f(t)e^{-j\omega t}dt \qquad (3\text{-}6)$$

while the discrete Fourier transform is given by

$$F_d(\omega) = \sum f(nT)e^{-j\omega nT} \qquad (3\text{-}7)$$

where T = sampling period and n ranges over the N time samples to be analyzed. More generally, we can write (3-7) as

$$F_d(\omega) = \sum_{n=-\infty}^{\infty} w(nT)\, f(nT)\, e^{-j\omega nT} \qquad (3\text{-}8)$$

where $w(nT) = 0$ for $|n| > N/2$. It can be shown that as a consequence

$$F_d(\omega) = \int_{-\infty}^{\infty} F(x)\, W(\omega - x)\, dx \triangleq F(\omega) * W(\omega) \qquad (3\text{-}9)$$

where $W(\omega)$ is the (unweighted) discrete Fourier transform of the window sequence $w(nT)$,

$$W(\omega) = \sum_{n=-\infty}^{\infty} w(nT)\ e^{-j\omega nT}$$

Equation (3-9) shows that the actual spectrum of $f(t)$ will be convolved with the transform $W(\omega)$ of the window function. Thus, if $F(\omega)$ consisted of impulse functions at the various multipath frequencies, the observed spectrum will be the sum of shifted (and weighted) replicas of $W(\omega)$.

For a uniform window [$w(nT) = 1$],

$$W(\omega) = \frac{\sin N\omega T/2}{\sin \omega T/2}$$

which has a 6 dB down width of $1.21/NT$ Hz and a first sidelobe of -13 dB (see figure 3-32). An exhaustive discussion of windows appears in [54]. For the bulk of our work, we have used a Hamming window (see figs. 3-32 and 3-33) which gives sidelobes below -43 dB and a 6 dB down width of $1.81/NT$ Hz. In certain cases, a Tukey 25% window was used to achieve better resolution of closely spaced signals. The Tukey window (see fig. 3-32 and fig. 3-34) has somewhat higher sidelobes than the Hamming window, but a substantially smaller 6 dB down width of $1.38/NT$ Hz.

The mathematical operation indicated by (3-8) was realized by:

(1) converting the digitized signals (typically 8 bit fixed point values) to floating point

(2) multiplying the data by the chosen window

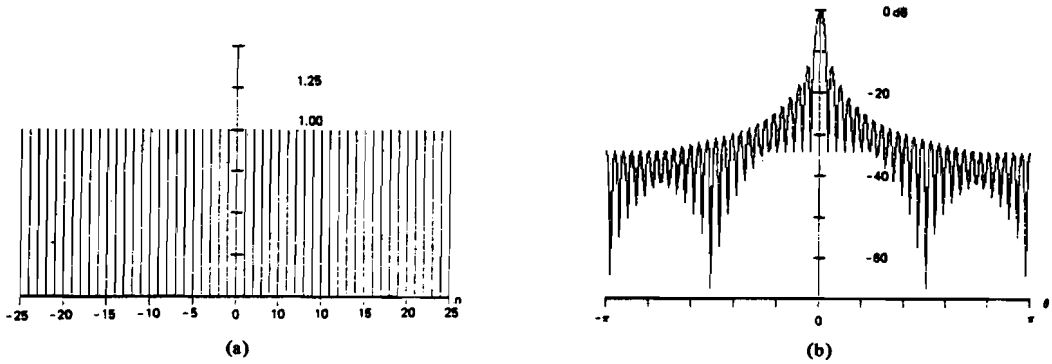

(a) (b)

(a) Rectangle window. (b) Log-magnitude of transform.

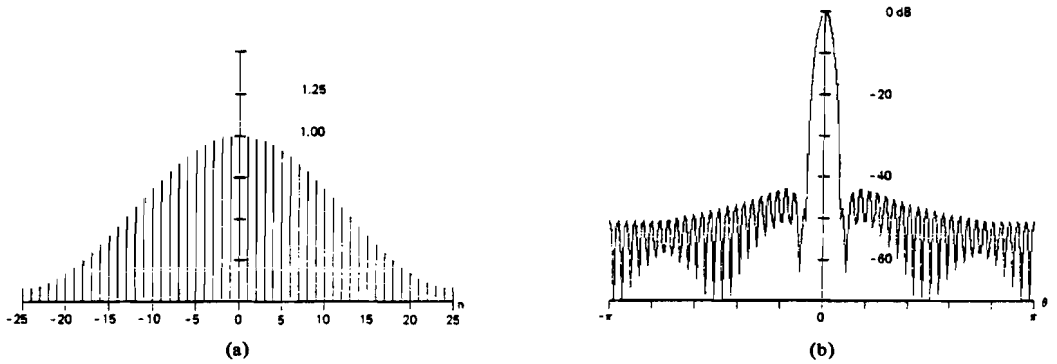

(a) (b)

(a) Hamming window. (b) Log-magnitude of Fourier transform.

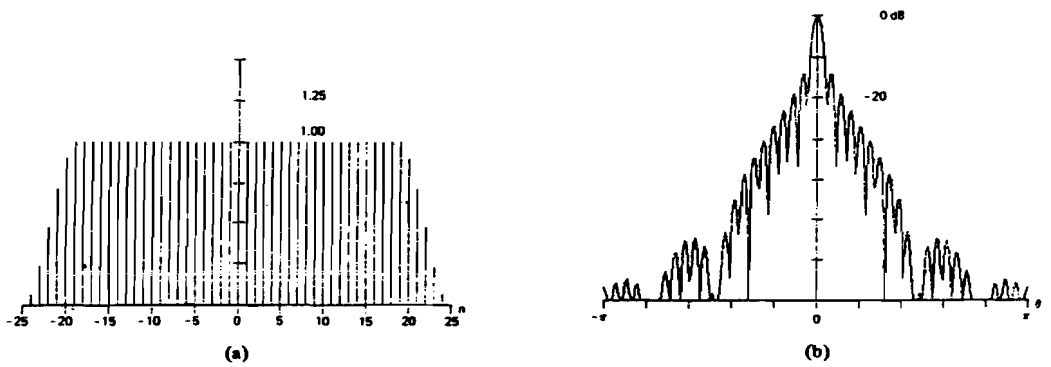

(a) (b)

(a) 25-percent cosine taper (Tukey) window. (b) Log-magnitude of transform.

Fig.3-32. Spectrum analysis windows used in data reduction (from [54]).

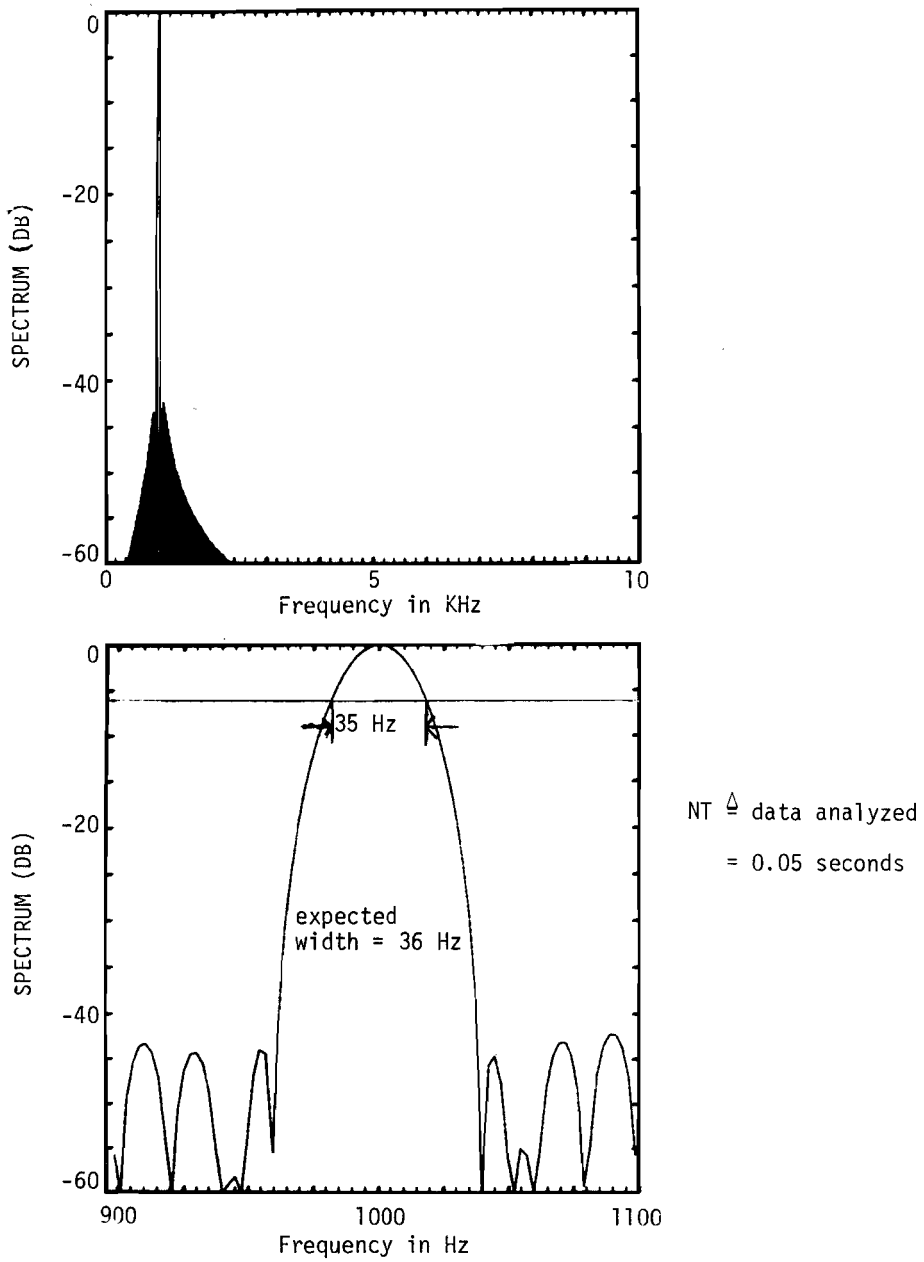

Fig.3-33. Hamming window applied to synthetic data.

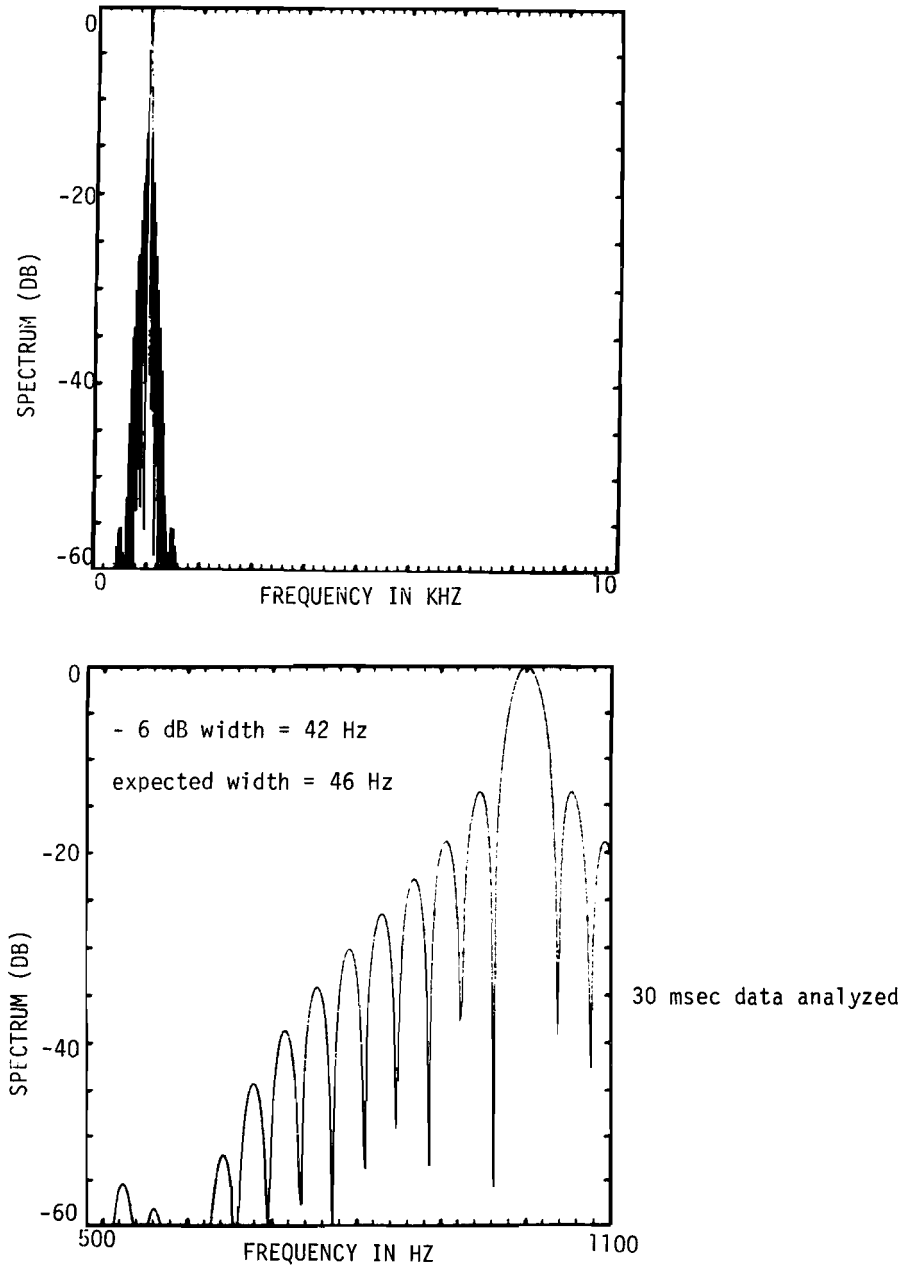

Fig.3-34. Tukey 25% window applied to synthetic data.

(3) adding zeros to the time sequence to be transformed to make a number of points to be transformed a power of 2, so that a FFT algorithm could be utilized.

(4) evaluating (3-8) at a discrete set of frequencies separated by $2\pi/NT$.

A side benefit of the time sequence extension in (3) was that the frequency estimates were then made over a finer grid so as to minimize the "scalloping loss" [54] which can occur if a signal frequency lies between the frequencies at which (3-8) is evaluated.

In some cases where the spectrum levels were quite low except in the vicinity of a few discrete components, every other data sample was skipped in the analysis so as to have twice the window width for a fixed transform size. This in some cases resulted in aliasing the various frequencies about the new effective sampling rate; however, the actual frequencies are easily determined from the usual aliasing equations [55].

The shape of the actual spectrum estimates $F_d(\omega)$ in the vicinity of a spectrum peak furnishes information on the time variation in multipath signal amplitude and phase coherence. Returning to (3-1), we observe that the spectrum near a given component is

$$F_{di}(\omega) \approx \int_{-T/2}^{T/2} w(t)\, w_m(t) e^{j(\omega_{io}-\omega)t}\, dt \qquad (3\text{-}10)$$

where

$w_m(t) = \rho_i(t)\, e^{j[\omega_i(t) - \omega_{io}]t}$ = window due to multipath signal variation

ω_{io} = mean frequency over the interval.

This spectrum will then be the effective window

$$W_{eff}(\omega) = W(\omega) * W_m(\omega) \qquad (3\text{-}11)$$

centered at ω_{io}. For example, if the variation in $\omega_i(t) - \omega_{io}$ is Δ Hz, the width of W_{eff} is approximately $\sqrt{\Delta^2 + [\text{width of } W(\omega)]^2}$. Consequently, if the shape of $F_d(\omega)$ closely resembles that of $W(\omega)$, it is suggested that $W_m(t)$ was approximately constant over the interval; i.e., the multipath signal was phase coherent and stable in amplitude.

Frequency and/or phase modulation of the received signal could arise from transmitter and/or receiver local oscillator drifts, receiver gain variations as well as the recording equipment. Since these changes could cause spectrum broadening which might be attributed to multipath signal changes, a concerted effort was made to quantify these effects.

To assess the analog recording and digitization facility, the output of a laboratory sinewave generator set to 1 kHz was recorded and digitized (at a sampling rate of 5000 samples/second). Fig. 3-35 shows the resulting digital spectra using a Hamming window. The observed 6 dB width of 33 Hz agrees quite well with the 35 Hz predicted theoretically. The sidelobes are seen to be quite similar to fig. 3-32 and 3-33 except for a 50 dB down peak at the second harmonic of the waveform generator frequency. It was concluded that the recording/digitizing system effects are essentially negligible.

To assess the short term stability of the transmitter and receiver local oscillators under controlled environmental conditions, a bench test was made in which the output of the TWT exciter was attenuated and then fed into the receiver. The demodulated signal was then recorded and digitized as would be the case with field data. Figs. 3-36 and 3-37 shows the spectra using 0.2 seconds of data and 0.8 seconds of data, respectively. We see that the spectrum width for 0.2 seconds of data is fairly close to that of the window, whereas the spectrum width with 0.8 seconds of data is 50% wider than the window width. This suggests that the time rate of change of the transmitter and receiver local oscillator frequencies would preclude obtaining increased frequency resolution by the use of data segments longer than 0.4 seconds. In both cases, the sidelobes away from the main peak were at least 40 dB down which suggests that even low level (e.g., -20 dB) multipath signals which are well separated from other signal frequencies could be easily detected.

Another potential source of spurious modulation effects is the aircraft power system and/or aircraft vibration. These were investigated by transmitting a signal from the antenna to the aircraft when parked in front of the hangar

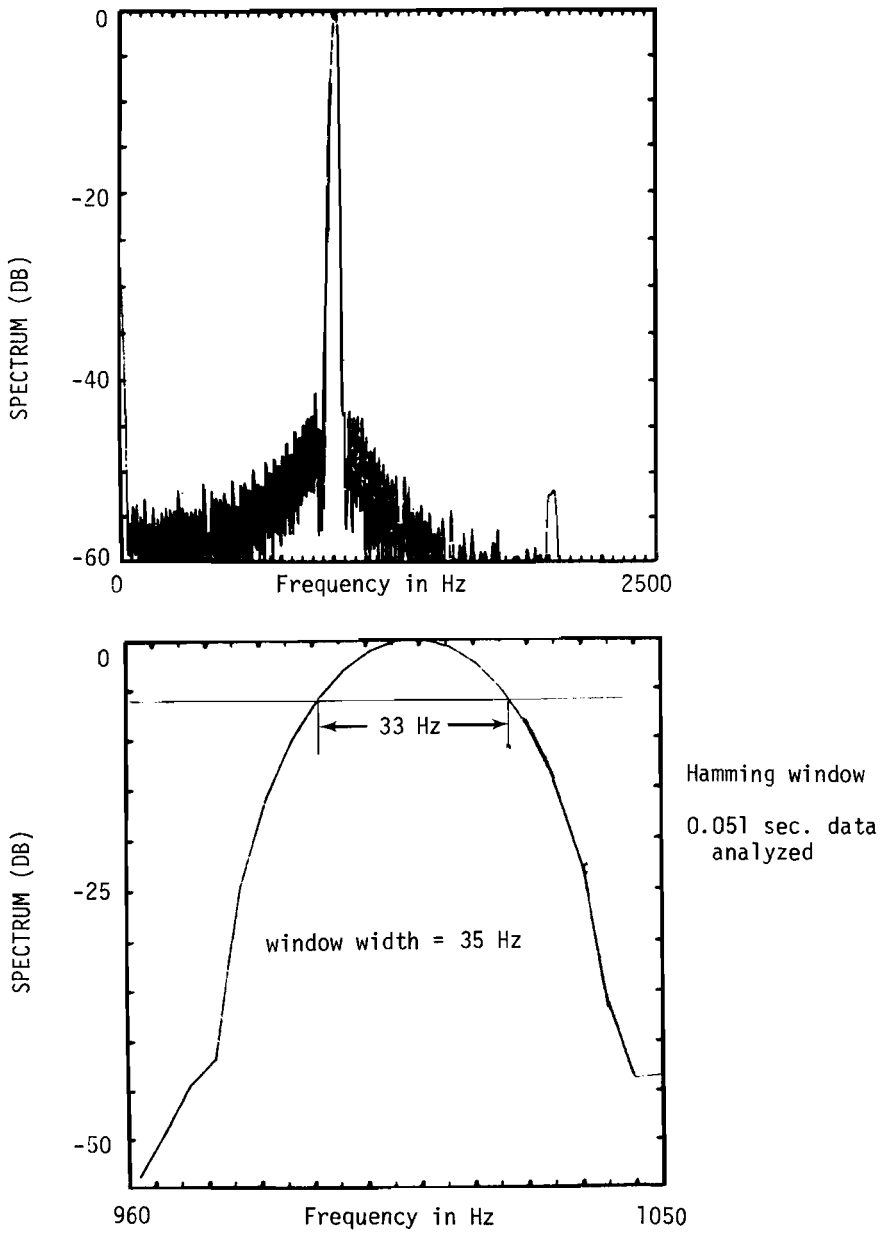

Fig.3-35. Spectrum of sinewave generator output.

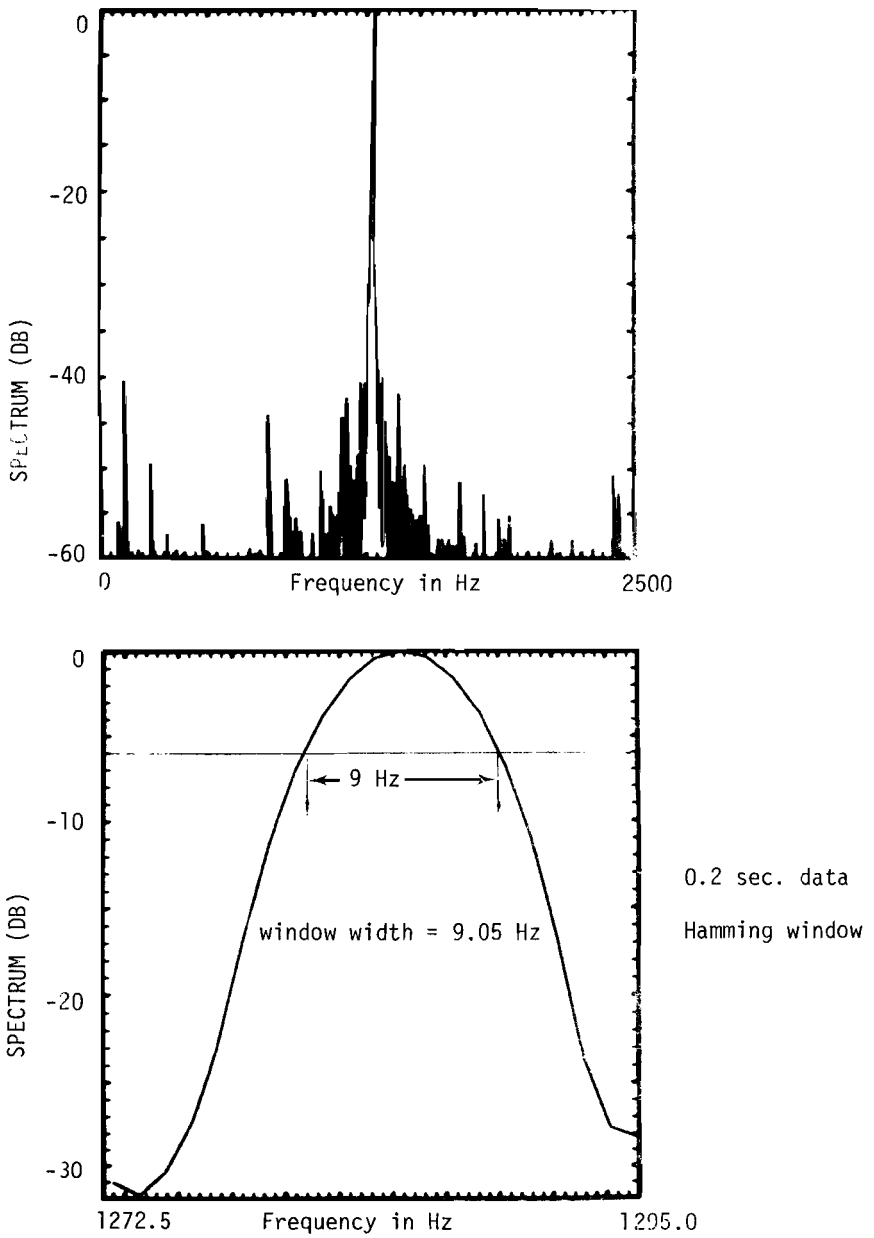

Fig.3-36. Spectrum of demodulated signal for bench test.

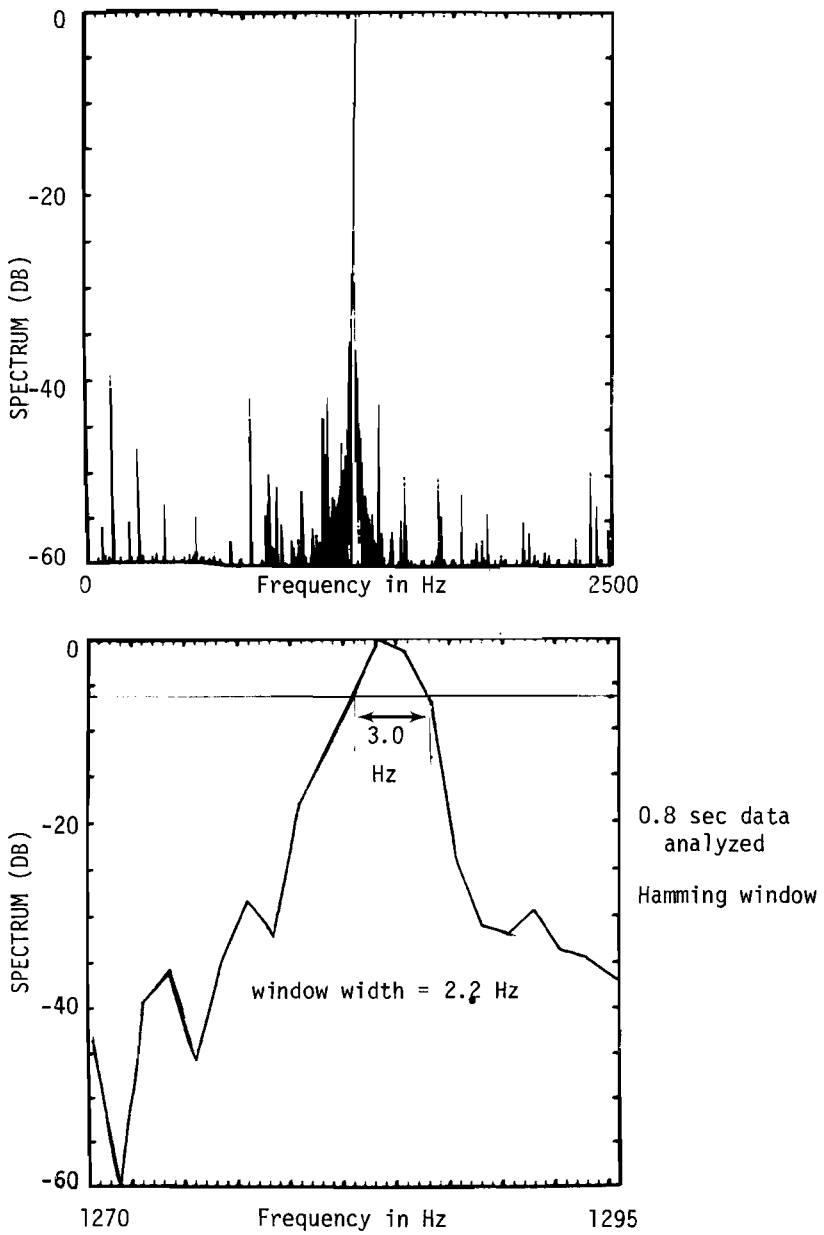

Fig.3-37. Demodulated signal spectrum for bench test.

with the engines running. Figures 3-38 and 3-39 show the spectrum of the demodulated signal for this experiment for two data samples separated 10 seconds in time. The spectrum widths are seen to be approximately the window width in keeping with the bench test data for 0.2 sec and 0.8 sec data lengths. The sidelobes away from the immediate main peak continued to be at least 35 dB down.

Sine a propeller driven aircraft was used for these experiments, shadowing by or reflections from the propellers could modulate the received signal and cause spectrum broadening and/or spurious lines. To minimize these effects for the flight profiles of interest, a twin engine aircraft was used and the receiving antenna was mounted well out on the nose. The generally clean data which was obtained in multipath free portions of the centerline approach data (see sections 4-7) suggests that propeller modulation effects were negligible for signals arriving from directly in front of the aircraft.

To quantify the extent of propeller modulation for signals arriving at angles well to the side of the aircraft heading, a flight was conducted at L.G. Hanscom airfield (Lincoln, Mass.).

The transmitter was sited beside the runway ILS localizer and the aircraft flew a profile at right angles to the extended runway centerline passing over the outer marker at an alititude of 1100 feet (and range 5 nmi). Figures 3-40 to 3-42 show the demodulated signal spectra for three different bearings of the transmitter from the aircraft velocity vector. We see that the dominant modulation components are at three times the engine rpm, corresponding to passage of the three propeller blades. Figure 3-43 summarizes the propeller modulation component levels versus bearing for two passes. One interesting feature which has not yet been fully explained* is the asymmetry in the modulation term levels about the direct signal frequency. It was concluded from these experiments that

*D. Vickers of the FAA MLS Program Office has suggested that the asymmetry may arise from reflection multipath from the propeller blades since both propellers rotate in the same direction (whereas on many similar twin engine aircraft the propellers rotate in opposite directions).

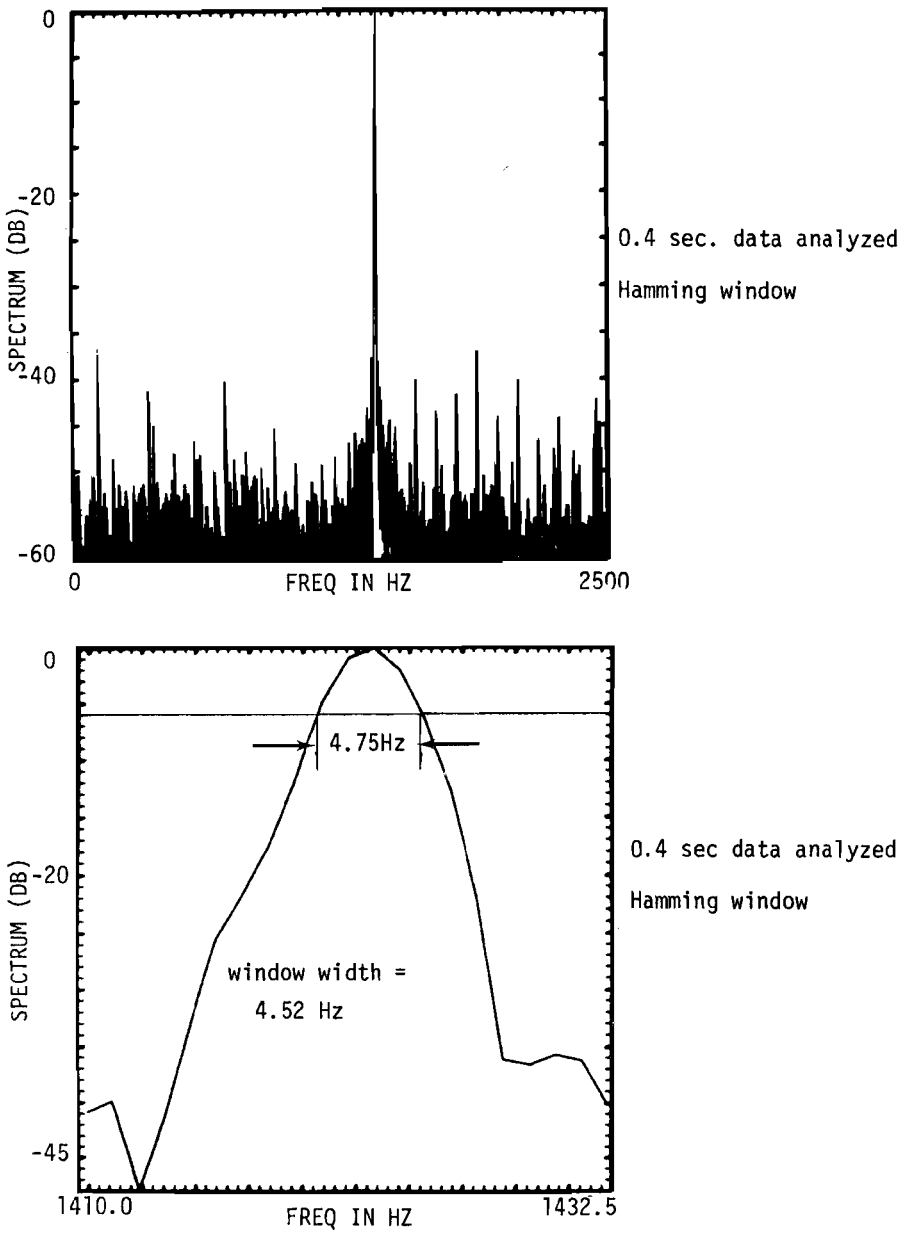

Fig.3-38. Spectrum of demodulated signal for stationary aircraft test.

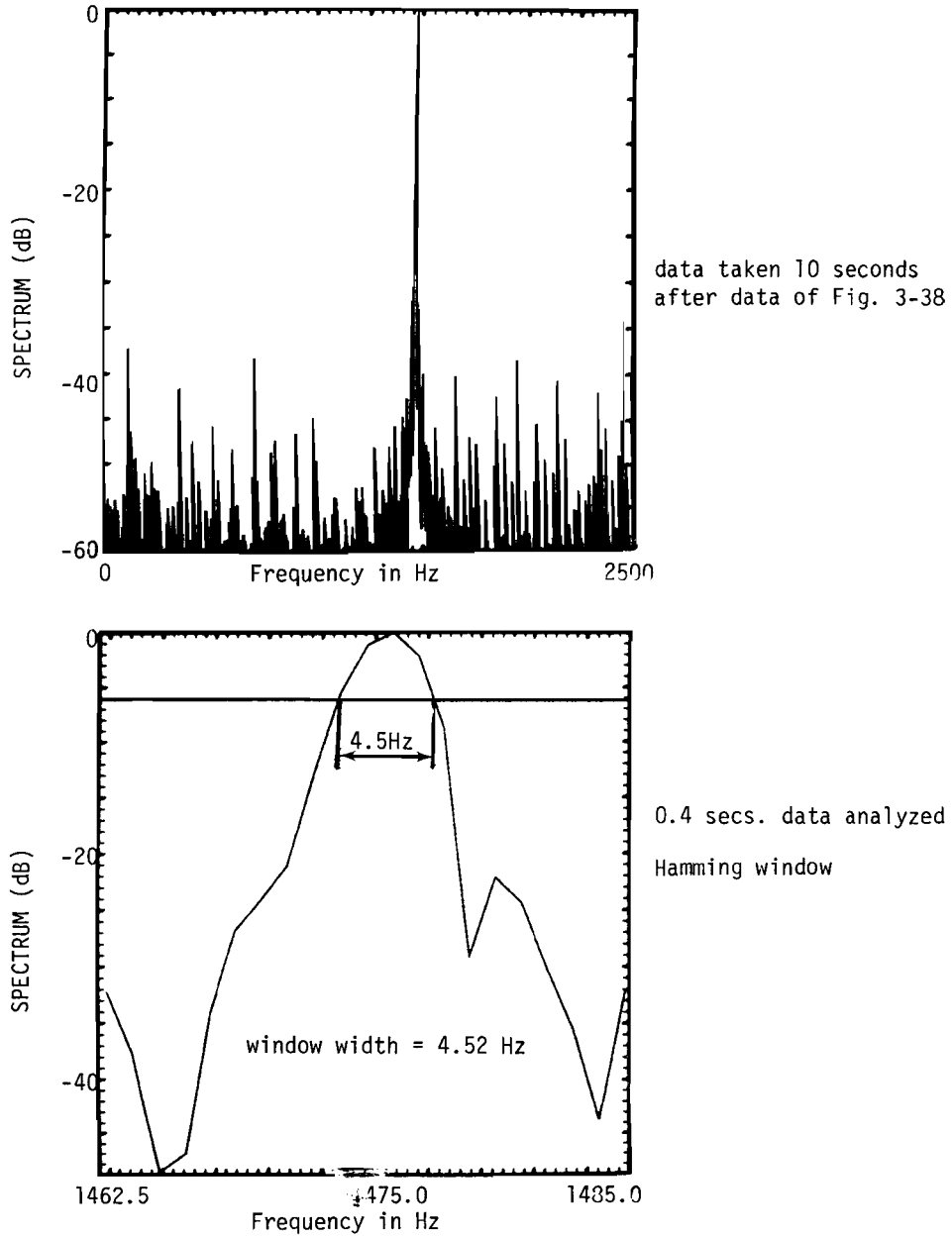

Fig.3-39. Demodulated signal spectrum for stationary aircraft test.

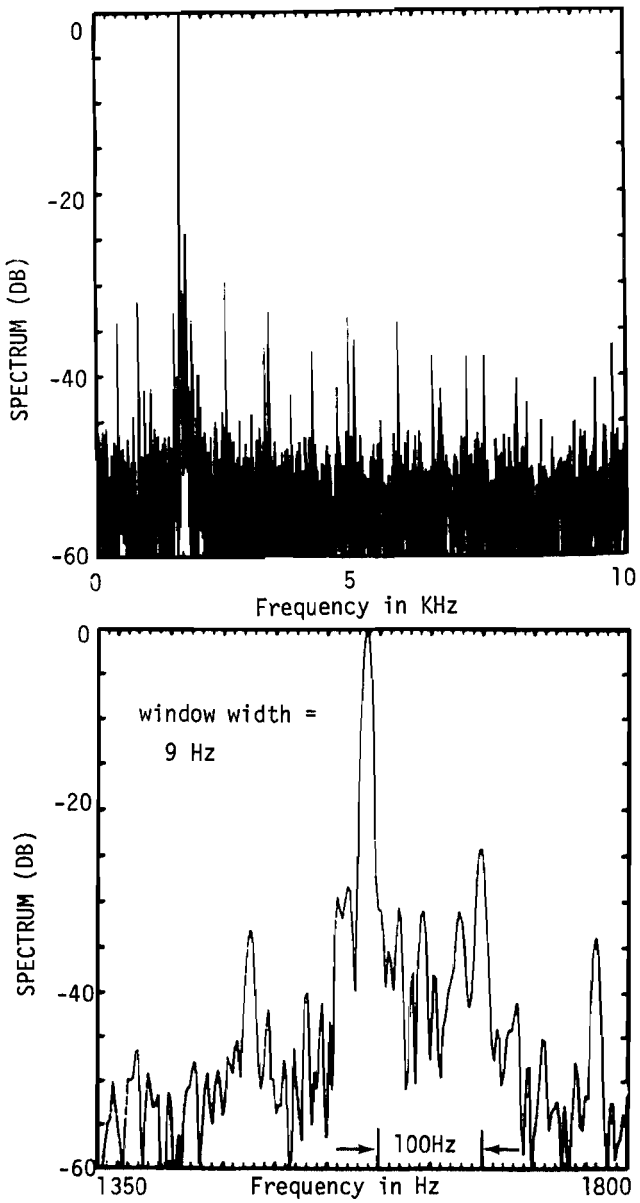

Fig. 3-40. Demodulated spectrum for Hanscom propeller modulation test.

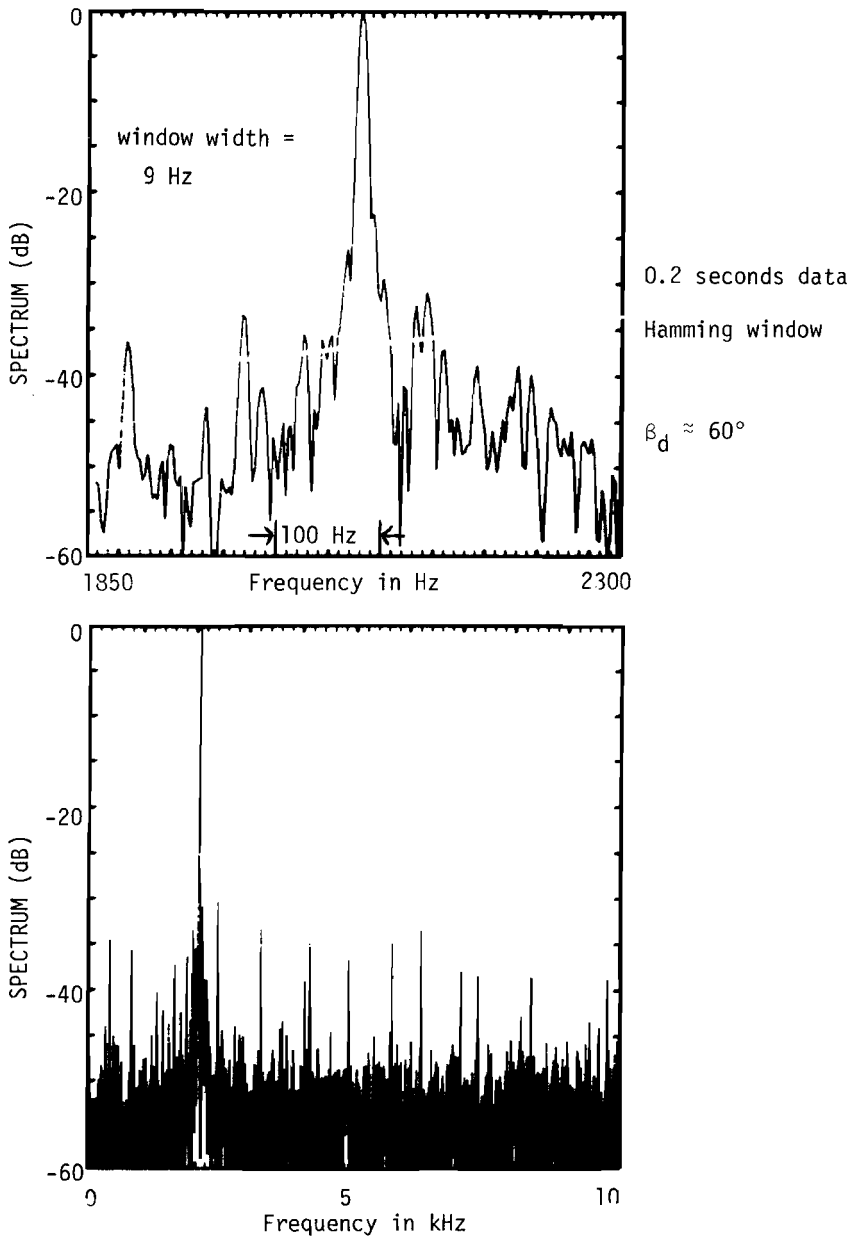

Fig. 3-41. Hanscom propeller modulation test spectrum.

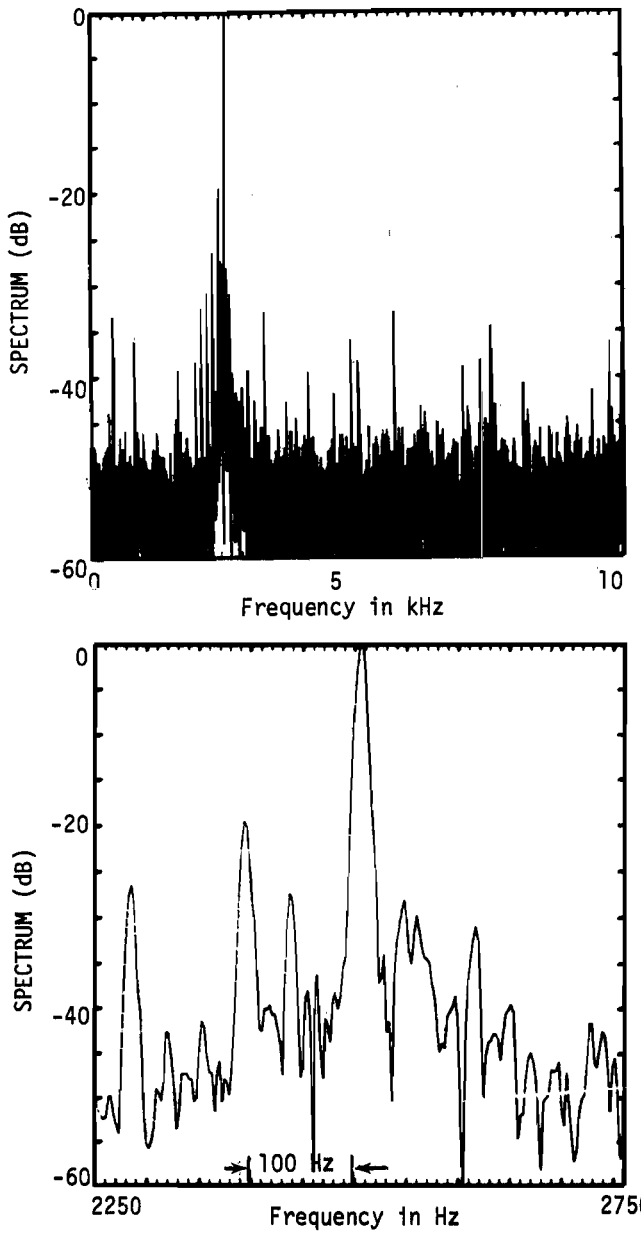

0.2 seconds data analyzed

Hamming window

$\beta_d \approx 90°$

Fig. 3-42. Hanscom propeller modulation test.

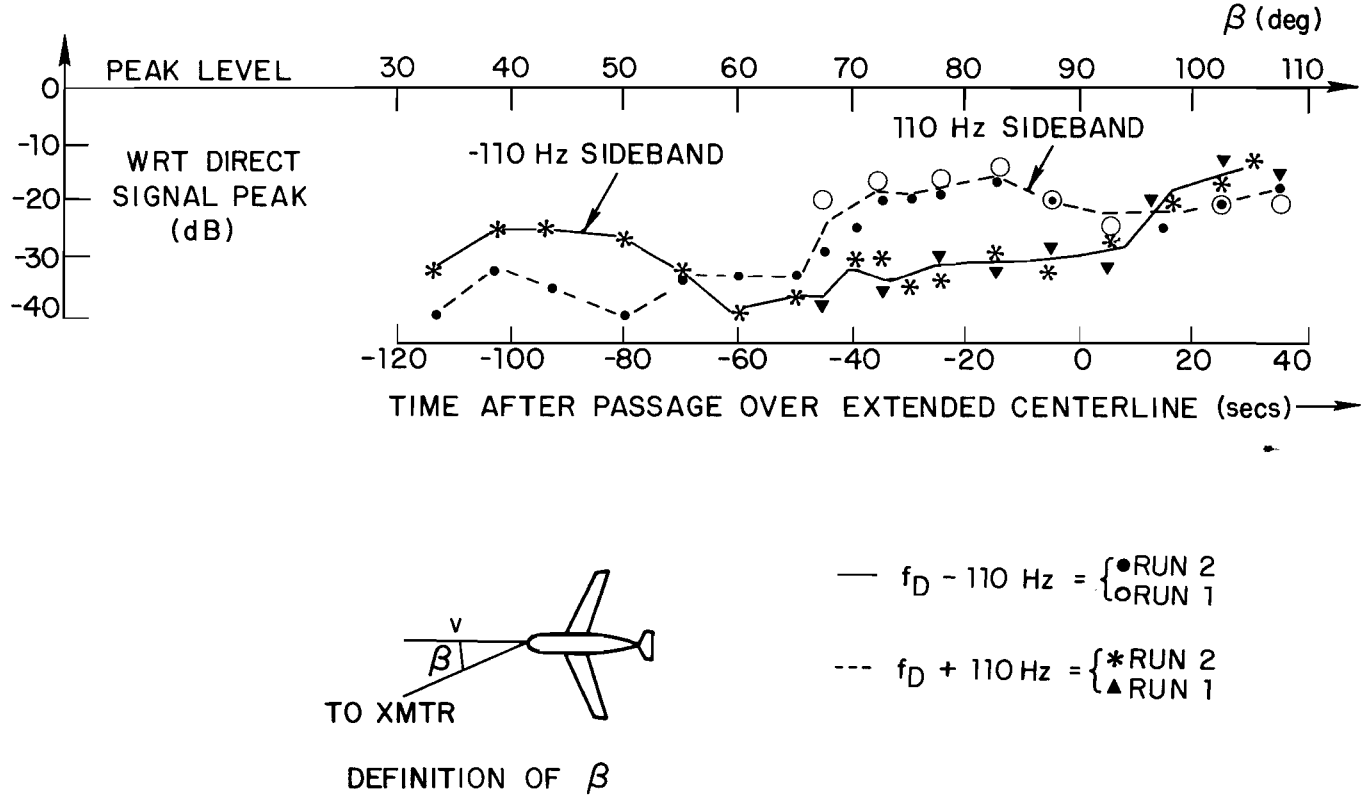

Fig. 3-43. Propeller modulation test sideband levels.

in the absence of any other effects (e.g., propeller modulation) that the experimental equipment and data analysis procedure was capable of resolving multipath signals of near equal level which were as close together as 10 Hz provided that the signal frequencies were stable over a 0.2 second period. Signal components which differed by as much as 20 dB in level could be resolved if they were at least 20 Hz apart in frequency. The chief exception to this would be cases where the geometry of the flight path and arriving signals was such that a weak multipath signal coincided with propeller modulation sidebands. Since most of the test environments were expected to yield scalloping frequencies in the hundreds of Hz and multipath with levels comparable to that of the direct signal were of greatest interest, it is concluded that significant multipath could be readily identified and quantified if it were indeed present with the postulated scalloping frequencies.

4. Lambert-St. Louis International Airport

a. Multipath Environment

Figure 3-44 shows an aerial photograph of Lambert-St. Louis International airport. Figure 3-45 is another aerial view which shows the reflection rays corresponding to the major anticipated multipath threats for an aircraft landing on runway 12R (currently a category I ILS runway). The major multipath threats were expected to be the large McDonnell Douglas aircraft factory buildings shown in Figures 3-46 to 3-49. The main factory building has predominantly masonry fronts (Gunite) punctuated by windows, while hangars 42 and 45 have several large vertical doors with windows.

The various low buildings (e.g., aircraft shelters) and a parking lot between the buildings and the threshold of runway 12R are expected to prevent some of the building reflections from reaching a receiver, especially if the receiver is at a low altitude. Similar circumstances arise for reflections from the terminal buildings.

The expected scalloping frequencies for a centerline approach at 116 knots are as follows:

BUILDING	SCALLOPING FREQUENCY (HZ)
McDonnell-Douglas main factory	700 - 800
McDonnell-Douglas Hangar 42 McDonnell-Douglas Hangar 45	560 - 690
Terminal buildings	40

The runway contour (shown in Fig. 3-50) is fairly flat over the airport proper. The transmitter antenna was sited to the immediate left of the ILS localizer as shown in Fig. 3-45 with a phase center height of approximately 5 feet. At the time the measurements were made, the ground was covered by approximately one foot of snow, but the runway was clear.

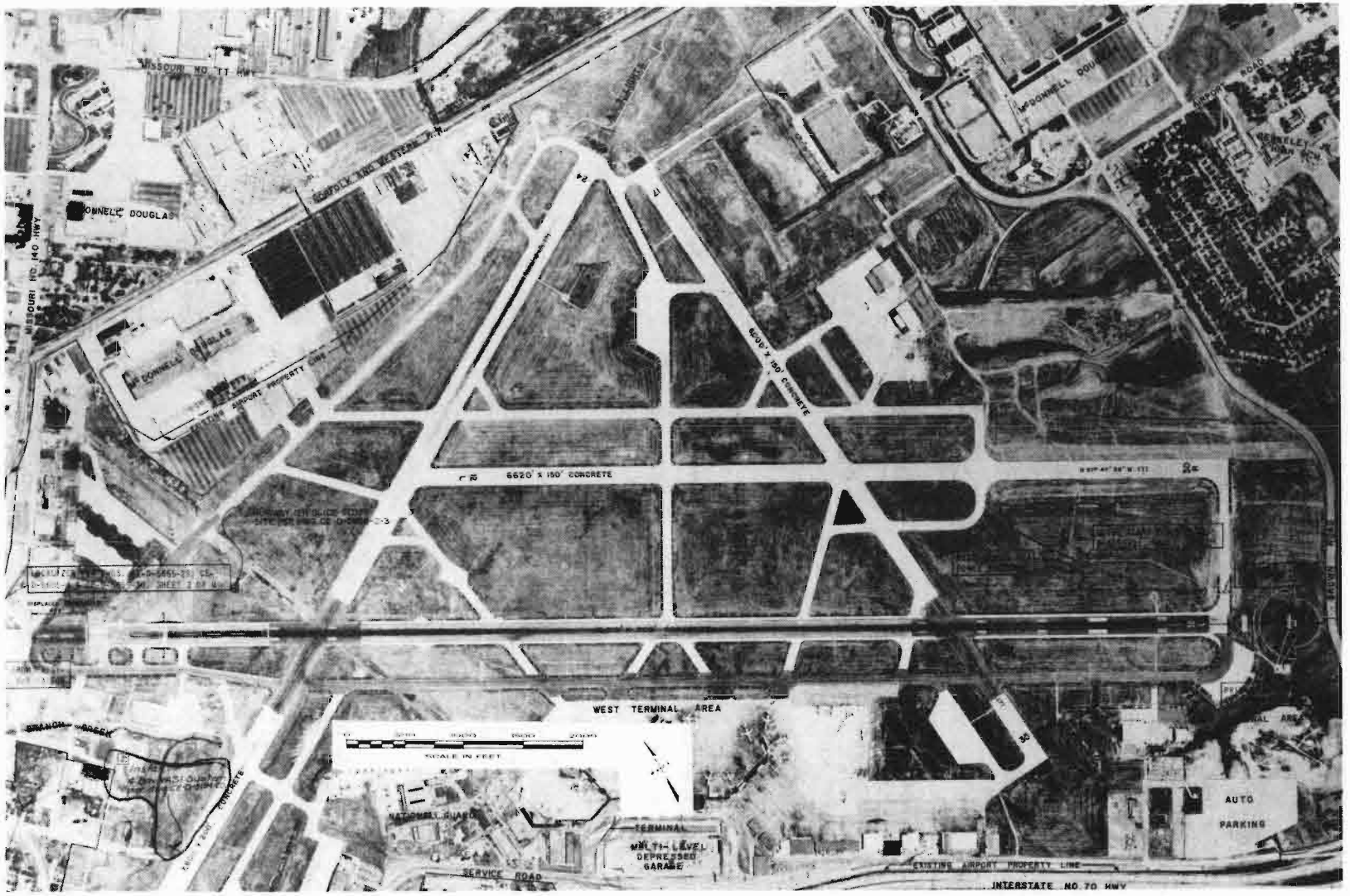

Fig. 3-44. Lambert-St. Louis International Airport.

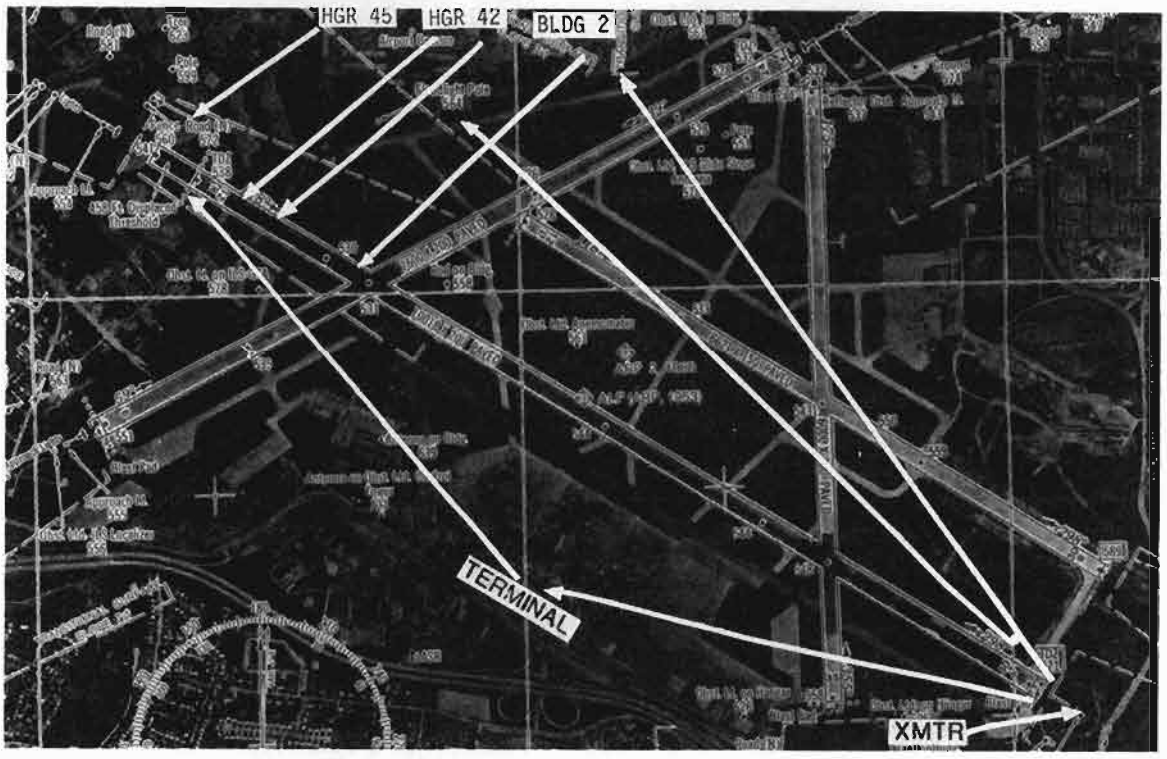

Fig. 3-45. Lambert-St. Louis International, St. Louis, Missouri, showing azimuth reflection paths.

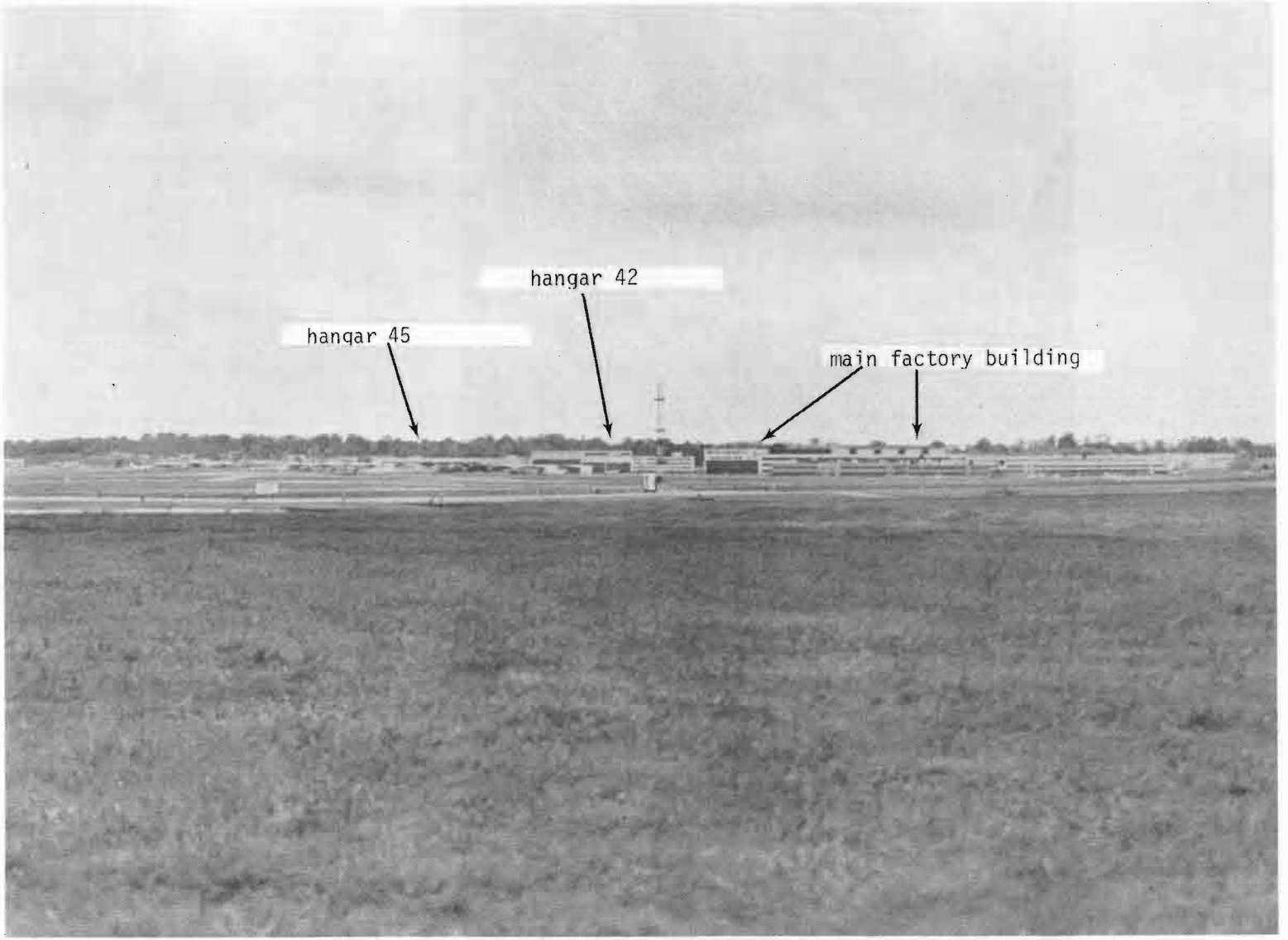

Fig. 3-46. McDonnell-Douglas buildings as seen from ILS localizer site.

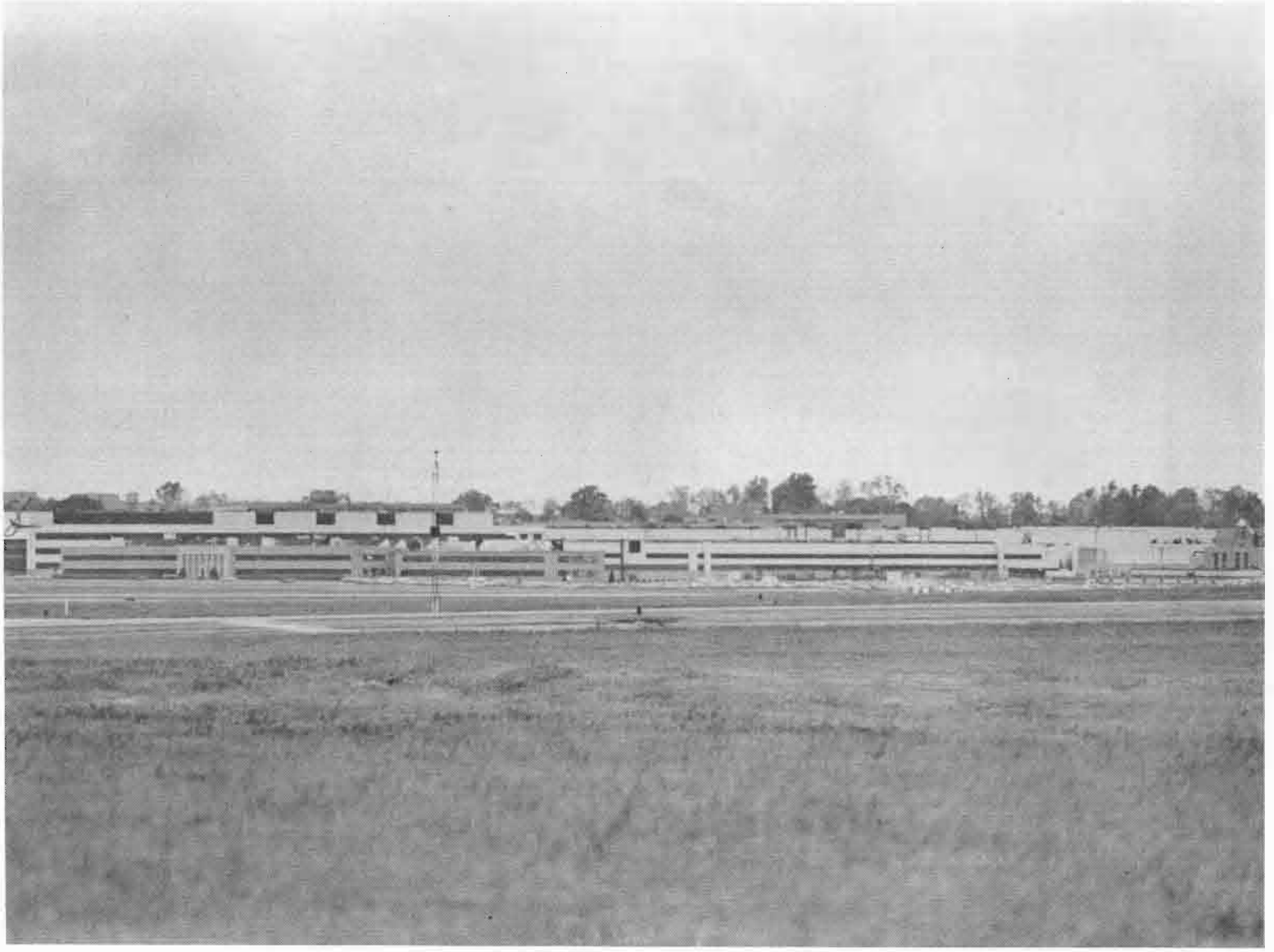

Fig. 3-47. McDonnell-Douglas main factory building.

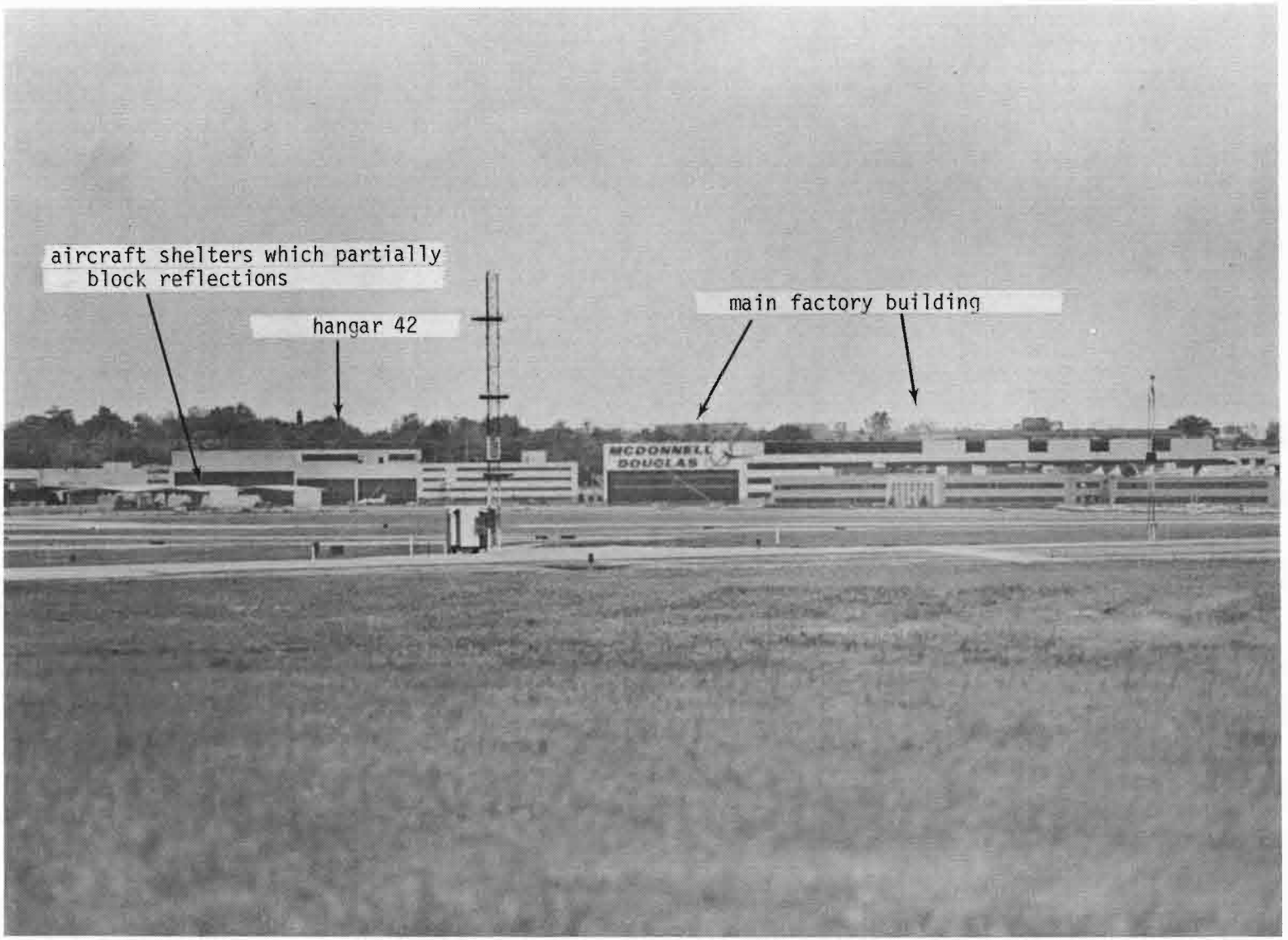

Fig. 3-48. McDonnell-Douglas aircraft hangars.

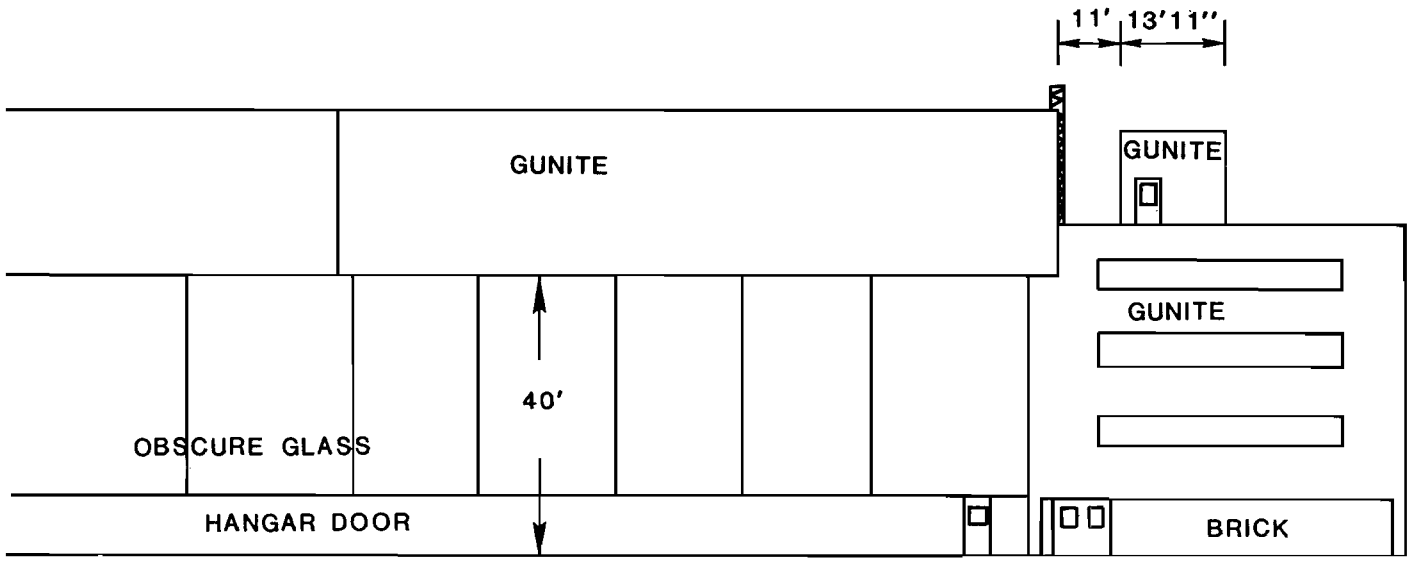

Fig. 3-49. Portion of McDonnell-Douglas hangar 42.

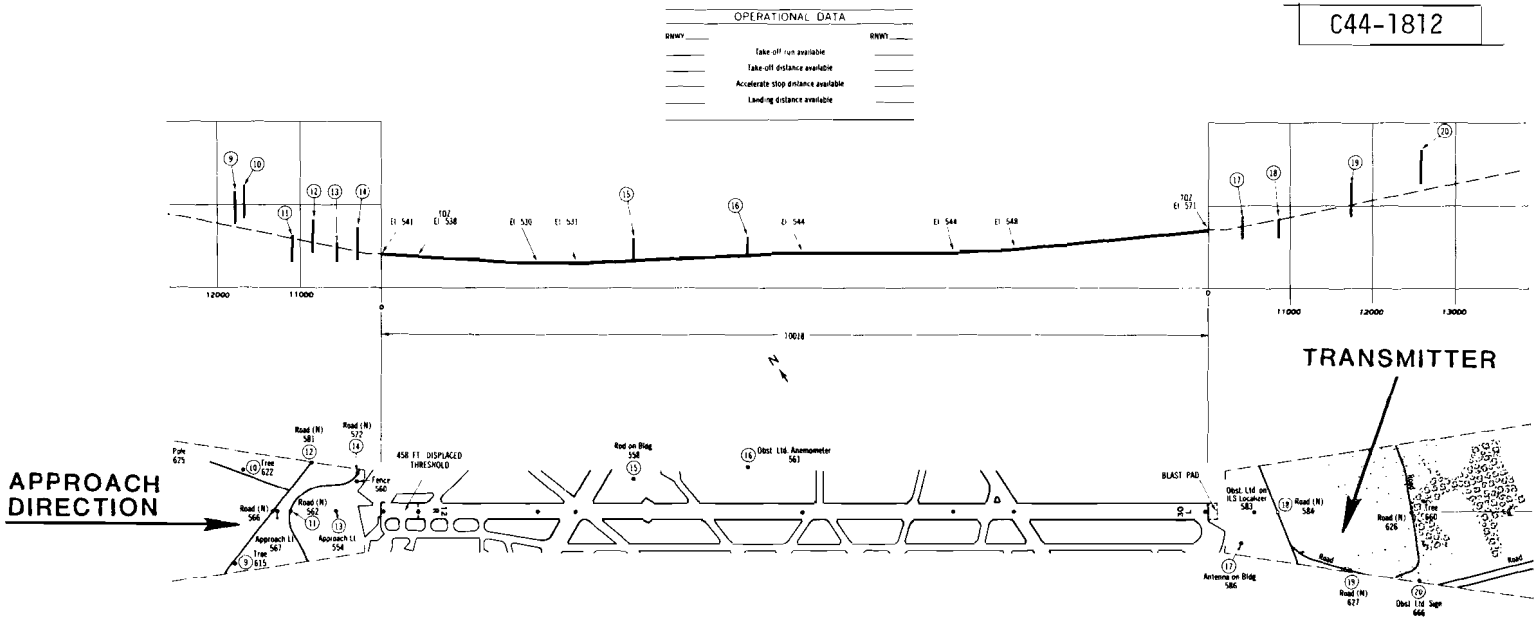

Fig.3-50. Runway 12R-30L contour at Lambert Field - St.Louis.

b. Measurements Made

Table 3-2 summarizes the measurements made at St. Louis. A total of six centerline approaches at 120 knots were made between the hours of 11 p.m. January 19 to 1 a.m. on January 20. This late hour was necessitated by the fact that runway 12R-30L is the main runway at a very active major airport. Passage over N. Lindberg Boulevard and Bridgeton Station Roads were used as the "event" recorded on the analog tape.

c. Spectrum Results

Runs 2, 3, 4, and 6 have been analyzed to date and representative results will be described in this section. The most distinctive characteristic of the St. Louis data vis-a-vis the data at the other airports was the very narrow spectral lines for the direct and multipath signals as well as very low overall level of background noise. Fig. 3-51 shows a typical spectrum in a region of low multipath, while Figs. 3-52 to 3-54 show the spectra for multipath at 30, 700 and 875 Hz scalloping frequencies, respectively. The principal spectral line widths are approximately that of the data window.

Fig. 3-55 shows the sequence of spectra at various points within the multipath region for hangars 42 and 45. The vertical scale on the spectrum plots is 0 dB to -30 dB for figure 3-55a and 0 dB to -60 dB for Fig. 3-55b. We see that the successive measurements made over disjoint sections of the flight path all yield narrow spectral lines at essentially identical locations. The "M/D values" shown on the right hand side of the figure were computed as follows:

(1) the direct signal level is taken to be the peak spectrum value in the "DBOUND" frequency region (indicated by a pair of dotted lines on the plot)

(2) the multipath signal is taken to be the peak spectrum value in the "MBOUND" frequency region (indicated by a second pair of dotted lines on the plot)

TABLE 3-2

FLIGHT PROFILES AND DEMODULATED DIRECT SIGNAL FREQUENCY CHARACTERISTICS FOR ST. LOUIS FLIGHTS

Run	Approximate glide path	Aircraft Height at threshold	Aircraft Height along runway	Demodulated direct signal frequency and stability
1	1° - 1.5°	20	10	stable at 10 kHz
2	1° - 1.5°	30	10	3 kHz at start, 2.7 kHz at end
3	1° - 1.5°	30	20	stable at 7.5 kHz
4	3°	40	30 - 40	stable at 6.0 kHz
5	3°	30	30	stable at 3 kHz
6	3°	100	40	stable at 4.3 kHz

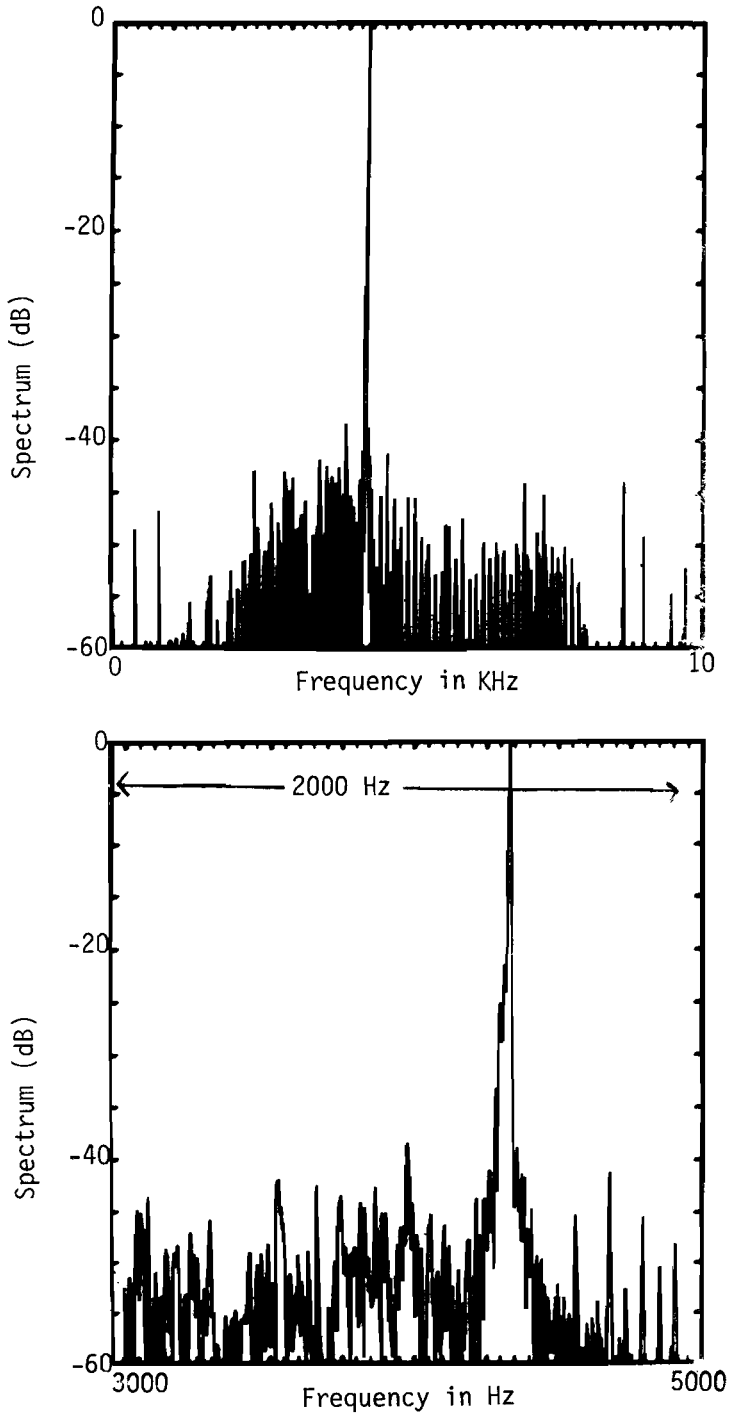

Fig. 3-51. Spectrum of demodulated signal at St. Louis.

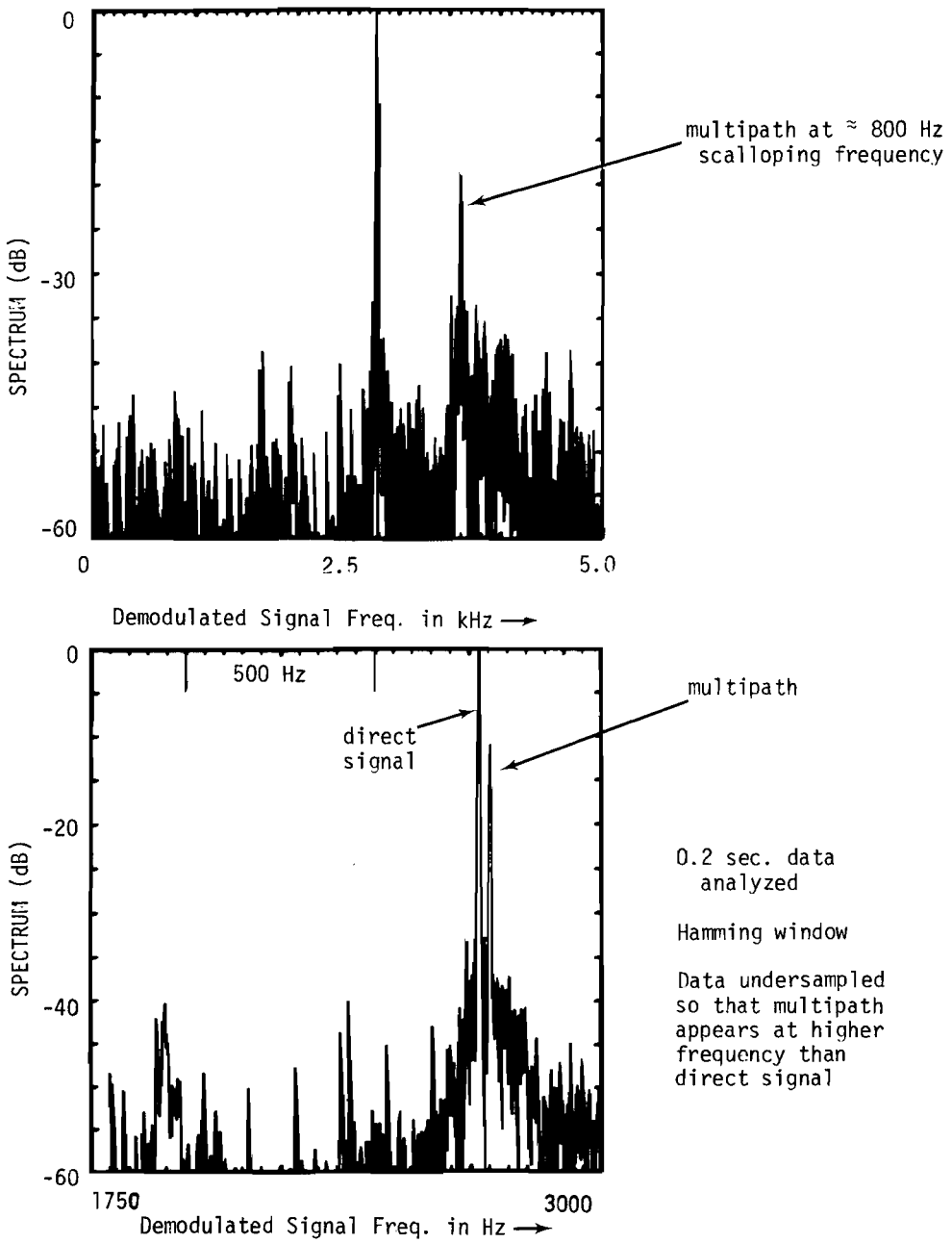

Fig.3-52. Example of St.Louis multipath at 30 Hz scalloping frequency.

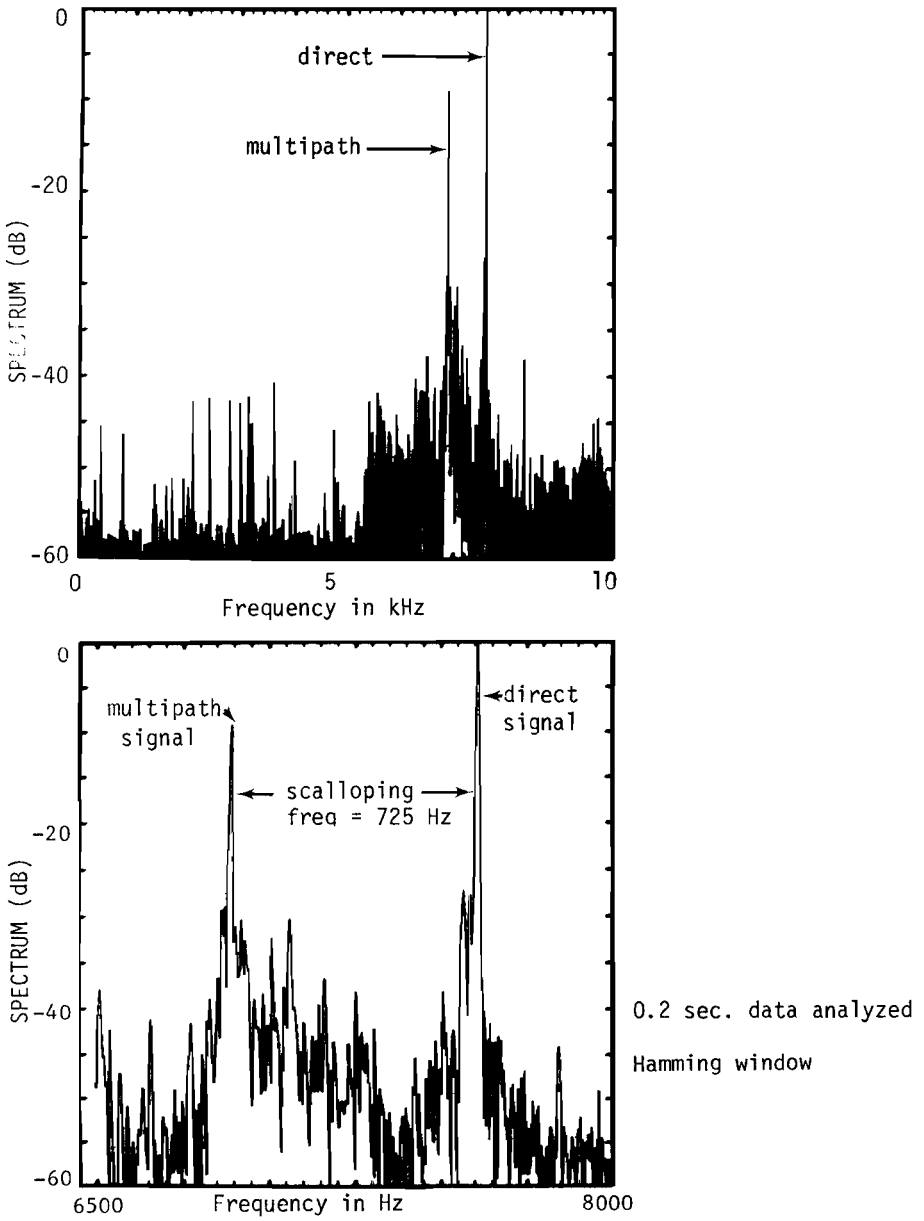

Fig.3-53. Example of St.Louis multipath near 700 Hz scalloping frequency.

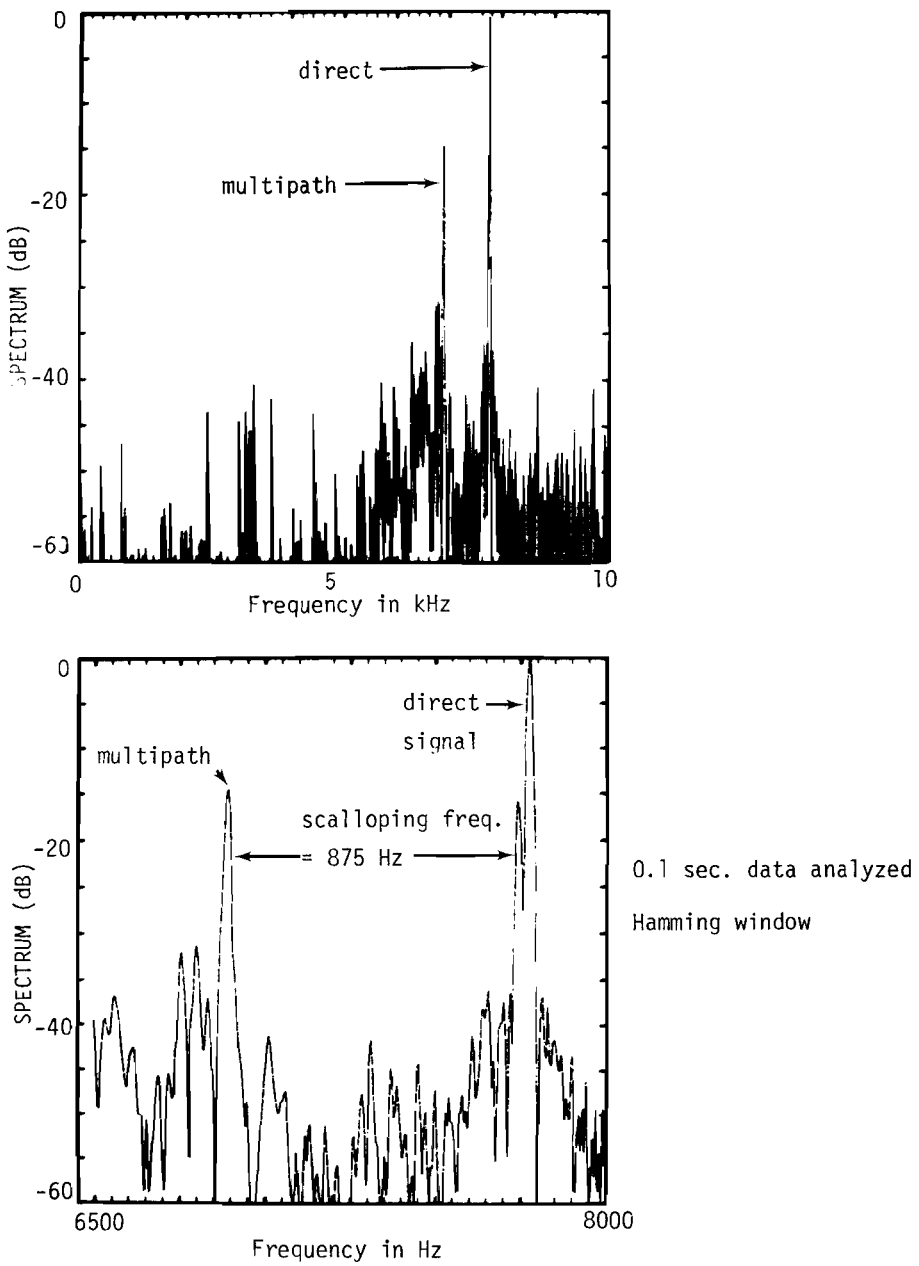

Fig.3-54. Example of St.Louis multipath near 875 Hz scalloping frequency.

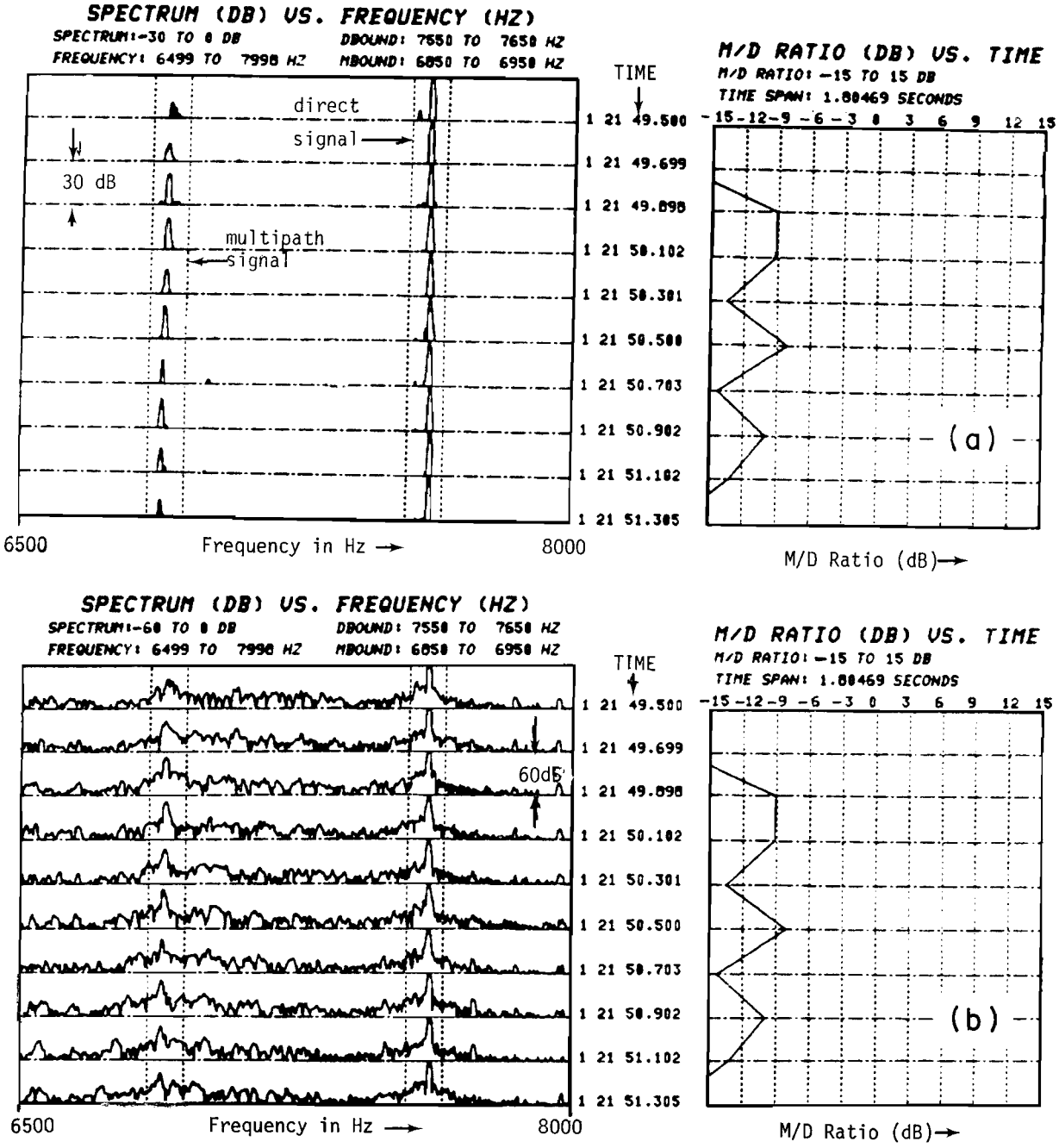

Fig.3-55. St.Louis spectra on run 3 at various points in expected multipath region for hangars 42 and 45.

(3) the "M/D ratio" is taken to be the ratio of the peak from (2) to the peak from (1)

In some cases where the multipath spectrum is noticeably wider than the direct signal, it could be argued that the area under the respective spectrum peaks (i.e., the energy) would be a better measure of the interference level. This refinement has not been incorporated in the data analysis to date.

Figure 3-56 summarizes the multipath levels versus time after the event marker for the components whose levels were within 20 dB of the direct signal level.

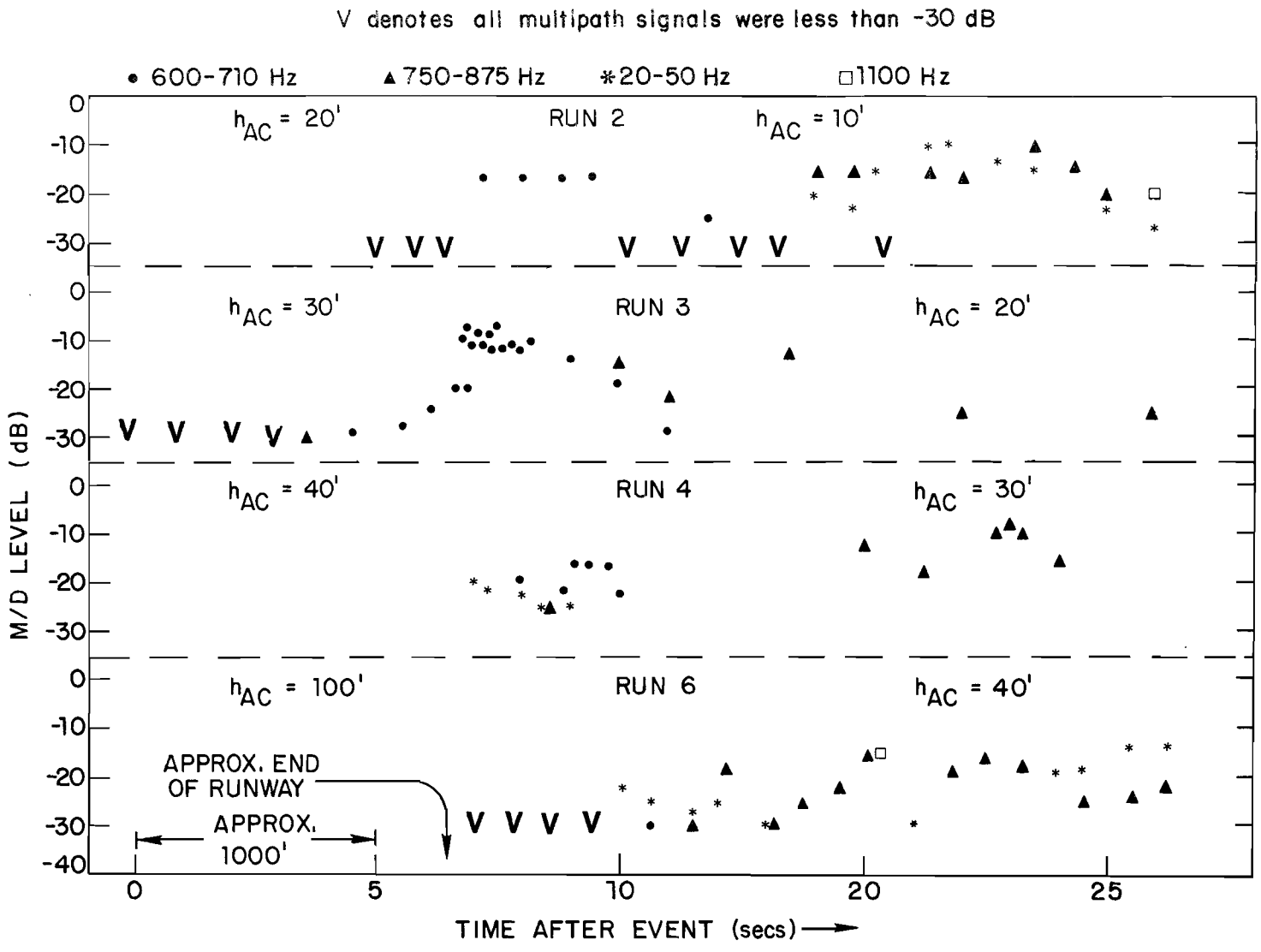

Fig. 3-56. Summary of Lambert Field multipath.

d. Summary

The multipath measurement data reduced to date from Lambert Field agrees well with the theoretical expectations in phase stability and multipath extent. Over analysis periods as long as 0.4 seconds, the observed spectrum widths were often comparable to those for a pure sinusoid. This high degree of coherence was observed for scalloping rates from 50 to 800 Hz. The peak multipath levels are not particularly high apparently due to low reflectivity of the building surfaces. Consequently, this runway at Lambert Field does not appear to be a good candidate for a stringent test of MLS capability to cope with high level out-of-beam azimuth multipath.

5. Tulsa International Airport

a. Multipath Environment

Fig. 3-57 shows a map of Tulsa International Airport together with reflection rays from the two buildings most likely to cause multipath threats for aircraft landing on runway 35R (currently a category I ILS runway). These buildings are the American Airlines (AA) and McDonnell-Douglas (M-D) hangars shown in Figs. 3-57 to 3-60. The large M-D building parallel to and behind the hangar can cause some multipath, but much of it is blocked by various small hangars and other buildings. The large M-D hangar has one building (outlined in Fig. 3-57) which partially blocks its multipath. In contrast, the multipath from the AA hangar is almost totally in the clear.

The expected scalloping frequencies for a centerline approach at 140 knots are as follows:

BUILDING	SCALLOPING FREQUENCY (HZ)
M-D hangar	690 - 880
M-D building	690 - 880
AA hangar	35 - 60

The runway contour (Fig. 3-61) shows a slight hump peaking near the intersection with runway 8-26. For this reason the transmitter antenna was raised to the top of the building housing the transmitter (Figure 3-62) for the runway 35-R ILS localizer. There was snow on the ground when the measurements were made, but the runway itself was clear.

b. Measurements Made

Table 3-3 summarizes the measurements made at Tulsa. A total of 8 centerline approaches at velocities ranging from 110 knots to 140 knots were flown on January 18, 1978 between 2 and 4 p.m. The road indicated on Fig. 3-57 was used for the "event" marker on the tape.

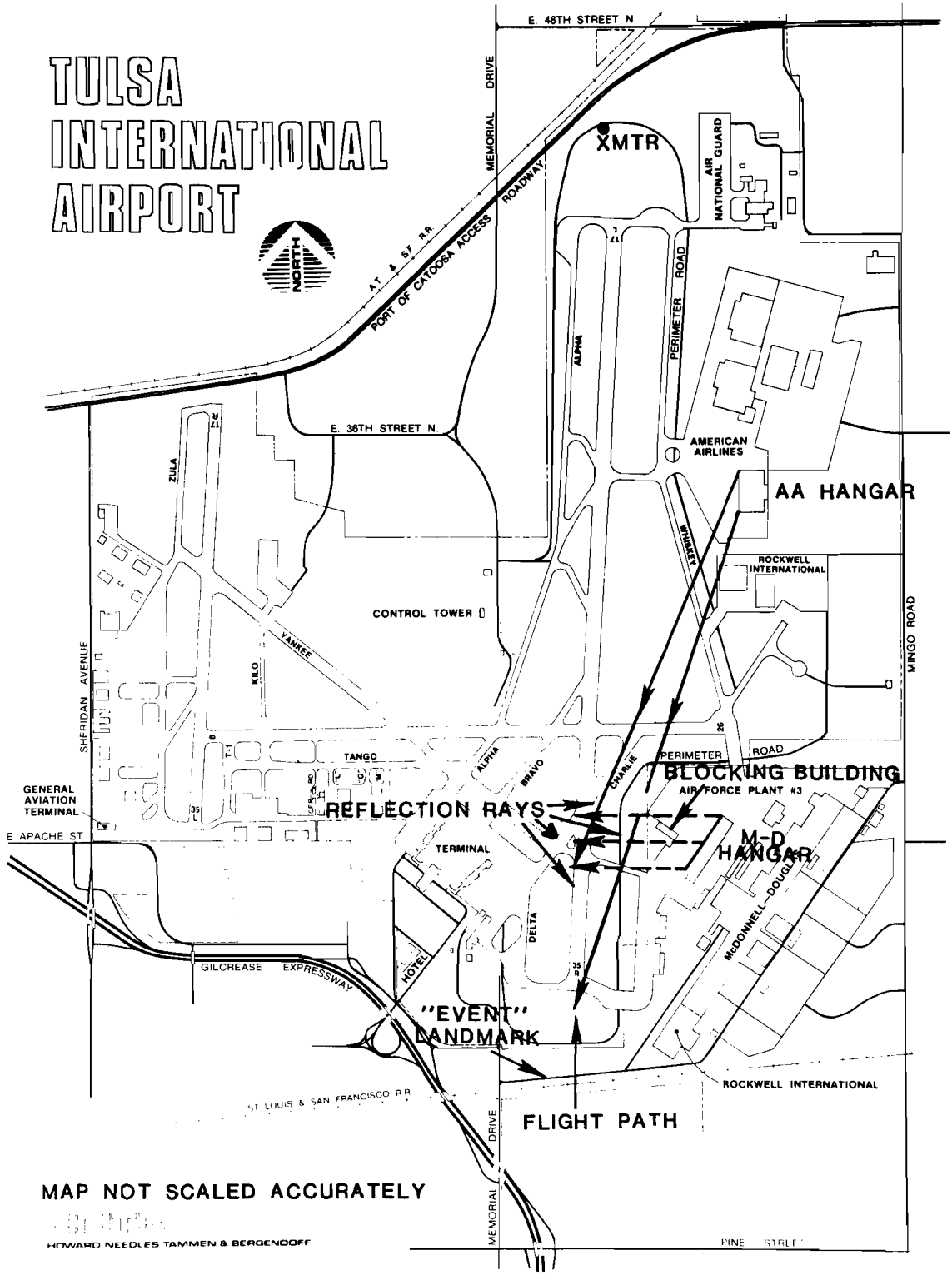

Fig. 3-57. Map of Tulsa International Airport.

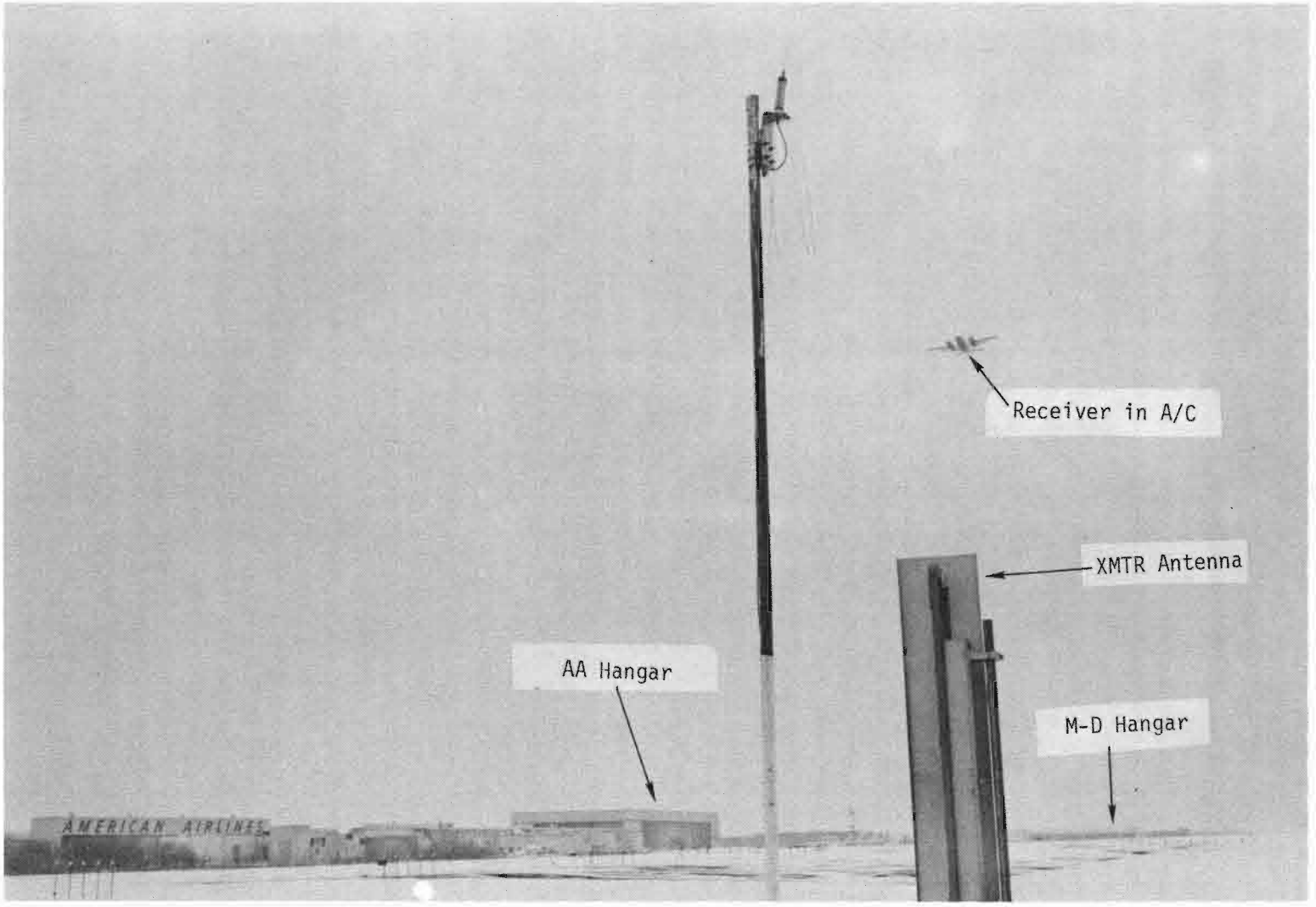

Fig. 3-58. View of buildings as seen from transmitter site.

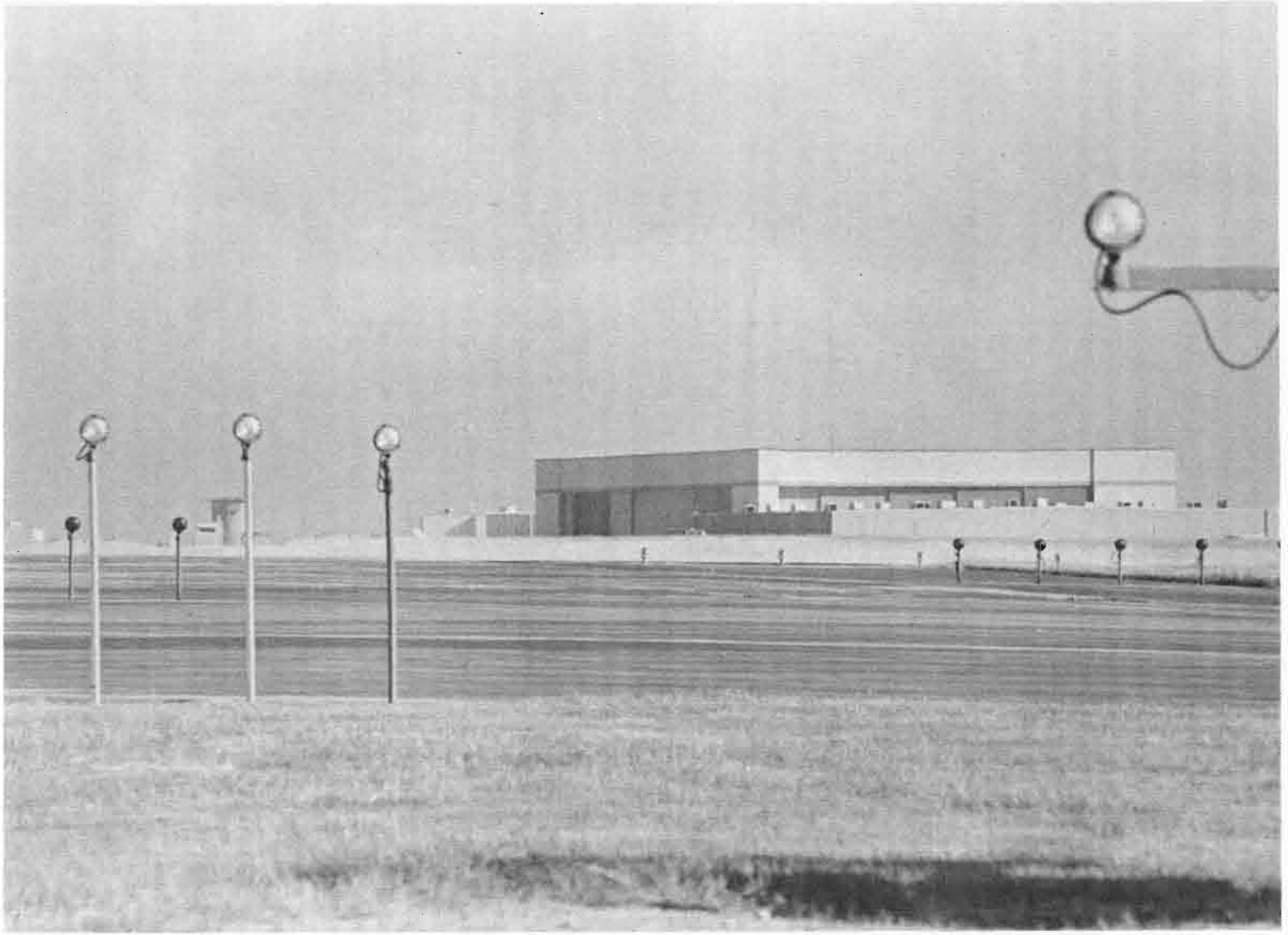

Fig. 3-59. American Airlines hangar as seen from threshold.

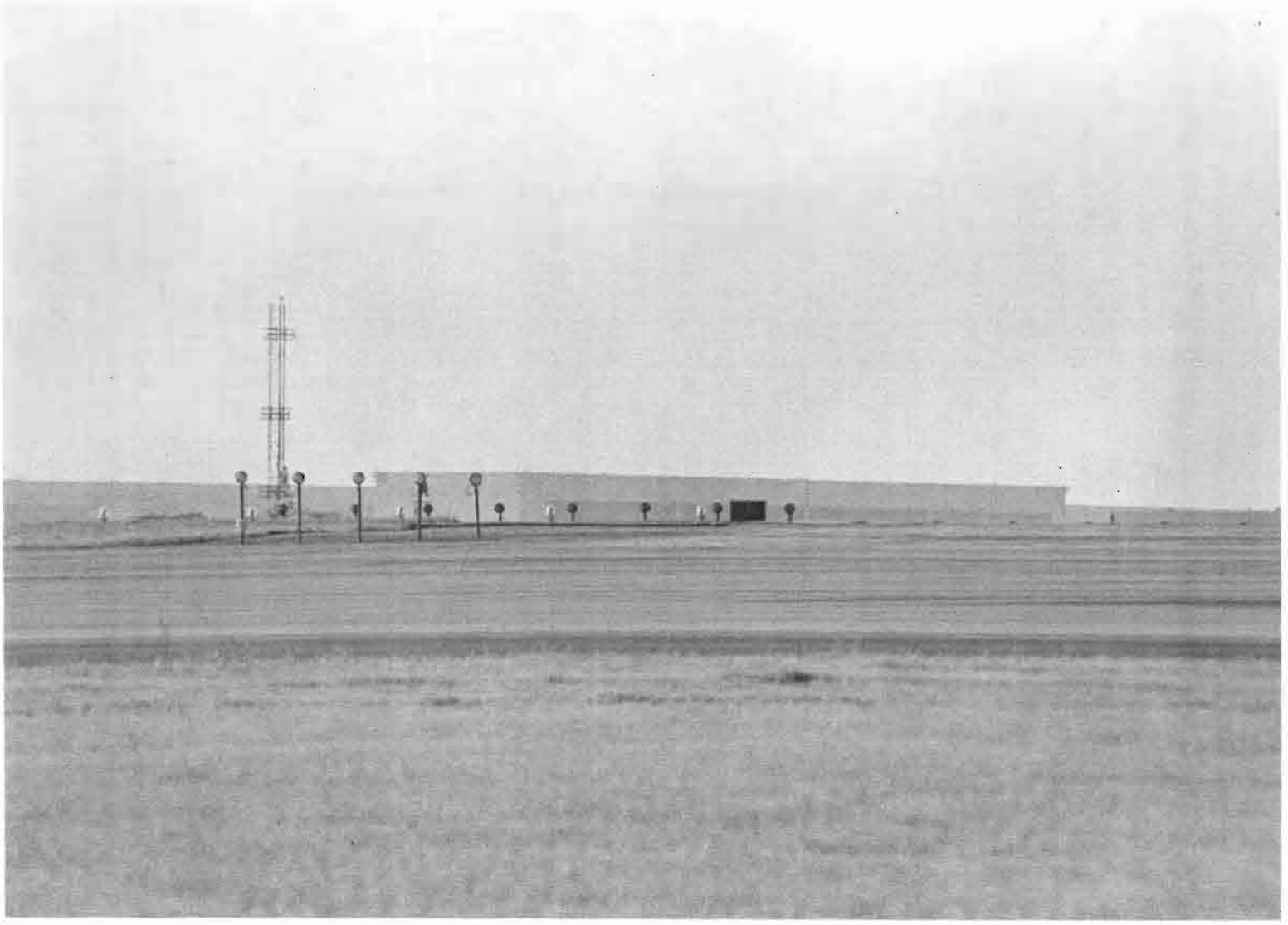

Fig. 3-60. McDonnell-Douglas hangar as seen from slope end of the runway.

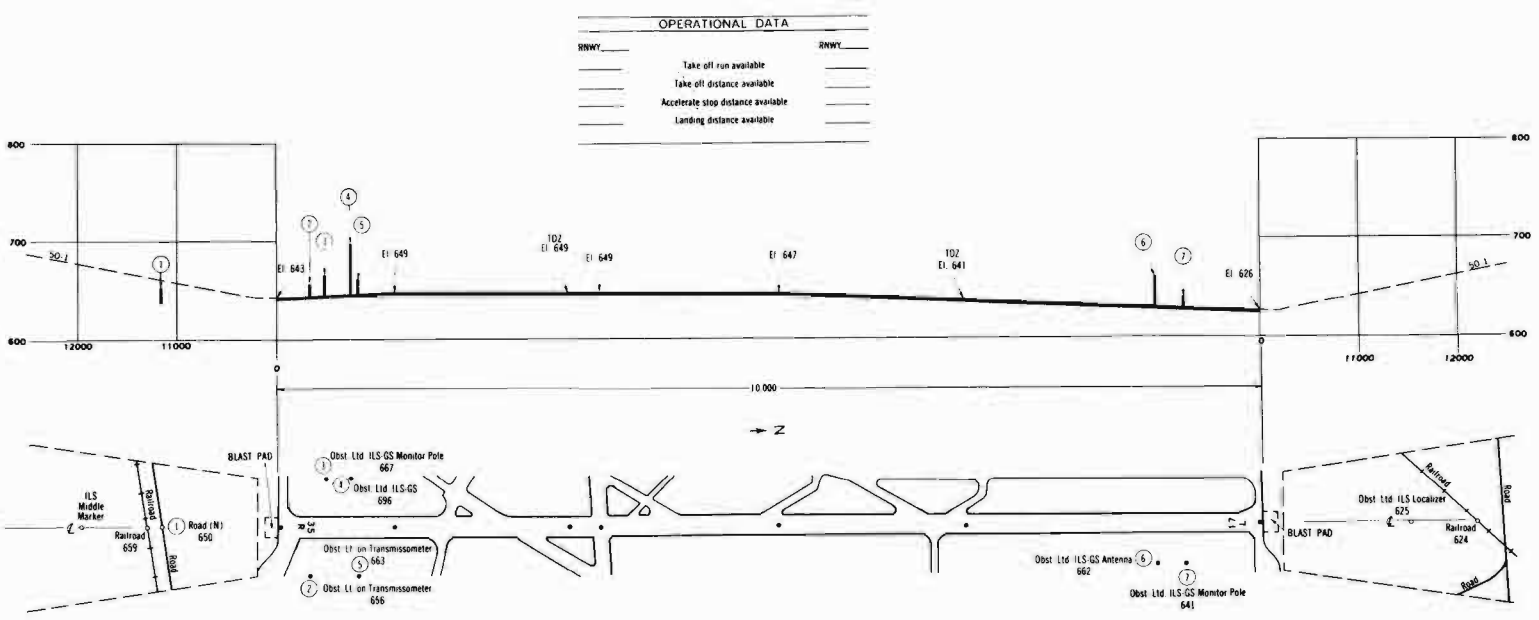

Fig. 3-61. Profile of runway 17L-35R.

Fig. 3-62. Transmitter on localizer shack.

TABLE 3-3

TULSA FLIGHT SUMMARY

Event marker = major road

RUN	VELOCITY (knots)	HT. ALONG RWY* (FT)	HT. AT THRESHOLD (FT)
1	120	25	100
2	120	5	100
3	120	35	100
4	120	50	2 dots below ILS glideslope full scale on approach.
5	140	20	
6	120	25	
7	125	20	
8	110	landed at first 1/3 of runway	normal

*average height over first third of runway

c. Spectrum Results

On several of the runs at Tulsa, the airborne and ground local oscillator drifts were such that the demodulated signal frequency passed through 0 Hz during the run, thus creating a difficult analysis task. The frequencies were stable on runs 5 and 8 so that a detailed analysis could be made. Thus, the results for runs 5 and 8 are presented and described in this section. Both the direct and reflected signals have relatively narrow spectral lines. The carrier frequency was stable for run 5 but appears to have drifted some during run 8. Fig. 3-63 shows the spectrum in a region of low multipath and Fig. 3-64 shows the spectrum in a region of multipath from both the AA and M-D hangars.

Fig. 3-65 presents a sequence of spectra at various points in the multipath region of the AA hangar, together with M/D levels for the 50 Hz scalloping signal at the right. We see some additional multipath at a scalloping frequency of about 800 Hz which corresponds to reflection off the large M-D building parallel to the M-D hangar. We expected to see reflection from the M-D hangar near the times 1/20/34.977 or 1/20/36.180, but it failed to appear. By making a fine time grid spectral analysis between 1/20/34.4 to 1/20/37.199 in Fig. 3-66 we see that a line at about 750 Hz does appear briefly peaking at about +2 dB. Evidently, at the receiver height of 20 to 25 feet, the specular reflection point is relatively high on the hangar and only the near corner is producing multipath.

Run 8 is similar to run 5 except that the plane is landing. This results in a lower specular point on the building, and the lower velocity causes the expected scalloping frequencies to be reduced by about 20 - 25%. We can see some drift in the demodulated signal carrier for the sequence of runs presented in Fig. 3-67. Here the M-D hangar multipath appears over a more extended region.

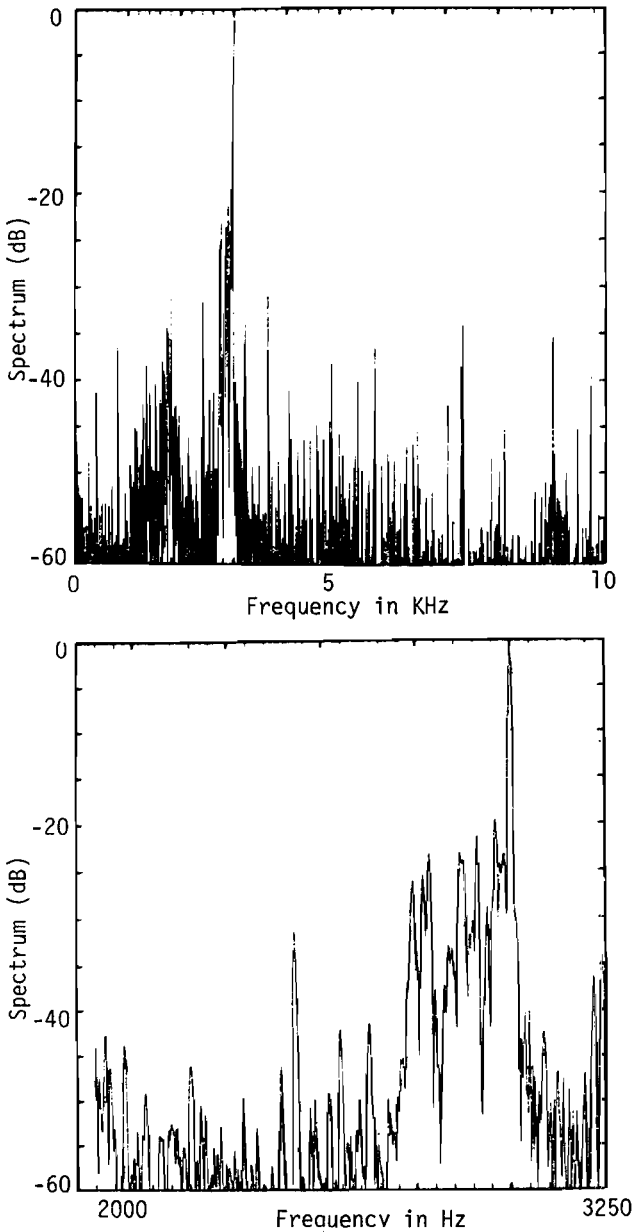

0.2 sec. data analyzed

Hamming window

Fig.3-63. Spectrum of demodulated signal at Tulsa and a blow-up of the 1900 to 3250 Hz section from run 5.

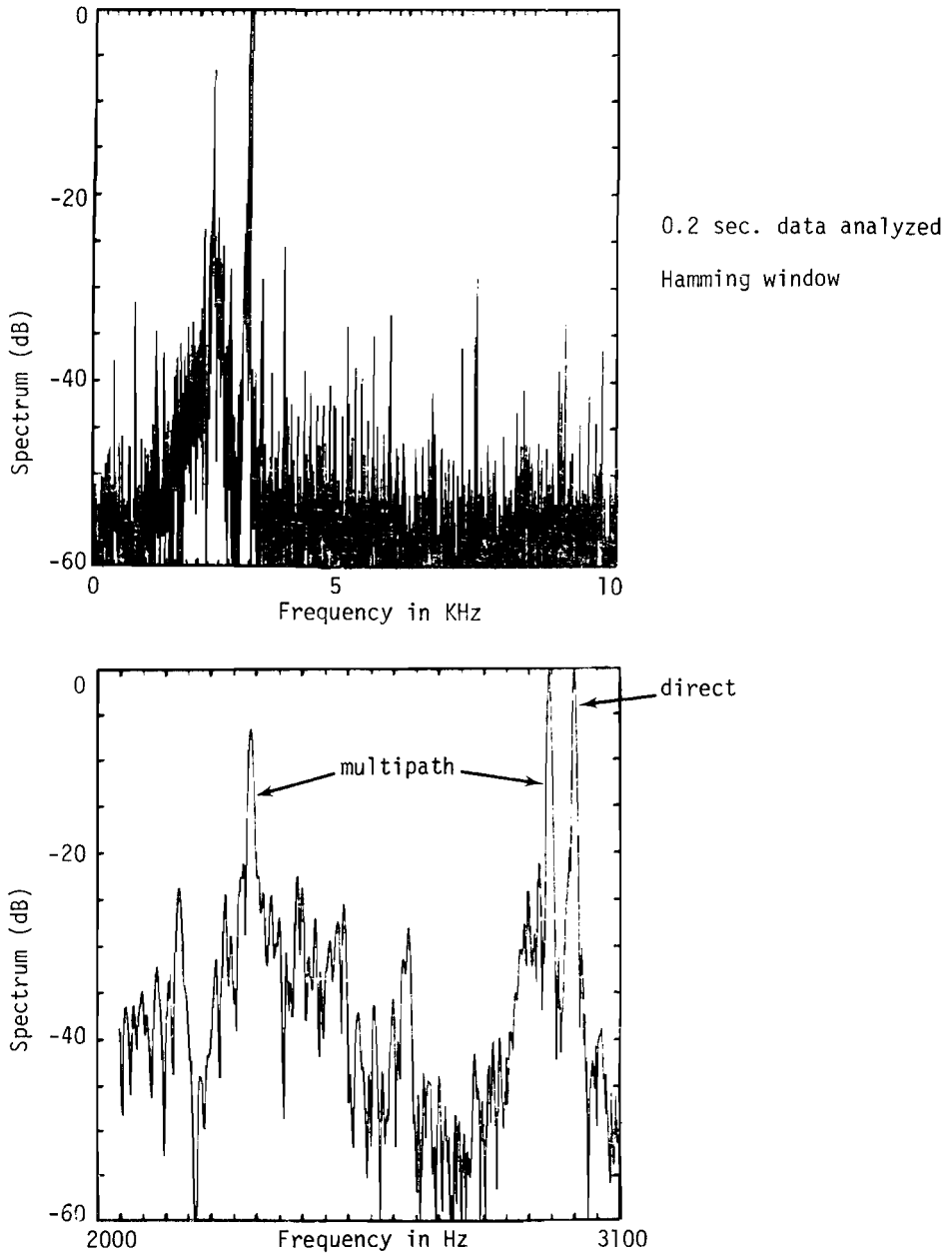

Fig.3-64. Example of Tulsa multipath spectrum containing both the 50 Hz scalloping frequencies and 2000 to 3100 Hz blow-up from run 5.

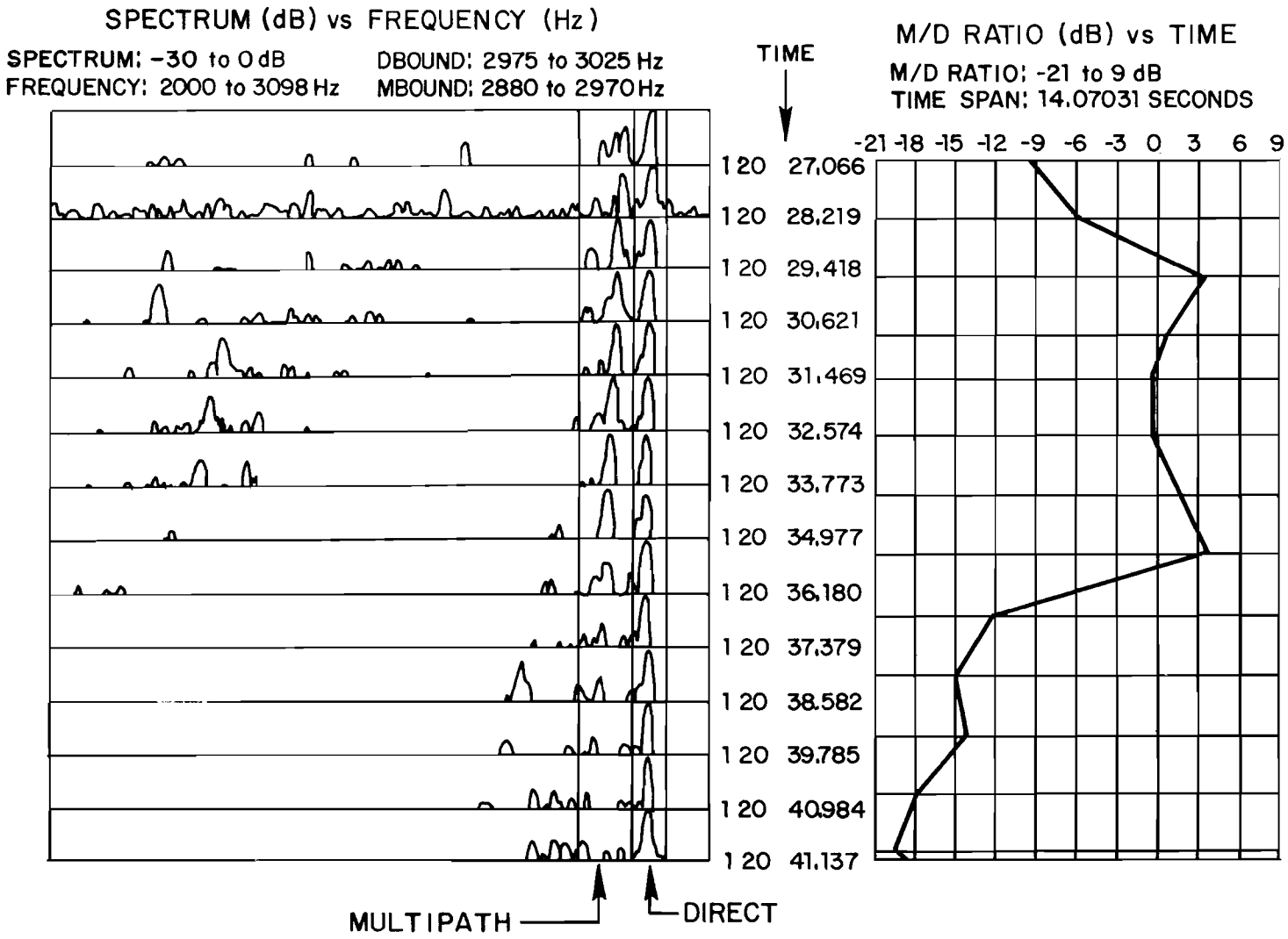

Fig. 3-65. Sequence of spectra for Tulsa run 5 in multipath region.

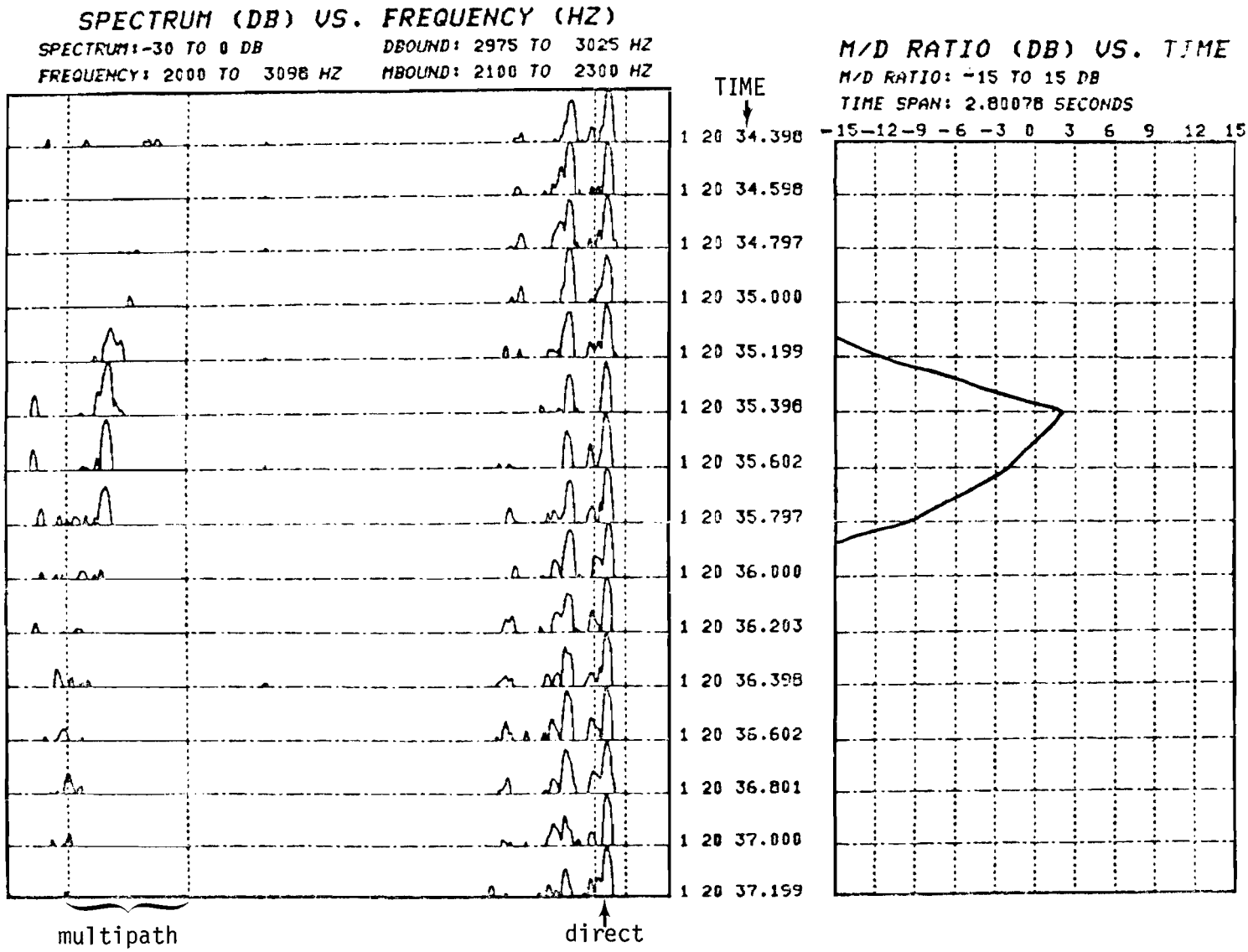

Fig.3-66. Blow-up of sequence of spectra for Tulsa run 5 from 1/20/34.298 to 1/20/37.199.

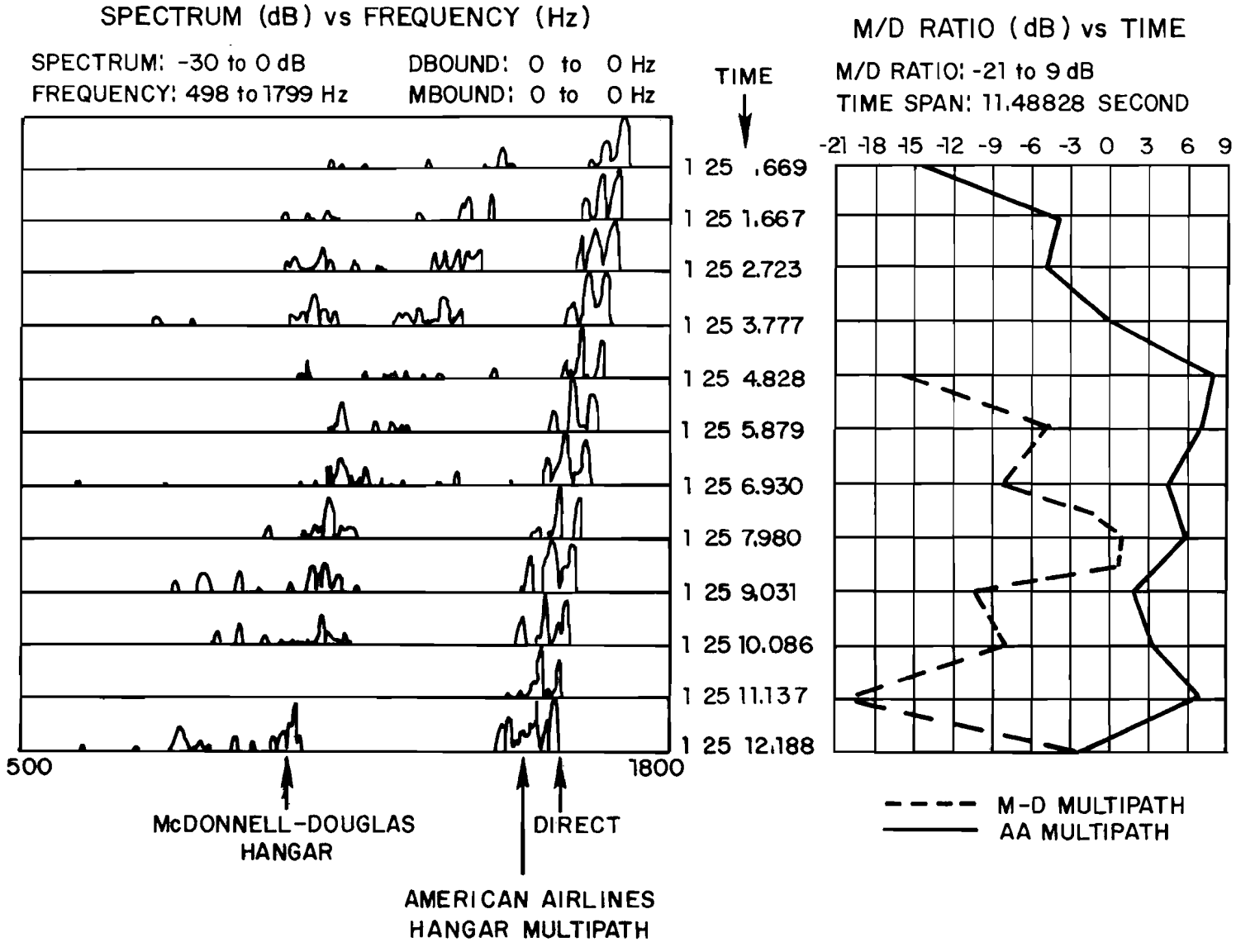

Fig. 3-67. Sequence of spectra for Tulsa run 8 in multipath region.

d. Summary

We have seen that the multipath measurements have agreed well with the theoretical expectation in multipath region extent, scalloping frequency, and reflection phase coherence.

The AA hangar produces high level multipath over an extensive range near threshold and into flare, but at relatively low scalloping frequency. The M-D hangar produces scalloping at about 650 - 700 Hz near flare, but is near or above 0 dB for only one second.

Tulsa represents a good choice for comparative multipath testing of resistance to high level multipath at low scalloping frequencies. The long duration (7 seconds) of high level multipath (> +3 dB M/D ratio) demonstrate the need for a high capability tracker and intrinsic resistance to out of beam multipath signals.

6. Wright Patterson Air Force Base

Wright Patterson Air Force Base has been the site of MLS testing as well as multipath measurements using directive antennas. Tests by the USAF with an early Doppler scan antenna showed very large azimuth errors (> 7.0°) in the flare region due to the multipath [56]. Multipath measurements by the U.S. Army and IITRI yielded multipath levels of +3 dB to +6 dB with vertical polarization [57]. It was suggested that no MLS using vertical polarization could function properly at WPAFB [57]. Thus, WPAFB seemed a logical candidate for the measurement program described here.

a. Multipath Environment

Fig. 3-68 shows an airport map of Wright-Patterson Air Force Base (WPAFB). Also shown in this figure are the reflection rays corresponding to the major anticipated multipath threats for an aircraft landing on runway 23. The major multipath threat was expected to be the building 206, as shown in Fig. 3-69 which is a photo taken at the west end of runway 23. Figs. 3-70 and 3-71 give more detailed pictures of the building 206. Building 206 consists of two main buildings with one lower cement building on each side and a lower building sticking out between them. Four end pillars and twenty doors constitute the building front, facing runway 23. The main building and the doors are 75 and 45 feet tall, respectively. Each door consists of interlaced glass windows and metal plates.

Some multipath might also be expected from the building 146, which is small as compared to building 206 (Figure 3-68). The relative location and size of buildings 206 and 146 can be more clearly seen in Fig. 3-68. Building 146 is about 25 feet tall and about one quarter as wide as building 206. Building 146 is about 500 feet east of building 206. The two buildings are oriented slightly differently with respect to runway 23, as indicated by the angles shown in Fig. 3-68.

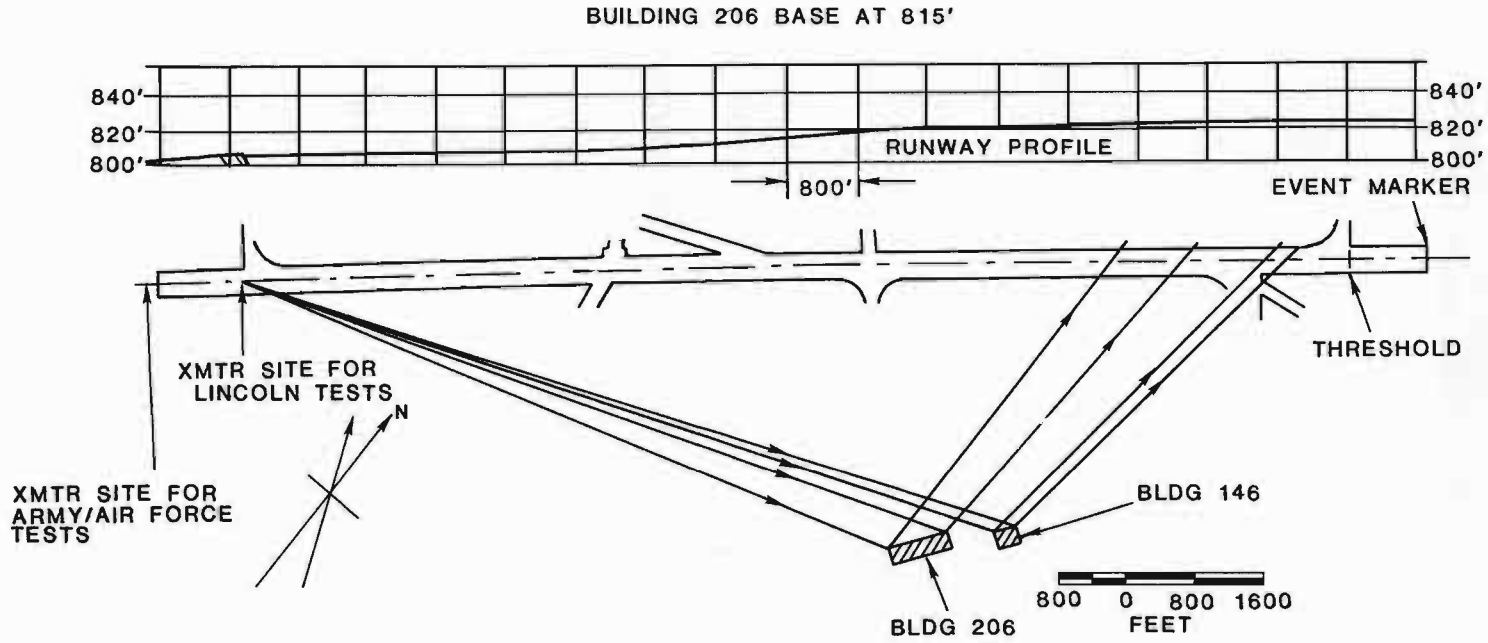

Fig. 3-68. Wright-Patterson Air Force Base.

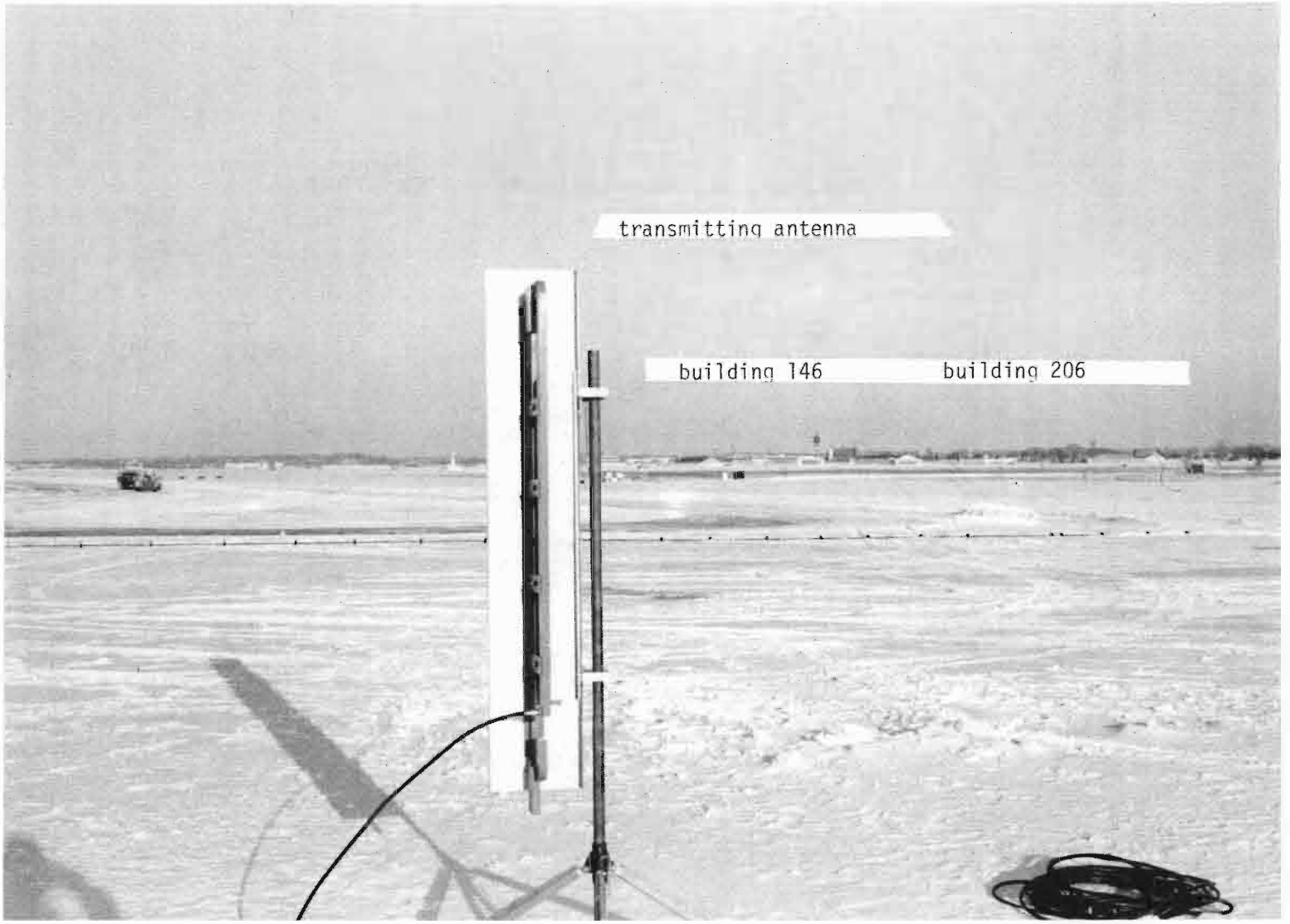

Fig. 3-69. Buildings 206 and 146 as seen from transmitting antenna.

Fig. 3-70. Building 206 at WPAFB from near the transmitter site.

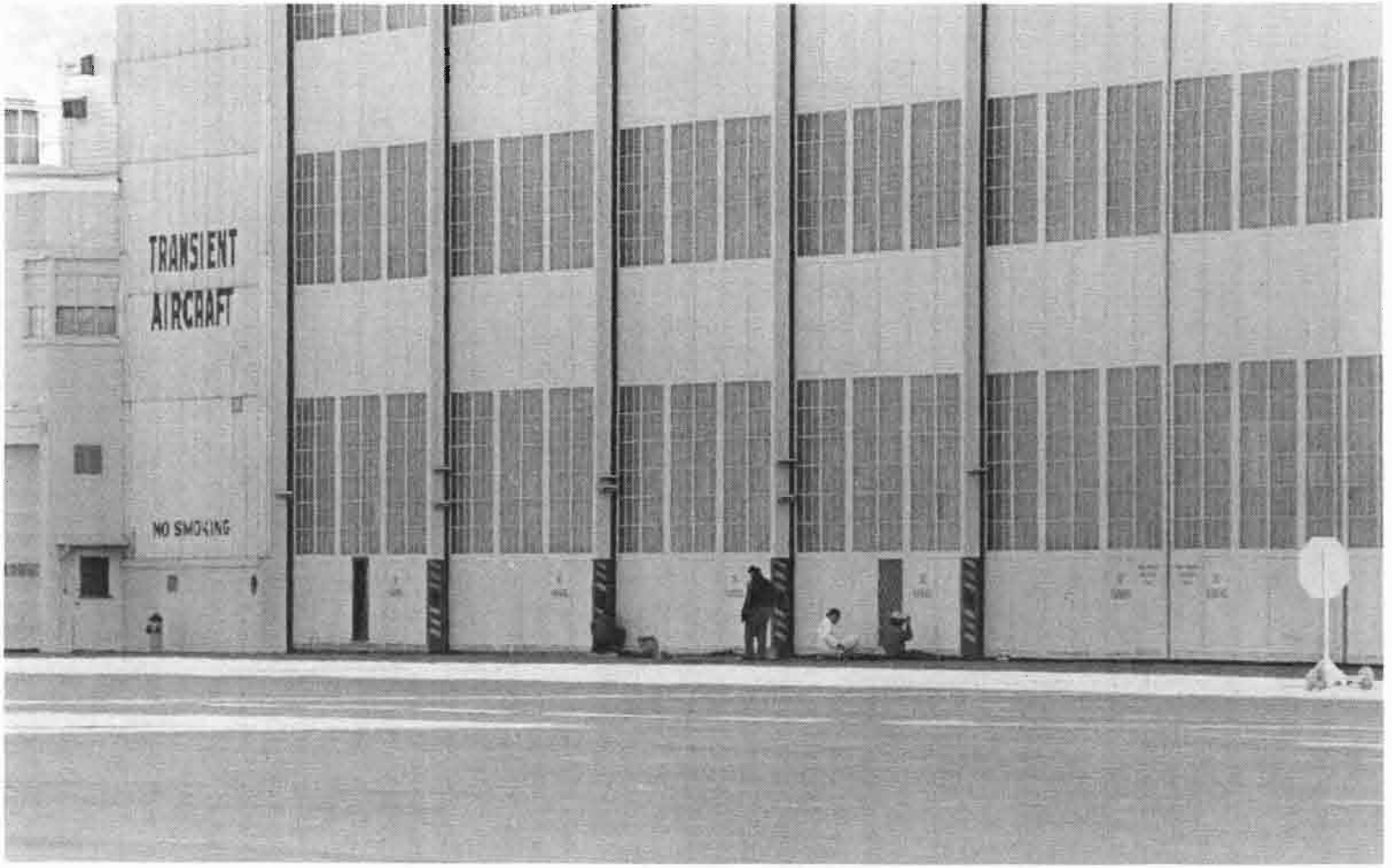

Fig. 3-71. Building 206.

The runway contour (also shown in Fig. 3-68) indicates an up slope from 800 feet elevation at the west end of runway 23 to 824 feet elevation at the east end. The ground at buildings 206 and 146 is 815 feet elevation. The transmitting antenna was located at about 1000 feet before the west end of the runway as shown in Figs. 3-68 and 3-69, with a phase center height of approximately 5 feet. This on-runway location was necessitated by the fact that the overrun area was not accessible due to deep snow. When the measurement was made, the ground was covered with some snow while the runway was partically clear, as can be seen in Fig. 3-69.

The expected scalloping frequencies for a centerline approach at 120 knots are as follows:

BUILDING	SCALLOPING FREQUENCY (HZ)
Building 206	360-410
Building 146	270-300

b. Measurements Made

Table 3-4 summarizes the measurements made at Wright-Patterson Air Force Base. A total of nine centerline approaches were made between the hours of 4 p.m. and 6 p.m. on 31 January 1978. Run #1 was at 110 knots and 50 feet above runway surface. Runs #2 through #8 were at 120 knots and 15-50 feet above runway surface. On Run #9, the aircraft landed on the runway. The aircraft was approaching the runway 23 from the east direction. The east end of the runway (about 1000 ft. from the landing threshold) was used as the "event mark" recorded on the analog tape.

c. Spectrum Analysis Results

Runs #3, #7, #8, and #9 have been analyzed to data and some representative results will be discussed in this section. The typical features which were observed in the majority of the spectra of the demodulated signals in the WPAFB measurements are: (1) the spectral peaks corresponding to the direct and the multipath signals were not as narrow as those observed in the St. Louis measurements; (2) the direct and the multipath signal spectra usually were of similar width; (3) on several occasions, two or three closely spaced peaks existed in the direct and the multipath signal spectra; and (4) the overall level of background noise was around -40 to -50 dB.

TABLE 3-4

WPAFB JANUARY 1978 FLIGHT PROFILES

RUN #	A/C SPEED (KNOTS)	HEIGHT* (FEET)	NOTES
1	110	50	snow plows in front of antenna
2**	120	20	snow plows in front of antenna
3**	120	15	snow plows in front of antenna
4	120	50	snow plows in front of antenna
5	120	50	snow plows on left hand side of runway
6	120	20	snow plows gone
7	120	20	snow plows gone
8	120	50	snow plows gone
9	105	landed	snow plows gone

These were all level flights, centerline approaches from the east end of runway 23

*Flight path height above runway surface

**No demodulated signals due to recording difficulties

Fig. 3-72 shows a typical spectrum of the demodulated signal in a region of low multipath. Figs. 3-73 and 3-74 show the spectra for the multipath at scalloping frequencies of 270 and 380 Hz, respectively. The scalloping frequency was estimated from the location of the highest peak in the multipath spectrum and that in the direct spectrum. The scalloping frequency was also estimated from the spectral analysis on the log-video signal. The scalloping frequency estimates from the demodulated and log-video signals agreed very well.

Fig. 3-75 shows the sequence of spectra at various points within the multipath region for building 206. The vertical scale of the spectrum is 0 to -30 dB for Fig. 3-75a and 0 to -60 dB for Fig. 3-75b. It is noticed that the successive measurements made over disjoint sections of the flight path all yield very similar spectra. The "M/D ratios" shown on the right hand side of this figure were estimated in the same way as described in Section 4-c. A similar display is shown in Fig. 3-76 for the multipath region caused by building 146.

Fig. 3-77 summarizes the multipath levels versus time after the "event mark" for the components whose levels were within 20 dB of the direct signal level. The largest M/D ratios observed are 0 dB to -1 dB for the building 206 and the building 146 multipath regions, respectively. It should be noted that the transmitting antenna pattern gain is down 2 dB in the direction of the buildings.

The above discussions are pertinent to runs #3, #7, and #8. Run #9 will be discussed separately here, since the aircraft was landing in this run in contrast to the level flight with constant aircraft speed in the other WPAFB runs. Fig. 3-78 shows the spectrum of the demodulated signal with very high multipath level. Fig. 3-79 summarizes the multipath levels and scalloping frequencies versus time after the "event mark" for the components whose levels were within 20 dB of the direct signal level. We see that the peak multipath level in this run is significantly higher than those in runs #3, #7, and #8.

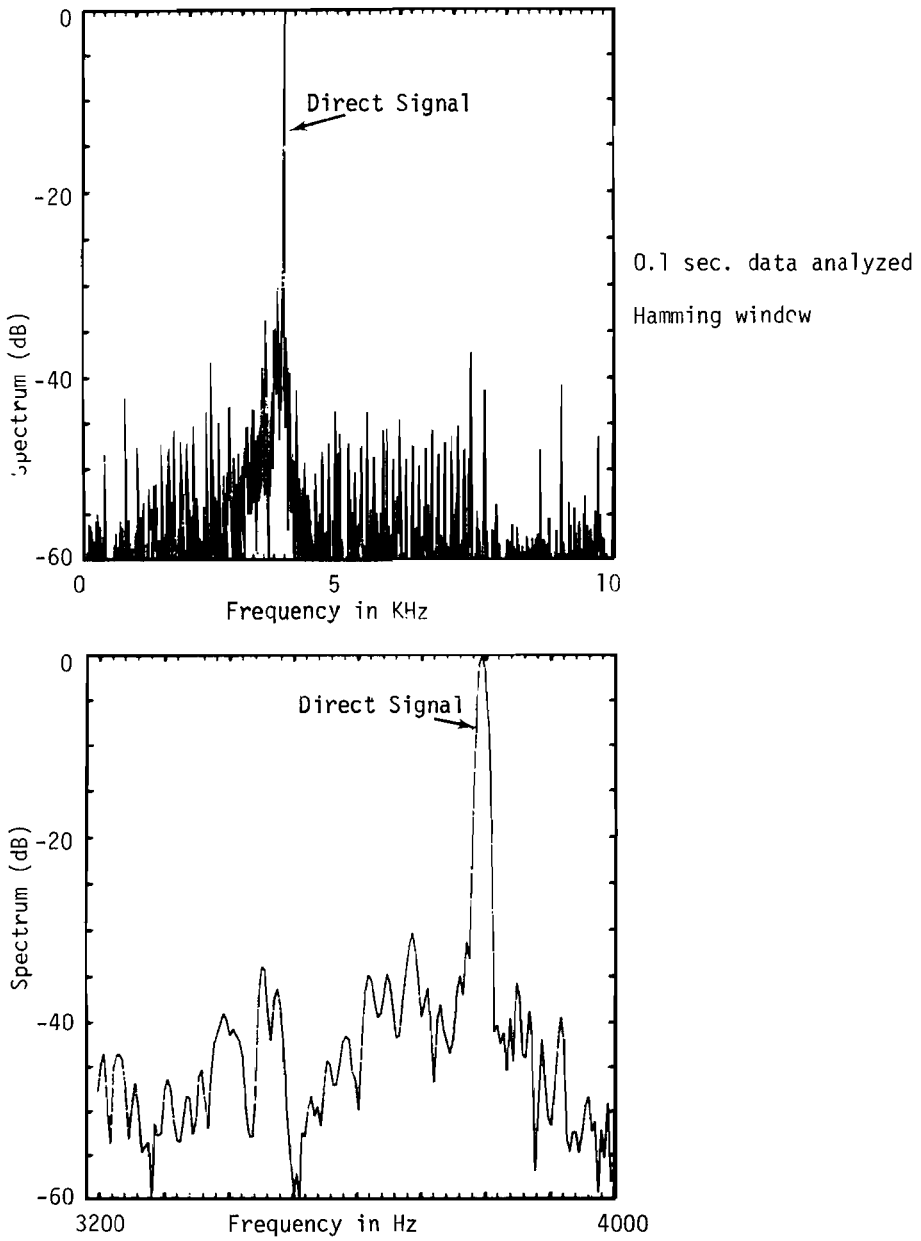

Fig.3-72. Spectrum of demodulated signal at WPAFB: example for low multipath region.

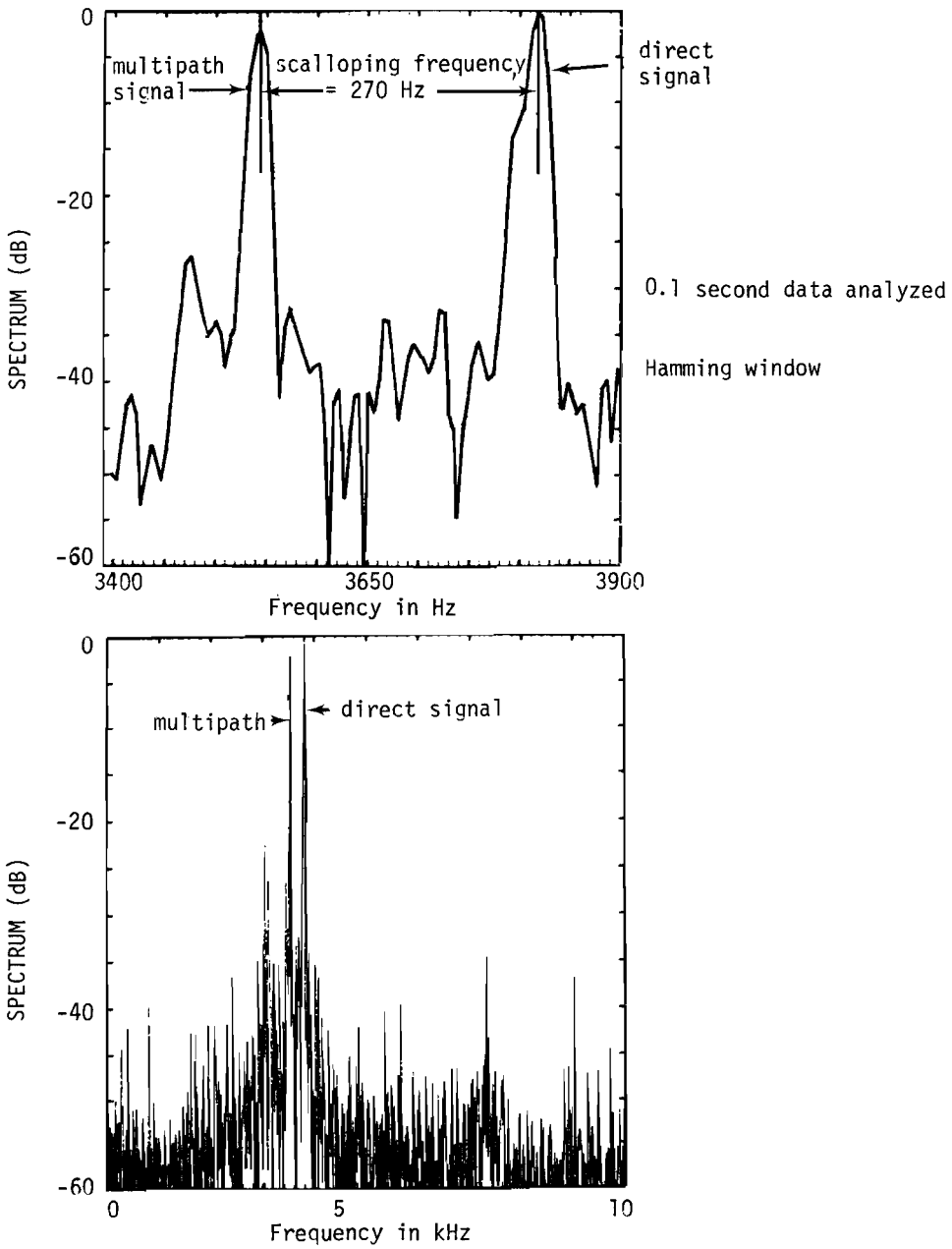

Fig.3-73. Spectrum of demodulated signal: example of WPAFB multipath at 270 Hz scalloping frequency.

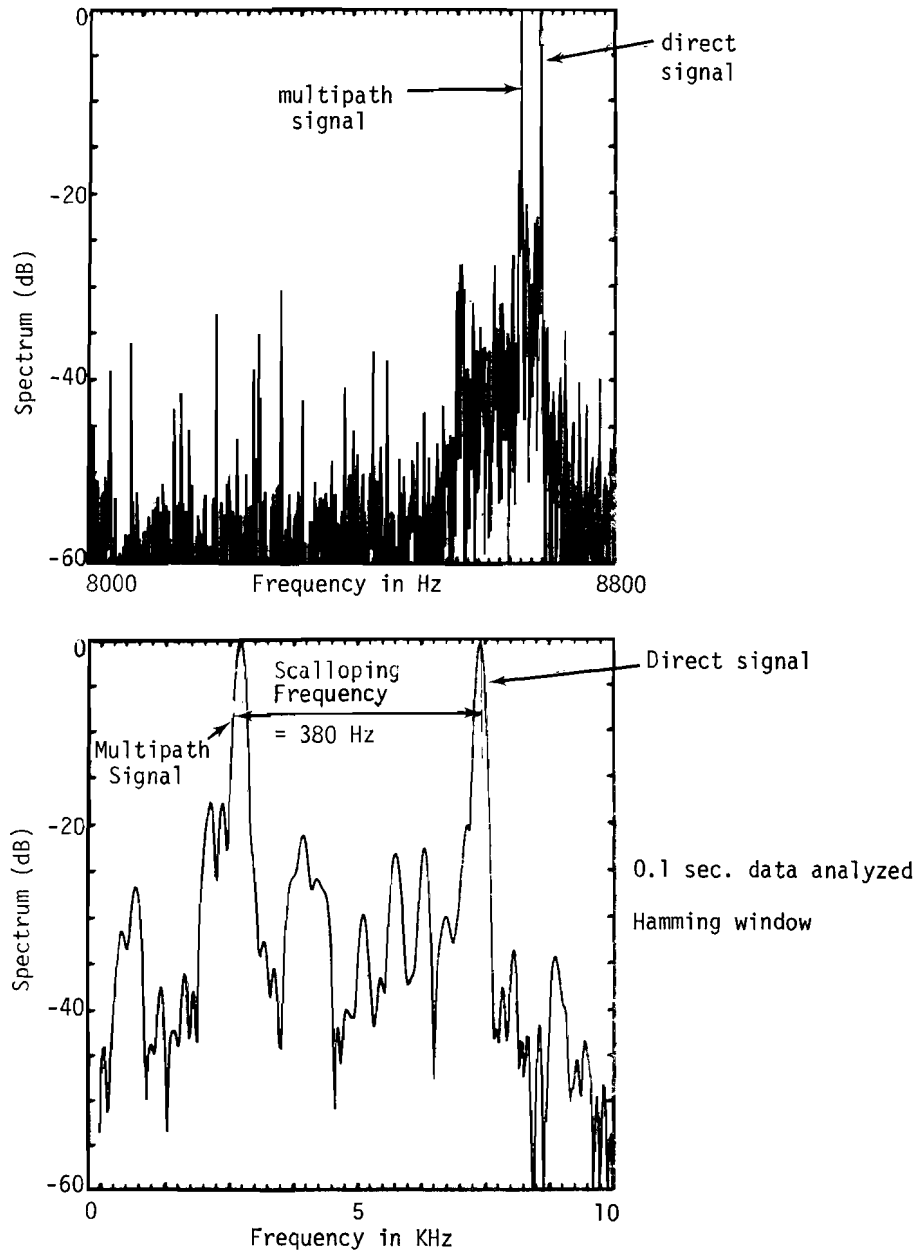

Fig. 3-74. Spectrum of demodulated signal: example of WPAFB multipath at 380 Hz scalloping frequency.

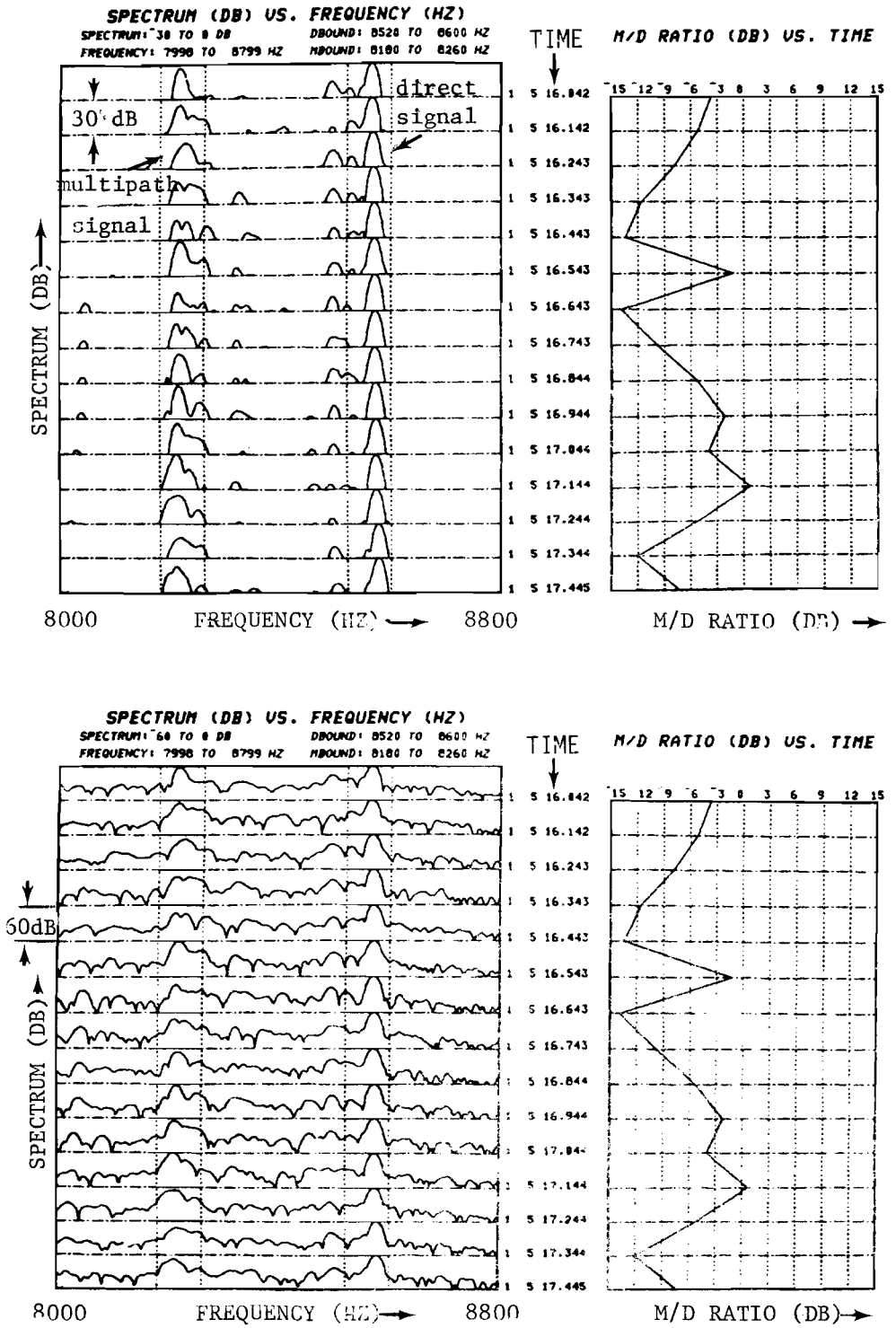

Fig. 3-75. WPAFB spectra on Run #3 at various points within the expected multipath region for building 206.

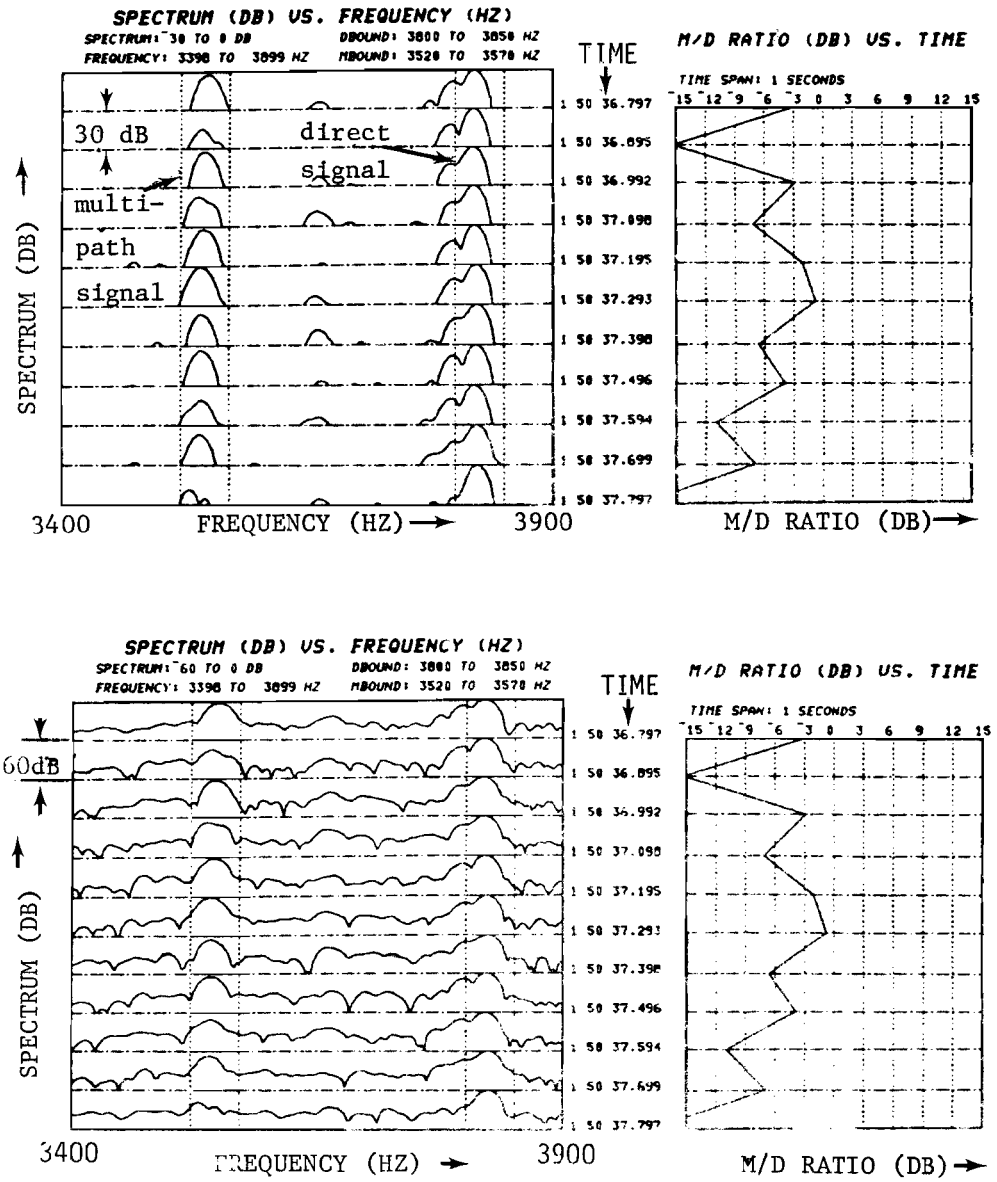

Fig. 3-76. WPAFB spectra on run #7 at various points within the expected multipath region for building 146.

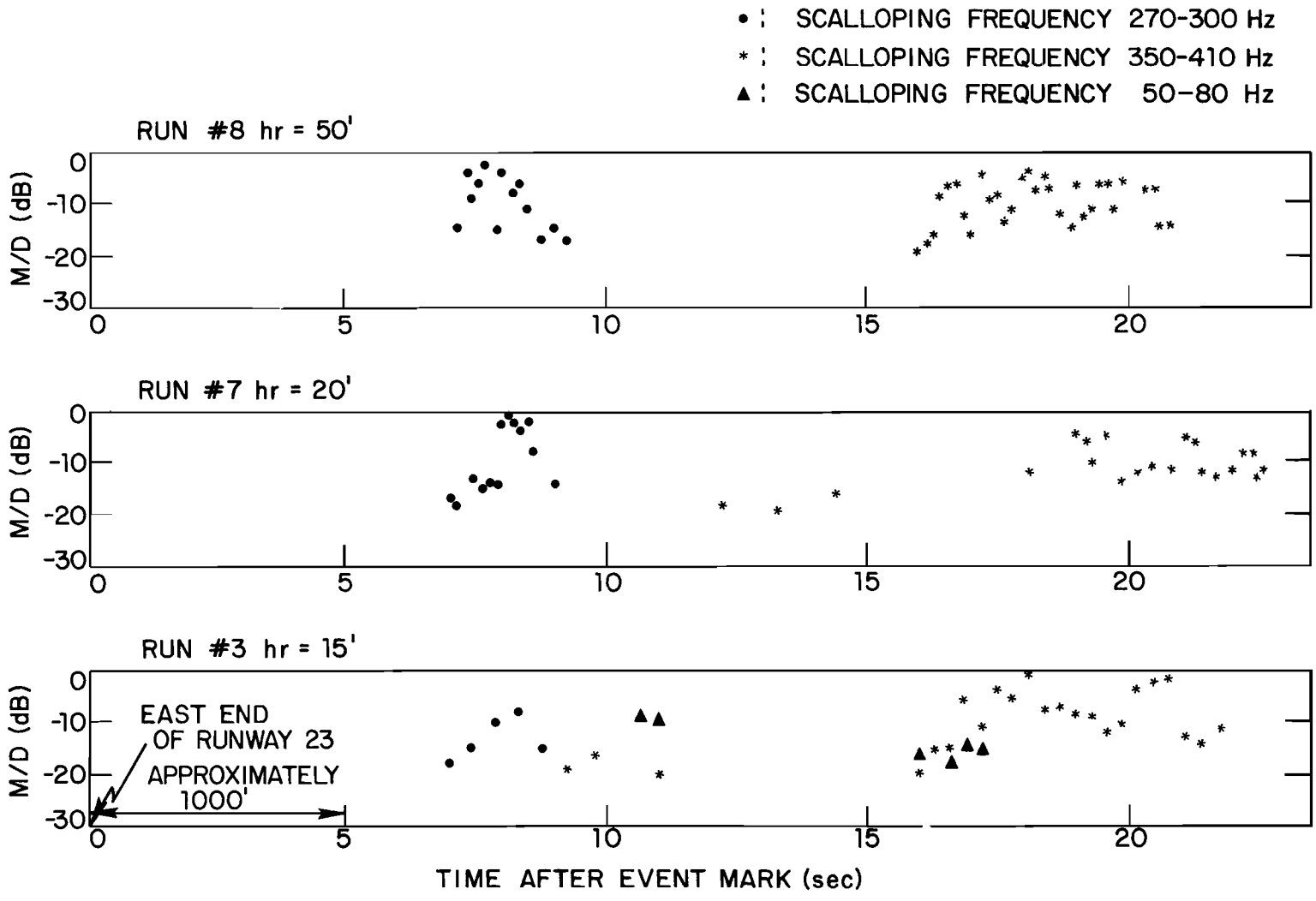

Fig. 3-77. Summary of WPAFB multipath.

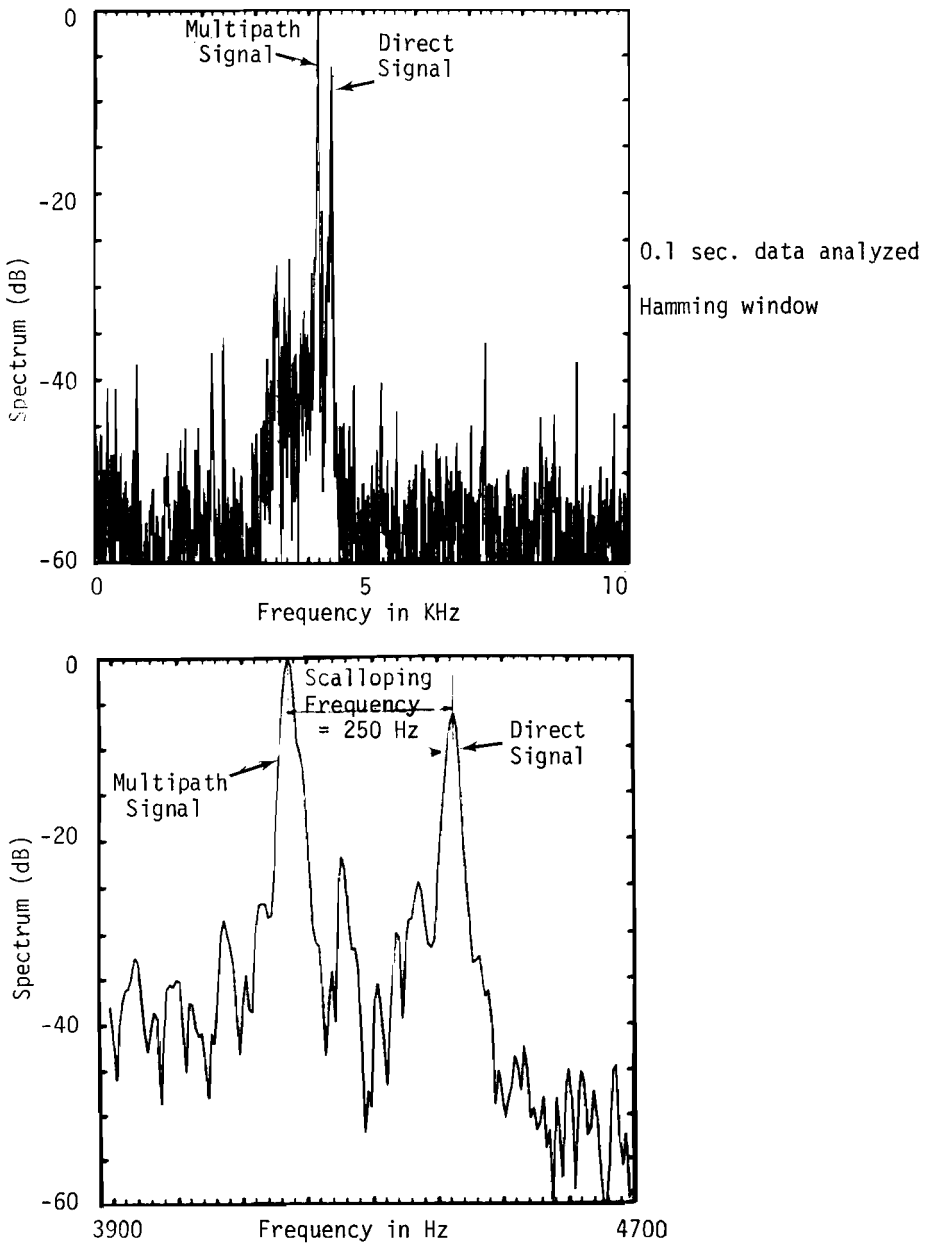

Fig. 3-78. Spectrum of the demodulated signal: example of WPAFB run #9.

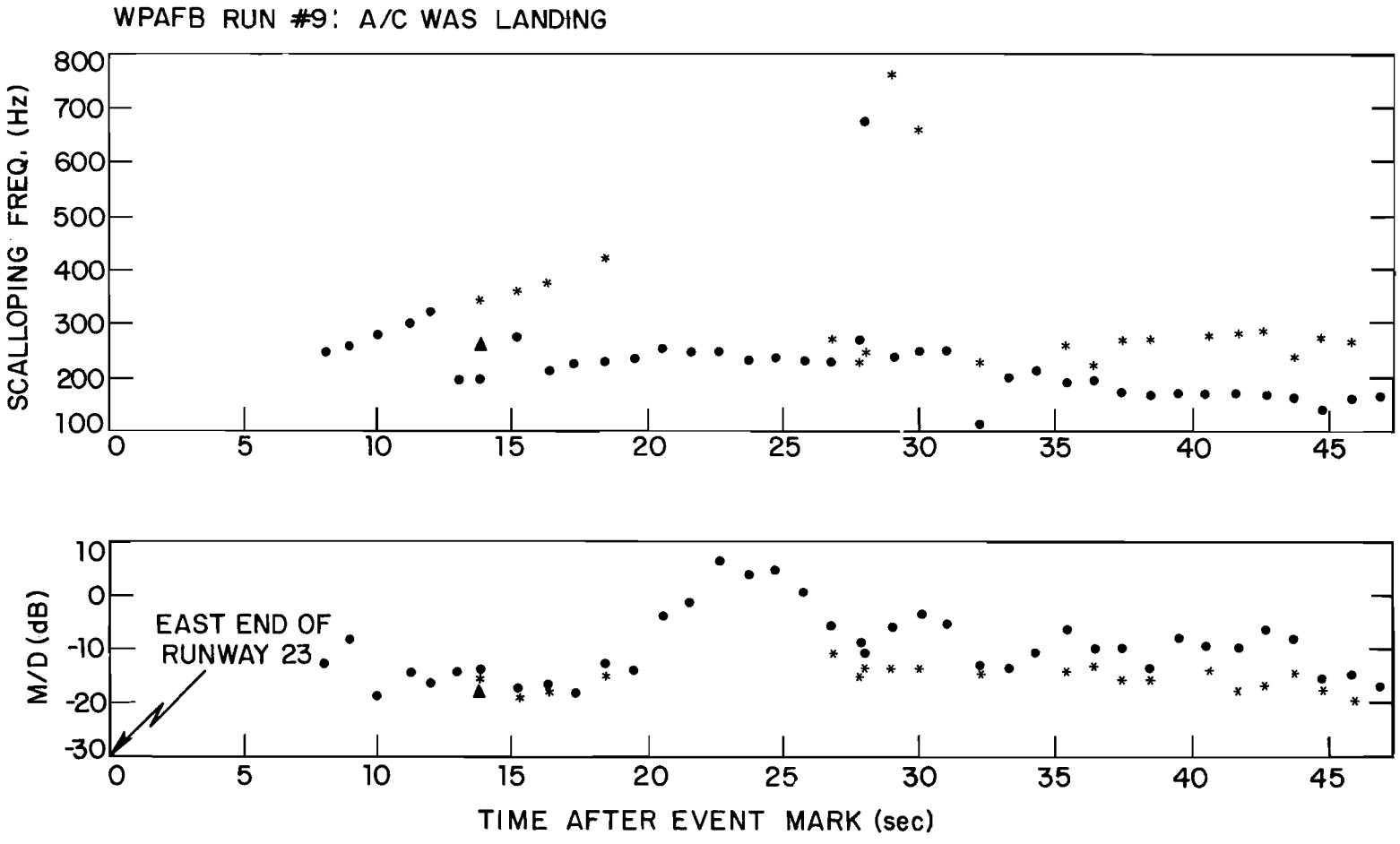

Fig. 3-79. Summary of WPAFB run #9 multipath.

d. Summary

The spectral analysis results of the multipath measurements at Wright Patterson Air Force Base agree reasonably well with the theoretical expectations in both scalloping frequencies and the multipath regions along runway 23. From the measurements, the first multipath region occurred at 7 to 9 seconds after the "event mark" (with aircraft speed at 120 knots) at the scalloping frequencies of 270 to 300 Hz. This corresponds to the theoretically predicted multipath region for building 206. Although the multipath region for building 146 is much narrower than that for building 206, to our surprise, the peak multipath level from building 146 is as high as that from building 206. The high multipath levels from these buildings suggest that the runway 23 at Wright Patterson Air Force Base might be a good candidate for a stringent test of MLS capability to cope with the high level out of beam azimuth multipath at high scalloping frequencies.

7. Miami International Airport

a. Multipath Environment

Fig. 3-80 shows an aerial photograph of Miami Internation Airport while Figs. 3-81 and 3-82 show maps of the airport area with reflection rays drawn on them. The major multipath threats on a curved approach were expected to be the large Eastern and Pan American hangars which are shown in Fig. 3-83. Fig. 3-84 shows details of these various buildings. The large Eastern hangar has vertical asbestos doors with vertical (trapezoidal shaped) corrugations.

The runway contour at Miami is quite flat (see Fig. 3-85). For the tests reported here, the transmitter was sited to the rear and side of the ILS localizer as indicated in Fig. 3-81 with a phase center height of approximately five feet. At the time the measurements were made, the terrain off the runway was grass covered. Fig. 3-86 shows the flight profiles and the expected multipath region for the large hangars.

b. Measurements Made

A total of eight flights were made at Miami between 9:30 a.m. and 11:30 a.m. on January 20. The flight profiles shown in Fig. 3-86 are radials emanating from the Miami VORTAC, thus it was possible to establish position along the radial DME distance. In all cases, the air speed was 150 knots. Table 3-5 summarizes the flights made and the received signal characteristics.

c. Spectrum Results

Runs 4, 5, and 7 have been analyzed in detail* to date and representative results will be reported in this section. Relative to data from the other airports, the Miami data shows a higher noise floor (due to the lower SNR when at

---

*Analysis of runs 1-3 showed that the direct signal frequency was so close to the sampling rate of 20 KHz that significant data interpretation problems arose due to aliasing effects. The analog tapes from these runs would have to be digitized at a higher sampling rate to extract useful data.

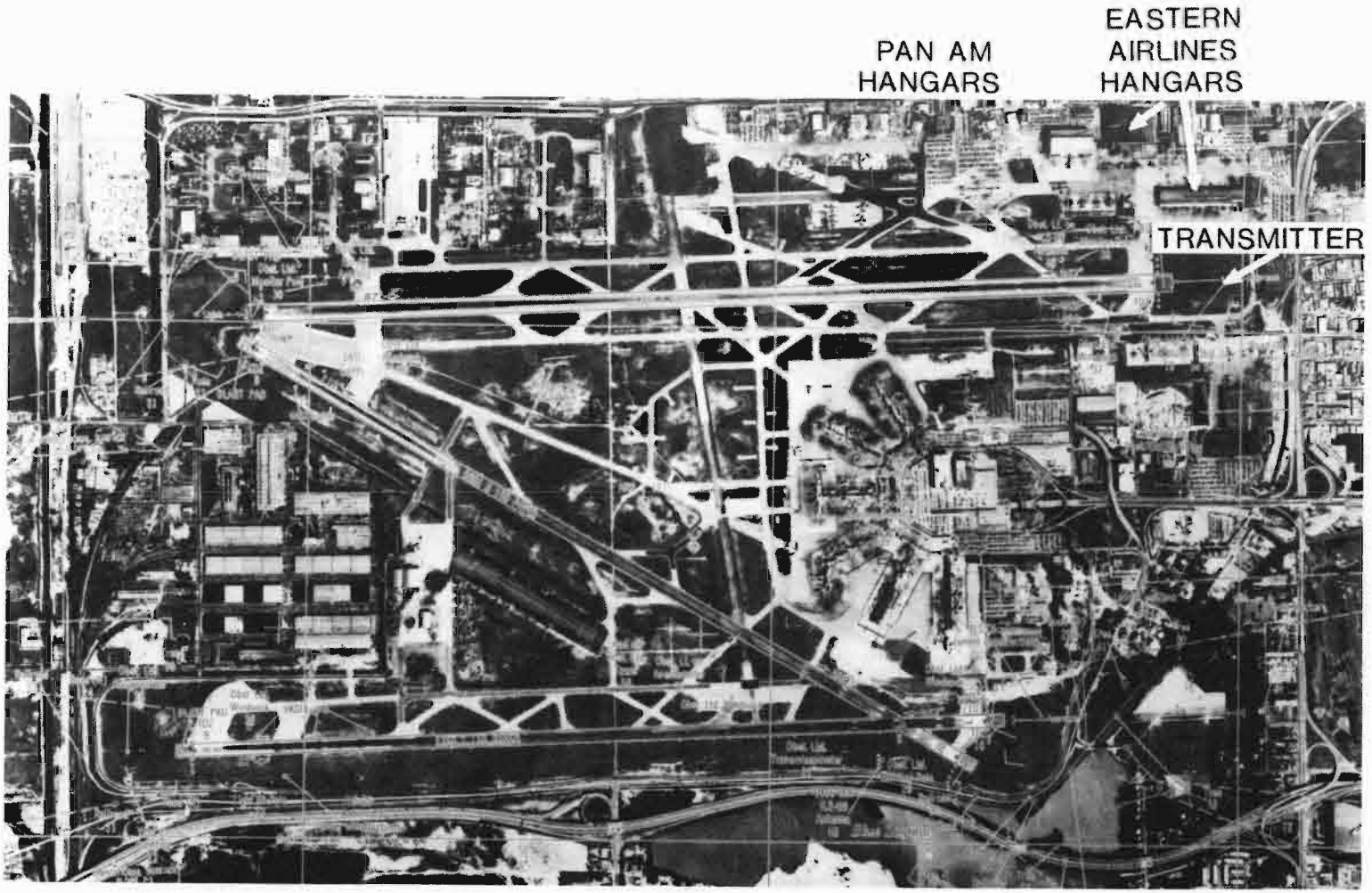

Fig. 3-80. Aerial view of Miami International Airport.

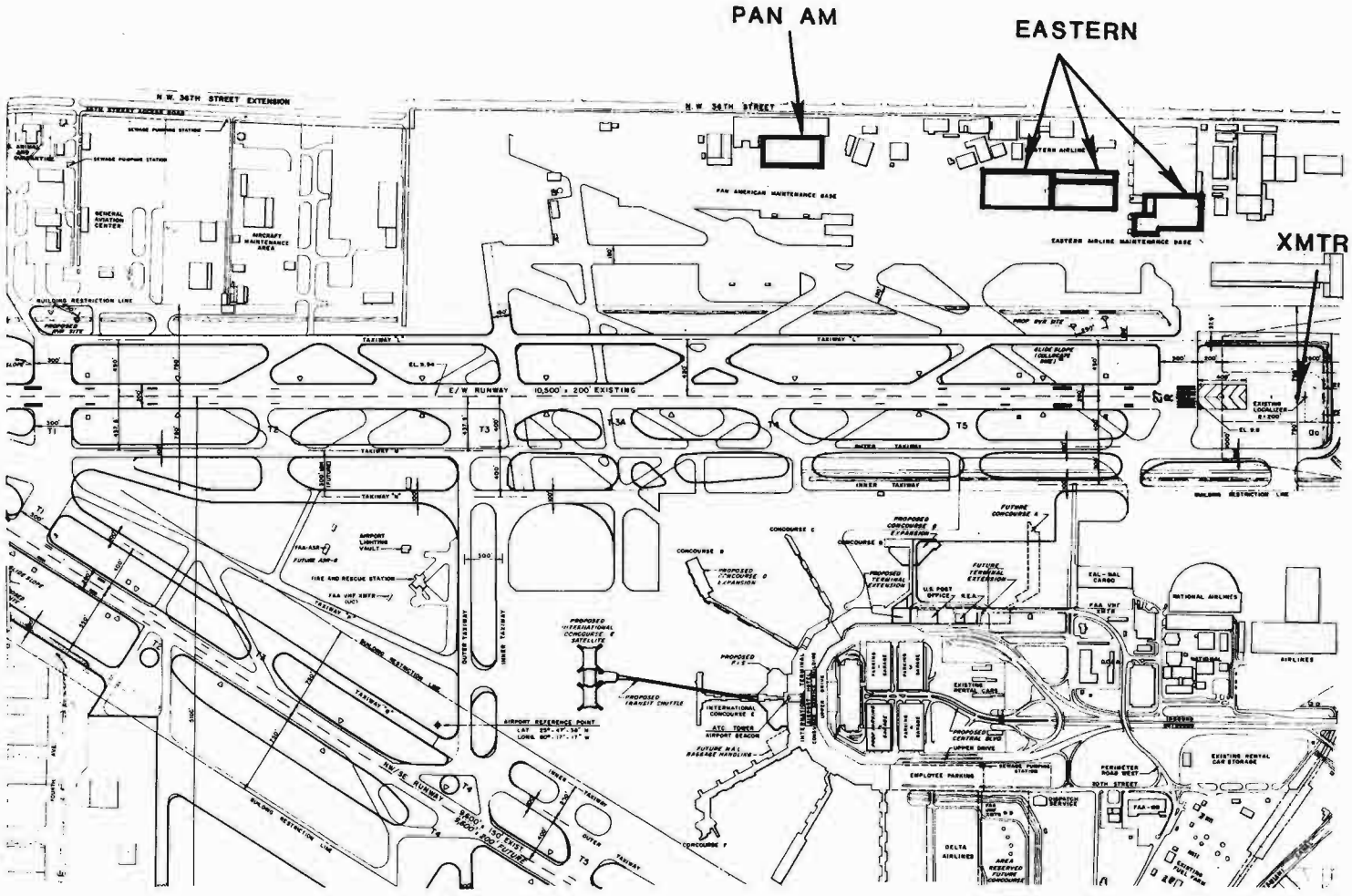

Fig. 3-81. Map of Miami International Airport.

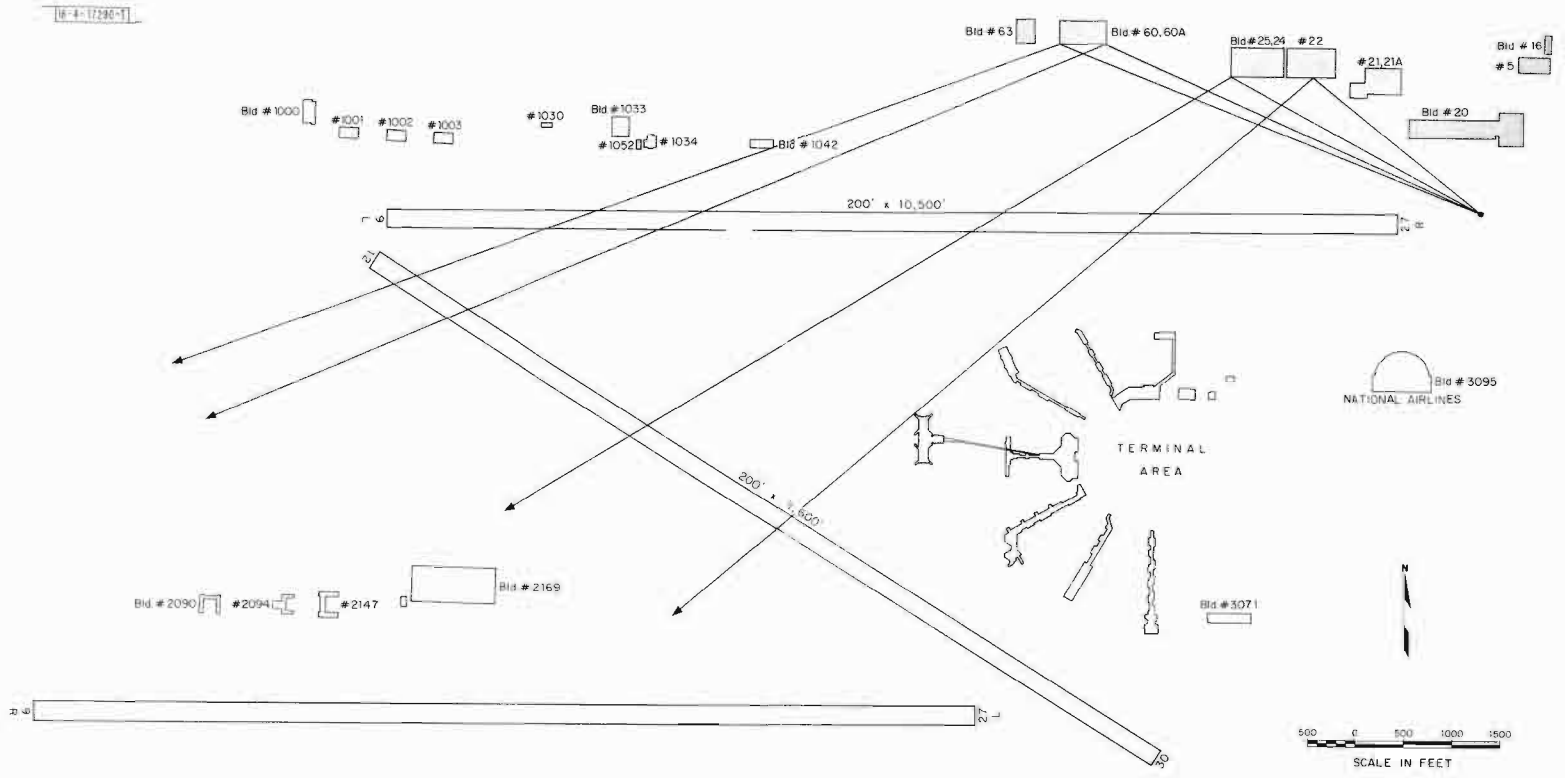

Fig. 3-82. Miami International Airport.

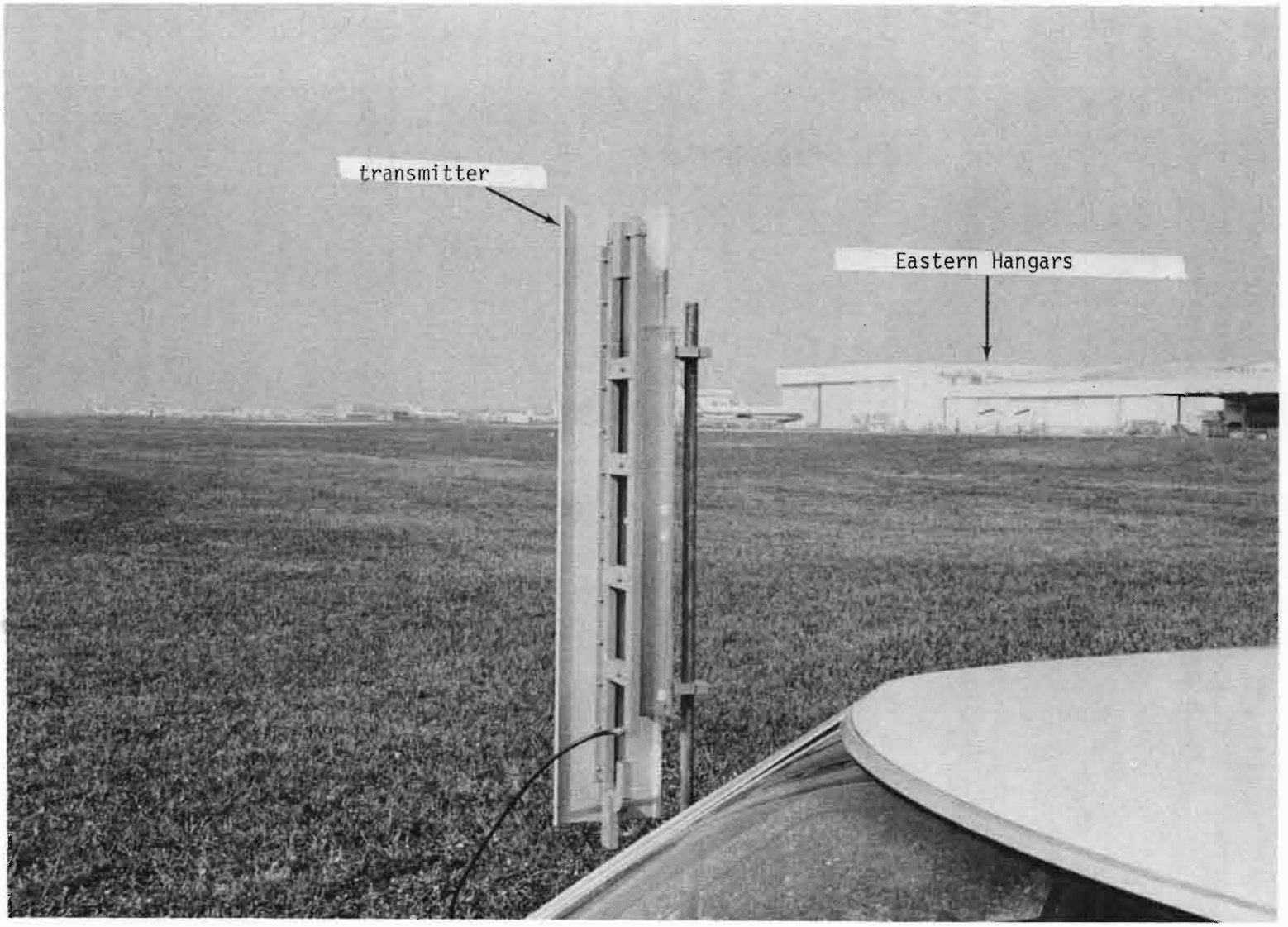

Fig. 3-83(a). View of Miami buildings from transmitter site.

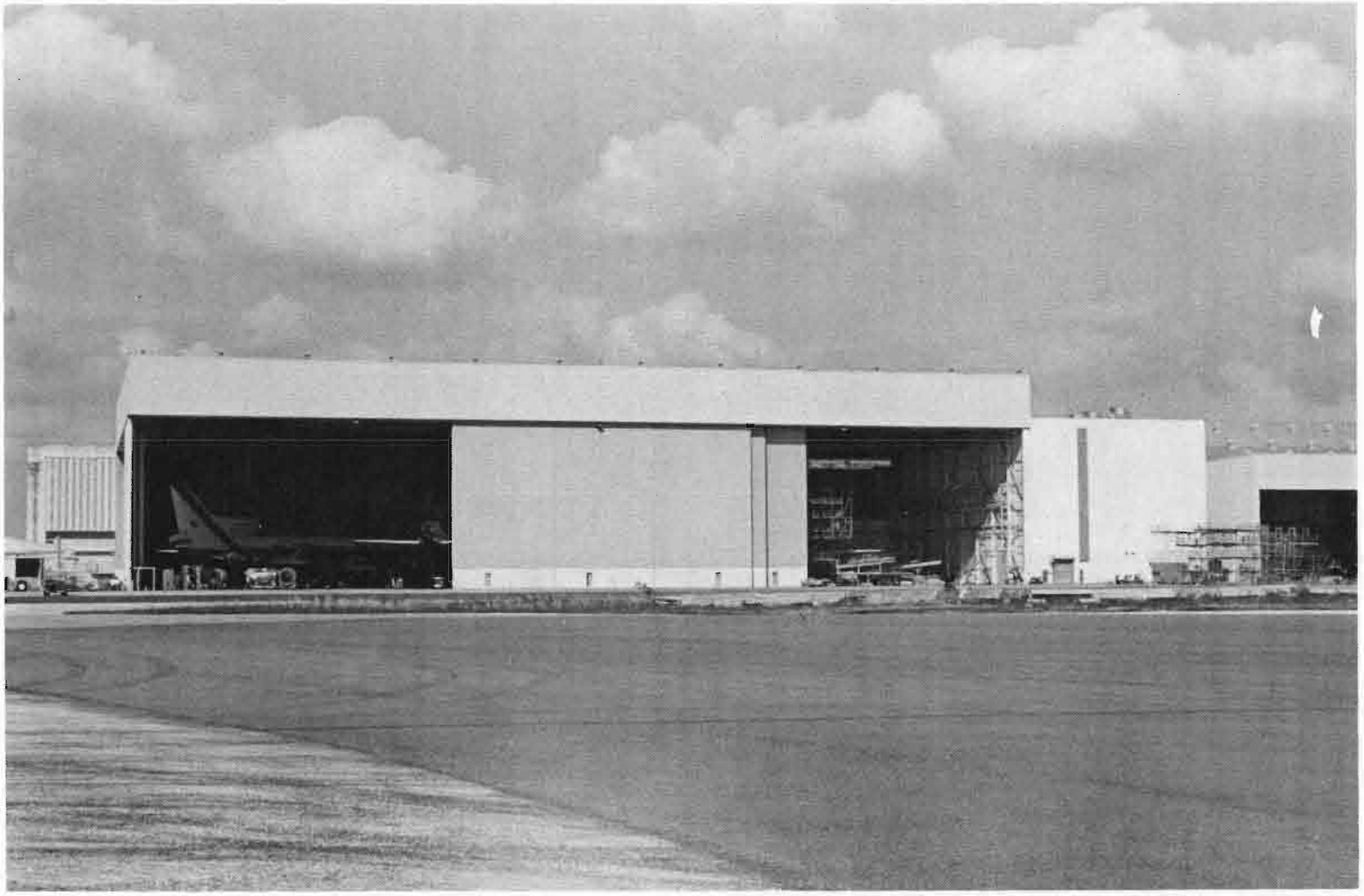

Fig. 3-83(b). Closeup of large Eastern Airlines hangar.

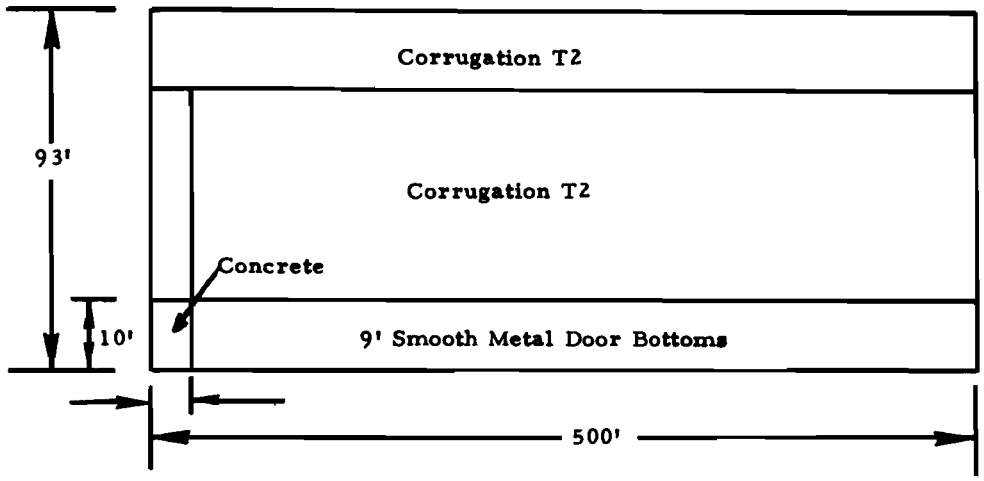

MIA, BUILDING 22 (Eastern hangar)

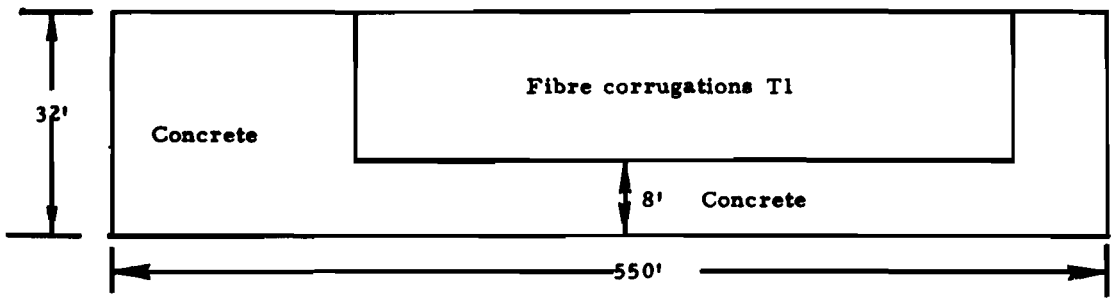

MIA, Building 21A (Eastern hangar)

Fig.3-84(a). Miami building details.

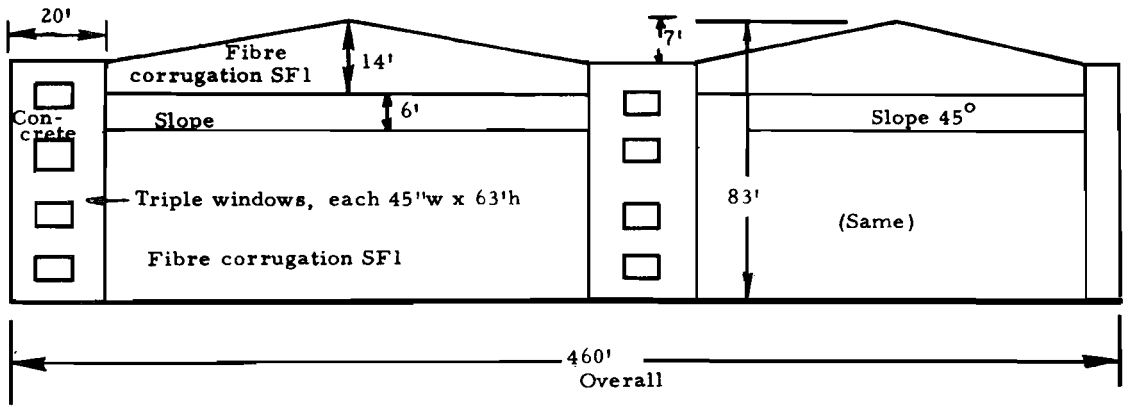

MIA, HANGAR BUILDINGS 60-60A (PAN AM HANGAR)

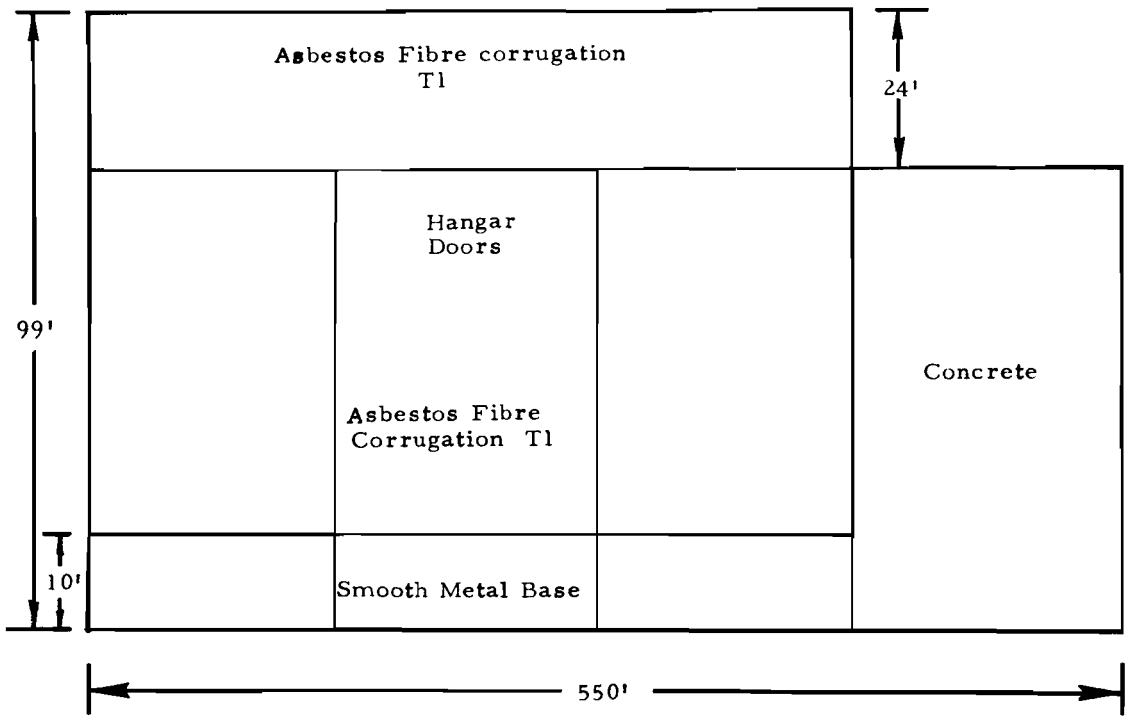

MIA, BUILDING 25-24 (PAN AM HANGAR)

Fig.3-84(b). Miami building details.

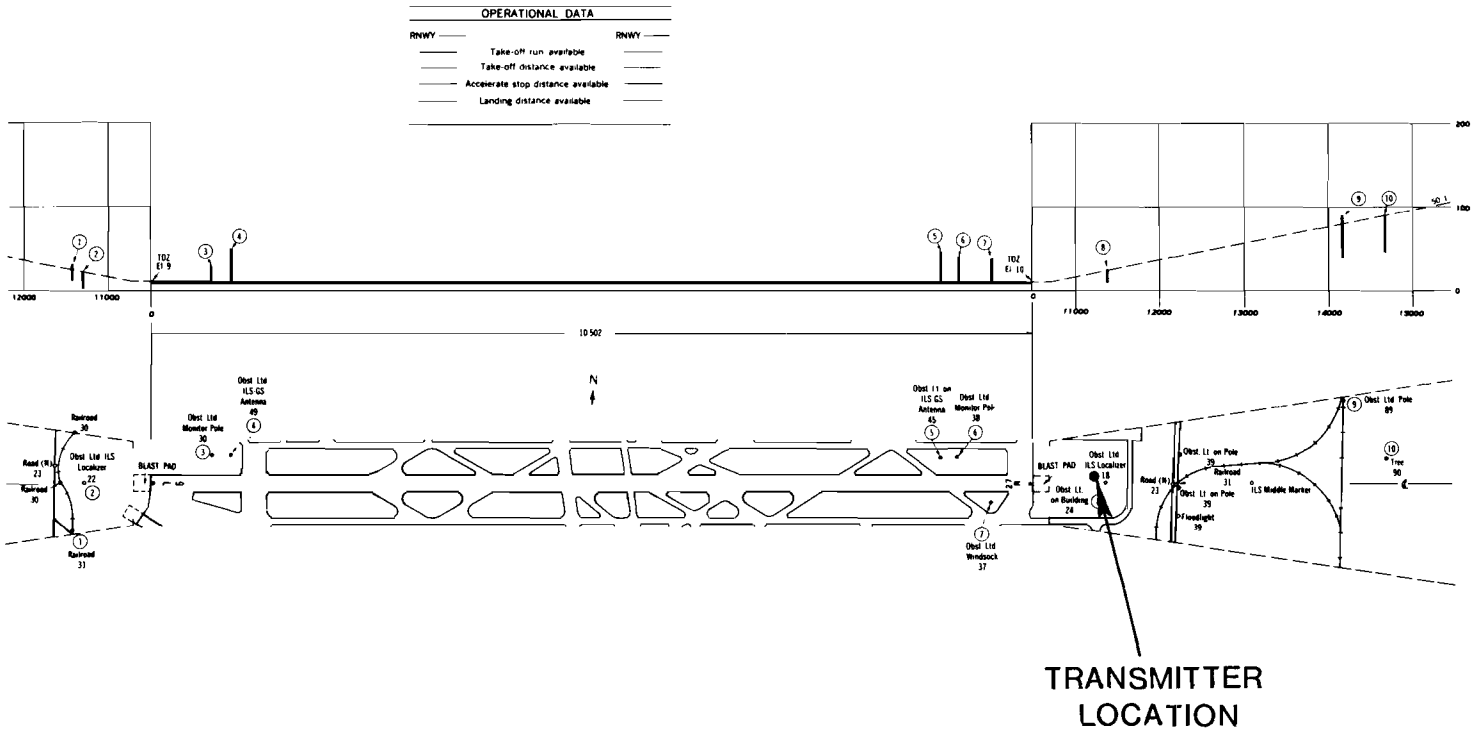

Fig. 3-85. Miami runway 9L-27R contour.

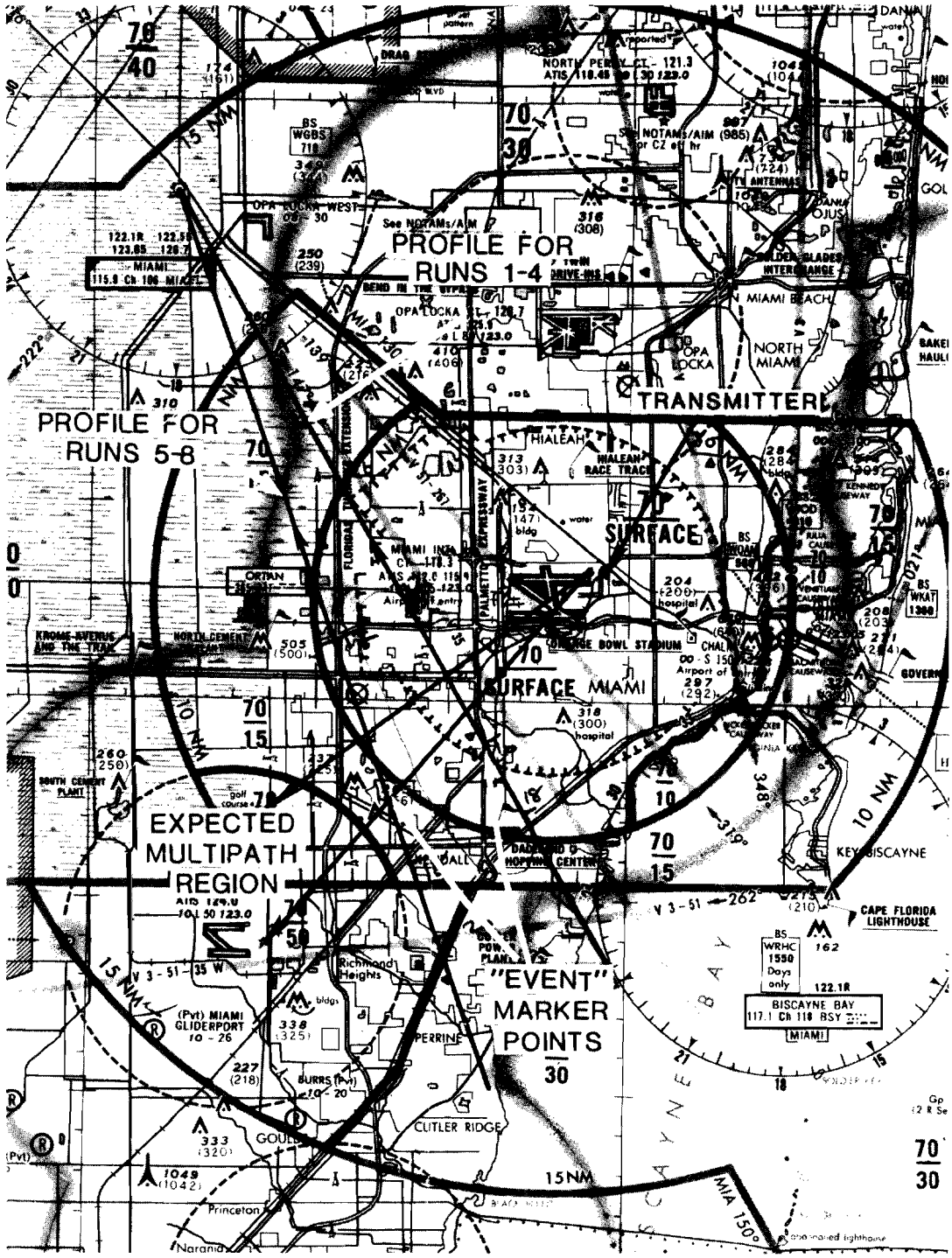

Fig. 3-86. Flight profiles and expected multipath regions for Miami measurements.

6 nmi) as well as noticeable propeller modulation effects. Fig. 3-87 shows typical spectra in regions of low multipath while Figs. 3-88 and 3-89 show spectra during a region of very high level multipath at a scalloping rate of 75 Hz. The multipath signal frequency here is greater than the direct signal frequency because the image transmitter is closer in heading to the velocity vector that is the actual transmitter [i.e., $\beta_m < \beta_d$ in eq. (3-1)].

Figures 3-90 and 3-91 show a sequence of spectra in the multipath region for the Eastern Airlines hangar. The vertical scale on the spectrum is 0 dB to -30 dB for the upper portion of each figure and 0 dB to -60 dB for the lower portion of the figure. In some cases, every other digital sample was used in the spectrum analysis so as to achieve better resolution for a fixed length transform. This results in the signals being aliased down in frequency and the relative positions interchanged (i.e., the apparent multipath is now below the apparent direct signal frequency). Figure 3-92 summarizes the multipath level results for the three runs as a function of time after the event marker.

d. Summary

The multipath measurement data reduced to date from Miami agrees reasonably well with the theoretical expectations in scalloping frequency, phase stability, and multipath region extent. Analysis of low level multipath was complicated by propeller modulation effects; however, there were regions of very high level multipath for time periods exceeding one second. Consequently, this runway appears to be a good candidate for a test of MLS capability to cope with high level out of beam multipath in the off centerline region.

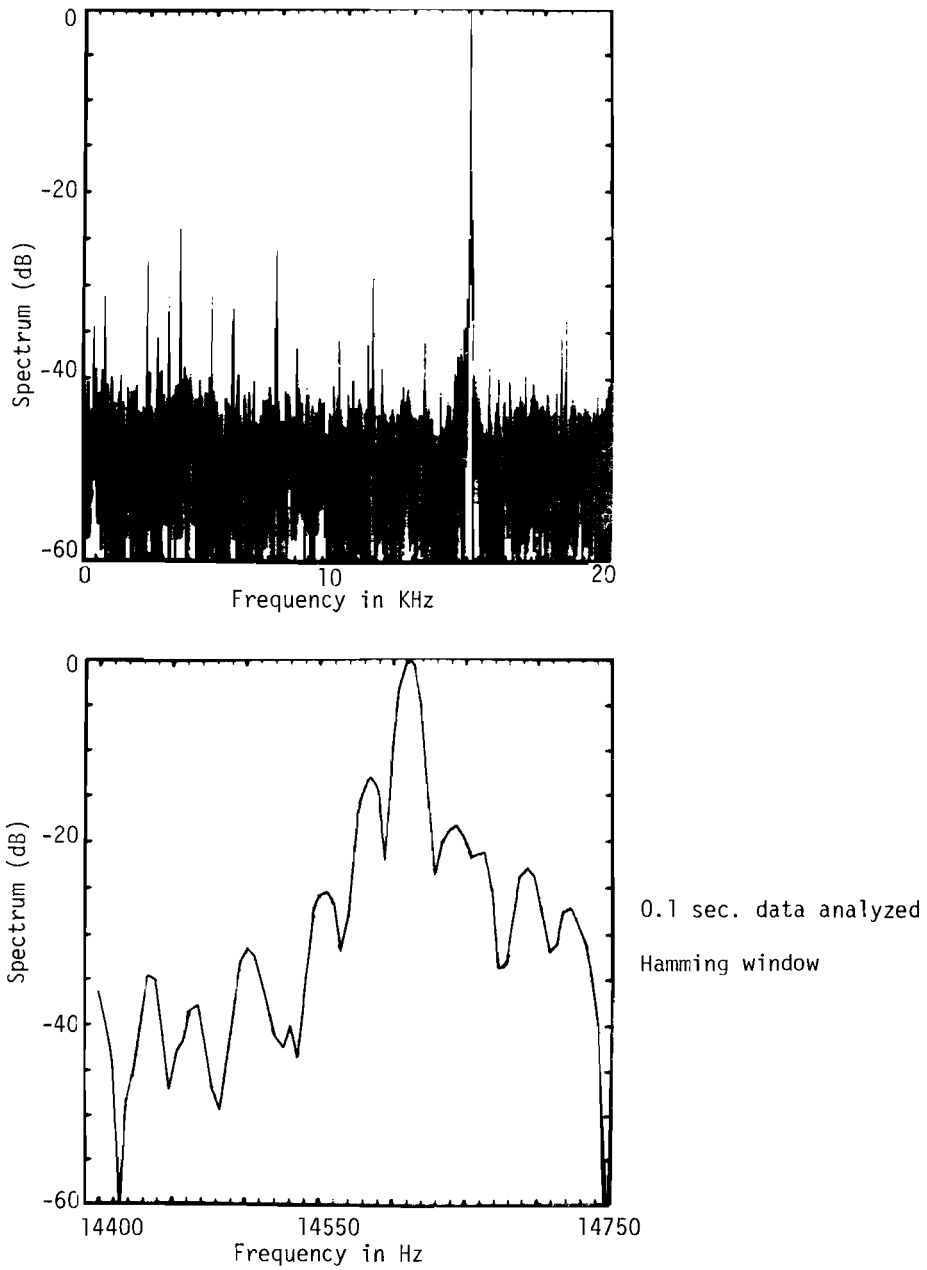

Fig. 3-87. Miami demodulated signal spectrum in low multipath region of run #7.

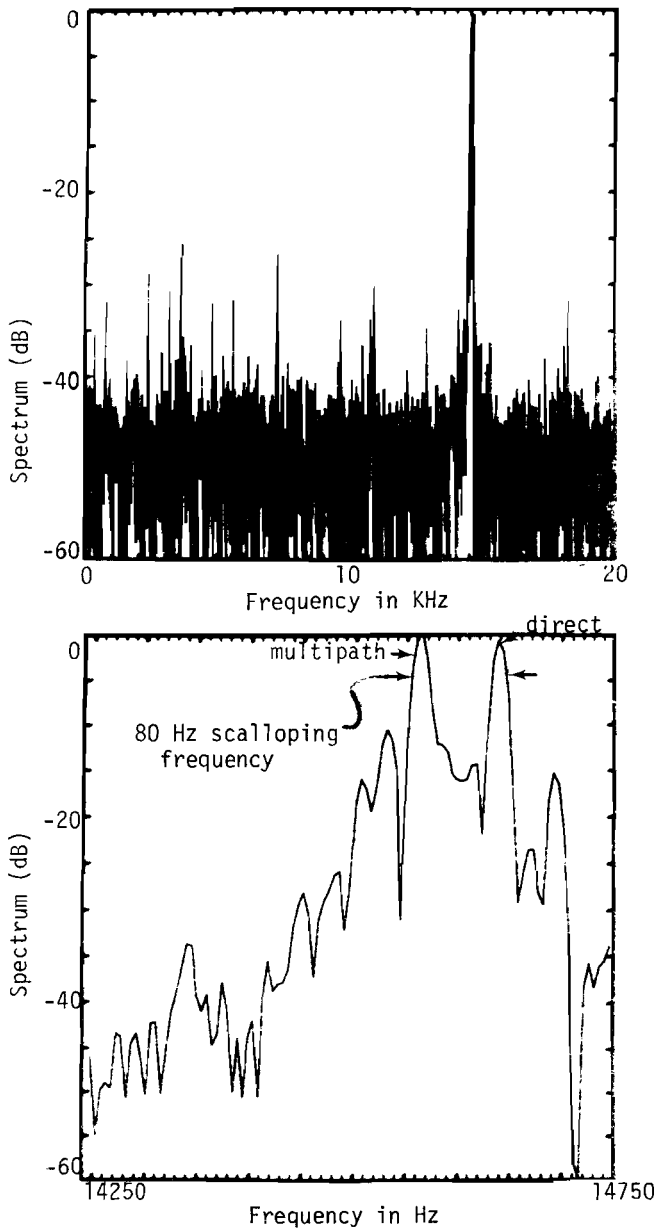

Fig. 3-88. Miami demodulated signal spectrum in high multipath region.

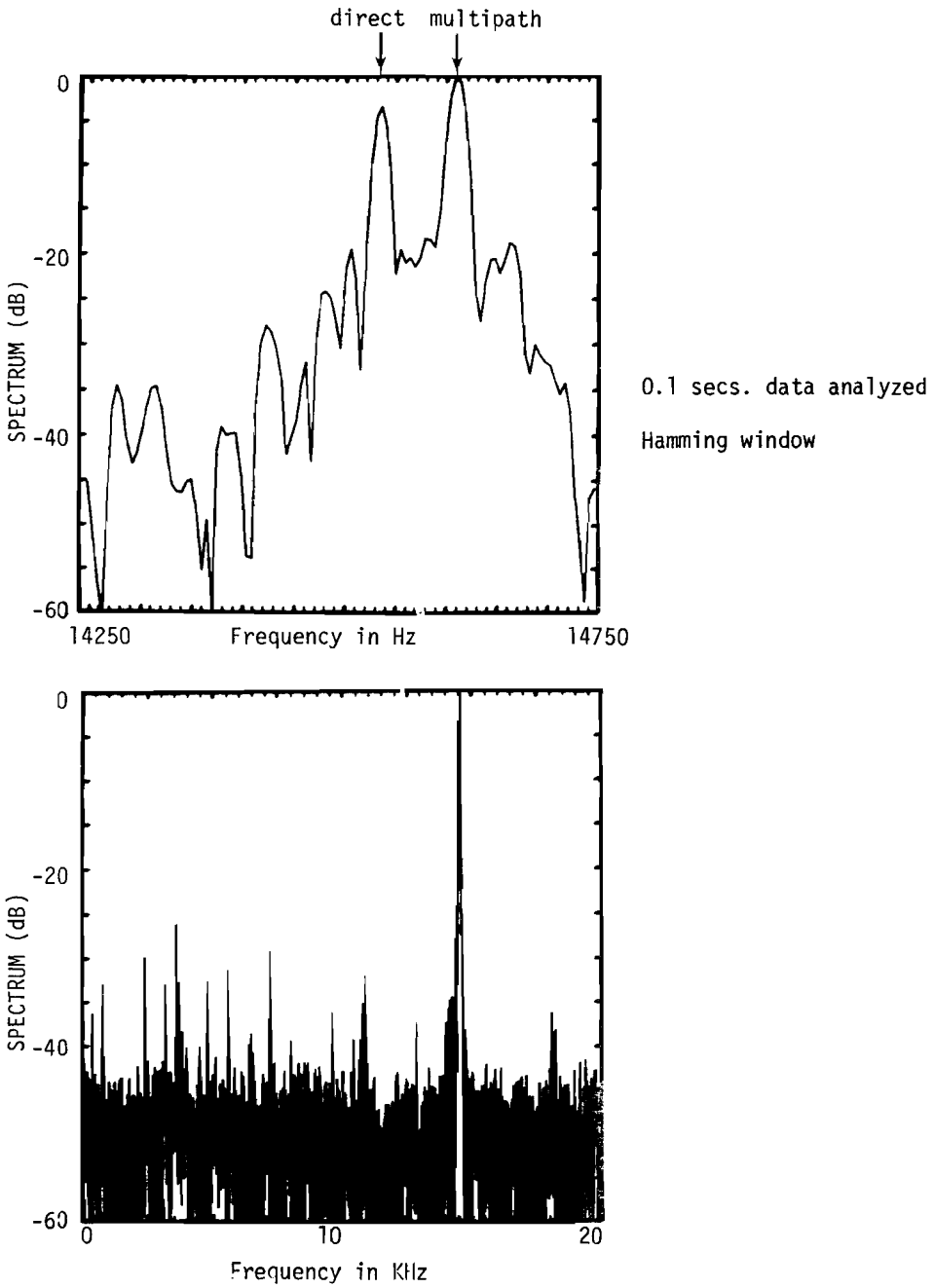

Fig. 3-89(a). Miami demodulated signal spectrum in high level multipath region on run #7.

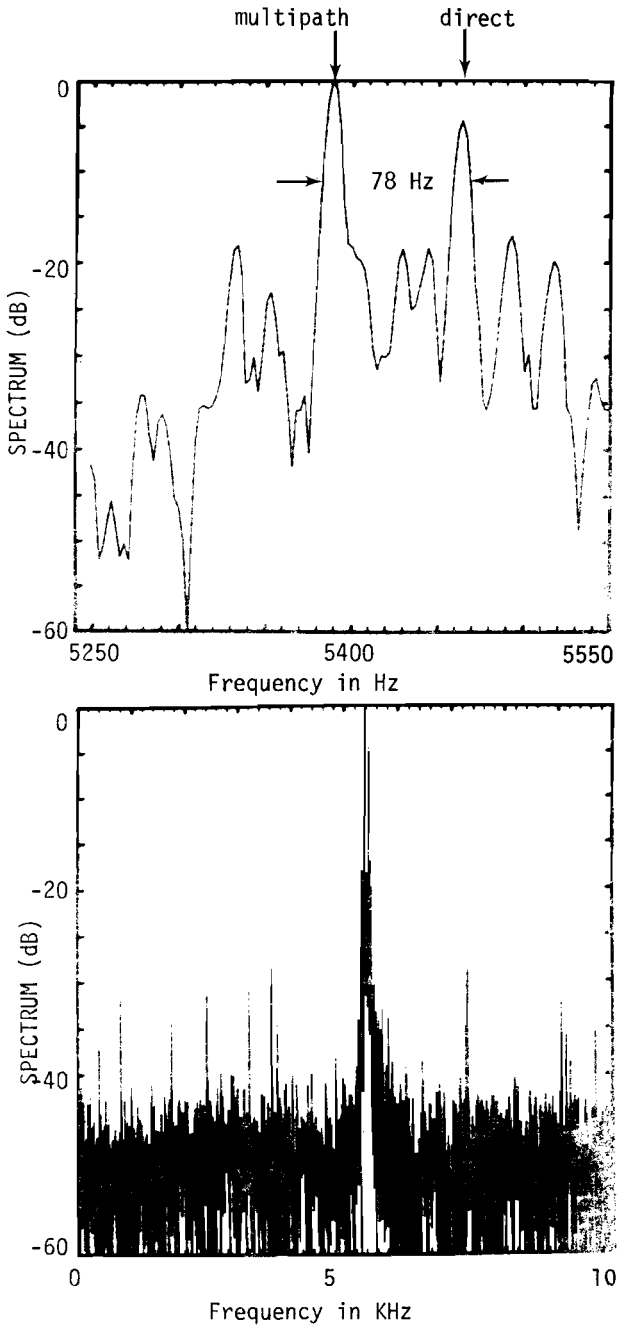

0.2 secs. data analyzed

Hamming window

data undersampled such that direct signal frequency now appears above multipath signal frequency

time region approximately same as in 3-89a

Fig. 89(b). Miami demodulated signal spectrum in high level multipath region on run #5.

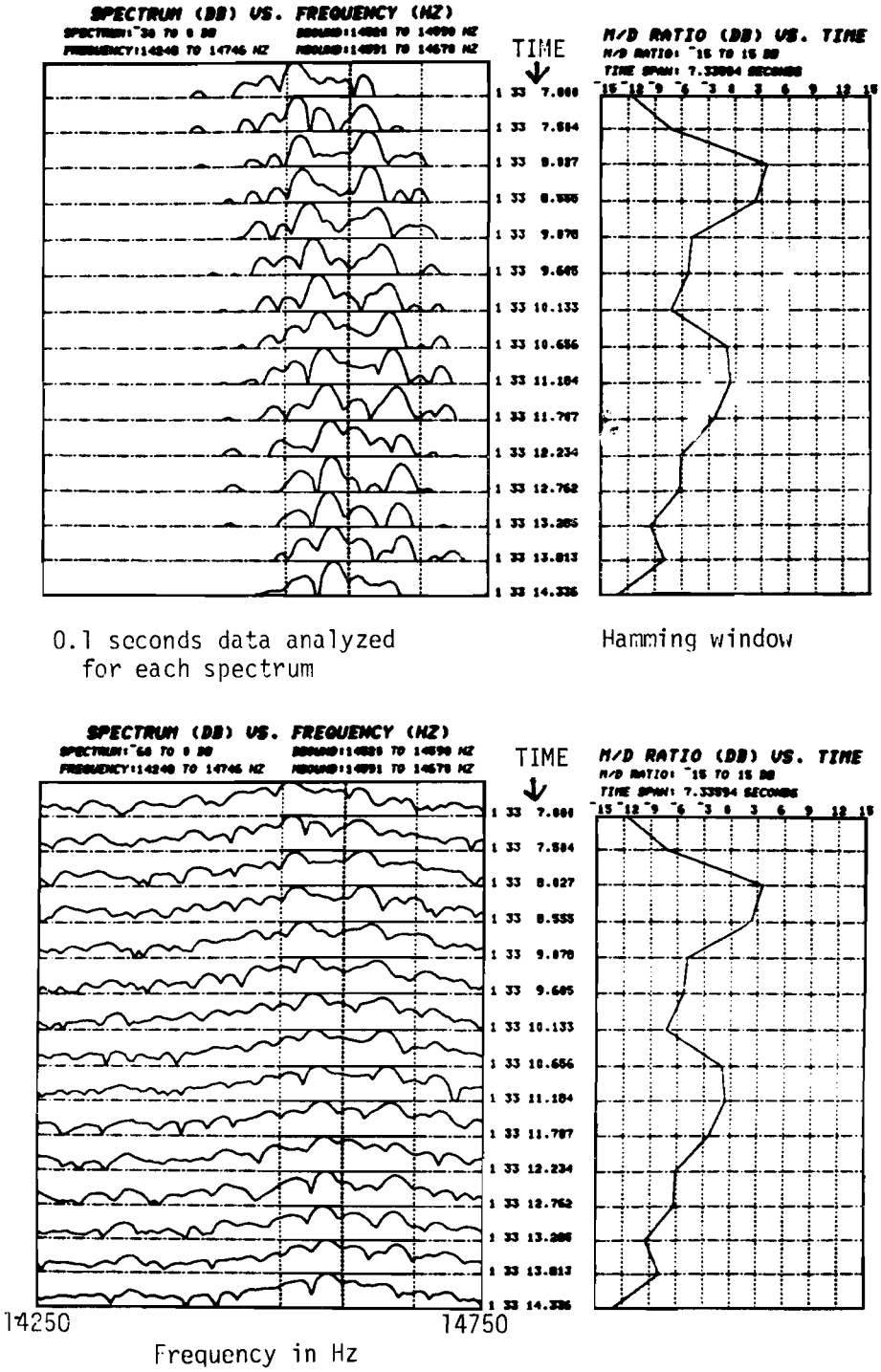

Fig. 3-90(a). Sequence of demodulated signal spectra for Miami run #5.

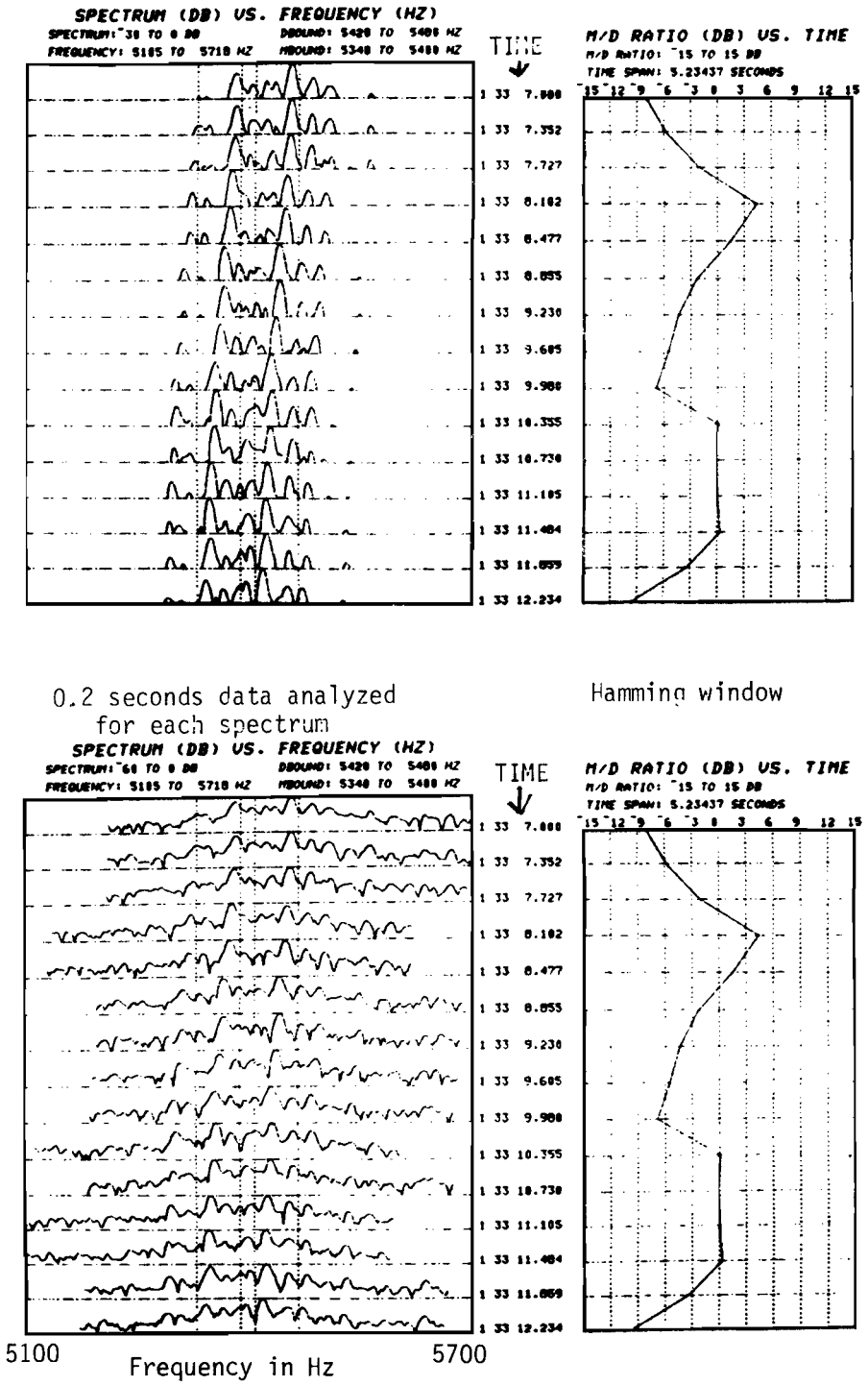

data undersampled such that direct signal frequency appears above multipath signal frequency.

Fig. 3-90(b). Sequence of demodulated spectra for Miami run #5.

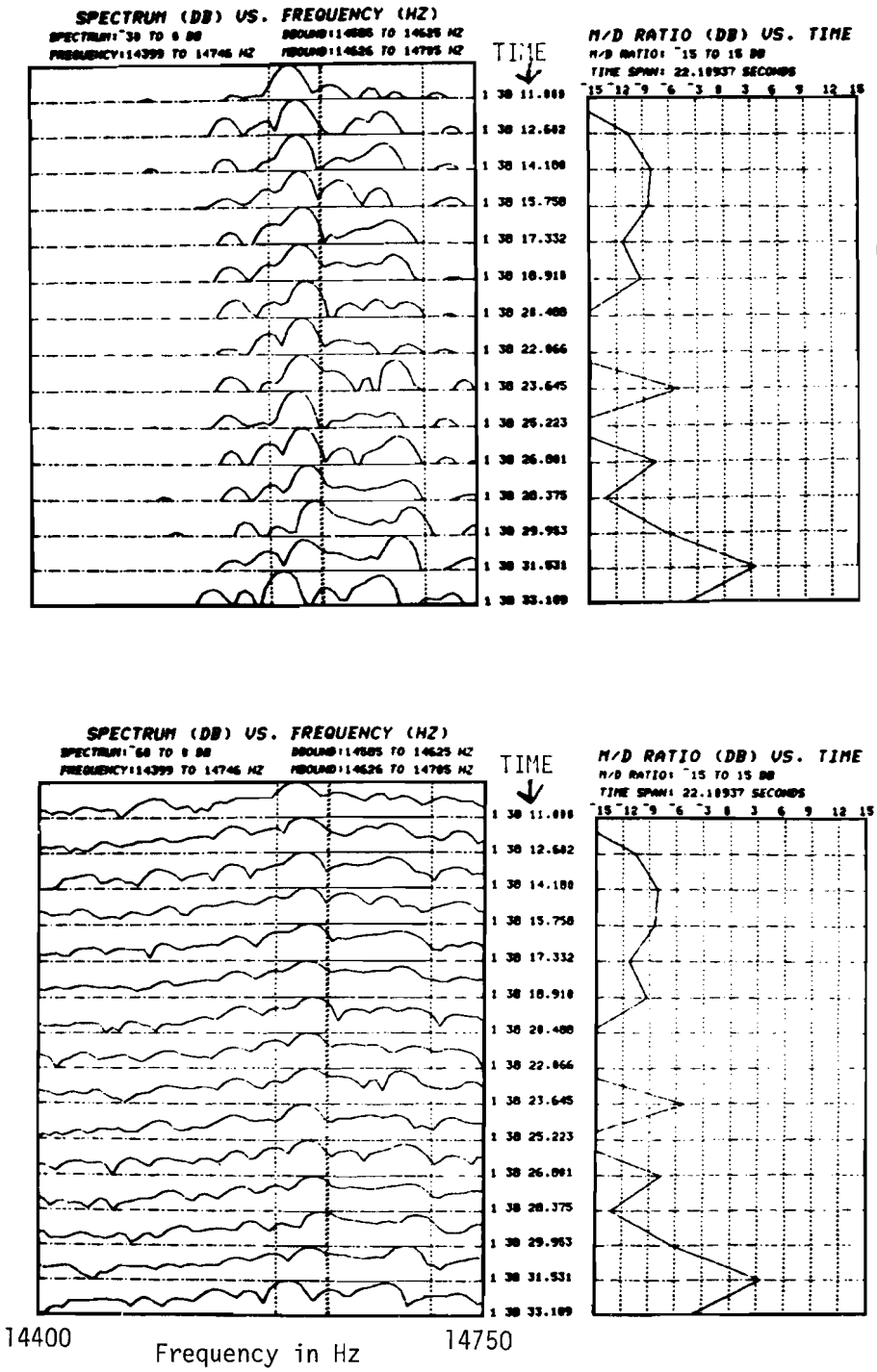

Fig. 3-91. Sequence of demodulated signal spectra for Miami run #7.

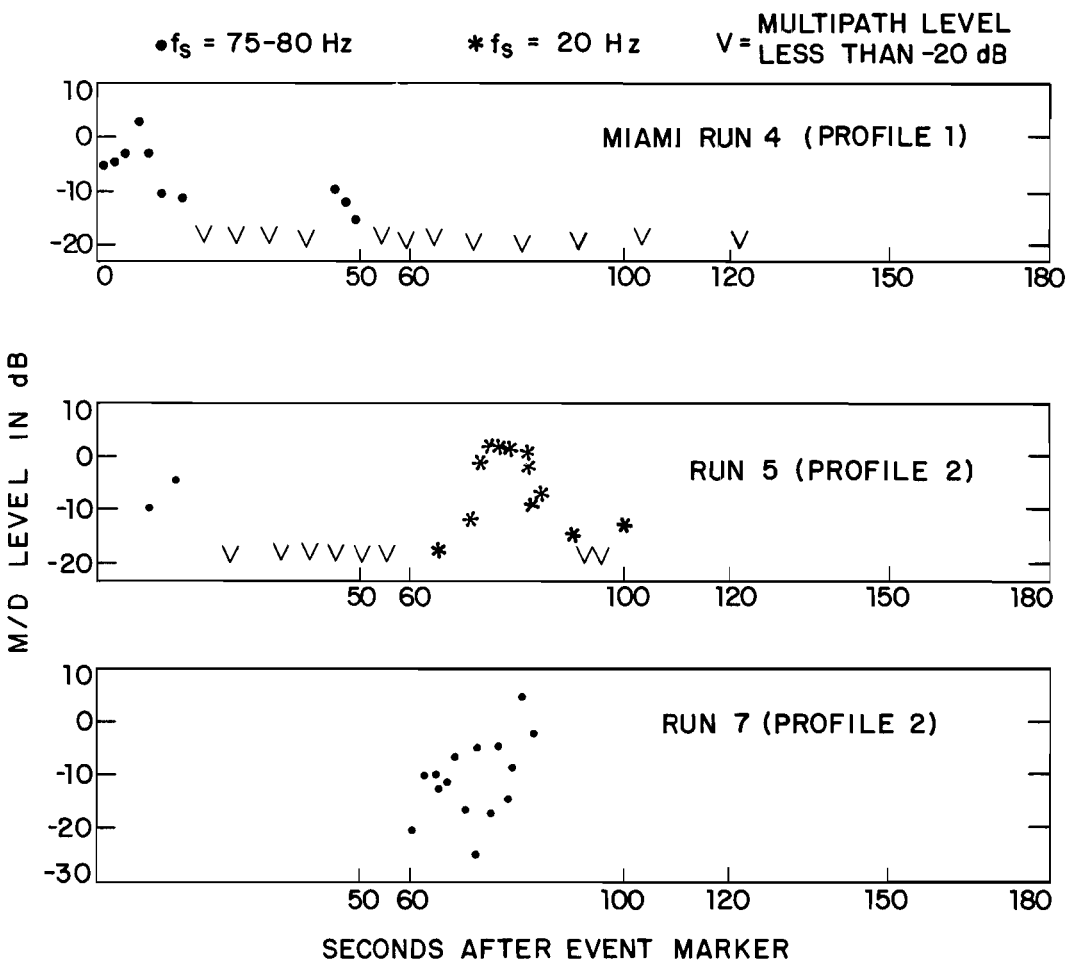

Fig. 3-92. Spectrum analysis results for Miami measurements.

8. Summary

This section has reported the preliminary results of an MLS azimuth multipath measurement program at four operational U.S. airports (St. Louis, Tulsa, Miami and Wright Patterson Air Force Base). The objectives of the measurement program were to:

1. confirm that azimuth multipath at major operational airports has the amplitude levels, scalloping frequencies, and phase coherence assumed in the computer simulations and analytical studies to date
2. provide data for choosing stressful MLS azimuth multipath test sites

and 3. obtain additional data for validation of the Lincoln MLS propagation model

The measurement technique of radiating a CW signal through a wide coverage antenna and performing spectral analysis on the (coherently demodulated) received signal to determine the mutlipath signal characteristics worked well.

Multipath signal levels as high or higher than that of the direct signal were observed at three of the four airports. The measured levels can be summarized as follows:

AIRPORT	PEAK MULTIPATH LEVELS (dB RELATIVE TO DIRECT)	SCALLOPING FREQUENCIES* (IN HZ)	MULTIPATH DURATION+ (SECS)	LOCATION
St. Louis International	-9	700	2	threshold
	-9	800	5	flare
Tulsa International	+3 to +8	50	7	threshold
	+1	800	0.3 to 1.0	flare
Wright-Patterson Air Force Base	0	400	2	flare
	-1	270	1	threshold
Miami International	+3	75	4	orbital flights at 6 nmi

+period that multipath remained within 6 dB of its peak level.

*at approximately 120 knots on final approach and 150 knots on orbital flights.

The principal focus in this section has been on further validating the salient features of the azimuth multipath in the AWOP comparative MLS multipath simulation studies [9, 28, 29, 64]:

1. high multipath levels over regions predicted by ray optics considerations
2. scalloping frequencies determined by the geometry of the transmitter, scatterer and flight profile
3. a high degree of stability (i.e., phase coherence) in the scalloping frequency over time periods corresponding to MLS azimuth measurement periods (30 msec for DMLS, 200 msec for DLS and TRSB).

All three of these features were confirmed by the results analyzed to date. The scalloping frequencies and regions of high multipath levels observed were shown to correspond to the expected regions. The widths of the spectral peaks were generally consistent with reflection phase stability over periods as long as 200 msec, and certainly consistent with reflection phase stability over periods of 30 msec.

C. Comparison of Simulation with Azimuth Multipath Field Data from Inhomogeneous Building Surfaces

1. Introduction

Many of the large buildings which border airport runways are aircraft hangars with sliding doors which are staggered so that they can be all pushed to the side of the doorway. Quite commonly these are oriented so that the hangar doors provide reflection multipath when on final approach. Thus, the nature of the scattered signal from such surfaces is a practically important issue, particularly for MLS techniques which are sensitive to coherent out of beam azimuth multipath. The preceding section presented the results of some of our field measurements to address this issue. In this section, we compare field measurements from the Sydney (Australia) International airport and WPAFB, Ohio with computer simulation results to see if the complex spatial variation of the multipath can be "explained" by the computer models.

Two aspects of the modeling process warrant special comment. The modeling of the hangar doors was accomplished by associating a reflecting plate with each individual door with the door orientation determined from airport maps, aerial photographs and on site measurement of the door staggering.* Doors of a single homogeneous surface material (e.g., flat metal) were represented by the appropriate dielectric constant. Doors with several surface materials (e.g., metal plates and glass windows) were treated as a homogeneous material with Fresnel reflection coefficient

$$\rho_{eff} \approx \sum f_i \rho_i \qquad (3\text{-}12)$$

where

f_i = fraction of door area represented by the ith material

ρ_i = Fresnel reflection coefficient for the ith material at the given angle of incidence.

*The actual on site measurements were by the Australian Department of Transportation and US Department of Defense personnel respectively.

The implicit assumption made in obtaining (3-12) was that the Fresnel zone radius was typically as large as the door itself.

In this connection, it should be noted that glass can be a significant reflector at microwave frequencies since its dielectric constant at microwave frequencies is not necessarily near unity. Figure 3-93 shows the results of theoretical and experimental measurements at L band by Cossor [76]. It can be shown (see[77] or any elementary wave propogation text book) that the reflection coefficient for a dielectric sheet is given by

$$\rho = \frac{j(\sqrt{\varepsilon'} - \frac{1}{\sqrt{\varepsilon'}}) \tan T}{2 + j\,(\sqrt{\varepsilon'} + \frac{1}{\sqrt{\varepsilon'}}) \tan T} \qquad (3\text{-}13)$$

where

$$\varepsilon' = \frac{\varepsilon - \sin^2 \theta_i}{\cos^2 \theta_i} \qquad (3\text{-}14)$$

$$T = \frac{2\pi d}{\lambda} \sqrt{\varepsilon' - \sin^2 \theta} \qquad (3\text{-}15)$$

ε = dielectric constant

d = glass thickness

Values for ε are typically in the range of 1.2 to 6.0 [77].

A second factor of considerable importance in azimuth multipath modeling is the effect of ground reflections from terrain on and off the runway as illustrated in figure 3-94. In practical modeling, two problems were encountered:

(a) data was not generally available on the off runway terrain profile at the time the studies were made

and

(b) the current building reflection model can only consider

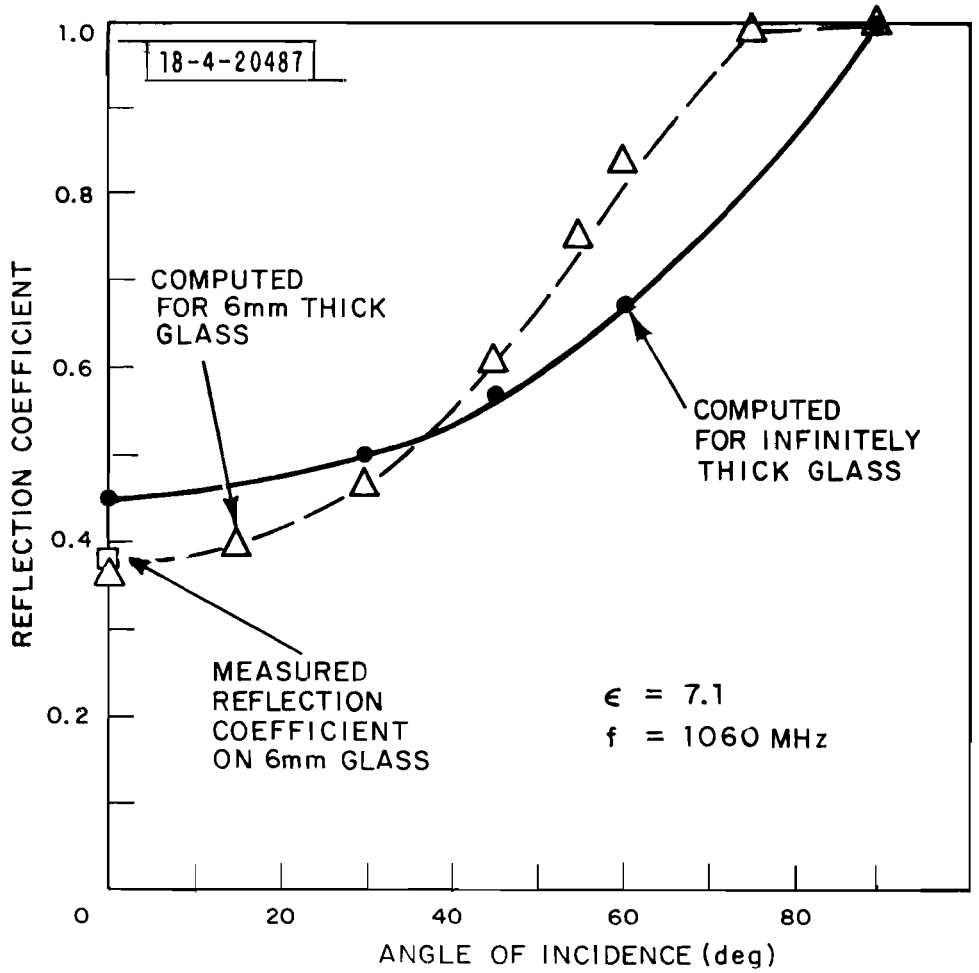

Fig. 3-93. Computed and measured reflection coefficient of glass at L band.

bg, cg involve ground reflection from terrain to the
side of the runway

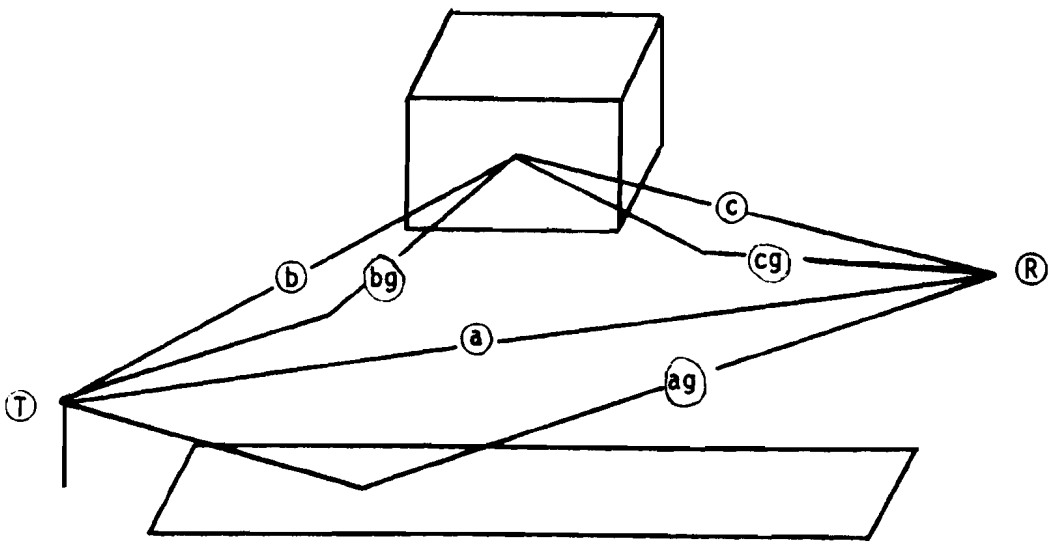

Measured "DIRECT" signal level depends on phase coherent sum of paths a and ag

Measured "MULTIPATH" signal level depends on phase coherent sum of paths
b, bg, c, cg

Fig. 3-94. Role of ground reflection paths in determining multipath/direct amplitude ratio.

the case of "multiple bounce" ground reflections over flat homogeneous terrain*

Since the principal effect of these various ground reflection paths is to change the M/D ratios, but not:

1. the scalloping frequency
2. rapid spatial variation in M/D level along the runway

or 3. the multipath azimuth angle

it was decided in most cases to utilize a flat earth model so that terrain would effect the computed direct and multipath returns in a similar fashion. The hope was that this would give M/D ratios which agree reasonably well with the field data.

2. Sydney International Airport

Runway 07L at Sydney airport (Australia) represents an airport geometry yielding azimuth multipath in the flare guidance region. Detailed airport data and field measurements were accomplished at Sydney by the Australian Dept. of Transport and the results made available to Lincoln.

The most striking differences between the Sydney field data and the multipath in the ICAO AWOP comparative scenarios [66] was the rapid fluctuations in the multipath level along the runway within the specular reflection region. A principal objective of the work reported here was to gain a better understanding of the impact of such spatial variation on system performance (especially for DMLS). As this spatial variation is believed to arise from the imhomogeneous character of the hangar fronts (staggered hangar doors), particular attention was paid to more accurately representing the building front features in the airport model. Also, the DMLS system model was refined to take into account better the effects of rapidly varying multipath. In this section of the report, we will discuss only the multipath spatial variation results. The DMLS study results will be presented in volume III of this report. However, we must emphasize that certain other airport features (e.g., off runway terrain contour) may not have been accurately represented in these simulations to permit the results to be extrapolated directly to an MLS flight test at Sydney.

*The height of this terrain can, however, be different from the height of the terrain along the runway centerline.

Section a discusses how the airport model was developed from the Australian building data. Section b presents the flight profiles utilized while Section c compares the computer simulation multipath level data with that obtained in field tests.

a. Airport Model

The locations of the building fronts were obtained from a cable map of Sydney airport (Figure 3-95) and an aerial photograph of the airport (Figure 3-96). The values obtained from these sources were cross checked against the Australian angle measurement data received in November 1977 (Figure 3-97) and are in fair agreement for the most part.*

The specific (x,y) plane coordinates assumed for the building edges were

building	x left	y left	x right	y right
1	6691	765	6881	676
2	6429	898	6687	778
3	6249	982	6429	989
83	6084	1061 (midpoint)	6230	990 (far end)

where the x axis coincides with the centerline of runway 07-25, and (0,0) is the threshold of rwy 07, the azimuth transmitter is at (-200,0) and the threshold of rwy 25 is (7903,0)

The hangar models used were based on Australian data (Figures 3-98 to 3-101). Also shown in these figures is various data related to the computer model for the given building:

(1.) the plate number assigned to a given door or wall in the simulation
(2.) the reflection coefficient (or dielectric constant) assumed for the plate (a conductivity of 0.1 mho/meter was assumed in all cases)
(3.) any additional dimensional assumptions made.

We were later informed that hangar #2 had one extra door with the last door being beside the eighth door. The revised building geometry is also shown in Fig. 3-99.**

*We were subsequently informed that the Australian value for the near edge of bldg. 1 (DOT) was in error.

**After the runs were completed, it was discovered that one of the doors (Plate B33) in hangar 83 was inadvertently misaligned in data entry. This results in a slight reduction in multipath level at one point along the flight path.

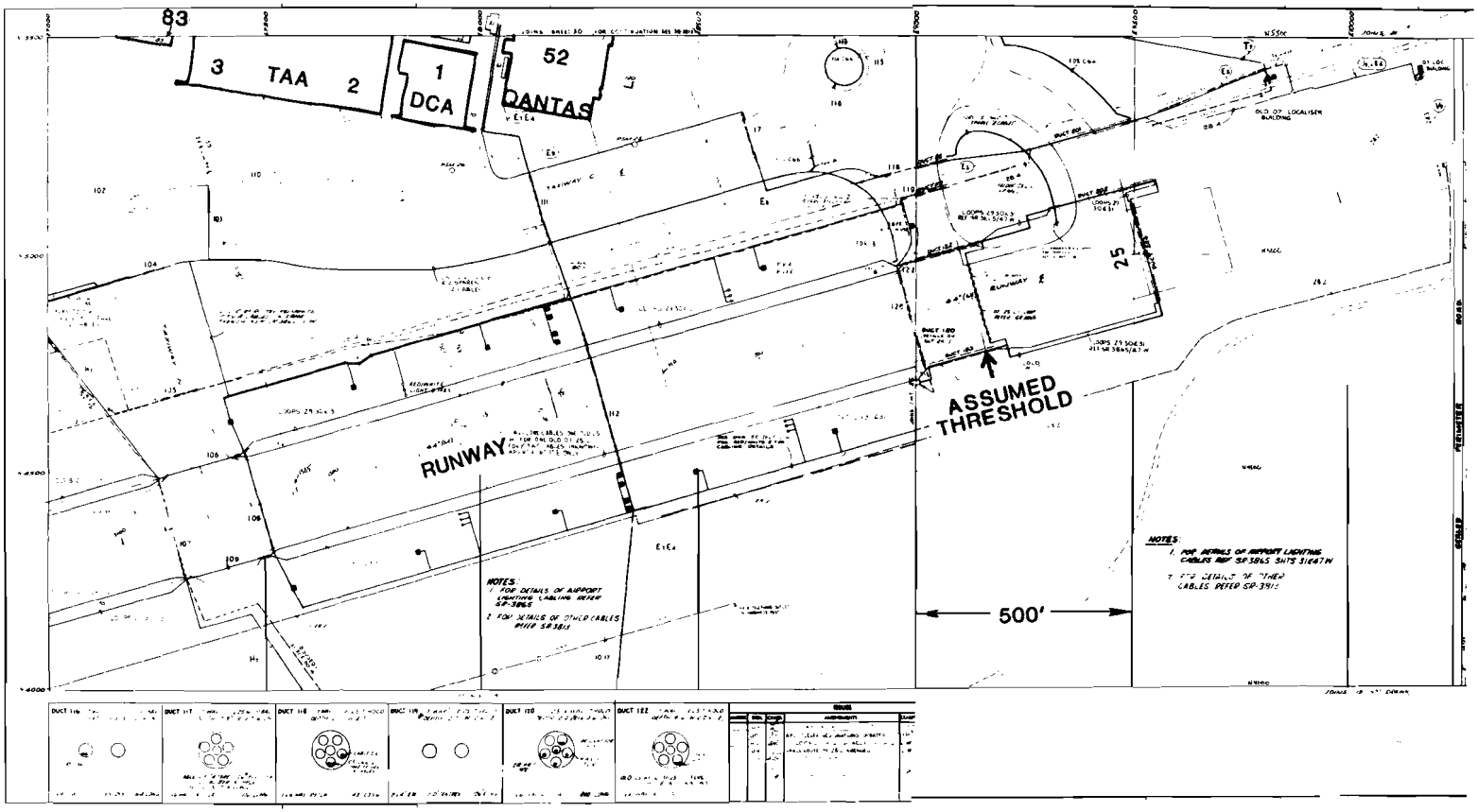

Fig. 3-95. Cable map of the end of runway 07-25 at Sydney Airport.

Fig. 3-96. Aerial photograph of Sydney Australia runway 07-25.

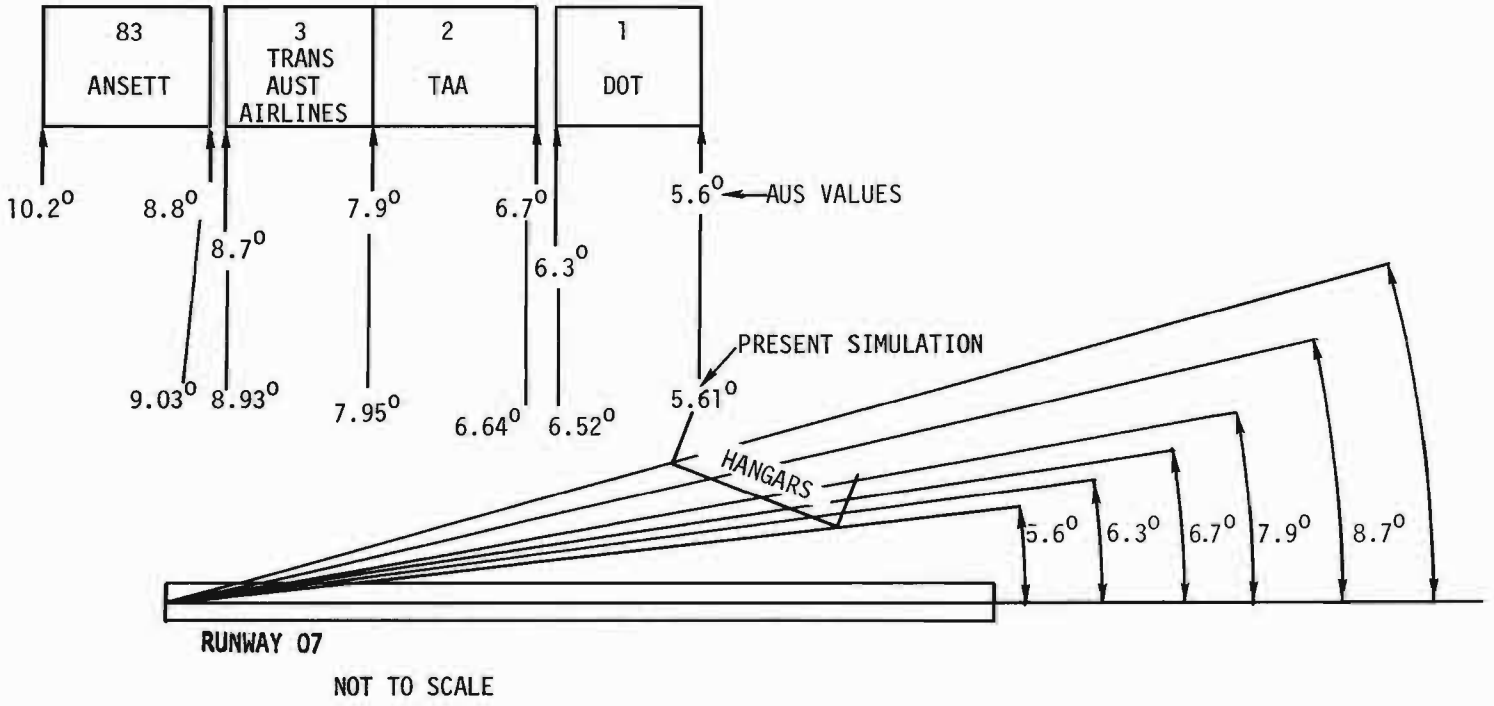

Fig. 3-97. Approx. angles subtended by hangars from survey point.

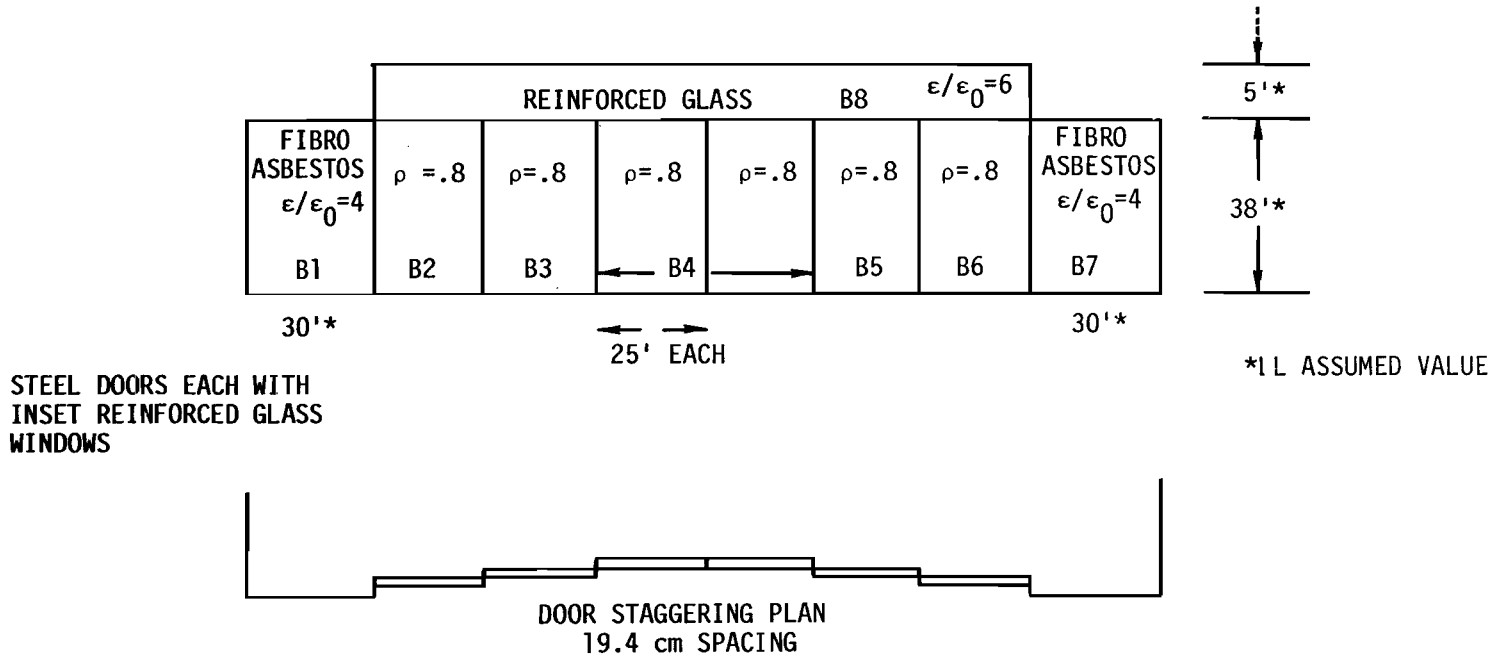

Fig. 3-98. DOT No. 1 hangar.

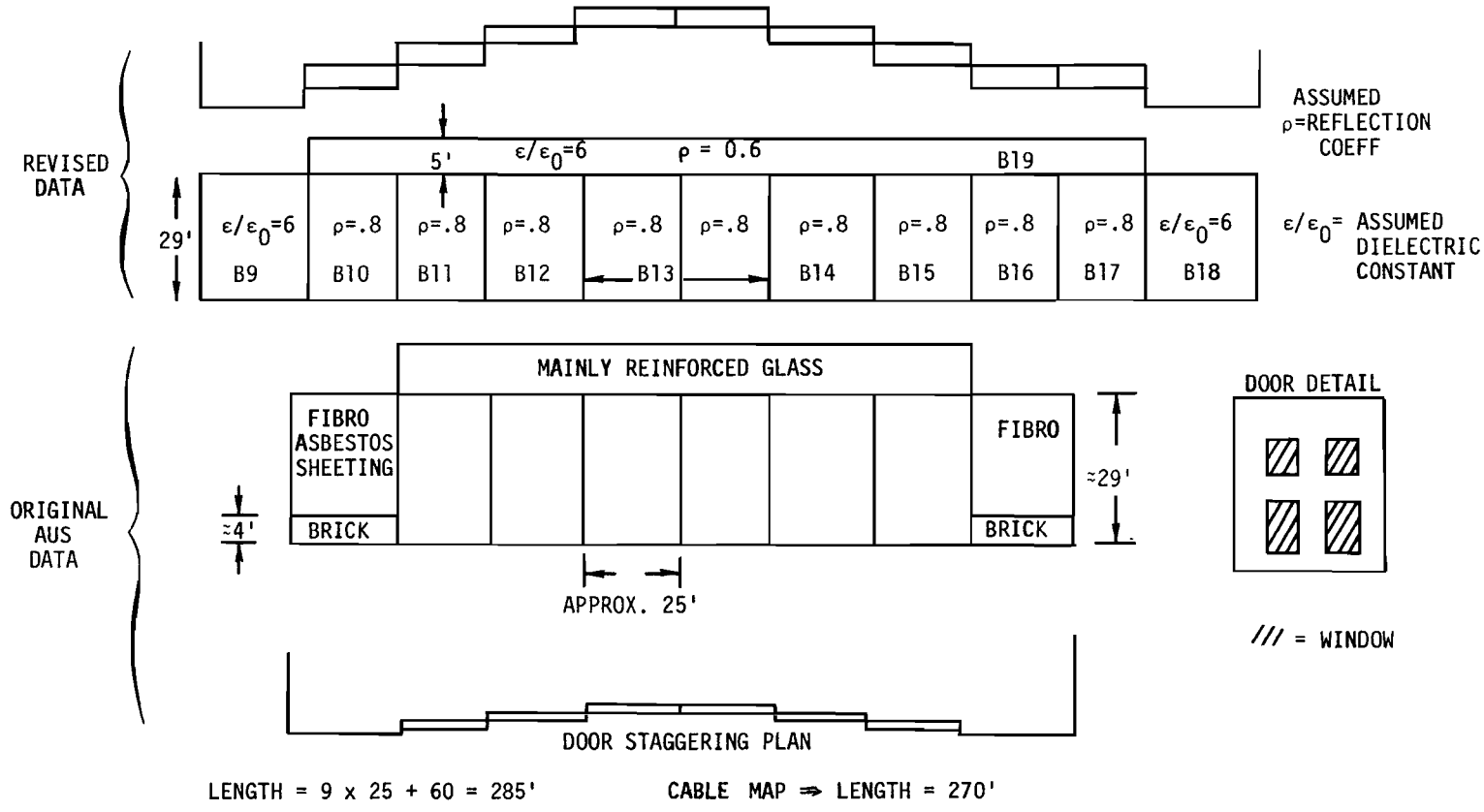

6 STEEL DOORS SMOOTH WITH REINFORCED GLASS INSET ≈1 cm p-p SURFACE ROUGHNESS
STAGGERED 20.4 cm RAIL TO RAIL

Fig. 3-99. TAA hangar No. 2.

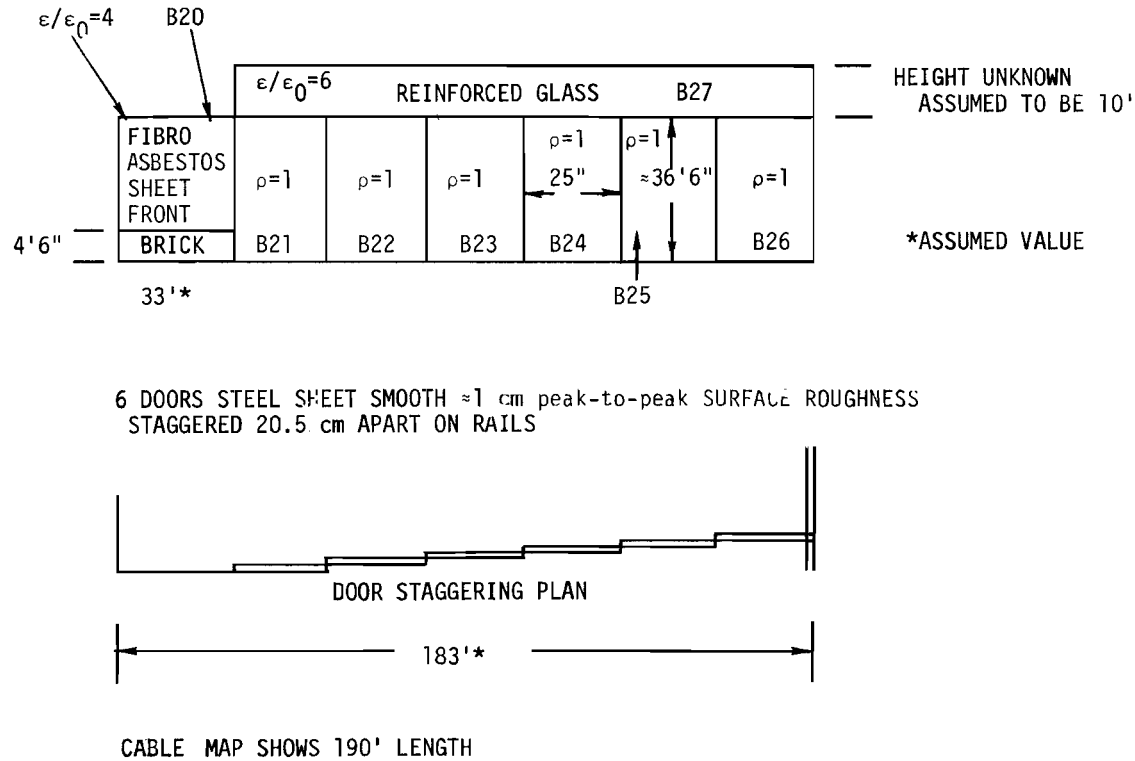

Fig. 3-100. Trans Australian Airlines Hangar #3.

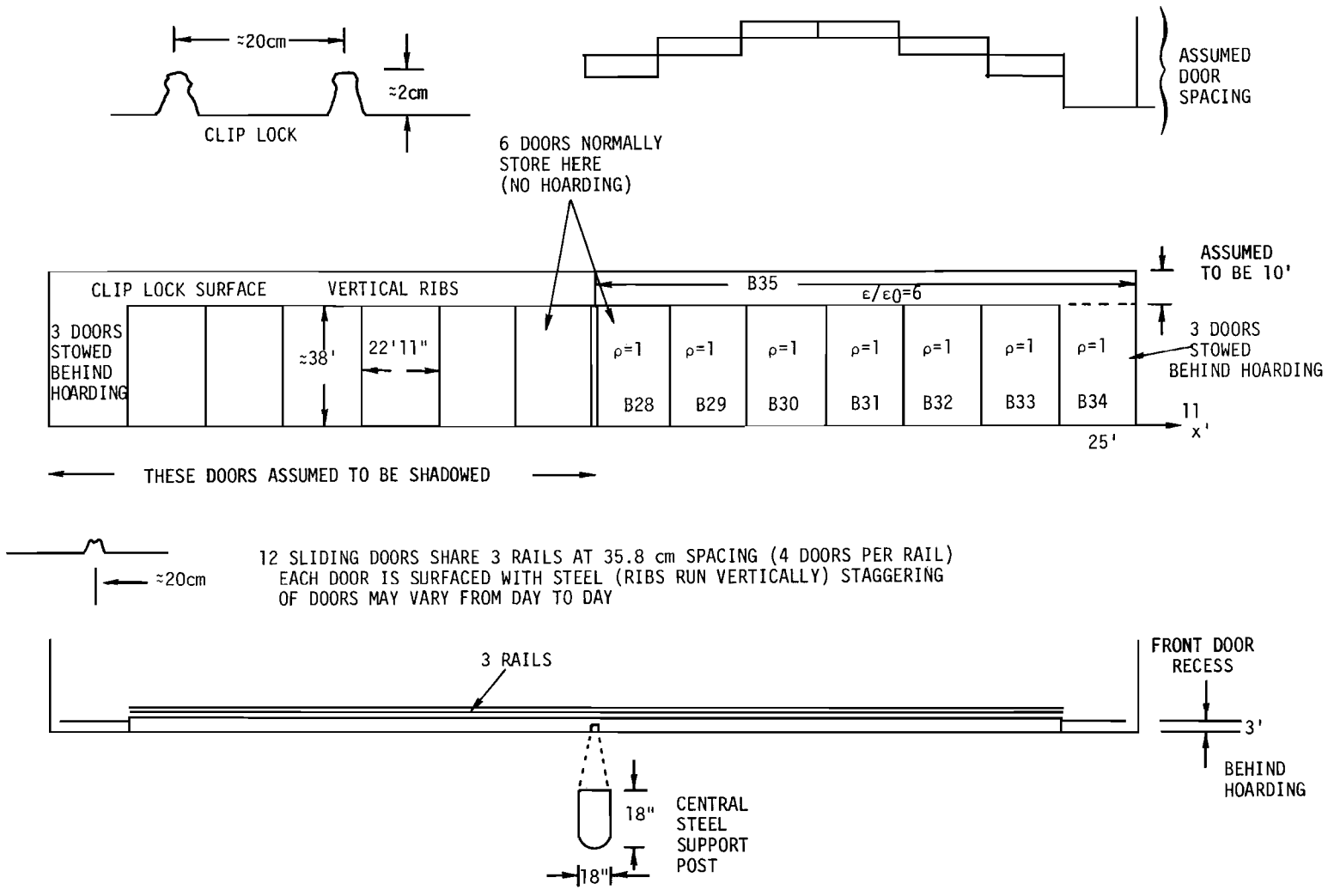

Fig. 3-101. ANSETT hangar No. 83.

The major airport factor which has not been considered in the current simulation is the effect of terrain profile. Figure 3-102 shows the runway terrain profile. We see that there is a possibility here of "focusing" ground reflections from the initial downslope and from the flat section which commences 1400 feet in front of the transmitter. This "focusing effect" can be represented by the current propagation program.

However, as was noted earlier, the irregularities in the off runway terrain shown in Fig. 3-103 cannot be represented easily in the current model. If the "focusing terrain" option were utilized for the direct signal and the flat earth model for the multipath signal, the considerable difference in terrain models might unduly bias the M/D levels. Thus, both terrains were considered to be flat for the results reported here.

b. Flight Profile

Preliminary analysis showed that the multipath region lies between the threshold of rwy 25 and the normal touchdown point, i.e., the flare region. Thus, the flight profile was intended to roughly approximate a flare approach. Typically, it consisted of linear segments between the waypoints shown below:

waypoint	x(ft)	velocity (knots) between points	height (ft)*
1	7903	111	50 (or, 40)
2	7203	107	29
3	7053	101 (or 105)	24.5
4	6903	96 (or 105)	20
5	6603		18.5

*with respect to the assumed threshold elevation

c. Comparison of Simulation Data With Field Multipath Data

In this section, we compare the simulation data with the Australian multipath measurement data. Three types of field data were provided:

(1.) M/D ratio versus distance along the runway for a taxiing aircraft as obtained by transmitting CW signals at different frequencies simultaneously through separate narrow beam antennas (2° BW) and plotting the net received signals versus time. One directional antenna was directed at various hangar complex features and the other along runway centerline.

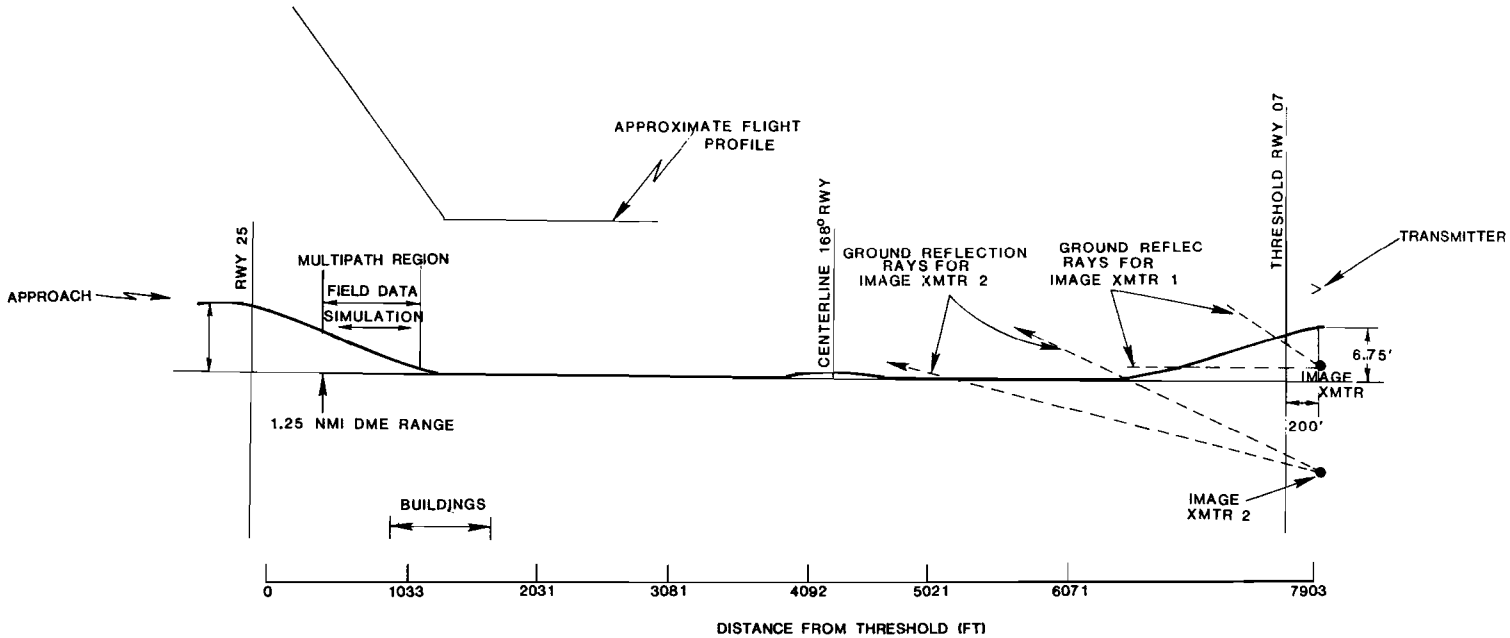

Fig. 3-102. Profile of Sydney runway 07-25.

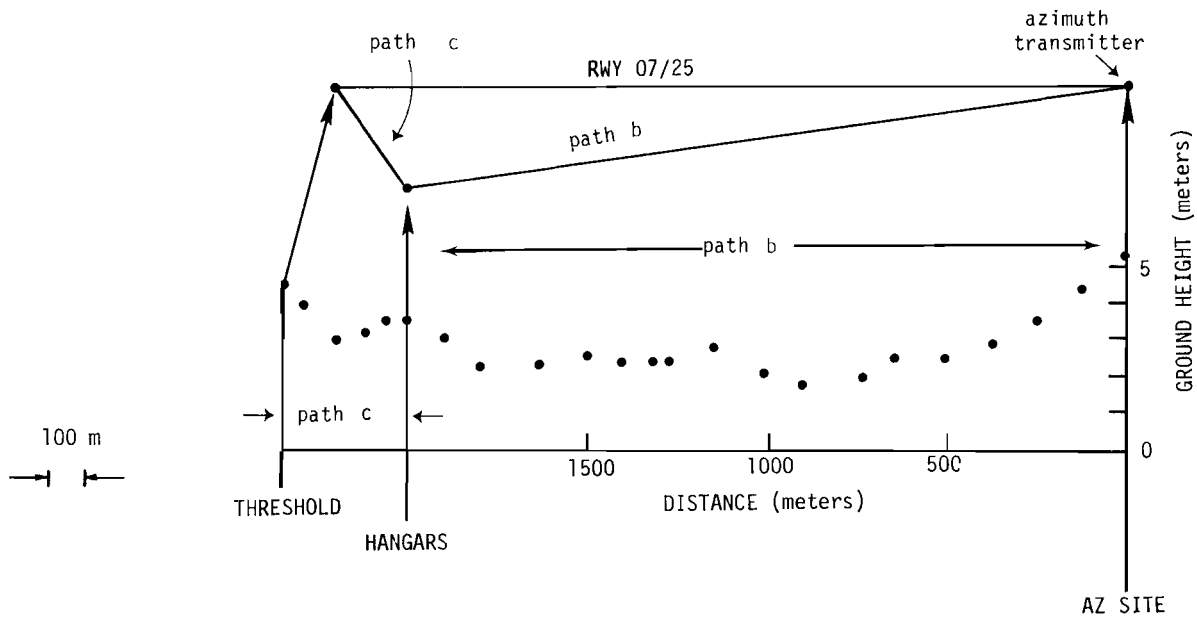

Fig. 3-103. Ground height profile at Sydney Airport along hangar reflection path.

(2.) M/D ratio at various flight path points as obtained from scope photographs of the scanning beam envelopes received during the flight tests.

(3.) scalloping in the net received signal envelope versus distance along the flight path when a CW signal was transmitted through an omni directional antenna.

Figure 3-104 shows one of the field data M/D level plots using method (1.). A high degree of spatial variation is evident, and raw* M/D values in excess of 0 dB occured. This data was viewed as being comparatively less useful than the other data due to:

(1.) the very compressed (and in some cases, incomplete) distance scale

(2.) the low aircraft antenna height

and (3.) uncertainty as to the aircraft antenna pattern.

Figure 3-105a shows the computed M/D ratio+ at points 2 feet apart for the flight profile with waypoints:

x (ft)	height (ft)	
7503	38	
6903	20	= a shortened version of the profile presented previously
6603	18	

Figures 3-105b and 3-105c show an expanded plot of the data in Figure 3-105a. Also plotted on Figure 3-105a are the M/D ratios** received in the Australian TRSB tests with their nominal position values and the result of shifting the Australian data by some 180 feet along the runway centerline. Figure 3-106 shows the Australian scope photos used to generate the M/D levels of figure 3-105.

We see that computer simulation yields a degree spatial variability quite similar to the field data and the M/D ratios are not badly inconsistent with the field data. The M/D levels computed for building 83 are low in the region from 1200 ft. from threshold as a consequence of assuming that the entire near half of that building was shielded by a fire station.

---

*i.e., uncorrected for transmitter or aircraft antenna gains.

+taking into account the various secondary paths in Figure 3-94.

**The raw Australian M/D values were increased by 2 dB to compensate for the reported characteristics of the aircraft antenna pattern.

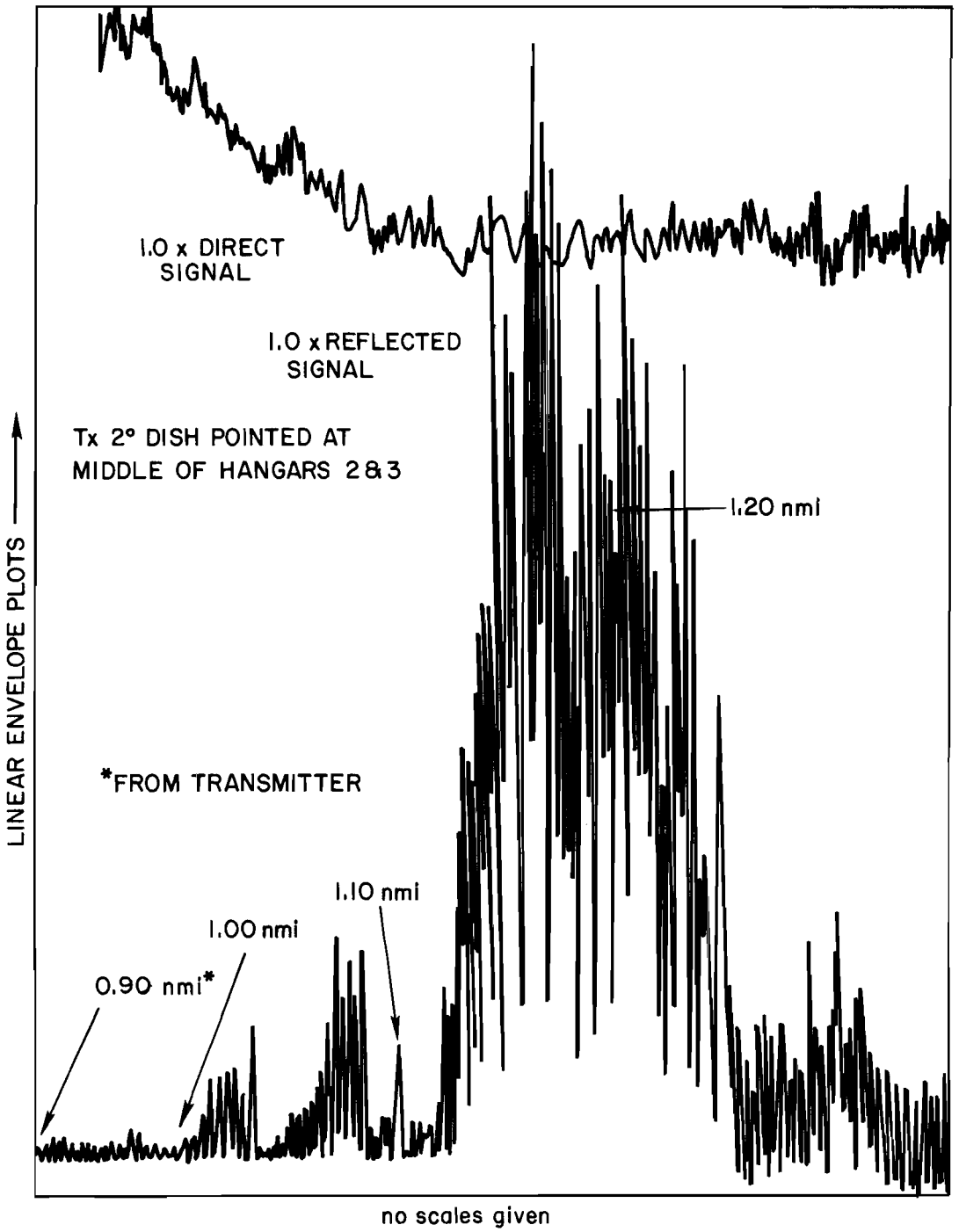

Fig. 3-104. Sydney M/D measurement for taxiing aircraft using two CW sources.

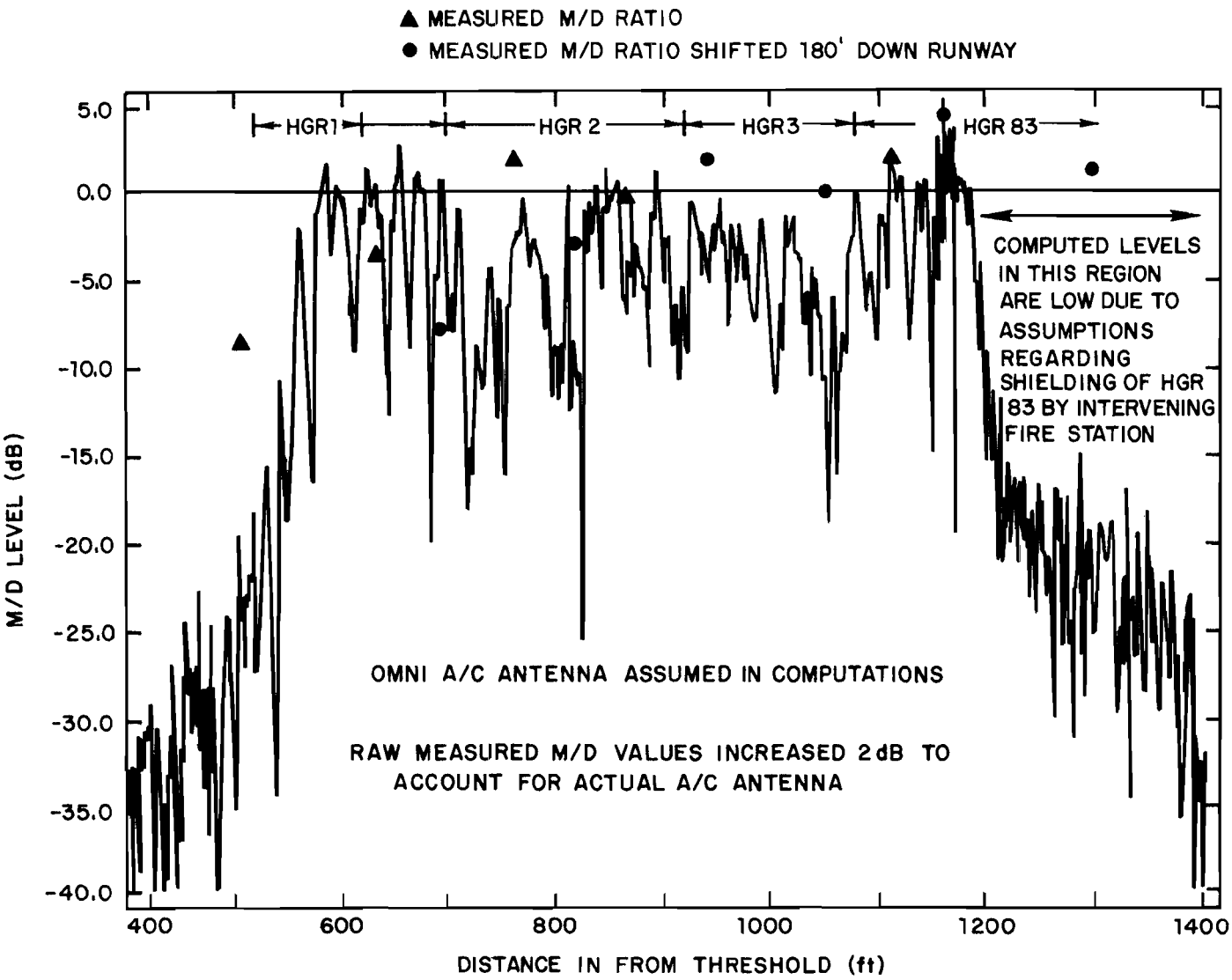

Fig. 3-105(a). Simulation results for received M/D levels.

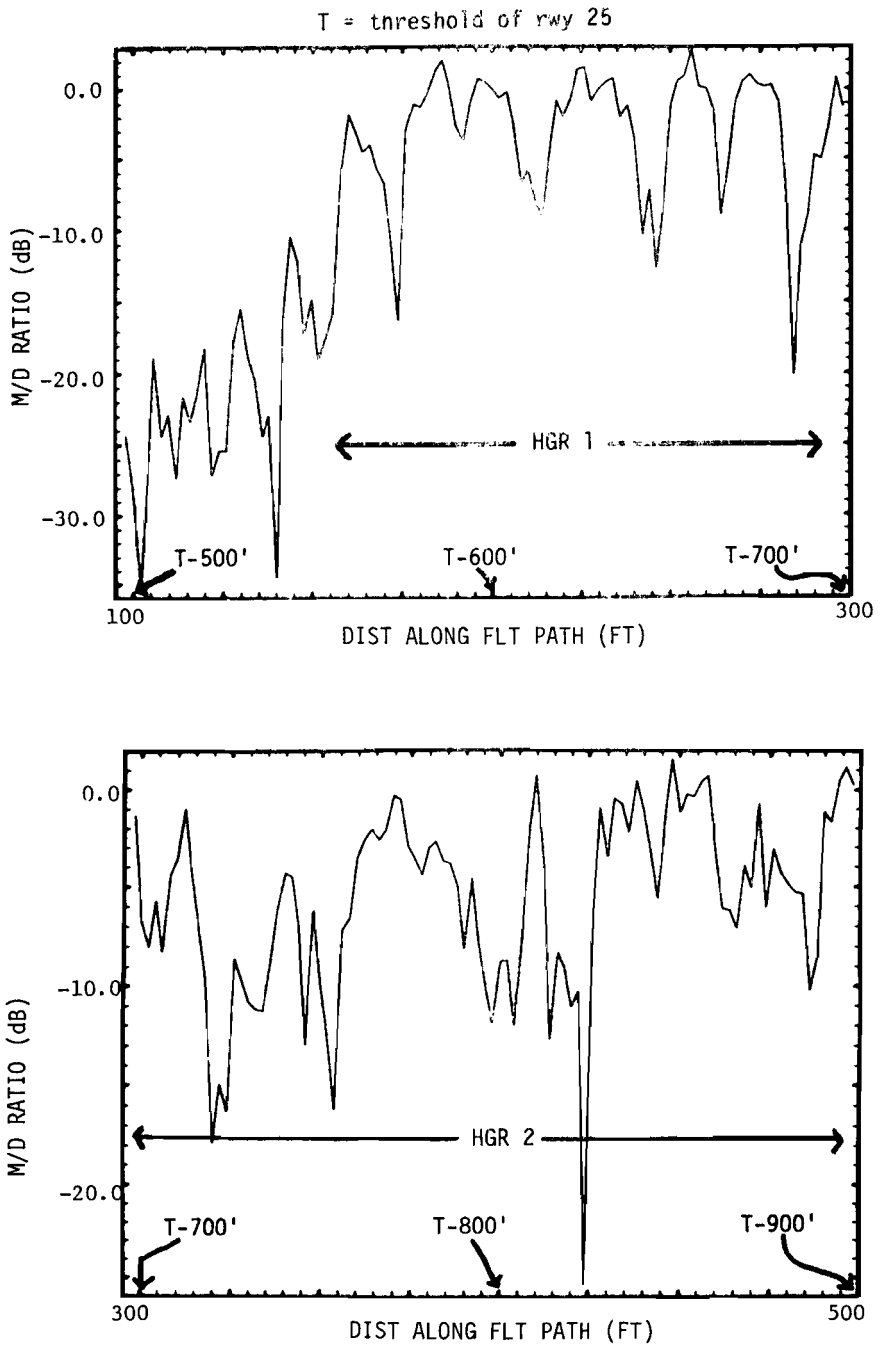

Fig. 3-105(b). Expanded plot of computed Sydney M/D ratio.

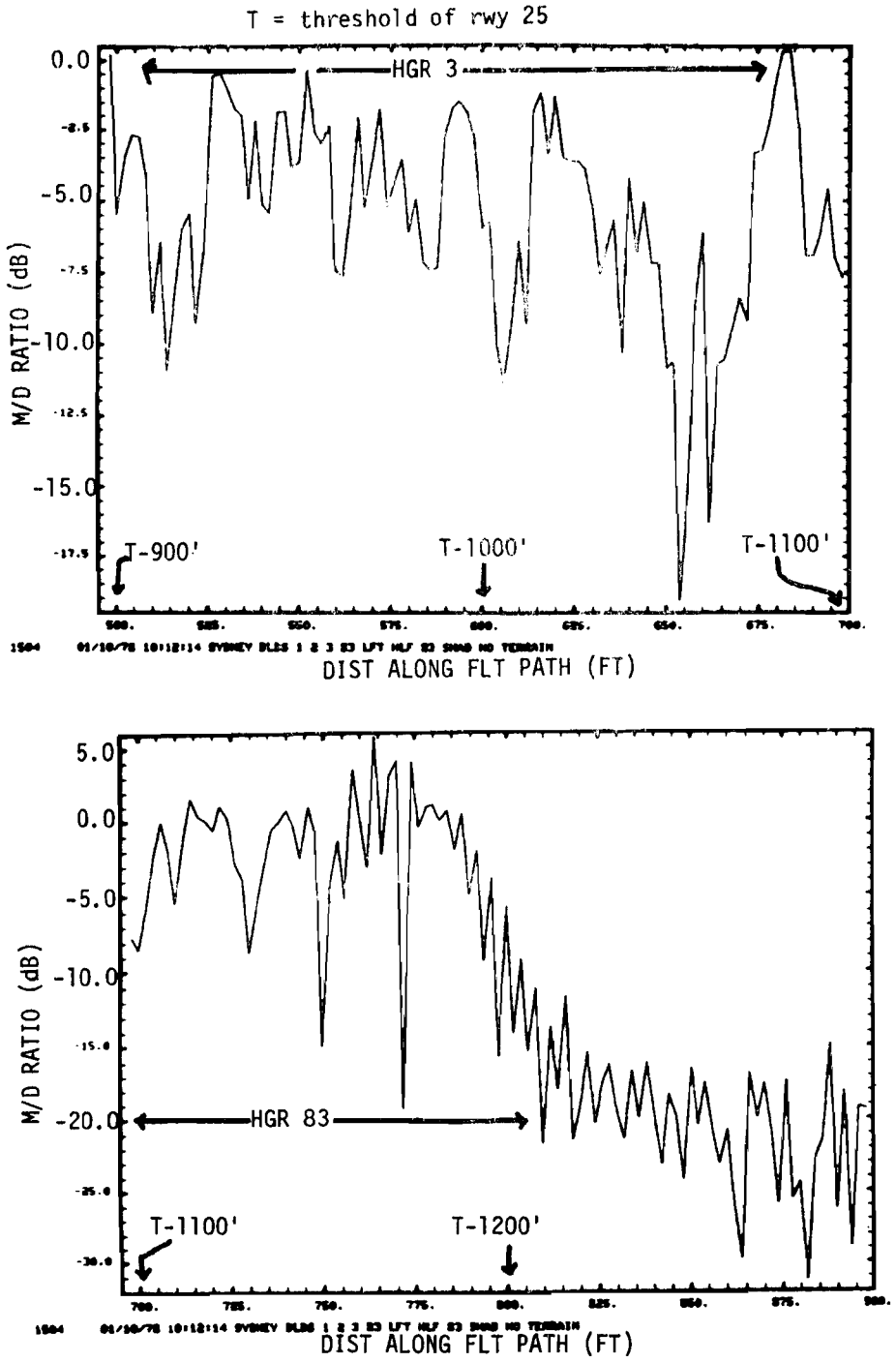

Fig. 3-105(c). Expanded plot of computed Sydney M/D ratio.

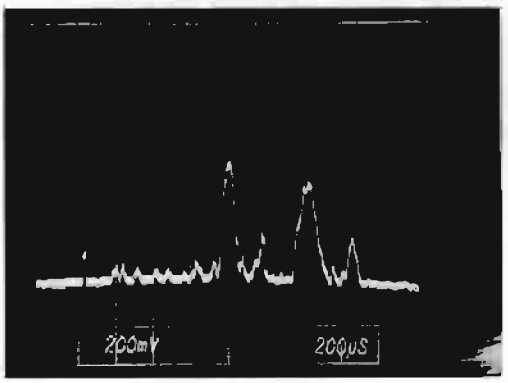

RUN 1 1.150 NMI

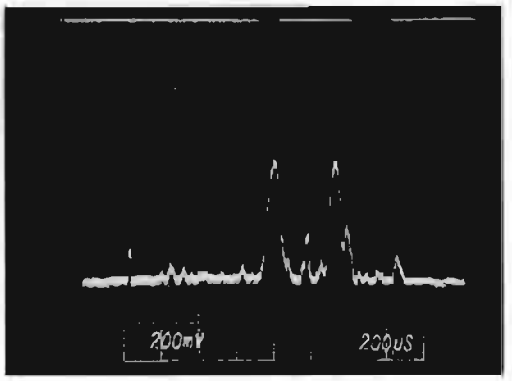

1.21 NMI RUN 1

NOTE: MULTIPATH > DIRECT SIGNAL

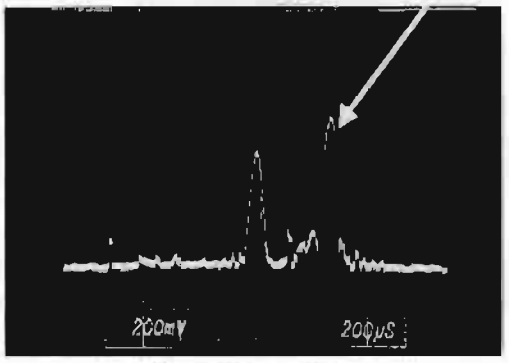

RUN 1 1.170 NMI

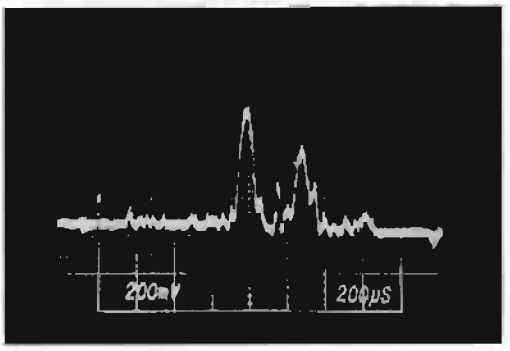

1.230 NMI RUN 1

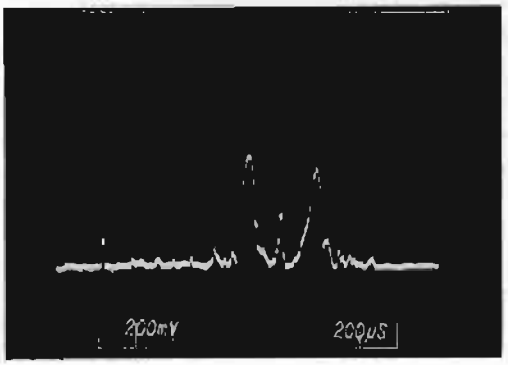

1.190 NMI RUN 1

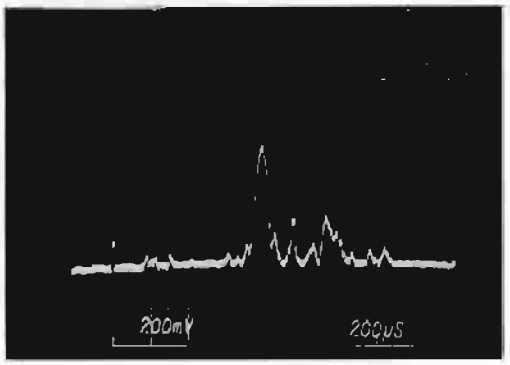

RUN 1 1.250 NMI

VERTICAL SCALE 5 DB/DIVISION
DIRECT SIGNAL APPEARS AT CENTER OF PHOTO.

ANGLE SCAN RATE IS 50 μSEC/DEG
(i.e., 400 μSEC = 8 DEG)

Fig. 3-106. TRSB received azimuth envelope data from Sydney flight test.

Another factor which might be affecting the hangar 1 multipath levels is the state of the hangar doors during the field trials. For the simulation, all doors were assumed closed. However, we were informed that this might not have been the case for hangar 1 when the tests were run. If some of the hangar doors were open, the M/D values would be lowered.

Experiments were also done radiating a CW signal through an omni antenna and recording the net received signal envelope during a flight. This experiment yields:

(a) direct indication of the degree of phase coherence between the direct and multipath signals received along the flight path - if there is a high degree of coherence (as postulated in the Lincoln simulations), the envelope will show a fine grain scalloping structure at the scalloping frequency (e.g., 400 Hz).

(b) an indication of the M/D level - the overall envelope will oscillate between the values $|D+M|$ and $|D-M|$ where M and D are the multipath and direct signal levels respectively.

The fine grain structure shows up quite dramatically in the Australian data as is shown in figure 3-107. In figure 3-108 we compare the computed overall envelope shape to the measured envelopes. The Lincoln value of M/D was reduced by 2 dB before computing the envelope to approximate the airborne antenna. The horizontal scales are approximately equal; it is not quite clear what the Australian vertical scale was. The Lincoln data has been translated approximately 180 feet to give what we felt was a better match to the experimental data. This was done on the grounds that there is some uncertainty as to the exact building locations.

As mentioned earlier, differences in the multipath region of hangar 1 may arise due to differences between the actual and assumed positions of the hangar doors. Also, the computed multipath region for building 83 should be less than that of the field data due to our having modeled only the far half of the hangar. Keeping these factors in mind, the agreement between the field data and simulation results for spatial variation in multipath level is regarded as reasonably good.

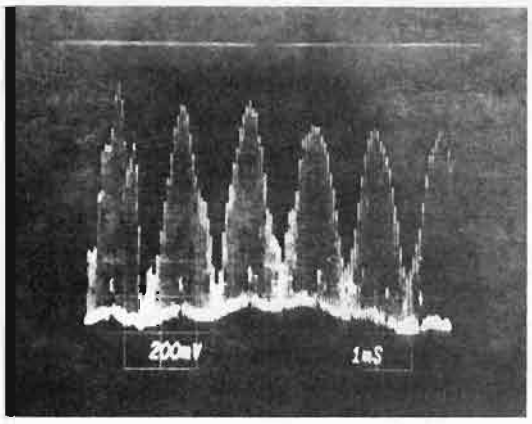

RUN 8 1.190 NMI + 200 MSEC

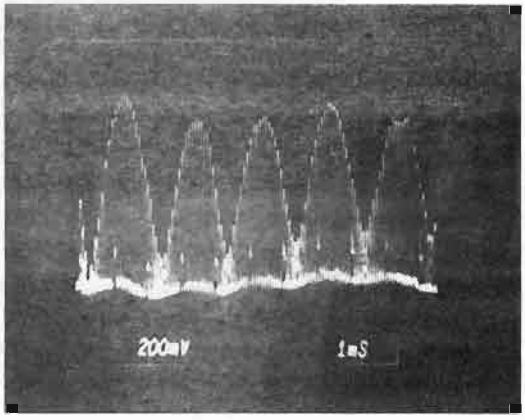

1.250 NMI RUN 8

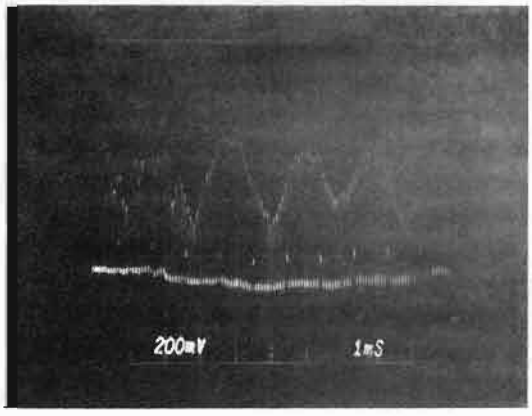

RUN 8 1.207 NMI

OMNI TRANSMITTER ANTENNA
LINEAR (VOLTAGE) SCALE

DEPTH OF FADE INDICATES
MULTIPATH LEVEL

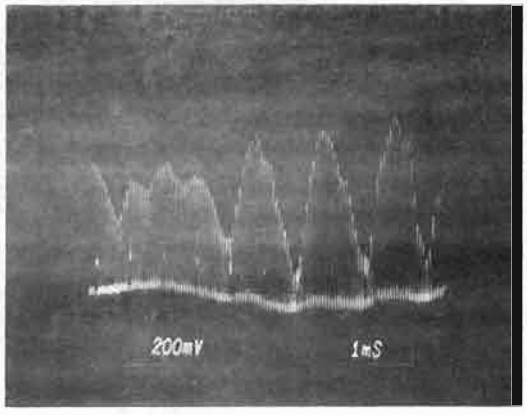

RUN 8 1.290 NMI

REGULARITY OF INTERFERENCE PATTERN
INDICATES PHASE COHERENCE
OF REFLECTED SIGNAL

Fig. 3-107. Scalloping in received CW signal level for Australian test.

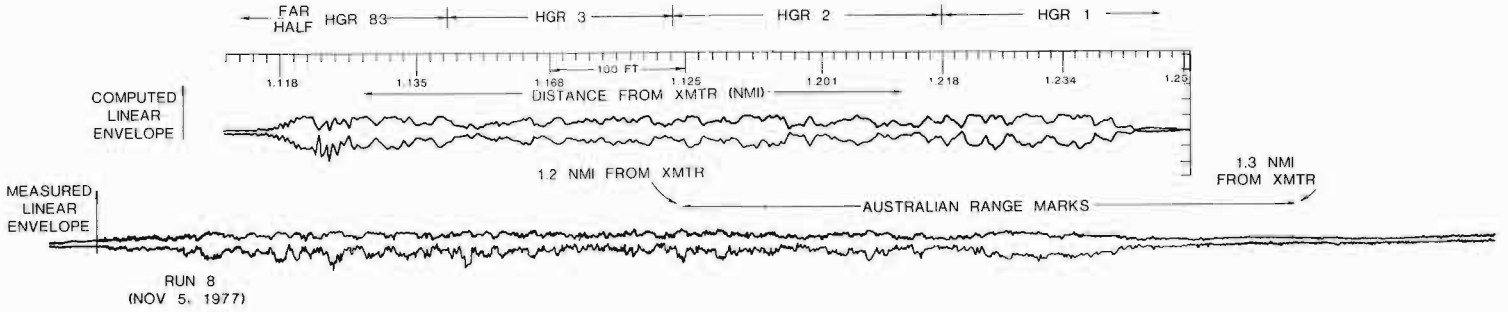

Fig. 3-108. Comparison of CW signal level scalloping Sydney runway 25-07.

3. Wright Patterson Air Force Base, Ohio

Multipath measurement experiments were carried out at Wright Patterson Air Force Base, Ohio (WPAFB) by Lincoln Laboratory and by a group with members from the US Air Force, Army and IITRI. The Lincoln data was discussed in section B of this chapter while the DOD/IITRI results have been presented in a series of US Army and USAF AFFDL reports [33-35, 56, 91]. Measurements were made on buildings with small and large scale surface irregularities with a variety of measurement geometries.

a. Bldg. 485 - an example of small scale irregularities.

Fig. 3-109 shows building 485 at area C of WPAFB. This is a concrete stucco building with narrow vertical windows separated by 22 foot sections of concrete structure with stucco finish. Each 22 foot panel is divided into three smaller panels which are in turn divided into small squares to emulate an ashlar curtain. The overall effect is one of considerable small scale irregularities superimposed on what is essentially a flat concrete wall.

The USAF/IITRI performed an experiment in which the building and the receiving van were simultaneously illuminated by a C band CW signal radiated from a wide coverage horn. The net recorded signal was recorded as the van moved along a taxiway/road parallel to the hangar as shown previously in figure 3-31.

For purposes of comparison, the building was modeled as a single flat concrete plate with dimensions corresponding to the building wall and dielectric constant $\varepsilon/\varepsilon_o = 4$.

Fig. 3-110 compares the field measurements with the simulation results. We see that the spatial period and the peak to peak amplitude variations show quite good agreement. The consistency in the spatial period shows that the small scale surface irregularities and/or windows on a surface which is otherwise flat do not change the basic nature from being essentially identical to those from a perfectly smooth surface. Similarly, the good agreement in peak-to-peak excursions shows that the fine scale surface roughness did not appreciably effect the specular reflection amplitude.

Fig. 3-109. WPAFB building 485 viewed from northwest.

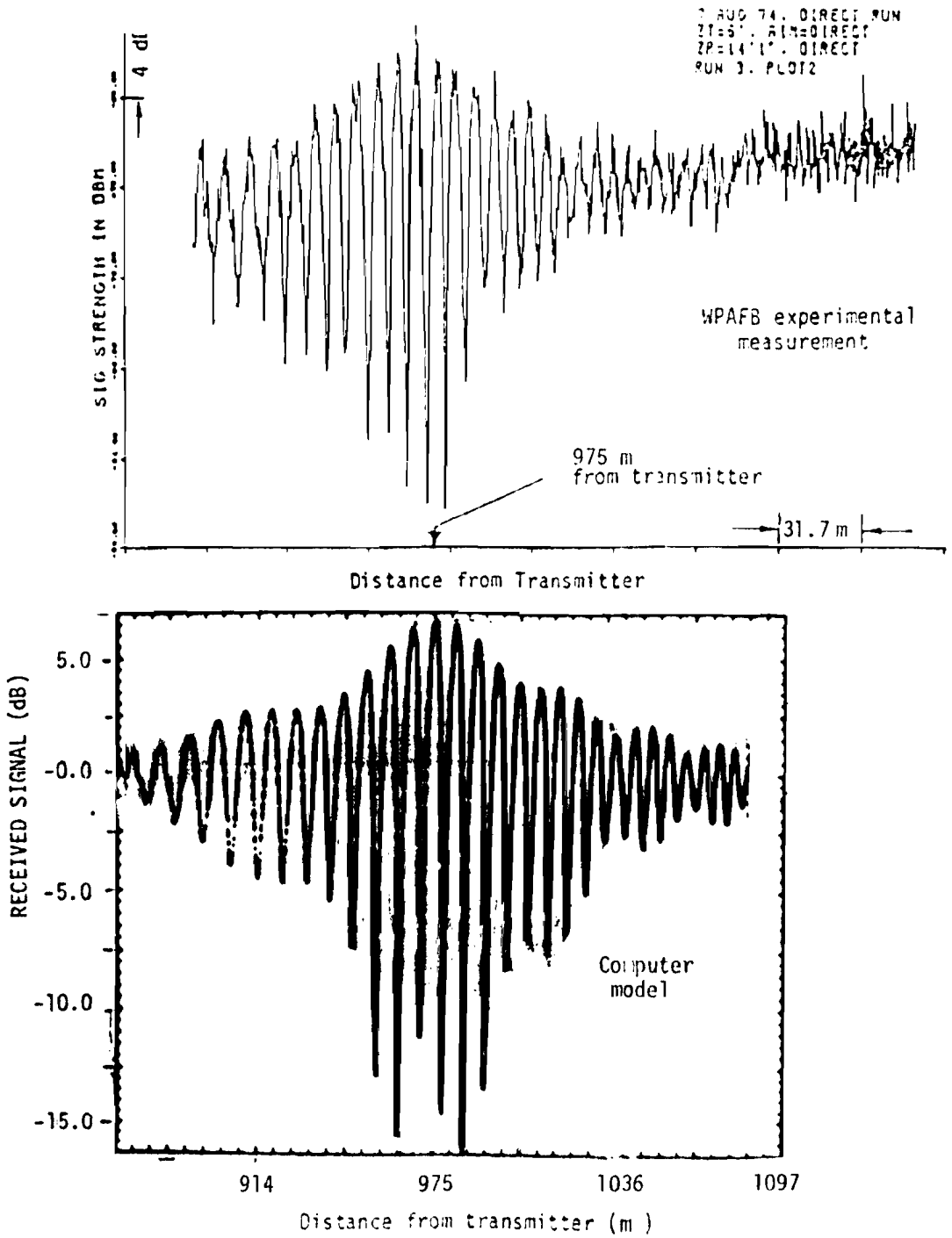

Fig. 3-110. Comparison of experimental data and computed results showing phase coherence for reflections from building 485 at Wright-Patterson Air Force Base.

b Bldg 206 - a structure with large scale periodic irregularities.

Bldg. 206 is a classical example of a vertical surface consisting of many flat plates (doors) which are set in from one another according to a periodic pattern. A photograph of this building and the reflection geometry were shown previously as figures 3-68 to 3-71. Long range reflection multipath measurements were made along the main runway by Lincoln (section B this chapter) and by a USAF, US Army/IITRI team [57].

These two sets of experimental data are complementary in that the USAF/ US Army/IITRI data yields an uncalibrated multipath signal level variation on a very fine spatial grid whereas the Lincoln data provides calibrated M/D levels averaged over a coarser spatial grid (e.g., average level over 20-50 foot intervals).

The USAF/US Army/IITRI measurement technique consisted of radiating a CW signal through a narrow beam dish which was aimed at the hangar and down the runway respectively. For a given transmitting antenna direction, the received signal level was then recorded as a van taxied down the runway centerline. To obtain multipath to direct signal ratios by this measurement technique it is necessary to merge the results of the pairs of runs taking into account any calibration factors which may have changed. Results of such merged runs have not yet been published; however, raw plots of the signal level variation along the runway were furnished to us. Examples of multipath level variation are shown in figures 3-111 and 3-112, while figure 3-113 shows an example of the direct signal level variation. The calibration data relating to figures 3-111, 3-112, and 3-113 was not available to us; however, it has been reported [57] that the peak M/D levels were on the order of + 3 dB to + 6 dB.

Two factors complicated the modeling effect. The first of these was the large number of discrete sizable flat plates associated with this building. Figure 3-114 shows the orientation of the various doors and other surfaces relative to the building front. Since the Fresnel zone radius of 25 feet was comparable to the single door width of 25 feet and much larger than the wire mesh grid imbedded in the windows, the individual doors were assumed to be flat

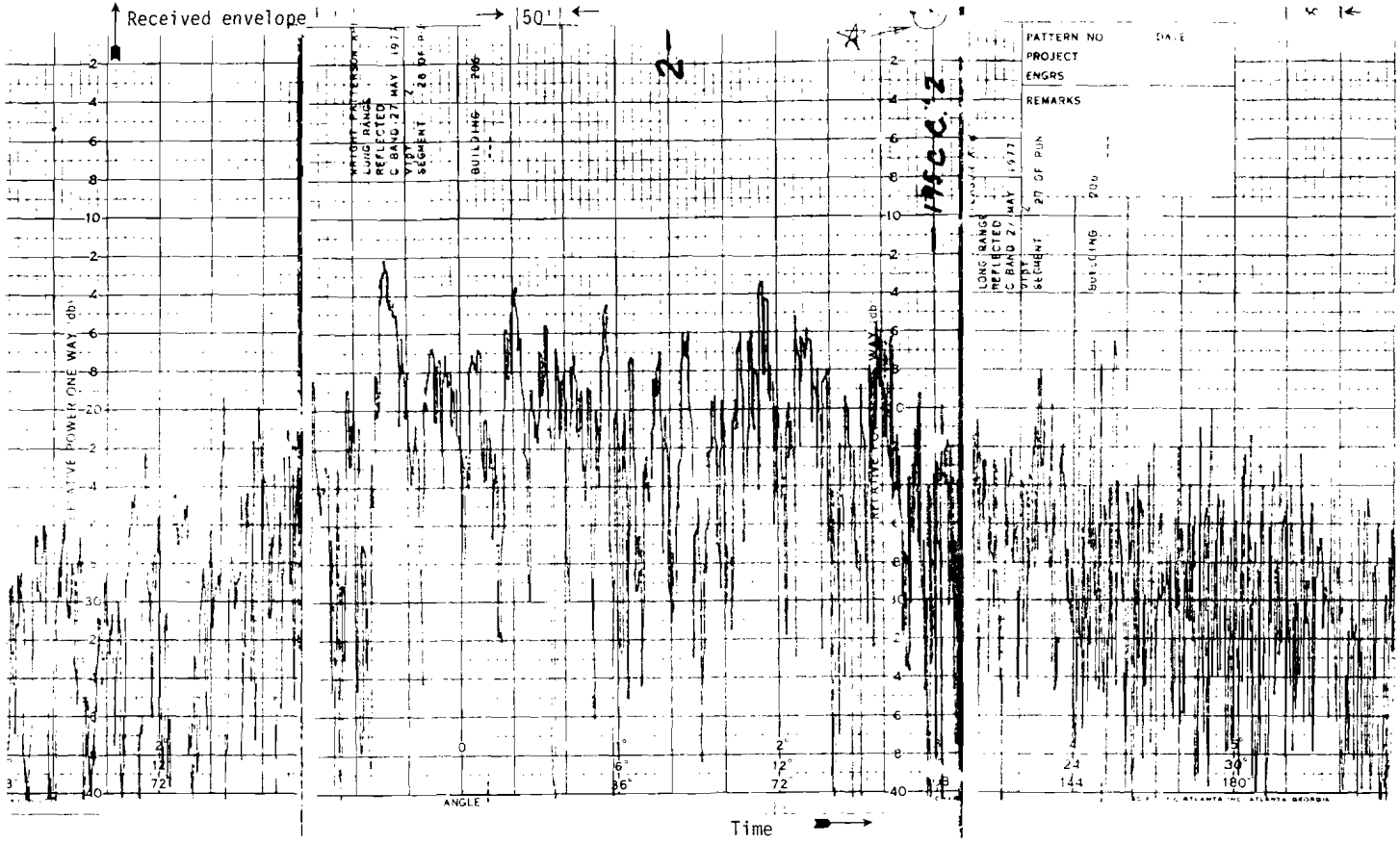

Fig. 3-111. Received bldg. 206 multipath signal level along WPAFB runway for receiver height of 50 ft.

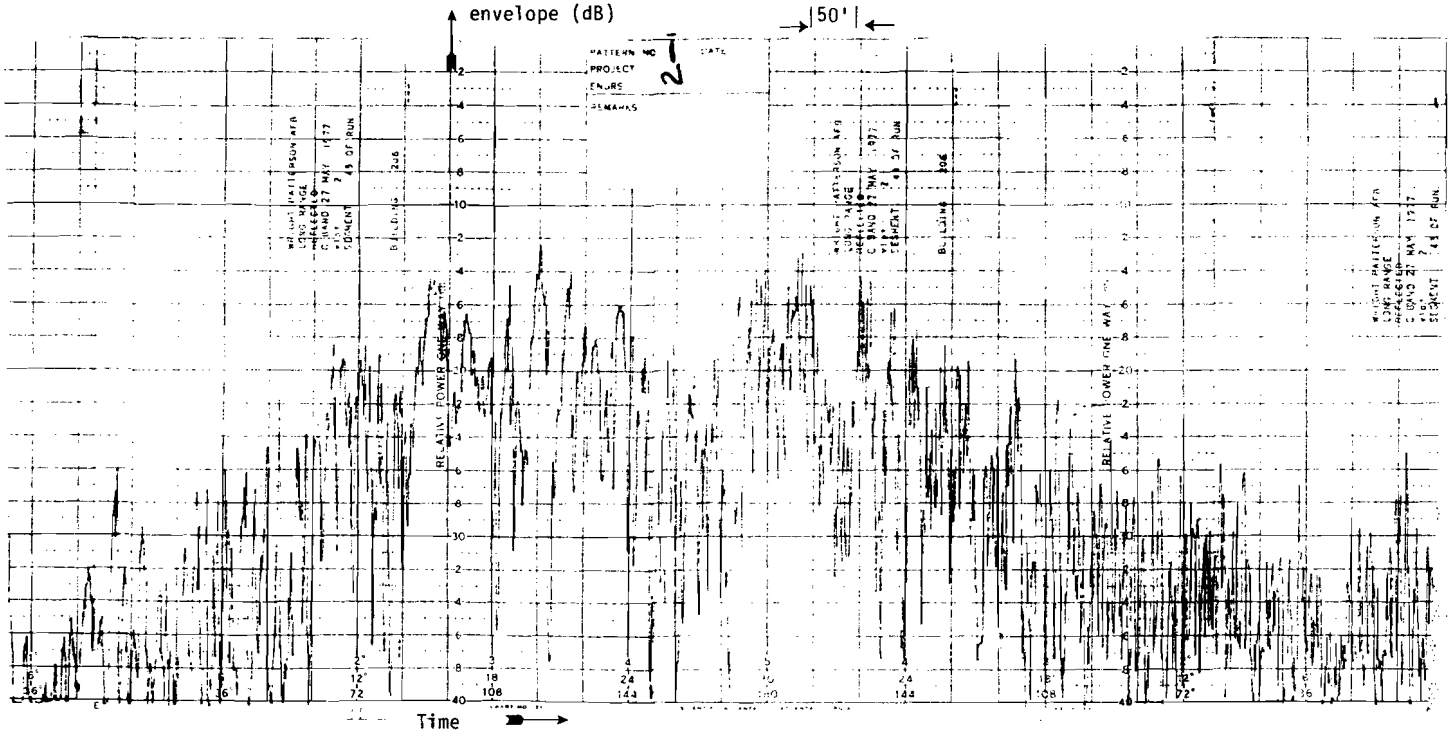

Fig. 3-112. Received building 206 multipath signal level along WPAFB runway for receiver height of 5 ft.

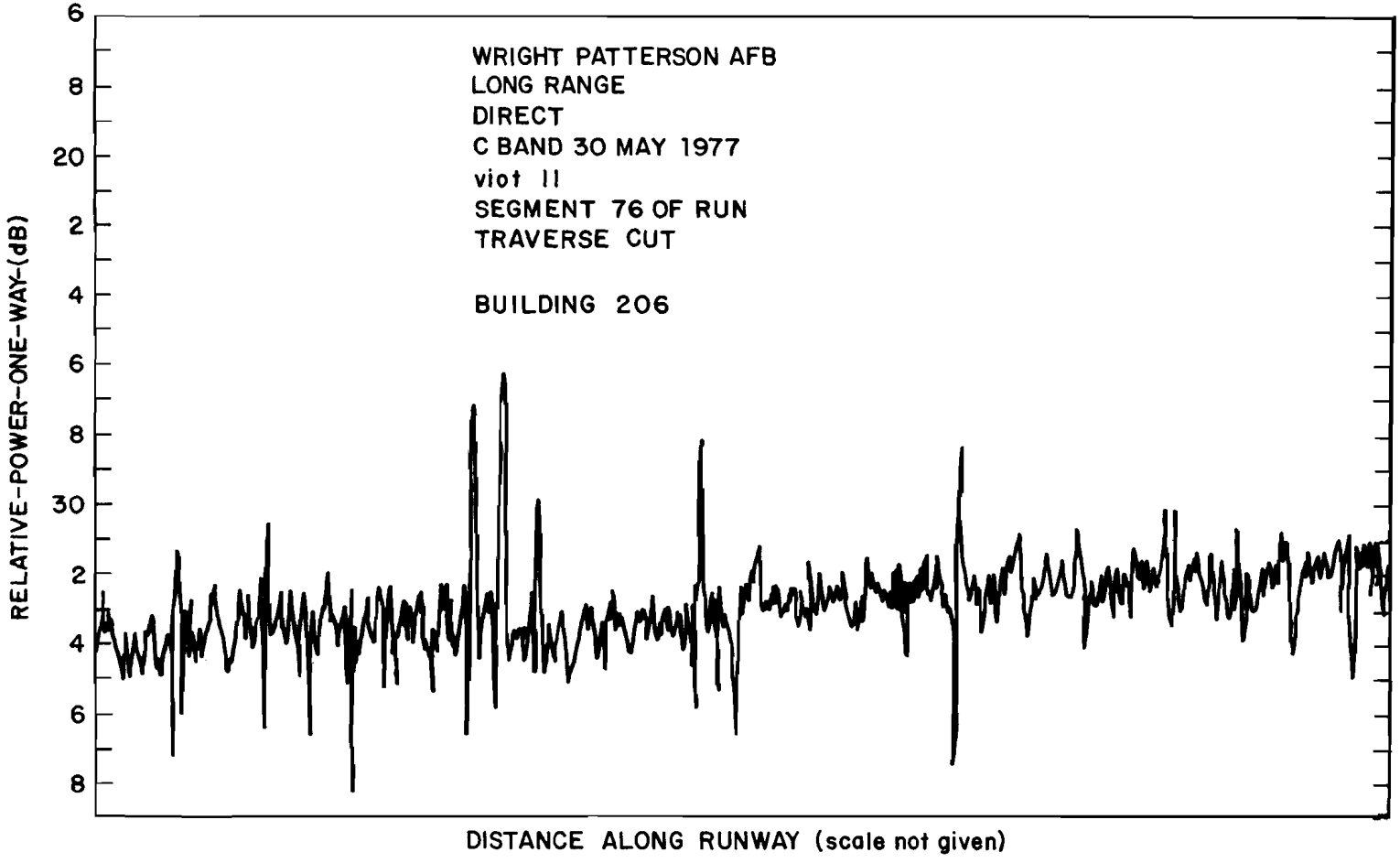

Fig. 3-113(a). Direct signal along WPAFB runway at height of 5 ft.

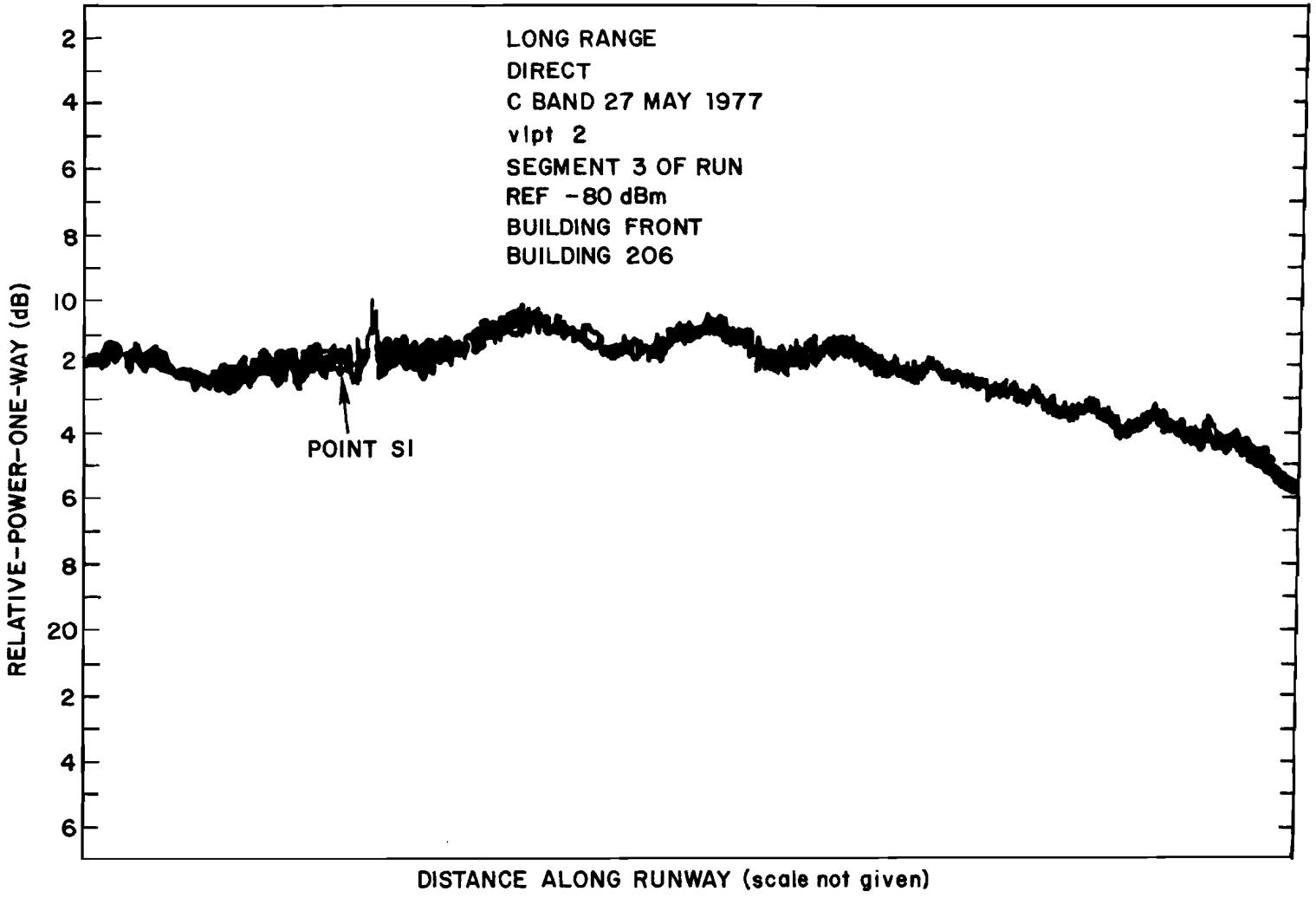

Fig. 3-113(b). Direct signal level variation along WPAFB runway at height of 50 ft.

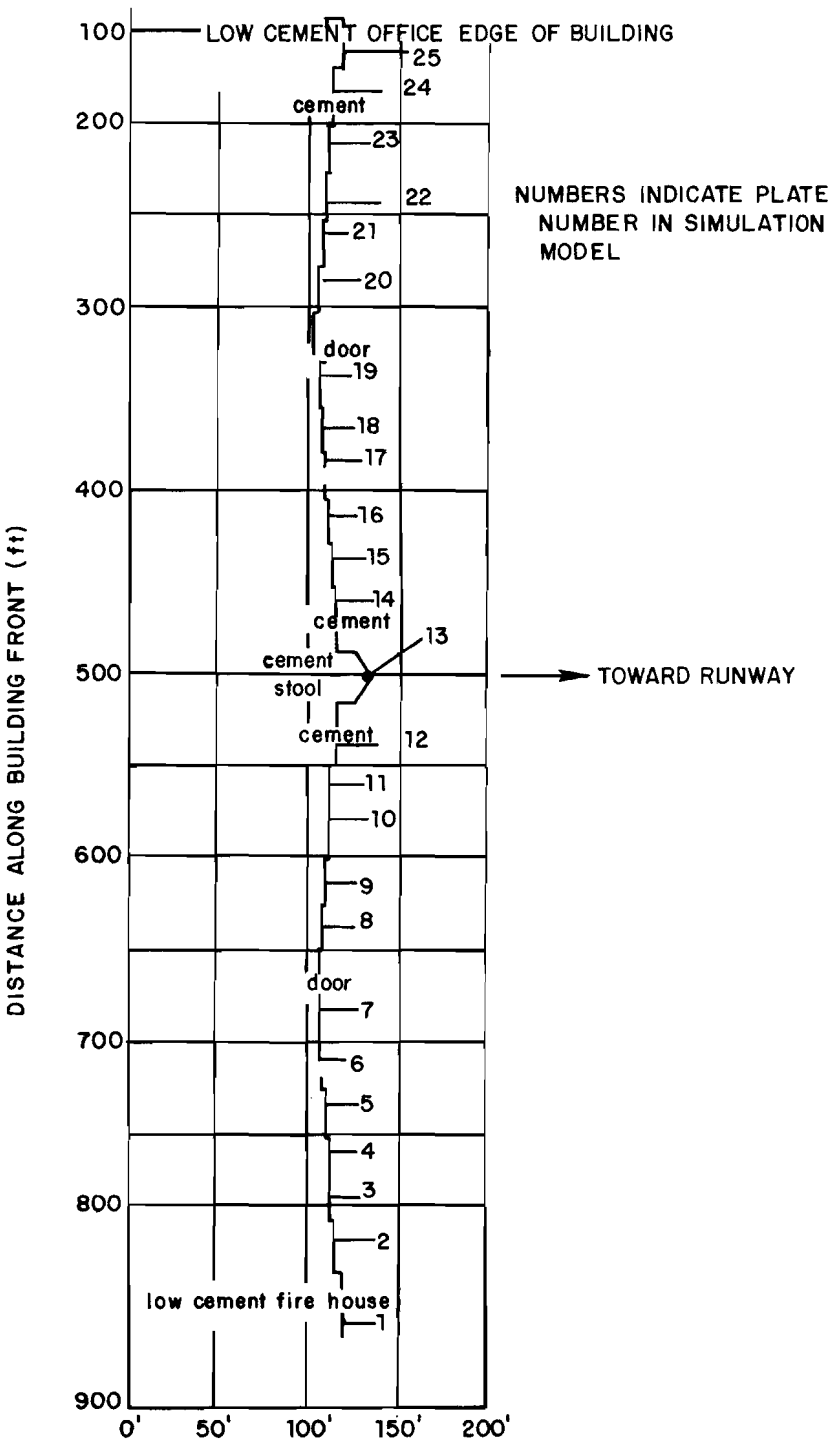

Fig. 3-114. Bldg 206 profile.

metal. The extent that this overestimated the actual reflection coefficient would become clearer when the simulation/field data comparison was accomplished. The concrete pillars to the side of the doors was modeled as a flat homogeneous material with dielectric constant 4.0.

The ground terrain on and off the runway also was a complicating factor. Figure 3-68 showed the terrain profile along the runway as well as a crude contour map of the off runway terrain profile. Since the off runway terrain was reasonably flat whereas the along runway terrain was concave, it was decided to model the runway profile by a series of four plates with appropriate slopes while the off runway terrain would be modeled as a homogeneous flat plate. Here again, any errors arising from this approximation would cause the overall multipath levels to be high or low, but not affect the nature of the fine variation.

Fig. 3-115 shows the computer generated airport map corresponding to a simulation of an aircraft flying at knots 20 feet above the runway in the building 206 specular reflection region. The azimuth transmitter was assumed to be at the transmitter location in the Lincoln tests. Fig. 3-116 shows the computed azimuth multipath levels for the six plates providing the largest multipath levels. We see that the significant specular reflections from an individual door are found over a region of approximately 30 feet. The specular reflection regions from adjacent staggered doors overlap so that constructive or destructive interference occurs on a spatial grid of approximately 40 feet.

Fig. 3-117 shows the computed (coherent) sum of the various direct and reflected signals. The fine grain spatial variation is seen to agree reasonably well with the fine grain structure shown in the Army/Air Force data* while the averaged multipath levels correspond fairly well to the measured M/D levels shown in figure 3-77. It also follows from the results of figures 3-115 and 3-116 that the composite received signal would have a spectrum centered at the nominal scalloping frequency (shown in fig 3-115) with a width of $\simeq$10-20 Hz, as was found in the Lincoln experiments reported in Section B of this chapter.

---

*The difference between the actual Army/Air Force and simulation transmitter positions and receiver heights is a second order effect on the spatial structure due to the large distances involved.

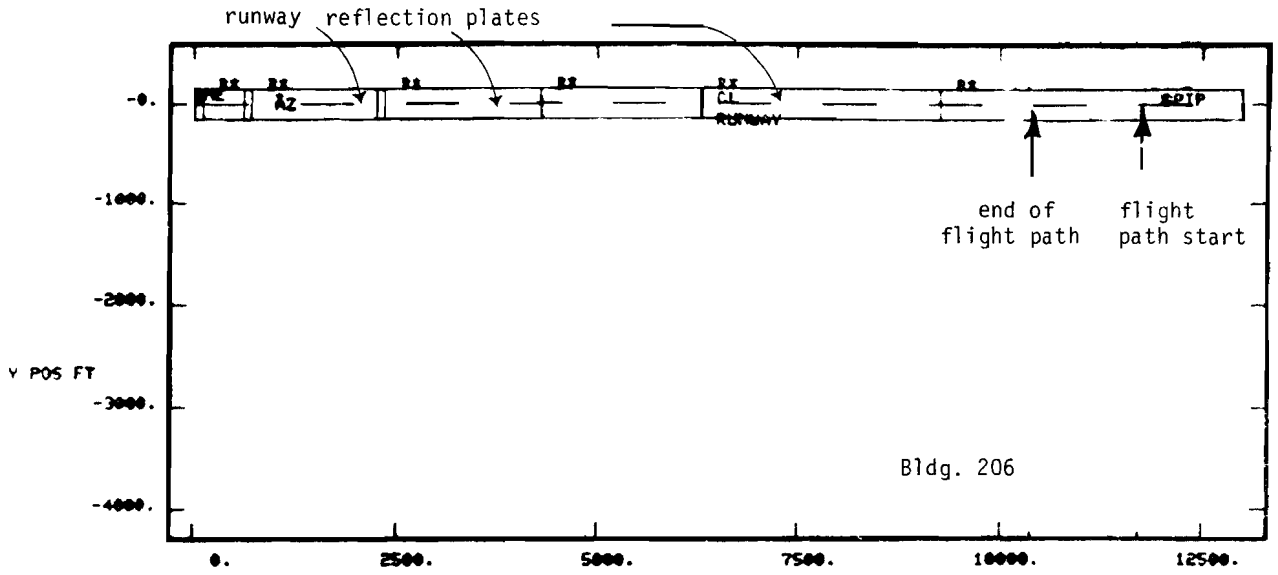

FLT PTH A
AZ SYSTEM

OBST	RANK	M/D(DB)	DIST	RDOP
B 1	25	-10.1	244.	-369.
B 2	4	-3.5	274.	-372.
B 3	11	-5.7	300.	-373.
B 4	24	-5.8	326.	-374.
B 5	21	-5.8	354.	-376.
B 6	22	-5.8	378.	-377.
B 7	1	-0.3	400.	-378.
B 8	23	-5.8	422.	-381.
B 9	20	-5.7	494.	-383.
B10	12	-5.7	518.	-384.
B11	14	-6.7	548.	-386.
B12	5	-3.9	576.	-386.
B13	26	-10.6	600.	-419.
B14	6	-3.9	658.	-391.
B15	16	-5.7	682.	-392.
B16	13	-6.7	714.	-394.
B17	18	-6.7	738.	-396.
B18	19	-6.7	748.	-394.
B19	2	-0.3	810.	-400.
B20	15	-6.7	834.	-400.
B21	17	-6.7	880.	-403.
B22	8	-6.5	912.	-406.

AZ SYSTEM

OBST	RANK	M/D(DB)	DIST	RDOP
B23	10	-5.6	946.	-407.
B24	3	-2.8	976.	-408.
B25	27	-11.7	1010.	-409.
B26	30	-80.0	0.	0.
B27	9	-5.6	1314.	-0.
B28	7	-4.4	1374.	-0.
B29	28	-11.8	0.	-0.
B30	31	-80.0	0.	0.
B31	32	-80.0	0.	0.

DIST = distance along flight path at point of peak M/D ratio

RDOP = scalloping frequency in Hz at point of peak M/D ratio

Fig.3-115. Airport map for simulation of WPAFB bldg. 206 reflections.

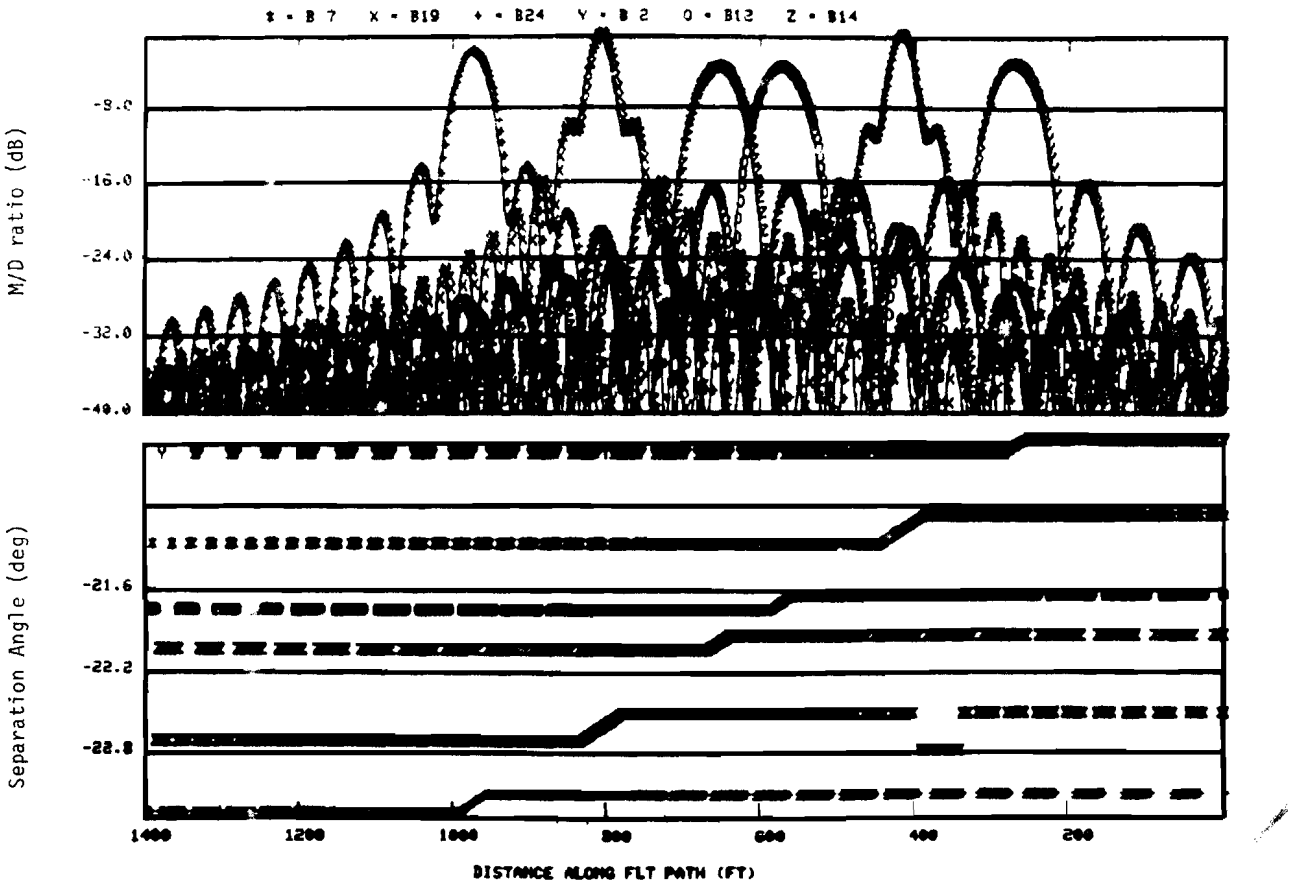

Fig.3-116. Computed multipath levels for six of WPAFB bldg. 206 doors.

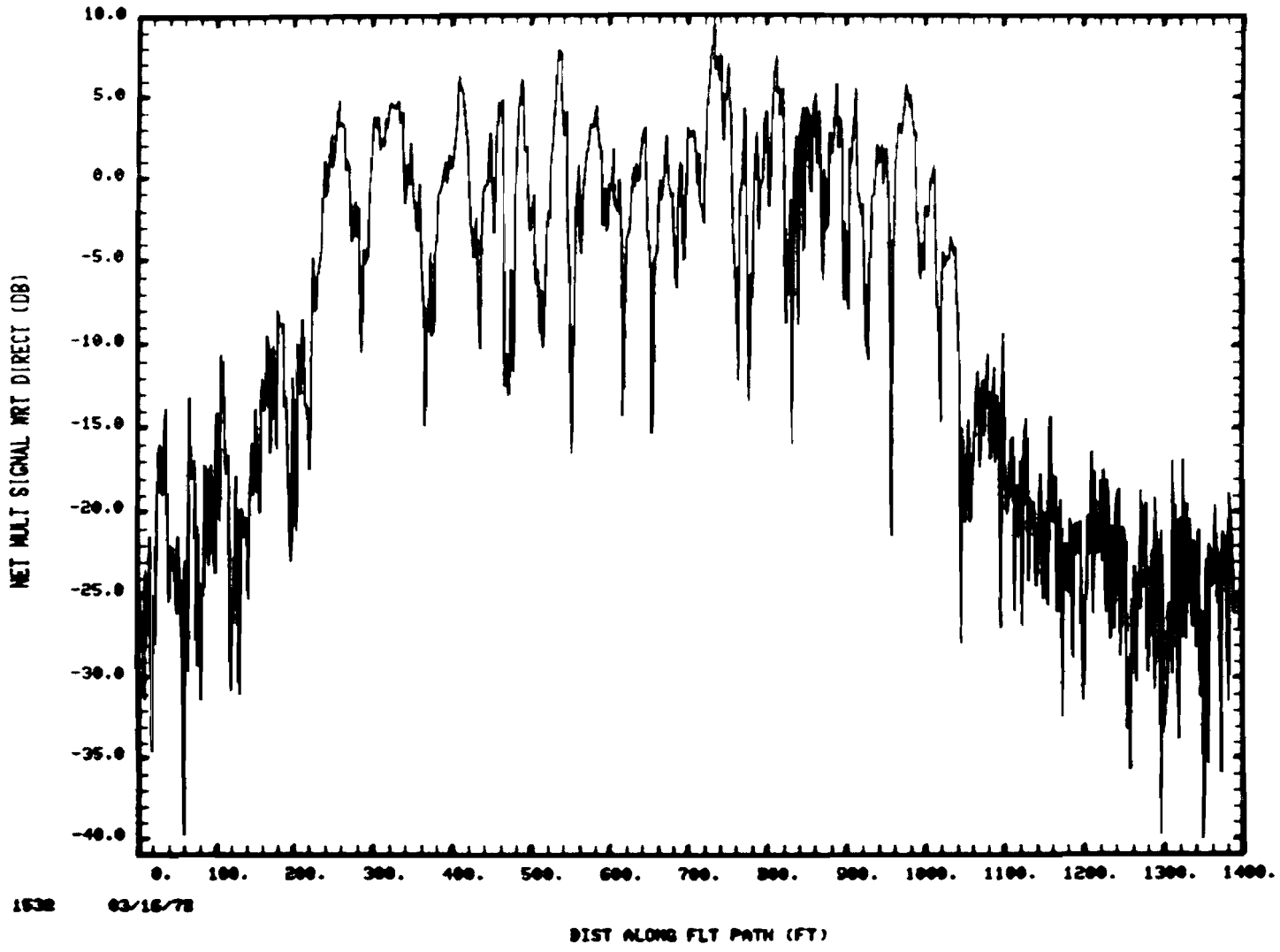

Fig.3-117. Computed bldg. 206 effective M/D level along WPAFB runway.

Considering the various airport model approximations (e.g., the modeling of the door surfaces and off runway terrain) and the very crude flight profile data, the agreement as to spatial structure and peak M/D levels is regarded as good.

4. Discussion of Results

In this section, we have presented a quantitative comparison of the propagation model predictions with the results of field measurements on structures whose walls contained a significant degree of irregularities. The fine grain irregularities (e.g., stucco on bldg. 485 and windows on the hangars) did not appear to significantly alter the spatial structure nor the levels of the specular reflection levels. The data on periodically staggered doors seems readily explainable by a simple model of dominant specular scattering from each door in succession coupled with destructive or constructive interference as the specular reflection spot moves from one door to the next. If the grazing angle on the wall is θ_g and D is the door staggering, the phase angle between the contributions from the two doors is $\phi(\text{deg}) \approx 720 \frac{D}{\lambda} / \sin\theta_g$. For the cases considered here, $D/\lambda \approx 3$ to 6 and $\theta g \approx 30°$ to 45° so that ϕ ranges over the full range of values from 0° to 360°. Thus, on the average, the multipath level at the transition points is reduced by approximately 3 dB over what it would have been for a flat surface. When the specular point lies in the middle of a door, the contributions from the adjacent doors could in some cases add up constructively such that a higher level is obtained than would have occured for a flat surface.

IV. SHADOWING MODEL REFINEMENTS

Diffraction of the received signal by structures and aircraft located close to the line of sight (LOS) between the MLS transmitter and receiver were found to be a common source of multipath errors in the various MLS field tests [17, 21, 31, 60, 62, 63, 73]. Consequently, considerable effort has gone into validating and refining the initial shadowing model [29]. The bulk of the validation data of the initial model is described in chapters II and IV of volume II in this report. This section describes the model refinements and their validation. The shadowing model assumptions are compared in table 4-1. The rationale for the assumptions which were not changed was presented in [29], so our discussion here will focus on the new features.

A. Incorporation of Additional Ground Reflection Terms

Australian field tests [16] and scale model range experiments [38] with the TRSB system showed that ground reflections on either side of a shadowing obstacle can in certain cases effect the net shadowing error. The initial model considered only the case of ground reflections between the ground antenna and the shadowing obstacle. To include the ground reflection terms between the shadowing obstacle and the receiver, it was necessary to introduce an image receiver as was done in the case of specular reflections from buildings or aircraft.

Although the mechanics of including these additional paths is a straightforward application of the corresponding building reflection model (see chapter III of [29]), there are certain subtle factors which merit some discussion. To understand these, we need to briefly review the basic model for shadowing by a rectangle. In free space, Huygen's principle states that the received signal at a point can be made up from wavelets which are retransmitted from an aperture plane such as shown in Fig. 4-1. Ground reflections give rise to the additional wavelet paths illustrated in Fig. 4-2. Thus, in determining the signal which was propagated through a rectangular opening in an opaque screen (per assumption 2 of table 4-1), we must

TABLE 4-1

COMPARISON OF INITIAL AND REFINED SHADOWING MODELS

INITIAL MODEL [29] ASSUMPTIONS	REFINED MODEL ASSUMPTIONS
(1) obstacles may be characterized by a set of nonoverlapping rectangular plates which coincide with their silhouette	same except in cases where an object dimension is comparable to a wavelength
(2) Babinet's principle is applicable, i.e., the received field with shadowing obstacle(s) = free space field - field propagated through rectangular openings in an opaque screen where the rectangle openings coincide with the sheets of (1)	same
(3) the rectangles are far enough away from transmitter and receiver such that the field propagating through a given rectangle can be adequately represented by Fresnel diffraction	same
(4) the variation of the diffracted signal phase as a function of position in the ground antenna aperture is the principal factor in determining the number and location of the diffraction rays.	the diffraction rays are obtained from a Fourier decomposition of the the (complex) diffracted signal amplitude along the aperture.
(5) ground reflections can be accounted for by suitable image transmitters.	image receivers are also included

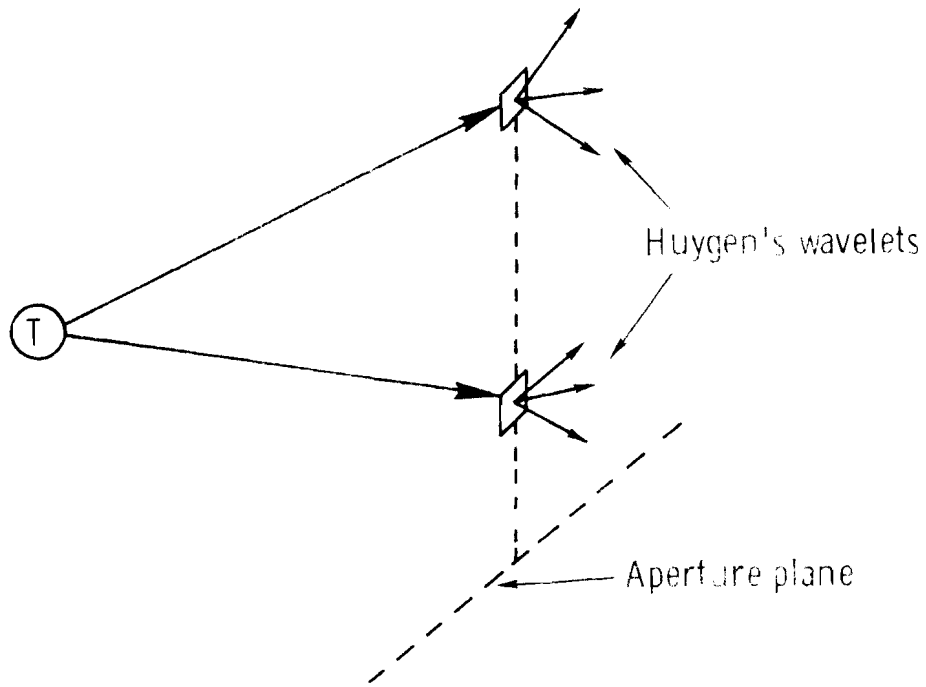

Fig.4-1. Huygen's principle.

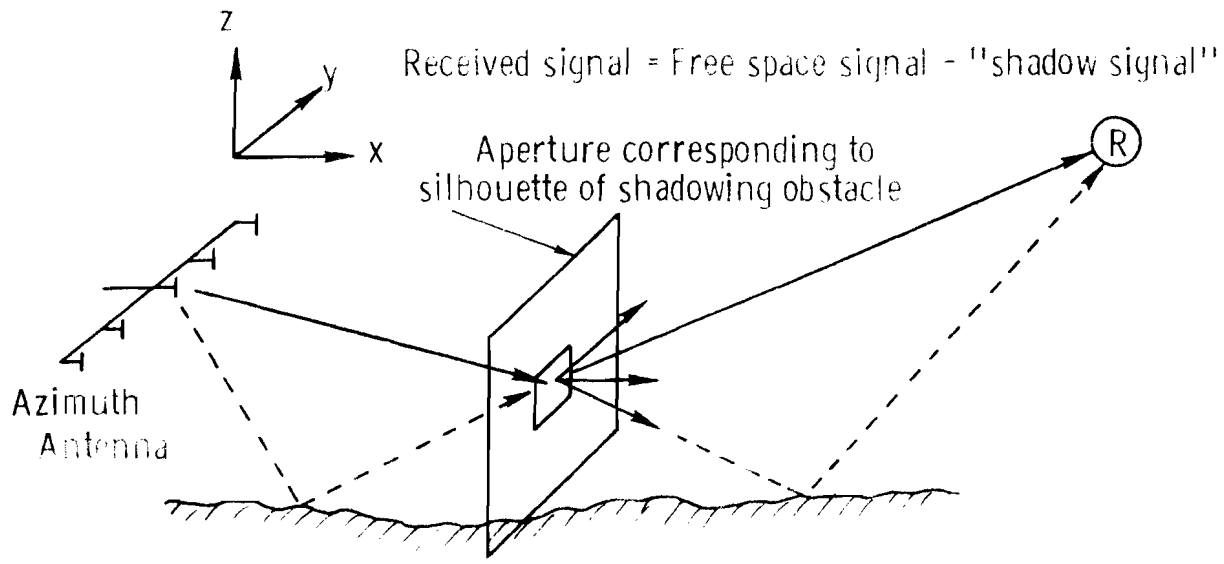

Fig.4-2. Huygen's principle applied to "shadowing signal" computation.

(1) take the unshadowed signal to be the sum of the direct signal and a "normal" ground reflection

and (2) introduce four shadowed signal components corresponding to the four wavelet paths of Fig. 4-2

As was the case with building and aircraft reflections [29], the diffraction signals on these four paths can be computed by considering all possible combinations of the ground antenna and its image together with the airborne antenna and its image.

However, a subtle difference now arises in the modeling when the LOS is blocked by an obstacle which has a large dimension in the direction of angle scan* In the initial model, there was only one diffraction path associated with the ground antenna and its image. When the LOS** was blocked, the diffraction ray at the angle of the LOS was combined with the LOS signal and the two treated as a single composite signal. This summation was deemed useful since only one rectangle could block a given LOS and, because it was possible to clearly distinguish between shadowing of the nominal direct signal versus the nominal ground reflection. However, the paths involving the image airborne antenna cannot be as easily allocated. Therefore, the separate identity of all signal components is maintained in the refined model, whether or not the LOS is blocked.

B. Refined Representation of Elevation Angles in Shadowing of MLS Azimuth

There is a small error introduced in the modeling when the ground antenna pattern is rapidly varying in the direction orthogonal to the scan direction (e.g., the elevation pattern of the azimuth array). When the direct signal LOS is blocked by an obstacle, the net direct signal propagates around the obstacle edges (e.g., the net azimuth signal at the direct signal angle propagates over the top of the obstacle). Thus, the net signal amplitude should be weighted by the ground antenna pattern in the direction of the obstacle edge as opposed to the pattern in the direction of the direct signal LOS.

*e.g., a very wide obstacle in front of an azimuth array.

**LOS here is from either the ground antenna or its image to the receiver.

The error introduced could be significant (e.g., several dB) if (1) a large obstacle were located close to the ground antenna and (2) the orthogonal pattern were rapidly varying at the angles of concern. Since the elevation pattern of the azimuth array is rapidly varying near the horizon, an option has been added to decompose the azimuth large obstacle blockage signal at the LOS azimuth angle into:

(1) a component at the LOS elevation angle with amplitude $A_{LOS} = -1$

(2) a component at the top edge of the obstacle with amplitude $A_{TOP} = .5 - (.5 + j.5)\ F(z_2)$

(3) a component at the bottom edge of the obstacle with amplitude $A_{BOT} = .5 + (.5 + j.5)\ F(z_1)$

where $F(\ )$, z_1 and z_2 are as defined in chapter VII of [29]. When the LOS corresponds to an image transmitter and/or an image receiver, the amplitudes above are weighted by the multiplicative factors described in chapters III and VII of [29].

C. Near Field Shadowing

1. Model Description

Shadowing of the ground antenna by objects (e.g., lighting structures or monitor poles) which are in the near field of the antenna is a problem of considerable practical importance, particularly for the azimuth array. The arguments used to provide the initial ray theory decomposition of the aperture field are not applicable in the near field case, since the amplitude and phase of the shadowed signal can vary rapidly as a function of position within the aperture. A fairly accurate approach to computing the error in such cases is the direct Fresnel integral approach due to Spiridon [30] which is described in Appendix B. However, a plane wave representation was deemed more appropriate for the present case since it would:

(1) permit the simultaneous consideration of reflection and shadowing phenomena within the context of the existing system models

(2) be able to utilize the far field antenna pattern models which had been validated from field tests

(3) yield insight into the error mechanism that would be useful in designing improved signal processors.

The basic ideas in the refined models are as follows:

(1) determine the received shadow signal* for the various elements of the ground antenna aperture by Fresnel diffraction

(2) since the aperture amplitude distribution of (1) is a strictly space limited function (e.g., it is zero for positions outside the aperture), it can be represented by a spatial Fourier series. The elements of the spatial Fourier series correspond to plane wave components.

(3) Plane wave components near the direct signal angle are of greatest concern.

The basis for (1) was discussed previously [29]. The Fourier series representation in (2) is a straightforward application of the classic sampling theorem [90]. The basis for (3) will be discussed subsequently.

The starting point for the mathematical development is the previous Fresnel integral expression for the signal diffracted through a rectangular screen

$$V = \frac{e^{j\pi/2}}{2} \left[F(\tilde{y}_2) - F(\tilde{y}_1)\right] \left[F(\tilde{z}_2) - (\tilde{z}_1)\right] V_o, \qquad (4\text{-}1)$$

Where

V_o = free space field

$$\tilde{y}_2 = \sqrt{2}(y_2 - y_s)\,(1 - \alpha_1^2)^{1/2}/R_f \quad , \qquad (4\text{-}2)$$

$$\tilde{y}_1 = \sqrt{2}(y_1 - y_s)\,(1 - \alpha_1^2)^{1/2}/R_f \quad , \qquad (4\text{-}3)$$

---

*the term "shadow signal" here refers to the signal propagating through one of the rectangular openings described in assumption (2) of Table 4-1

$$\tilde{z}_2 = \sqrt{2}(z_2 - z_s)\,(1 - \beta_1^2)^{1/2}/R_f \quad , \tag{4-4}$$

$$\tilde{z}_1 = \sqrt{2}(z_1 - z_s)\,(1 - \beta_1^2)^{1/2}/R_f \quad , \tag{4-5}$$

where α_1, β_1 are the direction cosines of the line of sight relative to the y', z'-axis, respectively, R_f is the Fresnel zone size and F(x) is the Fresnel integral as defined in [29]. The various displacements are defined in the rectangle oriented coordinate system shown in Fig. 4-3.

In Eq. (4-1), both V_o and V are functions of position within the ground array aperture by virtue of the dependence of y_s and z_s on ground antenna location. For the sake of exposition, we consider the case of an azimuth array where the shadowing rectangle is perpendicular to the x-axis, the line of sight lies along the x-axis and $\alpha_1 \approx 0$. With these assumptions, the received shadowing signal as a function of position within the ground antenna aperture is given by

$$V(y) = -\frac{V_o\, e^{j\pi/2}}{\sqrt{2}}\left[F(\tilde{y}_2 - \tilde{y}) - F(\tilde{y}_1 - \tilde{y})\right] \rho_z \tag{4-6}$$

where:

$$\tilde{y} = \sqrt{2}\ (K/R_f)y \tag{4-7}$$

y = lateral position along the antenna aperture relative to the antenna phase center

K = change in LOS y' value for a unit displacement along aperture ($\approx -R_r/(R_t + R_r)$]

$$\rho_z = [F(\tilde{z}_2) - F(\tilde{z}_1)]/\sqrt{2} \tag{4-8}$$

The function $V_{SH}(y) = 0$ for $|y| > L/2$, i.e., it is strictly space limited. By drawing the correspondence time $\longleftrightarrow$ y/λ, it follows from the sampling theorem for time series* that V(y) has a discrete Fourier series representation

$$V(y) = \sum_{m=-\infty}^{\infty} a_m\, e^{j2\pi \frac{y}{\lambda}(m\lambda/L)} \tag{4-9}$$

*See Appendix C.

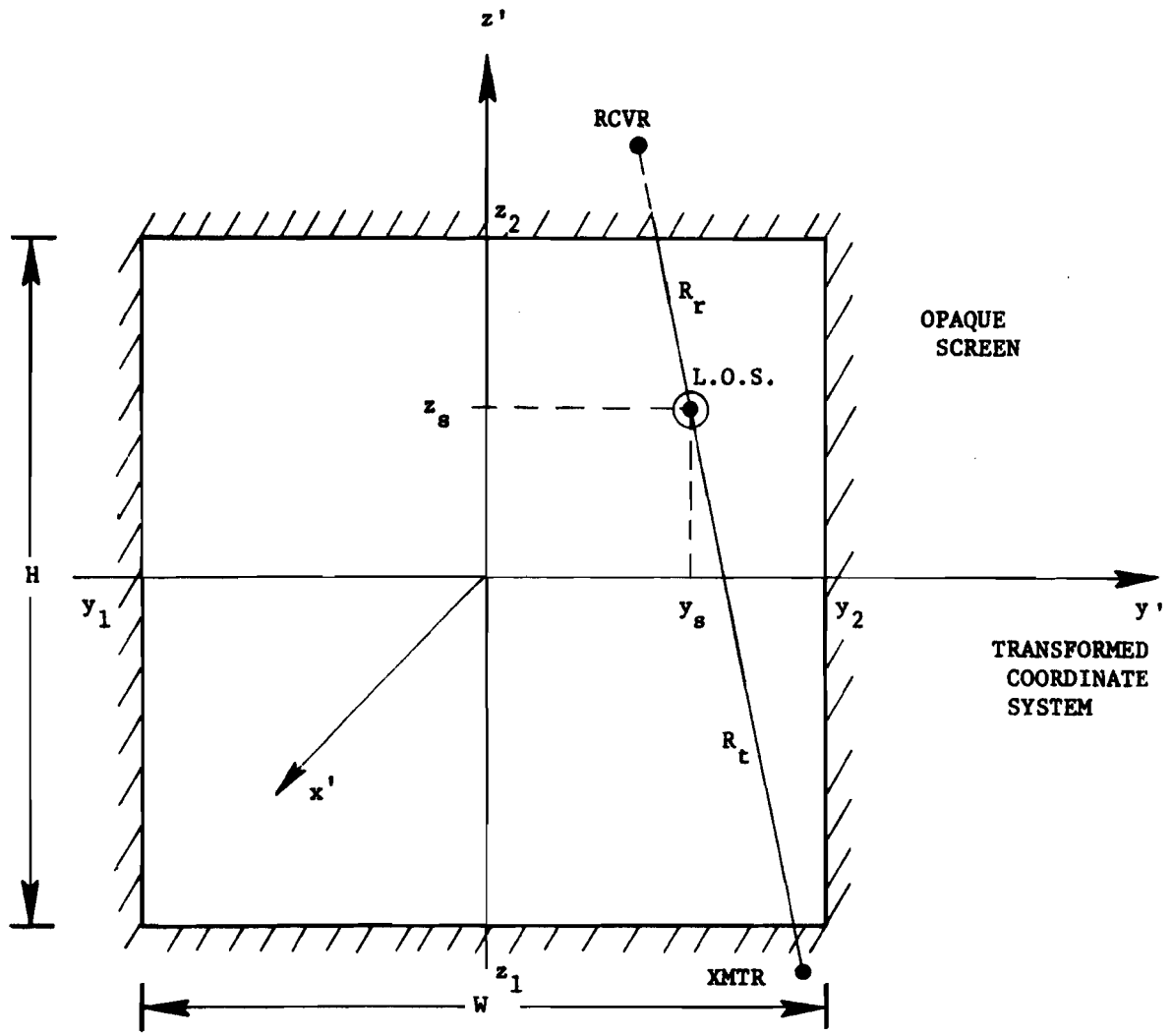

Fig. 4-3. Geometry for diffraction by rectangular opening in opaque screen.

where the Fourier coefficient (complex) amplitudes are given by

$$a_m = \int_{-L/2}^{L/2} V(y)\, e^{-j2\pi ym/\lambda}\, dy \qquad (4\text{-}10)$$

By drawing the further correspondence:*

$$\sin \theta_m = m\lambda/L \qquad (4\text{-}11)$$

we obtain:

$$V(y) = \sum_m a_m\, e^{j2\pi \frac{y}{\lambda} \sin \theta_m} \qquad (4\text{-}12)$$

which is the desired decomposition of the aperture distribution into plane waves at azimuths $\{\theta_m\}$ with complex amplitudes $\{a_m\}$.

In the actual computations, V(y) is numerically evaluated according to eq. (4-1) at a discrete set of equally spaced points within the aperture and the Fourier transform then computed at a discrete set of angles. N_p, the number of points within aperture at which V(y) is computed is user specified; numerical experiments to date have yielded similar results $11 \leq N_p \leq$ number of elements in the ground array.

Similarly, N_T, the number of Fourier decomposition terms is a user specified variable. The angles $\{\theta_m\}$ are centered about the direct signal azimuth (or, elevation) angle, with additional terms included for the:

(1) the vertical edge(s) of a large obstacle if that edge(s) is greater than λ/L away from all the elements of the LOS centered angle set

and (2) the center of a small obstacle if the center is greater than λ/L away from all the elements of the LOS centered angle set.

---

*This correspondence is valid for $|m\lambda/L| \leq 1$. The terms in (4-9) for $|m\lambda/L| > 1$ correspond to the evanescent waves of antenna theory.

To date, we have generally obtained good results for 5 terms centered on the LOS corresponding to the "inbeam" region for the TRSB system.

The basis for these choices of the expansion angles was a series of calculations for the shadowing situations such as the Australian scale model range geometry [38] shown in Fig. 4-4. Fig. 4-5 shows the plane wave magnitudes $|a_m|$ for the case of Fig. 4-4 based on 119 aperture evaluation points and L = 47 λ (a scaled version of the parameters of the Bendix testbed wide aperture TRSB antenna [66]). We see that the components at angles near the LOS are largest in magnitude until the LOS is well removed from the obstacle edge. When the LOS just intersects the obstacle edge,

(1) the component at the LOS angle has a magnitude $\simeq$ 1/2 of the direct signal (as would be expected from knife edge diffraction theory)

(2) the "inbeam" components at separation angles $\pm \lambda/L$ (= $\pm$ 1 "standard" beamwidths) have approximately equal magnitudes, but opposite signs.

Results such as shown in Fig. 4-5 are viewed as being of fundamental importance in the design of improved signal processors to reduce shadowing effects. The existence of shadowing components on both "sides" of the direct signal when the LOS is nearly blocked means that care must be taken in 1) utilizing a signal processor which attempts to determine the "side" of the direct signal with the least multipath and/or 2) projecting shadowing performance on the basis of simulation and/or bench test results where only a single multipath component is present.

2. Model Validation

The model validation has been accomplished by comparison with analytical results, Australian scale model range tests and full scale field tests on the TRSB and DMLS systems. As mentioned earlier, the comparison with field test data using the previous shadowing model is contained in volume II of this report. Here, we are concerned principally with those situations where the previous model was deficient; namely large obstacles with an edge near the LOS and obstacles within the near field of the antenna.

a. Shadowing By a Large Obstacle

The case of a large obstacle with one edge near the LOS is an

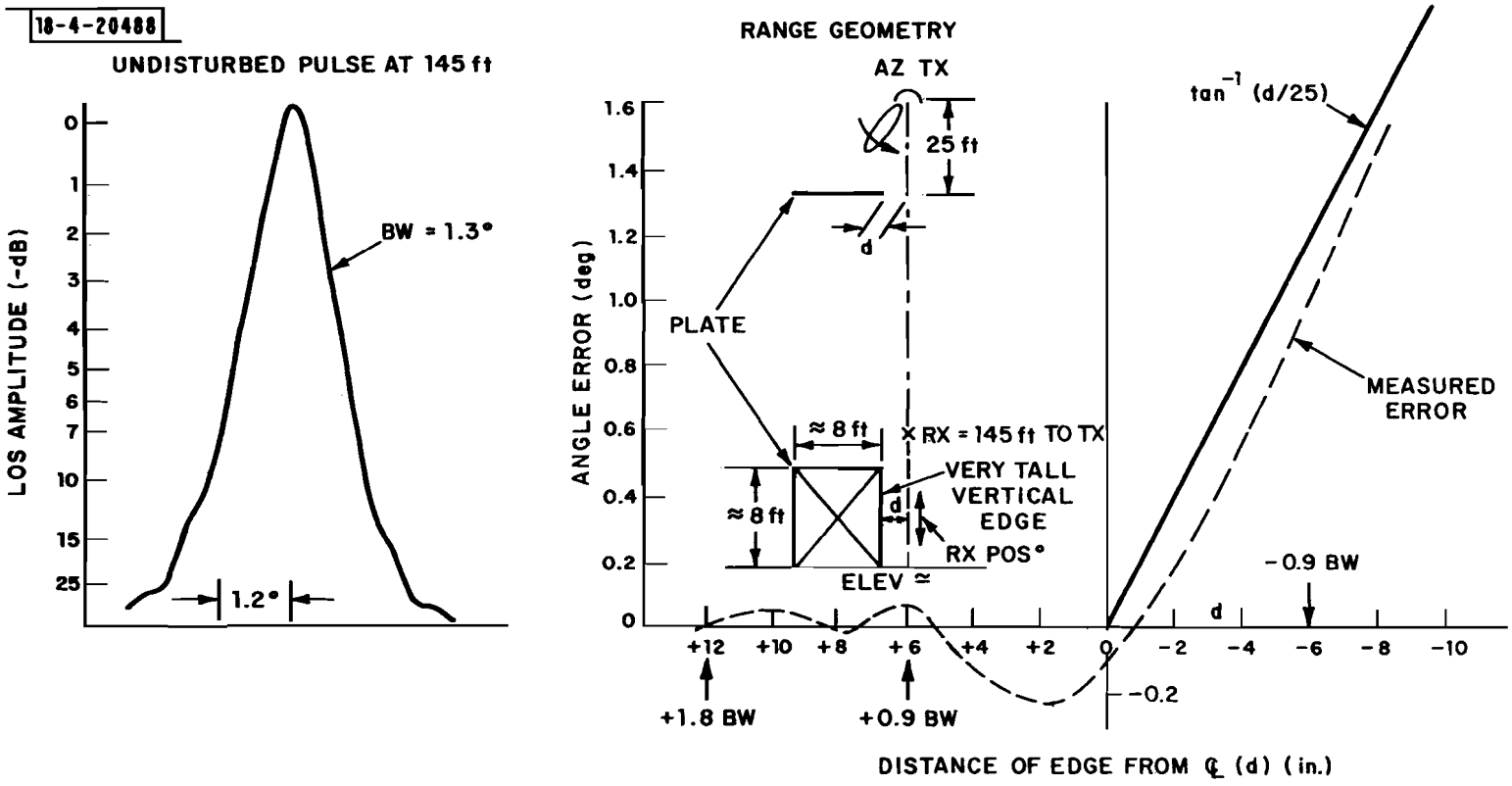

Fig. 4-4. Australian 20:1 scale model range data.

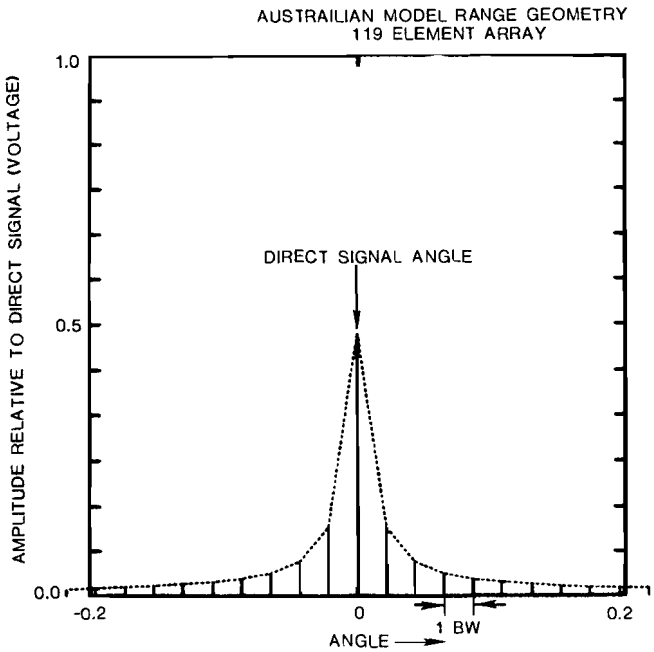

Fig.4-5(a). "Shadowing signal" components when LOS is at edge of blocking obstacle.

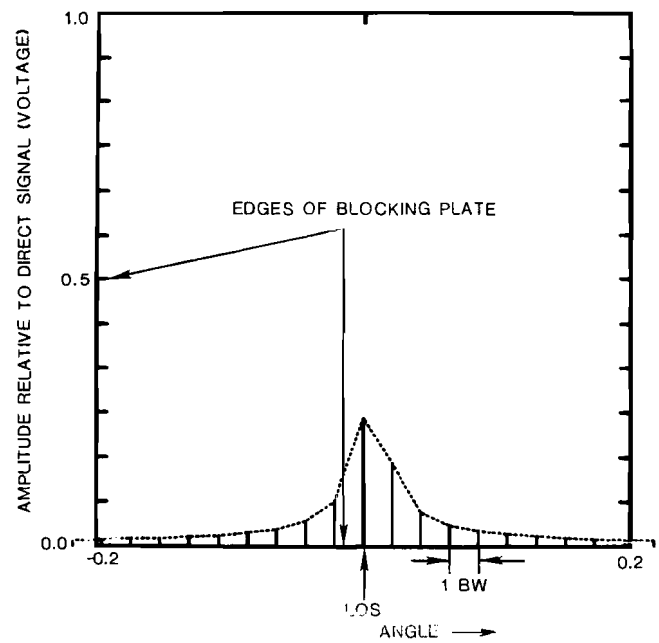

Fig.4-5(b). "Shadowing signal" components when LOS is 0.6 BW from the blocking plate.

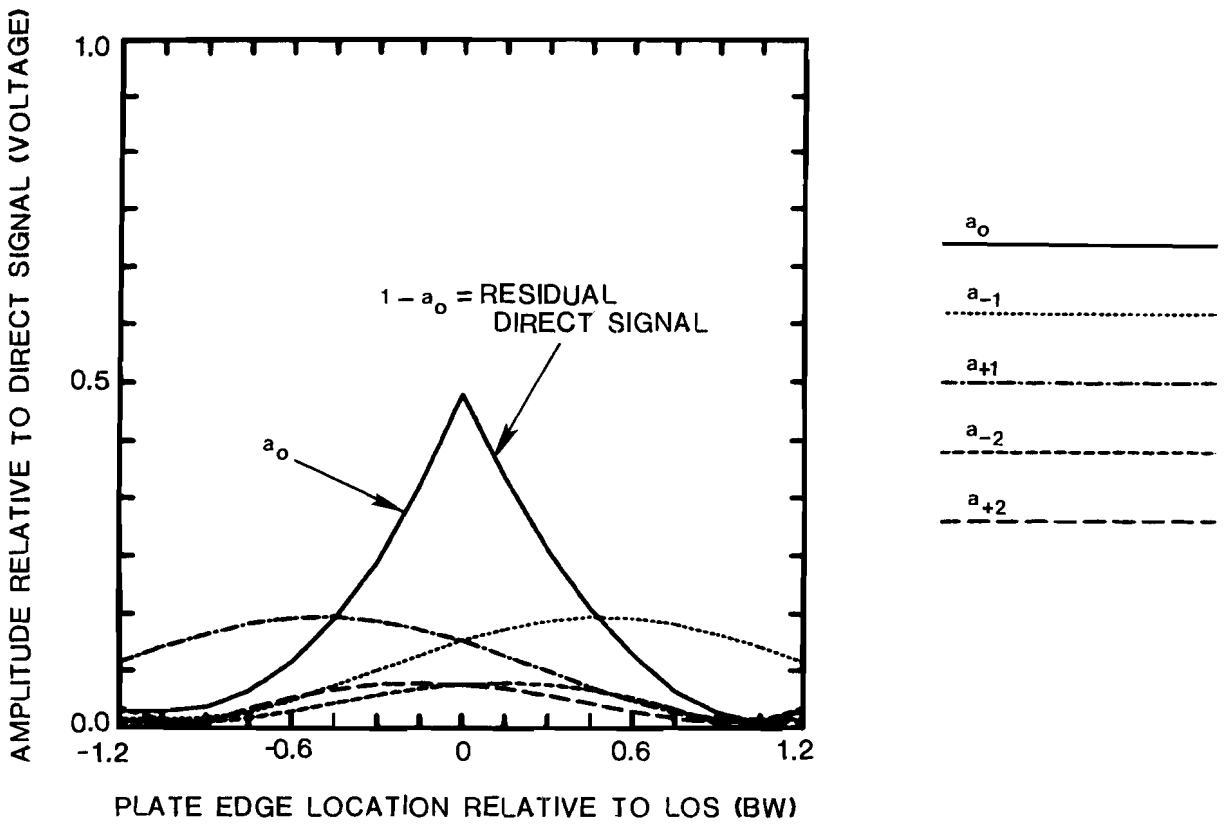

Fig.4-5(c). Variation in "shadow signal" component amplitudes vs LOS location.

important canonical case since the results for other obstacles can be obtained by superposition of the large obstacle results. In particular, we consider the azimuth case since that is the situation which was studied extensively in the Australian scale model work. Fig. 4-4 showed one such result. We note that when the LOS is blocked (d<0), the angle error increases proportional to the angular separation between the LOS and the edge. This 1:1 proportionality is expected from the following simplified physical model:

(1) The received signal is the sum of a signal propagating over the top with the direct signal azimuth angle code and a signal propagating around the edge with the angle code corresponding to the edge.

(2) When the LOS is much closer to the side edge than the top, then the edge coded signal dominates and the indicated azimuth is essentially that of the edge.

(3) Thus, as long as condition (2) holds, the angle error is the angle separation between the LOS and the edge.

This argument is quite reasonable physically and can be justified mathematically [29] when the physical separation between the edge and LOS (d in Fig. 4-4) is greater than the Fresnel zone radius and the obtacle is in the antenna far field. However, it yields a zero angle error when the LOS just intersects the blocking obstacle whereas it is clear the angle error cannot be zero since there is no signal received from the area on one side of the LOS.

Figs. 4-6 shows the computed evelopes and angle erros for a 1.3^{o} beamwidth line array with 119 aperture computation points. Comparing Fig. 4-6 to Fig. 4-4, we note that the behavior for large |d| is quite similar; however, the scale model errors and the computed errors differ as to the sign of the error when d=0. Figures 4-7 and 4-8 compare scale model and computed envelopes. These are similar when the LOS is clear (d<0); however, there is a noticeable bump on scale model envelopes which does not appear on the computed envelopes.

In an effort to better understand these differences, analytical studies were carried out for the case when a very wide and tall plate blocks the

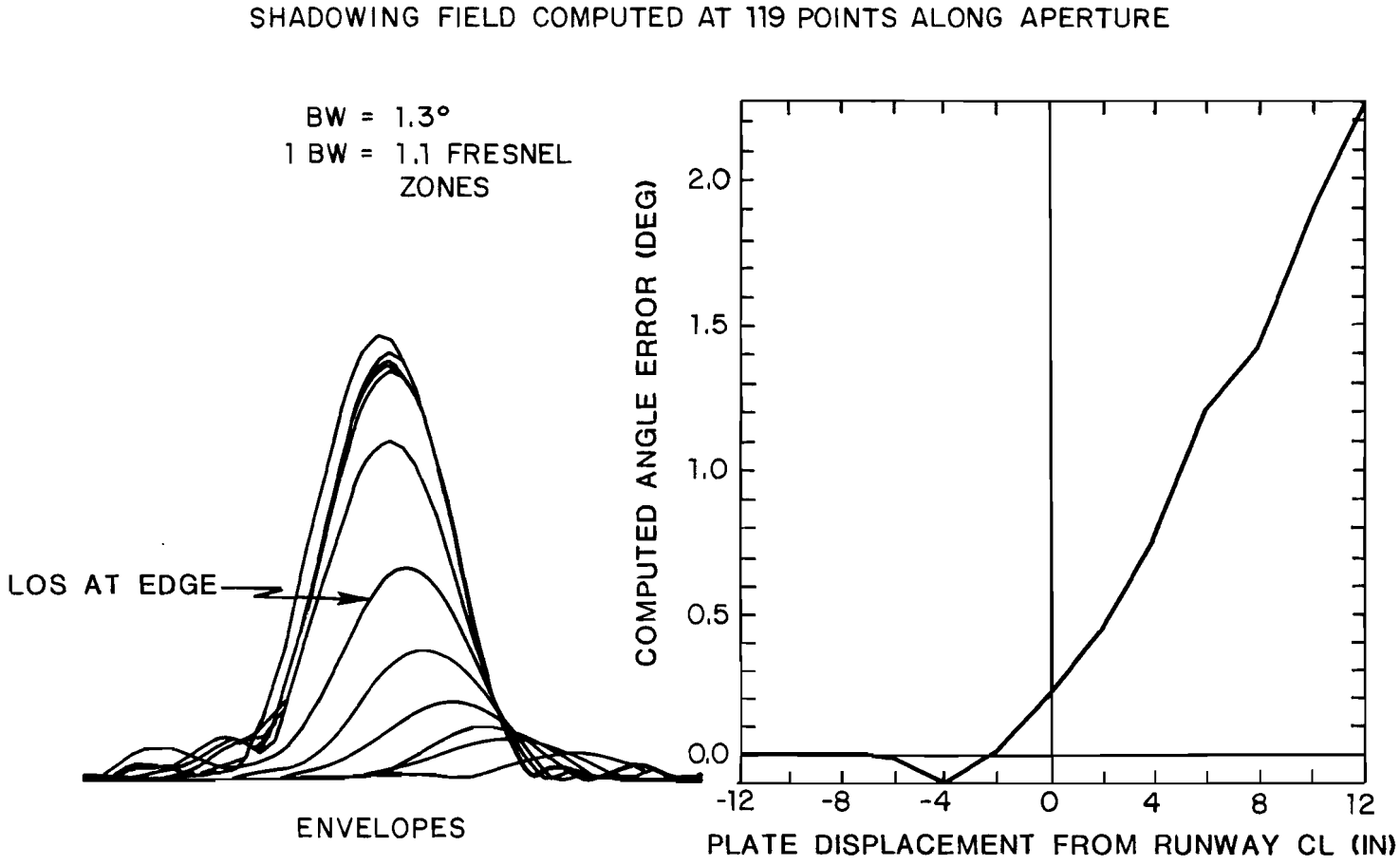

Fig. 4-6. Computed envelopes and errors for Australian shadowing case.

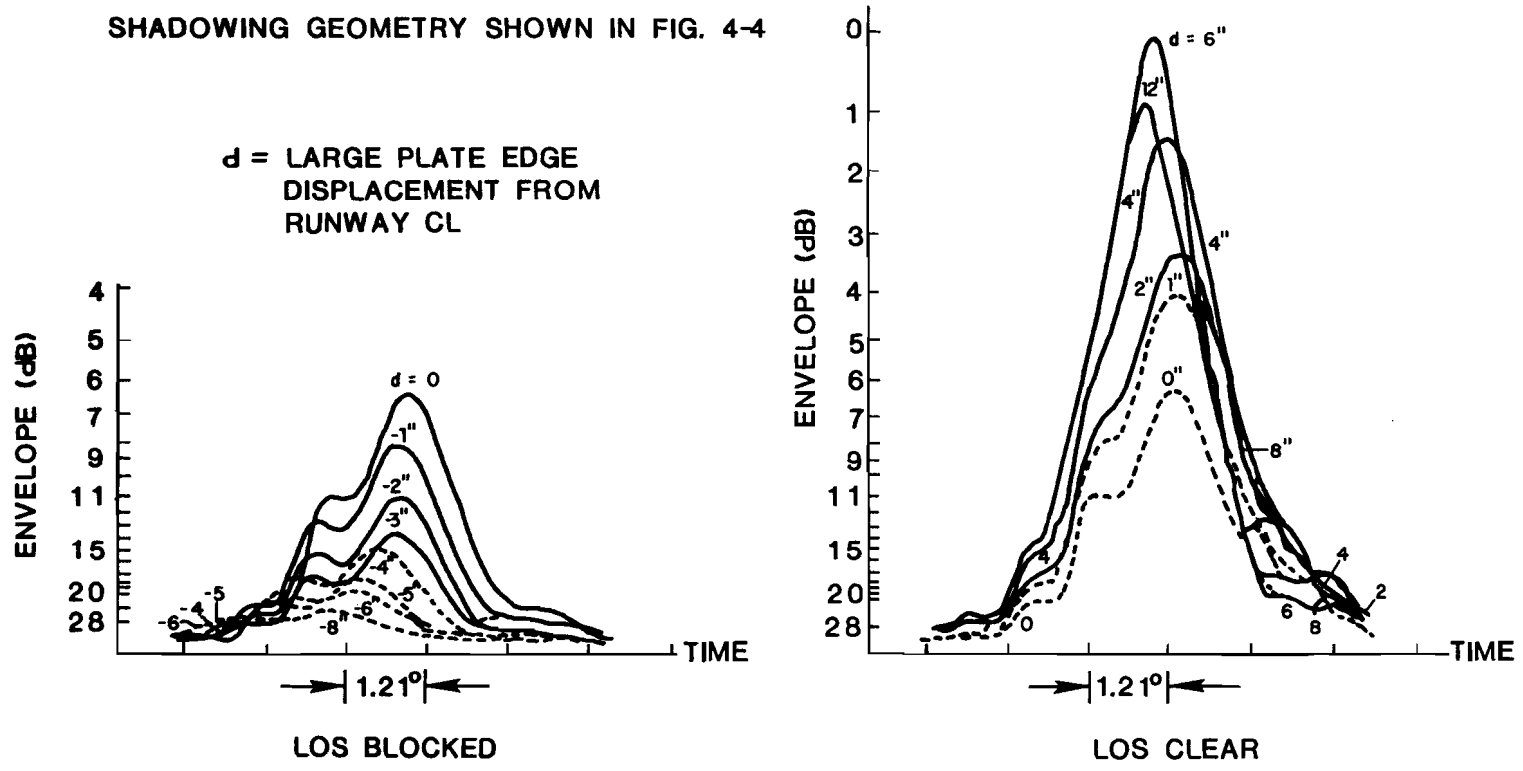

Fig. 4-7. Australian scale model range envelopes.

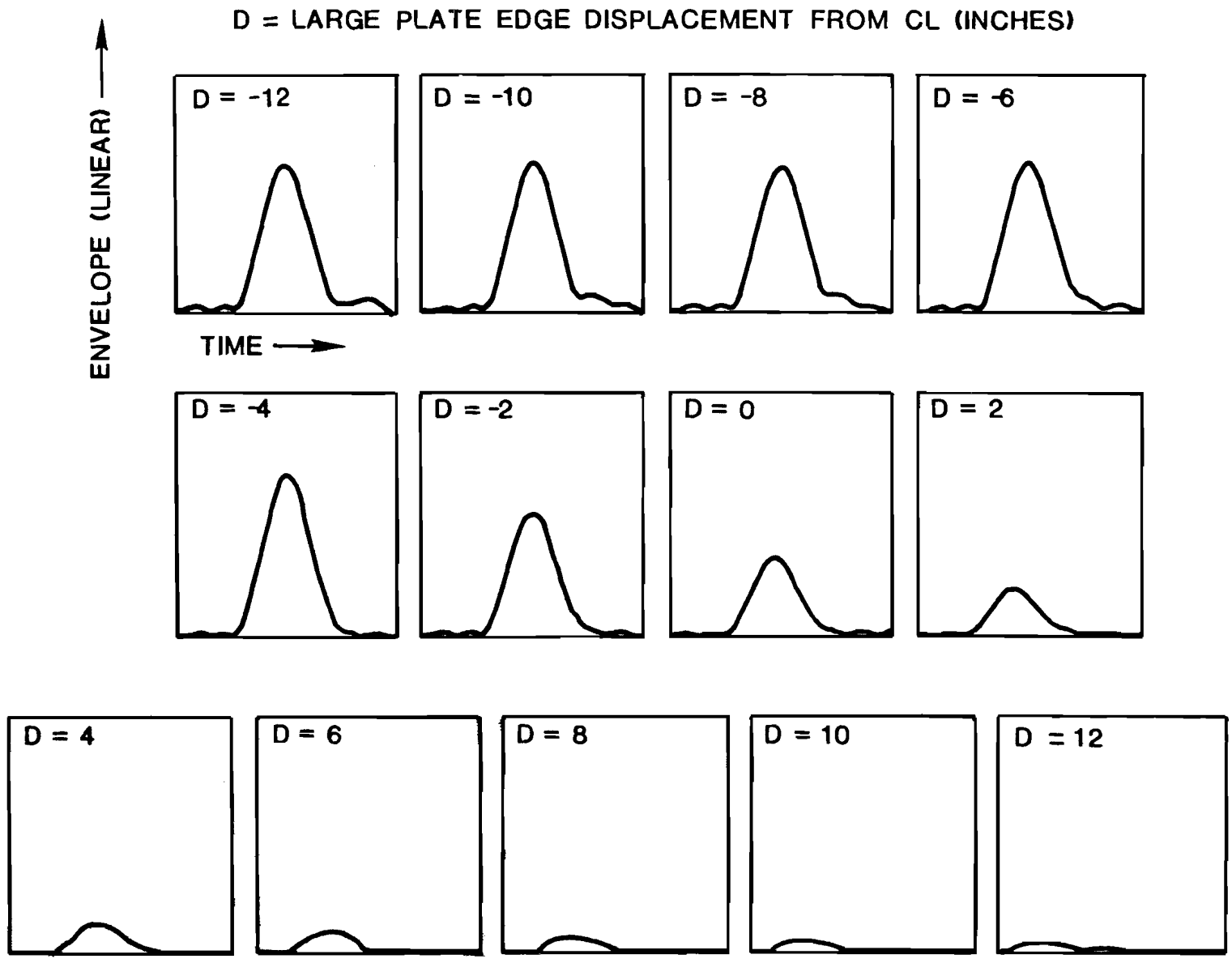

Fig. 4-8. Expanded view of computed envelopes for Australian scale model range geometry.

region y<0. In this case, eq. (4-6) becomes

$$V_{sh}(y) = + \frac{e^{j\pi/4}}{\sqrt{2}} F\left(\sqrt{2}\,\frac{Ky}{R_f}\right) - 0.5 \qquad (4\text{-}13)$$

For small values of the argument, $F(u) \sim u(1-j\pi u^2/6)$. Retaining only the linear term, we obtain

$$V_{sh}(y) = -0.5 + e^{j\pi/4}\ K\, y/R_f \qquad (4\text{-}14)$$

The net received envelope for for a receiver on centerline (see appendix C) is the aperture distribution weighted Fourier transform of the shadowing signal plus the direct signal [$V_{direct}(y) = 1$]:

$$V(u) = \left| 0.5 \int a(y)\, e^{j2\pi yu/\lambda} dy + \frac{e^{j\pi/4}}{R_f}\ K \int y\, a(y)\, e^{j2\pi yu/\lambda} dy \right|$$

$$= \left| 0.5\ \ G(u) + \frac{e^{j\pi/4}}{R_f}\,\frac{K\lambda}{2\pi}\ \ \frac{d\,G(u)}{du} \right| \qquad (4\text{-}15)$$

where

$u = \sin\theta$
θ= scan angle
$G(u)$= far field pattern of array with aperture weight $a(y)$.

This expression is equivalent to the expression obtained for an unshadowed direct signal plus an interfering signal of amplitude

$$\rho(u) = \frac{e^{\ j\pi/4} K\lambda}{\pi\ R_f}\ \ \frac{d\,G(u)}{du} \qquad (4\text{-}16)$$

The approximate TRSB dwell gate processor angle error is

$$\varepsilon \approx \frac{1}{2}\left[\frac{\mathrm{Re}\,[\rho(+t)]}{S\,(+t)} + \frac{\mathrm{Re}[\rho(-t)]}{S\,(-t)}\right] \qquad (4\text{-}17)$$

where $S(\pm\ t)$ is the slope of the beam pattern at the nominal threshold crossing angles $\pm t$.

For small beamwidths characteristic of MLS, $\sin\theta \sim \theta$, so that (4-17) becomes

$$\varepsilon = \frac{K}{\sqrt{2}\,\pi\,(R_f/\lambda)} \quad \text{radians} \qquad (4\text{-}18)$$

independent of the antenna pattern or beamwidth. The actual beamwidth/aperture enters in by restricing the region for which the approximation made in obtaining (4-14) is valid, while the beamshape (i.e., aperture weighting) affects the validity of eq. (4-14). Applying (4-18) to the shadowing geometry of Fig. 4-4 when d-0, we obtain

$$\varepsilon = 0.223°$$

which agrees quite well with the computed results in Fig. 4-6.

The validity of the linearized approximation to F(), used in obtaining eq. (4-14) improves as the distance between the obstacle and the transmitter increases (e.g., at a distance = $2L^2/\lambda$, the cubic term is $\frac{1}{8}$ that of the linear term). Thus, calculations of the error for a large plate with one edge on centerline were carried out as a function of distance to the obstacle with the results shown in Fig. 4-9. We see that the simplified analytical formula gives a result which is quite close to the Fourier decomposition results for "far-field" obstacle-transmitter separation. It is worth noting that eq. (4-18) was obtained without any use of the Fourier series decomposition [eq. (4-9)]. Thus, the good agreement shown also provides a degree of validation for the Fourier series decomposition modeling.

However, there still remains a discrepancy between the Australian scale model results and the various computational results as to the sign of the error when a large obstacle edge is very near the LOS. For the line arrays used in the US MLS program and modeled in the MLS multipath simulation, a variety of physical arguments can be advanced to support the error sign obtained above.* These line arrays have a well defined phase center which is stationary during the scan. The Australian full-size and scale model MLS azimuth arrays are typically

---

* e.g., the Huygen's wavelets, (recall Fig. 4-1), which reach the receiver all have the angle codes corresponding to the unblocked portion of the aperture plane. Since this unblocked portion in Fig. 4-4 corresponds to positive azimuths, the resulting indicated angle (and, angle error) on centerline for d=0 should be positive.

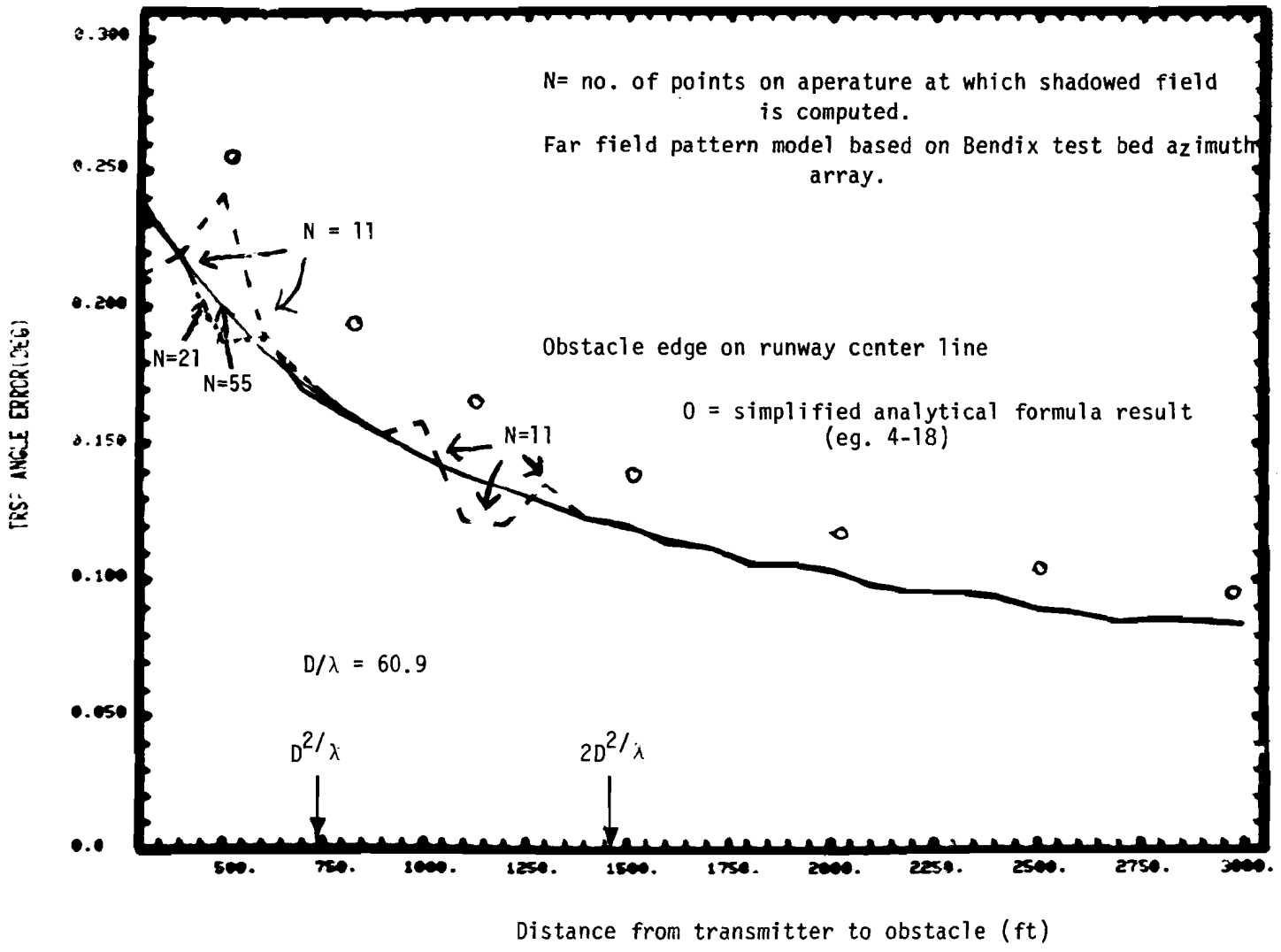

Fig.4-9. Comparison of refined shadowing model with simplified analytical formula for large obstacle just blocking the line of sight.

torus reflectors in which the illuminated portions of the reflector translates physically as the antenna scans. Consequently, the (small) differences which exist between the scale model range and computed results may have their origin in the method of antenna scanning.

Another factor which may also contribute to these differences is the effect of ground reflections on either side of the screen. As long as the signal propogating over the top of the blocking aperture is much smaller than the net received direct signal, this should not be an important factor. The effective height of the scale model range azimuth array phase center was not available, so exact quantitative calculations could not be carried out. However, since the signal propogating over the top of the blocking plate should be some 34 dB lower in amplitude than the X-O-R signal propogating around the plate, it seems unlikely that the ground reflections and the elevation pattern of the Australian scale model could account for all the differences.

B) Shadowing by a small obstacle

Shadowing errors due to small obstacles such as monitor poles located in the near field of the MLS ground antenna was observed in many of the MLS field trials. Unfortunately, in most of these cases, both precise tracking data and detailed data on the shadowing geometry were not available. One case where fairly detailed investigations were carried out occurred at the NAFEC test site of the Bendix phase 3 small community antenna. Fig. 4-10 shows the geometry for one of the van tests made at that site to better understand effects seen in the flight data on that system. Fig. 4-11 shows a close-up view of the monitor horn.

Figures 4-12 and 4-13 show the measured angle errors with the monitor pole down and up respectively. The difference between the two represents a combination of the error due to shadowing and tracker errors (the transmitter to receiver distances are quite small and the tracking theodolite data was not film corrected.) Also shown on Fig. 4-13 are several o's which are the difference between figures 4-12 and 4-13 at several selected angles. Due to the symmetry of the shadowing

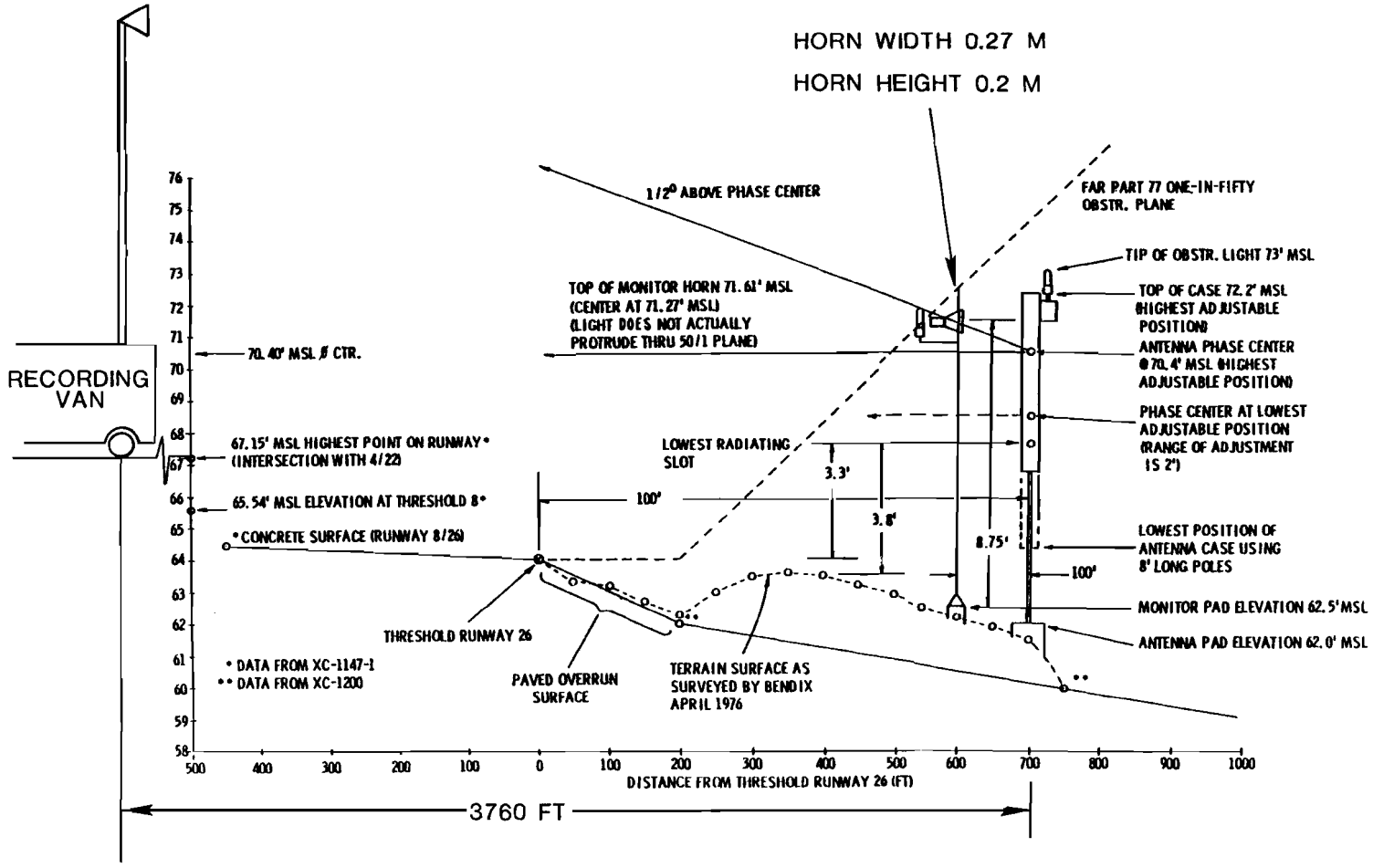

Fig. 4-10(a). SC AZ siting (elevation view), runway 26 at NAFEC.

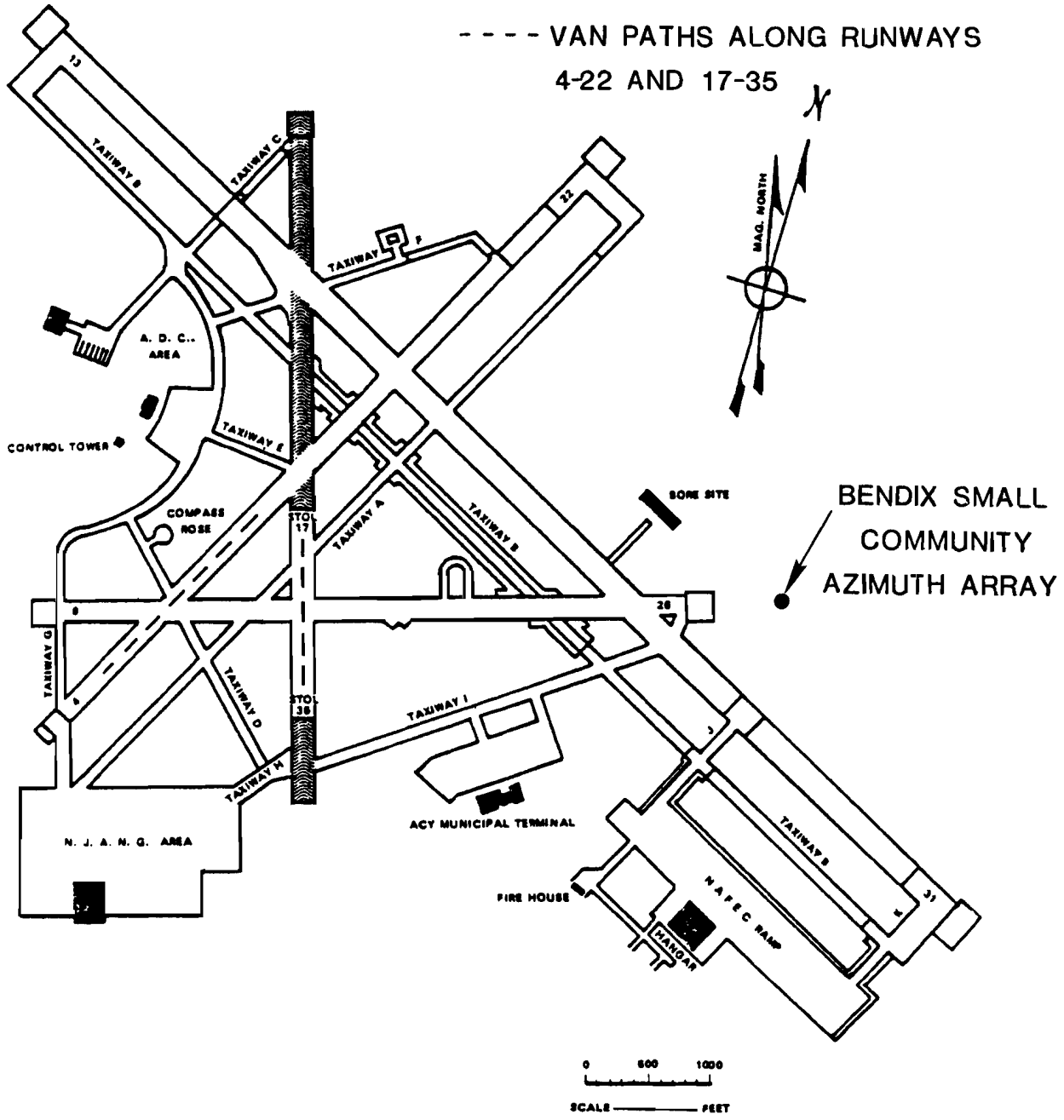

Fig. 4-10(b). Geometry for small community azimuth tests at NAFEC/Atlantic City Airport, Atlantic City, New Jersey.

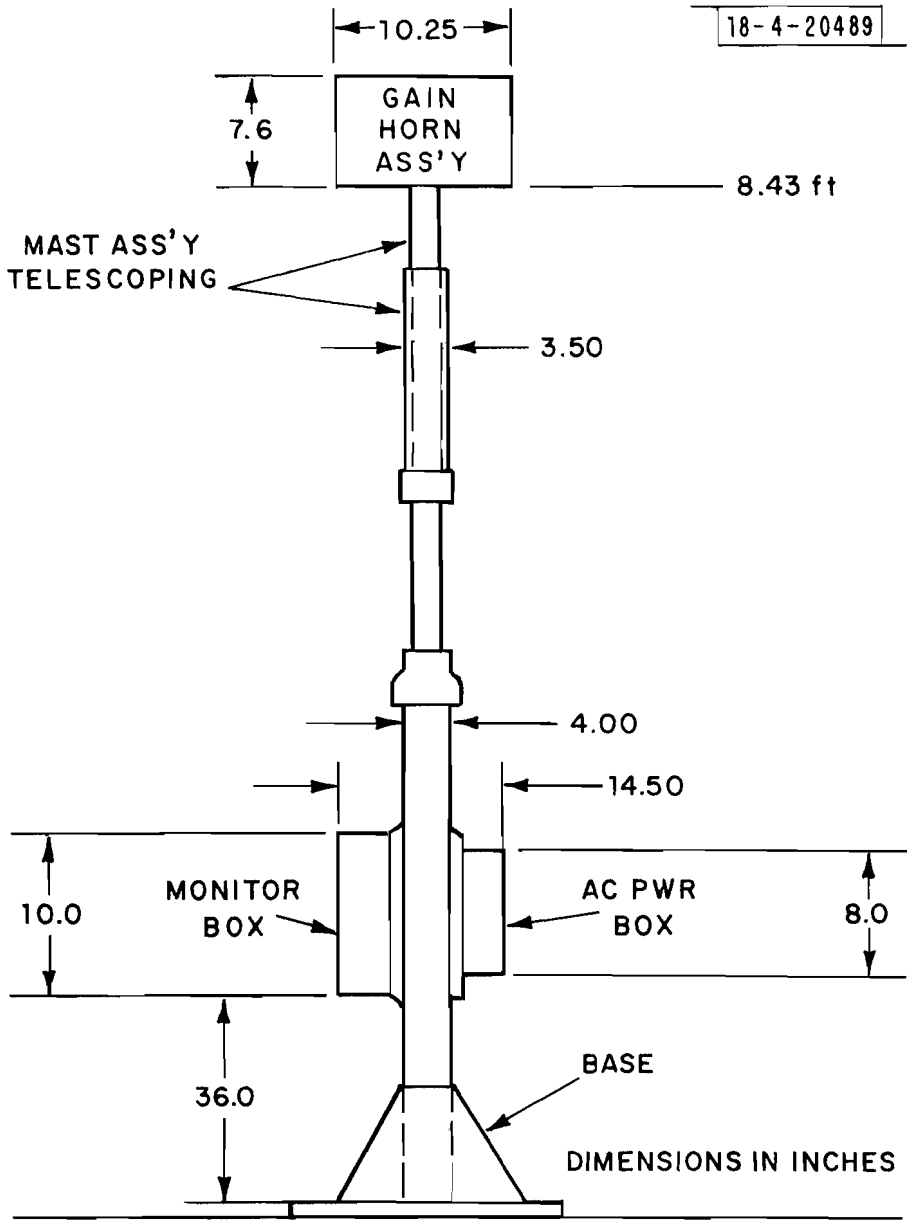

Fig. 4-11. Small community azimuth monitor.

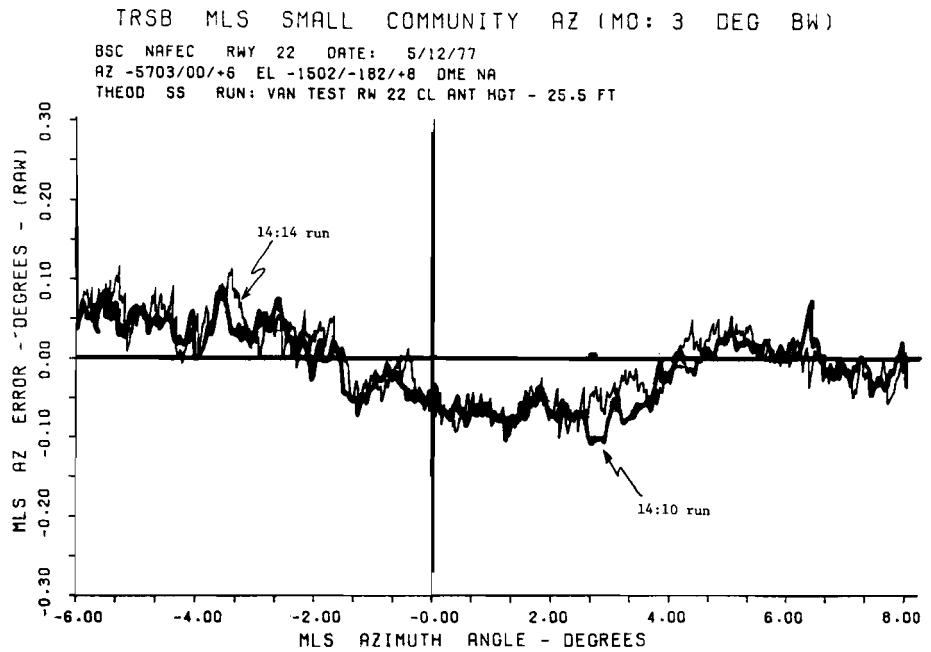

Fig.4-12(a). TRSB azimuth antenna error with monitor pole down.

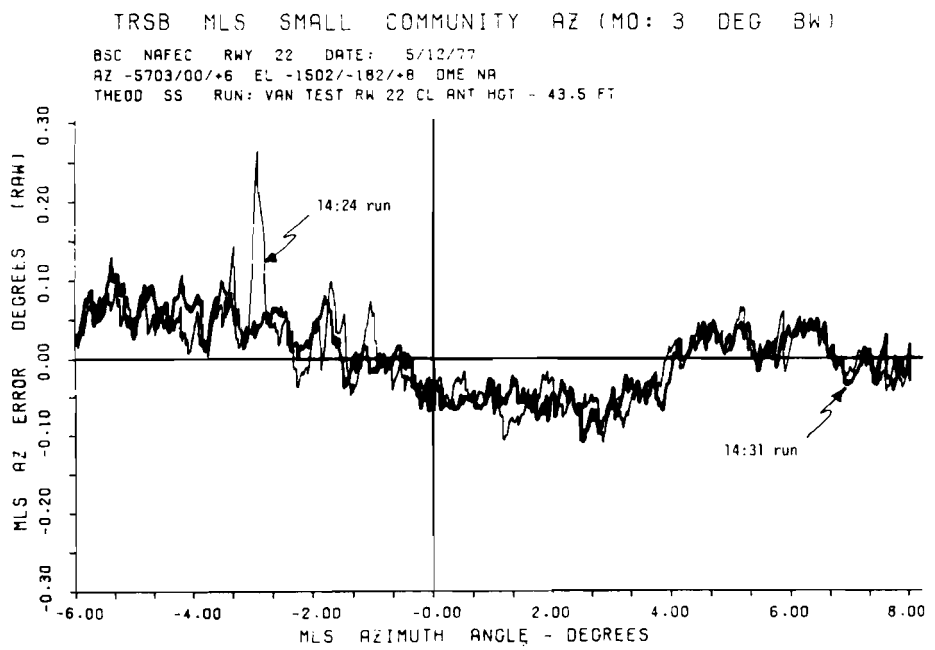

Fig.4-12(b). Bendix small community TRSB azimuth error with monitor pole down.

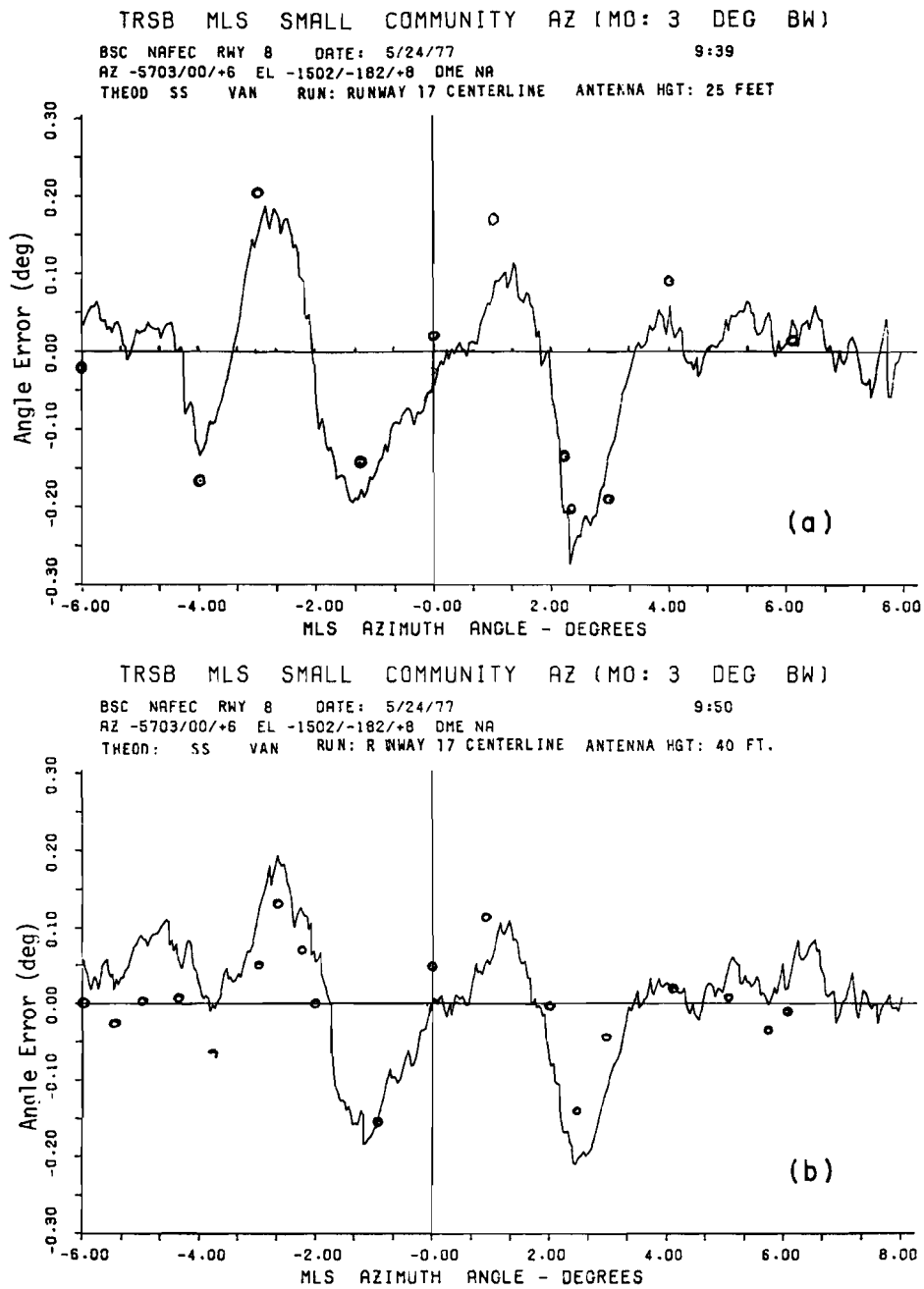

Fig.4-13(a-b). (a) TRSB angle error with normal monitor position. (b) Bendix small community TRSB azimuth errors with shadowing by monitor pole.

obstacle about runway centerline, the shadowing error should be antisymmetrical about centerline and zero on centerline. We see that the o's in Fig. 4-13 generally meet this condition to within a tolerance of 0.03° except at 3° (difference of 0.09°) and 4° (difference of .06°).

Since certain dimensions of the small community monitor structure were comparable to a wavelength, it was necessary to look more closely at the assumption that the pole could be modeled by its silhouette. It is well known [81] that when the object size is comparable to a wavelength, resonances can occur which substantially increase the radar backscatter reflection levels. The physical phenomena which is of concern here involves surface currents which "creep" around the object into the "not illuminated" region and then give rise to additional scattered signals.

Most of the scattering literature has focused on back scatter (due to the radar applications) whereas we are primarily concerned with forward scattering. Closed form results are not available for most objects of interest; however, some insight can be obtained from considering the results for spheres (which are "small" in both dimensions) and infinite cylinders (which are "small" in a single dimension).

Figure 4-14a shows results obtained by Barrick [81] for the scattering width of a vertical infinite cylinder with vertical polarization. The forward scattered field (i.e., "shadowing signal") is proportional to the square root of the scattering width:

$$E_s \approx \frac{\sqrt{\sigma}}{\sqrt{2\pi r}} \qquad (4\text{-}19)$$

where r = distance from obstacle to the ground antenna for a receiver which is very far away

and

$k_o = 2\pi/\lambda$.

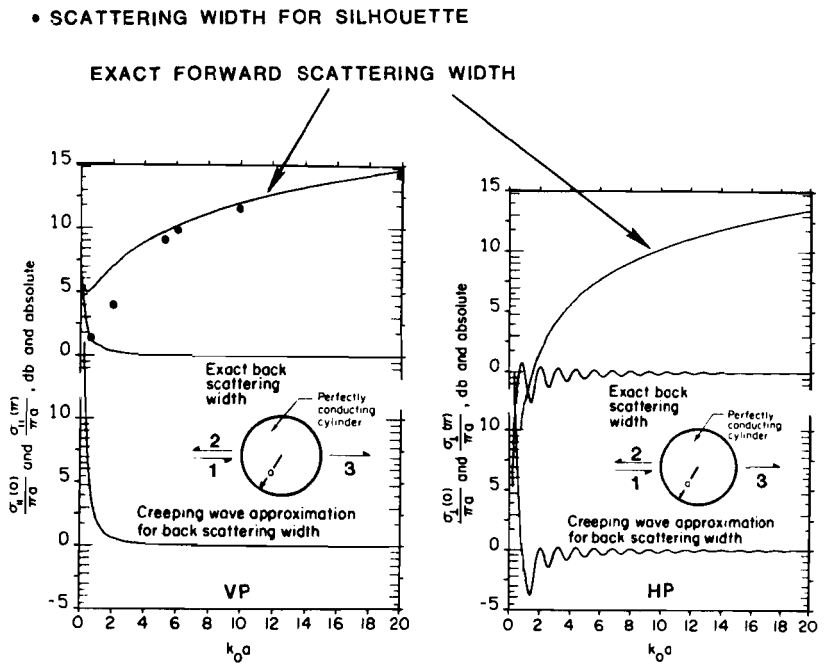

Fig.4-14(a). Exact solution and the creeping wave approximation for the backscattering widths, and exact forward scattering widths for an infinitely long, perfectly conducting circular cylinder.

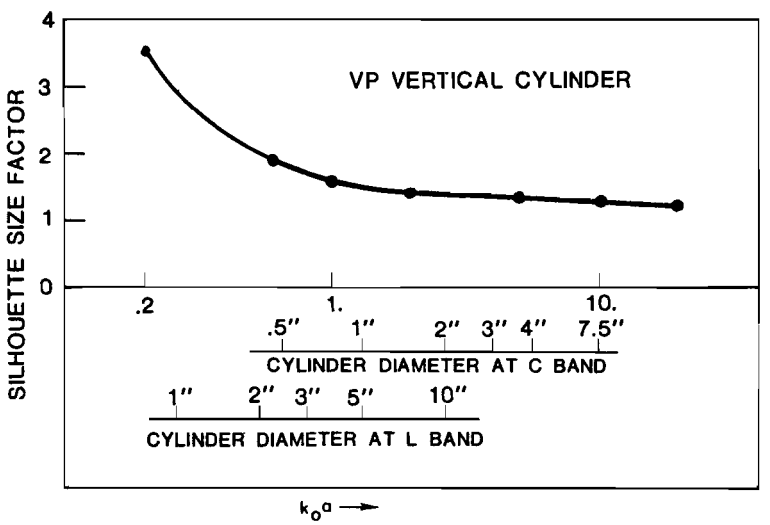

Fig.4-14(b). Factor by which cylinder silhouette dimension must be multiplied to yield equivalent forward scattered signal.

When the cylinder radius is very large, ($k_o a > 20$), Barrick [81] states that

$$\sigma = 4\, k_o a^2 \qquad (4\text{-}20)$$

The scattering amplitude expected from the silhouette is

$$E_s \approx \frac{\text{diameter}}{\text{Fresnel zone radius}} = \frac{2a}{\sqrt{\lambda r}} \qquad (4\text{-}21)$$

which agrees precisely with the amplitude obtained by substituting (4-20) into (4-19). Consequently, if the forward scattering is determined by the silhouette, the back scatter width in Fig. 4-14 should be proportional to ($k_o a^2$). The small dots in Fig. 4-14a correspond to the forward scattering width as $k_o a \rightarrow \infty$ being scaled down proportional to $(k_o a)^2$. We see that the exact widths become increasingly greater than those expected from the silhouette as $k_o a \longrightarrow 0$.* This suggests defining a width multiplication factor by which the cyclinder physical diameter should be increased so that the silhouette forward scattered amplitude is equal to the cyclinder forward scattered amplitude. This factor is plotted in Fig. 4-14b.

Exact computation results are not available for forward scattering by a finite length cyclinder typical of actual monitor poles. However, the discussion in Barrick [81] suggests that the forward scattered signal from a finite length cyclinder has the same functional dependence as does that from an infinite length cyclinder. Consequently, in modeling the monitor pole of Figure 4-11, the pole width of 4" ($k_o a = 4.6$) was increased by 15%.

Monitor boxes or horn antennas are typically small in both dimensions. To the best of our knowledge, no quantitative results are available for the forward scatter from such objects. However, some insight can be obtained by considering results for forward scatter from a sphere. Analogous to radar backscatter cross-section studies, the forward scattered field from a sphere is proportional

---

* This increase corresponds to the well-known phenomena in antennas whereby the gain of a vertically polarized azimuth array is decreased proportional to the horizontal width as long as that width is many wavelengths in extent, and then approaches a constant asymptotic value as the width becomes less than $\lambda/2$.

to the square root of the forward scattering cross-section

$$E_s \approx \frac{\sqrt{\sigma}}{\sqrt{4\pi r}} \quad . \tag{4-22}$$

Physical optics (ie., silhouette considerations) calculations yield

$$\sigma = \frac{4\,A^2}{\lambda_o^2} = k_o^2\,\frac{A^2}{\pi} \tag{4-23}$$

and

$$E_s = \frac{\text{area}}{R_f^2} = \frac{A}{\lambda_o r} \tag{4-24}$$

for an object of subtended area A. For spheres, (4-23) and (4-24) are accurate for $k_o a > 20$ [81]. Barrick [81] suggests the semiempirical formulas

$$\sigma = \pi a^2 \left[k_o\ a + \frac{2}{5}\right]^2 \quad \text{for } 1 \leq k_o a < 20 \tag{4-25}$$

and

$$\sigma = \pi a^2\ (k_o a)^4 \quad \text{for } k_o a < 0.5 \tag{4-26}$$

Proceeding as was the case for infinite cyclinders, we can define a size factor

$$F(k_o a) \triangleq \left[\frac{\sigma\ (k_o a)}{k_o^2\ \pi^2\ a^4}\right]^{1/4} \tag{4-27}$$

by which the physical dimensions should be multiplied so that the silhouette forward scattered field amplitude equals that of the sphere. Figure 4-15 plots F as a funtion of $k_o a$ using eqs. (4-25) and (4-26) in (4-27). We see that in contrast to cyclinders, the silhouette of a sphere <u>overbounds</u> the forward scattered signal amplitude when the object is quite small ($a < 0.1\ \lambda$). At C band, this effect is of little import since virtually all objects are at least one wavelength in diameter. However, at L band this "small object suppression effect" could be of some aid in reducing errors.

Returning to the modeling of the Bendix small community monitor structure we want to consider now the monitor box which is several wavelengths in extent horizontally and vertically. Very crudely approximating it as a sphere with $k_o a = 12$, we see that from Fig. 4-15 that the silhouette which approximates the sphere would be 2% larger than the sphere itself. This suggested that the

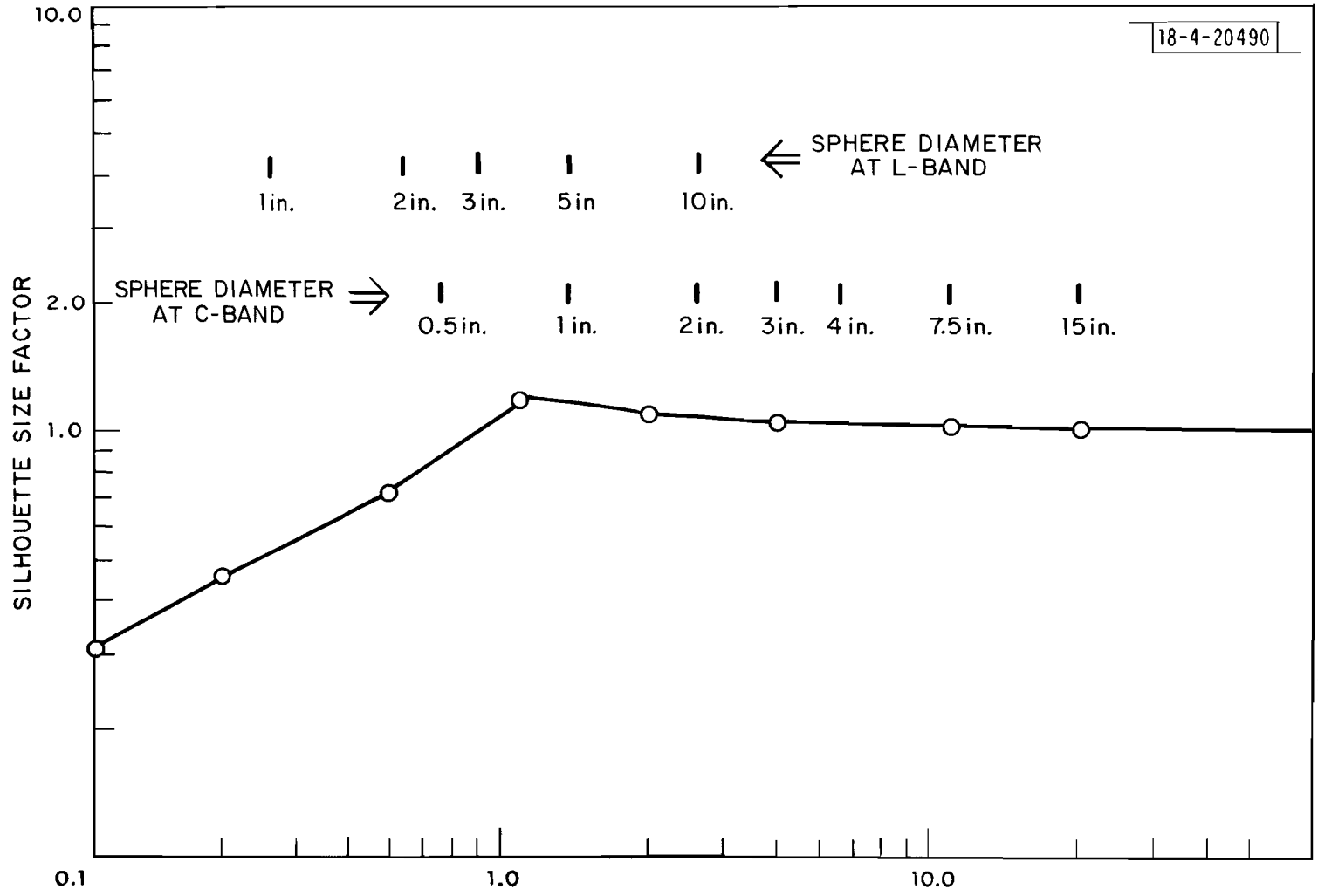

Fig. 4-15. Factor by which sphere silhouette diameter must be multiplied to yield equivalent forward scattered signal.

silhouette of the monitor box should correspond the physical dimensions of the box.

In Figures 4-16 and 4-17, we compare the computed errors using the refined shadowing model to the field data of Figure 4-13. We see that the spatial variation in the errors is quite similar; however, the model results generally give lower errors at the points of peak error. The field data at ±3° and ±4° has an error component not associated with the monitor, so lack of agreement at those angles may not be very significant.

Another factor which may not have been adequately modelled in this situation is the effects of the radiating aperture vertical distribution. The shadowing model implicitly assumes that the obstacle is in the far field of the azimuth antenna elevation pattern. This assumption may not be fully valid in the present case. To yield some indication of the sensitivity to this factor, the simulations were repeated for a phase center height 2 feet below that indicated in Fig. 4-10 with the results as shown in Fig. 4-18 and 4-19. We see that the errors here are closer to the experimental field data. This sensitivity of the error to relatively small changes in site geometry emphasizes the need for 1) very careful site surveys for assessment of shadowing effects by objects close to the transmitter, and 2) consideration of a full variety of operationally relevant shadowing geometries in site selection.

Figures 4-20 and 4-21 compare the computed errors using refined model with those obtained using the earlier simulation model. We see that the two results are essentially identical. Similarly, it was found that the number of aperture evaluation points in the refined model could be varied from 11 to 41 without significantly effecting the error.

This good agreement between the earlier and refined model is not surprising since the earlier model had been shown to agree well with a variety of experimental data at L bank [29] and C band (see volume 2 of this report). Practically, it suggests that the original "small obstacle" model (which requires significantly smaller computation time for multipath parameter computation

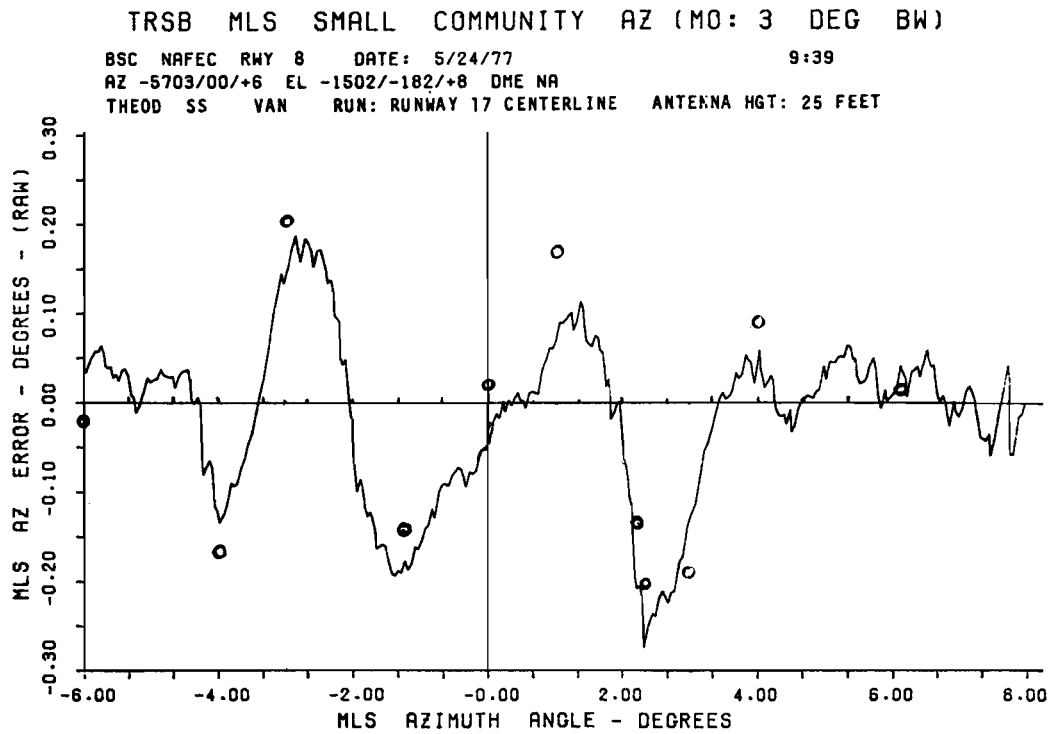

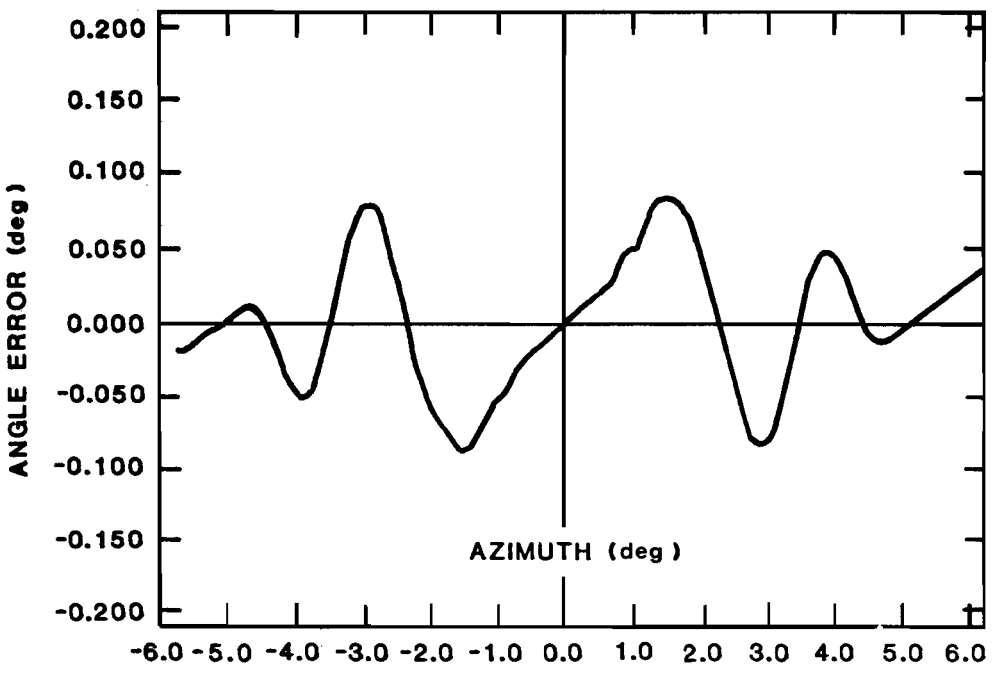

Fig.4-16. Comparison of field data and refined model simulation.

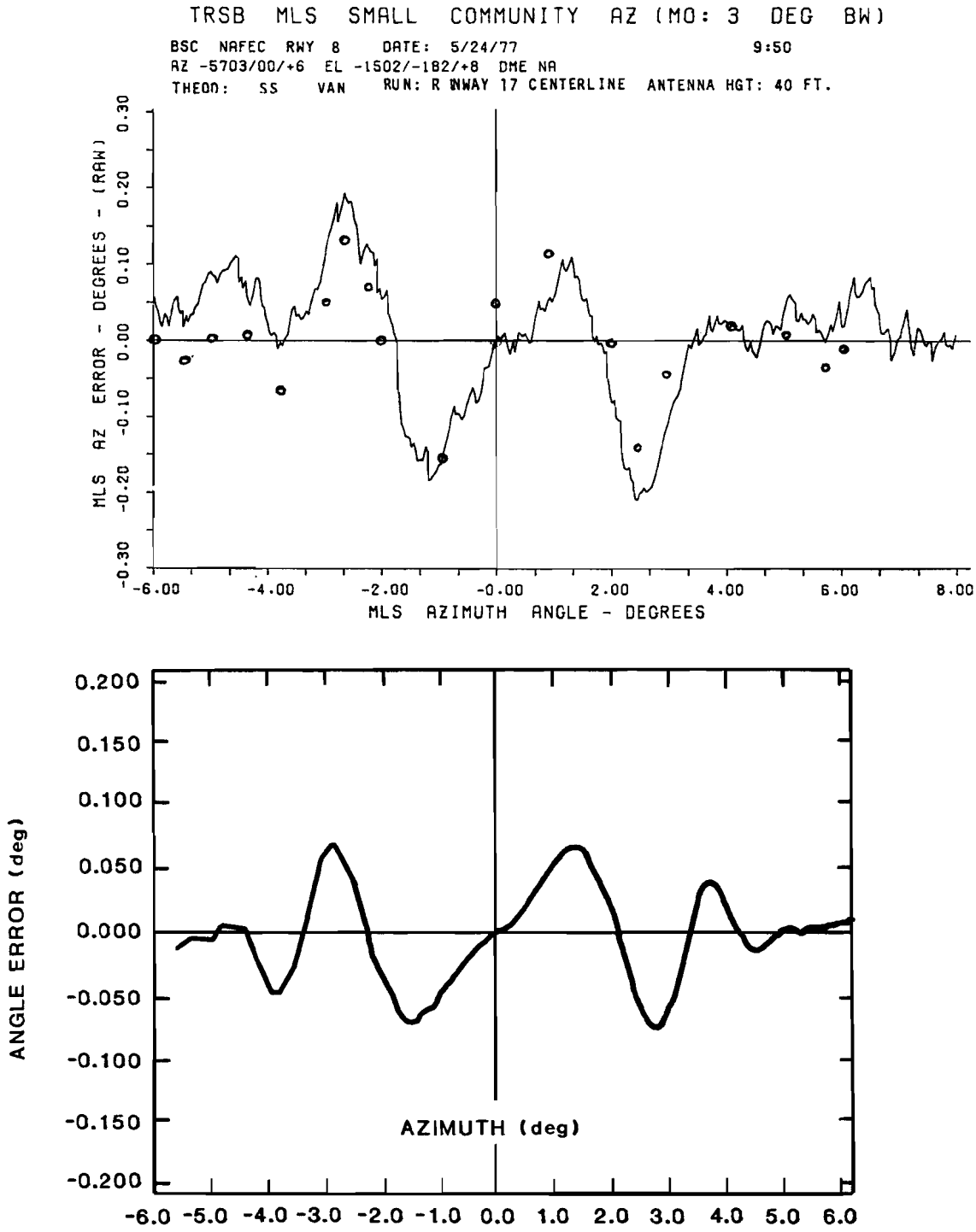

Fig.4-17. Comparison of field data and refined model.

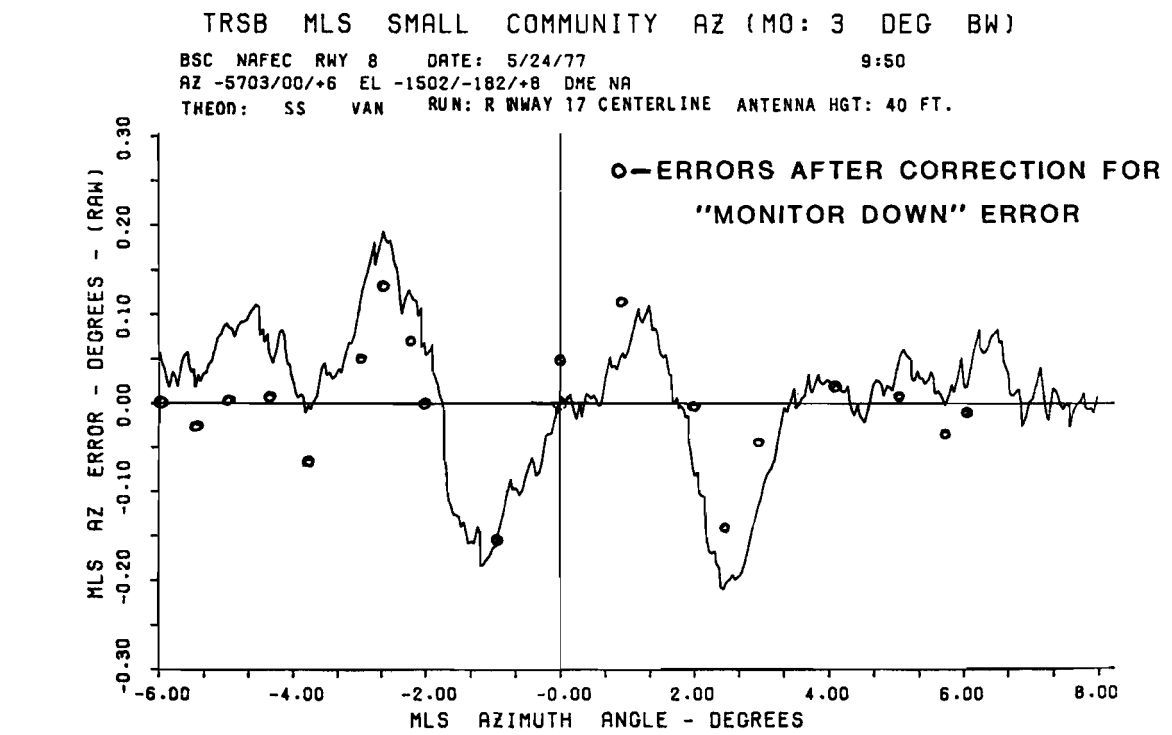

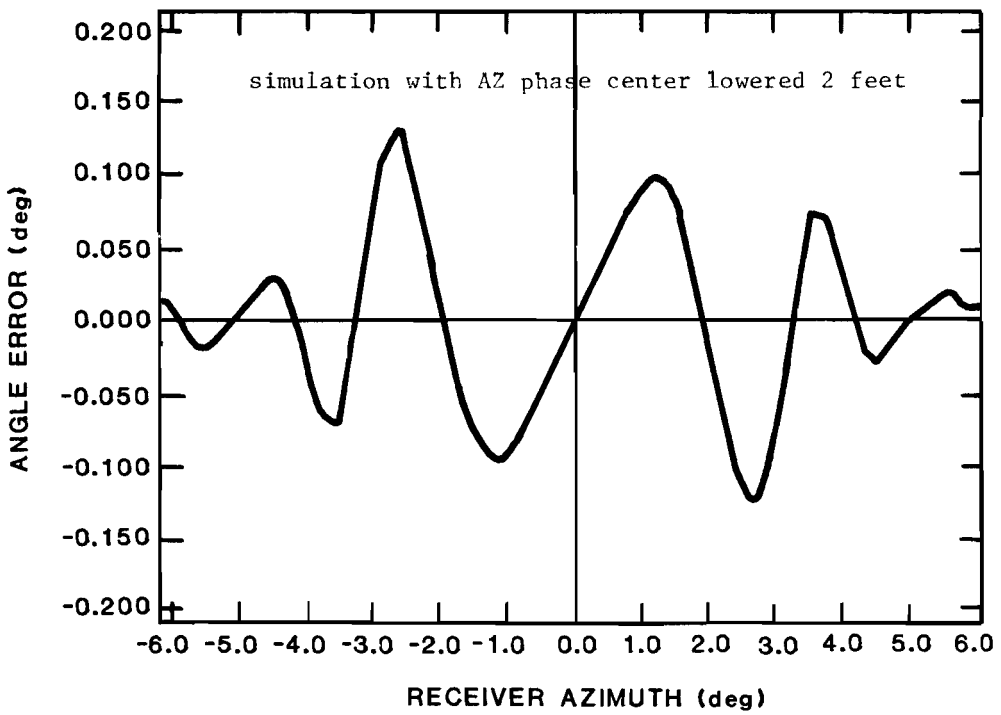

Fig.4-18. Comparison of field data and refined model simulation for two foot lower phase center.

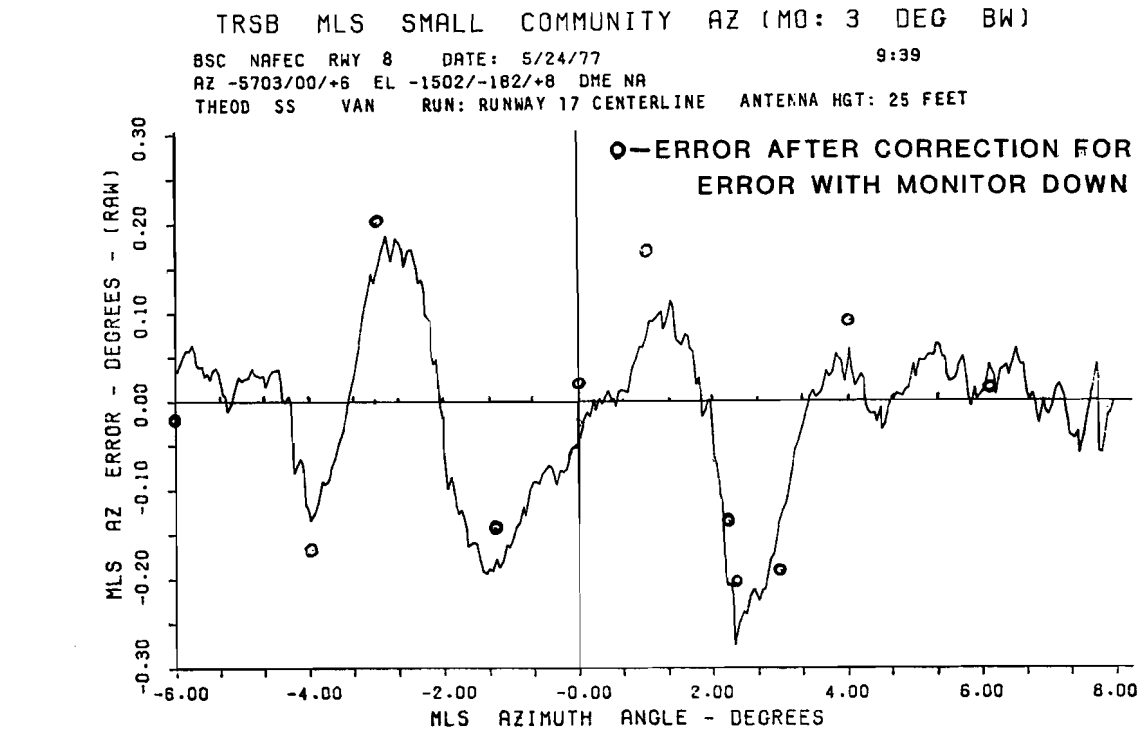

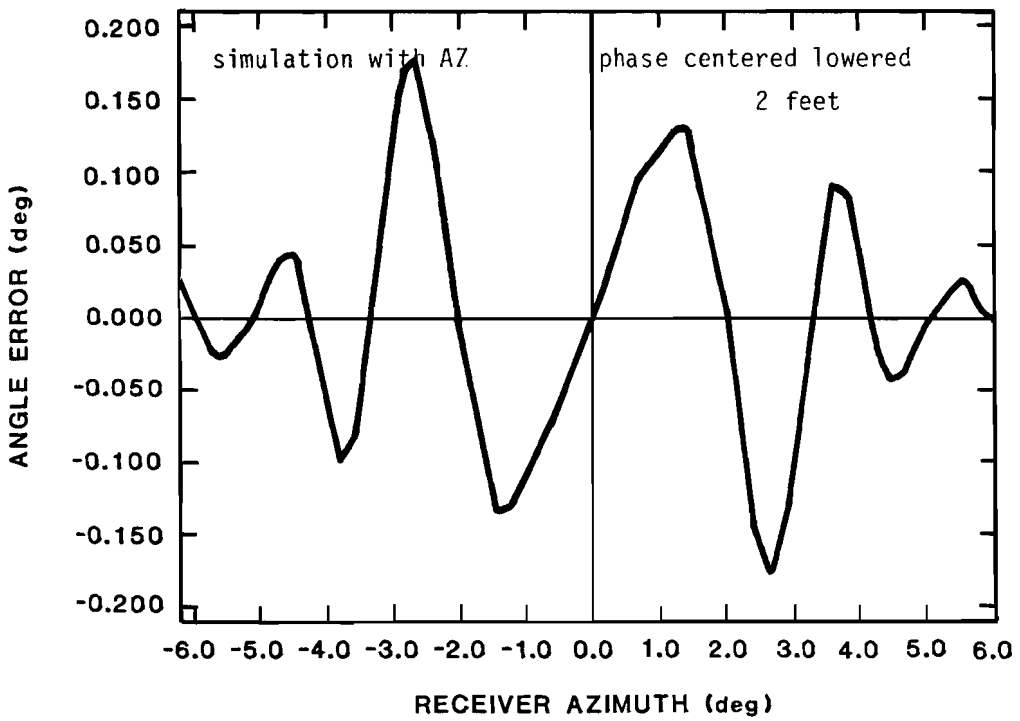

Fig.4-19. Comparison of field data and refined model simulation for two foot lower phase center height.

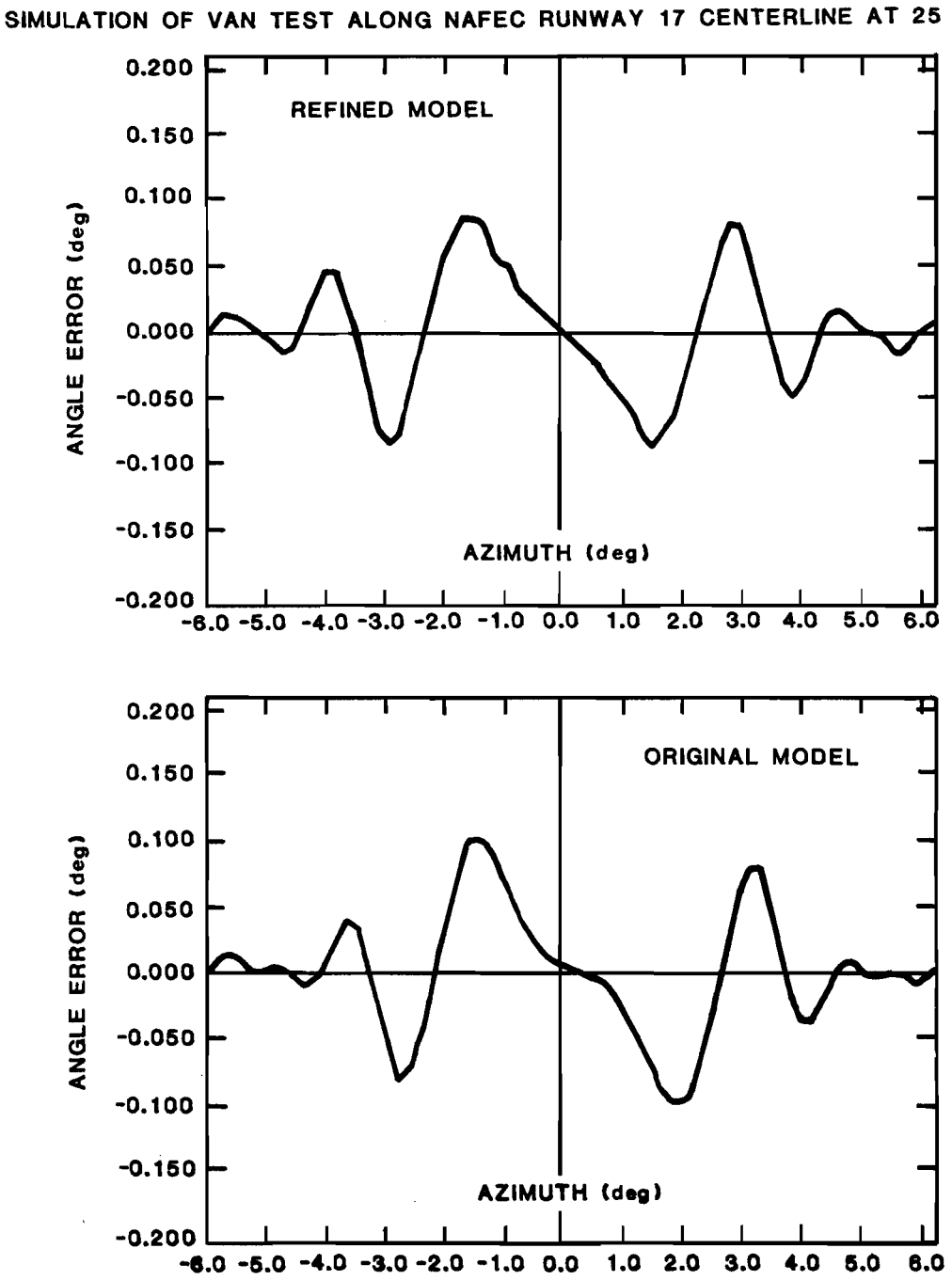

Fig.4-20. Comparison of original and refined shadowing models for Bendix small community azimuth shadowing geometry.

SIMULATION OF VAN TEST ALONG NAFEC RUNWAY 17 CENTERLINE AT 40 FT ALTITUDE

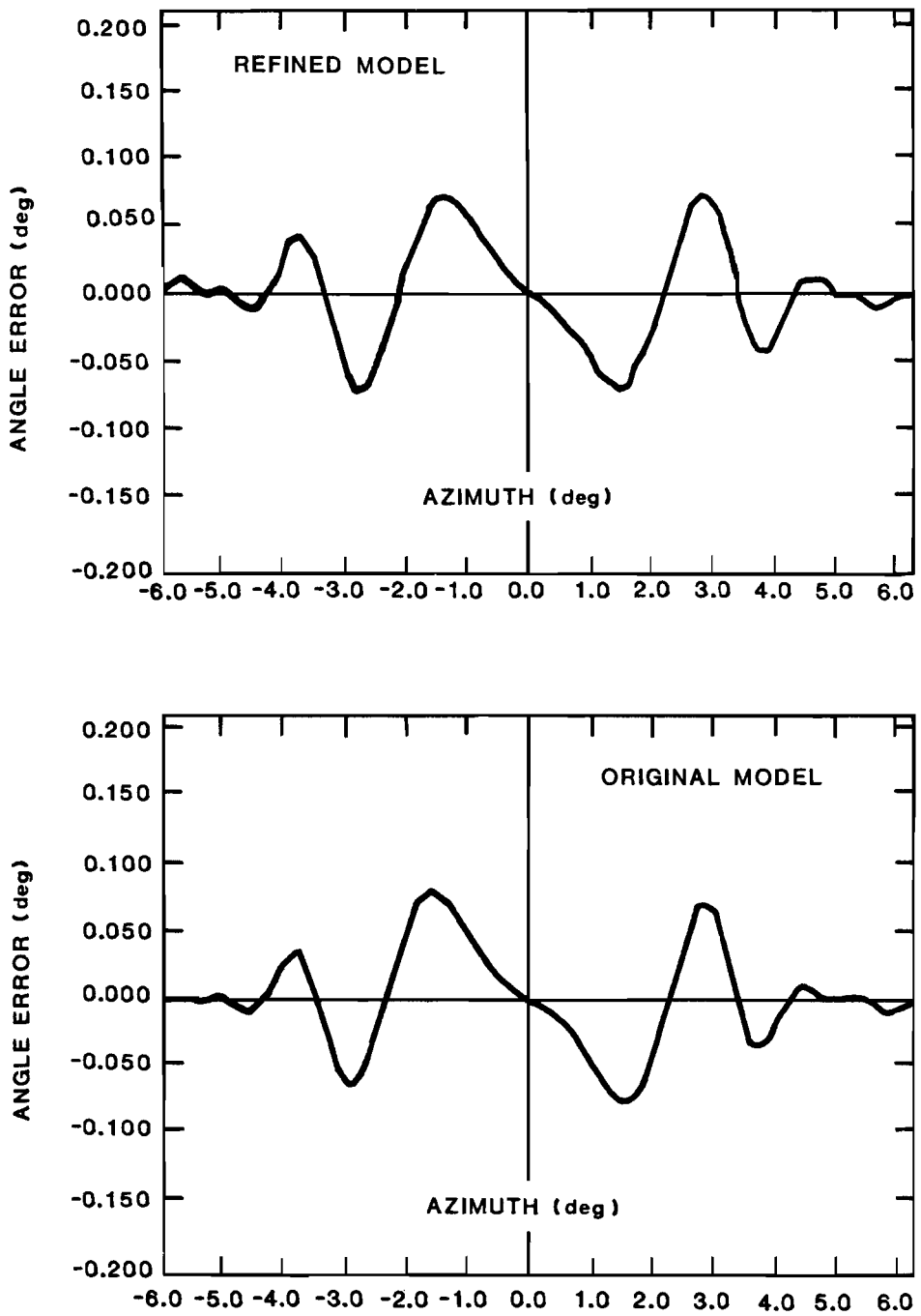

Fig.4-21. Comparison of original and refined shadowing models for Bendix small community azimuth shadowing geometry.

and system error computations) may be adequate in situations where the object in the antenna near field is small.*

D. Summary and Suggestions for Further Research

In this section we have described several refinements of the earlier shadowing model to give a more accurate representation of the effects due to ground reflections and shadowing obstacles which are near the ground antenna. The resulting data has been shown to agree reasonably well with analytical calculations, scale model data and full scale field tests. The validation comparisons above have indicated a need for carefully controlled experiments to better understand the effects of

1) type of ground antenna radiating aperture (e.g., torus versus line array)
2) elevation pattern of the azimuth array
3) size exaggeration effects which arise when the obstacle size is comparable to a wavelength.

Several other factors emerged during the course of the Australian scale model work [18, 37, 38, 80] which also merit additional studies. These factors include:

1. Effects of fuselage reflections on the shadowing error

It was found that the shadowing errors due to three dimenstional scale model aircraft differed from that for the corresponding silhouettes when the shadowing aircraft was at right angles to the LOS. It was suggested by the Australian researchers that fuselage reflections such as shown in Fig. 4-22 may cuase these effects. Such reflections can yield errors by two mechanisms:

1) "fully specular" paths (e.g., a and b in Fig. 4-22) yeild errors by the unusual specular reflection mechanism. For the current propogation model, the characteristics of these specular reflections can be obtained by positioning a

*Limited simulations with larger (e.g., 4 foot wide) obstacles show the earlier model gives larger errors than does the refined model as the shadowing obstacle nears the ground antenna.

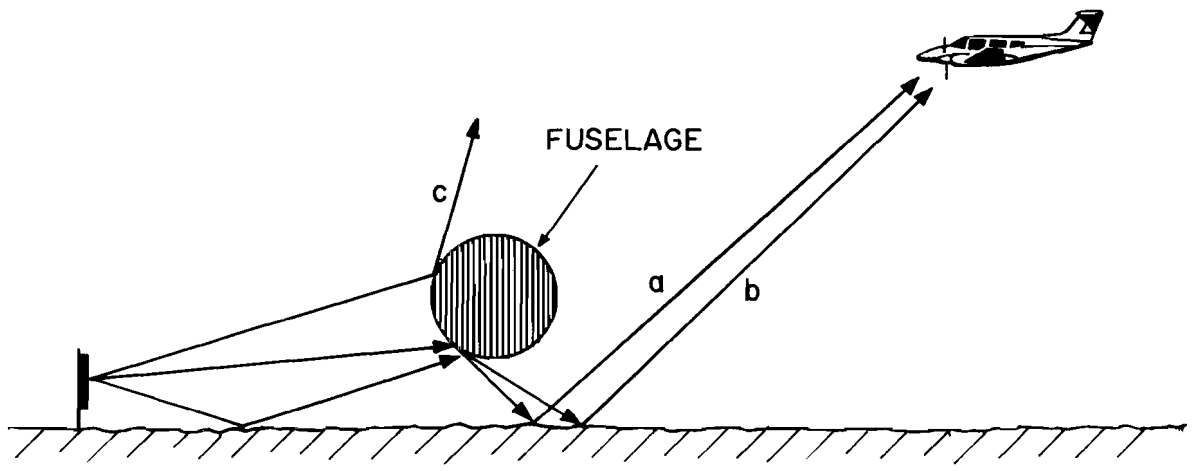

Fig. 4-22. Fuselage reflections in shadowing geometry.

specular reflecting aircraft coincident with the shadowing aircraft. However, in most cases the computed specular levels are very low due to the high degree of divergence at the curved surface.

2) "halo ray" paths (e.g., c in Fig. 4-22) affect the shadowing (diffraction) signals by reducing the illumination of the fuselage top and bottom edges. The effect of the "halo ray" reflections from the cyclindrical surface was investigated theoretically and experimentally by Neugebauer and Backynski [82], who concluded that with vertical polarization, the silhouette vertical extent should be increased to

$$H = D + 0.316\lambda\ (a/\lambda)^{1/3}\ (1 + r_1/r_2) \qquad (4\text{-}28)$$

where a/λ = fuselage radius in wavelengths

r_1 = distance from ground antenna to the shadowing aircraft

r_2 = distance from landing aircraft to the shadowing aircraft

D = fuselage diameter

For a B747 ($D \sim 20$ feet) at close distances ($r_1 \sim 1000$ feet), eq. (4-28) suggests a vertical extent increase of .3 feet. It seems unlikely such a change in the Australian scale models would yield closer agreement between the three dimensional model results versus those for a silhouette; a more plausible explanation (suggested by the Australians) may be differences in shadowing obstacle placement between the two experiments.

2. Effects of extended edges which are parallel to the LOS

It was found that where the edge of an obstacle is exactly or nearly parallel to the LOS, the diffracted signal level can be substantially lower than the silhouette (knife edge) loss shown in Fig. 4-23. Physically, this may be considered as arising from reflections of the diffraction rays generated by the initial blockage on the side of the obstacle. Fig. 4-24 shows measured attenuations on the University of Sydney scale model range for various edge lengths.

It was found that the differences between thick and thin edges were small when the path from the initial shadowing point to the receiver was 6° - 10° in

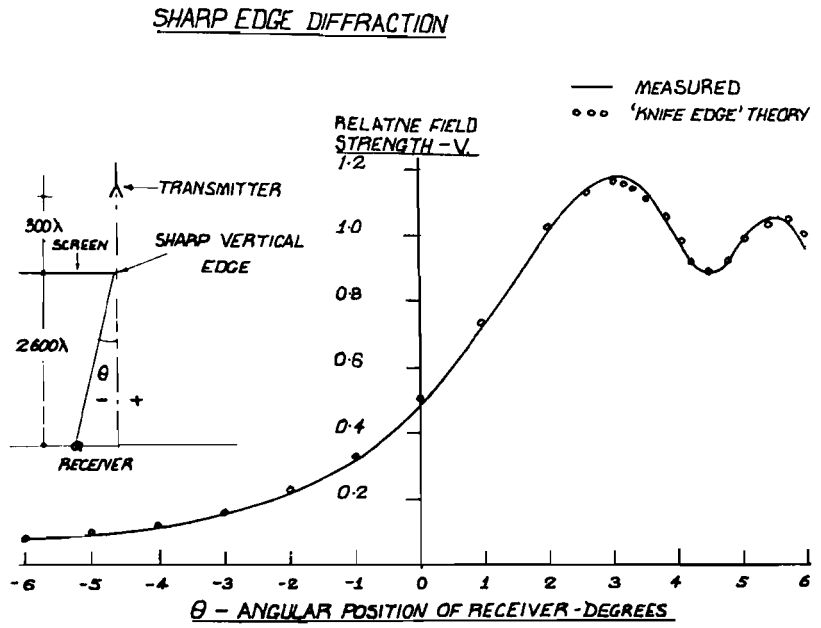

Fig. 4-23. Knite edge diffraction (from Oreb [80]).

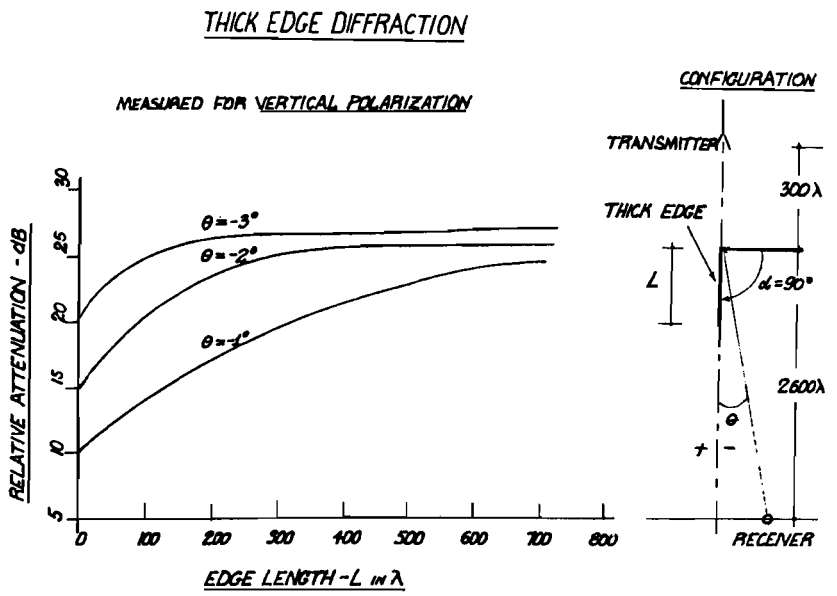

Fig. 4-24. Thick edge diffraction angles (from Oreb [80]).

the clear (i.e., $\alpha < 80°$-$84°$ in Fig. 4-23). This condition has been met by the buildings in the actual airport geometries we have examined to date. However, it would be of interest to know if there is an equivalent silhouette which might be utilized when the above condition is not met.

A more common operationally relevant situtation of a LOS parallel to an edge arises when aircraft are taxiing down a runway. The Australian scale model data in this case suggests that signals propogating beneath the fuselage are attenuated much more strongly than would be the case for a circular disk. This effect could be incorporated in the current shadowing model by extending the fuselage silhouette approzimation down to the ground. However, there needs to be additional research into the proper silhouette model for the sides and top of the fuselage.

V. CURVED FLIGHT PATHS IN MLS SIMULATIONS

Originally, flight paths for the MLS simulations were constrained to the piecewise linear functions in x,y,z with a maximum of 35 segments. A new program permits the insertion of curved segments between two linear segements under certain conditions. This section describes the method used by the program to generate the curved path.

A. Basic Approach

The intent in designing the curved path program was to allow the user to specify a path by giving some waypoints and having the program construct a smooth path through the points. If the user chooses his waypoints carefully, he can force the resulting path to closely approximate a desired shape.

The smoothness criterion chosen for cuved segments was that the path be continuous and differentiable, implying that the endpoints and slopes match in three dimensions at the waypoints. This still leaves considerable latitude in the choice of the curve fit function. The problem is solved sequentially by finding an x, y plane fit first and the z axis fit subsequently as illustrated in Fig. 5-1. The details of the procedures follow below.

B. x, y Plane Fit

Figure 5-2 shows four waypoints to be linked with linear segments directed from (1) to (2) and (3) to (4) and a curved segment from (2) to (3) The points depicted here are the x, y plane projections of the waypoints.

The connecting curve will be described in a polar coordinate system whose center is the intersection of the two lines through points (2) and (3) which are normal to the segment (1)(2) and (3)(4), respectively. For the present, we assume that there exists a unique intersection; the special cases are treated subsequently.

Letting (x_i,y_i), i = 1,4 denote the projected waypoints, the equations for the polar system center, c, (x_c,y_c) are:

$$y_c - y_2 = m_2(x_c - x_2) \tag{5-1}$$

$$y_c - y_3 = m_3(x_c - x_3) \tag{5-2}$$

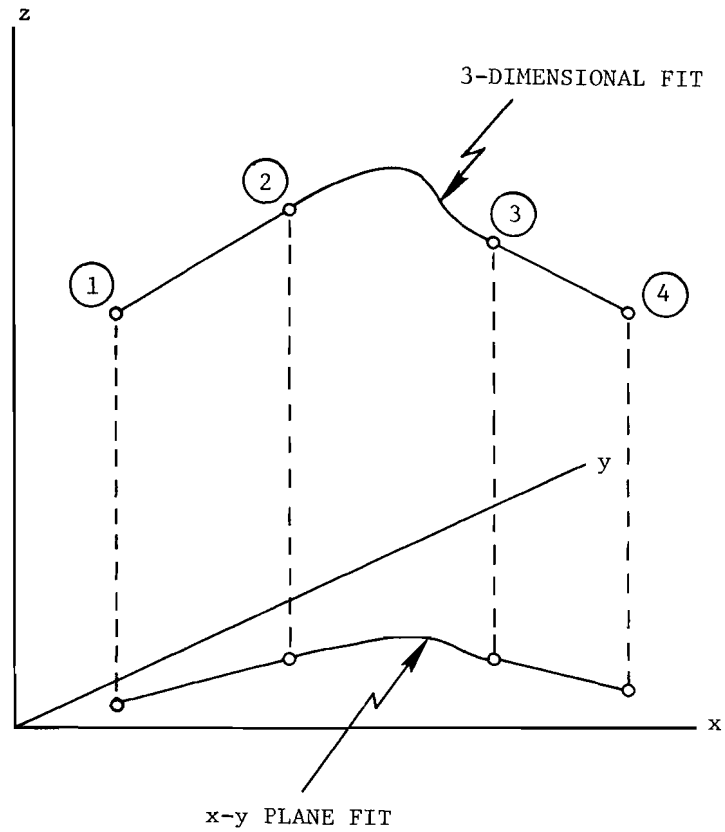

Fig.5-1. Three dimensional graph shows separate x, y plane and z-axis fits.

18-4-20492

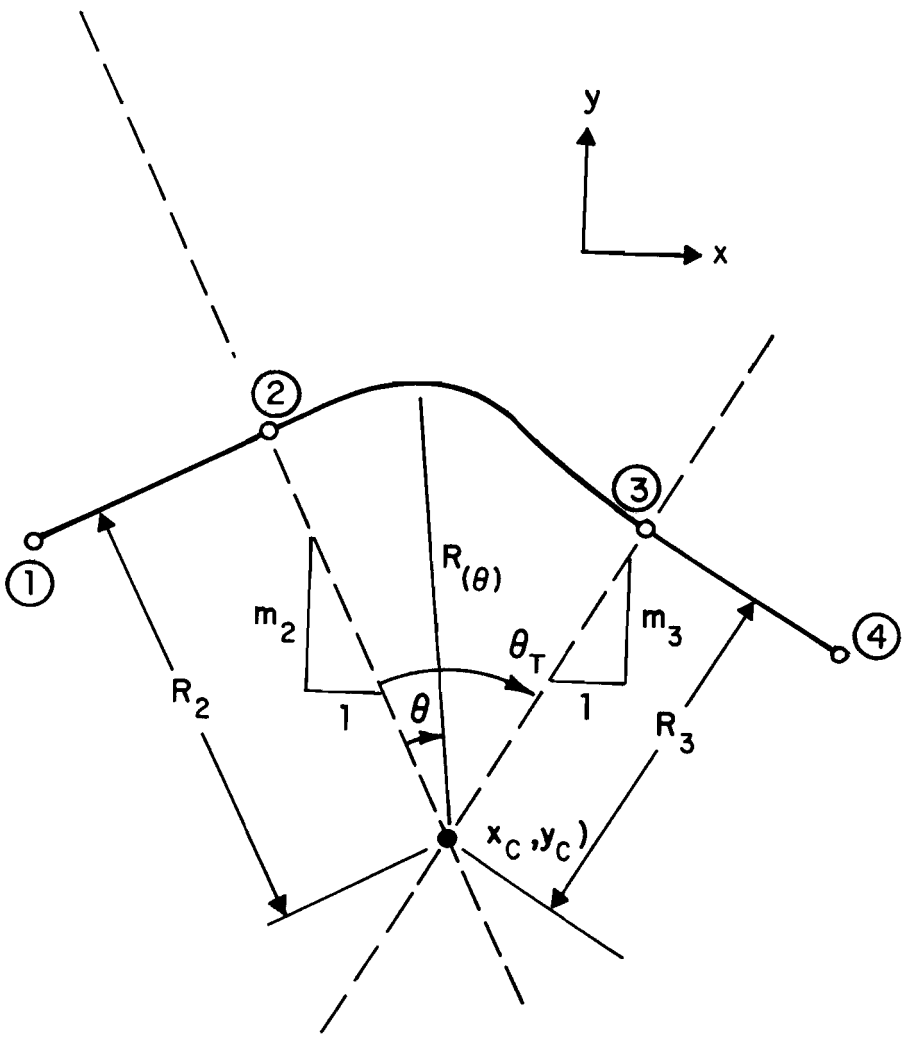

where m_2 and m_3 are the negative inverse slopes of the preceding and following segments:

$$m_2 = -\left(\frac{y_2-y_1}{x_2-x_1}\right)^{-1} \tag{5-3}$$

$$m_3 = -\left(\frac{y_4-y_3}{x_4-x_3}\right)^{-1} \tag{5-4}$$

The solution is

$$x_c = \frac{(m_3x_3-y_3) - (m_2x_2-y_2)}{m_3-m_2} \tag{5-5}$$

$$y_c = \frac{m_2m_3(x_3-x_2) + m_3y_2-m_2y_3}{m_3-m_2} \tag{5-6}$$

For computational purposes it is easier to compute x_c from (5) and then obtain y_c from (1):

$$y_c = m_2(x_c-x_2) + y_2 \tag{5-7}$$

The curve connecting ② and ③ is parameterized by an angle variable θ measured in the polar coordinate system centered at (x_c, y_c). Initially 0 at ②, θ increases or decreases to a value $\theta_T(|\theta_T| \leq 2\pi)$, the sign of θ_T depending on whether the desired rotation is counterclockwise (positive θ_T) or clockwise (negative θ_T). The rotation direction is determined by the heading at ② with respect to (x_c, y_c); see Section G for further discussion.

The x and y coordinates of the curve connecting ② and ③ are given as

$$x(\theta) = R(\theta)\cos(\theta + \theta_2) + x_c \tag{5-8}$$

$$y(\theta) = R(\theta)\sin(\theta + \theta_2) + y_c \tag{5-9}$$

where θ_2 is defined as the bearing of ②, measured from (x_c, y_c). The function $R(\theta)$ must be specified for θ between 0 and θ_T in a way that satisfies the polar version of the boundary conditions. The coordinate system has been defined so that the flight path is normal to the radius at the waypoints. Thus, besides the obvious conditions

$$R(0) = R_2 = ||② - ©|| \tag{5-10}$$

$$R(\theta_T) = R_3 = ||③ - ©|| \tag{5-11}$$

we also have

$$\dot{R}(0) = 0 \tag{5-12}$$

$$\dot{R}(\theta_T) = 0 \tag{5-13}$$

where $\dot{R}(\theta)$ stands for $\frac{d}{d\theta} R(\theta)$. Since there are four independent boundary conditions, the function $R(\theta)$ should have four free parameters. The function chosen with this property is cubic in θ, i.e.,

$$R(\theta) = a\left(\frac{\theta}{\theta_T}\right)^3 + b\left(\frac{\theta}{\theta_T}\right)^2 + c\left(\frac{\theta}{\theta_T}\right) + d \tag{5-14}$$

$$\dot{R}(\theta) = \frac{1}{\theta_T}\left[3a\left(\frac{\theta}{\theta_T}\right)^2 + 2b\left(\frac{\theta}{\theta_T}\right) + c\right] \tag{5-15}$$

The boundary conditions then are

$$R(0) = R_2 = d \tag{5-16}$$

$$R(\theta_T) = R_3 = a + b + c + d \tag{5-17}$$

$$\dot{R}(0) = \frac{c}{\theta_T} = 0 \tag{5-18}$$

$$\dot{R}(\theta_T) = \frac{1}{\theta_T}(3a + 2b + c) = 0 \tag{5-19}$$

from which one obtains the solutions

$$a = -2(R_3-R_2) \tag{5-20}$$

$$b = 3(R_3 - R_2) \tag{5-21}$$

$$c = 0 \tag{5-22}$$

$$d = R_2 \tag{5-23}$$

or

$$R(\theta) = (R_3-R_2)\left(\frac{\theta}{\theta_T}\right)^2\left[-2\left(\frac{\theta}{\theta_T}\right) + 3\right] + R_2 \tag{5-24}$$

$$\dot{R}(\theta) = 6\left(\frac{R_3-R_2}{\theta_T}\right)\left(\frac{\theta}{\theta_T}\right)\left[-\left(\frac{\theta}{\theta_T}\right) + 1\right] \tag{5-25}$$

Within the computer program, these formulas are written in terms of normalized radius and angle variables R and u:

$$R = \frac{R_3}{R_2} \tag{5-26}$$

$$u = \frac{\theta}{\theta_T} \tag{5-27}$$

i.e.,

$$R(\theta) = R_2 r\left(\frac{\theta}{\theta_T}\right) \tag{5-28}$$

$$\dot{R}(\theta) = \frac{R_2}{\theta_T}\dot{r}\left(\frac{\theta}{\theta_T}\right) \tag{5-29}$$

where

$$r(u) = (R-1)u^2(-2u + 3) + 1 \tag{5-29a}$$

$$\dot{r}(u) = \frac{d}{du} r(u) = 6(R-1)u(-u + 1) \tag{5-29b}$$

C. z-Coordinate Fit

The three dimensional curved path lies on the cylinder whose base is the x,y plane curve derived in Section B. The height of the curve is specified by a third coordinate, $z(\theta)$. The boundary conditions on $z(\theta)$ and $\dot{z}(\theta) = \frac{d}{d\theta} z(\theta)$ are determined by the positions and slopes of the leading and trailing linear segments. Since the slopes of the linear segments are not conveniently expressed in terms of $\dot{z}(\theta)$, we first derive a relation between $\dot{z}(\theta)$ and $\frac{dz}{ds}$, the rate of change of z with respect to arc length (s) along the curve.

In cylindrical coordinates, the element of arc is

$$ds = \sqrt{(dz)^2 + (Rd\theta)^2 + (dR)^2} \tag{5-30}$$

which is equivalent to

$$\left|\frac{ds}{d\theta}\right| = \sqrt{\dot{z}^2 + \dot{R}^2 + R^2} \tag{5-31}$$

Since

$$\dot{z}(\theta) = \frac{dz}{d\theta} = \frac{dz}{ds}\,\frac{ds}{d\theta} \tag{5-32}$$

we find from (31) that

$$\dot{z}^2 = \left(\frac{dz}{ds}\right)^2 (\dot{z}^2 + \dot{R}^2 + R^2) \tag{5-33}$$

or

$$\dot{z} = \frac{\pm \frac{dz}{ds}}{\sqrt{1 - \left(\frac{dz}{ds}\right)^2}} \sqrt{\dot{R}^2 + R^2} \tag{5-34}$$

The sign to be used in (34) is the same as the sign of θ_T. Equation (34) is true at any point on the curve. For the boundary conditions, we are only concerned with the endpoints, where we know that $\dot{R} = 0$. Therefore the z-coordinate slope conditions are computed as:

$$\dot{z}_2 = \dot{z}\Big|_{②} = \left.\frac{\pm R\left(\frac{dz}{ds}\right)}{\sqrt{1-\left(\frac{dz}{ds}\right)^2}}\right|_{②} \tag{5-35a}$$

$$\dot{z}_3 = \dot{z}\Big|_{③} = \left.\frac{\pm R\left(\frac{dz}{ds}\right)}{\sqrt{1-\left(\frac{dz}{ds}\right)^2}}\right|_{③} \tag{5-35b}$$

The $\frac{dz}{ds}$ boundary values are computed as the slopes of the two linear segments preceding and following the curved section:

$$\left.\frac{dz}{ds}\right|_{②} = \frac{z_2 - z_1}{||② - ①||} \tag{5-36}$$

$$\left.\frac{dz}{ds}\right|_{③} = \frac{z_4 - z_3}{||④ - ③||} \tag{5-37}$$

The curve fit for z is also a cubic in θ:

$$z(\theta) = a\left(\frac{\theta}{\theta_T}\right)^3 + b\left(\frac{\theta}{\theta_T}\right)^2 + c\left(\frac{\theta}{\theta_T}\right) + d \tag{5-38}$$

$$\dot{z}(\theta) = \frac{1}{\theta_T}\left[3a\left(\frac{\theta}{\theta_T}\right)^2 + 2b\left(\frac{\theta}{\theta_T}\right) + c\right] \tag{5-39}$$

The equations for the coefficients are

$$z_2 = d \tag{5-40}$$

$$z_3 = a + b + c + d \tag{5-41}$$

$$\theta_T \dot{z}_2 = c \tag{5-42}$$

$$\theta_T \dot{z}_3 = 3a + 2b + c \tag{5-43}$$

which have the solution

$$a = -2(z_3 - z_2) + \theta_T(\dot{z}_2 + \dot{z}_3) \tag{5-44}$$

$$b = 3(z_3 - z_2) - \theta_T(2z_2 + z_3) \tag{5-45}$$

$$c = \theta_T \dot{z}_2 \tag{5-46}$$

$$d = z_2 \tag{5-47}$$

Eqs. (24) and (38) completely determine the full three-dimensional curved path segment. The selection of the discrete flight path points and the velocity calculation are dealt with below.

D. Flight Path Positions and Velocities

On linear flight paths, successive evaluation points are uniformly separated by a distance D (denoted DINC in the programs). The same rule is applied to curved segments as well. In this case the next flight path point is found by computing the angular increment corresponding to an arc length increment $\Delta s = D$. From (31),

$$|\Delta\theta| \approx \frac{D}{\sqrt{\dot{z}^2(\theta) + \dot{R}^2(\theta) + R^2(\theta)}} \tag{5-48}$$

where θ indicates the polar angle of the present flight path point. The radius of the curve is usually >> D (D = 40 ft. is typical of many simulation cases), so that Eq. (48) is a sufficiently good approximation in all cases encountered so far.

Unlike the linear segment case, velocity components must be recomputed at each flight path point on a curved segment, even though the aircraft speed is constant on the segment. The rectangular coordinates corresponding to the polar frame are given by:

$$x = R(\theta)\cos(\theta + \theta_2) + x_c \tag{5-49}$$

$$y = R(\theta)\sin(\theta + \theta_2) + y_c \tag{5-50}$$

$$z = z(\theta) \tag{5-51}$$

The velocity components are obtained by differentiating these expressions with respect to time

$$v_x = \frac{dx}{dt} = \dot{R}(\theta)\frac{d\theta}{dt}\cos(\theta + \theta_2) - R(\theta)\frac{d\theta}{dt}\sin(\theta + \theta_2) \qquad (5\text{-}52)$$

$$v_y = \frac{dy}{dt} = \dot{R}(\theta)\frac{d\theta}{dt}\sin(\theta + \theta_2) + R(\theta)\frac{d\theta}{dt}\cos(\theta + \theta_2) \qquad (5\text{-}53)$$

$$v_z = \frac{dz}{dt} = \dot{z}(\theta)\frac{d\theta}{dt} \qquad (5\text{-}54)$$

The time rate of change of the parameter θ is obtained by noting that the arc length increments linearly in time at a rate given by the desired speed, V:

$$ds = \sqrt{\dot{z}^2 + \dot{R}^2 + R^2}\, d\theta = V\, dt \qquad (5\text{-}55)$$

or

$$\frac{d\theta}{dt} = \frac{V}{\sqrt{\dot{z}^2 + \dot{R}^2 + R^2}} \qquad (5\text{-}56)$$

E. Arc Length

An initilization routine computes the length of a curved segment when the flight path first reaches that segment. This is analogous to what happens on a linear segment, except that in the linear case the calculation is trivial. For the curved segment, differential arc length is numerically integrated along the curve since the integration cannot be accomplished analytically for the cubic formulas. The total angle θ_T is subdivided into 500 uniform increments and first-order integrated:

$$S = \int_0^{\theta_T} d\theta \sqrt{\dot{z}^2 + \dot{R}^2 + R^2} \qquad (5\text{-}57)$$

$$\approx \sum_{n=1}^{500} \left[\dot{z}(n\Delta\theta)^2 + \dot{R}(n\Delta\theta)^2 + R(n\Delta\theta)^2\right]^{1/2} \Delta\theta: \qquad \Delta\theta = \theta_T/500$$

F. Special Cases

Certain cases may arise in practice which do not strictly fit the mathematical formulation given thus far. Some of these are handled within the initialization program as exceptions; others remain as restrictions which can only be removed by additional alteration of the algorithms.

The exceptions treated here deal with the x, y plane projection of the flight path. The troublesome cases are:

(i) either (but not both) of the leading and trailing segments has zero slope in the x, y plane, or

(ii) the leading and trailing segments have equal slopes

1. One Segment with Zero Slope

Looking back to Eqs. (3) and (4), which define the slopes of the lines perpendicular to the leading and trailing segments, we see that m_2 (or m_3) becomes infinite if $y_2 - y_1$ (or $y_4 - y_3$) is zero. In either case the program would halt with a divide check at this point if left as indicated in Eqs. (3) and (4). This is an important case inasmuch as zero slope corresponds to a segment parallel to centerline in the MLS coordinate frame, and almost all the scenarios simulated to date contain at least one such segment (e.g., the final approach).

When only one segment has zero slope, the polar coordinate system determined by the intersection of the segment normals is well defined. Figures 5-3a and 5-3b illustrate the two cases. In the first, the leading segment has zero slope. The x-coordinate of the center is then obviously:

$$x_c = x_2 \tag{5-58}$$

which can be substituted into (2) to obtain

$$y_c = m_3 (x_2 - x_3) + y_3 \tag{5-59}$$

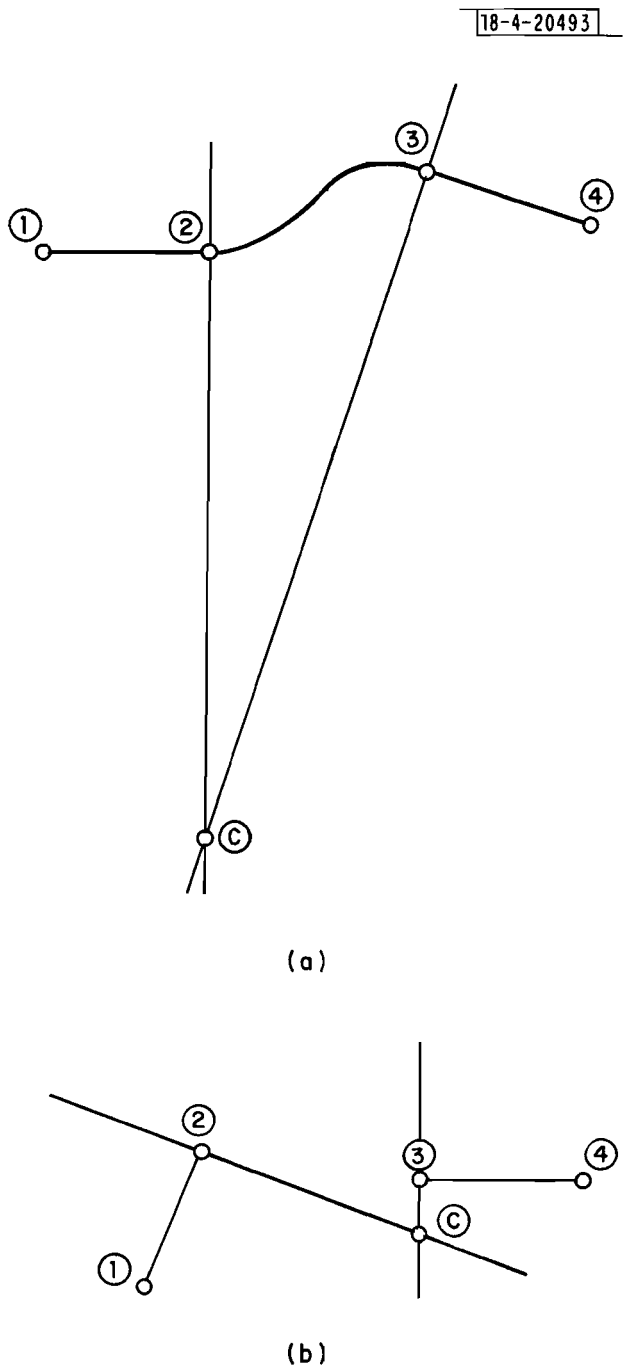

Fig. 5-3. Cases in which one segment has zero slope.

In the complementary case where the trailing segment has zero slope, the result is:

$$x_c = x_3 \tag{5-60}$$

$$y_c = m_2(x_3 - x_2) + y_2 \tag{5-61}$$

The case in which both slopes are zero is handled as an equal slope case.

2. Equal Slopes

Figure 5-4 illustrates the sort of flight path leading to an equal slope case. In any equal slope case, the polar system is undefined since the normals at the two ends of the curved segment do not intersect. Fortunately, a simple x, y coordinate fit exists which can easily be implemented using the formulas which have already been programmed. It can be shown that this algorithm generates the same path one would obtain by taking a limit of cases with nearly equal slopes.

As shown in Fig. 5-4b, a new rectangular coordinate system is constructed by translating the origin to point ② (beginning of the curved segment) and rotating so that the segments have zero slope in the new coordinates. Let

$$x_3' = x_3 - x_2 \tag{5-62}$$

$$y_3' = y_3 - y_2 \tag{5-63}$$

denote the coordinates of ③ (end of curved segment) after the translation. Rotation through angle ψ,

$$\psi = \tan^{-1}\left(\frac{y_3'}{x_3'}\right) \tag{5-64}$$

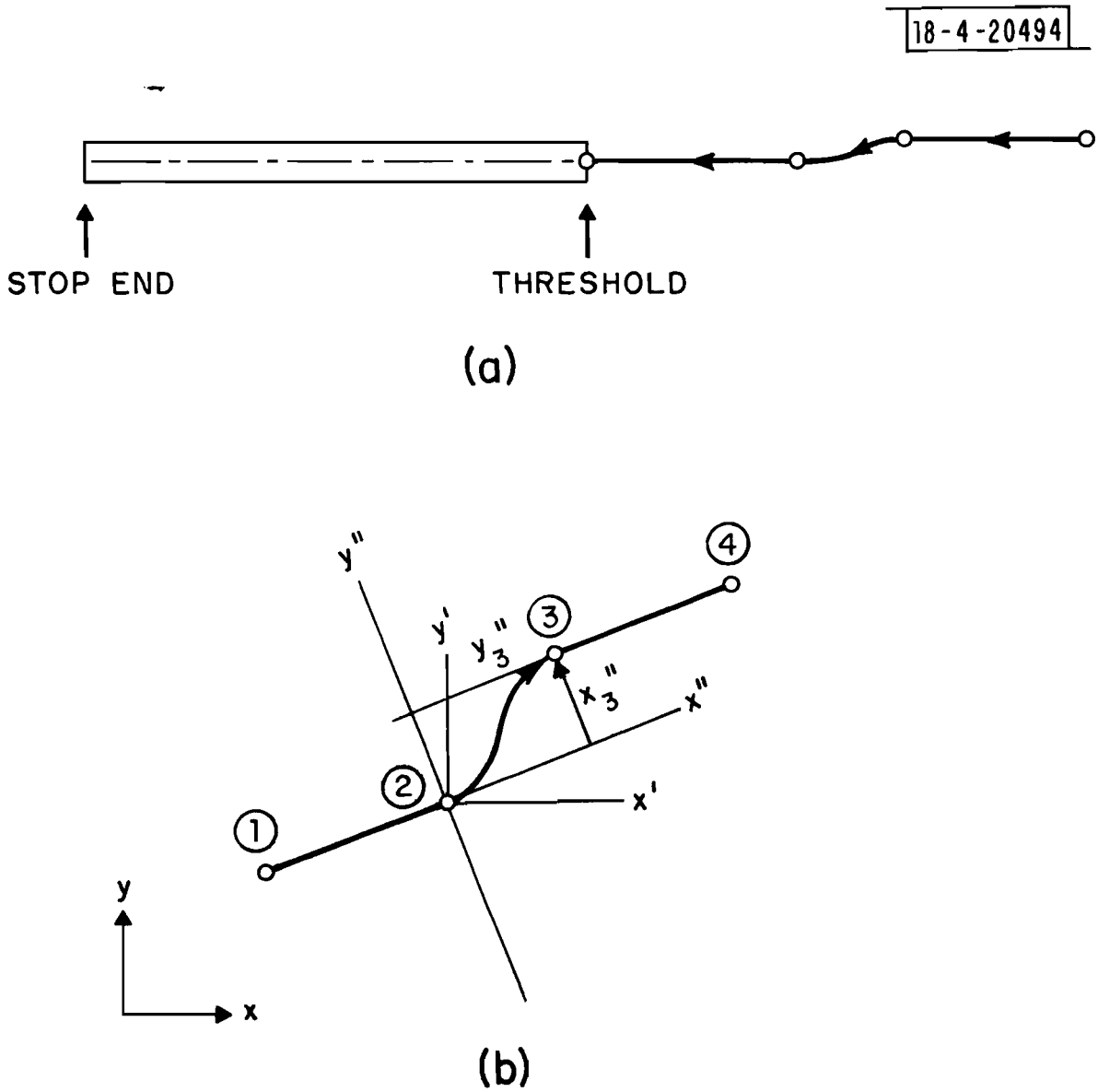

Fig. 5-4. Equal slope case.

produces new coordinates $(x_3", y_3")$:

$$\begin{pmatrix} x_3" \\ y_3" \end{pmatrix} = \begin{bmatrix} \cos\psi & \sin\psi \\ -\sin\psi & \cos\psi \end{bmatrix} \begin{pmatrix} x_3' \\ y_3' \end{pmatrix} = \begin{pmatrix} x_3'\cos\psi + y_3' \sin\psi \\ -x_3'\sin\psi + y_3' \cos\psi \end{pmatrix} \tag{5-65}$$

It is assumed in the program that $x_3" > 0$ (see Sec. G)

A function $Y(\cdot)$ and its derivative $\dot{Y}(\cdot)$ are needed with the properties:

$$Y(0) = 0 \tag{5-66}$$

$$Y(x_3") = y_3" \tag{5-67}$$

$$\dot{Y}(0) = 0 \tag{5-68}$$

$$\dot{Y}(x_3") = 0 \tag{5-69}$$

Again, a cubic can be used for this purpose. Conditions (66) and (68) show that there is no constant or linear term; hence we use

$$y(u) = au^3 + bu^2 \tag{5-70}$$

and find the solution

$$Y(x) = y_3" y\left(\frac{x}{x_3"}\right) \tag{5-71}$$

where

$$y(u) = u^2 (-2u + 3) \tag{5-72}$$

Use of the equal slope coordinate frame changes the z-coordiante boundary conditions. Paralleling the argument used in Section C, this time for the translated, rotated rectangular coordinate system, we have

$$ds = \sqrt{dx^2 + dy^2 + dz^2}$$

$$= \sqrt{1 + \left(\frac{dy}{dx}\right)^2 + \left(\frac{dz}{dx}\right)^2}\ dx \qquad (5\text{-}73)$$

$$\frac{dz}{dx} = \frac{dz}{ds}\frac{ds}{dx} = \frac{dz}{ds}\sqrt{1 + \left(\frac{dy}{dx}\right)^2 + \left(\frac{dz}{dx}\right)^2} \qquad (5\text{-}74)$$

or

$$\frac{dz}{dx} = \frac{\frac{dz}{ds}\sqrt{1 + \left(\frac{dy}{dx}\right)^2}}{\sqrt{1 - \left(\frac{dz}{ds}\right)^2}} \qquad (5\text{-}75)$$

Similarly to the polar case, we have $\frac{dy}{dx} = 0$ at the endpoints; thus

$$\left.\frac{dz}{dx}\right|_{②,③} = \left.\frac{\frac{dz}{ds}}{\sqrt{1 - \left(\frac{dz}{ds}\right)^2}}\right|_{②,③} \qquad (5\text{-}76)$$

In the computer program, z is calculated relative to the normalized parameter u which varies over (0,1) as the independent variable takes on its range. This parameter was implicitly introduced in Eqs. (70) and (71) to set up an x scale as follows:

$$x = ux_3'' \qquad (5\text{-}77)$$

Thus

$$\left.\frac{dz}{du}\right|_{②,③} = \left.\frac{x_3''\frac{dz}{ds}}{\sqrt{1 - \left(\frac{dz}{ds}\right)^2}}\right|_{②,③} \qquad (5\text{-}78)$$

Arc length in this case is computed by numerically integrating (73). The interval $(0, x_3'')$ is subdivided into 500 increments and a first order approximation to the arc length integral is used.

G. Derivation of Restrictions on the Curve Fit Algorithm

The curved path program characterizes linear segments by their slopes, and not as directed line segments (vectors). Thus, it fails to distinguish between the two cases shown in Fig. 5-5. Although both of these look like cases which the curved path program should accept, it will in fact treat them as identical (up to the 3rd waypoint) and in effect handle only one of them. The question is, of course, which one will it accept and how does the user choose his waypoints to avoid having the curved segment approach the trailing waypoint from the wrong side.

Fig. 5-6a and 5-6b illustrate the possibilities. Only runway plane projections of the flight path are considered in this section, because it is easily shown that the altitude fit causes no additional restrictions. It is assumed without loss of generality that the leading waypoint is at the origin and the heading is along the positive x-axis. The destination is on the unit circle at relative bearing θ, and the destination heading is ϕ. Only upper half-plane destinations ($0° \leq \theta \leq 180°$) need be considered, since every lower half-plane destination is the mirror image of an upper half-plane destination. In Fig. 5-6a, the destination is in the first quadrant ($0 \leq \theta < 90°$); Fig. 5-6b shows the second quadrant case. The two are treated separately below.

For any θ, the center of the polar coordinate system must lie on the y-axis due to the assumptions about the point of origin. The position of the polar center along the y-axis is determined by the slope of the destination heading, but is independent of its direction. The destination heading must be such that the radius function is a single-valued function of angle from origin to destination. For this to be the case the destination heading must be "out of" the angular sector formed by origin, polar center, and destination (OCD). From Fig. 5-6a we see that polar centers on the on the positive y-axis correspond to acceptable heading angles ϕ satisfying

$$\theta \leq \phi < \theta + 90° \tag{5-79}$$

Those on the negative y-axis correspond to

$$\theta - 90° < \phi \leq \theta \tag{5-80}$$

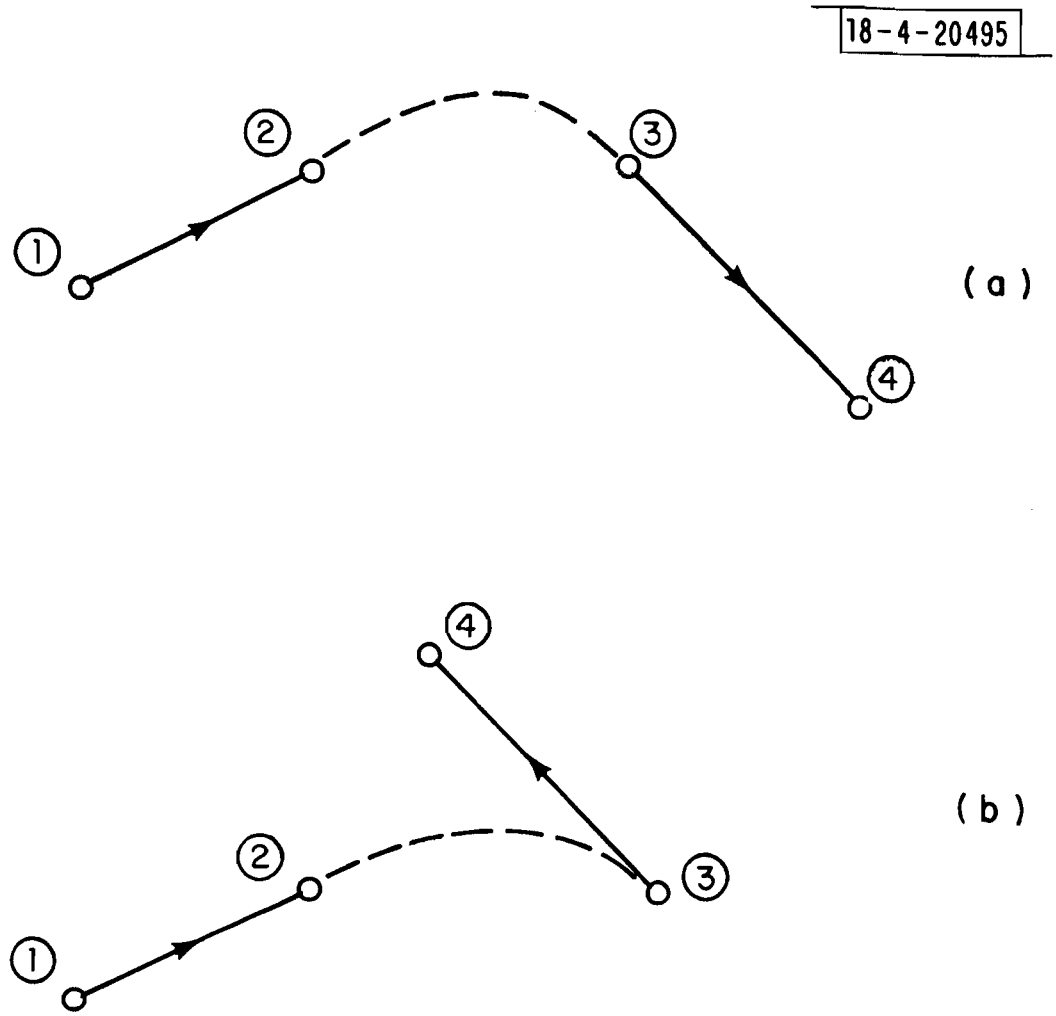

Fig. 5-5. Two cases with oppositely directed trailing segment.

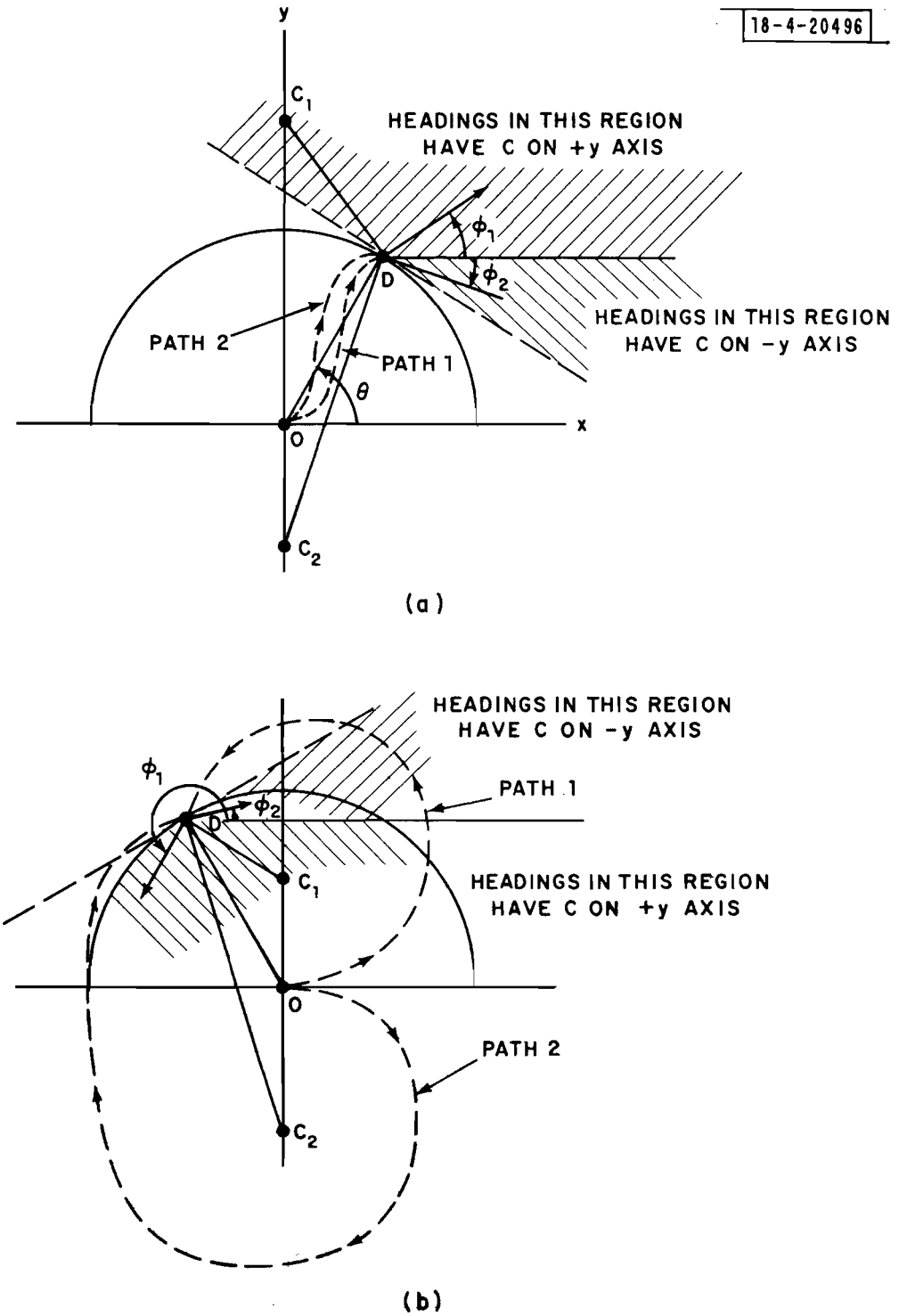

Fig. 5-6. Restrictions on destination heading.

Taken together, inequalities (79) and (80) show that the acceptable destination vectors lie within $\pm 90^0$ of the relative bearing θ.

From Figure 5-6b we reach a different conclusion for the cases in which the destination lies "behind" the origin, i.e., in the second quadrant. In those cases the flight path leaves the acute angular sector defined above (OCD) and must therefore terminate in the reentering direction. The eligible destination heading vectors are those pointing toward the origin side of the line tangent to the unit circle at the destination. These are vectors within $\pm 90^0$ of $\theta - 180^0$, i.e.,

$$\theta - 270^0 < \phi < \theta - 90^0 \tag{5-81}$$

These results can be expressed in a more compact form. Let $\underline{U}_i$ be the runway plane projection of the unit vector directed from waypoint (i) to (i+1). In Figure 5-7, $\underline{U}_1$ and $\underline{U}_3$ define the headings at the origin and destination, respectively; $\underline{U}_2$ is the bearing from origin to destination. The conditions derived above require that the vectors $\underline{U}_1$ and $\underline{U}_3$ both lie either within $\pm 90^0$ of $\underline{U}_2$ or in the complementary region, which is equivalent to having the inner products $\underline{U}_1 \cdot \underline{U}_2$ and $\underline{U}_3 \cdot \underline{U}_2$ be both positive or both negative. The first quadrant result can thus be stated as:

$$\underline{U}_1 \cdot \underline{U}_2 > 0 \text{ and } \underline{U}_3 \cdot \underline{U}_2 > 0 : \qquad 0^\circ \leq \theta < 90^\circ \tag{5-82}$$

and the second quadrant result is:

$$\underline{U}_1 \cdot \underline{U}_2 < 0 \text{ and } \underline{U}_3 \cdot \underline{U}_2 < 0 : \qquad 90^\circ < \theta \leq 180^\circ \tag{5-83}$$

A single expression covering both cases is:

$$(\underline{U}_1 \cdot \underline{U}_2)\ (\underline{U}_3 \cdot \underline{U}_2) > 0 \tag{5-84}$$

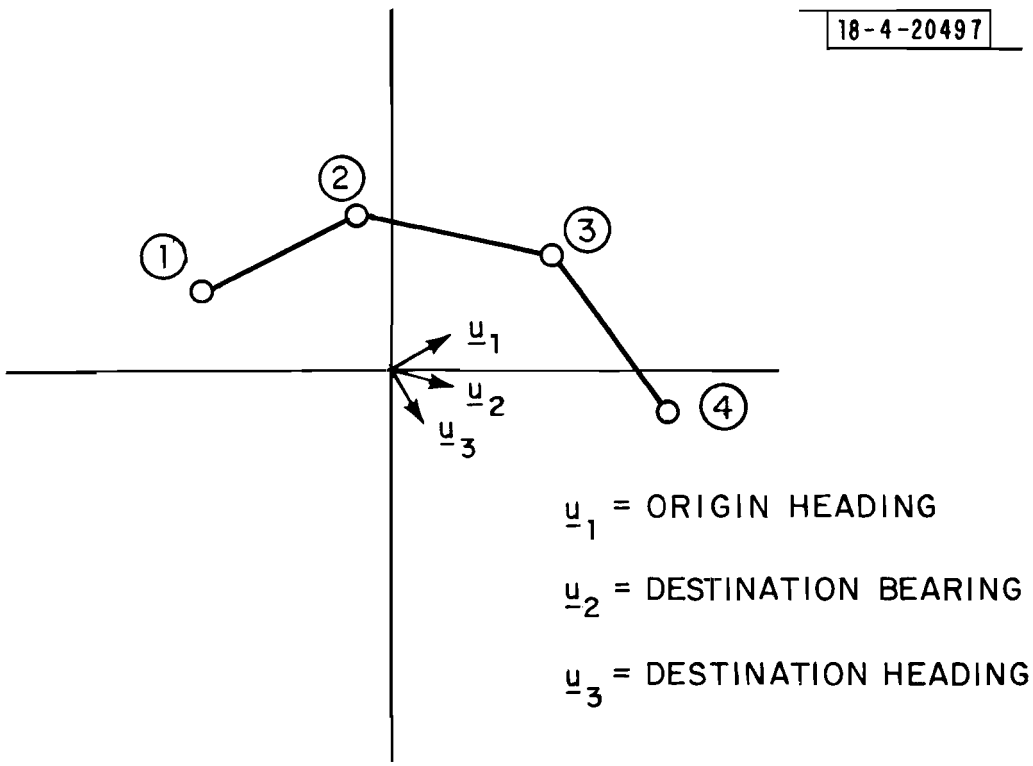

Fig. 5-7. Unit vectors for origin heading, destination bearing, and destination heading.

Certain exceptions are not covered by (84) and are treated individually below. These are:

(i) Parallel or antiparallel leading and trailing segments (because these were given a separate algorithm);

(ii) $\theta = 90°$, i.e., $\underline{U}_1 \cdot \underline{U}_2 = 0$; and

(iii) Destination heading perpendicular to bearing of destination relative to origin, i.e., $\underline{U}_3 \cdot \underline{U}_2 = 0$.

One other situation, which does not strictly lead to a mathematical exception, but nonetheless can produce unsuitable flight paths, is treated. It is:

(iv) Flight paths with small radius of curvature.

(i) Parallel (or antiparallel) Segments

The algorithm treating these cases was derived in Section F.2 (Equal Slopes). In the derivation of the curve fit the final transformed coordinate system was (except for an x, y scale factor) the same one we have been using for the restriction analysis, i.e., the coordinate and flight path origins coincide and the initial heading is along the positive x-axis. It was assumed there that the destination lay in the right-half plane and that acceptable destination headings are along the positive x-axis. In terms of the segment vectors defined earlier, this condition is:

$$\underline{U}_1 \cdot \underline{U}_2 > 0 \text{ and } \underline{U}_3 \cdot \underline{U}_2 > 0 \qquad (5\text{-}85)$$

Consistency with condition (84) would be achieved by adding an algorithm to solve the remaining cases. However, any such algorithm would not interface well with the ones already given, because it can be shown that the curves generated by nearly parallel segments do not have a bounded limit as the segments become parallel. Hence, the program does not accept the equal slope case in which $\underline{U}_1 \cdot \underline{U}_2 < 0$.

(ii) $\theta = 90°$

As indicated in Fig. 5-8a, the $\theta = 90°$ case has the property that the final radius is zero, which makes R = 0 in Eq. (26). That is, the destination and the polar center coincide. The position of the polar center is independent of the destination heading, so a valid slope match should not be expected. Indeed, it can be shown that the curve specified by (28), (29)

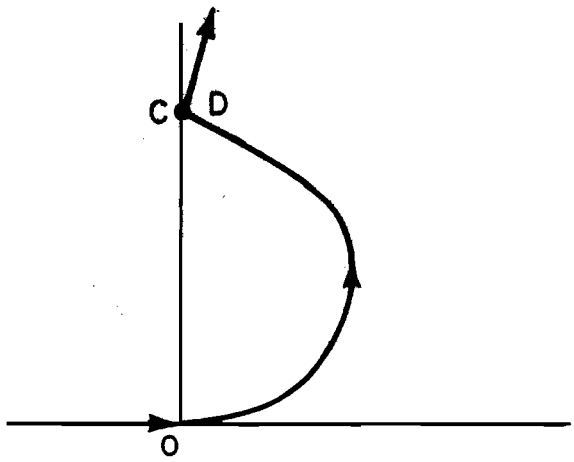

(a)

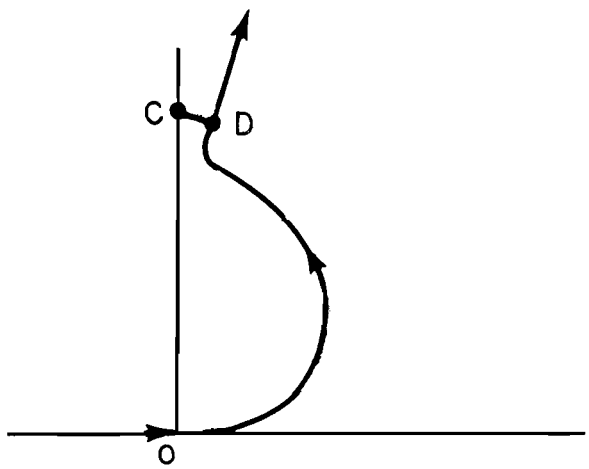

(b)

Fig. 5-8. Case of $\theta = 90°$.

comes into the endpoint perpendicular to the desired heading, if the angle θ_T (which as a polar system parameter is, strictly speaking, undefined) is taken to be the rotation between initial and final headings. In Figure 5-8b we show a case in which R <<1; note that the flight path makes a tight turn near the end in order to satisfy the boundary condition. When R = 0, there is no room for the turn, causing the heading error. Thus the condition:

$$\underline{U}_1 \cdot \underline{U}_2 = 0 \qquad (5\text{-}86)$$

is sufficient for the curve fit to fail.

(iii) Destination Heading Normal to Destination Relative Bearing

This case is converse to the previous one. In this case, the initial point is the center of the polar system, resulting in zero initial radius. This causes R = ∞ in Eq.(26) and the whole procedure is undefined from that point on. Thus the condition

$$\underline{U}_2 \cdot \underline{U}_3 = 0 \qquad (5\text{-}87)$$

must be avoided for the curve fit to work.

(iv) Small Radius of Curvature

In the analysis of the case R = 0, we have seen what happens when R <<1. A tight turn into the correct final heading occurs near the end of the flight path. For the R >> 1 case, the tight turn is at the beginning of the path; otherwise the problem is essentially the same. A good way to decide whether the resulting flight paths are reasonable would be to examine the instantaneous radius of curvature of the path at all points and require that it exceed some minimum. A less general but simpler criterion can be determined by looking at the radius of curvature at the path endpoints.

The standard formula for radius of curvature in rectangular coordinates (in two dimensions) is:

$$\rho(x) = \frac{[1 + \dot{Y}^2(x)]^{3/2}}{\left|\ddot{Y}(x)\right|} \tag{5-88}$$

where $\dot{Y}$, $\ddot{Y}$ are respectively, the first and second derivatives of Y with respect to x. In polar coordinates this transforms into:

$$\rho(\theta) = \frac{[R^2(\theta) + \dot{R}^2(\theta)]^{3/2}}{\left|R^2(\theta) + 2\dot{R}^2(\theta) - R(\theta)\ddot{R}(\theta)\right|} \tag{5-89}$$

where $\dot{R}$, $\ddot{R}$ are respectively the first and second derivatives of $R(\theta)$ with respect to θ. The curvature radius at each point along the curved path can be computed from (88) in the parallel segment case, and from (89) otherwise.

These formulas simplify at the path endpoints, where $\dot{R}$ and $\dot{Y}$ are zero.

$$\rho(x)\Big|_{0,\ x_3''} = \left.\frac{1}{\left|\ddot{Y}(x)\right|}\right|_{0,\ x_3''} \tag{5-90}$$

$$\rho(\theta)\Big|_{0,\ \theta_T} = \left.\frac{R^2(\theta)}{\left|R(\theta) - \ddot{R}(\theta)\right|}\right|_{0,\ \theta_T} \tag{5-91}$$

By differentiating (29) we see that:

$$\ddot{R}(0) = +R_2\,\frac{6(R-1)}{\theta_T^2} \tag{5-92}$$

$$\ddot{R}(\theta_T) = -R_2\,\frac{6(R-1)}{\theta_T^2} \tag{5-93}$$

Thus

$$\rho(\theta = 0) = \frac{R_2^2}{\left| R_2 - \frac{6}{\theta_T^2} (R_3 - R_2) \right|} \tag{5-94}$$

$$\rho(\theta = \theta_T) = \frac{R_3^2}{\left| R_3 + \frac{6}{\theta_T^2} (R_3 - R_2) \right|} \tag{5-95}$$

When $R \equiv R_3/R_2 >> 1$ the radius of curvature at $\theta = 0$ is small and can be approximated by

$$\rho(\theta=0) \approx \frac{\theta_T^2}{6} \frac{R_2^2}{R_3} << 1 \tag{5-96}$$

In opposite extreme ($R<<1$), the trouble occurs at the other endpoint,

$$\rho(\theta = \theta_T) \approx \frac{\theta_T^2}{6} \frac{R_3^2}{R_2} << 1 \tag{5-97}$$

Similar problems are encountered for the paths joining parallel segments. At the endpoints the radius of curvature formula (90) reduces to

$$\rho(x=0) = \rho(x=x_3'') = \frac{x_3''^2}{6 |y_3''|} \tag{5-98}$$

which is small whenever the distance between the segments along their common direction (x_3'') is small relative to the perpendicular distance between them ($|y_3''|$).

Appendix A Airborne Antenna Pattern Characterisitics

Airborne antenna pattern at C band can show substantial differences in gain as a function of bearing angle for different aircraft and/or different locations on a given aircraft. The Havaho aircraft flew in a basically level attitude on the flights reported here; hence it was deemed necessary to only characterize the airborne pattern at the horizon.

Since a simple blade was being used in an unobstructed locaion on the nose, the pattern was expected to be nearly omni directional with a slow variation if any. Thus, it was felt that the pattern need only be characterized over a fairly coarse angle grid.

A straightforward method of measuring the pattern over the desired range is via ground measurements over a flat surface at several angles as illustrated in Fig. A-1. The principal problem which arises with this approach is different ground reflection effects at the various angles. These were minimized by having:

1. the transmitter and receiver well apart so the ground reflection was essentially at the horizon
2. the aircraft antenna positioned over the same point of the ground for each measurement

and

3. choosing the transmitter and receiver heights so as to make measurements at a stationary point (i.e., maxima or a minima) in the signal vs distance plot

Specifically, values used were $h_t = 5$, $h_r = 6$ and $d = 300$ feet.

Data was recorded and analyzed as in the other experiments reported in Chapter III except that the spectrum plots were not normalized to yield 0 dB peak values. Figures A-2 and A-3 show typical unnormalized spectra. Figure

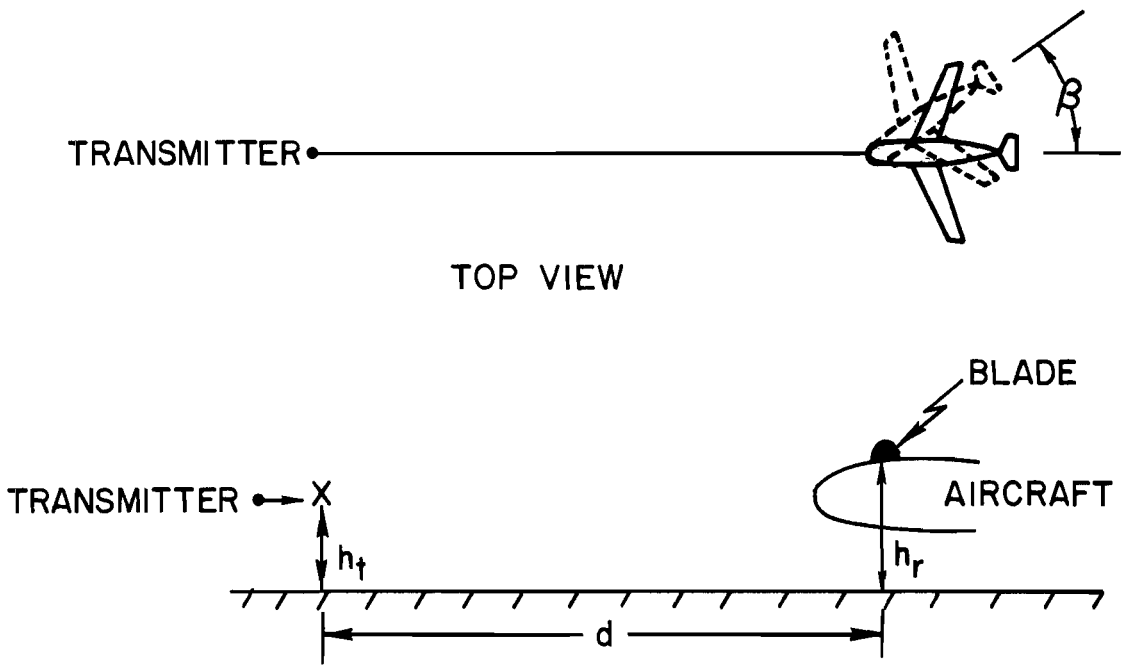

Fig. A-1. Measurements of aircraft antenna pattern by ground measurements.

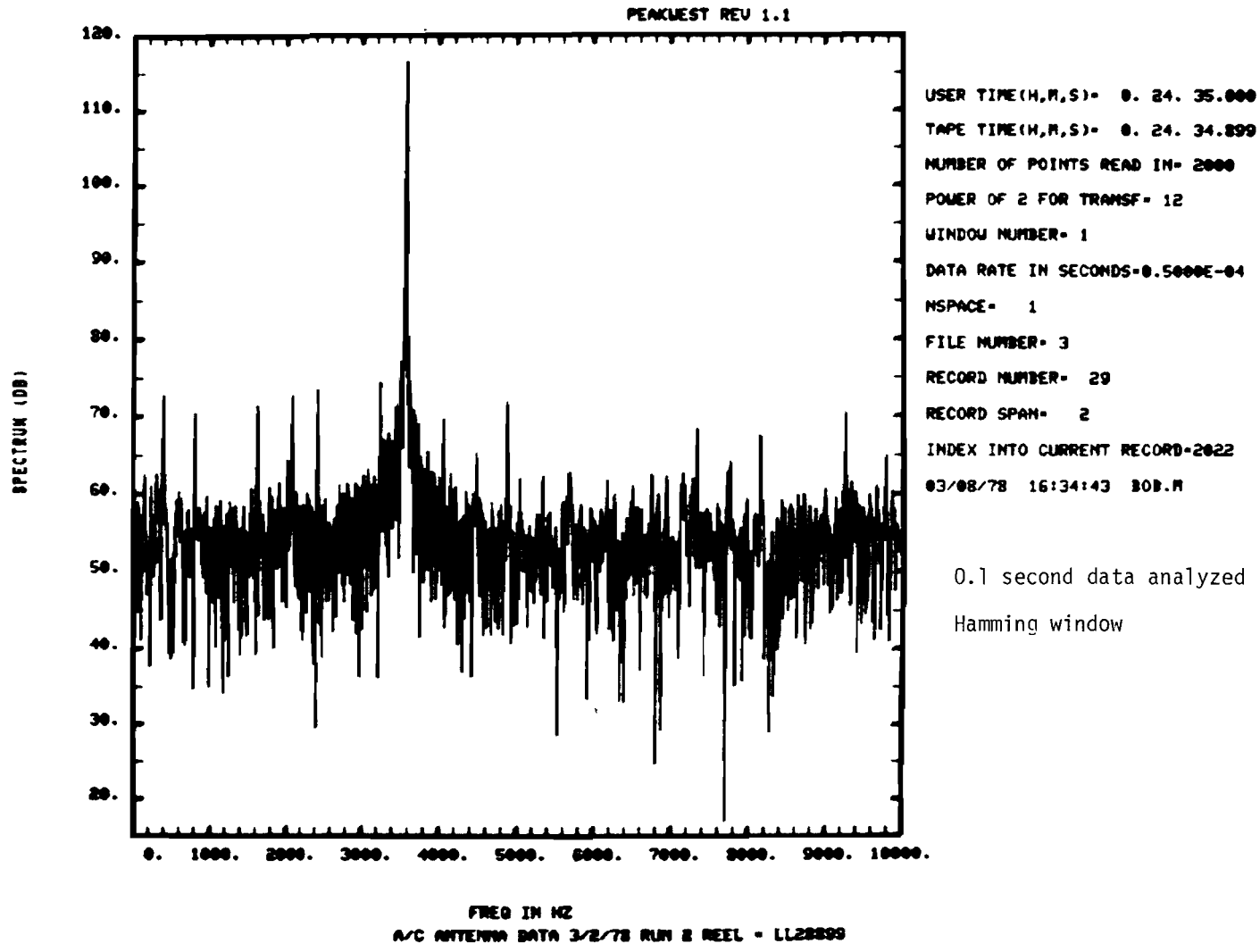

Fig. A-2. Demodulated signal spectrum for aircraft antenna pattern measurement.

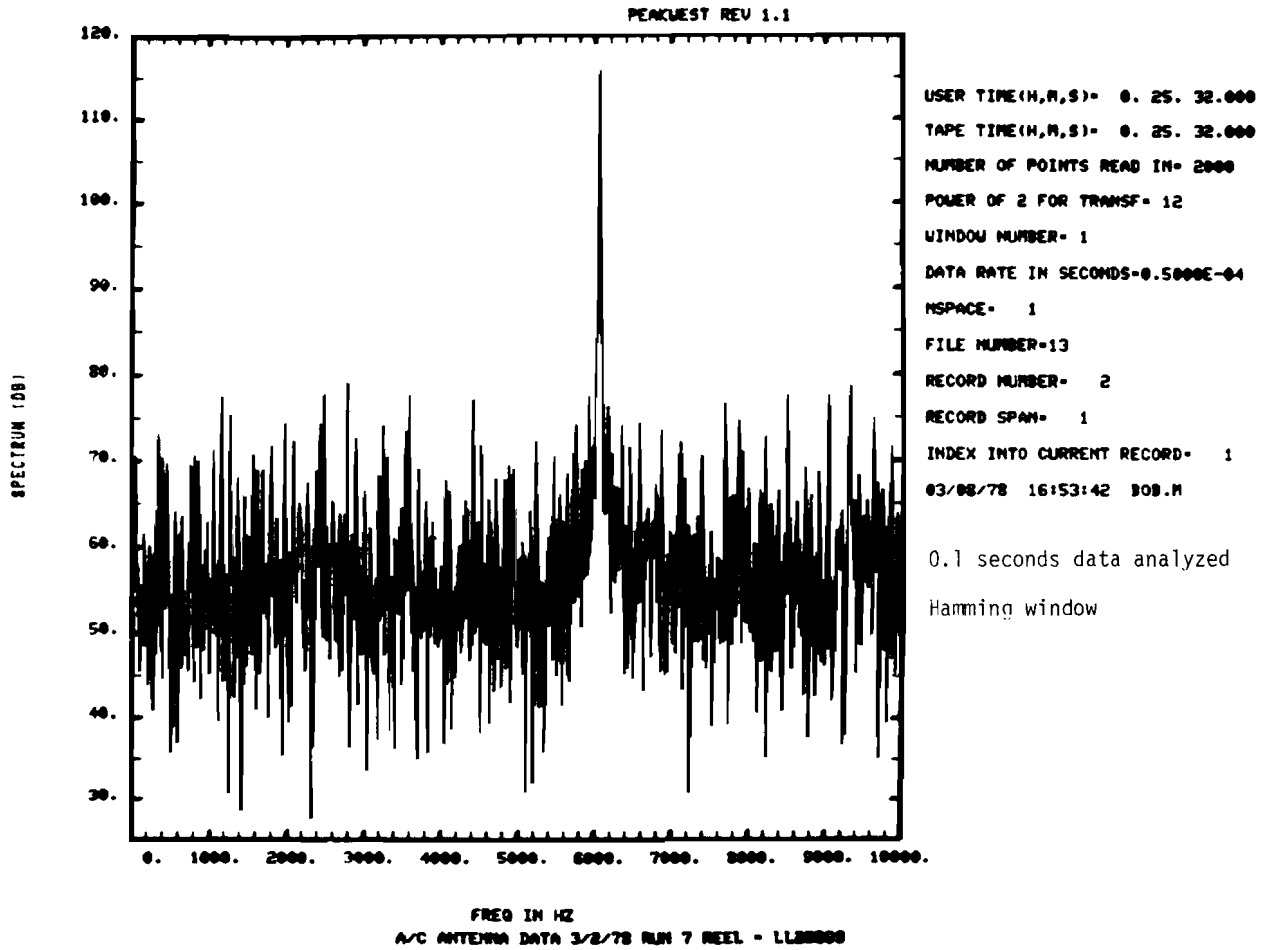

Fig. A-3. Demodulated signal spectrum for aircraft antenna pattern measurement.

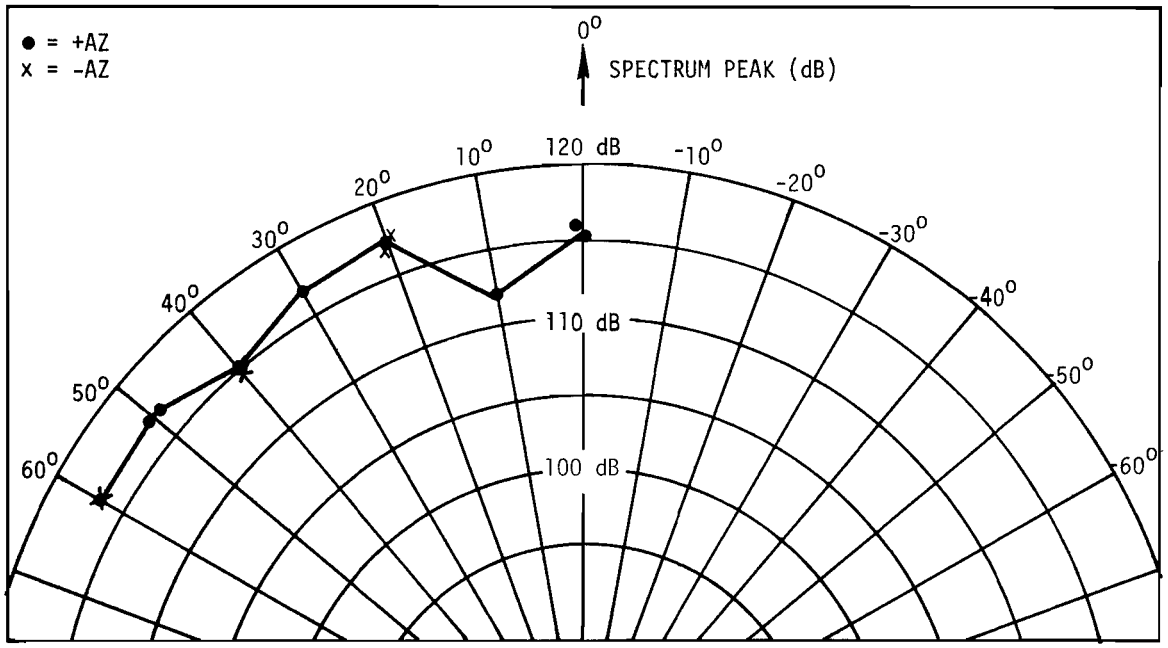

DATA FOR NEGATIVE AZIMUTHS TRANSFERRED TO POSITIVE AZIMUTH ANGLES

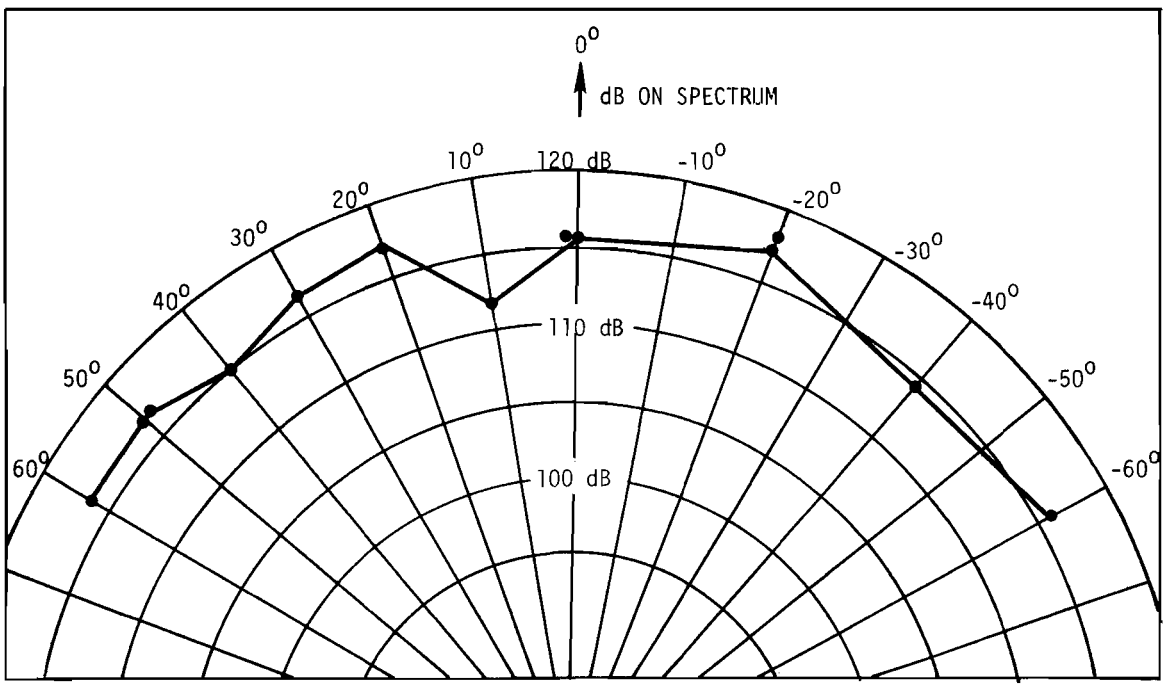

DATA NOT TRANSFERRED

Fig. A-4. Aircraft antenna pattern spectrum peak level vs aircraft rotation angle.

A-4 shows the measured spectrum peaks for the various measurements versus transmitter bearing from the receiver. The values for negative bearings have been transferred to the positive bearing side as the pattern should be symmetrical. The high degree of similarity in the results on either side suggests that the measurement procedure was quite adequate for this task. The pattern is seen to be quite flat out to 60^{o} as would be expected.

Appendix B Brief Description of Shadowing Model Due to Spiridon [30]

This appendix briefly describes a shadowing error model due to Spiridon [30] which may be useful for more accurate error calculations. The basic notion is to numerically sum the received signal from each element (e.g., dipole or column radiator) of the ground antenna with the signal from each element computed assuming Fresnel diffraction. The received signal is then processed in the same manner as the given system to be modeled.

For the TRSB system, this would involve computing the received envelope as*

$$r(t) = |R(t)| = \left|\sum_k a_k v(y_k) \exp\left(-j\, 2\pi \frac{y_k}{\lambda} \sin \theta t\right)\right| \qquad \text{(B-1)}$$

where

a_k = antenna aperture weight distribution

θ = antenna scan rate

$$v(y_k) = v_o(y_k) - v_{sh}(y_k) \qquad \text{(B-2)}$$

$$v_o(y_k) = \exp\left(-j\, 2\pi \frac{y_k}{\lambda} \sin \_\__d\right) \qquad \text{(B-3)}$$

$v_{sh}(y_k)$ = "shadowing signal" of eq. (4-6)

over a suitable time grid $\{t_i\}$. The envelope samples are then processed to yield an angle estimate as was done with the "standard" TRSB model. For DMLS, DLS, or monopulse radar (e.g., DABS), one typically computers (B-1) at a given time for several different $\{a_k\}$ and/or different element locations and then utilizes the usual receiver processing metrics being applied to the R(t).

The expression (B-1) does not explicitly take into account the orthogonal pattern of the antenna (e.g., elevation pattern of the azimuth array). One method of accomplishing this is the ray representation utilized in the MLS simulation model whereby multiplicative factors of the from $\rho\, G(E_i)$ are applied to the various terms of eq. (B-2). Alternatively, one can compute an effective orthogonal factor

$$\Gamma = \sum_m b_m(z_m) \quad v(z_m) \exp\left(-j2\pi \frac{z_m}{\lambda} \quad \sin E_d\right)$$

*for the sake of exposition, we assume here the case of an azimuth antenna.

where $b_m(z_m)$ = aperture illumination of the individual elements (e.g., power radiated from a slot at height z_m on a vertical slotted column.

$v(z_m)$ = $\tilde{\rho}$ of eq. (4-8) for a phase center height of z_m

E_d = direct signal elevation angle.

To the extent that the Fresnel integrals over the horizontal and vertical extents of the array can be factored (see appendix C of [29]), the factor Γ need be computed only once for all y_k.

One minor difficulty which arises with the above approach is determination of the a_k (and/or b_m) for an antenna in which only far field patterns are known, (e.g., reflector implementations). For exacting calculations, one could determine an approximate set by Fourier tranform of the experimental antenna pattern. Alternately, approximation of the field pattern by a known pattern (e.g., Chebyschev) whose coefficients are known should be adequate in most cases.

Appendix C Tutorial Derivation of Plane Wave Expansion Expression

In this appendix, we derive in a tutorial manner the representation of aperture shadowing by a sum of plane waves. The approach taken here draws heavily on the corresponding time series derivation by Papoulis [90]. Our starting point is the expression for the net received signal:

Received signal from a dipole located at position y

Aperture distribution

$$r(\mu) = \int_{-L/2}^{L/2} v(y)\ a(y)\ [\exp(j2\pi \tfrac{y}{\lambda} \mu)]\ dy \qquad \text{(C-1)}$$

The received signal from a given dipole, $v(y)$, could be computed by the previous Fresnel diffraction formula, but need not be. The essential feature is that the aperture distribution $\{a(y)\}$ be zero outside the array ends at $\pm L/2$. Now we form a periodic repetition of $v(y)$:

$$v^*(y) = v(y) \quad \text{for } |y| \leq L/2 \qquad \text{(C-2)}$$

$$v^*(y) = v(y-nL) \text{ for } |y-nL| \leq L/2 \qquad \text{(C-3)}$$

Since $v^*(y)$ is periodic, its Fourier transform $V^*(\mu)$ is a series of equidistant impulses

$$V^*(\mu) = \sum_m \delta(\mu - m\,\mu_o) \left[\int_{-L/2}^{L/2} v(y) \exp(\mp j2\pi \tfrac{y}{\lambda} m\mu_o)\, dy\right] \qquad \text{(C-4)}$$

where $\mu_o = \frac{\lambda}{L}$

By Fourier transform theory, $r(\mu)$ is a convolution:

$$r(\mu) = V^*(\mu) * P(\mu)/\lambda \qquad \text{(C-5)}$$

$$\text{where } P(\mu) = \int_{-L/2}^{L/2} a(y)\, e^{j2\pi \frac{y}{\lambda} \mu}\, dy \qquad \text{(C-6)}$$

But $P(\mu)$ is seen to be the far field pattern of the antenna in sin θ space, i.e.,

$$P(\mu)\Big|_{\mu=\sin\theta} = G(\theta) \qquad \text{(C-6)}$$

Thus, we see that the received signal can be represented as a weighted sum of far field patterns pointed at the angles

$$\theta_m = \sin^{-1}(m\mu_o) \qquad \text{(C-7)}$$

with weights

$$b_m = \int_{-L/2}^{L/2} v(y) \exp\left(\mp j2\pi \frac{y}{\lambda} m\mu_o\right) dy \qquad \text{(C-8)}$$

But this is equivalent to the received signal for a series of plane waves from angles θ_m and complex amplitudes b_m.

REFERENCES

1. RTCA SC-117 Final Report,"A New Guidance System for Approach and Landing," RTCA Document DO-148 (Dec. 1970).

2. "National plan for the Development of the Microwave Landing System," DOT/ NASA/DOD Planning Group (July 1971) AD-733268.

3. R. A. Rondini and R. H. McFarland, "Experimental Validation of Boeing 747 ILS Signal Scattering Calculations for Critical Area Determination," FAA SRDS (Jan. 1974) FAA-RD-74-57.

4. "Report of the Seventh Air Navigation Conference," ICAO Doc. 900 4-AN-CONF/7 (April 1972).

5. "Operational Requirements for an Advanced Approach and Landing Guidance System for the Post-1975 Period Prepared by the NATO Industrial Advisory Group (NIAG)," NATO NIAG document NIAG (71) D/1 (March 1971).

6. "The DME-Based-Landing System, DLS," as proposed by the Federal Republic of Germany developed by Standard Elektrik Lorenz AG. and Siemens, AG. (Sept. 1975).

7. "Doppler Microwave Landing Guidance System," proposal submitted by United Kingdom to the International Civil Aviation Organization (Nov. 1975).

8. "Recommendations for Selection of Scanning Beam Technique Using a Time Reference Signal Format for the U.S. Microwave Landing System - Issue Papers and Backup Documentation," Federal Aviation Administration ARD-700 (Jan. 1975).

9. S. Grashoff (chairman) "Report of the Sixth Meeting of the ICAO All-Weather Operations Panel," ICAO Doc. 9200, AWOP/6, (March 1977).

10. T. Breien, "Computer Analysis of MLS in Multipath Environment," IEE Conf. on the Future of All Weather Operations, (Nov. 1976).

11. H. A. Wheeler, "Multipath Effects in Doppler MLS," contained in Hazeltine Corp. Report "Microwave Landing System (MLS) Development Plan as proposed by Hazeltine Corp. During the Technique Analysis and Contract Definition Phase of the National MLS Development Program," FAA-RD-73-185 (Sept. 1972).

12. "Microwave Landing System (MLS) Development Plan as Proposed by Texas Instruments, Inc., During the Technique Analysis and Contract Definition Phase of the National MLS Development Program," FAA-RD-74-170, (1 Sept. 1972).

13. ITT/Gilfillan, "Microwave Landing System (MLS) Development Plan as Proposed by ITT/Gilfillan During the Technique Analysis and Contract Definition Phase," FAA-RD-74-118 (Sept. 1972).

14. P. Fombonne, "Position Errors in Microwave Landing Systems," Electronics and Civil Aviation Int. Conf., Paris, France (June 1972).

15. J. Benjamin and G. E. J. Peake, "Contributions to the UK Microwave Landing System Study (Phase 1)," Royal Aircraft Establishment, Tech. Memo RAD 1021 (May 1973).

16. "Interscan," proposal submitted by Australia to International Civil Aviation Organization (December 1975).

17. R. Giles "Study and Test Report on MLS Performance in Shadowing Conditions," ICAO AWOP Paper AWOP/6-BIP.45 (March 1977).

18. B. F. Oreb and J. G. Lucas, "A 1/20th Scale Millimetric Model of the Microwave Landing System," IEE Conf: Future of All Weather Operations (Nov. 1976).

19. L. N. Spinner and V. L. Bencivenga, "Advanced Scanning Beam Guidance System for All Weather Landing," FAA Syst. Res. Dev. Serv., Washington, D.C., RD 68-2 (Feb. 1968) AD 664 973.

20. V. L. Bencivenga, "Test and Evaluation of a Portable Scanning Beam Guidance System," (March 1972), FAA-RD-72-16.

21. F. X. Kelly, "Tests of Scanning-Beam Microwave Landing Systems at Difficult Sites," presented at technical seminar "Aviation - A Tool for Economic Development," First International Aerospace Show, Sao Paulo, Brazil (Sept. 1973).

22. Bendix Corp. "Refined Microwave Landing System (MLS) Program Development Plan (Phase III)," (Oct. 1974).

23. Texas Instruments, Inc., "Refined Microwave Landing System (MLS) Development Program Plan," DM74-03-04 (1 Oct. 1974).

24. ITT/Gilfillan, "Five Year MLS Development Program Plan (updated) Microwave Landing System," MLS-0420 (1 Oct. 1974).

25. Hazeltine Corp., "Refined Microwave Landing System (MLS) Development Program Feasibility Demonstration, Phase II," Report 11009 (1 Oct. 1974).

26. D. A. Shnidman, "The Logan MLS Multipath Experiment," Project Report ATC-55, Lincoln Laboratory, M.I.T. (23 Sept. 1975), DDC AD-A017083, FAA-RD-75-130.

27. D. A. Shnidman, "Airport Survey for MLS Multipath Issues," Project Report ATC-58, Lincoln Laboratory, M.I.T. DDC AD-A022937/7 (15 Dec. 1975), FAA-RD-75-195.

28. J. E. Evans, R. Burchsted, J. Capon, R. S. Orr, D. A. Shnidman, and S. M. Sussman, "MLS Multipath Studies, Volume I: Mathematical Models and Validation; Volume II: Application of Multipath Model to Key MLS Performance Issues," Project Report ATC-63, Lincoln Laboratory, M.I.T. (25 Feb. 1976), FAA-RD-76-3, DDC AD-A023040/9 and DDC AD-A025108/2.

29. J. Capon, "Multipath Parameter Computations for the MLS Simulation Computer Program," Project Report ATC-68, Lincoln Laboratory, M.I.T. (8 April 1976), FAA-RD-76-55, DDC AD-A024350/1.

30. A. Spiridon, "Impact of Obstacle Shadows in Monopulse Azimuth Estimate," Project Report ATC-50, Lincoln Laboratory, M.I.T. (17 July 1975), FAA-RD-75-91, DDC AD-A015139/9.

31. F. L. Frisbie, "Studies of Comparative Shadowing Behavior for DMLS and TRSB," ICAO AWOP Paper AWOP/6-BIP/50 (Feb. 1977).

32. P. S. Demko, "Polarization/Multipath Study," U.S. Army Electrom. Command Rep. VL-5-72 (Aug. 1971/June 1972).

33. A. E. Brindly, L. C. Calhoun, and T. N. Patton, (IITRI) "Multipath Environment Evaluation," Air Force Flight Dynamics Laboratory (Nov. 1974). AFFDL-TR-74-150.

34. IIT Research Institute "A Joint Army/Air Force Investigation of Reflection Coefficient at C and Ku Bands for Vertical, Horizontal, and Circular System Polarizations," (July 1976), AFFDL-TR-76-67.

35. A. E. Brindley, L. E. Calhoun, T. N. Patton, and L. Valcik, "Analysis, Test and Evaluation Support to the USAF Advanced Landing System Program," USAF Flight Dynamics Lab. (Aug. 1974), AFFDL-TR-74-62.

36. E. Bramley and S. Cherry, "Investigation of Microwave Scattering by Tall Buildings," Proc. IEEE, (Aug. 1973).

37. J. G. Lucas and B. F. Oreb, "MLS Modeling Work," Report from Air Navigation Group, School of Electrical Engineering, Univ. of Sydney, Australia, to Australian Dept. of Civil Aviation (1976).

38. B. F. Oreb and J. G. Lucas, "Blocking and Diffraction Due to an ICAO Sheet," personal communication to J. Evans (May 1977).

39. J. E. Evans, D. Karp, R. R. LaFrey, R. J. McAulay, and I. G. Stiglitz, "Experimental Validation of PALM - A System for Precise Aircraft Location," Technical Note 1975-29, Lincoln Laboratory, M.I.T. (29 April 1975), DDC AD-A010112/1.

40. J. E. Evans, "Aperture Sampling Techniques for Precision Direction Finding," paper presented at IEEE Electro 78, Boston, Massachusetts (May 1978)

41. J. E. Evans and S. M. Sussman, "Doppler Azimuth Reference Errors with Out-of-Beam Multipath," ICAO AWOP Working Group A Paper TH.BIP.3 (30 June 1976).

42. T. E. Bernard, "Analytical Studies of Techniques for the Computation of High-Resolution Wavenumber Spectra," Special Report No. 9, Texas Instruments Incorporated, Dallas, Texas (14 May 1969), Project No. VELAT/77701.

43. J. Capon, "High-Resolution Frequency-Wave Number Spectrum Analysis," Proc. of IEEE, 57, 1408 (1969).

44. N. O. Anderson, "On the Calculation of Filter Coefficients for Maximum Entropy Spectral Analysis," Geophysics, 39, 69 (1974).

45. J. P. Burg, "Maximum Entropy Spectral Analysis," Paper presented at the 37th meeting of the Society of Exploration Geophysicists, Oklahoma City, Oklahoma (31 October 1967).

46. R. T. Lacoss, "Data Adaptive Spectral Analysis Methods," Geophysics, 56, 661 (1971).

47. R. N. McDonough, "Maximum-Entropy Spatial Processing of Array Data," Geophysics, 39, 843 (Dec. 1974).

48. H. R. Radoski, P. F. Fouger, E. J. Zanalick, "A Comparison of Power Spectral Estimates and Applications of the Maximum Entropy Method," J. Geophy. Res., 80, No. 4, 619 (Feb. 1975)

49. T. E. Bernard, "The Maximum Entropy Spectrum and the Burg Technique," Advanced Signal Processing Technical Report No. 1, Texas Instruments Incorporated, Dallas, Texas (25 June 1975), ALEX(03)-TR-75-01.

50. J. Makhoul, "Linear Prediction; A Tutorial Review," Proc. IEEE, 63, 561 (1975).

51. T. P. McGarty, "Models of Multipath Propagation Effects in a Ground-to-Air Surveillance System," Technical Note 1974-7, Lincoln Laboratory, M.I.T. (25 February 1974), DDC AD-777241/1.

52. A. Spiridon, "Effects of Local Terrain and Obstacles Upon Near Horizon Gain of L-Band Beacon Antennas," Technical Note 1975-6, Lincoln Laboratory, M.I.T. (17 July 1975), DDC AD-A013732/3.

53. H. Berger and J. E. Evans, "Diversity Techniques for Airborne Communications in the Presence of Ground Reflection Multipath," Technical Note 1972-27, Lincoln Laboratory, M.I.T. (8 September 1972), DDC AD-752249.

54. F. Harris, "On the Use of Windows for Harmonic Analysis with the Discrete Fourier Transform," Proc. IEEE, 66, 51 (1978).

55. A. Oppenheim and R. Schafer, Digital Signal Processing, (Prentice Hall, 1975).

56. A. Brindley, L. Calhoun, T. Patton, and L. Valcik, "Analysis, Test and Evaluation Support to the USAF Advanced Landing System Program Vol. III Part 1 Doppler MLS Guidance Error Data (DOTS Tracking System)," AFFDL-TR-74-62, Vol. III, Part 1 (August 1974).

57. P. Demko,"Propagation Integrity for Microwave Landing Systems," In AGARD Conference Proceedings No. 240 Guidance and Control Design Considerations for Low-Altitude and Terminal-Area Flight (October 1977).

58. "Flight Trials of TRSB/Interscan Equipment at Sydney International Airport, Australia," Paper AWO/78-WP/88 presented by Australia at ICAO AWO Division Meeting, (April 1978).

59. "Tracked Flight Trials of Doppler MLS at Manchester Airport," Paper AWO/78-WP/123 presented by United Kingdom at ICAO AWO division meeting (April 1978).

60. "Tracked Flight Trials of Doppler MLS Azimuth System at Brussels National Airport," Paper AWO/78-WP/12 presented by the United Kingdom at ICAO AWO Division Meeting (Janauary 1977).

61. "Test Results for a Time Reference Scanning Beam (TRSB) 'Basic Narrow' MLS," Paper AWO/78-WO/119, presented by United States at ICAO AWO Division Meeting (April 1978).

62. "DMLS/TRSB Comparative Demonstration Test Results at Brussels National Airport, Brussels, Belgium," Paper AWO/78-WO/141, presented by United States at ICAO AWO Division Meeting (April 1978).

63. DMLS/TRSB Comparative Demonstration Test Results," Paper AWO/78-WP/153 presented by United States at ICAO AWO Division Meeting (April 1978).

64. J. E. Evans and D. A. Shnidman, "Multipath Characteristics of AWOP WG-A Multipath Scenarios," AWOP WG-A Paper TH.BIP/9 also Revision 1 (4 January 1977).

65. "Time Reference Scanning Beam Microwave Landing System," proposal submitted by the United States to the International Civil Aviation Organization (December 1975).

66. R. Butler (Rappoteur), "Report of the Multipath Subgroup of WG-A Held near Boston, Mass., 11-15 October 1976)," L.WP/3 in the report of ICAO AWOP Working Group A, Seventh Meeting, London (Nov. 1-12, 1976).

67. M. Whitney, "UK Presentations and Demonstrations of Doppler MLS in Multipath Environments," given at Royal Aircraft Establishment, Bedford, (1 Nov. 1976), CAA Paper 77003 (Feb. 1977).

68. M. Whitney, "DMLS Signal Processing," L.BIP/38 in Report of the Seventh Meeting of ICAO AWOP Working Group A, held in London, U.K. (2-12 Nov. 1976).

69. F. Frisbie, "TRSB Phase III Receiver Functional Description," Paper L.BIP/19 in the report of ICAO AWOP Working Group A, Seventh Meeting, London (Nov. 1976).

70. T. Bohr, "The Proposed DLS Airborne Equipment and DLS System Configuration," L.BIP/42 and L.BIP/43 in Report of ICAO AWOP Working Group A, Seventh Meeting, London (1-12 Nov. 1976).

71. J. Beneke, C. Wightman et. al., "Multipath and Performance Tests of TRSB Receivers," FAA-RD-77-66 (March 1977).

72. ICAO All Weather Operations Panel Working Group A, "Report of the Third Meeting Held in Melbourne During the Period 24-28 February 1975" (Feb. 1975).

73. "Validation of Computer Simulation by Comparison with Tests at Operational Airports," Paper AWO/78-WP/135 presented by the United States at ICOA AWO Division meeting (April 1978).

74. "Application and Validation of Computer Simulation to MLS Multipath Performance Assessment," Paper AWO/78-WP/138 presented by the United States at ICAO AWO Division meeting (Jan. 1978).

75. "Performance of Advanced Approach and Landing Systems (AALS)," Electronics Research Laboratory, Univ. of Trondheim, Norwegian Inst. of Tech. (March 1973).

76. "Study of the Radar Reflectivity Characteristics at SSR Frequency of Pilkington 'Insulight' Metallized Glass," Cosser Electronics Limited Report EF/S/055 (Sept. 1973).

77. A. Von Hippel, Dielectric Materials and Applications, (Chapman & Hall, Ltd., London 1954).

78. G. Bailey, Personal Communication (Feb. 1977).

79. F. L. Frisbie, "Comparison of DMLS and TRSB Acquisition/Validation in an Azimuth Multipath Environment," ICAO All Weather Operations Panel Working Paper AWOP-WP/322 (March 1977).

80. B. L. Oreb, "Modeling of the Microwave Landing System (MLS) at 104 GHz," PhD Thesis, Univ. of Sydney, Australia (1978).

81. G. T. Ruck, D. E. Barrick, W. D. Stuart and C. Krichbaum, Radar Cross Section Handbook, Volume 1 (Plenum, New York, 1970).

82. H. Neugebauer and M. Bachynski, "Diffraction by Smooth Cylindrical Mountains," Proc. of IRE, 41, 1619 (Sept. 1958).

83. I. M. Hunter, "Some Properties of Air-Derived and Ground-Derived Aircraft Landing Guidance Concepts," J. of British Institute of Navigation (1973).

84. K. D. Eckert, "DME Based System for Enroute/Terminal Navigation, All Weather Landing and Air Traffic Control," in AGARD Conference Proc., No. 240 Guidance and Control Design Considerations for Low-Altitude and Terminal Area Flight (Oct. 1977).

85. L. Armijo, K. Daniel, and W. Labuda, "Application of the FFT to Antenna Array Beamforming," EASCON '74 Conference Proceedings, Washington, D.C. (1974).

86. K. Kohler, "Synthetic Radio Direction Finding with Virtual Antenna Patterns," Electric Comm., 48, 299 (1973).

87. W. B. Kendall, "Unambiguous Accuracy of an Interferometric Angle-Measuring System," IEEE Trans. Space Electronics and Telemetry, 11, 67, (June 1965).

88. J. Duncan,"The Effect of Ground Reflections on an Interferometric Direction Finder," IEEE Trans. Aerospace Electron. Systems, AES-3, 927 (1967).

89. D. K. Barton, "Multipath Error in a Vertical Interferometer," Proc. of IEEE, 53, 543 (1965).

90. A. Papoulis, The Fourier Integral and Its Applications, (McGraw-Hill, New York, 1962).

91. M. F. Whitney, "Simulation of Phased Array Antenna Systems," Working Paper TH.WP-3 presented at the Hague Meeting of AWOP WG-A (July 1976).

92. J. Beneke et. al., "TRSB Multimode Digital Processor," Final Report, Calspan Corporation, Report No. FAA-RD-77 (April 1978).

93. Bendix Corp., "Microwave Landing System, Phase III (Basic Narrow and Small Community Configurations) Final Report, Volume 1," Report No. MLS-BCD-R-2801-1 (June 1978).

94. "Report of the All Weather Operations Division Meeting, 1978," International Civil Aviation Organization, Doc. 9242, AWO/78 (April 1978).

95. F. Frisbie, "Out of Coverage Indication (OCI) and Left/Right Guidance," ICAO AWOP Working Group A Background Information Paper L.BIP/20 (Nov. 1976).

96. Hazeltine Corp., "Cost Minimized Phased Array Circuit Technique (COMPACT)," (1976).

97. J. Sebring and J. Ruth, "MLS Scanning-Beam Antenna Implementation," Microwave J., 41 (Jan. 1974)

98. F. Pogust, "Microwave Landing Systems," IEEE Spectrum, 15, 30 (1978).

99. R. Kelly, H. Redlein and J. Shagena, "Landing Aircraft Under Poor Conditions," IEEE Spectrum, 15, 52 (1978).

100. A. Lopez, "Scanning-Beam Microwave Landing System - Multipath Errors and Antenna Design Philosophy," IEEE Trans on Ant. and Prop., AP-3, 290 (May 1977).

101. J. Kuznetsov,"Some Questions Concerning Reduction of Multipath Effect on Microwave Landing System Accuracy," ICAO AWOP 6 Paper WP/305 (1977).

102. F. L. Frisbie, "(Latest) Comparison of DMLS Computer Model with January 1977 DMLS Hybrid Simulator Azimuth Multipath Data," ICAO AWOP 6 Paper BIP/62 (1977).

103. H. L. Van Trees, Detection, Estimation and Modulation Theory Part I (John Wiley & Sons, New York, 1968).

104. M. Skolnik, Introduction to Radar Systems, (McGraw-Hill Book Company, New York, 1962).

105. D. K. Barton and H. R. Ward, Handbook of Radar Measurement (Prentice-Hall, New Jersey, 1969).

106. L. Jolley, Summation of Series (Dover, New York, 1961).

107. R. J. McAulay, "The Effects of Interference on Monopulse Performance," Technical Note 1973-30, Lincoln Laboratory, M.I.T. (1 August 1973), DDC AD-769336/9.